frontiers | Research Topics

Environmental remediation strategies of new and emerging chemical contaminants

Edited by
Vishal Tripathi, Sheikh Adil Edrisi, Becky Nancy Aloo,
Leonardo Fernandes Fraceto, Vaibhav Srivastava and Gaurav Pant

Published in
Frontiers in Microbiology
Frontiers in Environmental Science
Frontiers in Environmental Chemistry

ISSN 1664-8714
ISBN 978-2-8325-5583-5
DOI 10.3389/978-2-8325-5583-5

About Frontiers

Frontiers is more than just an open access publisher of scholarly articles: it is a pioneering approach to the world of academia, radically improving the way scholarly research is managed. The grand vision of Frontiers is a world where all people have an equal opportunity to seek, share and generate knowledge. Frontiers provides immediate and permanent online open access to all its publications, but this alone is not enough to realize our grand goals.

Frontiers journal series

The Frontiers journal series is a multi-tier and interdisciplinary set of open-access, online journals, promising a paradigm shift from the current review, selection and dissemination processes in academic publishing. All Frontiers journals are driven by researchers for researchers; therefore, they constitute a service to the scholarly community. At the same time, the *Frontiers journal series* operates on a revolutionary invention, the tiered publishing system, initially addressing specific communities of scholars, and gradually climbing up to broader public understanding, thus serving the interests of the lay society, too.

Dedication to quality

Each Frontiers article is a landmark of the highest quality, thanks to genuinely collaborative interactions between authors and review editors, who include some of the world's best academicians. Research must be certified by peers before entering a stream of knowledge that may eventually reach the public - and shape society; therefore, Frontiers only applies the most rigorous and unbiased reviews. Frontiers revolutionizes research publishing by freely delivering the most outstanding research, evaluated with no bias from both the academic and social point of view. By applying the most advanced information technologies, Frontiers is catapulting scholarly publishing into a new generation.

What are Frontiers Research Topics?

Frontiers Research Topics are very popular trademarks of the *Frontiers journals series*: they are collections of at least ten articles, all centered on a particular subject. With their unique mix of varied contributions from Original Research to Review Articles, Frontiers Research Topics unify the most influential researchers, the latest key findings and historical advances in a hot research area.

Find out more on how to host your own Frontiers Research Topic or contribute to one as an author by contacting the Frontiers editorial office: frontiersin.org/about/contact

Environmental remediation strategies of new and emerging chemical contaminants

Topic editors

Vishal Tripathi — Graphic Era University, India
Sheikh Adil Edrisi — Thapar Institute of Engineering & Technology, India
Becky Nancy Aloo — University of Eldoret, Kenya
Leonardo Fernandes Fraceto — São Paulo State University, Brazil
Vaibhav Srivastava — University of Allahabad, India
Gaurav Pant — Graphic Era University, India

Citation

Tripathi, V., Edrisi, S. A., Aloo, B. N., Fraceto, L. F., Srivastava, V., Pant, G., eds. (2024). *Environmental remediation strategies of new and emerging chemical contaminants*. Lausanne: Frontiers Media SA. doi: 10.3389/978-2-8325-5583-5

Table of contents

frontiers | Frontiers in Environmental Chemistry

TYPE Editorial
PUBLISHED 09 October 2024
DOI 10.3389/fenvc.2024.1500489

OPEN ACCESS

EDITED AND REVIEWED BY
Andrew Sweetman,
Lancaster University, United Kingdom

*CORRESPONDENCE
Vishal Tripathi,
vishalbiotechbhu@gmail.com

RECEIVED 23 September 2024
ACCEPTED 27 September 2024
PUBLISHED 09 October 2024

CITATION
Tripathi V, Edrisi SA, Aloo BN, Fraceto LF, Srivastava V and Pant G (2024) Editorial: Environmental remediation strategies of new and emerging chemical contaminants. *Front. Environ. Chem.* 5:1500489. doi: 10.3389/fenvc.2024.1500489

Editorial: Environmental remediation strategies of new and emerging chemical contaminants

Vishal Tripathi[1]*, Sheikh Adil Edrisi[2], Becky Nancy Aloo[3], Leonardo Fernandes Fraceto[4], Vaibhav Srivastava[5] and Gaurav Pant[6]

[1]Department of Biotechnology, Graphic Era (Deemed to be University), Dehradun, Uttarakhand, India, [2]Thapar School of Liberal Arts and Sciences, Thapar Institute of Engineering and Technology, Patiala, Punjab, India, [3]Department of Biological Sciences, University of Eldoret, Eldoret, Kenya, [4]Institute of Science and Technology, São Paulo State University, Sorocaba, Brazil, [5]Department of Botany, Faculty of Science, University of Allahabad, Pryagraj, India, [6]Department of Microbiology, Graphic Era (Deemed to be University), Dehradun, Uttarakhand, India

KEYWORDS

new and emerging pollutants, environmental pollution, bioremediation, phytoremediation, ecological risk

Editorial on the Research Topic
Environmental remediation strategies of new and emerging chemical contaminants

The industrial development of the 21st century has led to anthropogenic impacts on Earth. Through the rapid growth of pharmaceuticals, electronics, agrochemicals, and biotech industries which have transformed healthcare, enhanced agriculture, and improved technological innovations, these developments have also led to unprecedented pollution. One of the most severe challenges has been the emergence and proliferation of new and emerging pollutants (NEPs), including antibiotics, antidepressants, microplastics, microbeads, specialty chemicals, etc. These xenobiotic compounds can persist in the environment and exhibit complex behaviors with long-term ecological and health impacts. As the global community increasingly recognizes the hazards associated with NEPs, the need for advanced, sustainable remediation strategies has never been more urgent. This Research Topic, Environmental Remediation Strategies for New and Emerging Chemical Contaminants, aims to address the critical challenges posed by NEPs through innovative research and reviews. It seeks to provide new perspectives on the environmental and health risks associated with NEPs while highlighting novel, sustainable solutions for their remediation. The issue combines the recent advancements in sustainable technologies to tackle these challenges.

Among the NEPs, microplastics have become a serious pollutant affecting terrestrial and aquatic ecosystems. The study Nakei et al. provides a promising solution for tackling plastic pollution in terrestrial and aquatic environments. The study reveals that bioprospecting of agricultural soils, water bodies, and landfills containing plastic wastes can provide highly efficient microbial species for breaking down polyethylene polymers. The ever-increasing use of agrochemicals has led to widespread environmental pollution, demanding urgent measures for restoration and remediation. The paper, Hu et al. examines the enhanced biodegradation capabilities of the microorganisms for more efficient

breakdown of complex agrochemical NEPs as a promising approach for managing the agrochemical pollution. Further, the review Zhou et al. explores the toxicity and bioremediation options for the treatment of carbendazim contaminated residues in agroecosystems. Apart from agrochemicals, another insightful study, Li et al., is particularly helpful in dealing with soil pollution with explosive munition 2,4,6-trinitrotoluene (TNT) and its metabolites.

In recent times, the nano-revolution has also caused the release of nanoparticles (NPs) as an emerging contaminant into the environment, with its remediation remaining an important environmental issue and a global challenge. Carbon nanotubes (CNTs) are a group of NPs that severely impact human health and ecosystems due to their widespread use. In this regard, a study, Takahashi et al., explores applying green chemistry principles to synthesize environmentally friendly catalysts for the degradation of persistent organic pollutants like CNTs. Further, long-term stability and continuity of the CNTs degradation is explored in another study, Takahashi and Hori which provides another innovative approach for bioremediation of NEPs like CNTs. Taking the microbial degradation further, the study, Deng et al. provides three novel species of *Mycobacterium* isolated from polluted soil samples, characterized and evaluated for biodegradation of polycyclic aromatic hydrocarbons (PAHs), which are considered as priority pollutants. Apart from microbial remediation, the issue also explores physicochemical and organic amendments-based solutions for tackling the challenge of NEP remediation (Zha et al.; Zouari et al.).

Researchers have developed a combined waste water treatment approach addressing the challenge of NEP contamination in wastewater Kokilaramani et al. This study reports that photoelectrochemical oxidation offers an excellent solution for wastewater treatment, inhibiting the growth of harmful microbes responsible for biocorrosion and degrading the pollutants in the wastewater stream. Teymoorian et al.

While remediation technologies are of immense importance, understanding the ecological risks posed by NEPs is equally essential. The review, Ferreira et al., provides important insight into how the application of these drugs has increased in time, particularly during the Covid pandemic, and has led to worldwide pollution of biologically active micropollutants. The article emphasizes the microbial degradation of such pharmaceutical compounds through pure isolates and microbial consortia via *in vitro*, *in situ*, and *ex-situ* processes.

With the ever-growing challenge of NEP pollution, the 12 articles published in this Research Topic provide a comprehensive view of challenges, toxicity, and recent advancements in the remediation of NEPs. The present issue addresses the challenges regarding the sources and impacts of NEPs and their remediation. The contributions in this issue pave the way for sustainable pollution control strategies, ensuring cleaner ecosystems and healthier communities. This issue highlights the urgent need for continued innovation and multidisciplinary collaboration to provide effective solutions for the mitigation of NEPs. The Research Topic will be valuable for researchers, policymakers, industry persons, and environmental engineers. This issue's contribution will provide the foundation for future research offering solutions for a clean, green, and safer environment through the mitigation of NEPs.

Author contributions

VT: Conceptualization, Writing–original draft, Writing–review and editing. SE: Writing–review and editing. BA: Writing–review and editing. LF: Writing–original draft, Writing–review and editing. VS: Writing–original draft, Writing–review and editing. GP: Writing–review and editing.

Funding

The author(s) declare that no financial support was received for the research, authorship, and/or publication of this article.

Conflict of interest

The authors declare that the research was conducted in the absence of any commercial or financial relationships that could be construed as a potential conflict of interest.

The author(s) declared that they were an editorial board member of Frontiers, at the time of submission. This had no impact on the peer review process and the final decision.

Publisher's note

frontiers | Frontiers in Microbiology

TYPE Original Research
PUBLISHED 19 December 2022
DOI 10.3389/fmicb.2022.1077588

OPEN ACCESS

EDITED BY
Becky Nancy Aloo,
University of Eldoret, Kenya

REVIEWED BY
Surendra Sarsaiya,
Zunyi Medical University, China
Sameh Samir Ali,
Jiangsu University, China

*CORRESPONDENCE
Monica D. Nakei
mnakei@sua.ac.tz

SPECIALTY SECTION
This article was submitted to Microbiotechnology, a section of the journal Frontiers in Microbiology

RECEIVED 23 October 2022
ACCEPTED 17 November 2022
PUBLISHED 19 December 2022

CITATION
Nakei MD, Misinzo G, Tindwa H and Semu E (2022) Degradation of polyethylene plastic bags and bottles using microorganisms isolated from soils of Morogoro, Tanzania.
Front. Microbiol. 13:1077588.
doi: 10.3389/fmicb.2022.1077588

Degradation of polyethylene plastic bags and bottles using microorganisms isolated from soils of Morogoro, Tanzania

Monica D. Nakei[1]*, Gerald Misinzo[2], Hamisi Tindwa[1] and Ernest Semu[1]

[1]Department of Soil Science, Sokoine University of Agriculture, Morogoro, Tanzania, [2]Department of Veterinary Microbiology, Parasitology and Biotechnology, College of Veterinary Medicine and Biomedical Sciences, Sokoine University of Agriculture, Morogoro, Tanzania

Plastics are of great significance in today's world due to their extensive use such as packaging food and carrying other goods, which have improved the quality of human life. However, plastics have low biodegradability and are persistent in the environment, becoming a major source of pollution. With regard to the current methods used in the management of plastic wastes, the degradation of plastics using beneficial soil microorganisms has recently gained attention due to their ability to degrade different types of plastics including polyethylene (PE) polymers. The study herein was conducted to isolate and identify microorganisms from agricultural soils capable of degrading plastics. Soil samples were inoculated into nutrient, potato dextrose, and starch-casein agar for the isolation of bacteria, fungi, and actinomycetes, respectively. During isolation, fungi and bacterial plates were incubated for 5 days and for 14 days, respectively. The population of bacteria ranged from 1×10^5 to $1.21^5 \times 10^5$ and that of fungi from $1.60^4 \times 10^4$ to 8.6×10^4 whereby actinomycetes ranged from $1.04^5 \times 10^5$ to $2.99^5 \times 10^5$ CFU/g of soil. However, the tested microorganisms showed significant ($p \leq 0.05$) differences in the ability to degrade PE bags and bottles as depicted by the diameters of clear zones around the colonies. The diameters of clear zones ranged from 19.3 to 47.5 mm and 25.9 to 32.2 mm after 17 days for bacteria and actinomycetes, respectively, and those of fungi ranged from 30.0 to 66.3 mm after 13 days. Among the bacteria, actinomycetes, and fungi, unsequenced bacterial and actinomycete isolates B1 and A3 as well as *Aspergillus* sp. (F7) were the most efficient degraders of PE plastic bags. This retrospective study sheds light on our understanding and the need for the bioprospecting of agricultural soils, water bodies, and landfills containing plastic wastes that could lead to the identification of more efficient microbial species with the ability to degrade plastics.

KEYWORDS

actinomycetes, bacteria, fungi, biodegradation of plastics, polyethylene

1 Introduction

Plastics are of great significance in today's world due to their widespread use, which has enabled improvement in the quality of human life through the ease of packaging of foods and other items, thus lengthening their shelf life (Ilyas et al., 2018). Due to its demand, the global yield of plastics reached 368 million tons per annum in 2019, and this figure is expected to double over the next 20 years (Geyer et al., 2017; Plastic Europe, 2018). China and the European Union account for 29.4 and 18.5% of all the plastics used in the world, respectively (Plastic Europe, 2018; Ru et al., 2020). The mainly manufactured and widely used plastic types are polyethylene (PE) (36%), polypropylene (PP) (21%), and polyvinyl chloride (PVC) (12%), polyethylene-terephthalate (PET) 10%, polyurethane (PU) 10%, and polystyrene (PS) 10%, and others (Geyer et al., 2017). However, all these plastics are high molecular weight polymers whose biodegradability is low (Burke et al., 2012). Hence, plastics are persistent once introduced, after use, into the environment and are one of the sources of environmental pollution (Ostle et al., 2019). Their single-use and disposal both on land and in aquatic environments have resulted in their accumulation due to less, if any, biodegradation, making the environment unaesthetic, with possible health implications to humans, animals, and other organisms (Zalasiewicz et al., 2016; Bergmann et al., 2019; Jamieson et al., 2019; Ali et al., 2021a). Moreover, plastic polymers and additives that are frequently blended into commercial-grade plastics have also been shown to accumulate in marine species harvested for human consumption (Markic et al., 2018; Webb et al., 2019). In addition, it has been projected that up to 26 billion tons of plastic waste are likely to be produced by 2050 (Ru et al., 2020) and more than half to be thrown away into landfills that finally enter ecosystems such as oceans and lakes which will, perhaps, worsen the situation.

Currently, several methods including landfilling, incineration, and mechanical and chemical recycling have been used to dispose plastic waste (Ru et al., 2020). It is reported that between 9 and 12% of global waste is recycled and incinerated while 79% is discarded into landfills or the natural environment (Geyer et al., 2017). Landfilling is the preferred method of disposing plastic wastes in developing countries due to its low cost. However, the accumulated plastic wastes in landfills continue to occupy vast land that could be put to other uses. Incineration of plastic wastes can reduce the demand for landfills and recover heat energy, but this process generates secondary pollutants such as dioxins, carbon monoxide, and nitrogen oxides into the environment (Lear et al., 2021). Although mechanical recycling has been applied for reusing thermoplastic wastes, the properties of most recycled materials are compromised and the commercial value of resulting products is limited (Ru et al., 2020). As an alternative, chemical recycling has the potential to recover monomers and other chemicals from plastic wastes, but its success relies on the affordability of processes and the efficiency of catalysts (Rahimi and Garciá, 2017). These studies demonstrate that there is a need to explore an innovative recycling method to dispose plastic wastes.

Microorganisms from different ecosystems including agricultural soils, aquatic environments, and landfills have been observed to degrade different types of synthetic plastics (Ali et al., 2021b). Some of the identified microorganisms include bacteria such as *Bacillus, Pseudomonas*, *Azotobacter*, *Ralstonia*, and *Halomonas* spp. (Biki et al., 2021). *Pseudomonas* spp. can degrade low-density polythene (LDP), PP, PE, and nylon (Nanda et al., 2010; Pramila, 2012; Gupta and Devi, 2020; Skariyachan et al., 2021). Various species of *Streptomyces* have also been associated with the degradation of low-density polyethylene (LDPE) with varying degrees (Gupta and Devi, 2020). Examples of fungal degraders of PE, LDPE, and high-density polyethylene (HDPE) include *Aureobasidium*, *Rhodotorula, Kluyveromyces*, and *Aspergillus* (Muhonja et al., 2018; Aderiye et al., 2019). These studies provide evidence that several microorganisms are capable of degrading synthetic plastics. Although several studies on the biodegradation of plastic have been carried out, many have focused on the biodegradation of a single kind of plastic and there is a need to identify those with the potential to degrade different kinds of plastics.

The degradation of synthetic plastics by soil microorganisms is gaining the attention of different researchers (Ali et al., 2021a). Beneficial and non-pathogenic soil microorganisms that degrade organic matter in the soil are potential degraders of different types of synthetic plastic wastes, which enter agricultural soils. To achieve this it needs a careful isolation and identification of effective species from different groups of fungi, bacteria, and actinomycetes from different soil types including those with low carbon content. The present study focused on the determination of the potential of bacteria, actinomycetes, and fungi isolated from the soils of Morogoro, Tanzania, to degrade different polyethylene plastic bags and bottles and characterize the effective species based on the morphological and genetic attributes. The findings of this study will contribute to enriching the knowledge which the researchers could tap into, for the benefit of further studies, on the management of plastic waste through degradation by beneficial and non-pathogenic microorganisms recovered from agricultural soils. Since these microorganisms are not potential plant pathogens, the identified fungi, bacteria, and actinomycetes in this study can be used in agricultural soils to get rid of plastics, which hinder plant root growth and water movement.

2 Materials and methods

2.1 Survey for identification of dominant plastic wastes, collection of soil samples, and polyethylene plastic bags and bottles

Dominant plastic wastes in the study site were identified after surveying the area. During the survey, the plastics on the soil surface and sub-surface were observed to undergo degradation with time as evidenced by the strength of plastic material when broken or smashed by hands. The dominant plastic wastes were PE plastic bags and bottles. Plastic bags are used as temporary packaging materials after purchasing goods or food while plastic bottles are mainly used for packaging drinking water from industries. For uniformity in the degradation of plastics by microorganisms, plastic bags, and bottles of the same type (dominant plastic wastes) were purchased to conduct this experiment. Soil samples for isolating plastics-degrading microorganisms were collected in the vicinity of the Morogoro-Iringa Road at Kasanga village and within Sokoine University of Agriculture (SUA) maize fields, close to the Department of Agricultural Economics and Agribusiness building. The university is located at latitude 06°50′ S and longitude 37°38′ E and an altitude of 526 m above sea level (m.a.s.l). In total, four locations, three at Kasanga village (Kasanga 1, 2, and 3) and one at SUA farm were identified for soil sampling within the study site. These included sites that harbored plastic waste for different lengths of time, as well as those that visibly had not encountered any plastic waste. Kasanga 2 and 3 harbored plastics for about 10 years while SUA fields for 5 years but the deposition time depends on the time of plastic disposal. Kasanga 1 had few plastic pollutants most likely blown by the wind since the area is not exhibited with human activities. Kasanga 2 had less visible plastic wastes since the site is somehow far from the shops while Kasanga 3 had many plastic wastes since the place has many shops, a fresh vegetable market, a small market, and small local food courts as well as smallholder brick making enterprises. The SUA farm (maize fields) had many visible plastic wastes blown by the wind from the Mafiga village waste damping area in use for about 15 years. The soils with physical contact with plastics were sampled at 5–10 cm depth. Surface soils exposed to sunlight were not collected because the degradation of plastic wastes might be due to ultraviolet (UV) radiation instead of microorganisms (Volke-Sepulveda et al., 2002). The soil samples were transported to the Soil and Geological Sciences laboratory at SUA for the isolation of actinomycetes, bacteria, and fungi. Immediately upon the sample's arrival in the laboratory, soil samples were stored at 4°C in the refrigerator before isolation.

2.2 Isolation of bacteria, fungi, and actinomycetes from the soil samples

A total of 1 g of soil sample was suspended in 99 ml of sterile distilled water and afterward incubated at 28°C (Usha et al., 2011) on a rotary shaker at 150 runs per minute (rpm) (Siddique et al., 2014) for 30 min. Then, 10-fold dilutions from 10^{-1} to 10^{-6} of soil samples were prepared as previously described by Usha et al. (2011). Nutrient agar (NA) was prepared for the isolation of bacteria as described by Akmar et al. (2011). Potato dextrose agar (PDA) was used to isolate fungi from the soil following the procedure described by Kaiding and Kumar (2018). Starch-casein agar (SCA) was prepared for the isolation of *Streptomyces* as previously described by Balakrishna et al. (2012). Approximately, 1 ml aliquots of the 10^{-3}–10^{-6} suspensions were dispensed into sterile Petri dishes in triplicates followed by the addition of 15 ml of the molten media. The Petri dishes were then swirled gently to uniformly mix the inoculum with media and left to solidify at room temperature (25 ± 2°C). The plates for isolation of bacteria and fungi were incubated upside down at 30°C for 5 days for colonies to develop while those for the isolation of actinomycetes were incubated upside down at 30°C for 14 days. The plate count method was used for enumeration of microbial colonies per gram of soil sample. The obtained colonies were subcultured repeatedly in the respective media to obtain pure cultures of the microbes, which were subsequently preserved at 4°C.

2.3 Morphological characterization of the microorganisms

Actinomycetes and bacterial isolates were morphologically characterized based on the color and edges of their colonies, cell shapes, and Gram-stain reactions (Tachibana et al., 2010). The fungal isolates were characterized based on the back and front colony color and sporulation. The fungal isolates were stained using lactophenol cotton blue solution as described by Mathew et al. (2016) and Maitig et al. (2018). A drop of lactophenol cotton blue solution was placed on a slide, using an inoculating needle/loop, followed by careful spreading of a fungal culture to obtain a thin preparation on the slide. A coverslip was afterward placed on the drop and gently lowered to avoid air bubbles and left for about 5 min. The slides were observed under a light microscope (Olympus CX43) at 1,000× magnification with low power for screening in low intensity as previously described by Golding et al. (2016). The images of the colonies were captured using a digital camera (Nikon, Hong Kong, China) mounted onto the light microscope.

2.4 Molecular identification of selected microorganisms

The DNA was extracted from pure colonies of actinomycetes, bacteria, and fungi using mini-spin columns (Qiagen, Hilden, Germany), as per the manufacturer's instructions. Bacteria, actinomycetes, or fungi were digested using proteinase K (20 mg/L) for 3 h at 56°C. Digestion was followed by lysis and precipitation of proteins by heating at 56°C for 15 min and the addition of ethanol, respectively. The DNA was passed through the positively charged silica columns, washed using buffers, and eluted using nuclease-free water. The DNA was stored at –20°C until further use for polymerase chain reaction (PCR). Amplification of 16S rDNA of actinomycetes and bacteria was performed using universal 27F and 1492R primers, as previously described by Isik et al. (2014). The PCR amplification conditions included an initial denaturation at 95°C for 10 min, followed by 40 cycles of denaturation at 95°C for 1 min, annealing at 62°C for 30 s, and extension at 72°C for 30 s, followed by a single final extension at 72°C for 10 min. The amplification of 5.8S rDNA and flanking ITS regions of fungi was performed using ITS1 and ITS4 primers (Iwen et al., 2002). The PCR amplification conditions included an initial denaturation at 95°C for 10 min, followed by 40 cycles consisting of denaturation at 95°C for 30 s, annealing at 57°C for 45 s and extension at 72°C for 1 min, and a final extension at 72°C for 10 min. The amplified DNA fragments were separated by electrophoresis using a 1.2% agarose, visualized, and imaged using a gel documentation system after staining with GelRed. PCR amplicons resulting from 5.8S rDNA and 16S rDNA amplification were sequenced using the dideoxynucleotide cycle sequencing method on an ABI 3500 genetic analyzer (Applied Biosystems, Foster City, CA, United States).

2.5 Degradation of polyethylene plastic bags and bottles of plastics by actinomycetes, bacterial isolates, and fungal isolates

The ability of the actinomycetes, bacterial isolates, and fungal isolates to degrade different types of plastics was carried out using the Bushnell and Haas mineral agar medium (Bushnell and Haas, 1940) supplemented with different types of plastics. The PE powder was obtained from ground plastics sieved through a 0.6-mm sieve. After sieving, 1 g of PE powder was added to 1,000 ml (0.1% w/v) of this mineral salt medium and mixed for 1 h at 120 rpm using a shaker. The pH of the medium was adjusted to 7.0 ± 0.2 and autoclaved at 1.05 Kg/cm^2 at 121°C for 15 min. The medium was left to cool to 50°C and dispensed into Petri dishes until the solidification of the media. The isolated microorganisms were transferred onto the plates and incubated at 27°C for up to 21 days while periodically observing for the formation of clear zones around the colonies, which evidenced the plastic degradation. The diameters of such colonies and the clear zones formed around them were measured using a ruler. Cultures that had larger clear zones were selected and tested for their comparative efficiency in degrading the plastics using the completely randomized design (CRD) with four replications in the Bushnell and Haas medium. The diameters of clear zones around the colonies were measured on days 5, 7, 9, 11, and 13 for fungi and on days 5, 8, 11, 14, and 17 for bacteria and actinomycetes.

3 Statistical analysis

The diameter of clear zones for each isolate of actinomycetes, bacteria, and fungi was subjected to the analysis of variance to test the significance of variation due to site, isolates, time, and their interactions. Analysis was performed using GenStat (15th Edition). Differences among treatment means were separated using Tukey's *post-hoc* tests at $p \leq 0.05$. Actinomycetes and bacteria were identified based on 16S rDNA nucleotide sequencing followed by nucleotide identity search at GenBank using the Basic Local Alignment Search Tool (BLAST). Nucleotide sequencing and identity search using BLAST of 5.8S rDNA and the flanking intergenic spacer regions (ITS1 and 2) were used to identify the fungi. The quality of nucleotide sequences was analyzed visually using the sequence scanner v.1.0 (Applied Biosystems, Foster City, CA, United States). The nucleotide sequences obtained using forward primers were overlapped with reverse complement sequences of reverse primers using notepad (Microsoft Windows 8.1, 2013). The nucleotide sequences obtained were used to search for the similarity to other publicly available nucleotide sequences at GenBank using BLAST. The identities of the actinomycetes, bacteria, and fungi were inferred based on the highest nucleotide identity following BLAST.

4 Results

4.1 Isolated microorganisms

Table 1 shows the total counts of microbial populations of the soils used in the present study. The population of actinomycetes was higher than that of bacteria and fungi whereby the fungi population was lower than that of bacteria.

TABLE 1 Microbial populations of the studied soils.

Soil	CFU/g soil		
	Bacteria	Fungi	Actinomycetes
Kasanga 1 (few plastics)	1.00×10^5	3.73×10^4	1.04×10^5
Kasanga 2 (few plastics)	1.12×10^5	8.10×10^4	1.34×10^5
Kasanga 3 (many plastics)	1.00×10^5	1.60×10^4	2.99×10^5
SUA farm (many plastics)	1.21×10^5	4.70×10^4	1.57×10^5

4.2 The abilities of isolated actinomycetes, bacteria, and fungi in degrading polyethylene plastic bags

The abilities of the microorganisms from the soils of Kasanga 1, Kasanga 2, Kasanga 3, and SUA farm to degrade plastic bags are shown in Table 2. Clearly, different isolates showed differences in abilities to degrade ground plastic bags as depicted by the differences in the diameters of clear zones surrounding the colonies. Bacterial isolates from the soil collected from the SUA farm recorded the smallest clear zone diameter of 1 mm and the largest diameter of 54 mm. The smallest average clear zone diameter was recorded in isolates from Kasanga 1 soil, and the largest one, 27.8 mm, was in isolates collected from the SUA farm soil. Fungal isolates from Kasanga 3 displayed a minimum clear zone diameter of 5.3 mm while a maximum diameter of 66.0 mm was recorded in an isolate from Kasanga 1 soil. The smallest average clear zone diameter, 27.7 mm, was recorded in fungal isolates from Kasanga 2 soil while the largest one, 39.1 mm, was in fungal isolates from Kasanga 1 soil. On the other hand, the isolates of actinomycetes collected from Kasanga 2 soil displayed the smallest clear zone diameter, 11.0 mm; whereas, the largest one, 58.3 mm, was recorded in isolates from Kasanga 2 soil. Actinomycete isolates from the SUA farm soil showed the smallest average clear zone diameter, 25.9 mm, while those from Kasanga 1 soil displayed the largest clear zone diameter, 35.3 mm.

4.3 The abilities of isolated actinomycetes, bacteria, and fungi in degrading polyethylene plastic bottles

The abilities of the microorganisms to degrade ground plastic bottles are presented in Table 3. Among microbial groups of actinomycetes bacteria and fungi, there were clear differences in their abilities to degrade the ground plastic bottles. Bacterial isolates from the soil collected Kasanga 1 recorded a minimum clear zone diameter of 1 mm whereas a maximum diameter of 56 mm was observed in a bacterial isolated from the SUA farm soil. Moreover, the smallest average clear zone diameter, 12.8 mm, was observed in bacterial isolates from Kasanga 1 soil while the highest zone, 30.0 mm, was displayed by bacterial isolates from the SUA farm soil. Fungal isolates from Kasanga 3 displayed a minimum clear zone diameter of 5 mm while a maximum diameter of 73.7 mm was achieved in an isolate from Kasanga 2 soil. Fungal isolates from Kasanga 3 soil displayed the smallest average diameter of clear zone, 23.3 mm with the

TABLE 2 Screening the abilities of isolated bacteria, fungi, and actinomycetes from four different soils in degrading ground plastic bags.

Soil + organism	Number of isolates tested	Number showing biodegradation ability	Diameter of clear zone			SD
			Smallest (mm)	Largest (mm)	Mean	
Kasanga 1						
Bacteria	14	13	9.7	32.0	15.1	5.6
Fungi	13	13	28.7	66.0	39.1	10.2
Actinomycetes	5	5	22.0	52.0	35.3	12.0
Kasanga 2						
Bacteria	–	–	–	–	–	–
Fungi	5	5	15.7	57.7	32.6	24.1
Actinomycetes	20	19	11.0	58.3	27.2	18.2
Kasanga 3						
Bacteria	16	16	9.7	34.0	16.6	5.9
Fungi	16	14	5.3	52.7	27.7	15.8
Actinomycetes	5	5	22.0	51.0	34.8	12.6
SUA farm						
Bacteria	11	11	1.0	54.0	27.8	16.2
Fungi	8	8	22.0	57.0	33.2	19.1
Actinomycetes	7	7	36.0	52.9	25.9	24.7

(–), not observed; SD, standard deviation.

TABLE 3 Screening the abilities of isolated bacteria, fungi, and actinomycetes from four different soils in degrading ground plastic bottles.

Soil + organism	Number of isolates tested	Number showing biodegradation ability	Diameter of clear zone			SD
			Smallest (mm)	Largest (mm)	Mean	
Kasanga 1						
Bacteria	14	13	1.0	42.7	12.8	10.5
Fungi	13	13	16.7	55.0	39.7	12.4
Actinomycetes	5	5	10.0	48.0	32.2	10.8
Kasanga 2						
Bacteria	–	–	–	–	–	–
Fungi	5	5	47.3	73.7	59.3	11.1
Actinomycetes	20	19	30.0	60.0	36.9	14.8
Kasanga 3						
Bacteria	16	16	5.0	46.0	17.3	8.9
Fungi	16	14	5.0	58.7	23.3	18.3
Actinomycetes	5	5	22.0	43.0	32.3	8.8
SUA farm						
Bacteria	11	11	8.7	56.0	30.3	16.7
Fungi	8	8	12.0	66.7	48.2	19.5
Actinomycetes	7	7	16.0	43.0	30.0	10.1

(–), not observed; SD, standard deviation.

largest one, 48.2 mm being in isolates obtained from SUA farm soil. On the other hand, the minimum diameter of the clear zone, 10.0 mm, was observed in the actinomycete isolate from Kasanga 1 while the maximum of 60.0 mm in the isolate was collected from Kasanga 2 soil. Actinomycetes from the SUA farm soil displayed the smallest average diameter of the clear zone (30.0 mm) while the largest one (36.9 mm) was in isolates collected from Kasanga 2 soil.

4.4 Morphological characterization of plastic-degrading microorganisms

The macro- and micromorphological features of the actinomycete, bacterial, and fungal isolates as examined on the culture plates with the naked eye and under the light microscope, respectively, are presented in Figure 1. Generally, the actinomycetes were mainly large dry colonies, with the colors of aerial mycelia varying from white to grayish to blue-gray, with the reverse color almost brownish for all actinomycetes. Bacterial colonies were slimy and shiny on the surface, with whitish to yellow colors. Fungal colonies were more profuse, with substantial sporulation. The microscopic features showed actinomycetes and fungi to be filamentous, but bacteria to be single-celled entities.

The macroscopic and microscopic features of bacteria and actinomycetes are summarized in Table 4. The shapes of the colonies, cells, color, and the Gram reaction for most of the bacterial isolates varied from one to another. The color of the colonies varied from yellow to white, with small to relatively large colonies. The cells varied from cocci to rod chains and/or groups. The rod-like bacteria could be of the genus *Bacillus*. The colony characteristics of the actinomycetes varied in appearance/color but were compact in size. The colors of the colonies varied from white, grayish, to bluish, and the mycelia were the characteristic of the genus *Streptomyces* when grown/cultured in SCA appeared dry on the surface.

Under the microscopic observations, some of the isolates developed a black substrate mycelium with sporulated aerial mycelium. The detailed morphological features of fungi are summarized in Table 5. The colors of the colonies of the fungi varied from white-brown, grayish-brown, to deep green in the front side of the colonies, with moderate sporulation, while the reverse of the colonies for most of the cultures showed a deep dirty brown color.

4.5 Molecular identification of plastic-degrading microorganisms

Amplification of 16S rDNA for bacteria and actinomycetes and of 5.8S rDNA and flaking ITS1 and ITS2 for fungi produced PCR products with sizes ranging between 300 and 800 bp (Figure 2). The DNA was of good quality and quantity for DNA sequencing. The identity of the species of bacteria, actinomycetes, and fungi based on 16S rDNA nucleotide sequences is shown in Table 6. The isolates that degraded plastics and their amplified DNA could not be sequenced are shown in Table 7. The sequenced isolates of bacteria, actinomycetes and fungi belonged to different species including

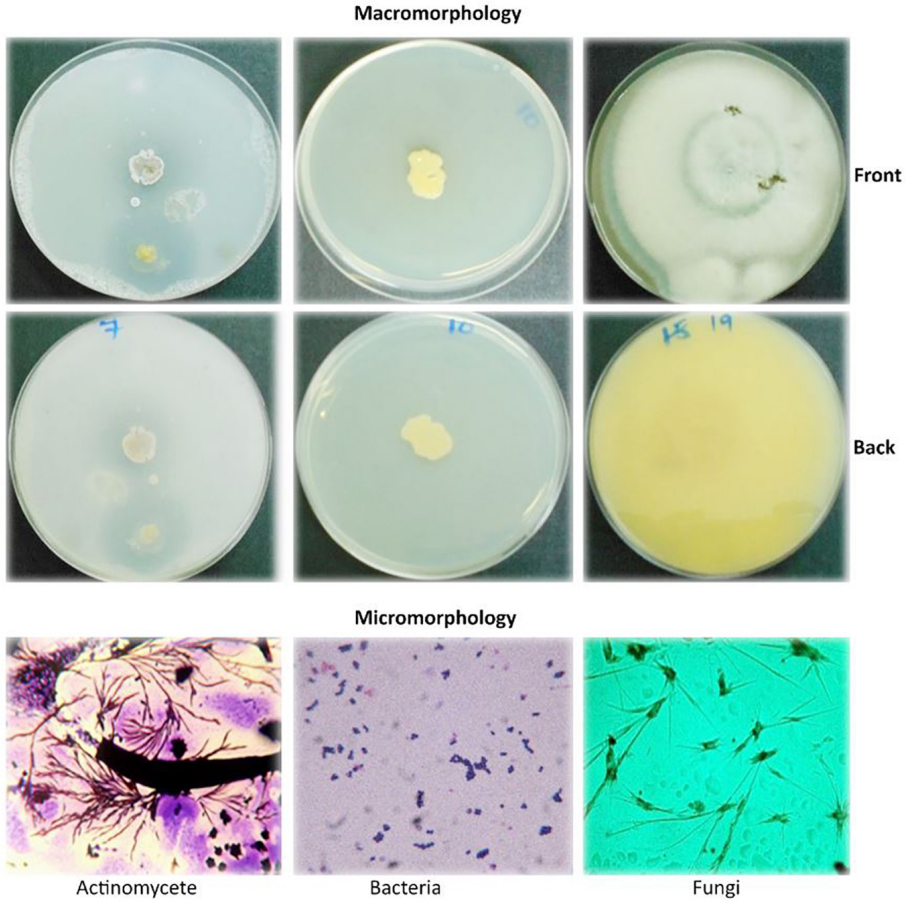

FIGURE 1
Macromorphological and micromorphological characteristics of the actinomycetes, bacteria, and fungi studied for the degradation of plastics.

Bacillus cereus, Sinomonas sp., and *Cellulosimicrobium* sp. while actinomycetes included *Streptomyces werraensis* and *S. rochei* (Table 6). The fungal isolates that degraded, on the other hand, belonged to different species including *Eupenicillium rubidurum*, *Phoma* sp., *Neosartorya fischeri*, *Aspergillus terreus*, *Aspergillus* sp., and *Talaromyces islandicus*. *Aspergillus terreus* appeared in two different soils of Kasanga 2 and SUA farm.

4.6 Comparative degradation of ground plastic bags by fungi (5–13 days), bacteria, and actinomycetes (5–17 days) isolates

The comparative degradation of plastic bags by actinomycetes, bacteria, and fungi is shown in Figure 3. There was a clear variation in the diameters of clear zones for actinomycetes, bacteria, and fungi in degrading ground plastic bags on solidified Bushnell and Haas agar medium. There were differences in growth among species of fungi during the degradation of plastic bags from the 5th to the 13th day. The minimum diameter of 9.1 mm was observed in *Aspergillus terreus* (F5) during the 5th day and the maximum diameter of 30.2 mm was observed in *Phoma* sp. (F2). The growth continued to vary from the 7th, 9th, and 11th days and, finally, on the 13th day, the minimum clear zone diameter was 33.3 mm, which was observed in the same isolate which is *Aspergillus terreus* F5 and the maximum diameter was 66.3 mm, observed in the same species which was *Phoma* sp. F2 isolate. The clear zone diameter of other fungal isolates was intermediate. *Phoma* sp. F2 was the most efficient, and *Aspergillus terreus* F5 was the least efficient in degrading the ground plastic bags. The minimum clear zone diameter of 6.2 mm recorded by bacteria on the 5th day was observed in unsequenced isolate B7 and the maximum, 7.2 mm in B1. The variation in growth continued from the 8th, 11th, and 14th day; finally, on the 17th day, the minimum clear zone diameter of 21.7 mm was recorded in the same isolate B7 and the maximum, 47.5 mm in isolate B1. This indicates that the bacterial isolate B1 was

TABLE 4 Morphology of plastic-degrading bacteria and actinomycetes.

Isolate	Colony morphology	Shape	Color	Gram stain
Bacteria				
B1	White, large, irregular shape	Large rods with ovoid ends	Purple	+
B2	Yellow, large with raged ends	Cocci in short chains	Purple	+
B3	White, small, round	Cocci rods	Pink	–
B4	Yellow, small	Cocci in groups	Pink	–
B5	White, small	Cocci in groups	Purple	+
B6	White, large, raged ends	Cocci in tetrads	Purple	+
B7	White, large, irregular shape	Large rods with ovoid ends	Purple	+
B8	White, small	Cocci in groups	Purple	+
Actinomycetes				
A1	Whitish, large, and dry colony	Filamentous	Gram+	
A2	White, large, and dry	Filamentous	Purple	+
A3	White to dark, large, and dry	Filamentous	Purple	+
A4	Grayish, large, and dry	Filamentous	Purple	+
A5	Whitish with a brown shadow, large, and dry ring	Filamentous	Purple	+
A6	Bluish, large, and dry	Filamentous	Purple	+
A7	Whitish, large, and dry	Filamentous	Purple	+
A8	Whitish, large, and dry	Filamentous	Purple	+

TABLE 5 Morphology of plastics-degrading fungi.

Isolate code	Colony morphology		Sporulation	Microscopic features
	Front	Back		
F1	Grayish-green, cotton like	Brownish color	Moderate	Smooth walls conidia which are globose to subglobose with phialides like ampulliform
F2	Grayish-brown, powdery/granular	Brownish color	Moderate	Conidia a produced in abundance within the pycnidia on narrow thread-like phialides, which are pycnidial wall cell, Conidia globose to cylindrical
F3	Whitish-bluish, cotton like	Deep brownish	Moderate	Short conidiophores branching from one foot cell, globose to hemispherical vesicle, branched straight phialides
F4	White to brown	Deep dirty brown	Moderate	Long conidiophores branching from one foot cell, globose to hemispherical vesicle, branched straight phialides
F5	White to brown	Deep dirty brown	Moderate	Long conidiophores branching from one foot cell, globose to hemispherical vesicle, branched straight phialides
F6	Deep green with white periphery	Brown	Moderate	Conidia globose to subglobose, conidiophore are on the surface hyphae
F7	White to brown	Deep dirty brown	Moderate	Long conidiophores branching from one foot cell, globose to hemispherical vesicle, branched straight phialides
F8	White to brown	Deep dirty brown	Moderate	Long conidiophores branching from one foot cell, globose to hemispherical vesicle, branched straight phialides

efficient as the B7 in degrading ground plastic bags. In the case of actinomycetes, there was somehow unpredictable variation in the growth of colonies and the formation of clear zones. The variation started from the 5th day as in fungi and bacteria whereby the minimum clear zone diameter of 3.3 mm was recorded in *Streptomyces weraensis* (A2) while the maximum, 5.3 mm, was displayed by another unsequenced isolate A6. Surprisingly, on the 17th day, isolate A6, which displayed the largest clear zone diameter, was the one with the smallest clear zone diameter of 27.2 mm while the largest one, 32.2 mm, was displayed by isolate A3. Despite the unpredictable growth variation among three isolates of actinomycetes, isolate A3 which had the highest clear zone diameter on the 17th day was observed to consistently display the highest clear zone diameter from the 8th, 11th, and 14th days. After 13 days, most of the fungal colonies were bigger, covering the whole plates of which it was not possible to measure the diameter of clear zones. On the other hand, bacteria and actinomycetes had slow growth whereby after 17 days, most of the colonies were observed to degrade.

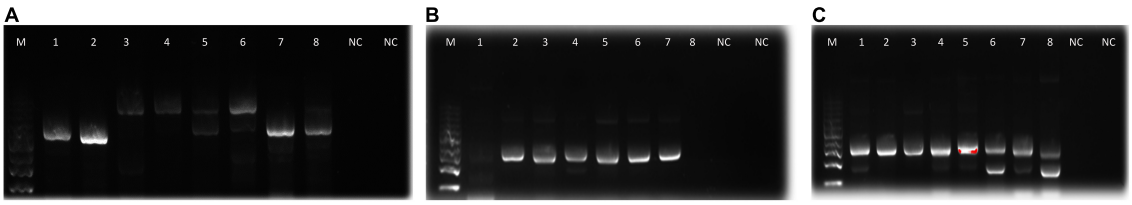

FIGURE 2
Agarose gel electrophoresis bands of PCR products from the microbial isolates **(A)**: fungi, **(B)**: actinomycetes, and **(C)**: bacteria. M, molecular weight marker; 1–8, bands for DNA samples; NC, negative control.

TABLE 6 Identity of plastic-degrading bacteria, actinomycetes, and fungi.

Current isolate/Strain	Location	Identification	Similarity of current isolate to GenBank		Type of plastic degraded
			Accession numbers	% identity	
Bacteria					
B2	SUA farm	*B. cereus*	KC683896	100	PE plastic bag
B3	SUA farm	*Sinomonas* sp.	HE793513	100	PE plastic bottle
B4	SUA farm	*Sinomonas* sp.	KJ504159	100	PE plastic bottle
B5	Kasanga 3	*Cellulosimicrobium* sp.	EU307933	100	PE plastic bottle
B6	Kasanga 3	*Cellulosimicrobium* sp.	LN846832	99	PE plastic bottle
Actinomycetes					
A2	Kasanga 3	*S. werraensis*	KM215730	99	PE plastic bag
A8	Kasanga 1	*S. rochei*	KF444515	100	PE plastic bottle
Fungi					
F1	Kasanga 3	*Eupenicillium rubidurum*	HQ608058	100	PE plastic bag
F2	Kasanga 1	*Phoma* sp.	EF423518	100	PE plastic bag
F3	Kasanga 3	*Neosartorya fischeri*	AF455538	99	PE plastic bag
F4	Kasanga 2	*A. terreus*	KC119206	100	PE plastic bottle
F5	Kasanga 2	*A. terreus*	KC119206	100	PE plastic bag
F6	SUA farm	*Talaromyces islandicus*	NR_103664	100	PE plastic bottle
F7	Kasanga 1	*Aspergillus* sp.	KF367546	100	PE plastic bottle
F8	SUA farm	*A. terreus*	KM491895	99	PE plastic bottle

TABLE 7 Microbial isolates that their DNA could not be sequenced.

Bacterial isolate	Location	Actinomycete isolate	Location
B1	Kasanga 1	A1	SUA farm
B7	Kasanga 2	A3	Kasanga 1
B8	Kasanga 2	A4	SUA farm
		A5	Kasanga 2
		A6	Kasanga 2
		A7	Kasanga 3

4.7 Comparative degradation of ground plastic bottles by fungi (5–13 days), bacteria, and actinomycetes (5–17 days) isolates

The comparative degradation of plastic bags by fungi, bacteria, and actinomycetes is shown in Figure 4. There was a clear variation in the diameters of clear zones for fungi, bacteria, and actinomycetes in degrading ground plastic bottles on solidified Bushnell and Haas agar medium. There were differences in growth among species of fungi during the degradation of plastic bags from the 5th to the 13th day. The minimum diameter of 5.1 mm was observed in *Talaromyces islandicus* (F6) during the 5th day and the maximum diameter of 21.8 mm was observed in *Aspergillus terreus* (F4). The growth continued to vary from the 7th, 9th, and 11th days and, finally, on the 13th day, the minimum clear zone diameter was 30.2 mm, which was observed in the same isolate, which is *Talaromyces islandicus* (F6), and the maximum diameter was 61.1 mm, which is *Aspergillus terreus* (F4). *Aspergillus terreus* (F4) was the most efficient and *Talaromyces islandicus* (F6) was the least efficient in degrading the ground plastic bags. The minimum clear zone diameter of 2.1 mm recorded by bacteria on the 5th day was observed in *Sinomonas* sp. (B4) and the maximum, 5.3 mm, was observed in another isolate

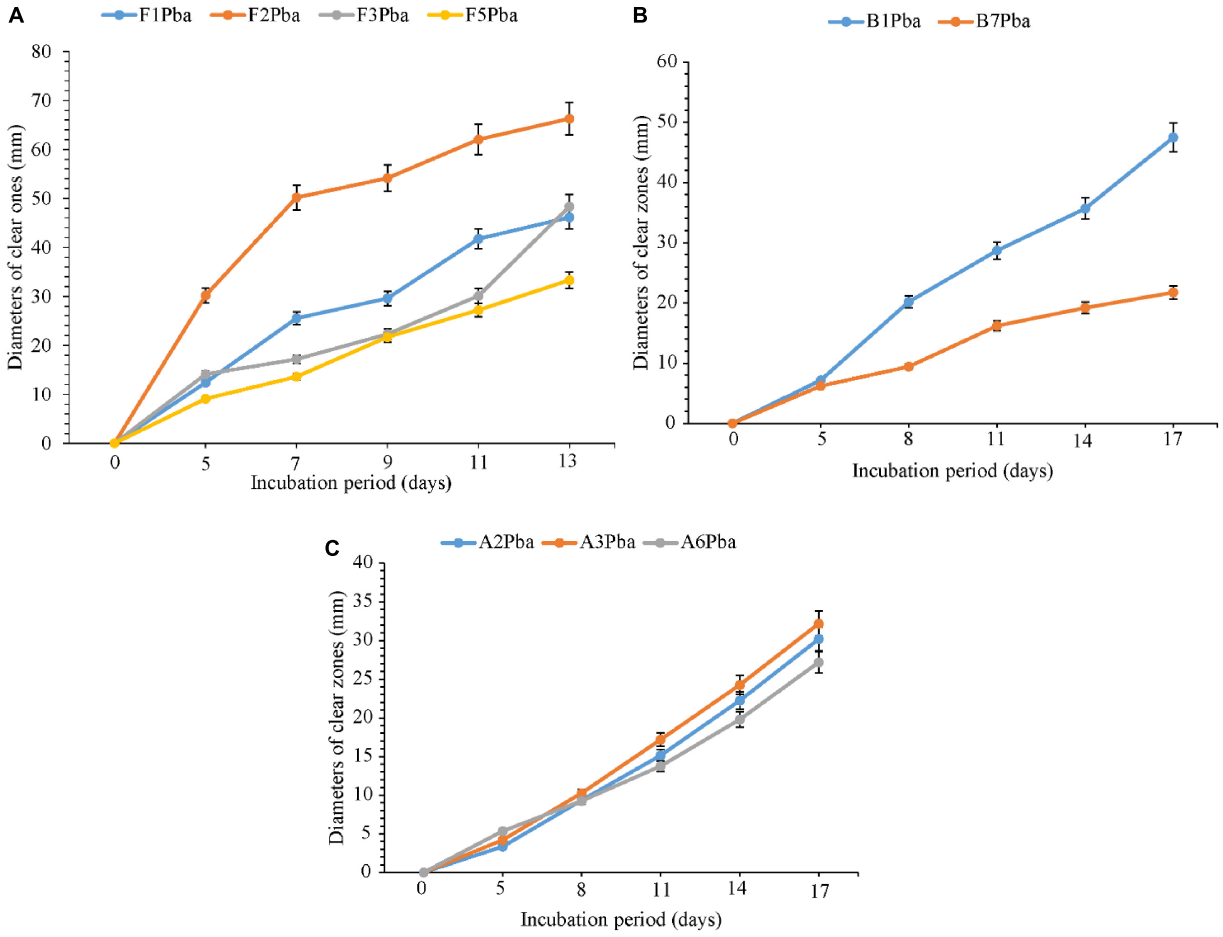

FIGURE 3
Comparative ability of the **(A)** fungi, **(B)** bacteria, and **(C)** actinomycetes in degrading ground plastic bags. Error bars represent the mean ± SD of three independent biological replicates (the names of species coded with letters F represent fungi, B represents bacteria, and A represents actinomycetes, and the numbers represent their positions in a particular group as shown in Table 6).

of *Sinomonas* sp. (B3). The variation in growth continued from the 8th, 11th, and 14th days; finally, on the 17th day, the minimum clear zone diameter of 19.3 mm was recorded in the same isolate *Sinomonas* sp. (B4) and the maximum, 33.6 mm, in *Bacillus cereus* (B2). This indicates that the bacterial *Bacillus cereus* (B2) was more efficient than other isolates in degrading ground plastic bottles. In the case of actinomycetes, the variation started from the 5th day as in fungi and bacteria whereby the minimum clear zone diameter of 2.5 mm was recorded in unsequenced isolate A4 while the maximum, 6.3 mm, was displayed by *Streptomyces rochei* (A8). Despite the variation in growth and formation of clear zones among the tested isolates of actinomycetes, *Streptomyces rochei* (A8) consistently displayed the highest clear zone diameter from the 5th to 17th days. The growth of fungi, bacteria, and actinomycetes followed the same trend as in plastic bags. There was an overgrowth of fungal colonies after 13 days and a degradation of colonies for bacteria and actinomycetes after 17 days.

4.8 Comparative efficiency of fungi, bacteria, and actinomycetes in degrading plastic bags and bottles

The comparative abilities of fungi, bacteria, and actinomycetes in degrading ground plastic bags and bottles in their final days of incubation were analyzed to assess whether the variation in the growth was either or not significant (Table 8). There was a significant ($p < 0.001$) variation in the abilities of the tested isolates in degrading both plastic bags and bottles. Unsequenced bacterial isolate, B1 from Kasanga 1 soil, was significantly ($p < 0.001$) effective in degrading the plastic bags as it displayed the largest clear zone diameter of 47.5 mm. On

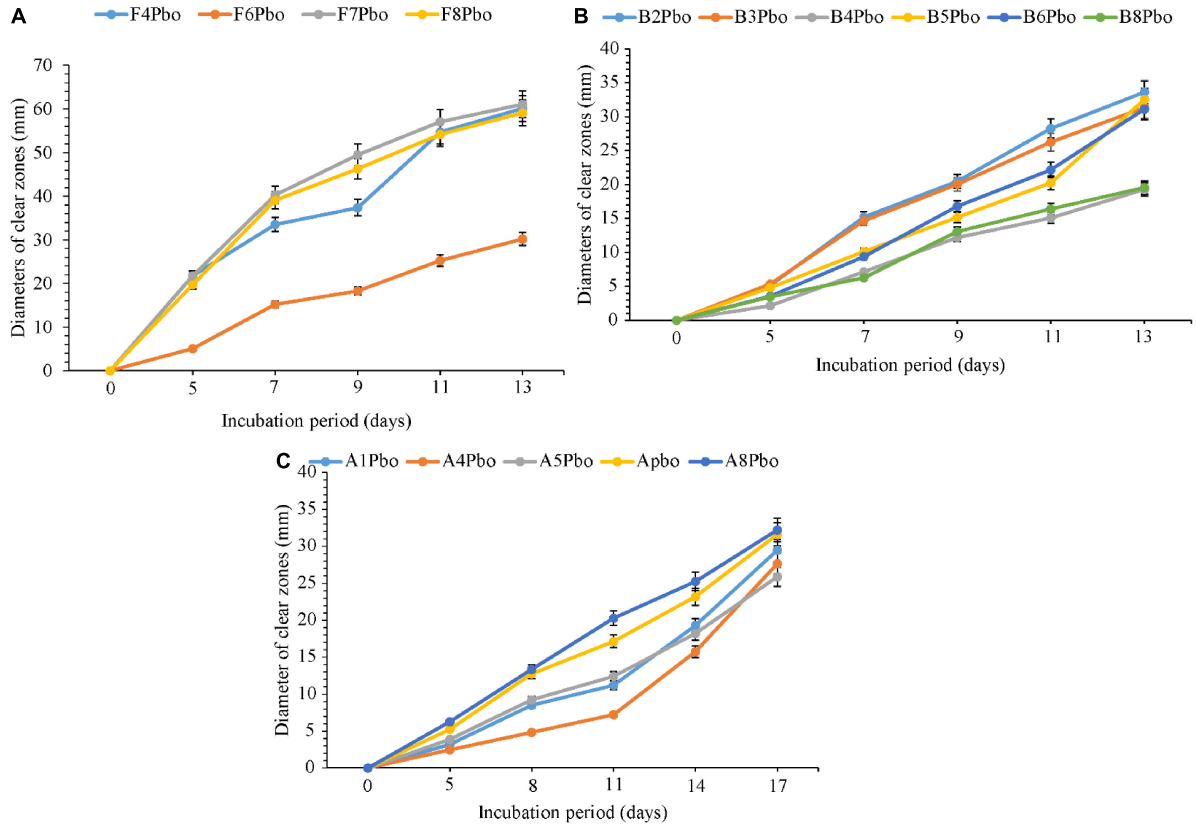

FIGURE 4
Comparative ability of the **(A)** fungi, **(B)** bacteria, and **(C)** actinomycetes in degrading ground plastic bottles. Error bars represent the mean ± SD of three independent biological replicates (the names of species coded with letters F represents fungi, B represents bacteria, and A represents actinomycetes, and the numbers represent their positions in a particular group as shown in **Table 6**).

the other hand, *Bacillus cereus* (B2) isolated from SUA farm soil was significantly ($p < 0.001$) effective in degrading the ground plastic bottles by displaying the largest clear zone diameter of 33.6 mm. On the other hand, actinomycetes were significantly ($p < 0.001$) effective in degrading plastic bags and bottles. *Streptomyces weraensis* (A2) from Kasanga 3 soil displayed the largest clear zone diameter of 30.2 mm in degrading the plastic bags, and *Streptomyces rochei* (A8) from SUA farm soil displayed the largest clear zone diameter of 32.2 mm in degrading the plastic bottles. On the other hand, *Aspergillus* sp. (F7) from Kasanga 1 soil was significantly ($p < 0.001$) effective in degrading the plastic bags by displaying the largest clear zone diameter of 61.1 mm. In contrast, *Phoma* sp. (F2) isolated from Kasanga 1 soil was significantly ($p < 0.001$) more effective in degrading the plastic bottles than the rest of the fungal species.

5 Discussion

The microbial populations in all soils varied from as low as 1.60×10^4 CFU/g soil (fungi, Kasanga 3 soil) (4.20 log CFU/g soil) to 1.57×10^5 CFU/g soil, which is the population of actinomycetes from SUA farm soil (5.20 log CFU/g soil). These results seem to indicate a relatively low capacity of the soils to sustain higher microbial populations above 10^5 CFU/g of soil. Similar observations were made by Akande and Adekayode (2019) while comparing the levels of microbial populations isolated from different types of soils.

Under the microscopic observations, some actinomycete isolates developed a black substrate mycelium with sporulated aerial mycelium. These observations are similar to the phenomenon explained by Ng et al. (2013) that *Streptomyces* can form a non-fragmenting substrate mycelium that may bear spores, and in most genera, a well-developed aerial mycelium with spore chains that can be long or very short. The microscopic features observed for the fungi were conidiophores, conidia, and phialides, which are the common characteristics of *Aspergillus* and *Penicillium* (Golding et al., 2016).

The identified bacterial species included *B. cereus, Sinomonas* sp., and *Cellulosimicrobium* sp. while actinomycetes included *S. werraensis* and *S. rochei*. The fungal isolates were identified as *E. rubidurum, Phoma* sp., *N. fischeri, A. terreus,* and *T. islandicus*. *Aspergillus terreus* appeared

TABLE 8 Comparative efficiency of different bacteria, actinomycetes, and fungi in degrading polyethylene plastics bag and bottle on the 13th (fungi) and 17th days (bacteria and actinomycetes).

Isolate	Location	Degradation ability, clear zone diameter (mm)	Type of plastic degraded
Bacteria on 17th day			
B1	Kasanga 1	47.5 ± 0.01^{b}	Plastic bag
B7	Kasanga 3	21.7 ± 0.02^{a}	Plastic bag
Bacillus cereus (B2)	SUA farm	33.6 ± 0.02^{d}	Plastic bottle
Sinomonas sp. (B3)	SUA farm	31.4 ± 0.02^{b}	Plastic bottle
Sinomonas sp. (B4)	SUA farm	19.3 ± 0.03^{a}	Plastic bottle
Cellulosimicrobium sp. (B5)	Kasanga 3	32.5 ± 0.02^{c}	Plastic bottle
Cellulosimicrobium sp. (B6)	Kasanga 3	31.1 ± 0.02^{b}	Plastic bottle
B8	Kasanga 1	19.6 ± 0.01^{a}	Plastic bottle
Actinomycetes on 17th day			
Streptomyces weraensis (A2)	Kasanga 3	30.2 ± 0.03^{b}	Plastic bag
A3	Kasanga 1	32.2 ± 0.02^{c}	Plastic bag
A6	Kasanga 2	27.2 ± 0.02^{a}	Plastic bag
A1	SUA farm	29.5 ± 0.01^{c}	Plastic bottle
A4	SUA farm	27.6 ± 0.02^{b}	Plastic bottle
A5	Kasanga 2	25.9 ± 0.01^{a}	Plastic bottle
A7	Kasanga 3	31.6 ± 0.01^{d}	Plastic bottle
Streptomyces rochei (A8)	SUA farm	32.2 ± 0.03^{e}	Plastic bottle
Fungi on 13th day			
Aspergillus terreus (F4)	Kasanga 2	60.1 ± 0.02^{c}	Plastic bag
Talaromyces islandicus (F6)	SUA farm	30.2 ± 0.03^{a}	Plastic bag
Aspergillus sp. (F7)	Kasanga 1	61.1 ± 0.01^{d}	Plastic bag
Aspergillus terreus (F8)	SUA farm	59.1 ± 0.02^{b}	Plastic bag
Eupenicillium rubidurum (F1)	Kasanga 3	46.1 ± 0.02^{b}	Plastic bottle
Phoma sp. (F2)	Kasanga 1	66.3 ± 0.03^{d}	Plastic bottle
Neosartorya fischeri (F3)	Kasanga 3	48.3 ± 0.02^{c}	Plastic bottle
Aspergillus terreus (F5)	Kasanga 2	33.3 ± 0.04^{a}	Plastic bottle

Different letters represent the significantly at $P = 0.05$.

in two different soils of the Kasanga and SUA farm. Differences were observed among these microorganisms in their comparative abilities to degrade the ground PE plastic bags. This observation is in line with that of Gajendiran et al. (2016) who identified five bacterial species, including *Streptococcus* and *Staphylococcus*, and eight fungal species of *Aspergillus*. Different genera/species of bacteria and *Streptomyces* degrade the plastics such as PE (Gupta and Devi, 2020). In the study by Deepika and Madhuri (2015), for instance, significant differences in weight loss of LDPE as compared to initial weight were attributed to their degradation by *Pseudomonas* sp., *A. niger,* and *A. flavus*. On screening of the ability of different microorganisms in degrading polyethylene, fungi were more efficient than bacteria and actinomycetes. Shah et al. (2016) also observed the ability of *B. subtilis* to degrade polyurethane. Various research studies have also reported on the abilities of different genera/species of fungi on degrading different types of plastics. Raaman et al. (2012) reported the biodegradation of plastics by *Aspergillus* spp., including *A. terreus* isolated from polythene-polluted sites around Chennai in India. Other studies have observed *Eupenicillium* sp., *Talaromyces* sp., and *Penicillium simplicissimum* to have the ability to degrade PE (Sowmya et al., 2015). In general, the results presented in **Table 6** on the involvement of different genera/species further confirm the diversity of bacteria, fungi, and actinomycetes genera and/or species that can degrade plastics. Other studies have similarly shown that different genera/species of bacteria, including *Pseudomonas* sp. (Nanda et al., 2010), *Streptococcus* spp., *Staphylococcus* spp., *Micrococcus* spp. and *Moraxella* spp., *B. subtilis*, *B. amylolyticus*, and *Arthrobacter defluvii* (Prabhat et al., 2013), actinomycetes, *Streptomyces* sp. (Deepika and Madhuri, 2015), and fungi, including *A. niger*, *A. japonicus*, *A. terreus, A. flavus,* and *Mucor* sp. (Ibrahim et al., 2011; Raaman et al., 2012), exhibited the ability to degrade LDPE.

Differences in the abilities of various microorganisms to degrade plastics might be due to the differences in environments from where they are isolated. However, the main mechanisms for microbial degradation of PE plastics

are oxidation of the PE surface and formation of carbonyl groups, which cause deterioration and fragmentation of the material (Ali et al., 2022). Nanda et al. (2010) investigated the same phenomenon by comparing three *Pseudomonas* sp. from three different isolation sources, namely, sewage sludge dump, household garbage dump, and textile effluents drainage site. They observed that *Pseudomonas* sp. from sewage sludge dump degraded polyhydroxyalkanoate (PHA), a natural plastic, more efficiently by 46.2%, as compared to its ability to degrade by 29.1% of a synthetic PE. In contrast, *Pseudomonas* sp. from the household garbage dump gave the lowest biodegradability of 31.4% and 16.3% for the natural plastic and synthetic PE, respectively. However, *Pseudomonas* sp. isolated from the textile effluent drainage site gave an intermediate biodegradability of 39.7 and 19.6% for the natural plastic and synthetic PE, respectively. Thus, the differences in plastic biodegradation between and within species of a microorganism, as presently observed using the diameters of the clear zones, can always be expected.

The growth rate of the microorganisms was slow (2–3 days), although the nutrients were amply available. This indicates that the organisms were not yet well-adapted to the available carbon source, plastics. The growth of bacteria and actinomycetes from the 5th to the 13th days and up to the 17th day for fungi increased, implying that microorganisms had adapted to the available foreign carbon source. The degradation rate of *Pseudomonas* sp., increased until the 21st day after which it took a sudden deep (Nanda et al., 2010), implying that *Pseudomonas* sp. had metabolized the available basal media nutrients before utilizing the carbon sources from the PE. The degradation of the colonies for bacteria and actinomycetes is an implication that the microbe cannot reach the available carbon beyond the clear zone. The microorganisms differ in their speed of degradation of plastics, and this might be due to the differential capacity of the enzymes produced to catalyze the degradation of the plastics (Shah et al., 2008). This demonstrates that biodegradation is dependent on polymer characteristics, organism type, and nature of pre-treatment. For the case of this study, the maximum time for growth was 21 days observed in *Pseudomonas* sp.

It should be noted that not all species occurring in nature exhibit the ability to degrade plastics. This is because they might be different/distinct strains. For example, two isolates of *A. terreus* were isolated from Kasanga 2 soil: *A. terreus*-F4 degraded ground plastic bottle and *A. terreus*-F5 degraded a ground plastic bag. Another isolate of *A. terreus*-F8 was isolated from the SUA farm, and it degraded the ground plastic bottle. These may not be the same strain. It is also possible that a given organism, for example, *A. terreus*, will have other strains that have a greater ability to degrade a given type of plastic while others do not. Ibrahim et al. (2011) observed strains of *A. terreus* that degraded PE by 58.0% as tested using colony diameter on Petri dishes. This is an indication that while the organism used in these two different studies cited was *A. terreus*, they could be two distinct strains as depicted by their huge difference in the extent of their degradation of PE. Therefore, it should not be assumed that any isolates of the same genus/species automatically have the equal capability of degrading a given plastic.

6 Conclusion

The higher demand for single-use plastics and their disposal in the environment is a serious environmental polluting component. The available management strategies have been used for many years, but still, the yield of plastic pollutants is increasing in the environment. It is high time to explore the new sustainable and environmentally safe technique of plastic degradation by beneficial soil microorganisms in removing the plastic pollutants from the environment. The soils used in this study contained microorganisms that were capable of degrading ground PE plastic bags and bottles as indicated by large clear zones of up to 66.3 mm by *Phoma* sp. (F2) in degrading the plastic bottles and 61.1 mm by *Aspergillus* sp. (F7) in plastic bags within 13 days. Moreover, this study revealed that the microbial degradation of plastics is widespread, among bacteria, fungi, and actinomycetes. Different genera/species including *Bacillus cereus* (bacteria), *Streptomyces werraensis* (actinomycete), *Aspergillus*, and *Phoma* sp. (fungi) that degrade PE plastics were identified in this study. Some could not be identified currently, calling for further study on them. The identified isolates especially the highly efficient ones hold the potential to be exploited industrially (in fermenters) or environmentally (in landfills) to degrade the waste plastics. Therefore, bioprospecting of agricultural soils, water bodies, and landfills containing plastic wastes could lead to the identification of more efficient microbial species with the ability to degrade plastics.

Data availability statement

The datasets presented in this study can be found in online repositories. The names of the repository/repositories and accession number(s) can be found in this article.

Author contributions

MN: original draft preparation. HT, GM, and ES: review and editing. All authors: conceptualization, methodology, experiments, read, and agreed to the published version of the manuscript.

Funding

This research was supported by the Alliance for a Green Revolution in Africa (AGRA).

Acknowledgments

We thank all the staff and technical experts from two laboratories at Sokoine University of Agriculture (SUA), the Laboratory of Soil Science in the Department of Soil and Geological Sciences (DSGS), and the Microbiology Laboratory at the College of Veterinary Medicine and Biomedical Sciences for their guidance and support during the sampling of soils and laboratory analyses, microbial isolation, characterization, and testing the biodegradability of plastics.

Conflict of interest

The authors declare that the research was conducted in the absence of any commercial or financial relationships that could be construed as a potential conflict of interest.

Publisher's note

All claims expressed in this article are solely those of the authors and do not necessarily represent those of their affiliated organizations, or those of the publisher, the editors and the reviewers. Any product that may be evaluated in this article, or claim that may be made by its manufacturer, is not guaranteed or endorsed by the publisher.

References

Aderiye, B. I., Akinyeye, R. O., Sulaimon, A., Oluwole, O. A., Kehinde, F. J., Ojo, O. E., et al. (2019). Monitoring fungal biodegradation of Low-Density Polyethylene [LDPE] from plastic wastes dump sites using FT-IR spectra. *Microbiol. Res. J. Int.* 26, 1–15. doi: 10.9734/mrji/2018/44851

Akande, G. M., and Adekayode, F. O. (2019). Identification of soil microbial population under different land use. *Trop. Plant Res.* 6, 90–100. doi: 10.22271/tpr.2019.v6.i1.013

Akmar, H. N., Asma, I., Venugopal, B., Latha, L. Y., and Sasidharan, S. (2011). Identification of appropriate sample and culture method for isolation of new thermophilic bacteria from hot spring. *Afr. J. Microbiol. Res.* 5, 217–221. doi: 10.5897/AJMR10.462

Ali, S. S., Elsamahy, T., Al-Tohamy, R., Zhu, D., Mahmoud, Y. A., Koutra, E., et al. (2021a). Plastic wastes biodegradation: Mechanisms, challenges and future prospects. *Sci. Total Environ.* 780, 146–590. doi: 10.1016/j.scitotenv.2021.146590

Ali, S. S., Elsamahy, T., Koutra, E., Kornaros, M., El-Sheekh, M., Abdelkarim, E. A., et al. (2021b). Degradation of conventional plastic wastes in the environment: A review on current status of knowledge and future perspectives of disposal. *Sci. Total Environ.* 771, 144–719. doi: 10.1016/j.scitotenv.2020.144719

Ali, S. S., Elsamahy, T., Zhu, D., and Sun, J. (2022). Biodegradability of polyethylene by efficient bacteria from the guts of plastic-eating waxworms and investigation of its degradation Mechanism. *J. Hazard. Mater.* 443:130287. doi: 10.1016/j.jhazmat.2022.130287

Balakrishna, G., Shanker, A. S., and Pindi, P. K. (2012). Isolation of phosphate solibulizing actinomycetes from forest soils of mahabubnagar district. *IOSR J. Pharmacy* 6, 44–48.

Bergmann, M., Mützel, S., Primpke, S., Tekman, M. B., Trachsel, J., and Gerdts, G. (2019). White and wonderful? Microplastics prevail in snow from the alps to the arctic. *Sci. Adv.* 5:eaax1157. doi: 10.1126/sciadv.aax1157

Biki, S. P., Mahmud, S., Akhter, S., Rahman, J., Rix, J. J., Al Bachchu, A., et al. (2021). Polyethylene degradation by *Ralstonia* Sp. Strain SKM2 and *Bacillus* Sp. Strain SM1 isolated from Land Fill Soil Site. *Environ. Technol. Innov.* 22, 101–495. doi: 10.1016/j.eti.2021.101495

Burke, C. S., Salas, E., Smith-Jentsch, K., and Rosen, M. A. (2012). *Measuring Macrocognition in Teams: Some Insights for Navigating the Complexities*. Boca Raton, FL: CRC Press, doi: 10.1201/9781315593173-4

Bushnell, L. D., and Haas, H. F. (1940). *The Utilization of Certain Hydrocarbons by Microorganisms*. Manhattan, NY: Kansas Agricultural Experiment Station.

Deepika, S., and Madhuri, R. J. (2015). Biodegradation of low density polyethylene by micro-organisms from garbage soil. *J. Exp. Biol. Agric. Sci.* 3, 15–21.

Gajendiran, A., Krishnamoorthy, S., and Abraham, J. (2016). Microbial degradation of Low-Density Polyethylene (LDPE) by *Aspergillus clavatus* Strain JASK1 Isolated from Landfill Soil. *3 Biotech* 6, 1–6. doi: 10.1007/s13205-016-0394-x

Geyer, R., Jambeck, J. R., and Law, K. L. (2017). Production, use, and fate of all plastics ever made. *Sci. Adv.* 3:e1700782. doi: 10.1126/sciadv.1700782

Golding, C. G., Lamboo, L. L., Beniac, D. R., and Booth, T. F. (2016). The scanning electron microscope in microbiology and diagnosis of infectious disease. *Sci. Rep.* 6:26516. doi: 10.1038/srep26516

Gupta, K. K., and Devi, D. (2020). Characteristics investigation on biofilm formation and biodegradation activities of *Pseudomonas Aeruginosa* Strain ISJ14 colonizing Low Density Polyethylene (LDPE) Surface. *Heliyon* 6:e04398. doi: 10.1016/j.heliyon.2020.e04398

Ibrahim, I. N., Maraqa, A., Hameed, K. M., Saadoun, I. M., and Maswadeh, H. M. (2011). Assessment of potential plastic-degrading fungi in jordanian habitats. *Turk. J. Biol.* 35, 551–557. doi: 10.3906/biy-0901-9

Ilyas, M., Ahmad, W., Khan, H., Yousaf, S., Khan, K., and Nazir, S. (2018). Plastic waste as a significant threat to environment – a systematic literature review. *Rev. Environ. Health* 33, 383–406. doi: 10.1515/reveh-2017-0035

Isik, K., Gencbay, T., Ozdemir-Kocak, F., and Cil, E. (2014). Molecular identification of different actinomycetes isolated from east black sea region plateau soil by 16S RDNA gene sequencing. *Afr. J. Microbiol. Res.* 8, 878–887. doi: 10.5897/ajmr2013.6174

Iwen, P. C., Hinrichs, S. H., and Rupp, M. E. (2002). Utilization of the internal transcribed spacer regions as molecular targets to detect and identify human fungal pathogens. *Med. Mycol.* 40, 87–109. doi: 10.1080/mmy.40.1.87.109

Jamieson, A. J., Brooks, L. S. R., Reid, W. D. K., Piertney, S. B., Narayanaswamy, B. E., and Linley, T. D. (2019). Microplastics and synthetic particles ingested by deep-sea amphipods in six of the deepest marine ecosystems on earth. *R. Soc. Open Sci.* 6:180667. doi: 10.1098/rsos.180667

Kaiding, P., and Kumar, R. (2018). Isolation and identification of soil mycoflora in different crop fields at salur mandal plant taxonomy view project soil microbiology view project. *Pelag. Res. Library* 3, 2020–2026.

Lear, G., Kingsbury, J. M., Franchini, S., Gambarini, V., Maday, S. D. M., Wallbank, J. A., et al. (2021). Plastics and the microbiome: Impacts and solutions. *Environ. Microb.* 16, 1–19. doi: 10.1186/s40793-020-00371-w

Maitig, A. M. A., Alhoot, M. A. M., and Tiwari, K. (2018). Isolation and screening of extracellular protease enzyme from fungal isolates of soil. *J. Pure Appl. Microbiol.* 12, 2059–2067. doi: 10.22207/JPAM.12.4.42

Markic, A., Niemand, C., Bridson, J. H., Mazouni-Gaertner, N., Gaertner, J. C., Eriksen, M., et al. (2018). Double trouble in the south pacific subtropical gyre: increased plastic ingestion by fish in the oceanic accumulation zone. *Mar. Pollut. Bull.* 136, 547–564. doi: 10.1016/j.marpolbul.2018.09.031

Mathew, J. J., Vazhacharickal, P. J., Sajeshkumar, N. K., and Ashokan, A. (2016). Amylase Production by *Aspergillus* Niger through Submerged Fermentation Using Starchy Food Byproducts as Substrate Customer Satisfaction View Project SERVICE QUALITY IN BANKS View Project Amylase Production by Aspergillus Niger through Submerged Fermentati. *Int. J. Herb. Med.* 4, 34–40.

Muhonja, C. N., Makonde, H., Magoma, G., and Imbuga, M. (2018). Biodegradability of polyethylene by bacteria and fungi from dandora dumpsite nairobi-kenya. *PLoS One* 13:e0198446. doi: 10.1371/journal.pone.0198446

Nanda, S., Sahu, S., and Abraham, J. (2010). Studies on the biodegradation of natural and synthetic polyethylene by *Pseudomonas* Spp. *J. Appl. Sci. Environ. Manage.* 14, 57–60. doi: 10.4314/jasem.v14i2.57839

Ng, Y. K., Hewavitharana, A. K., Webb, R., Shaw, P. N., and Fuerst, J. A. (2013). Developmental cycle and pharmaceutically relevant compounds of salinispora actinobacteria isolated from great barrier reef marine sponges. *Appl. Microbiol. Biotechnol.* 97, 3097–3108. doi: 10.1007/s00253-012-4479-0

Ostle, C., Thompson, R. C., Broughton, D., Gregory, L., Wootton, M., and Johns, D. G. (2019). The rise in ocean plastics evidenced from a 60-year time series. *Nat. Commun.* 10:1622. doi: 10.1038/s41467-019-09506-1

Plastic Europe (2018). *An Analysis of European Plastics Production. Demand and Waste Data*. Madrid: Plastic Europe.

Prabhat, S., Bhattacharyya, S., Vishal, V., Kalyan, R. K., Vijai, K., Pandey, K. N., et al. (2013). Studies on isolation and identification of active microorganisms during degradation of polyethylene/starch film. *Int. Res. J. Environ. Sci.* 2, 83–85.

Pramila, R. (2012). *Brevibacillus Parabrevis*, *Acinetobacter Baumannii* and *Pseudomonas* Citronellolis – Potential Candidates for Biodegradation of Low Density Polyethylene (LDPE). *J. Bacteriol. Res.* 4, 9–14. doi: 10.5897/jbr12.003

Raaman, N., Rajitha, N., Jayshree, A., and Jegadeesh, R. (2012). Biodegradation of Plastic by *Aspergillus* Spp. isolated from polythene polluted sites around chennai. *J. Acad. Ind. Res.* 1, 313–316.

Rahimi, A. R., and Garciá, J. M. (2017). Chemical recycling of waste plastics for new materials production. *Nat. Rev. Chem.* 1:46. doi: 10.1038/s41570-017-0046

Ru, J., Huo, Y., and Yang, Y. (2020). Microbial degradation and valorization of plastic wastes. *Front. Microbiol.* 11:442. doi: 10.3389/fmicb.2020.00442

Shah, A. A., Hasan, F., Hameed, A., and Ahmed, S. (2008). Biological degradation of plastics: A comprehensive review. *Biotechnol. Adv.* 26, 246–265. doi: 10.1016/j.biotechadv.2007.12.005

Shah, Z., Gulzar, M., Hasan, F., and Ali Shah, A. (2016). Degradation of polyester polyurethane by an indigenously developed consortium of *Pseudomonas* and *Bacillus* species isolated from soil. *Polymer Degrad. Stabil.* 134, 349–356. doi: 10.1016/j.polymdegradstab.2016.11.003

Siddique, S., Syed, Q., Adnan, A., and Qureshi, F. A. (2014). Isolation, characterization and selection of avermectin-producing Streptomyces avermitilis strains from soil samples. *Jundishapur J. Microbiol.* 7, 1–7. doi: 10.5812/jjm.10366

Skariyachan, S., Taskeen, N., Kishore, A. P., Krishna, B. V., and Naidu, G. (2021). Novel Consortia of *Enterobacter* and *Pseudomonas* Formulated from cow dung exhibited enhanced biodegradation of polyethylene and polypropylene. *J. Environ. Manage.* 284:112030. doi: 10.1016/j.jenvman.2021.112030

Sowmya, H. V., Ramalingappa, B., Nayanashree, G., Thippeswamy, B., and Krishnappa, M. (2015). Polyethylene degradation by fungal consortium. *Int. J. Environ. Res.* 9, 823–830.

Tachibana, K., Hashimoto, K., Yoshikawa, M., and Okawa, H. (2010). Isolation and characterization of microorganisms degrading nylon 4 in the composted soil. *Polymer Degrad. Stabil.* 95, 912–917. doi: 10.1016/j.polymdegradstab.2010.03.031

Usha, R., Sangeetha, T., and Palaniswamy, M. (2011). Screening of polyethylene degrading microorganisms from garbage soil. *Libyan Agric. Res. Center J. Int.* 2, 200–204.

Volke-Sepulveda, T., Saucedo-Castaneda, G., Gutierrez-Rojas, M., Manzur, A., and Favela-Torres, E. (2002). Thermally treated low density polyethylene biodegradation by *Penicillium pinophilum* and *Aspergillus niger*. *J. Appl. Polymer Sci.* 83, 305–314. doi: 10.1002/app.2245

Webb, S., Ruffell, H., Marsden, I., Pantos, O., and Gaw, S. (2019). Microplastics in the New Zealand Green Lipped Mussel *Perna canaliculus*. *Mar. Pollut. Bull.* 149:110641. doi: 10.1016/j.marpolbul.2019.110641

Zalasiewicz, J., Waters, C. N., Ivar do Sul, J., Corcoran, P. L., Barnosky, A. D., Cearreta, A., et al. (2016). The geological cycle of plastics and their use as a stratigraphic indicator of the anthropocene. *Anthropocene* 13, 4–17. doi: 10.1016/j.ancene.2016.01.002

frontiers | Frontiers in Environmental Science

TYPE Original Research
PUBLISHED 13 June 2023
DOI 10.3389/fenvs.2023.1184257

OPEN ACCESS

EDITED BY
Vishal Tripathi,
Graphic Era University, India

REVIEWED BY
Jong-Rok Jeon,
Gyeongsang National University, Republic of Korea
Xiaojia He,
Chemical Insights Research Institute, United States

*CORRESPONDENCE
Katsutoshi Hori,
khori@chembio.nagoya-u.ac.jp

RECEIVED 11 March 2023
ACCEPTED 31 May 2023
PUBLISHED 13 June 2023

CITATION
Takahashi S, Taguchi F and Hori K (2023), Contribution of the Fenton reaction to the degradation of carbon nanotubes by enzymes.
Front. Environ. Sci. 11:1184257.
doi: 10.3389/fenvs.2023.1184257

Contribution of the Fenton reaction to the degradation of carbon nanotubes by enzymes

Seira Takahashi, Fumiko Taguchi and Katsutoshi Hori*

Department of Biomolecular Engineering, Graduate School of Engineering, Nagoya University, Nagoya, Japan

The widespread use of carbon nanotubes (CNTs) has raised concerns about the human health and ecological effects of CNTs released into the environment. Bacteria play an important role in bioremediation and waste treatment, and their enzymes are mostly responsible for the degradation of contaminants. However, there are still only a few reports about the bacterial degradation of CNTs, and evidence showing the involvement of bacterial enzymes in CNT degradation with their mechanisms has never been reported. The purpose of this study is to clarify whether CNTs can be degraded by bacterial enzymes. In this study, the degradation of oxidized (carboxylated) single-walled CNTs (O-SWCNTs) by mt2DyP, a dye-decolorizing peroxidase of *Pseudomonas putida* mt-2, a common soil bacterium, was investigated. After incubation of O-SWCNTs with recombinant mt2DyP and its substrate H_2O_2 for 30 d, the optical absorbance and Raman spectra revealed the degradation of O-SWCNTs. However, inactivation of the enzyme was observed within 60 min of the start of incubation, suggesting that the degradation of O-SWCNTs occurred nonenzymatically. The inactivation of mt2DyP was accompanied by the release of iron, the active center metal, and degradation of O-SWCNTs was significantly inhibited in the presence of diethylenetriamine pentaacetic acid, a chelating agent, indicating that O-SWCNTs were degraded by the Fenton reaction with iron released from mt2DyP and H_2O_2. The same phenomenon was observed with P450, which is also a heme enzyme. Furthermore, we investigated the contribution of the Fenton reaction to the O-SWCNT degradation by horseradish peroxidase (HRP), which was reported to enzymatically and rapidly degrade O-SWCNTs. Our results revealed that the degradation of O-SWCNTs in the presence of HRP is also mainly due to the Fenton reaction, with negligible enzymatic degradation. This contradicts the report showing enzymatic degradation of O-SWCNTs by HRP but supports the subsequent report quantitatively showing very slow transformation of O-SWCNTs by HRP. The current results emphasize that the Fenton reaction, which has received little attention in CNT degradation by heme enzymes, must be taken into consideration and will contribute to the development of a simple disposal method for CNTs, utilizing the Fenton reaction with bacteria/bacterial enzymes and H_2O_2.

KEYWORDS

carbon nanotubes, degradation, heme enzyme, Fenton reaction, bacteria

1 Introduction

Carbon nanotubes (CNTs) have been applied in a wide range of fields, such as electronics (Xiang et al., 2018), energy storage (Yang et al., 2019b; Chen et al., 2021), drug delivery (Ho et al., 2021), biosensor devices (Sireesha et al., 2018; Anzar et al., 2020; Zhao et al., 2021), and water treatment (Dong et al., 2021), owing to their excellent mechanical strength, optical properties, and electrical and thermal conductivity (Dresselhaus et al., 2004; Byrne et al., 2018). Among CNTs, single-walled CNTs (SWCNTs) have particularly excellent physical properties for application. The technology for highly efficient production of SWCNTs has been established in recent years, and the problem of high production costs has been solved (Hata et al., 2004; Almarasy et al., 2021). This will lead to the expansion of the CNT market and the development of a wider range of applications. With the use of CNTs becoming more widespread, the amount of CNTs released into the environment is expected to increase, either accidentally or as waste, raising concerns about their impact on human health and ecosystems. Recent studies have reported that some CNTs exhibit toxicity to plants, animals, and microorganisms (Chen et al., 2015b; Kumarathasan et al., 2015; Hatami, 2017; Mendonca et al., 2017; Chen et al., 2018).

To date, knowledge of the biodegradation and remediation of CNTs is lacking, although many efforts have been made to understand these processes. Since Allen et al. reported the degradation of oxidized (carboxylated) SWCNTs (O-SWCNTs), which are functionalized SWCNTs, by horseradish peroxidase (HRP) (Allen et al., 2008; Allen et al., 2009), the biodegradation of CNTs by incubation with heme enzymes from several organisms, such as human myeloperoxidase (Kagan et al., 2010), human eosinophil peroxidase (Andon et al., 2013), bovine lactoperoxidase (Bhattacharya et al., 2015), fungal manganese peroxidase (Zhang et al., 2014) and lignin peroxidase (Chandrasekaran et al., 2014) in the presence of their oxidizing substrate H_2O_2, has been reported. However, Flores-Carvantes et al. were the first to quantitatively investigate the enzymatic degradation of CNTs and estimated a half-life of 80 years for CNT degradation by HRP (Flores-Cervantes et al., 2014), which is significantly different from a previous report (Allen et al., 2009). Quantitative studies and reproducibility have not yet been conducted for enzymes other than HRP. There is still much, that is, not well understood about the enzymatic degradation of CNTs.

Bacteria have an immense and diverse metabolic system and play an important role in environmental bioremediation and waste treatment. However, there are still only a few reports of bacterial degradation of CNTs. The degradation of CNTs by bacterial cometabolism with additional carbon sources has been reported, but the mechanism remains to be elucidated (Zhang et al., 2013; You et al., 2017). *Labrys* sp. WJW was shown to utilize carbon nanomaterials, including CNTs, as the sole carbon source for growth via an extracellular biogenic Fenton-like reaction using siderophores that are secreted only under iron-deficient conditions (Wang et al., 2020). Though bacterial enzymes significantly contribute to the bacterial treatment of contaminants, their involvement in CNT degradation has not yet been confirmed. Elucidation of the function of bacterial enzymes in the degradation of CNTs may lead to more rapid remediation and waste treatment of CNTs under a wide range of conditions using bacteria.

Fungal enzymes involved in the degradation of lignin, a huge persistent organic compound, have attracted attention for their potential to degrade other persistent organic compounds (Kadri et al., 2017; Singh et al., 2021), including CNTs (Chandrasekaran et al., 2014; Zhang et al., 2014). However, white-rot fungi that secrete lignin-degrading enzymes have a limited habitat and are more difficult to apply to waste treatment than bacteria. The purpose of this study is to clarify the degradation behavior of CNTs by bacterial heme enzymes. We focused on dye-decolorizing peroxidases (DyPs), which are widely found mainly in bacteria and have been studied for their ability to degrade lignin (Singh et al., 2013; Colpa et al., 2014; Rahmanpour and Bugg, 2015; Yang et al., 2018). Thus, we investigated the degradation of O-SWCNTs by DyP from *Pseudomonas putida* mt-2 (mt2DyP), a common soil bacterium reported to have high lignin degradation capacity (Bugg et al., 2011). O-SWCNTs were degraded by incubation with mt2DyP. However, the degradation of O-SWCNTs proceeded nonenzymatically via the Fenton reaction with iron released from the enzyme. The same phenomenon was observed with other heme enzymes. The results of this study provide insight that will lead to the accurate evaluation of CNT biodegradation and the development of new remediation and/or waste treatment methods.

2 Materials and methods

2.1 Materials

Dispersion of O-SWCNTs (Product No. ZEONANOR-SG101) was produced and provided by Zeon Nanotechnology Co., Ltd. (Japan). 2SYN medium consisted of 2% glucose, 4% soytone, 0.5% yeast extract, 0.015% $CaCl_2 \cdot 2H_2O$, and 50 μg/ml neomycin. The pH of the 2SYN medium was adjusted to 7.2 with NaOH and H_2SO_4. Hemin chloride, 30% H_2O_2, diethylenetriaminepentaacetic acid (DTPA), 2,2′-azino-bis(3-ethylthiazoline-6-sulfonate) (ABTS), ferrozine, methanol, and acetonitrile were purchased from FUJIFILM Wako Pure Chemical Co., Ltd. (Japan). 3′-(p-hydroxyphenyl) fluorescein (HPF) was purchased from Goryo Chemical, Inc. (Japan). Lyophilized HRP type VI, the same enzyme used by Allen et al. (2009), was purchased from Sigma-Aldrich, Ltd. (United States).

2.2 Recombinant protein production

To produce recombinant enzymes, the *Brevibacillus* secretory expression system (TaKaRa Bio Inc., Japan) was used according to the manufacturer's instructions. First, for the cloning of DyP and cytochrome P450 homologs from *Pseudomonas putida* mt-2 (mt2DyP and mt2P450, respectively), polymerase chain reaction (PCR) primers were designed on the basis of the DNA sequence of *P. putida* KT2440. They consisted of a sequence (20 bases) amplifying a target gene and a 15-base 5′ overhang that was identical to the pBIC3 expression vector (Table 1). Chromosomal DNA from *P. putida* mt-2 was extracted and purified using a commercial kit (Cica Geneus DNA extraction reagent, Kanto Chemical Co. Inc., Japan)

TABLE 1 Primer sets for constructs.

Target genes	Primer sets
mt2DyP	Forward: 5′-GATGACGATGACAAAATGCCGTTCCAGCAAGGTCT-3′
	Reverse: 5′-CATCCTGTTAAGCTTTCAGGCCCGCAGCAAGGGGC-3′
mt2P450	Forward: 5′-GATGACGATGACAAAATGTCCGAAACCATTCGTGT-3′
	Reverse: 5′-CATCCTGTTAAGCTTACACGAATGGTTTCGGACAT-3′

for PCR as a template. The resulting PCR fragments were mixed with the plasmid vector and competent cells of *Brevibacillus choshinensis* to obtain transformants. Transformed cells were grown in 2SYN medium supplemented with 30 μM hemin chloride for 48 h at 30°C, and recombinant protein with an N-terminal His6-tag was extracellularly produced in the culture supernatant. After removing the cells by centrifugation, the culture supernatant was applied onto a Ni Sepharose column (Ni-Sepharose 6 Fast Flow column, GE Healthcare, Sweden), which was then washed with binding buffer (20 mM sodium phosphate, 500 mM NaCl, 20 mM imidazole, pH 7.4). The recombinant protein was eluted with elution buffer (20 mM sodium phosphate, 500 mM NaCl, 500 mM imidazole, pH 7.4). The obtained eluate was subjected to ultrafiltration using a centrifugal concentrator (Vivaspin Turbo 15, 10,000 MWCO, Sartorius, Germany) to remove imidazole and exchange buffer into ultrapure water (resistivity at 25°C, >18 MΩ cm; TOC, <5 ppb). The recombinant protein was further purified by gel filtration using an AKTA purifier system (GE Healthcare Bio-Sciences AB, Sweden) equipped with a column (Superdex G-75, Pharmacia, Sweden), as needed. The protein sample was loaded onto the gel filtration column pre-equilibrated with 20 mM phosphate buffer (pH 7.0) and eluted with the same buffer at a flow rate of 2.0 ml/min. The fractions containing the enzyme were collected, and the buffer was exchanged by ultrafiltration. All abovementioned purification steps were performed at 4°C, and the effluent from the column was monitored by absorbance at 280 nm. The protein purity was assessed by SDS-PAGE on a 12.5% polyacrylamide gel. The concentration of protein was measured with a bicinchoninic acid protein assay kit (Pierce, Thermo Fisher Scientific, United States). Purified enzymes were stored at −30°C until further use.

2.3 Holoenzyme reconstitution

Holoenzymes were reconstituted by incubating purified enzyme in an aqueous solution of hemin chloride at twice the molar concentration of the enzyme for 2 h at room temperature (25°C). The excess hemin was removed by passing the mixture through a Ni Sepharose 6 Fast Flow column, and imidazole in the eluate was removed in the same manner as described above. The spectral characteristics of holoenzymes were obtained using a UV-Vis spectrophotometer (Cary 60 UV-Vis, Agilent Technologies, United States). Purified and reconstituted enzymes were stored at −30°C until further use.

2.4 Incubation of O-SWCNTs with enzymes

The enzyme was added to the O-SWCNT dispersion diluted with ultrapure water and incubated for 24 h at 4°C in the dark; thereafter, phosphate-buffered saline (PBS) and H_2O_2 were added to initiate the reaction. For incubation with mt2DyP or mt2P450, the 5 ml reaction mixture contained 30 μg/ml O-SWCNTs, 4 μM enzyme, and 1, 10, or 100 mM H_2O_2 in PBS (adjusted to pH 7.0) and was incubated at 37°C in the dark for 30 d, with a daily supply of each concentration of H_2O_2 chaser using a pipette. DTPA was added to the reaction mixture at a final concentration of 200 μM when its inhibition for CNT degradation was investigated. For incubation with HRP, the 5 ml reaction mixture contained the same concentrations of O-SWCNTs (30 μg/ml) and the enzyme (4 μM = 160 μg/ml) as above in PBS (adjusted to pH 6.0), and the reaction was initiated with 40 μM H_2O_2 and incubated for 30 d at 25°C in the dark with a daily supply of 1 μM H_2O_2 chaser using a pipette (Allen et al., 2009; Flores-Cervantes et al., 2014). HRP stock solution was prepared by dissolving lyophilized powder of HRP into ultrapure water at 5 mg/ml. During the incubation, samples were taken periodically, an equal volume of 5% sodium dodecyl sulfate (SDS) was added to disperse the O-SWCNT aggregate, sonicated for 10 min, and the absorbance at 750 nm (A_{750}) was measured to calculate the concentration of O-SWCNTs from a calibration curve prepared using stocks of O-SWCNT dispersions. It was confirmed that the 10 min sonication itself did not alter the A_{750} and physical property (Raman spectrum) of O-SWCNTs (Supplementary Figure S1). Incubation of O-SWCNTs with free iron was performed under the same conditions as for incubation with enzymes, except that the enzyme was replaced by the same molar concentration of $FeCl_3$.

The release of free iron from holoenzymes during incubation with O-SWCNTs was measured colorimetrically using ferrozine, following a previous method with slight modifications (Paumann-Page et al., 2013). Briefly, a 1 ml sample taken from the incubated mixture was lyophilized and resuspended in 60 μl of ultrapure water. An equal volume (60 μl) of 1.13 mM ascorbic acid solution in 0.2 M HCl was added and left for 5 min at room temperature. The protein was then precipitated by adding 60 μl of 11.3% trichloroacetic acid, and the samples were left on ice for 5 min followed by a short fast spin at 4°C. To the supernatant, 72 μl of 10% ammonium acetate was added, followed by 18 μl of 6.1 mM ferrozine, and the absorbance at 563 nm (A_{563}) was measured after 5 min at room temperature (ε = 28,000 $M^{-1}cm^{-1}$). Hydroxyl radical (·OH) concentration of O-SWCNT suspension was measured using a fluorescent probe (HPF, 5 μM) (Hessler et al., 2012; Wang et al., 2020).

2.5 Measurement of enzyme activity

The enzyme activity during incubation with O-SWCNTs was determined by the initial velocity assay using ABTS as a substrate. The reaction was initiated by adding 10 µl of 100 mM H_2O_2 to 990 µl of the reaction buffer containing 15 µl of 30 mM ABTS and the sample solution (25 µl for mt2DyP/mt2P450 or 5 µl for HRP). As the buffer solution, acetate buffer of the optimum pH for each enzyme was used for mt2DyP or mt2P450, and PBS (adjusted to pH 6.0) was used for HRP. The absorbance of oxidized ABTS at 413 nm (A_{413}) was continuously monitored for 30 s after the start of the reaction at room temperature (25 °C), and the enzyme activity was calculated from the slope of the linear approximation of the absorbance change. When the optimum pH of enzymes was determined, the enzyme activity for ABTS oxidation was measured in a Britton-Robinson buffer (50 mM phosphoric acid, 50 mM boric acid, and 50 mM acetic acid mixed with NaOH to the desired pH in the range of 3–9) containing 0.1 µM of purified enzyme.

To validate enzyme activity assays, the activity of HRP was measured using Amplex Red or ABTS as substrates, following the method employed in previous studies by Allen et al. (2009) and by Flores-Cervantes et al. (2014) or in this study. To follow the previous studies, we performed the assay under conditions described in their papers, including the concentrations of H_2O_2 and Amplex Red, the buffer used, and temperature. HRP solutions of various concentrations (0.6, 1.2, 2.4, and 4 µM) were prepared by dissolving lyophilized HRP into PBS (pH 6.0). Instead of sample solution, 500 µl of the HRP solution of various concentrations (or PBS for 0 µM) was added to a mixture of 468 µl of ultrapure water, 30 µl of 800 µM H_2O_2, and 2 µl of 10 mM Amplex Red (dissolved in dimethyl sulfoxide). Therefore, the final concentrations of HRP in this assay ranged from 0 to 2 µM. The mixture was gently mixed for 5 min at room temperature, and the UV-vis spectrum (300–700 nm) of oxidized Amplex Red was acquired. The relative activity of each HRP solution was determined from the absorbance at 570 nm (A_{570}) of the UV-vis spectrum obtained. To validate our assay method in this study, the HRP activity was assayed using ABTS as a substrate under the conditions described above. Instead of sample solution, 5 µL of the HRP solution prepared above (0.6, 1.2, 2.4, or 4 µM) or PBS (for 0 µM) was added to 995 µl of the reaction mixture so that its final concentration ranged from 0 to 20 nM. The enzyme activity was determined by the initial velocity assay described above and the UV-vis spectrum (350–700 nm) of oxidized ABTS was also acquired 30 s after the start of the reaction. The activity of HRP was also assayed using Amplex Red instead of ABTS as a substrate, although basically following the method in this study. The reaction was initiated by adding 10 µl of 100 mM H_2O_2 to a mixture of 987 µl of PBS, 2 µl of 10 mM Amplex Red, and 1 µl of HRP solution of various concentrations (0.6, 1.2, 2.4, or 4 µM), and A_{570} was monitored at room temperature. HRP activity was determined from the initial velocity assay at various final concentrations of HRP (from 0 to 4 nM). The UV-vis spectra of oxidized ABTS at different HRP concentrations were also acquired 30 s after the start of the reaction.

2.6 Instrumental analyses

For Raman spectroscopy, samples were subjected to ultracentrifugation at 28000 rpm for 30 min, the supernatant was discarded by decantation, and the pellet was resuspended in methanol through sonication. Specimens were prepared by drop-casting approximately 100 µl of the samples on carbon tape or glass microscope slide and drying. All spectra were collected on a micro-Raman spectrometer (inVia Reflex, Renishaw, UK) using an excitation wavelength of 532 nm. The samples were scanned from 1000 to 1900 cm^{-1} to visualize the D-band and G-band of O-SWCNTs. Spectra were collected with a 10 s exposure time and averaged across 5 scans per sample. Samples analyzed by Raman spectroscopy were also used for X-ray photoelectron spectroscopy (XPS) (ESCALAB250, VG Scientific, UK). XPS was performed using monochromatized Al Kα radiation ($h\nu$= 1486.6 eV) as an X-ray source.

To analyze the degradation products of O-SWCNTs using high-performance liquid chromatography (HPLC), 3-ml samples taken from the incubated O-SWCNT suspension were lyophilized, resuspended in 200 µL methanol by vortexing for 1 min, and centrifuged again at 10000 rpm for 1 min. The supernatant was filtered through a 0.22 µm membrane filter (Millex-GV, Millipore, Ireland), and 20 µl of the filtrate was injected into an HPLC system (LC-20AT, Shimadzu, Japan) equipped with a reverse-phase C18 column (InertSustain C18, 4.6 × 150 mm, 5 µm, GL sciences, Japan) and a UV detector (SPD-10A VP, Shimadzu, Japan). The mobile phase, acetonitrile solution with a linear gradient from 0% to 70% for the initial 5 min followed by 70% isocratic elution, flowed at 1 mL/min. The detection wavelength was set to 254 nm based on the compounds identified as O-SWCNT degradation products in a previous study (Allen et al., 2009). In liquid chromatography-mass spectrometry (LC-MS), the column and separation conditions followed HPLC analysis. Approximately 10 µl of the sample was injected into the HPLC (1200 Series, Agilent, United States) tandem mass spectrometer (Compact, Bruker Daltonics, United States) and analyzed for positive ions using electrospray mass spectrometry.

2.7 Statistical analysis

The standard errors (SE) were calculated from three independent experiments. The quantitative data are expressed as the mean with SE (mean ± SE). Details about each figure are provided in the legend. Significance was calculated by Student's *t*-test, and 95% confidence intervals (Cls) and *p* values of 0.05 or less were considered to indicate a statistically significant correlation or difference.

3 Results

3.1 O-SWCNT degradation during incubation in the presence of DyP from *Pseudomonas putida* mt-2

First, we attempted to clone the gene encoding DyP of *P. putida* mt-2. Although the whole genome of this strain was not revealed, we found a gene homologous to E-type DyPs (PP_3248 gene; accession number, NC_002947.4) in the genome of *P. putida* KT2440, the strain that lost the plasmid from the strain mt-2 (Regenhardt et al., 2002; Singh and Eltis, 2015). Utilizing this information for PCR, we

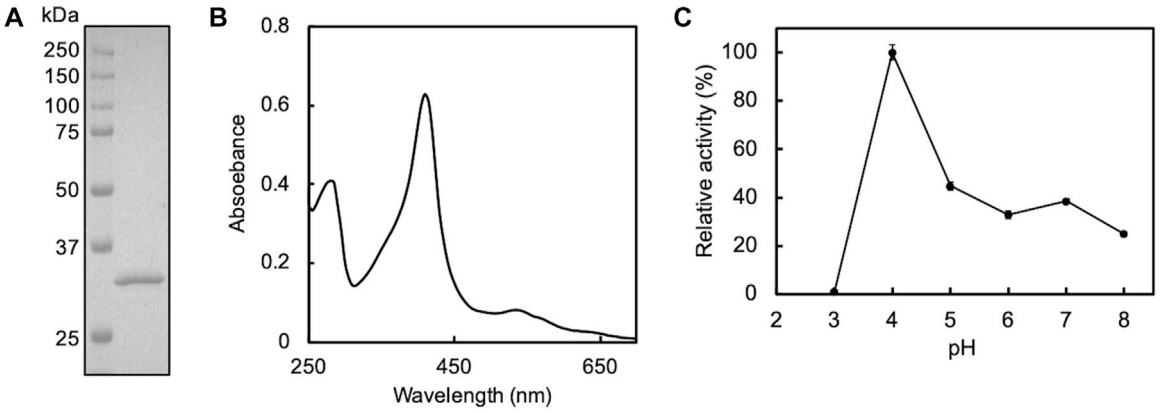

FIGURE 1
SDS-PAGE **(A)** and UV-Vis spectrum **(B)** of purified mt2DyP and the pH dependence of the enzyme activity on the ABTS substrate **(C)**. Error bars indicate the SE from three independent assays.

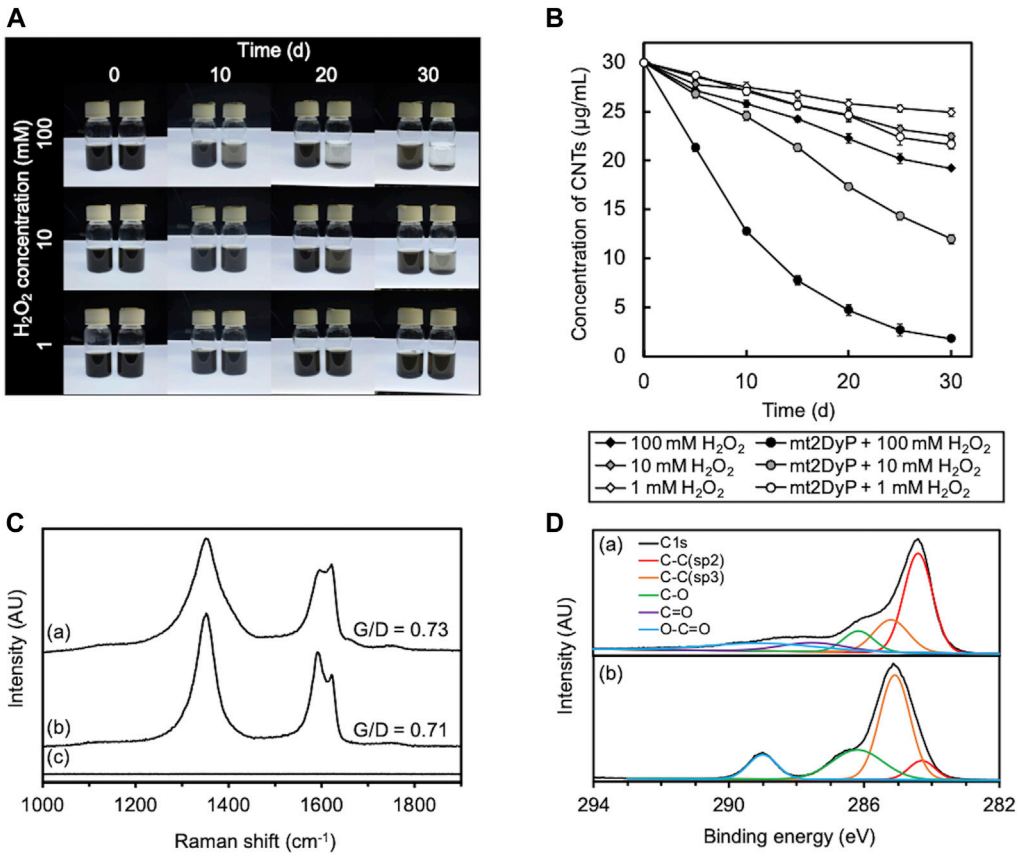

FIGURE 2
Degradation of O-SWCNTs during incubation at 37°C in the presence of mt2DyP under different H_2O_2 concentration conditions (1, 10, and 100 mM). **(A)** Photographs of the appearance of the O-SWCNT suspensions during incubation with (right) and without (left) mt2DyP at different time points (0, 10, 20, and 30 d). **(B)** Time courses of the O-SWCNT concentrations in suspensions incubated with and without mt2DyP. Error bars indicate the SE from three independent incubations. **(C)** Raman spectra (excitation wavelength, 532 nm) of untreated O-SWCNTs **(A)** and O-SWCNTs incubated with mt2DyP at an H_2O_2 concentration of 100 mM for 25 d **(B)** and 30 d **(C)**. AU, arbitrary units. **(D)** XPS spectra of untreated O-SWCNTs **(A)** and O-SWCNTs incubated with mt2DyP at an H_2O_2 concentration of 100 mM for 25 d **(B)**. AU, arbitrary units.

successfully obtained the amplicon of mt2DyP, whose DNA sequence was completely identical to that of the DyP gene of strain KT2440. The cloned DNA was used for the production of the recombinant protein by *B. choshinensis*. The secreted enzyme was purified from the culture supernatant and subjected to SDS-PAGE to confirm its isolation and purity in the sample. As a result, a band was detected on the gel at ~32 kDa, corresponding to the molecular mass of mt2DyP with a 6 × His tag (Figure 1A). The reconstituted mt2DyP exhibited an absorbance maximum at 410 nm, a Soret band derived from heme, with a Reinheit Zahl (RZ) value (A_{410}/A_{280} ratio), an indicator for heme insertion, of 1.5 (Figure 1B), which was comparable to those of DyP from other bacteria (Chen et al., 2015a; Rahmanpour et al., 2016; Habib et al., 2019). The oxidation activity of mt2DyP for ABTS, a standard substrate of peroxidase, was examined at various pH values. This revealed that the enzyme activity was the highest at pH 4 (Figure 1C), which was similar to the optimum pH values of DyPs previously reported (Roberts et al., 2011; Li et al., 2012; Santos et al., 2014; Chen et al., 2015a). Then, CNTs were incubated in the presence of mt2DyP at pH 7, which is close to normal environmental conditions, to obtain useful information for predicting the environmental fate of CNTs, even though it is different from the optimum conditions.

A photograph of the appearance of the O-SWCNT suspensions during incubation in the presence of mt2DyP under different H_2O_2 concentrations (1, 10, 100 mM) is shown in Figure 2A. The black color of the O-SWCNTs decreased with the passage of time in the suspensions with 10 and 100 mM H_2O_2. Because biologically derived materials have no absorbance near 750 nm, the concentration of O-SWCNTs can be obtained by measuring A_{750} (Yang et al., 2019a) after adding SDS to remove proteins adsorbed on O-SWCNTs and dispersing the CNT aggregate. The O-SWCNT concentrations calculated from the A_{750} values of these samples are shown in Figure 2B The degradation of O-SWCNTs was more pronounced at higher H_2O_2 concentrations. The measurement of A_{750} also revealed that the O-SWCNTs degraded at 1 mM H_2O_2, although there was little change in appearance observed over time.

The degradation of O-SWCNTs was also confirmed by Raman spectroscopy. The G-band (graphite) peak at 1591 cm^{-1} and the D-band (disordered) peak at ~1350 cm^{-1} that were present in the Raman spectra of pristine O-SWCNTs are characteristic Raman bands of graphitic carbon materials (Figure 2C) (Allen et al., 2008; Flores-Cervantes et al., 2014; You et al., 2017). The ratio of G-band to D-band (G/D) decreased with incubation with mt2DyP, which was consistent with the trend observed during CNT degradation in previous studies, and suggested an increase in O-SWCNT surface defects and amorphous carbon (Andon et al., 2013; Chandrasekaran et al., 2014; You et al., 2017; Wang et al., 2020). After incubation with mt2DyP for 30 d, both peaks disappeared, indicating the disappearance of O-SWCNTs. XPS analysis was performed to investigate in more detail the changes in the chemical composition of O-SWCNTs during incubation with mt2DyP. The main peak of C1s spectrum shifted to the lower binding energy because the peak attributed to sp2 C-C identified in pristine O-SWCNTs decreased and that attributed to sp3 C-C increased during incubation with mt2DyP (Figure 2D). In addition, oxygen functional groups (C-O and O-C=O) increased after the incubation. These results suggest that the graphite frame in O-SWCNTs was oxidized, supporting the above interpretation obtained from the Raman spectral change.

Subsequently, the degradation products of O-SWCNTs that were produced by incubation with mt2DyP were analyzed by HPLC. After 7 d of incubation, a peak unobserved at the beginning of incubation appeared at a retention time of 3.3 min, which was expected to be the peak of an O-SWCNT degradation product (Figures 3A, B). To identify this degradation product, the samples were subjected to LC-MS. A mass to charge (m/z) value of 132.1 was observed only in the sample after incubation with mt2DyP (Figures 3C, D), which corresponds to cinnamaldehyde, one of the previously reported degradation products of O-SWCNTs and pristine SWCNTs by HRP or Fenton reaction (Allen et al., 2009).

3.2 Degradation mechanism of O-SWCNTs by incubation in the presence of mt2DyP

To determine whether the enzyme truly remained active during the degradation of the CNTs for as long as a month, the enzymatic activity to oxidize ABTS of mt2DyP during incubation with O-SWCNTs was measured over time. Surprisingly, at every H_2O_2 concentration, mt2DyP was inactivated within 1 h after the start of the incubation (Figure 4A). This implies that degradation of O-SWCNTs proceeded in the presence of mt2DyP, even after the enzyme was inactivated. In the absence of H_2O_2, the activity of mt2DyP was largely maintained, indicating that H_2O_2 caused inactivation of the enzyme. In fact, heme enzymes are known to be inactivated by heme degradation by H_2O_2, releasing free iron (Villegas et al., 2000; Valderrama et al., 2002; Nagababu and Rifkind, 2004; Albertolle and Guengerich, 2018).

We supposed that the degradation of O-SWCNTs may have been caused by the Fenton reaction with iron released by the inactivation of mt2DyP. Measurement of the concentration of free iron in the samples revealed its increase during the incubation along with the inactivation of mt2DyP (Figure 4B). To confirm that free iron released from the enzyme mainly contributed to the degradation of O-SWCNTs via the Fenton reaction, incubation with mt2DyP was performed in the presence of DTPA, a chelating agent. The percentage of O-SWCNTs remaining after 30 d of incubation in the presence or absence of DTPA is shown in Figure 5. The degradation of O-SWCNTs was significantly inhibited by the addition of DTPA. The formation of ·OH, the main product of the Fenton reaction, was also detected in the samples (Supplementary Figure S2). In addition, when the enzyme was replaced by free iron at the same stoichiometric concentration as that of mt2DyP in the incubation, the rate of O-SWCNT degradation was similar to that in the incubation with the enzyme (Supplementary Figure S1). These results confirmed our hypothesis that O-SWCNTs were degraded by the Fenton reaction caused by iron released from mt2DyP's heme. This suggested that the same phenomenon may occur in the presence of other heme enzymes.

3.3 Degradation of O-SWCNTs by incubation in the presence of another heme enzyme of *P. putida*

Cytochrome P450, a heme enzyme found in many organisms, including bacteria, was examined as another heme enzyme for

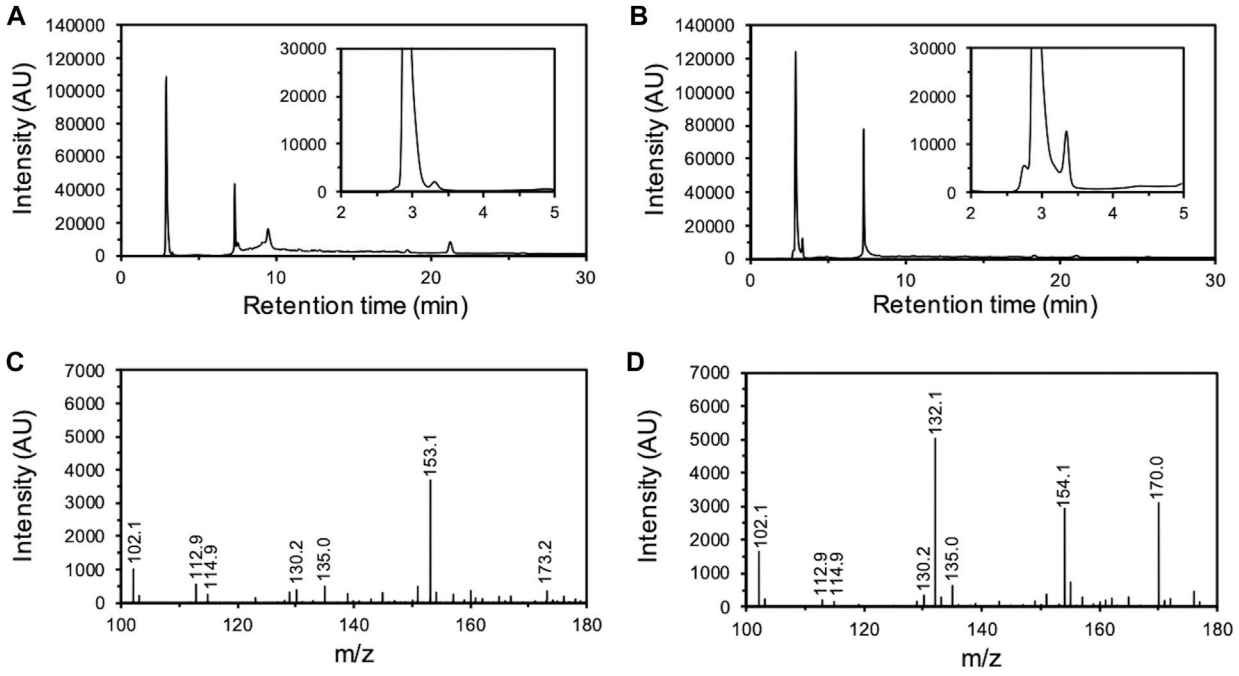

FIGURE 3
Analysis of O-SWCNT degradation products formed by incubation with mt2DyP. HPLC chromatograms of samples after 0 d **(A)** and 7 d **(B)** of incubation. LC-MS spectrum of samples after 0 d **(C)** and 7 d **(D)** of incubation. AU, arbitrary units.

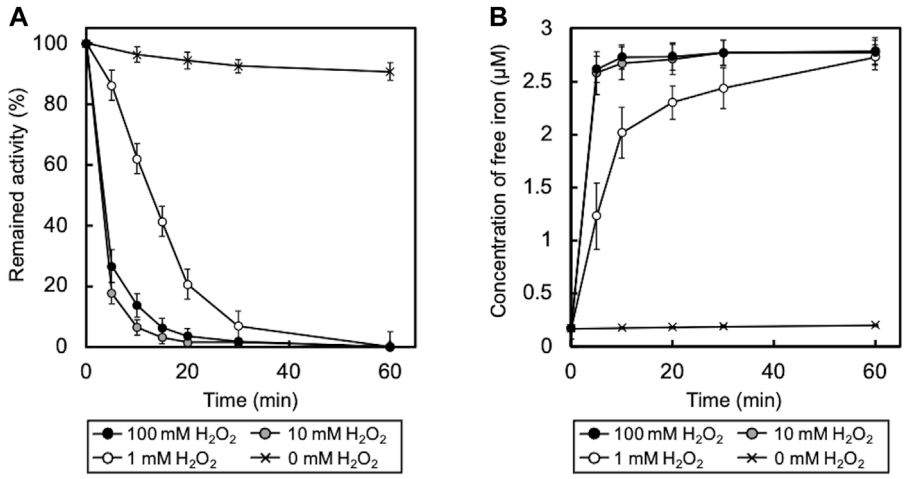

FIGURE 4
(A) Time course of enzyme activity of mt2DyP during incubation with O-SWCNTs. Error bars indicate the SE from three independent incubations. **(B)** Time course of free iron concentration in samples during incubation. Error bars indicate the SE from three independent incubations.

O-SWCNT degradation. We designed PCR primers on the basis of the DNA sequence of the cytochrome P450 gene (PP_1955 gene; accession number, NC_002947.4) on the genome of *P. putida* KT2440 for the cloning of a cytochrome P450 homolog from *P. putida* mt-2, mt2P450, and successfully obtained the amplicon by PCR using chromosomal DNA of mt-2 as a template. The DNA sequence of this amplicon was completely identical to that of the cytochrome P450 gene of strain KT2440, and this cloned DNA was used for recombinant protein production by *B. choshinensis*. On the SDS-PAGE gel of purified mt2P450, a band was detected at ~45 kDa corresponding to the molecular mass of mt2P450 with a 6 × His tag (Supplementary Figure S4A). The reconstituted mt2P450 exhibited an absorbance maximum at 410 nm, similar to mt2DyP, with an RZ value (A_{410}/A_{280} ratio) of 0.4 (Supplementary Figure S4B). Because there are no reports of the RZ value for cytochrome P450, it is impossible to evaluate the RZ value of mt2P450 in comparison with

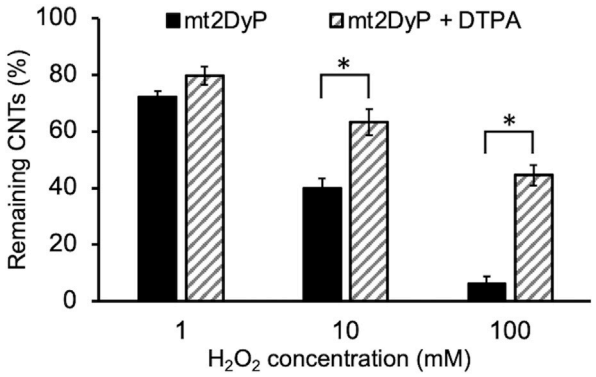

FIGURE 5
Concentration of O-SWCNTs after 30 d of incubation at 37°C with mt2DyP in the presence of DTPA (the initial O-SWCNT concentration is considered to be 100%). Error bars indicate the SE from three independent incubations. *$p < 0.05$ means significantly different (Student's t-test).

others. The ABTS oxidation activity of mt2P450 was highest at pH 5 (Supplementary Figure S4C). As expected, the incubation of O-SWCNTs in the presence of mt2P450 resulted in its degradation. As in the case with mt2DyP, when incubated with mt2P450 in the presence of 10 or 100 mM H_2O_2, the black color of the samples became distinctly transparent over time (Figure 6A). The concentration of O-SWCNTs measured with A_{750} decreased with incubation time, and the decrease was faster with higher H_2O_2 concentrations (Figure 6B). The change in Raman and XPS spectra during incubation in the presence of mt2P450 also showed the same tendency as that in the presence of mt2DyP. The G/D ratio decreased at 25 d of incubation with mt2P450 at 100 mM H_2O_2 in the Raman spectrum, and both the G- and D-band peaks in O-SWCNTs disappeared after 30 d of incubation (Figure 6C). The XPS spectrum showed a decrease in the sp2 C-C peak and an increase in the sp3 C-C peak and oxygen functional group peaks during the incubation with mt2P450 (Figure 6D). HPLC and LC-MS analyses of degradation products of O-SWCNTs by incubation with mt2P450 showed similar peaks to those observed in the case of incubation with mt2DyP (Supplementary Figure S5). The release of free iron accompanied by the inactivation of mt2P450 enzymatic activity and the formation of ·OH during incubation with O-SWCNTs was also observed (Figure 6E; Supplementary Figure S6). In the absence of H_2O_2, the enzyme activity was largely maintained, indicating that H_2O_2 also caused inactivation of mt2P450 (Figure 6E). It was described above that the degradation rates of O-SWCNT were almost identical when mt2P450 was replaced by free iron of the same stoichiometric concentration (Supplementary Figure S3); note that the molar concentrations (4 μM) of mt2P450 and mt2DyP used for incubation with O-SWCNTs were same. These results confirmed that O-SWCNTs were degraded by the Fenton reaction caused by iron released from mt2P450, a heme enzyme other than mt2DyP, inactivated by H_2O_2 during incubation in the presence of H_2O_2.

3.4 Degradation of O-SWCNTs by incubation in the presence of HRP

Most previous studies on the enzymatic degradation of CNTs have been performed without consideration of the Fenton reaction, despite the use of heme enzymes (Allen et al., 2008; Andon et al., 2013; Chandrasekaran et al., 2014; Zhang et al., 2014; Bhattacharya et al., 2015). Therefore, it is unclear whether O-SWCNT degradation in these studies was solely due to enzymatic reactions. To investigate the contribution of the Fenton reaction to the degradation, O-SWCNTs were incubated with HRP under the same experimental conditions as described by Allen et al. (2009), including H_2O_2 concentration (40 μM at the initial and 1 μM/d for the chaser), temperature, and pH; however, the O-SWCNTs used, their concentration, and the enzyme concentration differed (enzyme concentration was higher in this study). No visible reduction in the black color of the O-SWCNT suspension was observed even after 30 d of incubation with HRP (Figure 7A), unlike the results shown in the article by Allen et al. (2009). The measurement of A_{750} revealed that the concentration of O-SWCNTs decreased by 4.6% after 30 d of incubation (Figure 7B). However, the addition of DTPA inhibited the decrease in the O-SWCNT concentration to 1.3%. In addition, more than 80% inactivation of HRP was observed after 10 d of incubation with O-SWCNTs (Figure 7C), accompanied by the release of free iron into the solution (Figure 7D). Even when HRP was replaced by free iron at the same stoichiometric concentration, the degradation rate of O-SWCNTs was almost identical (Supplementary Figure S7). HRP was also not inactivated in the absence of H_2O_2 (Supplementary Figure S8). These results imply that the Fenton reaction by iron released from HRP inactivated by H_2O_2 greatly contributed to the degradation of O-SWCNTs and that enzymatic degradation was negligible.

The rapid inactivation of HRP observed in this study differed from the results of the previous studies by Allen et al. (2009) and by Flores-Cervantes et al. (2014), in which the activity of HRP was maintained for long periods of time. The methods used to measure HRP activity differed between this study and the previous studies. Therefore, we assessed the validity of both methods. To validate the previous assay methods, we measured the oxidation of Amplex Red by HRP at different concentrations, according to the assay conditions described in the previous studies. As a result, the UV-vis spectrum of oxidized Amplex Red was unchanged even when the HRP concentration was changed (Figure 8A). In accordance with the previous studies, the relative activity for Amplex Red oxidation by HRP at different concentrations was determined from A_{570} of the UV-vis spectra. The relative activity was independent of the HRP concentration (Figure 8B), suggesting inaccuracy in the enzyme activity measurements in the previous studies. To validate the assay method used in this study, we also measured the oxidation of ABTS by HRP at different concentrations. As shown in Figures 8C, D, the UV-vis spectrum of oxidized ABTS was changed by the HRP concentration, and the relative activity determined from the slope of the linear approximation of A_{413} change (Fig. S9) depended on the HRP concentration. Thus, it was demonstrated that the HRP activity was accurately measured by the method used in this study.

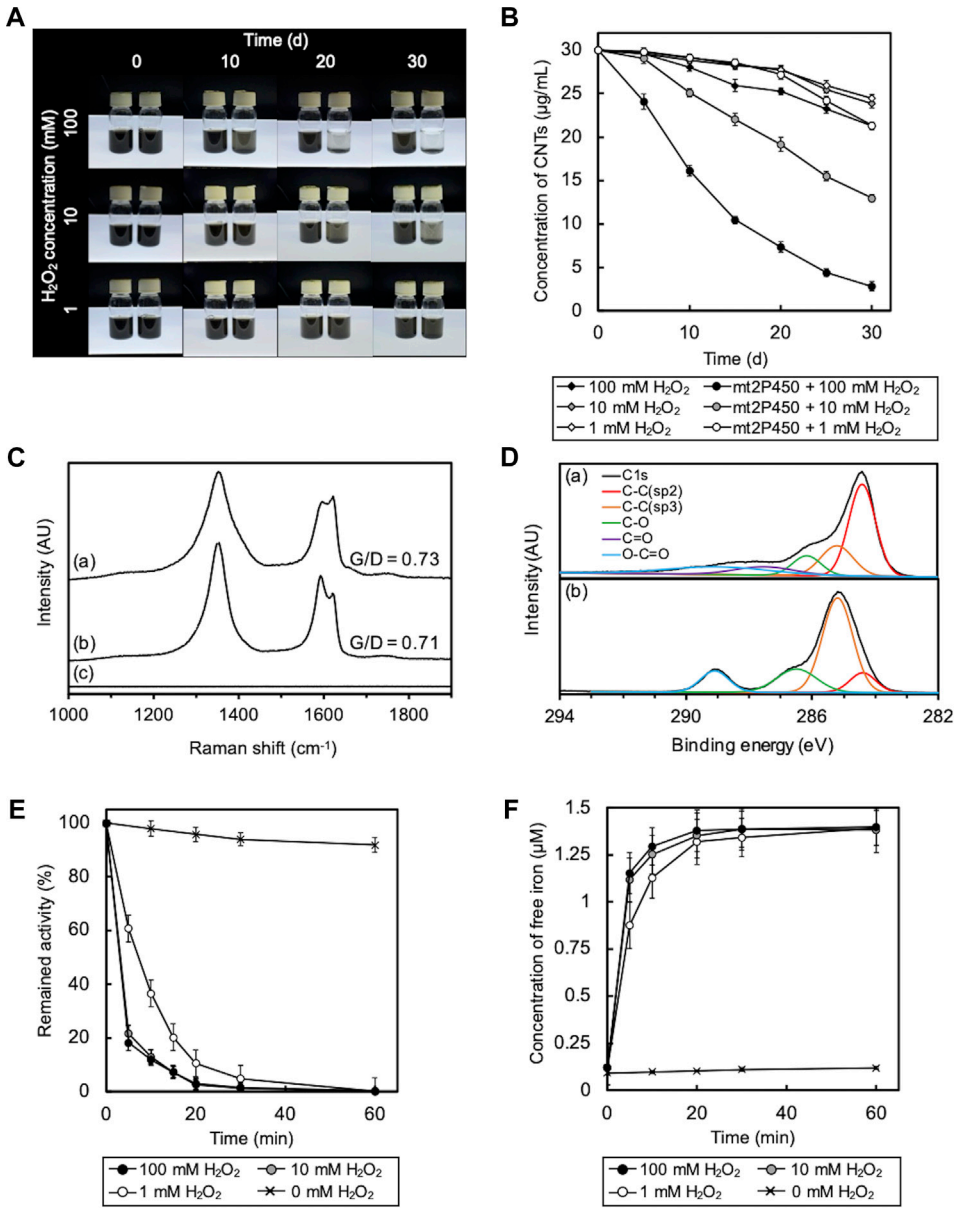

FIGURE 6
Degradation of O-SWCNTs during incubation in the presence of mt2P450 under different H_2O_2 concentration conditions (1, 10, and 100 mM) at 37 °C. **(A)** Photographs of the degradation of O-SWCNTs by incubation with mt2P450 (right) and without mt2P450 (left) at different time points (0, 10, 20, and 30 d). **(B)** Time course of the O-SWCNT concentrations in samples incubated with and without mt2P450. Error bars indicate the SE from three independent incubations. **(C)** Raman spectra (excitation wavelength, 532 nm) of untreated O-SWCNTs **(A)** and O-SWCNTs incubated with mt2P450 at an H_2O_2 concentration of 100 mM for 25 d **(B)** and 30 d **(C)**. AU, arbitrary units. **(D)** XPS spectra of untreated O-SWCNTs **(A)** and O-SWCNTs incubated with mt2P450 at an H_2O_2 concentration of 100 mM for 25 d **(B)**. AU, arbitrary units. **(E)** Time course of enzyme activity of mt2P450 during incubation with O-SWCNTs. Error bars indicate the SE from three independent incubations. **(F)** Time course of free iron concentration in samples during incubation. The color of the marker indicates the concentration of H_2O_2: 1 mM (white), 10 mM (gray), and 100 mM (black). Error bars indicate the SE from three independent incubations.

4 Discussion

At least under the experimental conditions used in this study, the degradation of O-SWCNTs in the presence of a heme enzyme was found to be primarily due to the Fenton reaction because the degradation proceeded during and after inactivation of the enzyme but was significantly inhibited by DTPA. This would have been the case even in O-SWCNT degradation in the presence of HRP, which was previously shown to enzymatically degrade O-SWCNTs (Allen et al., 2009). Flores-Cervantes et al. first quantitatively investigated CNT degradation by heme enzymes and showed that O-SWCNTs were biotransformed by HRP by 0.51% in 30 d (Flores-Cervantes et al., 2014), which was largely different from the rapid degradation (became colorless within 10 d) in the article by Allen et al. (2009). Of course, not all experimental

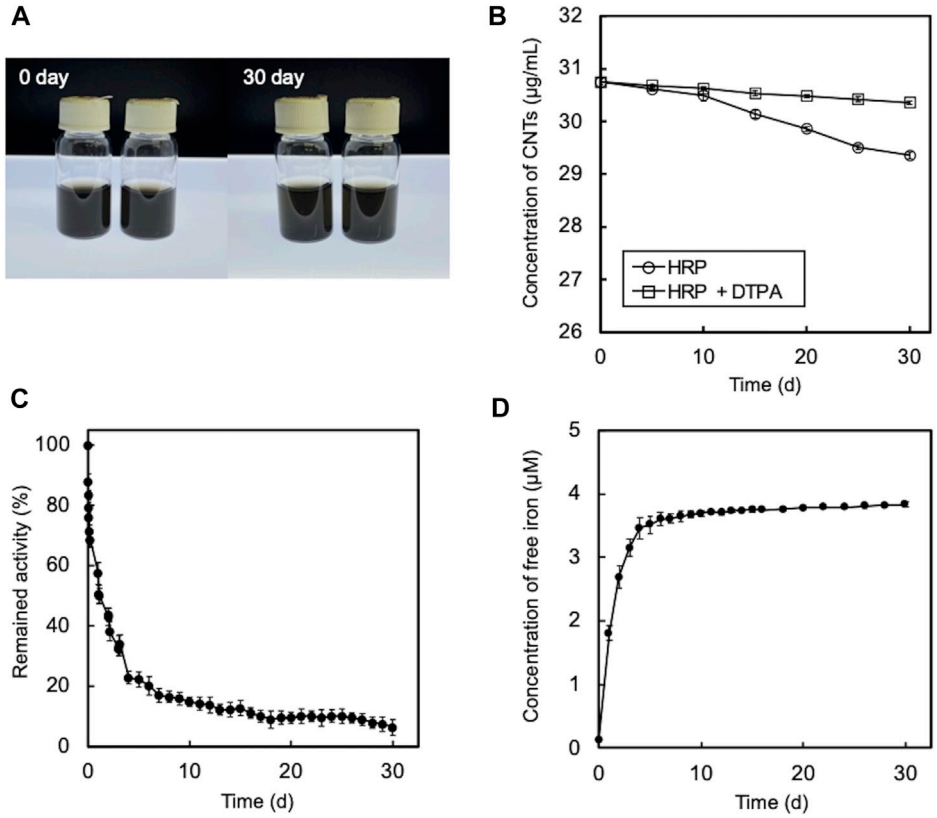

FIGURE 7
Degradation of O-SWCNTs during incubation at 25°C in the presence of HRP and 40 μM H_2O_2. **(A)** Photographs of the degradation of O-SWCNTs by incubation with (right) and without HRP (left). **(B)** Time course of the O-SWCNT concentrations in samples incubated with HRP. The color of the marker indicates with (white) and without (black) DTPA. Error bars indicate the SE from three independent incubations. **(C)** Time course of the enzyme activity of HRP during incubation with O-SWCNTs. Error bars indicate the SE from three independent incubations. **(D)** Time course of free iron concentration in samples during incubation. Error bars indicate the SE from three independent incubations.

conditions in these two studies were the same, but the difference in results between the two studies was too great. Therefore, to date, the degradation of CNTs by HRP is still not well-understood. Our results support the results of the study by Flores-Cervantes et al. (2014).

In addition, this study revealed that the assay methods to determine the activity of HRP during incubation with CNTs in the previous studies (Allen et al., 2009; Flores-Cervantes et al., 2014) were not accurate. This should be because the concentration of H_2O_2 used in the previous studies was too low relative to that of HRP. The assays were performed at the molar concentration ratio of HRP to H_2O_2 of 1:20 in the previous studies, whereas it was 1: 50000 in this study. Since a lack of substrate leads to underestimation of the enzyme activity, an excess of substrates relative to the enzyme concentration is usually employed to accurately measure peroxidase activity (Zhao et al., 1992; Monier et al., 2010; Yu et al., 2019). In addition, in the previous studies, the enzyme activity was determined by measuring the absorbance at one time point, 5 min after the start of the reaction; this method has rarely been used for measuring peroxidase activity. By contrast, we determined the enzyme activity by continuously monitoring the change in the absorbance for 30 s from the start of the reaction to get the slope of the linear approximation; this initial velocity assay is common for measuring peroxidase activity. Under the assay conditions used in this study, the absorbance of oxidized ABTS increased gradually and linearly for 30 s from the start of the reaction, and the slope of the approximate line depended on the HRP concentration (Fig. S9). We also attempted to monitor the change in the absorbance of oxidized Amplex Red under the conditions used in the previous studies. As a result, Amplex Red was instantly oxidized at the start of the reaction, and the change in absorbance could not be measured accurately; the reaction ended before the start of absorbance measurement at time 0, and absorbance did not change or conversely decreased thereafter (Supplementary Figure S10), suggesting that the assay conditions used in the previous studies were inappropriate. Thus, the initial velocity assay is also useful to validate the assay conditions. We examined HRP activity using Amplex Red as a substrate, following our assay conditions with a slight modification; the molar concentration ratio of HRP to H_2O_2 was set at 1: 250000 because Amplex Red is more sensitive than ABTS as a substrate for HRP. Under these conditions, the absorbance was saturated at around 2 min and therefore, measurement of the absorbance at one time point of 5 min cannot determine the

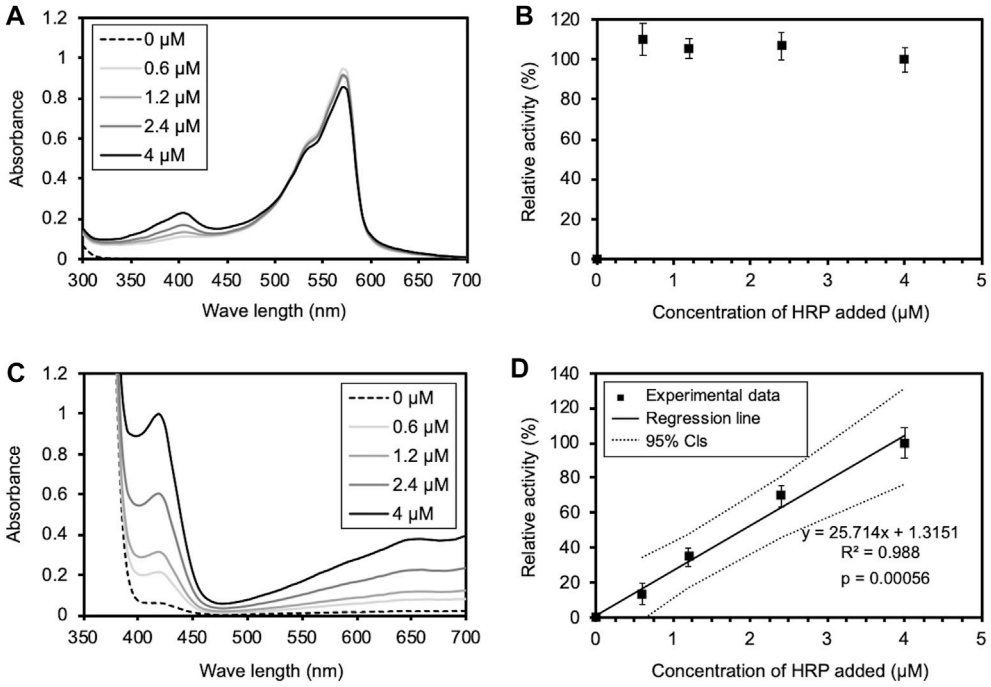

FIGURE 8
Validation of enzyme activity assays used in the previous and this studies. **(A)** The UV-Vis spectrum of oxidized Amplex Red under the assay conditions in the previous studies. 500 μl of a HRP solution of various concentrations (0, 0.6, 1.2, 2.4, and 4 μM) was added to the equal volume of the reaction mixture. The final concentrations of Amplex Red, H_2O_2, and HRP in PBS (pH 6.0) were 20, 24 μM, and 0, 0.3, 0.6, 1.2, and 2 μM. **(B)** Relative activity of Amplex Red oxidation at different HRP concentrations, determined from A_{570} of the UV-Vis spectrum in **(A)**, according to the previous studies. The activity at the highest HRP concentration is shown as 100%. Error bars indicate the SE from three independent assays. **(C)** The UV-Vis spectrum of oxidized ABTS under the assay conditions in this study. 5 μl of a HRP solution of various concentrations (0, 0.6, 1.2, 2.4, and 4 μM) was added to 995 μl of the reaction mixture. The final concentrations of ABTS, H_2O_2, and HRP in PBS (pH 6.0) were 0.45, 1 mM, and 3, 6, 12, and 20 nM. **(D)** Relative activity of ABTS oxidation at different HRP concentrations, determined from A_{413} of the UV-Vis spectrum in **(C)**. The activity at the highest HRP concentration is shown as 100%. Error bars indicate the SE from three independent assays. The solid and dotted lines indicate a regression line and 95% confidence intervals, respectively. The statistical *p*-value is also provided.

correct enzyme activity (Supplementary Figure S11). As shown in Supplementary Figure S12, it was revealed that HRP activity can be accurately measured under appropriate conditions even using Amplex Red. The precise activity assay in this study showed that the activity of HRP is not maintained for very long during incubation with CNTs in the presence of H_2O_2. In the presence of an oxidizing substrate, H_2O_2, and the absence of a reducing substrate, the inactivation of peroxidase is accelerated by heme degradation, called suicide inactivation (Valderrama et al., 2002). The fast inactivation of HRP observed in this study implies that CNTs were not utilized as a reducing substrate, i.e., they were not enzymatically oxidized. However, on one hand, since there are various types of CNTs with different numbers of walls, morphologies, and attached functional groups, further investigation is needed to rule out the possibility that there are CNTs that are susceptible to enzymatic degradation by HRP. On the other hand, the results of this study emphasize that the Fenton reaction, which has received little attention in the degradation of CNTs by heme enzymes, must be taken into consideration as well as quantitative analyses for accurate assessment of CNT degradation, and that accurate measurement of enzyme activity is essential.

At each H_2O_2 concentration, even in the control sample without enzyme, O-SWCNTs were slightly degraded (Figures 2B, 6B). This occurred probably due to trace amounts of residual iron used as a catalyst for O-SWCNT synthesis (Hata et al., 2004). In addition, the degradation of O-SWCNTs proceeded to some extent even in the presence of DTPA (Figure 5). This occurred probably because chelating agents reduce the rate of the Fenton reaction but do not prevent it completely (Li et al., 2005). Thus, the Fenton reaction, which is highly dependent on the H_2O_2 concentration, is more effective and stable than the enzymatic reaction in the degradation of CNTs, suggesting that its contribution to degradation should be carefully considered. The O-SWCNT degradation rates were much higher for mt2DyP and mt2P450 than for HRP, which is likely due to the much higher H_2O_2 concentrations used for the mt2 enzymes than for HRP. Conversely, the inactivation of HRP was slower than that of the mt2 enzymes, probably for the same reason. In this study, degradation experiments were performed at pH 7, which is not optimal for mt2DyP and mt2P450, to match the natural environmental conditions. Moreover, H_2O_2 concentrations were high enough to inactivate enzymes. Therefore, degradation experiments should be conducted at the optimum pH and H_2O_2 concentrations for enzymes to confirm whether enzymatic degradation of O-SWCNTs truly occurs.

There is an estimation that 1 g of soil contains 10^{10}–10^{11} bacteria (Horner-Devine et al., 2003). Enzymes externally secreted by bacteria are also abundant in soil, and the activity and role of enzymes after secretion into the soil have been extensively studied (Burns et al., 2013). Soil enzymes also include heme enzymes such as peroxidase (Sinsabaugh, 2010). Iron is widely distributed in the environment, mostly as iron oxide minerals that are less efficient than free iron in the Fenton reaction (Huang et al., 2013; Lai et al., 2021). Therefore, the external addition of H_2O_2 to release free iron from reproducible heme enzymes into the environment and induce the Fenton reaction is expected to be an effective method of CNT degradation for environmental remediation and waste treatment. In fact, Fenton or Fenton-like reactions using H_2O_2 have been studied as a relatively inexpensive method for the remediation of environments contaminated with various toxic substances (Vicente et al., 2011; Yap et al., 2011; Sun et al., 2014; Yu et al., 2019b; Li et al., 2023). These studies applied H_2O_2 concentrations similar to or higher than those used in this study but much lower than those used for disinfection purposes (Zeng and Wu, 2021). Therefore, our results will contribute to the development of a simple disposal method for CNTs without the risk of secondary contamination.

5 Conclusion

O-SWCNTs can be degraded in the presence of bacterial heme enzymes via the Fenton reaction with externally added H_2O_2 and iron released from the inactivated enzymes. Under the experimental conditions in this study, even in the presence of HRP, the degradation of O-SWCNTs was primarily due to the Fenton reaction, and enzymatic degradation was negligible. The obtained results suggest that the Fenton reaction, which has received little attention in CNT degradation by heme enzymes, must be taken into consideration and will contribute to the development of a simple disposal method for CNTs, utilizing the Fenton reaction with bacteria/their enzymes and H_2O_2.

Data availability statement

The original contributions presented in the study are included in the article/Supplementary Materials, further inquiries can be directed to the corresponding author.

Author contributions

ST: Investigation, methodology, formal analysis, writing—Original draft. FT: Investigation, methodology. KH: Conceptualization, planning, writing—Review and editing. All authors contributed to the article and approved the submitted version.

Acknowledgments

We thank Zeon Nanotechnology Co., Ltd. for providing the O-SWCNT sample. We also thank Kanie of Friend Microbe Inc. (Japan) for the helpful discussion about this study. The preprint of the paper has been submitted to ChemRxiv (https://doi.org/10.26434/chemrxiv-2021-t6n20-v2). The authors declare that this study received a contribution from Zeon Nanotechnology Co. Ltd. The company was not involved in the study design, collection, analysis, interpretation of data, the writing of this article or the decision to submit it for publication.

Conflict of interest

The authors declare that the research was conducted in the absence of any commercial or financial relationships that could be construed as a potential conflict of interest.

Publisher's note

All claims expressed in this article are solely those of the authors and do not necessarily represent those of their affiliated organizations, or those of the publisher, the editors and the reviewers. Any product that may be evaluated in this article, or claim that may be made by its manufacturer, is not guaranteed or endorsed by the publisher.

Supplementary material

The Supplementary Material for this article can be found online at: https://www.frontiersin.org/articles/10.3389/fenvs.2023.1184257/full#supplementary-material

References

Albertolle, M. E., and Guengerich, F. P. (2018). The relationships between cytochromes P450 and H2O2: Production, reaction, and inhibition. *J. Inorg. Biochem.* 186, 228–234. doi:10.1016/j.jinorgbio.2018.05.014

Allen, B. L., Kichambare, P. D., Gou, P., Vlasova, I. I., Kapralov, A. A., Konduru, N., et al. (2008). Biodegradation of single-walled carbon nanotubes through enzymatic catalysis. *Nano Lett.* 8 (11), 3899–3903. doi:10.1021/nl802315h

Allen, B. L., Kotchey, G. P., Chen, Y. N., Yanamala, N. V. K., Klein-Seetharaman, J., Kagan, V. E., et al. (2009). Mechanistic investigations of horseradish peroxidase-catalyzed degradation of single-walled carbon nanotubes. *J. Am. Chem. Soc.* 131 (47), 17194–17205. doi:10.1021/ja9083623

Almarasy, A. A., Hayasaki, T., Abiko, Y., Kawabata, Y., Akasaka, S., and Fujimori, A. (2021). Comparison of characteristics of single-walled carbon nanotubes obtained by super-growth CVD and improved-arc discharge methods pertaining to interfacial film formation and nanohybridization with polymers. *Colloids Surfaces a-Physicochemical Eng. Aspects* 615, 126221. doi:10.1016/j.colsurfa.2021.126221

Andon, F. T., Kapralov, A. A., Yanamala, N., Feng, W. H., Baygan, A., Chambers, B. J., et al. (2013). Biodegradation of single-walled carbon nanotubes by eosinophil peroxidase. *Small* 9 (16), 2721–2729. doi:10.1002/smll.201202508

Anzar, N., Hasan, R., Tyagi, M., Yadav, N., and Narang, J. (2020). Carbon nanotube - a review on synthesis, properties and plethora of applications in the field of biomedical science. *Sensors Int.* 1, 100003. doi:10.1016/j.sintl.2020.100003

Bhattacharya, K., El-Sayed, R., Andon, F. T., Mukherjee, S. P., Gregory, J., Li, H., et al. (2015). Lactoperoxidase-mediated degradation of single-walled carbon nanotubes in the presence of pulmonary surfactant. *Carbon* 91, 506–517. doi:10.1016/j.carbon.2015.05.022

Bugg, T. D. H., Ahmad, M., Hardiman, E. M., and Singh, R. (2011). The emerging role for bacteria in lignin degradation and bio-product formation. *Curr. Opin. Biotechnol.* 22 (3), 394–400. doi:10.1016/j.copbio.2010.10.009

Burns, R. G., DeForest, J. L., Marxsen, J., Sinsabaugh, R. L., Stromberger, M. E., Wallenstein, M. D., et al. (2013). Soil enzymes in a changing environment: Current knowledge and future directions. *Soil Biol. Biochem.* 58, 216–234. doi:10.1016/j.soilbio.2012.11.009

Byrne, C., Subramanian, G., and Pillai, S. C. (2018). Recent advances in photocatalysis for environmental applications. *J. Environ. Chem. Eng.* 6 (3), 3531–3555. doi:10.1016/j.jece.2017.07.080

Chandrasekaran, G., Choi, S. K., Lee, Y. C., Kim, G. J., and Shin, H. J. (2014). Oxidative biodegradation of single-walled carbon nanotubes by partially purified lignin peroxidase from *Sparassis latifolia* mushroom. *J. Industrial Eng. Chem.* 20 (5), 3367–3374. doi:10.1016/j.jiec.2013.12.022

Chen, C., Shrestha, R., Jia, K., Gao, P. F., Geisbrecht, B. V., Bossmann, S. H., et al. (2015a). Characterization of dye-decolorizing peroxidase (DyP) from *Thermomonospora curvata* reveals unique catalytic properties of A-type DyPs. *J. Biol. Chem.* 290 (38), 23447–23463. doi:10.1074/jbc.M115.658807

Chen, D. R., Adusei, P. K., Chitranshi, M., Fang, Y. B., Johnson, K., Schulz, M., et al. (2021). Electrochemical activation to enhance the volumetric performance of carbon nanotube electrodes. *Appl. Surf. Sci.* 541, 148448. doi:10.1016/j.apsusc.2020.148448

Chen, M., Zhou, S., Zhu, Y., Sun, Y. Z., Zeng, G. M., Yang, C. P., et al. (2018). Toxicity of carbon nanomaterials to plants, animals and microbes: Recent progress from 2015-present. *Chemosphere* 206, 255–264. doi:10.1016/j.chemosphere.2018.05.020

Chen, Q. L., Wang, H., Yang, B. S., He, F., Han, X. M., and Song, Z. H. (2015b). Responses of soil ammonia-oxidizing microorganisms to repeated exposure of single-walled and multi-walled carbon nanotubes. *Sci. Total Environ.* 505, 649–657. doi:10.1016/j.scitotenv.2014.10.044

Colpa, D. I., Fraaije, M. W., and van Bloois, E. (2014). DyP-Type peroxidases: A promising and versatile class of enzymes. *J. Industrial Microbiol. Biotechnol.* 41 (1), 1–7. doi:10.1007/s10295-013-1371-6

Dong, Y. D., Zhang, H., Zhong, G. J., Yao, G., and Lai, B. (2021). Cellulose/carbon composites and their applications in water treatment - a review. *Chem. Eng. J.* 405, 126980. doi:10.1016/j.cej.2020.126980

Dresselhaus, M. S., Dresselhaus, G., Charlier, J. C., and Hernandez, E. (2004). Electronic, thermal and mechanical properties of carbon nanotubes. *Philosophical Trans. R. Soc. a-Mathematical Phys. Eng. Sci.* 362 (1823), 2065–2098. doi:10.1098/rsta.2004.1430

Flores-Cervantes, D. X., Maes, H. M., Schaffer, A., Hollender, J., and Kohler, H. P. E. (2014). Slow biotransformation of carbon nanotubes by horseradish peroxidase. *Environ. Sci. Technol.* 48 (9), 4826–4834. doi:10.1021/es4053279

Habib, M. H., Rozeboom, H. J., and Fraaije, M. W. (2019). Characterization of a new DyP-peroxidase from the alkaliphilic cellulomonad, cellulomonas bogoriensis. *Molecules* 24 (7), 1208. doi:10.3390/molecules24071208

Hata, K., Futaba, D. N., Mizuno, K., Namai, T., Yumura, M., and Iijima, S. (2004). Water-assisted highly efficient synthesis of impurity-free single-walled carbon nanotubes. *Science* 306 (5700), 1362–1364. doi:10.1126/science.1104962

Hatami, M. (2017). Toxicity assessment of multi-walled carbon nanotubes on *Cucurbita pepo* L. under well-watered and water-stressed conditions. *Ecotoxicol. Environ. Saf.* 142, 274–283. doi:10.1016/j.ecoenv.2017.04.018

Hessler, C. M., Wu, M. Y., Xue, Z., Choi, H., and Seo, Y. (2012). The influence of capsular extracellular polymeric substances on the interaction between TiO2 nanoparticles and planktonic bacteria. *Water Res.* 46 (15), 4687–4696. doi:10.1016/j.watres.2012.06.009

Ho, N. T., Siggel, M., Camacho, K. V., Bhaskara, R. M., Hicks, J. M., Yao, Y. C., et al. (2021). Membrane fusion and drug delivery with carbon nanotube porins. *Proc. Natl. Acad. Sci. U. S. A.* 118 (19), 4118. doi:10.1073/pnas.2016974118

Horner-Devine, M. C., Leibold, M. A., Smith, V. H., and Bohannan, B. J. M. (2003). Bacterial diversity patterns along a gradient of primary productivity. *Ecol. Lett.* 6 (7), 613–622. doi:10.1046/j.1461-0248.2003.00472.x

Huang, W. Y., Brigante, M., Wu, F., Hanna, K., and Mailhot, G. (2013). Effect of ethylenediamine-N,N'-disuccinic acid on Fenton and photo-fenton processes using goethite as an iron source: Optimization of parameters for bisphenol A degradation. *Environ. Sci. Pollut. Res.* 20 (1), 39–50. doi:10.1007/s11356-012-1042-6

Kadri, T., Rouissi, T., Brar, S. K., Cledon, M., Sarma, S., and Verma, M. (2017). Biodegradation of polycyclic aromatic hydrocarbons (PAHs) by fungal enzymes: A review. *J. Environ. Sci.* 51, 52–74. doi:10.1016/j.jes.2016.08.023

Kagan, V. E., Konduru, N. V., Feng, W. H., Allen, B. L., Conroy, J., Volkov, Y., et al. (2010). Carbon nanotubes degraded by neutrophil myeloperoxidase induce less pulmonary inflammation. *Nat. Nanotechnol.* 5 (5), 354–359. doi:10.1038/Nnano.2010.44

Kumarathasan, P., Breznan, D., Das, D., Salam, M. A., Siddiqui, Y., MacKinnon-Roy, C., et al. (2015). Cytotoxicity of carbon nanotube variants: A comparative *in vitro* exposure study with A549 epithelial and J774 macrophage cells. *Nanotoxicology* 9 (2), 148–161. doi:10.3109/17435390.2014.902519

Lai, C., Shi, X. X., Li, L., Cheng, M., Liu, X. G., Liu, S. Y., et al. (2021). Enhancing iron redox cycling for promoting heterogeneous Fenton performance: A review. *Sci. Total Environ.* 775, 145850. doi:10.1016/j.scitotenv.2021.145850

Li, J., Liu, C., Li, B. Z., Yuan, H. L., Yang, J. S., and Zheng, B. W. (2012). Identification and molecular characterization of a novel DyP-type peroxidase from *Pseudomonas aeruginosa* PKE117. *Appl. Biochem. Biotechnol.* 166 (3), 774–785. doi:10.1007/s12010-011-9466-x

Li, X. M., Xu, J. L., and Yang, Z. L. (2023). Insight on efficiently oriented oxidation of petroleum hydrocarbons by redistribution of oxidant through inactivation of soil organic matter coupled with passivation of manganese minerals. *J. Hazard. Mater.* 443, 130192. doi:10.1016/j.jhazmat.2022.130192

Li, Y. C., Bachas, L. G., and Bhattacharyya, D. (2005). Kinetics studies of trichlorophenol destruction by chelate-based Fenton reaction. *Environ. Eng. Sci.* 22 (6), 756–771. doi:10.1089/ees.2005.22.756

Mendonca, M. C. P., Rizoli, C., Avila, D. S., Amorim, M. J. B., and de Jesus, M. B. (2017). Nanomaterials in the environment: Perspectives on *in vivo* terrestrial toxicity testing. *Front. Environ. Sci.* 5, 71. doi:10.3389/fenvs.2017.00071

Monier, M., Ayad, D. M., Wei, Y., and Sarhan, A. A. (2010). Immobilization of horseradish peroxidase on modified chitosan beads. *Int. J. Biol. Macromol.* 46 (3), 324–330. doi:10.1016/j.ijbiomac.2009.12.018

Nagababu, E., and Rifkind, J. M. (2004). Heme degradation by reactive oxygen species. *Antioxidants Redox Signal.* 6 (6), 967–978. doi:10.1089/ars.2004.6.967

Paumann-Page, M., Furtmuller, P. G., Hofbauer, S., Paton, L. N., Obinger, C., and Kettle, A. J. (2013). Inactivation of human myeloperoxidase by hydrogen peroxide. *Archives Biochem. Biophysics* 539 (1), 51–62. doi:10.1016/j.abb.2013.09.004

Rahmanpour, R., and Bugg, T. D. H. (2015). Characterisation of dyp-type peroxidases from *Pseudomonas fluorescens* pf-5: Oxidation of Mn(II) and polymeric lignin by Dyp1B. *Archives Biochem. Biophysics* 574, 93–98. doi:10.1016/j.abb.2014.12.022

Rahmanpour, R., Rea, D., Jamshidi, S., Fulop, V., and Bugg, T. D. H. (2016). Structure of *Thermobifida fusca* DyP-type peroxidase and activity towards Kraft lignin and lignin model compounds. *Archives Biochem. Biophysics* 594, 54–60. doi:10.1016/j.abb.2016.02.019

Regenhardt, D., Heuer, H., Heim, S., Fernandez, D. U., Strompl, C., Moore, E. R. B., et al. (2002). Pedigree and taxonomic credentials of *Pseudomonas putida* strain KT2440. *Environ. Microbiol.* 4 (12), 912–915. doi:10.1046/j.1462-2920.2002.00368.x

Roberts, J. N., Singh, R., Grigg, J. C., Murphy, M. E. P., Bugg, T. D. H., and Eltis, L. D. (2011). Characterization of dye-decolorizing peroxidases from *Rhodococcus jostii* RHA1. *Biochemistry* 50 (23), 5108–5119. doi:10.1021/bi200427h

Santos, A., Mendes, S., Brissos, V., and Martins, L. O. (2014). New dye-decolorizing peroxidases from *Bacillus subtilis* and *Pseudomonas putida* MET94: Towards biotechnological applications. *Appl. Microbiol. Biotechnol.* 98 (5), 2053–2065. doi:10.1007/s00253-013-5041-4

Singh, A. K., Bilal, M., Iqbal, H. M. N., and Raj, A. (2021). Lignin peroxidase in focus for catalytic elimination of contaminants ? A critical review on recent progress and perspectives. *Int. J. Biol. Macromol.* 177, 58–82. doi:10.1016/j.ijbiomac.2021.02.032

Singh, R., and Eltis, L. D. (2015). The multihued palette of dye-decolorizing peroxidases. *Archives Biochem. Biophysics* 574, 56–65. doi:10.1016/j.abb.2015.01.014

Singh, R., Grigg, J. C., Qin, W., Kadla, J. F., Murphy, M. E. P., and Eltis, L. D. (2013). Improved manganese-oxidizing activity of DypB, a peroxidase from a lignolytic bacterium. *Acs Chem. Biol.* 8 (4), 700–706. doi:10.1021/cb300608x

Sinsabaugh, R. L. (2010). Phenol oxidase, peroxidase and organic matter dynamics of soil. *Soil Biol. Biochem.* 42 (3), 391–404. doi:10.1016/j.soilbio.2009.10.014

Sireesha, M., Babu, V. J., Kiran, A. S. K., and Ramakrishna, S. (2018). A review on carbon nanotubes in biosensor devices and their applications in medicine. *Nanocomposites* 4 (2), 36–57. doi:10.1080/20550324.2018.1478765

Sun, S. P., Zeng, X., Li, C., and Lemley, A. T. (2014). Enhanced heterogeneous and homogeneous Fenton-like degradation of carbamazepine by nano-Fe3O4/H2O2 with nitrilotriacetic acid. *Chem. Eng. J.* 244, 44–49. doi:10.1016/j.cej.2014.01.039

Valderrama, B., Ayala, M., and Vazquez-Duhalt, R. (2002). Suicide inactivation of peroxidases and the challenge of engineering more robust enzymes. *Chem. Biol.* 9 (5), 555–565. doi:10.1016/S1074-5521(02)00149-7

Vicente, F., Rosas, J. M., Santos, A., and Romero, A. (2011). Improvement soil remediation by using stabilizers and chelating agents in a Fenton-like process. *Chem. Eng. J.* 172 (2-3), 689–697. doi:10.1016/j.cej.2011.06.036

Villegas, J. A., Mauk, A. G., and Vazquez-Duhalt, R. (2000). A cytochrome c variant resistant to heme degradation by hydrogen peroxide. *Chem. Biol.* 7 (4), 237–244. doi:10.1016/S1074-5521(00)00098-3

Wang, J. W., Ma, Q., Zhang, Z. J., Li, S. Z., Diko, C. S., Dai, C. X., et al. (2020). Bacteria mediated Fenton-like reaction drives the biotransformation of carbon nanomaterials. *Sci. Total Environ.* 746, 141020. doi:10.1016/j.scitotenv.2020.141020

Xiang, L., Zhang, H., Hu, Y. F., and Peng, L. M. (2018). Carbon nanotube-based flexible electronics. *J. Mater. Chem. C* 6 (29), 7714–7727. doi:10.1039/c8tc02280a

Yang, C. X., Yue, F. F., Cui, Y. L., Xu, Y. M., Shan, Y. Y., Liu, B. F., et al. (2018). Biodegradation of lignin by *Pseudomonas* sp Q18 and the characterization of a novel

bacterial DyP-type peroxidase. *J. Industrial Microbiol. Biotechnol.* 45 (10), 913–927. doi:10.1007/s10295-018-2064-y

Yang, M., Zhang, M. F., Nakajima, H., Yudasaka, M., Iijima, S., and Okazaki, T. (2019a). <p>Time-dependent degradation of carbon nanotubes correlates with decreased reactive oxygen species generation in macrophages</p>. *Int. J. Nanomedicine* 14, 2797–2807. doi:10.2147/Ijn.S199187

Yang, Z. F., Tian, J. R., Yin, Z. F., Cui, C. J., Qian, W. Z., and Wei, F. (2019b). Carbon nanotube- and graphene-based nanomaterials and applications in high-voltage supercapacitor: A review. *Carbon* 141, 467–480. doi:10.1016/j.carbon.2018.10.010

Yap, C. L., Gan, S. Y., and Ng, H. K. (2011). Fenton based remediation of polycyclic aromatic hydrocarbons-contaminated soils. *Chemosphere* 83 (11), 1414–1430. doi:10.1016/j.chemosphere.2011.01.026

You, Y., Das, K. K., Guo, H., Chang, C. W., Navas-Moreno, M., Chan, J. W., et al. (2017). Microbial transformation of multiwalled carbon nanotubes by *Mycobacterium vanbaalenii* PYR-1. *Environ. Sci. Technol.* 51 (4), 2068–2076. doi:10.1021/acs.est.6b04523

Yu, B., Cheng, H., Zhuang, W., Zhu, C. J., Wu, J. L., Niu, H. Q., et al. (2019a). Stability and repeatability improvement of horseradish peroxidase by immobilization on amino-functionalized bacterial cellulose. *Process Biochem.* 79, 40–48. doi:10.1016/j.procbio.2018.12.024

Yu, Q. Q., Feng, L., Chai, X. N., Qiu, X. H., Ouyang, H., and Deng, G. Y. (2019b). Enhanced surface Fenton degradation of BPA in soil with a high pH. *Chemosphere* 220, 335–343. doi:10.1016/j.chemosphere.2018.12.141

Zeng, Y. C., and Wu, G. (2021). Electrocatalytic H2O2 generation for disinfection. *Chin. J. Catal.* 42 (12), 2149–2163. doi:10.1016/S1872-2067(20)63781-0

Zhang, C., Chen, W., and Alvarez, P. J. J. (2014). Manganese peroxidase degrades pristine but not surface-oxidized (carboxylated) single-walled carbon nanotubes. *Environ. Sci. Technol.* 48 (14), 7918–7923. doi:10.1021/es5011175

Zhang, L. W., Petersen, E. J., Habteselassie, M. Y., Mao, L., and Huang, Q. G. (2013). Degradation of multiwall carbon nanotubes by bacteria. *Environ. Pollut.* 181, 335–339. doi:10.1016/j.envpol.2013.05.058

Zhao, J. G., Henkens, R. W., Stonehuerner, J., Odaly, J. P., and Crumbliss, A. L. (1992). Direct electron-transfer at horseradish-peroxidase colloidal gold modified electrodes. *J. Electroanal. Chem.* 327 (1-2), 109–119. doi:10.1016/0022-0728(92)80140-Y

Zhao, K., Veksha, A., Ge, L., and Lisak, G. (2021). Near real-time analysis of para-cresol in wastewater with a laccase-carbon nanotube-based biosensor. *Chemosphere* 269, 128699. doi:10.1016/j.chemosphere.2020.128699

frontiers | Frontiers in Environmental Science

TYPE Original Research
PUBLISHED 05 September 2023
DOI 10.3389/fenvs.2023.1240633

OPEN ACCESS

EDITED BY
Gaurav Pant,
Graphic Era (Deemed to be University), India

REVIEWED BY
Vivek Verma,
Thapar Institute of Engineering and Technology, India
Sumit Pal,
Indian Agricultural Research Institute (ICAR), India

*CORRESPONDENCE
Tiefeng Zhou,
dun0816qi@163.com

RECEIVED 15 June 2023
ACCEPTED 08 August 2023
PUBLISHED 05 September 2023

CITATION
Zha Y, Zhao L, Wei J, Niu T, Yue E, Wang X, Chen Y, Shi J and Zhou T (2023), Effect of the application of peanut shell, bamboo, and maize straw biochars on the bioavailability of Cd and growth of maize in Cd-contaminated soil.
Front. Environ. Sci. 11:1240633.
doi: 10.3389/fenvs.2023.1240633

Effect of the application of peanut shell, bamboo, and maize straw biochars on the bioavailability of Cd and growth of maize in Cd-contaminated soil

Yan Zha[1], Lin Zhao[1], Jiqian Wei[2], Tianxin Niu[1], Erkui Yue[1], Xianbo Wang[3], Yi Chen[4], Jiang Shi[1] and Tiefeng Zhou[5]*

[1]Laboratory of Molecular Biology, Institute of Crop and Ecology, Hangzhou Academy of Agricultural Sciences, Hangzhou, China, [2]Hangzhou Agricultural Technology Extension Center, Hangzhou, China, [3]Laboratory of Plant Molecular Biology and Proteomics, Institute of Biotechnology, Hangzhou Academy of Agricultural Sciences, Hangzhou, China, [4]Institute of Fishers Institute, Hangzhou Academy of Agricultural Sciences, Hangzhou, China, [5]Hangzhou Academy of Agricultural Sciences, Hangzhou, China

Biochar is a versatile, carbon-rich, organic material that can effectively immobilize Cd in the soil. In this study, peanut shell biochar (SP), maize straw biochar (MS), and bamboo straw biochar (BS) were applied in different proportions to evaluate their effects on the remediation of Cd-contaminated farmland soil and plant growth. The results revealed that both single and mixed applications of biochar substantially increased corn biomass and chlorophyll content compared to the unamended control treatment, while the malondialdehyde (MDA) and proline contents were largely unaffected. The bamboo straw block biochar with maize straw biochar at a mass ratio of 2:1 (DBM) significantly increased the dry total biomass of maize (+107.24% compared to the unamended soil). SP application has highly increased the SPAD value. PB with BS application at a mass ratio of 1:1 (MSB) significantly decreased the soluble sugar content (+21.81% compared to the unamended control soil). Soil pH was increased by the application of biochar alone and in combination with feedstocks. The soil content of Fe/Mn oxide-bound (OX) and exchangeable-bound Cd (EX) was decreased, whereas that of carbonate-bound Cd (CA), residue-bound Cd (RE), and organic-bound Cd (OM) contents increased. The Cd content in corn grains under MSB and SP application was markedly reduced by 42.62% and 31.48%, respectively, compared to the unamended control soil. Overall, MSB and SP applications were effective in improving soil quality and crop growth.

KEYWORDS

biochar, cadmium, remediation, maize, soil properties

1 Introduction

Many soils worldwide are contaminated with heavy metals due to industrial production, industrial activities, waste disposal, and improper management of pesticides and chemicals (Duan et al., 2016; Zhang A F et al., 2017; Zhang R H et al., 2017; Xie et al., 2021; Aown et al., 2022). Among the global environmental concerns related to soil, heavy metal pollution is particularly acute in China. According to a 2014 publication by the National Soil Pollution Survey Bulletin (NSPSB), approximately 19.4% of China's arable soils are plagued by heavy

metal contamination (about 2.0×10^7 ha of agricultural soil), of which cadmium (Cd) is the most concerning (Department of Environmental Protection, 2014). Cd in the soil can combine with soil colloids, organic matter, and minerals. It can also exist in the soil pore water environment in the ionic form (such as Cd^{2+}, $CdOH^+$, and $CdCl^+$) (Wan et al., 2018). The Cd content in soil pores and its morphology are the main reasons for its biological effects on soil. Given the persistency of characteristics of heavy metals such as Cd and their detrimental impact on food security and human health, it is imperative to introduce stabilizing substances into the soil. The addition of stabilizing substances plays a key role in achieving this objective, preventing the entry of Cd into critical pathways of food crops (Zhao et al., 2015; Li et al., 2016).

Biochar is capable of binding heavy metal ions and reducing their harmful effects through surface precipitation, absorption, ion exchange, and electrostatic binding due to its high specific surface area; physicochemical properties, e.g., abundant surface oxygen-containing functional groups; and high pH (Liang et al., 2017; Michal et al., 2022). Crop straw is rich in organic carbon (OC), phosphorus (P), nitrogen (N), trace elements, and potassium (K) (Cui et al., 2019). In recent years, biochar prepared by straw pyrolysis has been widely used for agricultural carbon sequestration and soil fertility improvement (Holatko et al., 2022; Yang et al., 2022; Sun et al., 2023). In addition to remediating heavy metal and organic compound-contaminated soils, biochar also acts as a catalyst, positively influencing crop growth and enhancing yield (Xu et al., 2019; Zha et al., 2022). Cui et al. (2019) found that long-term incubation tests confirmed the stability of wheat straw biochar, which effectively decreased Cd bioavailability by approximately 90% compared to the control. The findings from Bashir et al. (2018a); Bashir et al. (2018b) revealed that the utilization of biochar triggered a substantial decline in the bioavailability of Cd and chromium (Cr), achieving reductions of 85% and 63%, respectively. China is the world's largest producer of bamboo and has abundant bamboo charcoal resources (Liu et al., 2011; Xu et al., 2012). Peanut, being one of the crucial oil crops globally, boasts significant importance. Furthermore, peanut shell biochar exhibits a notable ability to uptake Cd (Christou et al., 2017). Maize straw efficiently adsorbs heavy metals and reduces Cd bioavailability in plants and soils (Gondek et al., 2018). However, biochar prepared from these different species has different physical and chemical properties (Michal et al., 2022; Ángela et al., 2022). Due to these differences in the physico-chemical properties of biochar, it is possible that biochar application alone will not alleviate soil heavy metal pollution.

As one of the primary staple crops in China, maize occupies a significant position in agriculture. Its remarkable growth rate and high yield make it the preferred cereal for phytoremediation of soil contaminated with heavy metals (Bai et al., 2017; Sarwar et al., 2017; Huerta et al., 2022). Previous studies have demonstrated that in maize cultivated in Cd-contaminated soil, the heavy metal concentration in the seeds of most maize varieties exceeds the safety standard (Yang et al., 2018; Zha et al., 2023). This study sought to establish an effective means of immobilizing Cd in contaminated soil, with the specific aim of ensuring the safety of maize cultivation. In this study, maize was used as an experimental material. The effect of the type of biochar and the amount needed to be applied to soil to control Cd pollution is unclear. Thus, the principal goal of this study was to investigate the practicality of utilizing different types of biochar in varying mass ratios and to assess the effects of different biochar combinations on soil and plant properties.

2 Materials and methods

2.1 Soil and biochar characterization

Surface soil samples (0–20 cm) were specifically gathered from a paddy field situated in Wangyan Village, Qiantan Town, Jiande City, which is positioned west of Hangzhou City in Zhejiang Province (29°39′25″ N, 119°35′38″ E). The soil samples collected from this area have been continuously impacted by surface runoff pollution from a nearby mine for a span of 30 years. Following an "S" pattern, five sampling points were carefully determined within the collection area to ensure representative coverage. To maintain uniformity, the soil was left to air-dry for 7 days and subsequently sieved using a 2-mm pore-size sieve. This preparatory step was performed prior to conducting various physico-chemical analyses. The soil analysis revealed a pH value of 6.78 and an electrical conductivity (EC) value of 1.58 dS m^{-1}. Additionally, the organic matter content of the soil was determined to be 0.92%. Measured in mg kg^{-1} DW (dry weight), the total concentrations of Cd, Pb, Zn, and Cr in the soil were 4.57, 53.10, 176.98, and 135.93, respectively. According to the soil environmental quality agricultural land pollution risk control (GB15618-2018), the chosen agricultural land soil initially revealed contamination only by Cd, while the levels of other elements remained below the specified thresholds.

The carbonization of peanut shell biochar (SP) and bamboo biochar (BS) was carried out by Henan Lize Environmental Protection Technology Company at a temperature of 700°C. A continuous slow pyrolysis machine was employed to produce maize (variety: Qianjiangnuo NO.3) straw block biochar (MS) by subjecting it to a final temperature of 550°C for a retention time of 30 min at the Hangzhou Academy of Agricultural Sciences at approximately 700°C in a batch pyrolysis facility. The physicochemical properties of the biochars and heavy metal-contaminated soil are shown in Table 1.

2.2 Greenhouse experiment

The treatments included Cd-contaminated soil amended with single biochar (SP, BS, and MS), mixtures of two biochars in equal mass ratios (MSB, MSM, and MBM), and mixtures of two biochars in a 1:2 (w/w) ratio (DSB, DSM, and DBM) (Table 2). Under greenhouse conditions, after sterilizing the corn seeds with hydrogen peroxide, 10 seeds were sown in each pot. One week after seedling emergence, three uniformly growing corn plants were retained in each pot. The experimental setup involved growing maize in plastic pots filled with 20 kg of air-dried soil. The soil was enriched with a 5% mixture of biochars ($W_{biochar}/W_{soil}$). Unamended soil was designated as the control group. Five replicates were organized for each treatment. The experiment plants were maize (variety: Qianjiangnuo NO.3), which can accumulate heavy metals. In each pot, five maize seeds were

TABLE 1 Physicochemical properties of Cd-contaminated soil and biochars.

Treatment	Soil	Peanut shell biochar	Maize straw block biochar	Bamboo straw biochar
pH	6.86	9.87	7.94	6.78
Moisture (%)	nd	0.03	0.04	0.04
Volatile matter (%)	nd	15.37	23.96	40.64
Ash (%)	nd	41.09	5.33	19.58
Pb ($mg{\cdot}kg^{-1}$)	53.10	14.07	7.24	10.04
Zn ($mg{\cdot}kg^{-1}$)	176.98	39.53	32.04	35.66
Cr ($mg{\cdot}kg^{-1}$)	135.93	32.02	27.23	37.2
Cd ($mg{\cdot}kg^{-1}$)	4.57	0.78	1.04	0.47

TABLE 2 Ratios of biochars for treatments.

Treatment	Peanut shell biochar	Bamboo straw block biochar	Maize straw biochar
CK	0	0	0
SP	1	0	0
BS	0	1	0
MS	0	0	1
MSB	1	1	0
MSM	1	0	1
MBM	0	1	1
DSB	2	1	0
DSM	2	0	1
DBM	0	2	1

sown. Following a 6-day germination period, three seedlings exhibiting robust growth were selected. Fertilizers (K_2SO_4–DAP–urea) were administered at a rate of 120–50–25 kg ha^{-1} applying irrigation water. Two rounds of urea fertilizer application were conducted (i.e., initially applied in conjunction with other fertilizers, and a subsequent application was conducted after a 15-day period).

After 82 days, the maize plants were harvested. The plants were dissected into four distinct parts (roots, stems, leaves, and grains). Each part was then gathered and prepared for laboratory analysis. A 15-min immersion of maize roots in a solution containing 20 mM of Na2EDTA was carried out to facilitate the removal of heavy metal ions attached to the root surface. Following the immersion, the roots underwent a comprehensive cleaning process using deionized water. All roots, stems, leaves, and grains underwent a thorough washing process, which was repeated three times. The four distinct plant parts were subjected to a drying process at 65°C for 72 h, allowing them to reach a constant weight. The biomass of each part was then confirmed using a balance (Setra Systems Inc. Boxborough, MA, and United States). The chlorophyll content was determined using the Soil and Plant Analyzer Development (SPAD) method (SPAD) (SPAD-TYS-A (Jinkeli, Inc., Beijing).

2.3 Analysis method of soil and plant

Soil and plant samples were collected simultaneously on the 82nd day after planting. Di-acid digestion was carried out on the dry weights (0.5 g) of both the soil and different maize parts. Nitric acid (HNO_3) and perchloric acid ($HClO_4$) were combined in a 1:3 ratio for the digestion process, ensued by heating on a hot plate at 250°C. Following filtration, the samples were subjected to Cd analyses using an atomic absorption spectrophotometer (AAS) (z2000, Hitachi, Tokyo, Japan). Samples of soil were digested by acidic solutions for available P and K analyses and were estimated in terms of the method elaborated by Page (1982). Soil Cd in the active state was determined by diethylenetriaminepentaacetic acid (DTPA) leaching and inductively coupled plasma–atomic emission spectrometry (ICP-AES) (HJ 804-2016). Soil samples were processed using the method reported by Tessier et al. (1979). The soil cadmium morphology can be segmented into five states: exchangeable state (EX), organic-bound state (OM), iron- and manganese oxide-bound state (OX), residual state (RE), and carbonate-bound state (CA).

The determination of proline content, MDA levels, and soluble sugar content involved was performed using the Saradhi method with acid ninhydrin solution (Aila and Saradhi, 1991), thiobarbituric

TABLE 3 Maize dry biomass production in Cd-contaminated soil amended with biochars.

Treatments	Total biomass	Root biomass	Stem biomass	Leave biomass	Bract biomass	Grain biomass
	(g·plant^{-1})	(g·plant^{-1})	(g·plant^{-1})	(g·plant^{-1})	(g·plant^{-1})	(g·plant^{-1})
CK	403.36 ± 22.37 g	22.35 ± 2.15 g	85.76 ± 6.01 f	49.15 ± 3.08 h	36.17 ± 2.33 e	209.93 ± 12.77 e
SP	472.33 ± 26.18 f	30.14 ± 1.58 f	113.15 ± 8.51 e	59.28 ± 3.04 g	40.84 ± 2.61 de	228.92 ± 17.63 de
BS	596.54 ± 34.26 d	56.15 ± 3.13 d	154.98 ± 10.7 c	92.35 ± 5.75 d	47.89 ± 3.21 c	245.17 ± 14.35 cd
MS	522.79 ± 35.06 ef	51.34 ± 2.81 d	132.57 ± 7.82 de	80.93 ± 4.11 e	42.51 ± 2.64 d	215.44 ± 11.61 e
MSB	494.47 ± 20.83 ef	38.41 ± 1.64 e	118.99 ± 10.43 e	77.74 ± 3.88 ef	39.26 ± 2.05 de	220.07 ± 12.48 de
MSM	486.16 ± 27.16 ef	36.55 ± 2.43 e	120.94 ± 9.73 e	69.83 ± 3.37 f	40.02 ± 2.42 de	218.82 ± 15.62 de
MBM	538.71 ± 31.65 e	59.34 ± 3.68 c	146.78 ± 8.61 cd	80.91 ± 4.23 e	39.84 ± 1.93 de	211.84 ± 14.53 e
DSB	700.97 ± 35.83 c	68.93 ± 3.12 b	178.83 ± 14.95 b	115.49 ± 6.53 c	69.31 ± 4.13 b	268.41 ± 17.22 c
DSM	763.02 ± 35.43 b	73.54 ± 5.55 b	196.48 ± 12.76 b	130.58 ± 7.25 ab	73.41 ± 3.65 b	289.01 ± 15.87 ab
DBM	835.91 ± 42.02 a	99.83 ± 6.5 a	208.67 ± 16.98 a	145.73 ± 6.63 a	79.75 ± 4.88 a	301.93 ± 18.14 a

The abbreviations of biochar treatments are given in Table 1. CK, unamended control. Error bars indicate standard deviation (n = 3). Different letters indicate statistically significant differences ($p < 0.05$).

acid (TBA) colorimetry (Duan et al., 2018), and anthrone colorimetry (Tashiro et al., 1997).

2.4 Statistical analysis

One-way analysis of variance (ANOVA) was performed using IBM SPSS 17.0 statistical software (SPSS Inc., Chicago, United States) to determine the significance of differences between the treatments. Tukey's range test ($p = 0.05$) was employed to compare the mean values and detect significant differences between the treatments. All tables and figures were created using Excel and Origin 8.0, respectively.

3 Results

3.1 Effect of biochars on maize biomass

In this study, the maize total biomass and root, stem, and leaf biomass in all amended samples of biochar were significantly higher than those in the unamended control sample ($p < 0.05$) (Table 3). The DBM treatments resulted in the highest biomass, followed by the DSM and DSB treatments. The maize total biomass amended with DBM, DSM, and DSB was 3.47, 2.49, and 2.08 times, respectively, higher than that of the unamended control. Grains subjected to the BS, DSB, DSM, and DBM treatments displayed prominently higher biomass than the unamended control ($p < 0.05$). The bract biomass under BS, MS DSB, DSM, and DBM was significantly higher than that of the unamended control ($p < 0.05$). The highest total biomass and different parts of the biomass of maize were observed in DBM treatment. The application of DBM significantly increased the total biomass and root, stem, leaf, grain, and bract biomass in maize by 346.67%, 143.32%, 196.50%, 43.83%, 120.49%, and 107.24%, respectively.

3.2 Effect of biochars on maize physiology properties

As shown in Figure 1, both individual and mixed biochar treatments significantly increased maize chlorophyll content, as indicated by increased SPAD values (Figure 1A). The application of SP, DBM, and DSB significantly increased the SPAD in maize by 21.81%, 17.91%, and 17.51%, respectively. The findings deliver compelling evidence that the application of biochar had a significant alleviating influence on heavy metal stress.

In this study, the concentration of proline was lower in all amended treatments of biochars, except MSB treatments (Figure 1B). However, the difference was statistically nonsignificant. As shown in Figure 1C, the MDA concentration in all treatments of biochars was lower than in the control. Nevertheless, no statistically significant differences were observed between the biochar treatments and the control conditions. The soluble sugar concentration was significantly lower in all treatments than in the control ($p < 0.05$) (Figure 1D). The application of MSB, MSM, and DSB significantly decreased the soluble sugar concentration in maize by 24.24%, 22.37%, and 21.83%, respectively.

3.3 Effects of biochars on soil physical and chemical properties

Soil pH decreased significantly in the soil amended with BS, MS, and DSB ($p < 0.05$) (Figure 2A). Soil pH was positively influenced by the addition of SP, MSB, and MSM, surpassing the levels recorded in the BS-, MS-, and DBM-treated soils. Notably, MSB displayed the highest impact, resulting in a substantial increase of 0.34 units compared to the unamended soil.

The EC was significantly higher under all amended biochar samples than in the control ($p < 0.05$) (Figure 2B). The application of DSB, DSM, and DBM significantly increased the EC in soil by 259.49%, 198.73%, and 188.61%, respectively.

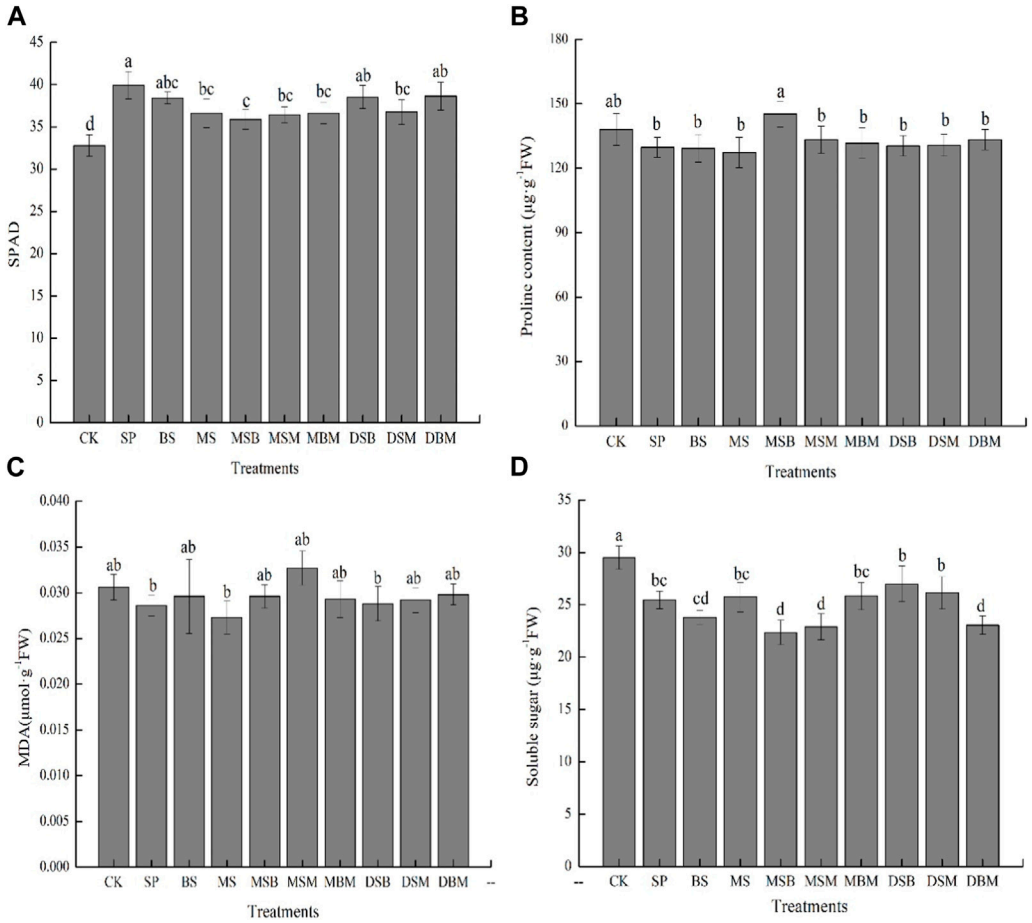

FIGURE 1
SPAD values **(A)**, proline contents **(B)**, MDA contents **(C)**, and soluble sugar contents **(D)** of maize grown in Cd-contaminated soils amended with biochars. The abbreviations for biochar treatments are reported in Table 2. Error bars indicate standard deviation (n = 3). Different letters indicate statistically significant differences ($p < 0.05$).

The available P content was significantly higher in soils amended with SP, BS, MS, DSB, DSM, and DBM than in the control ($p < 0.05$) (Figure 2C). The application of MS, DSM, and DBM markedly elevated the available P content in soil by 34.49%, 29.83%, and 25.78%, respectively. The available K content was significantly higher in soils after the application of biochars ($p < 0.05$) (Figure 2D). The soil treatments with MSB and SP exhibited significantly higher available K content than the other biochar treatments ($p < 0.05$). The application of MSB increased the available K content in the soil by 61.16%, while SP increased the available K content by 60.43%.

3.4 Effects of biochars on Cd content

In this study, the Cd content was higher in biochar-amended soils than in the unamended control soil. The Cd content amended with BS, MS, and DSB was significantly higher in amended soils than in the unamended control soil ($p < 0.05$) (Figure 3). Significant enhancements in soil Cd content were observed when BS and MS were used, with increases of 13.97% and 13.32%, respectively. All applications of biochar decreased the exchangeable Cd contents in soil. The inclusion of SP and DBM resulted in a substantial decline in the soil exchangeable Cd content, with reductions of 45.69% and 44.57%, respectively ($p < 0.05$).

3.5 Effects of biochars on Cd morphology in contaminated soil

Because the Cd concentration varied greatly among the different biochars, studying the changes in the proportion of each form of Cd under the different biochar treatments could more intuitively reflect the effect of biochar on the morphological transformation of Cd. Figure 4 indicates a significant difference in soil's exchangeable-bound (EX-bound) Cd content between the biochar treatments and the control (CK) ($p < 0.05$). The soil EX-bound Cd concentration was reduced by 45.30% and 46.37% under the DSB and DBM treatments, respectively (Figure 4A). The soil CA-bound Cd concentration under the biochar treatments was significantly higher than that of the CK and was considered too high for safe maize cultivation under the DSB treatment, with an increase of 96.32% compared to the CK (Figure 4B). The soil OX-bound Cd concentration under the MSB, MBM, DSB, DSM, and DBM treatments was significantly lower than that of the CK, with decreases of 19.49%, 22.68%, 34.28%, 22.17%, and

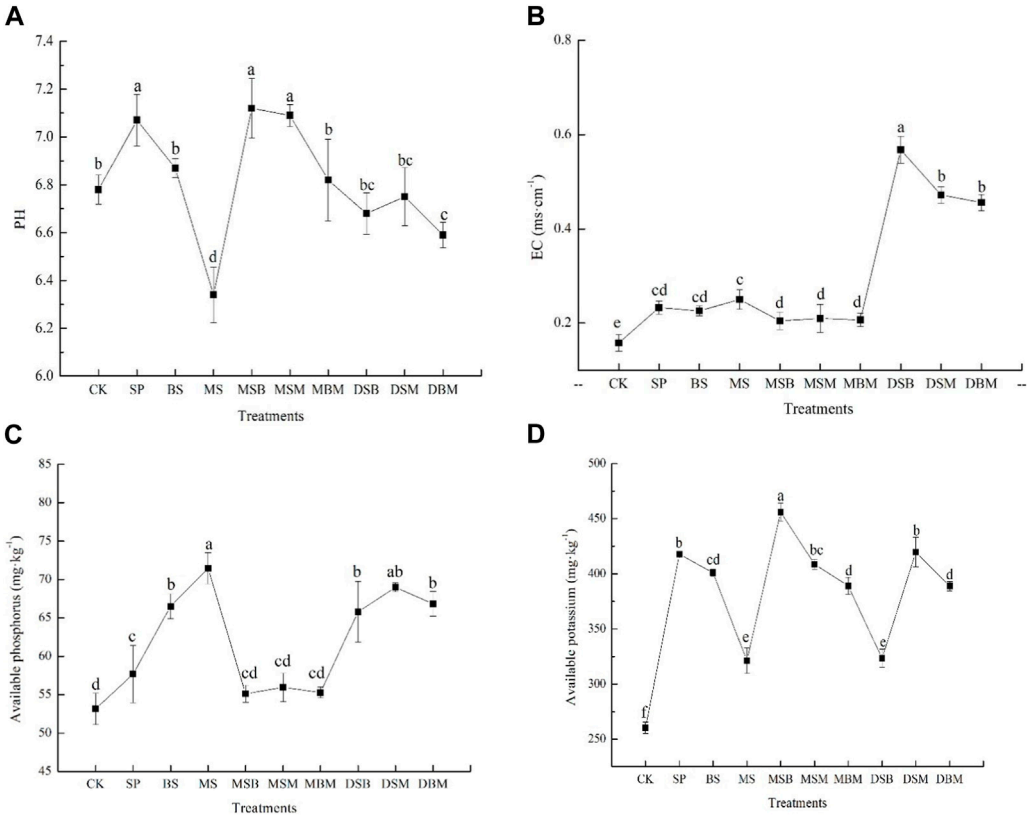

FIGURE 2
pH **(A)**, EC **(B)**, available phosphorus **(C)**, and available potassium **(D)** in soils contaminated with Cd and amended with biochars. The abbreviations for biochar treatments are reported in Table 2. Error bars indicate standard deviation (n = 3). Different letters indicate statistically significant differences ($p < 0.05$).

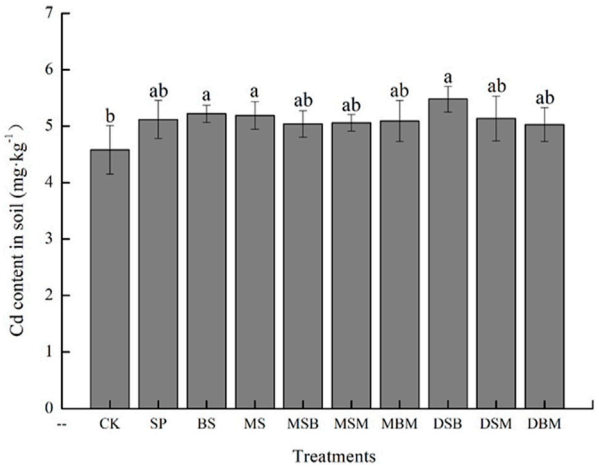

FIGURE 3
Cd content in soil in Cd-contaminated soil amended with biochars. The abbreviations for biochar treatments are reported in Table 2. Error bars indicate standard deviation (n = 3). Different letters indicate statistically significant differences ($p < 0.05$).

22.22%, respectively (Figure 4C). The soil OM-bound Cd concentration increased under the different biochar treatments compared to the CK, with increases of 105.53%, 175.60%, 78.75%, 81.00%, and 95.11% under the SP, BS, MS, DSM, and DBM treatments, respectively (Figure 4D). The soil RE-bound Cd concentration increased under the different biochar treatments, with 19.19%, 21.60%, 24.07%, 41.79%, 19.25%, and 13.96% increases compared to the CK under the MSB, MSM, MBM, DSB, DSM, and DBM treatments, respectively (Figure 4E). In conclusion, the application of biochar induced the conversion of soil Cd from the more active form to the more stable form, thus reducing the harmful effects of soil Cd.

3.6 Effects of biochars on Cd accumulation in the tissues of maize

The Cd concentration in different parts of maize was as follows: root > leaf > stem > grains (Figure 5). In this study, the Cd content in different parts of maize was lower under biochar-amended samples than in the control. The application of SP, BS, MSB, MBM, DSB, DSM, and DBM significantly decreased the Cd content in maize root ($p < 0.05$) (Figure 5A). The lowest Cd content in maize root was observed in treatments of SP and DBM, which decreased the Cd content by 52.99% and 47.55%, respectively. However, the application of MS and MSM increased the Cd content in maize root by 1.90% and 65.22%, respectively. Treatment of the soil with SP, BS, MSB, and DBM significantly decreased the Cd content in maize leaf ($p < 0.05$) (Figure 5B). The lowest Cd content in maize

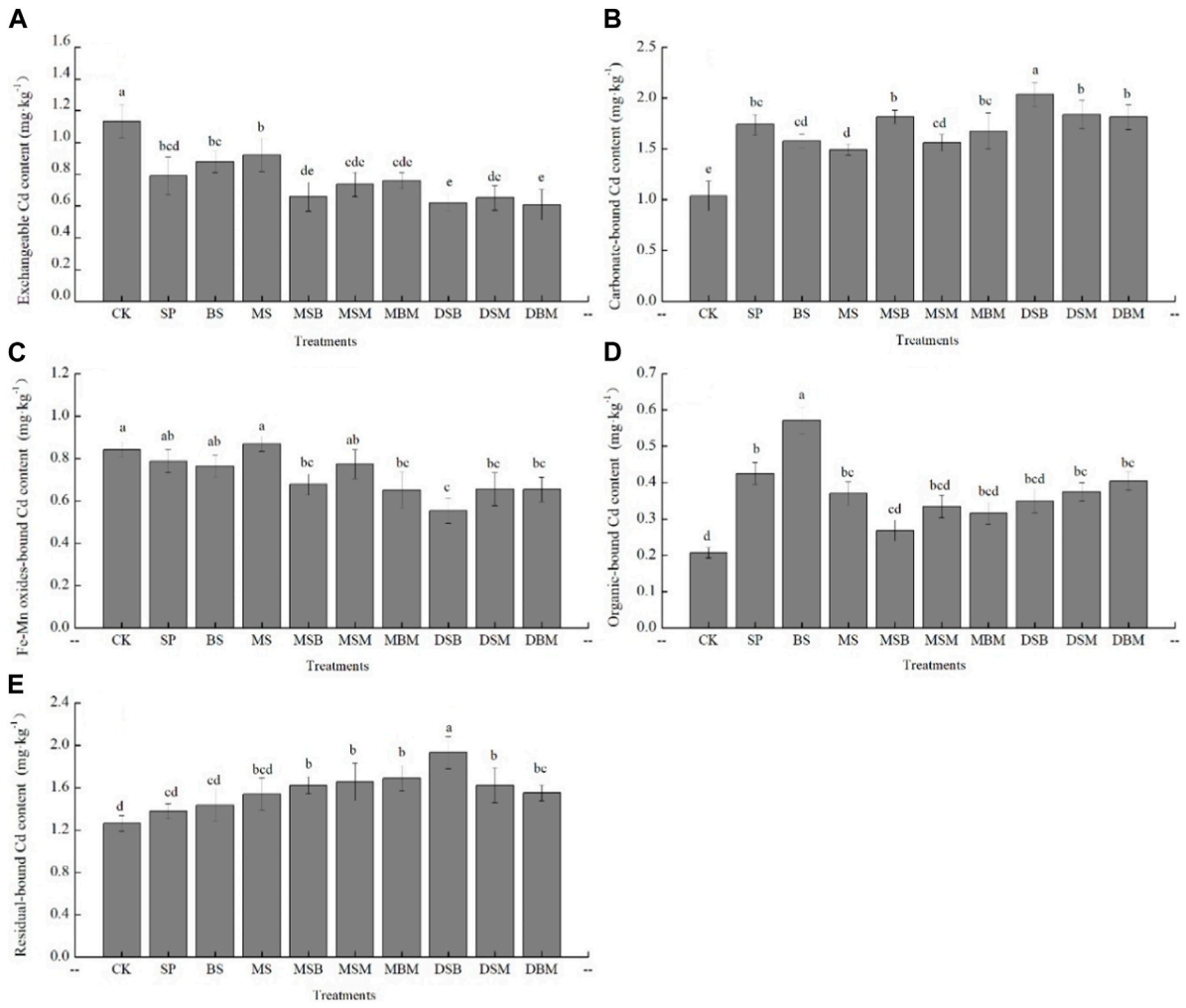

FIGURE 4
Exchangeable, carbonate, Fe-Mn oxides, organic and residual-bound Cd content in Cd-contaminated soil amended with biochars. The abbreviations for biochar treatments are reported in Table 2. Error bars indicate standard deviation (n = 3). Different letters indicate statistically significant differences ($p < 0.05$).

root was observed in treatments of the application of SP and MSB, which decreased the Cd content in maize leaves by 42.62% and 31.48%, respectively. The application of SP, MSB, and DBM significantly decreased the Cd content in maize stem ($p < 0.05$) (Figure 5C). The lowest Cd content in maize stem was observed in treatments of MSB, which decreased the Cd content by 46.37%. Treatments of soil with SP, BS, MSB, MBM, DSB, and DBM significantly decreased the Cd content in maize grains ($p < 0.05$) (Figure 5D). The application of SP and DBM significantly decreased the Cd content in maize grain by 32.68% and 43.14%, respectively.

4 Discussion

4.1 Effects of biochars on Cd accumulation in the tissues of maize

Biochar application can increase soil nutrient cycling, improve soil physicochemical properties, and increase soil N content, all of which positively affect plant growth (Jin et al., 2019; Yu et al., 2019; Ángela et al., 2022). Sun et al. (2023) found that N increased by 23.95% under 29.4 mg ha^{-1} biochar application, which substantially improved soil fertility. Higher levels of biochar application contribute to N retention in the soil and promote plant growth (Chan et al., 2007; Guerena et al., 2013). Another study found that the application of phosphorus fertilizer and biochar increased wheat yield, possibly owing to improvements in soil physical properties and organic matter (Mahmoud et al., 2017). The different types of biochar treatments in the present study increased maize plant biomass by varying degrees, which may be due to differences in the physicochemical properties of biochar prepared from peanut shells, bamboo, and maize stover (Michal et al., 2022). In this study, an increase in corn biomass corresponded to an increase in soil effective phosphorus and potassium. This suggests that biochar application is highly effective in improving soil fertility and promoting plant growth (Yang et al., 2022).

Chlorophyll is an important indicator of the plant response to different environmental stresses, and reactive oxygen species

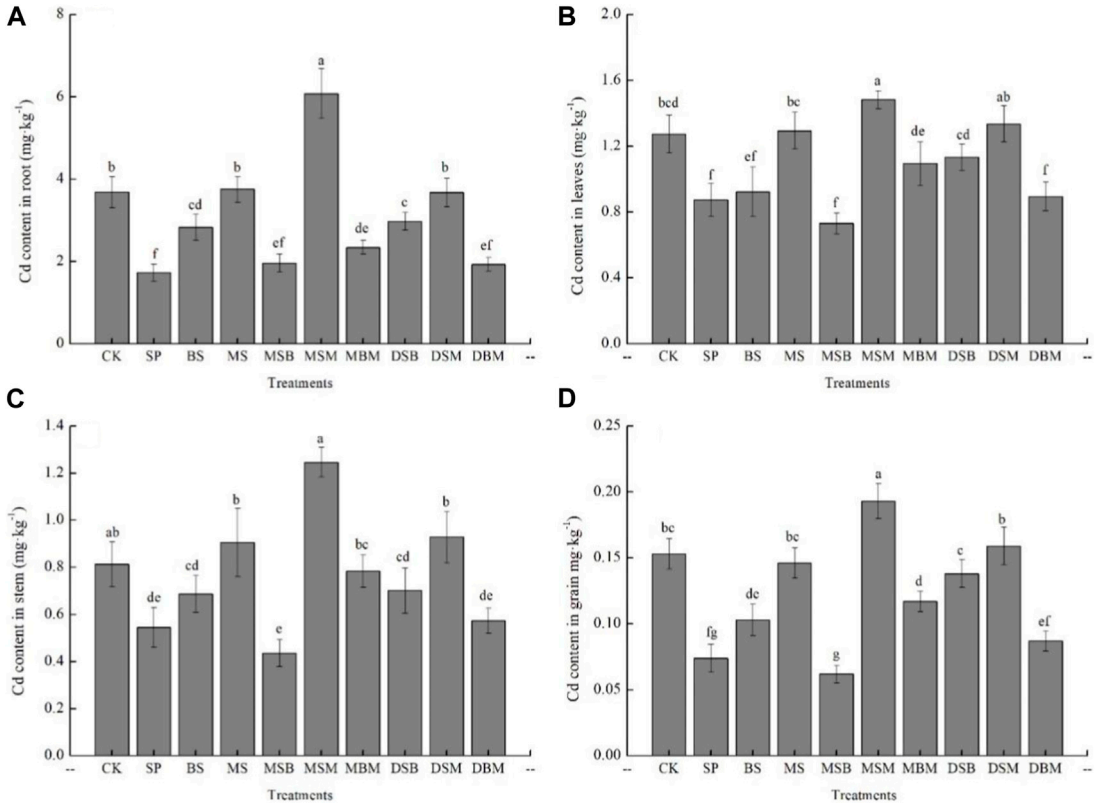

FIGURE 5
Cd content on the maize root, leave, stem and grain in Cd-contaminated soil amend with biochars. The abbreviations for biochar treatments are reported in Table 2. Error bars indicate standard deviation (n = 3). Different letters indicate statistically significant differences ($p < 0.05$).

production disrupts protein complexes and inhibits chlorophyll production (Oliveira, 2012; Jia et al., 2018). In the present study, the chlorophyll content of maize plants was effectively increased by applying biochar alone or in combination. Related studies have found that the addition of biochar to heavy metal-contaminated soil can increase plant chlorophyll content and reduce oxidative stress, favoring plant growth.

Proline is an important physiological indicator for maintaining the osmotic balance between protoplasts and the environment and resisting the damage caused by heavy metal ions (Schat et al., 2010). The content of proline in plant leaves was lower under no-stress conditions (Liu et al., 2015). Ángela et al. (2022) found that biochar improved antioxidant defenses in plants, which is a clear advantage for plant growth under stress conditions. Another study concluded that the addition of biochar reduced Cr toxicity by decreasing antioxidant enzyme activity. Plants were, therefore, less stressed (Younis et al., 2015). The addition of biochar to the soil improved the physiological characteristics of maize in heavy metal-contaminated soil, and these results may be related to the significant reduction in exchangeable Cd concentration in the contaminated soil after biochar addition. In this study, the effect of each treatment on maize proline was insignificant, probably because heavy metal stress itself had only a small effect on proline. MDA is an important physiological indicator of the degree of damage to the plant membrane system (Abdelhafez et al., 2014), and the difference in the MDA content between different biochar treatments in this study was not significant, probably because the amount of biochar applied was less. Soluble sugar is a sensitive index of plant response to heavy metal stress, and its content decreases with the increase in heavy metal concentration (Zhang et al., 2014). In this study, the soluble sugar content under the MSB, MSM, and DSB treatments was prominently lower than that of the single-biochar strategy, which indicated that the biochar application was effective in reducing soil Cd stress.

4.2 Effects of biochar on soil properties

Throughout the biochar production process of pyrolysis, alkaline cations (such as Ca, Mg, K, and Na) present in the biomass are converted into distinct alkaline compounds (e.g., ash comprising oxides, hydroxides, and carbonates). This process results in the dissolution of these alkaline compounds, thereby increasing the pH level of the soil (Houben et al., 2013; Kelly et al., 2014). The soil pH under the SP, MSB, and MSM treatments was significantly higher than that of the untreated soil, which may be because peanut shell biochar has a high pH. In addition, the presence of iron and manganese oxides in soil contributes to its amphiphilic colloidal properties, with their adsorption primarily governed by the negative surface charge. Through its interaction with the soil, biochar plays a role in elevating soil pH by decreasing the concentrations of H^+, Fe^{3+}, Al^{3+}, and Mn^{2+} ions in the soil solution (Liu et al., 2014). In this

study, significantly higher EC values were uncovered in soils modified with multiple types of biochar compared to the control, implying that elevated pH levels could influence the movement of heavy metals and enhance the cationic exchange capacity of the soil. The current study showed that the addition of biochar affected Cd adsorption, which may be the key reason for the reduction in Cd bioavailability in maize compared to that in the control. Sousa et al. (2018) found that the addition of a composite mixture of biochar and manure affected the adsorption of Cr and reduced its translocation from roots to stems (Sousa et al., 2018). In addition, Xia et al. (2020) found that the continuous addition of biochar altered the physical properties of the soil, such as pH and moisture and water-holding capacity, which led to changes in environmental conditions for soil microbes and nitrogen (N) cycling. This may also be the main reason for the reduction in N loss and the increase in soil fertility (Thangarajan et al., 2018).

4.3 Effects of biochar on the total Cd concentration and soil Cd morphology

The research conducted by Yang et al. (2016) demonstrated an inverse correlation between soil pH and the $CaCl_2$-extractable Cd concentration in heavy metal-contaminated soil, which was observed in soils that received supplementation with bamboo charcoal biochar and rice straw biochar (Yang et al., 2016). The biochar increased the soil pH, resulting in the precipitation of Cd as $CdCO_3$ (Xu et al., 2016). Yin et al. (2016) used 1%–2% rice straw biochar to treat agricultural soils in mining areas and found a significant reduction in the soil inter-root pore water Cd concentration (Yin et al., 2016). Corn straw biochar prepared by Gao et al. (2017) reduced the extractable Cd content in agricultural soils by 91% (Gao et al., 2017). In this study, the increase in the soil Cd content and decrease in the effective Cd content under different biochar treatments were mainly related to the increase in pH. The introduction of biochar into the soil increased its pH, triggering the hydrolysis of heavy metal cations. Consequently, oxide precipitates were formed, leading to a decrease in the exchangeable Cd concentration within the soil. Additionally, multiple investigations have revealed that biochar implementation can significantly affect the sorption and desorption behavior of heavy metals in soil.

The biotoxicity and harmful effects of heavy metals are not only related to their contents but are also determined by their fugitive forms. Following soil amendment due to the application of different biochars, the CA-bound Cd, RE-bound Cd, and OM-bound Cd concentrations increased and the OX-bound Cd concentration decreased, indicating that the application of biochar promoted the conversion of soil Cd from the active to the stable state. Biochar can interact with soil Cd by electrostatic adsorption, ion exchange, complexation, co-precipitation, and cation–π-bonding interactions, thus changing the fugitive form of soil Cd from the highly active form to the less active form, and finally achieving the passivation of soil Cd (Xia et al., 2020; Zhang et al., 2020). Biochar treatment significantly reduced the oxide-bound metal fraction. Jiang et al. observed a similar metal immobilization effect of biochar. In this study, biochar application reduced the oxide-bound metal fraction, but the differences between treatments were small. The Fe and Mn oxide-bound Cd is a transitional form, which is generally not easily absorbed and utilized by plants, but it is converted to the active state with changes in soil environmental conditions.

It has been documented that an increase in soil pH leads to an increase in negative charges on clay minerals, hydrated oxides, and organic matter surfaces. Consequently, the sorption capacity of these components for Cd^{2+} boosts, facilitating the formation and precipitation of $CdCO_3$ and $Cd(OH)_2$. This may have been responsible for the increase in CA-bound Cd (Chen et al., 2020). The increase in the OM-bound Cd concentration in soil may have been due to the abundance of OM-bound Cd in soil and the high concentrations of carboxyl, aldehyde, ketone, and aromatic substances in the carboxyl groups of biochar and crop straw decomposition products. The ability to retain ions was enhanced, gradually manifesting distinct colloidal characteristics (Li et al., 2017). In this study, the OM-bound Cd content of biochar under the MSM and MBM treatments increased, probably due to the higher ion retention ability of biochar produced from peanut shells and corn stover and biochar applied with bamboo charcoal and corn stover.

Biochar application in acidic rice soils caused a higher residual fraction of Cd, which can be attributed to the robust inner-sphere complexation between the metals and biochar particles (Zhu et al., 2015; Cui et al., 2016). The increase in the reducible fraction of Cd after biochar application could be attributed to the adsorption of Fe/Mn oxides (Fang et al., 2016), which in turn further increased the adsorption of Cd onto Fe and Mn oxides (Li et al., 2013).

4.4 Effects of biochar on the total Cd concentration in maize

The findings of this investigation demonstrated that biochar significantly reduced the harmful biological effects of soil Cd, and thus the uptake and transport of Cd by maize. A significant reduction of Cd was achieved by adopting diverse biochar types in combination. The addition of biochar derived from bean stalk and rice straw, as highlighted by Zheng's study, exhibited a significant reduction in the Cd content within rice roots, shoots, husks, and seeds (Zheng et al., 2012), which was proven to be consistent with the findings of this study. Liu et al. (2014) observed a substantial decline in the Cd concentration in crops following the application of bamboo stalk biochar. Aown et al. (2022) applied a biochar mixture to reduce bioavailable extractable Cr concentrations in soil by 36%, and soil Cd bioavailability was lower in the composite, amended treatment than in the control treatment (Aown et al., 2022). These findings suggested that biochar application can effectively immobilize Cd, reducing its mobility in the soil and inhibiting its uptake and accumulation in the aboveground tissues of crops. Additionally, Mohamed et al. (2018) found that the Cd concentration was higher in the belowground parts of wheat than in the aboveground parts (Mohamed et al., 2018), which was consistent with the pattern observed in this study. The Cd concentration in the root system of maize was higher than

that in the straw, confirming that maize reduces the toxic effect of Cd by fixing it in the root system and inhibiting its transfer to the aboveground tissues. In summary, the utilization of biochar contributed to the mineral nutrition provided to the crop, which in turn weakened the synergistic effect between Cd and other cationic metals and nonmetals.

5 Conclusion

Both individual and mixed-biochar applications increased maize plant biomass to varying degrees and enhanced maize Cd stress tolerance by increasing leaf chlorophyll content and decreasing soluble sugar content. In addition, both individual and mixed applications of biochar effectively increased the soil pH, which might have led to the conservation of N nutrients and an increase in soil fertility, which is an obvious advantage for plant growth under heavy metal stress. The Cd content of maize grains under the SP treatment was reduced to 0.1 mg kg^{-1}, which met the national standard for food safety and the limit of contaminants in food. This study confirmed that different mass ratios mixed with different biochars are important in immobilizing Cd in contaminated soil to ensure food security. Therefore, it can be concluded that the application of biochar in Cd-contaminated soil is an option for improvements in soil quality and crop growth. In the future, it will be necessary to evaluate the long-term effects of biochar application on soils and crops contaminated with heavy metals through field trials.

Data availability statement

The original contributions presented in the study are included in the article/Supplementary Material, further inquiries can be directed to the corresponding author.

Author contributions

Conceptualization: YZ; methodology: YZ and LZ; validation: YC and TN; formal analysis: XW; investigation: YZ; resources: JS; data curation: YZ; writing—original draft preparation: YZ; writing—review and editing: YZ; visualization: XB; supervision: EY and LZ; project administration: JS and TZ; funding acquisition: YZ. All authors contributed to the article and approved the submitted version.

Funding

This work is supported by the Natural Science Foundation of Zhejiang Province (LQ20C030007), the Hangzhou Agricultural and Social Development Scientific Research Project (20201203B108, 20201203B119), the Science and Technology Innovation Fund of Hangzhou Academy of Agricultural Sciences (2022HNCT-08), and the Zhejiang Provincial Key Research and Development Project (2019C02035).

Conflict of interest

The authors declare that the research was conducted in the absence of any commercial or financial relationships that could be construed as a potential conflict of interest.

Publisher's note

All claims expressed in this article are solely those of the authors and do not necessarily represent those of their affiliated organizations, or those of the publisher, the editors, and the reviewers. Any product that may be evaluated in this article, or claim that may be made by its manufacturer, is not guaranteed or endorsed by the publisher.

References

Abdelhafez, A. A., Li, J., and Abbas, M. H. H. (2014). Feasibility of biochar manufactured from organic wastes on the stabilization of heavy metals in a metal smelter contaminated soil. *Chemosphere* 117 (1), 66–71. doi:10.1016/j.chemosphere.2014.05.086

Aila, P., and Saradhi, P. P. (1991). Proline accumulation under heavy metal stress. *J. Plant Physiol.* 138 (5), 554–558. doi:10.1016/S0176-1617(11)80240-3

Ángela, M. G., Jorge, P., and Carolina, E. (2022). Overview of the use of biochar from main cereals to stimulate plant growth. *Front. Plant Sci.* 13, 912264. doi:10.3389/fpls.2022.912264

Aown, A., Muhammad, A., Muhammad, N., Abdul, L., Saqib, B., Amjad, A., et al. (2022). Synergistic use of biochar and acidified manure for improving growth of maize in chromium contaminated soil. *Int. J. Phytoremediation* 22 (1), 52–61. doi:10.1080/15226514.2019.1644286

Bai, Y. C., Zuo, W. G., Zhao, H. T., Mei, L. J., Gu, C. H., Guan, Y. X., et al. (2017). Distribution of heavy metals in maize and mudflat saline soil amended by sewage sludge. *J. Soils Sediments* 17 (6), 1565–1578. doi:10.1007/s11368-016-1630-z

Bashir, S., Hussain, Q., Akmal, M., Riaz, M., Hu, H., Ijaz, S. S., et al. (2018b). Sugarcane bagasse-derived biochar reduces the cadmium and chromium bioavailability to mash bean and enhances the microbial activity in contaminated soil. *J. Soil Sediments* 18 (3), 874–886. doi:10.1007/s11368-017-1796-z

Bashir, S., Zhu, J., Fu, Q., and Hu, H. (2018a). Cadmium mobility, uptake and anti-oxidative response of water spinach (Ipomoea Aquatic) under rice straw biochar, zeolite and rock phosphate as amendments. *Chemosphere* 19, 579–587. doi:10.1016/j.chemosphere.2017.11.162

Chan, K. Y., Van Zwieten, L., Meszaros, I., Downie, A., and Joseph, S. (2007). Agronomic values of greenwaste biochar as a soil amendment. *Soil Res.* 45, 629–634. doi:10.1071/SR07109

Chen, X., He, H. Z., Chen, G. K., and Li, H. S. (2020). Effects of biochar and crop straws on the bioavailability of cadmium in contaminated soil. *Sci. Rep.* 10 (1), 9528. doi:10.1038/s41598-020-65631-8

Christou, A., Theologides, C. P., Coasta, C., Kalavrouziotis, I. K., and Varnavas, S. P. (2017). Assessment of toxic heavy metals concentrations in soils and wild and cultivated plant species in Limni abandoned copper mining site, Cyprus. *J. Geochem. Explor.* 178, 16–22. doi:10.1016/j.gexplo.2017.03.012

Cui, L., Noerpel, M. R., Scheckel, K. G., and Ippolito, J. A. (2019). Wheat straw biochar reduces environmental cadmium bioavailability. *Environ. Int.* 126, 69–75. doi:10.1016/j.envint.2019.02.022

Cui, L. Q., Pan, G. X., Li, L. Q., Bian, R. J., Liu, X. Y., Yan, J. L., et al. (2016). Continuous immobilization of cadmium and lead in biochar amended contaminated paddy soil: a five-year field experiment. *Ecol. Eng.* 93, 1–8. doi:10.1016/j.ecoleng.2016.05.007

Department of Environmental Protection (2014). *Ministry of Land and Resources. National survey of soil pollution*. Beijing: Department of Environmental Protection. Ministry of Land and Resources.

Duan, C., Fang, L., Yang, C., Chen, W., Cui, Y., and Li, S. (2018). Reveal the response of enzyme activities to heavy metals through *in situ* zymography. *Ecotox Environ. Safe* 156, 106–115. doi:10.1016/j.ecoenv.2018.03.015

Duan, Q. M., Lee, J. C., Liu, Y. S., Chen, H., and Hu, H. Y. (2016). Distribution of heavy metal pollution in surface soil samples in China: a graphical review. *Bull. Environ. Contam. Toxicol.* 97 (3), 303–309. doi:10.1007/s00128-016-1857-9

Fang, S. E., Tsang, D. C. W., Zhou, F. S., Zhang, W. H., and Qiu, R. L. (2016). Stabilization of cationic and anionic metal species in contaminated soils using sludge-derived biochar. *Chemosphere* 149, 263–271. doi:10.1016/j.chemosphere.2016.01.060

Gao, J. K., Lv, J. L., Wu, H. M., Dai, Y. C., and Nasir, M. (2017). Impacts of wheat straw addition on dissolved organic matter characteristics in cadmium-contaminated soils: insights from fluorescence spectroscopy and environmental implications. *Chemosphere* 193, 1027–1035. doi:10.1016/j.chemosphere.2017.11.112

Gondek, K., Mierzwa, H. M., and Kopeć, M. (2018). Mobility of heavy metals in sandy soil after application of composts produced from maize straw, sewage sludge and biochar. *J. Environ. Manage* 210, 87–95. doi:10.1016/j.jenvman.2018.01.023

Guerena, D., Lehmann, J., Hanley, K., Enders, A., Hyland, C., and Riha, S. (2013). Nitrogen dynamics following field application of biochar in a temperate North American maize-based production system. *Plant Soil* 365, 239–254. doi:10.1007/s11104-012-1383-4

Holatko, J., Hammerschmiedt, T., Kucerik, J., Baltazar, T., Radziemska, M., Havlicek, Z., et al. (2022). Soil properties and maize yield improvement with biochar-enriched poultry litter-based fertilizer. *Basel)* 15 (24), 9003. doi:10.3390/ma15249003

Houben, D., Evrard, L., and Sonnet, P. (2013). Mobility, bioavailability and Ph dependent leaching of cadmium, zinc, and lead in a contaminated soil amended with biochar. *Chemosphere* 92, 1450–1457. doi:10.1016/j.chemosphere.2013.03.055

Huerta, E. R., Arnienta, M., Dubrovsky, J., and Bernal, J. M. G. (2022). Bioaccumulation of heavy metals and as in maize (Zea mays L) grown close to mine tailings strongly impacts plant development. *Ecotoxicology* 31, 447–467. doi:10.21203/rs.3.rs-827219/v1

Jia, R., Qu, Z., You, P., and Qu, D. (2018). Effect of biochar on photosynthetic microorganism growth and iron cycling in paddy soil under different phosphate levels. *Sci. Total Environ.* 612, 223–230. doi:10.1016/j.scitotenv.2017.08.126

Jin, Z., Chen, C., Chen, X., Hopkins, I., Zhang, X., Han, Z., et al. (2019). The crucial factors of soil fertility and rapeseed yield - a five year field trial with biochar addition in upland red soil, China. *Sci. Total Environ.* 649, 1467–1480. doi:10.1016/j.scitotenv.2018.08.412

Kelly, C. N., Peltz, C. D., Stanton, M., Rutherford, D. W., and Rostad, C. E. (2014). Biochar application to hardrock mine tailings: soil quality, microbial activity, and toxic element sorption. *Appl. Geochem* 43, 35–48. doi:10.1016/j.apgeochem.2014.02.003

Li, H., Dong, X., da Silva, E, B., de Oliveira, L. M., Chen, Y., and Ma, L. Q. (2017). Mechanisms of metal sorption by biochars: biochar characteristics and modifications. *Chemosphere* 178, 466–478. doi:10.1016/j.chemosphere.2017.03.072

Li, M. Y., Ly, D., Zhang, Y., and Gao, Y. D. (2013). Influence of pyrolysis temperatures of biochar obtained from the rice straw on cadmium forms. *J. Soil Water Conserv.* 27 (6), 2511–2519. (in Chinese). doi:10.13870/j.cnki.stbcxb.2013.06.010

Li, S., Chen, J., Islam, E., Wang, Y., Wu, J., Ye, Z., et al. (2016). Cadmium-induced oxidative stress, response of antioxidants and detection of intracellular cadmium in organs of moso bamboo (Phyllostachys pubescens) seedlings. *Chemosphere* 153, 107–114. doi:10.1016/j.chemosphere.2016.02.062

Liang, J., Yang, Z. X., Tang, I., Zeng, G. M., Yu, M., Li, X. D., et al. (2017). Changes in heavy metal mobility and availability from contaminated wetland soil remediated with combined biochar-compost. *Chemosphere* 181, 281–288. doi:10.1016/j.chemosphere.2017.04.081

Liu, D., Li, S., Islam, E., Chen, J., Wu, J., Ye, Z., et al. (2015). Lead accumulation and tolerance of moso bamnoo (phyllostachys pubecens) seedlings: applications of phytoremediation. *J. Zhejiang Univ. Sci. B* 16 (2), 123–130. doi:10.1631/jzus.B1400107

Liu, X. L., Zeng, Z. X., Chen, Q. W., and Zou, H. L. (2014). Effects of biochar and lime additives on non-point load of heavy metals in paddy soil. *J. Hydraul. Eng.* 45, 682–690. doi:10.13243/j.cnki.slxb.2014.06.007

Liu, Y. X., Wang, Y. Y., Lu, H. H., Linson, L. P., Brar, S. K., and He, L. I. (2011). Lead accumulation and tolerance of moso bamboo (phyllostachys pubescens) seedlings: applications of phytoremediation. *J. Zhejiang Univ. Sci. B*, 123–130. doi:10.1631/jzus.B1400107

Mahmoud, E., Beshbeshy, T. R., El-Kader, A., El-Shall, B., and Khalafallah, N. (2017). Biochar impacts on physical properties and wheat yield of salt affected soils. *Int. J. Sci. Res. Publ.* 2 (1), 1–10.

Michal, K., Sarka, S., Jiri, S., Monika, T., Jan, H., Leona, K., et al. (2022). The effect of pyrolysis temperature and the source biomass on the properties of biochar produced for the agronomical applications as the soil conditioner. *Mater. (Basel)* 15 (24), 8855. doi:10.3390/ma15248855

Mohamed, I., Ali, M., Ahmed, N., Abbas, M. H. H., Abdelsalam, M., Azab, A., et al. (2018). Cow manure-loaded biochar changes Cd fractionation and phytotoxicity potential for wheat in a natural acidic contaminated soil. *Ecotox Environ. Safe* 2162, 348–353. doi:10.1016/j.ecoenv.2018.06.065

Oliveira, H. (2012). Chromium as an environmental pollutant: insights on induced plant toxicity. *J. Bot.* 2012, 1–8. doi:10.1155/2012/375843

Page, A. L. (1982). *Method of soil analysis, part 2, Chemical and microbiological properties*. Second ed. Wisconsin, USA: American Society of Agronomy, Inc. Soil Science Society of America, Inc.

Sarwar, N., Imran, M., Shaheen, M. R., Ishaque, W., Kamran, M. A., Matloob, A., et al. (2017). Phytoremedia-tion strategies for soils contaminated with heavy metals: modifications and future perspectives. *Chemosphere* 171, 710–721. doi:10.1016/j.chemosphere.2016.12.116

Schat, H., Sharma, S. S., and Vooijs, R. (2010). Heavy metal-induced accumulation of free proline in a metal-tolerant and a nontolerant ecotype of silene vulgaris. *Physiol. Plant.* 101 (3), 477–482. doi:10.1111/j.1399-3054.1997.tb01026.x

Sousa, R. S. D., Nunes, L., Lima, A. B. D., Melo, W. J. D., Antunes, J. E. L., and Araujo, A. (2018). Chromium accumulation in maize and cowpea after successive applications of composted tannery sludge. *Acta Sci. Agron.* 40, 35361–35460. doi:10.4025/actasciagron.v40i1.35361

Sun, J., Lu, X. R., Wang, S., Tian, C. K., Chen, G. S., Luo, N. N., et al. (2023). Biochar blended with nitrogen fertilizer promotes maize yield by altering soil enzyme activities and organic carbon content in black soil. *Int. J. Environ. Res. Public Health* 20 (6), 4939. doi:10.3390/ijerph20064939

Tashiro, C., Takahashi, H., Kanaya, M., Hirakida, I., and Yoshida, R. (1997). Hardening property of cement mortar adding heavy metal compound and solubility of heavy metal from hardened mortar. *Cem. Concr. Res.* 7 (3), 283–290. doi:10.1016/0008-8846(77)90090-4

Tessier, A., Campbell, P. G. C., and Bisson, M. (1979). Sequential extraction procedure for the speciation of particulate trace metals. *Anal. Chem.* 51 (7), 844–851. doi:10.1021/ac50043a017

Thangarajan, R., Bolan, N. S., Kunhikrishnan, A., Wijesekara, H., Xu, Y., Tsang, D. C. W., et al. (2018). The potential value of biochar in the mitigation of gaseous emission of nitrogen. *Sci. Total Environ.* 612, 257–268. doi:10.1016/j.scitotenv.2017.08.242

Wan, Y., Camara, A. Y., Yu, Y., Wang, Q., Guo, T., Zhu, L., et al. (2018). Cadmium dynamics in soil pore water and uptake by rice: influences of soil-applied selenite with different water managements. *Environ. Pollut.* 240, 523–533. doi:10.1016/j.envpol.2018.04.044

Xia, Y., Luo, H. N., Li, D., Chen, Z., Yang, S., Liu, Z., et al. (2020). Efficient immobilization of toxic heavy metals in multi-contaminated agricultural soils by amino-functionalized hydrochar: performance, plant responses and immobilization mechanisms. *Enviro Pollu* 261, 114217. doi:10.1016/j.envpol.2020.114217

Xie, Y. X., Dong, C., Chen, Z. Y., Liu, Y. J., Zhang, Y. Y., Gou, P. X., et al. (2021). Successive biochar amendment affected crop yield by regulating soil nitrogen functional microbes in wheat-maize rotation farmland. *Environ. Res.* 194, 110671. doi:10.1016/j.envres.2020.110671

Xu, P., Sun, C. X., Ye, X. Z., Xiao, W. D., Zhang, Q., and Wang, Q. (2016). The effect of biochar and crop straws on heavy metal bioavailability and plant accumulation in a Cd and Pb polluted soil. *Ecotoxicol. Environ. Saf.* 132, 94–100. doi:10.1016/j.ecoenv.2016.05.031

Xu, W. J., Mohammad, S., Penttinena, P., Shuzhen, H., and Liu, D. (2019). Bioavailability of heavy metals in contaminated soil as affected by different mass ratios of biochars. *Enviro Techno* 2019, 1609096. doi:10.1080/21622515.2019.1609096

Xu, Z. Y., Tang, M., Chen, H., Ban, Y. H., and Zhang, H. H. (2012). Microbial community structure in the rhizosphere of Sophora viciifolia grown at a lead and zinc mine of northwest China. *Sci. Total Enviro* 09 (435–436), 453–464. doi:10.1016/j.scitotenv.2012.07.029

Yang, Q., Li, Z., Lu, X. N., Duan, Q. N., Huang, L., and Bi, J. (2018). A review of soil heavy metal pollution from industrial and agricultural regions in China: pollution and risk assessment. *Sci. Total Envir* 642, 690–700. doi:10.1016/j.scitotenv.2018.06.068

Yang, W., Feng, G., Jia, Y. L., Yang, Y. X., Gao, X. Y., Gao, L. H., et al. (2022). Impact of single biochar application on maize growth and water-fertilizer productivity under different irrigation regimes. *Front. Plant Sci.* 13, 1006827. doi:10.3389/fpls.2022.1006827

Yang, X., Liu, J., McGrouther, K., Huang, H., Lu, K., Guo, X., et al. (2016). Effect of biochar on the extractability of heavy metals (Cd, Cu, Pb, and Zn) and enzyme activity in soil. *Environ. Sci. Pollut. Res.* 23, 974–984. doi:10.1007/s11356-015-4233-0

Yin, D. X., Wang, X., Chen, C., Peng, B., Tang, C. Y., and Li, H. L. (2016). Varying effect of biochar on Cd, Pb and as mobility in a multi-metal contaminated paddy soil. *Chemosphere* 152, 196–206. doi:10.1016/j.chemosphere.2016.01.044

Younis, U., Athar, M., Malik, S. A., Raza, S., and Mahmood, S. (2015). Biochar impact on physiological and biochemical attributes of spinach (*Spinacia oleracea* L) in nickel contaminated soil. *Glob. J. Environ. Sci. Manage* 1 (3), 245–254. doi:10.7508/gjesm.2015.03.007

Yu, H., Zou, W., Chen, J., Chen, H., Yu, Z., Huang, J., et al. (2019). Biochar amendment improves crop production in problem soils: a review. *J. Environ. Manag.* 232, 8–21. doi:10.1016/j.jenvman.2018.10.117

Zha, Y., Zhao, B., and Niu, T. X. (2022). Bamboo biochar and zinc oxide nanoparticles improved the growth of maize (Zea mays L) and decreased cadmium uptake in Cd contaminated soil. *Agriculture* 12 (9), 1507doi. doi:10.3390/agriculture12091507

Zha, Y., Zhao, L., Niu, T. X., Yue, E. K., Wang, X. B., and Shi, J. (2023). Multi-target element-based screening of maize varieties with low accumulation of heavy metals (HMs) and metalloids: uptake, transport, and health risks. *Agriculture* 13, 1123. doi:10.3390/agriculture13061123

Zhang, A. F., Cheng, G., Hussain, Q., Zhang, M., Feng, H., Dyck, M., et al. (2017). Contrasting effects of straw and straw-derived biochar application on net global warming potential in the Loess Plateau of China. *Field Crop Res.* 205, 45–54. doi:10.1016/j.fcr.2017.02.006

Zhang, A., Li, X., Xing, J., and Xu, G. (2020). Adsorption of potentially toxic elements in water by modified biochar: a review. *J. Envir Chemi Engin* 8 (4), 104196. doi:10.1016/j.jece.2020.104196

Zhang, R. H., Li, Z. G., Liu, X. D., Wang, B. C., Zhou, G. L., Huang, X. X., et al. (2017). Immobilization and bioavailability of heavy metals in greenhouse soils amended with rice straw-derived biochar. *Ecol. Eng.* 98, 183–188. doi:10.1016/j.ecoleng.2016.10.057

Zhang, X. K., He, L. Z., Sarmah, A. K., Lin, K. D., Liu, Y. K., Li, J. W., et al. (2014). Retention and release of diethyl phthalate in biochar-amended vegetable garden soils. *J. Soil. Sediment.* 14, 1790–1799. doi:10.1007/s11368-014-0929-x

Zhao, F. J., Ma, Y. B., Zhu, Y. G., Tang, Z., and McGrath, S. P. (2015). Soil contamination in China: current status and mitigation strategies. *Environ. Sci. Technol.* 49, 750–759. doi:10.1021/es5047099

Zheng, R. L., Cai, C., Liang, J. H., Huang, Q., Chen, Z., Huang, Y. Z., et al. (2012). The effects of biochars from rice residue on the formation of iron plaque and the accumulation of Cd, Zn, Pb, as in rice (Oryza sativa L) seedlings. *Chemosphere* 89, 856–862. doi:10.1016/j.chemosphere.2012.05.008

Zhu, Q. H., Wu, J., Wang, L, L., Yang, G., and Zhang, X, H. (2015). Effect of biochar on heavy metal speciation of paddy soil. *Water Air Soil Poll.* 226, 429. doi:10.1007/s11270-015-2680-3

frontiers | Frontiers in Microbiology

TYPE Original Research
PUBLISHED 08 September 2023
DOI 10.3389/fmicb.2023.1225746

OPEN ACCESS

EDITED BY
Vishal Tripathi,
Graphic Era University, India

REVIEWED BY
Anukool Vaishnav,
Agroscope, Switzerland;
Durgesh K. Jaiswal,
Savitribai Phule Pune University, India

*CORRESPONDENCE
Yanchun Yan
✉ yanyanchun@caas.cn;
Yu-Qin Zhang
✉ yzhang@imb.pumc.edu.cn

†These authors have contributed equally to this work and share first authorship

RECEIVED 30 May 2023
ACCEPTED 28 August 2023
PUBLISHED 08 September 2023

CITATION
Deng Y, Mou T, Wang J, Su J, Yan Y and Zhang Y-Q (2023) Characterization of three rapidly growing novel *Mycobacterium* species with significant polycyclic aromatic hydrocarbon bioremediation potential.
Front. Microbiol. 14:1225746.
doi: 10.3389/fmicb.2023.1225746

Characterization of three rapidly growing novel *Mycobacterium* species with significant polycyclic aromatic hydrocarbon bioremediation potential

Yang Deng[1,2†], Tong Mou[1,2†], Junhuan Wang[3†], Jing Su[1], Yanchun Yan[3*] and Yu-Qin Zhang[1,2*]

[1]Institute of Medicinal Biotechnology, Chinese Academy of Medical Sciences and Peking Union Medical College, Beijing, China, [2]State Key Laboratory of Dao-di Herbs, Beijing, China, [3]Graduate School of Chinese Academy of Agricultural Sciences, Beijing, China

Mycobacterium species exhibit high bioremediation potential for the degradation of polycyclic aromatic hydrocarbons (PAHs) that are significant environmental pollutants. In this study, three Gram-positive, rapidly growing strains (YC-RL4^T, MB418^T, and HX176^T) were isolated from petroleum-contaminated soils and were classified as *Mycobacterium* within the family *Mycobacteriaceae*. Genomic average nucleotide identity (ANI; < 95%) and digital DNA–DNA hybridization (dDDH; < 70%) values relative to other *Mycobacterium* spp. indicated that the strains represented novel species. The morphological, physiological, and chemotaxonomic characteristics of the isolates also supported their affiliation with *Mycobacterium* and their delineation as novel species. The strains were identified as *Mycobacterium adipatum* sp. nov. (type strain YC-RL4^T = CPCC 205684^T = CGMCC 1.62027^T), *Mycobacterium deserti* sp. nov. (type strain MB418^T = CPCC 205710^T = KCTC 49782^T), and *Mycobacterium hippophais* sp. nov. (type strain HX176^T = CPCC 205372^T = KCTC 49413^T). Genes encoding enzymes involved in PAH degradation and metal resistance were present in the genomes of all three strains. Specifically, genes encoding alpha subunits of aromatic ring-hydroxylating dioxygenases were encoded by the genomes. The genes were also identified as core genes in a pangenomic analysis of the three strains along with 70 phylogenetically related mycobacterial strains that were previously classified as *Mycolicibacterium*. Notably, strain YC-RL4^T could not only utilize phthalates as their sole carbon source for growth, but also convert di-(2-ethylhexyl) phthalate into phthalic acid. These results indicated that strains YC-RL4^T, MB418^T, and HX176^T were important resources with significant bioremediation potential in soils contaminated by PAHs and heavy metals.

KEYWORDS

***Mycobacterium adipatum*, *Mycobacterium deserti*, *Mycobacterium hippophais*, genome, bioremediation potential**

Highlights

- Polycyclic aromatic hydrocarbons (PAHs) are significant environmental pollutants caused by human industrial activities.
- The bioremediation of PAHs is a promising method of pollutant mitigation and *Mycobacterium* species have been previously reported to hold considerable bioremediation potential.
- In this study, three novel species of *Mycobacterium* were isolated from polluted soil samples, formally characterized, and evaluated for bioremediation potential.
- The three strains were found to exhibit considerable potential for bioremediation of PAHs due to their physiological and genomic characteristics.
- Thus, these newly described species represent an important resource for bioremediation efforts.

Introduction

The *Mycobacterium* genus encompasses a large group of Gram-positive, rod-shaped, acid-fast bacteria of the phylum *Actinomycetota*, that was first proposed by Skerman et al. (1980). Early classification of *Mycobacterium* was based on growth rate, pigmentation, and clinical significance (Runyon, 1959). Indeed, the fundamental taxonomic division of the group was connected to growth rate, such that species were defined as either slow or rapid growers. Rapid growers exhibit visible growth from dilute inocula within 7 days, while slow growers require over 7 days to achieve visible growth. Subsequently, immunological methods, in addition to comparisons of cell wall components, homologous enzyme sequences, DNA–DNA homologies, plasmid profiles, and restriction endonuclease analyses were used to complement the quantitative growth studies and infer natural relationships among *Mycobacterium* strains. Stahl and Urbance conducted a thorough phylogenetic analysis of *Mycobacterium* in 1990 based on comparison of 16S rRNA sequences, revealing phylogenetic relationships that were consistent with previous classifications (Stahl and Urbance, 1990). Lévy-Frébault and Portaels further proposed minimal standards for describing *Mycobacterium* species in 1992 (Lévy-Frébault and Portaels, 1992). These standards included acid-alcohol staining fastness, DNA G + C content levels, and mycolic acid presence. The recommended minimal standards for describing a new slowly growing *Mycobacterium* species were consequently based on phenotypic and genomic analyses. Takewaki et al. (1994) revealed species-specific restriction site profiles within amplified *dnaJ* genes in 1994 that could differentiate most *Mycobacterium* species based on a combination of PCR and restriction fragment length polymorphism analyses. The relationships among mycobacterial species were also concomitantly evaluated using the sequences of 23S rRNA gene spacers (Stone et al., 1995) in addition to those of several housekeeping genes including *hsp65* (Kim et al., 2005), *gyrB* (Kasai et al., 2000), *rpoB* (Tortoli, 2012), and *gyrA* (Guillemin et al., 1995). Gupta et al. (2018) proposed a revision of mycobacteria taxonomy in 2018 that redistributed the 150 species of *Mycobacterium* into five genera based on synapomorphies. The four newly proposed genera comprised the non-tuberculous mycobacteria and included *Mycobacteroides*, *Mycolicibacter*, *Mycolicibacterium*, and *Mycolicibacillus*. Non-tuberculous mycobacteria exhibit diverse genomic backgrounds and physiological characteristics, but produce remarkably similar disease manifestations within at-risk populations. Consequently, Tortoli et al. (2019) suggested not renaming clinically important organisms in 2019, including non-tuberculous mycobacteria, suggesting that the use of the previously established *Mycobacterium* genus exhibited the advantage of avoiding confusion in health care settings. The genus *Mycobacterium* currently comprises 195 species with validly published names.[1] The primary ecological niche for some *Mycobacterium* is the diseased tissue of warm-blooded hosts. Most human infections are caused by either *M. leprae* or *M. tuberculosis*, although other *Mycobacterium* strains are opportunistic pathogens of humans, particularly in immunocompromised individuals (Hartmans et al., 2006). However, most *Mycobacterium* species are non-pathogenic to humans and are inhabitants of many natural environments, including freshwaters and soils (Falkinham, 2009). In addition, several strains of *Mycobacterium* have been isolated from soils contaminated with polycyclic aromatic hydrocarbons (PAHs) like gasoline and coal tar (Willumsen et al., 2001; Hormisch et al., 2004; Zhang et al., 2012).

PAHs have become a significant environmental concern due to their potential toxic, mutagenic, and carcinogenic properties (Zeng et al., 2004). *Mycobacterium* species are typical PAH-degrading bacteria and can degrade high molecular weight PAHs by introducing two oxygen atoms to PAH compounds through dioxygenase enzymes (Khan et al., 2001). *M. vanbaalenii* PYR-1 was first shown to degrade low molecular weight compounds like 4-ring pyrene (Pereira et al., 2020). The unique cell wall layer of mycobacteria, including the presence of mycolic acids, plays an important role in mycobacterial degradation of hydrophobic PAHs (Abbasnezhad et al., 2011). Indeed, pyrene-degrading mycobacteria can degrade diverse PAHs, including naphthalene, phenanthrene, and fluoranthene, and even five-ring compounds like benzo[α]pyrene via co-metabolic biodegradation, subsequently using these compounds as carbon sources (Kweon et al., 2011). Zeng et al. (2017) revealed that the PdoAB dioxygenase from *Mycobacterium* sp. NJS-P exerts versatile functions in oxidizing various PAHs, including up to five-ring compounds like benzo[α]

Abbreviations: DPG, diphosphatidylglycerol; PE, phosphatidylethanolamine; PI, phosphatidylinositol; ANI, average nucleotide identity; dDDH, digital DNA–DNA hybridization; PAHs, polycyclic aromatic hydrocarbons; PAH-RHDs, polycyclic aromatic hydrocarbons ring-hydroxylating dioxygenases.

1 https://lpsn.dsmz.de/genus/mycobacterium

pyrene. Further, *pdoAB* can be induced during bacterial growth on pyrene and phenanthrene, implicating its function in PAH degradation. *Mycobacterium* species in rhizosphere soils have also been shown to accelerate the degradation of organic contaminants like PAHs and enhance plant resistance to soil pollution (Dai et al., 2020). Moreover, Yang et al. (2021) recently observed that the pyrene-degrading bacterium, *Mycobacterium* sp. Pyr9 exhibited diverse plant growth-promoting characteristics and a high tolerance to harsh environments, suggesting a high potential for bioremediation application (Yang et al., 2021). Thus, pyrene-degrading *Mycobacterium* strains may contribute to improving the safety of agricultural products and human health in PAHs polluted environments.

Phthalates are widely used industrial compounds and intensively studied environmental pollutants that exhibit endocrine disrupting properties. Strain NK0301 was the first *Mycobacterium* strain observed to degrade phthalates. It could degrade di-(2-ethylhexyl) phthalate (DEHP) into 2-ethylhexanol and 1,2-benzenedicarboxylic acid (Nakamiya et al., 2005). Wright et al. (2020) subsequently observed that the marine phthalate-degrading strain *Mycobacterium* sp. DBP42 could degrade diverse phthalates by transforming them into phthalic acid (PA) via di-alkyl phthalate esters (DAPs), and was also able to utilize PA as a growth substrate via the protocatechuate branch of the *β*-ketoadipate pathway.

Notably, some rapidly growing mycobacterial strains that were previously classified as *Mycolicibacterium* are also phthalate-degrading bacteria. Fourteen molecular markers (4 CSIs and 10 CSPs) are unique to members of the former *Mycolicibacterium* genus, supporting its monophyly and genetic cohesiveness. These strains could be distinguished from other *Mycobacteriaceae* genera, in addition to other bacteria, based on the presence of conserved signature indels in genes encoding the LacI family transcriptional regulator, cyclase, CDP-diacylglycerol–glycerol-3-phosphate 3-phosphatidyltransferase, and CDP-diacylglycerol–serine O-phosphatidyltransferase (Gupta et al., 2018). A novel DEHP-degrading marine bacterium was identified in 2021 as *Mycolicibacterium phocaicum* RL-HY01 that was isolated from intertidal sediments polluted by municipal wastewaters. The strain could transform DEHP into PA by *β*-oxidation and de-esterification and was further utilized within the gentisate branch of the *β*-ketoadipate pathway (Ren et al., 2021). Strain YC-RL4^T was previously isolated from petroleum-contaminated soil and belonged to the *Mycobacterium* genus. The strain could utilize phthalates as their sole carbon source for growth and could also transform DEHP into PA via MEHP (mono (2-ethylhexyl) phthalate), with PA further being utilized for growth via the benzoic acid (BA) degradation pathway (Ren et al., 2016). Currently, limited research could be referred on the degradation of polycyclic aromatic hydrocarbons (PAHs) in environmental pollution by strains of the genus *Mycobacterium*. Especially, the taxonomic status of these PAHs-degrading strains and the clear understanding of the functional genes and metabolic pathways involved in PAHs degradation are still unclear. In this study, strain YC-RL4^T (= CPCC 205684^T = CGMCC 1.62027^T) and two other strains that were closely related to each other were characterized, and their functional genes, metabolic pathways and potential for degrading PAHs were evaluated. Furthermore, this study also identified that these strains with PAHs degradation potential also possessed the potential heavy metal resistance. This remarkable bioremediation potential held significant importance for their future applications in the field of bioremediation. Polyphasic taxonomic analyses revealed that the three strains were novel *Mycobacterium* species with considerable application potential for the bioremediation of PAH-degrading soils.

Materials and methods

Strain acquisition

Strain YC-RL4^T was isolated from a petroleum-contaminated soil sample collected from Heze City (35°16′ N, 115°28′ E), Shandong Province, China, as described by Ren et al. (2016). Strain MB418^T was isolated from a gravel soil sample collected from the Gurbantunggut desert (45°22′ N, 88°20′ E) in Xinjiang. Strain HX176^T was isolated from rhizosphere soil associated with a medicinal plant in Xinjiang (43°36′ N, 82°11′ E). About 2 g of each sample was suspended in 18 mL of 0.85% (w/v) NaCl solution. Then, 200 μL of 10^{-4} diluted soil suspensions were spread on humic acid agar medium, as previously described (Deng et al., 2022). After incubation for 2 weeks at 28°C, visible colonies were picked and streaked on peptone yeast glucose (PYG) medium containing peptone (3 g L^{-1}), yeast extract (5 g L^{-1}), glycerol (10 g L^{-1}), betaine hydrochloride (1.25 g L^{-1}), sodium pyruvate (1.25 g L^{-1}), and agar (15 g L^{-1}), with adjustment to pH 7.2. The cultures were again incubated at 28°C to obtain isolated colonies. Purified isolates were maintained in glycerol suspensions (20%, v/v) at −80°C.

The reference strain *M. fluoranthenivorans* JCM 14741^T was obtained from the Japan Collection of Microorganisms (JCM), while strains *M. frederiksbergense* DSM 44346^T and *M. litorale* DSM 45785^T were acquired from the German Collection of Microorganisms and Cell Cultures (DSMZ).

Phenotypic properties

Strain growth was evaluated on glucose–yeast extract–malt extract agar (GYM; DSMZ medium 65), Middlebrook 7H10 agar (MB7H10; Difco), nutrient agar (NA; Difco), and tryptic soy agar (TSA; Difco), with incubation at 28°C for 48–72 h. Cell motility was examined by microscopic observations and inoculation on semisolid GYM medium with 0.3% agar (w/v). The growth conditions of strains YC-RL4^T, MB418^T, and HX176^T were evaluated over temperature, pH, and salt tolerance ranges. The temperature range of growth was determined in MB7H10 mediu (Difco) at 4, 15, 20, 22, 25, 28, 30, 32, 35, 37, 45, and 50°C. The growth range across pH was determined in GYM medium at pH 4.0–10.0, at intervals of 1.0 unit. NaCl tolerance was determined with cultivation at 28°C in modified GYM medium (pH 7.0, without Na^+ and Cl^-), and with NaCl supplemented at concentrations of 0–10.0% (w/v) at increasing increments of 1.0%. All growth condition assays were performed in triplicate.

Biochemical and physiological tests were conducted for strains YC-RL4^T, MB418^T, HX176^T and other closely related strains. Oxidase activity was investigated using the API oxidase reagent (bioMérieux) according to the manufacturer's instructions. Catalase activity was evaluated via production of bubbles after addition of a drop of 3% (v/v) hydrogen peroxide. Voges–Proskauer, H_2S production, and starch hydrolysis tests were evaluated using a biochemical identification kit (Huankai Microbial) according to the manufacturers'

instructions. Additional biochemical characteristics including enzymatic activities, acid production from fermentation, and assimilation of carbon sources were evaluated using API ZYM, API 50CH, and Biolog GEN III MicroPlates (Biolog) according to the manufacturers' instructions. API strip and Biolog results were recorded every 24 h after incubation at 28°C until all reactions had stabilized. The API and Biolog tests were performed in duplicate using consistent conditions.

Chemotaxonomic characterization

Biomass for chemotaxonomic investigations of strains was obtained by cultivation in flasks on a rotary shaker (180 r.p.m.) using ISP2 broth as the medium and with incubation at 28°C for 3 days, except that cellular fatty acids and cell-wall mycolic acids extraction and analyses were conducted using cultures grown on Middlebrook 7H10 (MB7H10) medium. Cellular polar lipids were extracted, detected with two-dimensional TLC silica-gel 60 F_{254} thin-layer plates (10 × 10 cm, Merck), and analyzed, as previously described (Minnikin et al., 1984). Menaquinones were extracted and purified using reverse-phase HPLC, also as previously described (Minnikin et al., 1984). Cellular fatty acids were extracted, methylated, and analyzed using the Sherlock Microbial Identification System (MIDI) with the standard ACTIN1 database (version 6.0) according to the manufacturer's instructions (Sasser, 2006). Diagnostic isomers of diaminopimelic acid in whole cell hydrolysates (6 N HCl, 120°C, 30 min) of the strains were subjected to thin-layer chromatography on cellulose plates (10 × 20 cm, Merck) using a previously described solvent system (Schleifer and Kandler, 1972). The cell-wall mycolic acids were determined following saponification, extraction and derivatization, and then separated using a gradient of methaand 2-propanol via high-performance liquid chromatography (HPLC) as recommended by the Sherlock Mycobacteria Identification System Operating Manual Version 1.0 (MIDI) (Butler and Guthertz, 2001; Zimenkov et al., 2015).

Phylogenetic analysis

16S rRNA genes of strains were amplified using PCR and the universal bacterial primers 27F (5′-AGAGTTTGATCCTGG CTCAG-3′) and 1492R (5′-GGTTACCTTGTTACGACTT-3′). Purified PCR products were cloned into the vector pMD19-T (TaKaRa) and recombinant plasmids were transformed into *Escherichia coli* DH5α cells, followed by sequencing in Sangon Biotech (Shanghai, China). The 16S rRNA gene sequences of the isolates were compared with publicly available sequences in the EzBioCloud platform[2] to determine the approximate taxonomic affiliations of the strains (Yoon et al., 2017a). Multiple sequence alignments and phylogenetic reconstructions of 16S rRNA genes were performed in MEGA (version 11) (Tamura et al., 2021). A phylogenetic tree was then inferred using neighbor-joining methods, and evolutionary distances were calculated using the Kimura 2-parameter substitution model (Shamsuzzaman et al., 2023). Maximum Parsimony and Maximum Likelihood phylogenetic methods were also used to evaluate the phylogenetic affiliations of the strains. The topologies of the resultant phylogenetic trees were evaluated using bootstrap analysis with 1,000 replicates (Deng et al., 2023).

Genome sequencing and gene annotation

Genome sequencing was conducted on an Illumina HiSeq 4,000 system platform at the BGI sequencing company (Shenzhen, China). To prepare sequencing libraries, genomic DNA was randomly sheared to construct three read libraries with lengths of 300 bp using a Bioruptor ultrasonicator (Diagenode, Denville, NJ, United States) and physico-chemical methods. The paired-end fragment libraries were then sequenced on the Illumina platform. Low quality reads (those with consecutive bases covered by fewer than five reads) were discarded. The sequenced reads were then assembled using the SOAPdenovo (version 1.05) assembly software program (Li et al., 2010). Estimated completeness and contamination values for the genomes were estimated using the CheckM pipeline (Parks et al., 2015). Digital DNA–DNA hybridization (dDDH) and average nucleotide identity (ANI) values between the strains and related strains were calculated using the Genome-to-Genome Distance Calculator (GGDC, version 3.0)[3] (Auch et al., 2010) and with the ezbiocloud platform (Yoon et al., 2017b), respectively. Genome-based phylogeny of supermatrix approach from protein sequences of the bac120 gene set (a collection of 120 single-copy protein sequences prevalent in bacteria) was constructed by using EasyCGTree version 3.0[4] as described previously (Zhang et al., 2020). Evolutionary distances were calculated using the IQ-Tree software program (version 1.6.1) (Nguyen et al., 2015). The genome sequences of the strains of interest were downloaded from the NCBI genome database.[5]

Protein sequences encoded by the strains were predicted and annotated using the NCBI Prokaryotic Genome Annotation Pipeline (PGAP). Gene prediction was conducted for the genome assemblies using glimmer3[6] with Hidden Markov models. tRNA, rRNA, and sRNA identification was conducted with tRNAscan-SE (Chan et al., 2021), RNAmmer (Lagesen et al., 2007), and the Rfam database (Gardner et al., 2009), respectively. Tandem repeat annotation was conducted using the Tandem Repeat Finder[7], with minisatellite and microsatellite DNAs identified based on the numbers and lengths of repeat units. Functional annotation was also conducted based on the best hits within BLAST analyses. In addition, general functional annotations were identified by comparisons against several databases included the Kyoto Encyclopedia of Genes and Genomes (KEGG), Clusters of Orthologous Groups (COG), Non-Redundant Protein (NR), Swiss-Prot, Gene Ontology (GO), TrEMBL, and EggNOG databases. Predictions of gene clusters involved in natural product formation were conducted using antiSMASH (Blin et al., 2019).

2 http://www.ezbiocloud.net/identify

3 http://ggdc.dsmz.de/ggdc.php
4 https://github.com/zdf1987/EasyCGTree
5 https://www.ncbi.nlm.nih.gov/genome/
6 http://www.cbcb.umd.edu/software/glimmer/
7 http://tandem.bu.edu/trf/trf.html

Pan-genome analysis

The bacterial pan-genome analysis (BPGA) pipeline (version 1.3) was used to assess the genomic diversity among *Mycobacterium* strains using default settings (Chaudhari et al., 2016). A total of 73 protein datasets were used for the pan-genome analysis, including for strains YC-RL4^T, MB418^T, HX176^T, and 70 related mycobacterial strains that were previously classified as "*Mycolicibacterium*." Orthologous gene/protein clusters (homologous families) were identified using the USEARCH clustering tool (Kim et al., 2014).

Results and discussion

Phenotypic properties of the novel strains

Cells of strains YC-RL4^T, MB418^T, and 205372^T were Gram-positive, non-motile and rod-shaped. The three isolates grew well on GYM and MB7H10 agar, with weak growth on NA and TSA agar. Colonies of strains YC-RL4^T and HX176^T grown on GYM medium and incubated for 48 h were 1.0–2.5 mm in diameter, opaque, ivory, and convex with a smooth surface. Colonies of strain HX176^T grown on GYM medium incubated for 48 h were 1.0–3.2 mm in diameter, dry, rough, and orange-colored with undulated/scalloped edges. All strains grew over the pH range of 6.0–7.0 (optimum: 7.0). Strain YC-RL4^T grew in the presence of 0–5.0% (w/v) NaCl (optimum: 0–3.0%, w/v), and 10–37°C (optimum: 28°C), while strain MB418^T grew at 0–5.0% (w/v) NaCl (optimum 0–3.0%, w/v), and 15–45°C (optimum: 28°C), and strain HX176^T grew in the presence of 0–4.0% NaCl (w/v) (optimum: 0–2.0%), and at 15–28°C (optimum: 28°C). All strains exhibited positive catalase reactions, but negative results for oxidase, starch hydrolysis, Voges–Proskauer, and H_2S production tests. All strains exhibited positive enzymatic activities for alkaline phosphatase, esterase (C4), leucine arylamidase, lipase (C14), naphthol-AS-BI-phosphohydrolase, and valine arylamidase, based on API ZYM strip tests. None of the strains could produce acid from fermentation of amidon, amygdalin, arbutin, D-arabinose, D-ardonitol, D-cellobiose, D-fucose, D-galactose, D-lactose, D-maltose, D-mannitol, D-melezitose, D-melibiose, D-raffinose, D-sorbitol, D-trehalose, D-turanose, dulcitol, erythritol, gentiobiose, glycogen, inulin, L-arabitol, L-fucose, L-rhamnose, L-sorbose, L-xylose, mehyl-α-D-glucopyranoside, mehyl-α-D-mannopyranoside, mehyl-β-D-xylopyranoside, N-acetylglucosamine, potassium 5-ketogluconate, salicin, or xylitol. The major differentiating features among strains YC-RL4^T, MB418^T, HX176^T, and other species are shown in Table 1.

TABLE 1 Physiological characteristics of strains YC-RL4^T, MB418^T, HX176^T, and closely related *Mycobacterium* type strains.

Characteristic	1	2	3	4	5	6
NaCl tolerance (%, w/v)	0–5.0	0–5.0	0–5.0	0–5.0	0–4.0	0–3.0
Growth temperature range (°C)	10–37	4–37	15–37	15–45	15–28	10–45
Gelatin hydrolysis	–	–	–	–	+	–
Nitrate reduced to nitrite	+	+	+	–	–	+
Carbon sources used for growth						
D-trehalose	–	–	–	–	–	+
α-D-glucose	+	–	–	+	–	+
D-mannose	+	w	+	+	–	–
D-fructose	–	+	+	+	–	+
D-galactose	–	–	–	+	–	–
D-sorbitol	–	–	–	+	w	+
D-mannitol	–	+	+	+	w	+
D-arabitol	–	–	–	+	w	+
myo-inositol	–	+	+	+	w	–
Glycerol	+	+	+	w	–	w
D-fructose-6-PO_4	w	+	w	–	w	w
Glycyl-L-proline	–	–	+	–	–	–
L-glutamic acid	+	+	+	–	–	–
D-gluconic acid	+	–	–	+	+	+
Quinic acid	–	+	–	+	w	–
D-saccharic acid	–	–	+	+	+	–
Methyl pyruvate	w	–	+	w	–	–
α-keto-glutaric acid	–	–	+	–	–	–
L-malic acid	+	+	+	–	–	+
Bromo-succinic acid	–	w	w	–	–	+
Tween 40	+	w	+	w	–	+
α-hydroxy-butyric acid	w	–	+	w	–	–
β-hydroxy-D,L-butyric Acid	+	+	+	–	+	+
α-keto-butyric acid	–	+	+	w	–	–
Formic acid	w	+	–	–	–	–
API ZYM results						
Cystine arylamidase	+	+	+	+	–	+
Trypsin	+	+	+	+	–	+
α-chymotrypsin	–	w	w	+	–	w
Acid phosphatase	+	+	+	+	–	+
β-galactosidase	–	+	–	–	–	–
α-glucosidase	+	+	+	+	–	+
β-glucosidase	–	+	+	+	–	+

(Continued)

Chemotaxonomic properties of strains

Strains YC-RL4^T, MB418^T, and HX176^T exhibited chemotaxonomic properties consistent with their classification as *Mycobacterium*. The strains produced whole organism hydrolysates rich in *meso*-diaminopimelic acid (*meso*-A_2pm), arabinose, galactose, glucose, mannose, and ribose. MK-9 (H_2) was the predominant menaquinone and the polar lipid profile contained diposphatidylglycerol (DPG), phosphatidylethanolamine (PE), and phosphatidylinositol (PI) (Supplementary Figure S1). The three strains

TABLE 1 (Continued)

Characteristic	1	2	3	4	5	6
Acid production from substrates (API 50CH)						
Glycerol	+	+	+	–	–	–
Erythritol	–	–	–	–	–	+
D-ribose	–	–	–	–	+	–
D-xylose	+	+	w	–	–	+
D-ardonitol	–	–	–	–	–	+
D-glucose	+	+	+	–	+	–
D-fructose	+	+	–	–	+	+
D-mannose	w	–	+	–	–	–
L-sorbose	–	–	–	–	–	+
L-rhamnose	–	–	–	–	–	+
Inositol	+	+	–	–	–	–
D-mannitol	–	+	–	–	–	+
D-sorbitol	–	–	–	–	–	+
D-cellobiose	–	–	–	–	–	+
D-trehalose	–	–	+	–	–	–
Gentiobiose	–	–	–	–	–	+
D-arabitol	–	–	–	+	–	+
L-arabitol	–	–	–	–	–	+

Strains: 1, YC-RL4^T; 2, *M. fluoranthenivorans* JCM 14741^T; 3. *M. frederiksbergense* DSM 44346^T; 4, MB418^T; 5, HX176^T; 6, *M. litorale* DSM 45785^T.
+, positive; w, weakly positive; –, negative activities/growth.

nevertheless exhibited differences in several chemotaxonomic characteristics relative to other *Mycobacterium* strains. The fatty acid profile of strain YC-RL4^T comprised major levels of $C_{16:0}$ (15.3%) and $C_{17:1}\omega7c$ (15.3%), while the fatty acid profile of strain MB418^T exhibited major levels of $C_{17:1}\omega7c$ (47.7%) and sum in feature 9 (iso-$C_{17:1}\omega9c$/$C_{16:0}$ 10-methyl) (43.3%). Strain HX176^T exhibited higher levels of $C_{17:1}\omega7c$ (43.2%) and $C_{19:1}$ trans 7 (30.9%), but lower $C_{16:0}$ levels (8.8%), while also lacking sum in feature 9 (Supplementary Table S1). In addition, only the polar lipid profiles of strains MB418^T and HX176^T included glycolipids (GLs), contrasting with that of strain YC-RL4^T that lacked GLs (Supplementary Figure S1). The HPLC profile of cell-wall mycolic acids from strain YC-RL4^T, containing 60–70 carbon atoms of mycolic acids as the main peaks, was a little similar to that observed for *M. fluoranthenivorans* JCM 14741^T and *M. frederiksbergense* DSM 44346^T while quite different from that of strains MB418^T, and HX176^T. The HPLC pattern of cell-wall mycolic acids from strains MB418^T and HX176^T were more similar to that of *M. litorale* DSM 45785^T than others, and the chromatogram of strain MB418^T was distinct from that of strain HX176^T (Supplementary Figure S2).

Phylogenetic analyses

Nearly complete 16S rRNA gene sequences for strain YC-RL4^T (1,527 bp, accession OQ096616), MB418^T (1,509 bp, accession OP522341), and HX176^T (1,508 bp, accession OQ096617) were obtained. BLAST searches of the 16S rRNA gene sequences against the GenBank database indicated that strains YC-RL4^T, MB418^T, and HX176^T were closely related to *Mycobacterium* species of the family *Mycobacteriaceae* even though they were previously classified as the genus *Mycolicibacterium*. Strain YC-RL4^T was most closely related to *M. fluoranthenivorans* JCM 14741^T and *M. frederiksbergense* DSM 44346^T, with 16S rRNA gene sequence similarities of 99.3 and 99.2%, respectively. The 16S rRNA gene of MB418^T exhibited 98.5% nucleotide similarity to 16S rRNA genes of *M. celeriflavum* DSM 46765^T and *M. moriokaense* DSM 44221^T, but with 97.2% similarity to the 16S rRNA genes of strain YC-RL4^T, and 96.2–98.3% similarity to 16S rRNA genes of other various *Mycobacterium* type strains. The 16S rRNA gene sequence of strain HX176^T exhibited a nucleotide similarity of 98.3% to that of *M. litorale* DSM 45785^T, 98.0% to that of strain YC-RL4^T, and similarities of 95.8–97.9% to those from other *Mycobacterium* type strains (Supplementary Table S2). Phylogenetic analysis of the 16S rRNA gene sequences of the three isolates with other mycobacterial strains that were previously classified as "*Mycolicibacterium*" revealed that the strains belonged to the genus *Mycobacterium*. The 16S rRNA gene sequence of strain YC-RL4^T formed a sub-clade with that of the type strain *M. fluoranthenivorans* JCM 14741^T, which were together related to the 16S rRNA gene of *M. frederiksbergense* DSM 44346^T, consistent with BLAST comparisons. The 16S rRNA gene of strain MB418^T formed a well-supported sub-clade with the 16S rRNA gene of strain HX176^T, which were together associated with that of *M. litorale* DSM 45785^T (Figure 1). The whole-genome phylogenomic analysis recapitulated the 16S rRNA gene phylogenetic analysis, with the exception of the strain YC-RL4^T genome being most closely related to that of *M. frederiksbergense* DSM 44346^T (Supplementary Figure S3), contrasting with the 16S rRNA gene phylogenetic analysis.

Genomic characteristics

The genomes of strains YC-RL4^T, MB418^T, and HX176^T were estimated to be 99.95, 100.00, and 100.00% complete, with estimated contamination of 0.62, 0.30, and 0.45%, respectively. The draft genome sizes of strains YC-RL4^T, MB418^T, and HX176^T were 6.1, 5.6, and 5.9 Mbp, respectively, and were assembled from two contigs with an N50 length of 5,801,417 bp; 15 contigs with an N50 length of 710,882 bp; and 41 contigs with an N50 length of 302,245 bp, respectively (Supplementary Table S3). The genomic sequence for strain YC-RL4^T encoded 5,881 total genes including 47 tRNA, 6 rRNA, 4 other ncRNA, and 83 pseudo genes. The genome of strain MB418^T encoded 5,444 total genes including 47 tRNA, 3 rRNA, 3 other ncRNA, and 98 pseudo genes. The genome of strain HX176^T encoded 5,692 genes including 46 tRNA, 4 rRNA, 3 other ncRNA, and 64 pseudo genes. The genomic G + C content of all three strains ranged between 66.5 and 69.3%. ANI values calculated between strains YC-RL4^T, MB418^T, HX176^T, and other *Mycobacterium* species were all <86.9%, with corresponding dDDH values all <31.8% (Supplementary Table S4). The values were lower than the thresholds used to delineate bacterial species (i.e., ANI < 95–96% and dDDH <70%) (Kim et al., 2014), thereby indicating that the strains represented novel, uncharacterized species.

FIGURE 1
Neighbor-joining phylogenetic reconstruction of 16S rRNA gene sequences from strains YC-RL4^{T}, MB418^{T}, and HX176^{T} along with those from other *Mycobacterium*. Bootstrap values above 50% are shown as percentages of 1,000 replicates. The 16S rRNA gene sequence of *Streptomyces albus* CAS922^{T} (GenBank accession MN218527) was used as the outgroup. Scale bar indicates 0.01 nt substitutions per alignment site.

Functional gene complements

Polycyclic aromatic hydrocarbons ring-hydroxylating dioxygenases (PAH-RHDs) are critical for PAH degradation by aerobic bacteria, because they catalyze the initial oxidation of O_2 atoms to form cisdihydrodiol and this step controls the PAH degradation rate (Kim et al., 2007; Chemerys et al., 2014). Among PAH-RHDs, aromatic ring-hydroxylating dioxygenases are particularly important in the aerobic bacterial degradation of aromatic compounds, because they catalyze the oxidation of the compounds during degradation. They typically catalyze the addition of two hydroxy groups to vicinal carbons, thereby disrupting aromaticity and yielding dihydrodiol compounds with *cis*, *cis* stereochemistry. The enzymes are biotechnologically important because they act as biocatalysts in the stereospecific synthesis of chiral synthons and the degradation of aromatic pollutants (Kahl and Hofer, 2003). Multiple genes encoding dioxygenases were identified in the genomes of strains YC-RL4^{T}, MB418^{T}, and HX176^{T}. Specifically, four genes putatively encoding alpha subunits with homology to aromatic ring-hydroxylating dioxygenases were encoded by the genome of strain YC-RL4^{T}, while genes putatively encoding alpha subunits of aromatic ring-hydroxylating dioxygenases were identified in the genomes of strains MB418^{T} and HX176^{T} (Supplementary Table S5).

Strains of the genus *Mycobacterium* could degrade PAHs to central intermediates via the *o*-phthalate and the *β*-ketoadipate pathway (Kim et al., 2007; Augelletti et al., 2020). The *o*-phthalate degradation pathway of Gram-positive bacteria involves oxygenation to form 3,4-dihydro-3,4-dihydroxyphthalate, dehydrogenation to 3,4-dihydroxyphthalate, and finally decarboxylation to generate protocatechuate (Bhattacharyya et al., 2023). Genes (*phtAa*) were identified that encoded homologous proteins involved in the degradation of phthalate in the genomes of strains YC-RL4^T, MB418^T, and HX176^T (Supplementary Table S5). Thus, these three strains could likely degrade various types of phthalates, as previously suggested. In addition, genes of the *β*-ketoadipate pathway cluster (*pcaC*, *pcaD*, *pcaG*, and *pcaH*) were also identified in the genomes of strains YC-RL4^T, MB418^T, and HX176^T (Supplementary Table S5), suggesting that anthracene degradation by these strains could proceed through the ortho-cleavage of protocatechuate (protocatechuic acid [PCA] 3,4-dioxygenase) (Habe et al., 2005). These protocatechuate catabolic genes were required for the complete degradation of PAHs to TCA cycle intermediates. Consequently, strains YC-RL4^T, MB418^T, and HX176^T exhibited the potential for the bioremediation of PAHs and smaller ring aromatics.

Although heavy metals naturally exist in many environments (Masindi and Muedi, 2018), the ubiquitous distribution of heavy metals in natural environments is a consequence of global industrialization and urbanization that has led to negative impacts on human and environmental health. Microorganisms have adapted multiple resistance mechanisms to overcome the physiological stress from heavy metal exposure (Sherpa et al., 2020). Several genes were identified in the genomes of strains YC-RL4^T, MB418^T, and HX176^T that encoded heavy metal resistance proteins. For example, the three strains exhibited the potential to mediate copper toxicity via copper-resistant genes (*copC*) identified in all of their genomes. Further, the copper-resistance gene *copD* was also identified in the genomes of strain MB418^T and HX176^T. Free form copper is highly toxic due to its ability to produce radicals during cycling between oxidized Cu(II) and reduced Cu(I) forms. Consequently, intracellular copper must remain complexed within a tightly controlled copper homeostatic system. Importantly, Cop proteins sequester excess copper in periplasms and outer membranes (Arnesano et al., 2003). Consequently, these proteins might confer copper resistance to strains YC-RL4^T, MB418^T, and HX176^T by helping to sequester and accumulate copper in periplasms with copper binding proteins, thereby preventing toxic levels of copper from entering the cytoplasm.

In addition to the above, genes (*merA* and *merB*) that encoded mercury reductase enzymes were identified in the strain YC-RL4^T genome that enable resistance to mercury stress. Mercury toxicity arises from the strong affinity of monomethyl-Hg and Hg^{2+} to sulfur atoms in cysteine residues and, hence, interference with protein structure and function. The mercury reductase encoded by *merA* and *merB* reduced the toxicity of Hg2+ to Hg^0 (Møller et al., 2014). Specifically, organomercurial lyase (MerB) catalyzed the protonolysis of the carbon-mercury bond, resulting in the formation of ionic mercury and reduced hydrocarbon. The ionic mercury (Hg^{2+}) was subsequently reduced to less reactive elemental mercury (Hg^0) by mercuric reductase (MerA) (Di Lello et al., 2004). The presence of these genes involved in PAH-degradation and metal resistance genes in the genomes of these strains suggested that strains YC-RL4^T, MB418^T, and HX176^T could be applied in bioremediation of soils contaminated with both PAHs and heavy metals.

Pangenomic analyses

The pan-genomes of strains comprise the entire gene repertoire for a given species across several populations, and their analysis can be informative for understanding the distribution of core, important genes shared by all strains of a species, in addition to strain-specific accessory genes that may be more dispensable (Reis and Cunha, 2021). A total of 401,362 protein-coding genes (Table 2) were encoded by the genomes of strains YC-RL4^T, MB418^T, HX176^T, and 70 other related strains of the genus *Mycobacterium*, comprising 51,712 homologous families based on cluster analysis. A total of 734 core genes were shared by the 73 strains and comprise the core genome identified in this study. The core genes accounted for approximately 13.5% of the pan-genome for the 73 strains of the genus *Mycobacterium*. The identification of the "open" pangenome based on consideration of increasing numbers of strains was fit with a powerlaw regression function [$f(X) = 5991.36\times^{0.50}$], while the core genome identification fit an exponential regression [$f(X) = 2838.85e^{-0.03X}$; Figure 2]. Thus, the relatively extensive open pangenome of the strains indicates that they have considerable repertoires of accessory genes, possibly due to extensive horizontal gene exchanges with various microbial species (Coyte et al., 2022). Aromatic ring-hydroxylating dioxygenase alpha subunit-encoding genes were identified in all of the 73 genomes, suggesting it was an important core gene shared by all strains and plays a critical role in PAH degradation by the strains. In addition, the copy numbers of these genes varied among different strains. The lowest number of copies was observed in the genome of *M. brumae* DSM 44177^T, while the largest number of copies was observed in the genome of strain *M. gadium* DSM 44077^T.

A functional classification of core, accessory, and unique genes was performed based on comparison to the COG database, revealing clear differences between core and accessory genes. Core genes were most associated with the COG categories of R (general function prediction only; 13.0% of genes), J (translation, ribosomal structure, and biogenesis; 12.4%), E (amino acid transport and metabolism; 9.1%) and I (lipid transport and metabolism; 8.2%) (Figure 3), while accessory and unique genes were most associated with the COG categories R (general function prediction only; 16.3 and 17.0%, respectively), K (transcription; 13.0 and 12.6%), and Q (secondary metabolite biosynthesis, transport, and catabolism; 8.8 and 9.3%). Thus, core genes were mostly involved in basic physiological functions, resulting in the overall prevailing phenotypes of the strains. In contrast, accessory genes related to tachytely evolution could increase the gene and functional diversity of their respective genomes. These accessory genes may be involved in metabolic pathways that critically ensure adaptations or functioning in variable ecological niches that differ among species (Vernikos et al., 2015).

Secondary metabolite biosynthesis gene cluster analysis

Polyketide synthesis operons and others involved in non-ribosomal peptide synthesis (NRPS) are common in the genomes

TABLE 2 Pan-genome information for *Mycobacterium* strains evaluated in this study, including strains YC-RL4^T, MB418^T, HX176^T, and 70 others.

GenomeID	Organism name	No. of core genes	No. of accessory genes	No. of unique genes	No. of exclusively absent genes
1	HX176^T	734	4,190	505	1
2	YC-RL4^T	734	4,432	266	0
3	MB418^T	734	4,101	494	4
4	*Mycobacterium agri* JCM 6377^T	734	4,399	935	5
5	*Mycobacterium aichiense* DSM 44147^T	734	4,496	176	1
6	*Mycobacterium alvei* JCM 12272^T	734	4,245	365	5
7	*Mycobacterium anyangense* JCM 30275^T	734	3,827	435	0
8	*Mycobacterium arabiense* DSM 45768^T	734	4,536	445	1
9	*Mycobacterium aromaticivorans* JCM 16368^T	734	4,511	265	1
10	*Mycobacterium aubagnense* JCM 15296^T	734	4,297	497	0
11	*Mycobacterium aurum* NCTC 10437^T	734	4,495	164	2
12	*Mycobacterium austroafricanum* DSM 44191^T	734	4,836	333	0
13	*Mycobacterium bacteremicum* DSM 45578^T	734	4,441	225	0
14	*Mycobacterium boenickei* JCM 15653^T	734	5,063	129	1
15	*Mycobacterium brisbanense* DSM 44680^T	734	5,304	617	2
16	*Mycobacterium brumae* DSM 44177^T	734	2,383	476	27
17	*Mycobacterium canariasense* DSM 44828^T	734	5,050	567	1
18	*Mycobacterium celeriflavum* DSM 46765^T	734	3,610	144	1
19	*Mycobacterium chitae* JCM 12403^T	734	3,700	366	8
20	*Mycobacterium chlorophenolicum* DSM 43826^T	734	5,165	495	2
21	*Mycobacterium chubuense* DSM 44219^T	734	4,542	103	3
22	*Mycobacterium conceptionense* CCUG 50187^T	734	4,820	264	0
23	*Mycobacterium confluentis* DSM 44017^T	734	4,021	394	1
24	*Mycobacterium cosmeticum* DSM 44829^T	734	5,020	174	0
25	*Mycobacterium crocinum* DSM 45433^T	734	4,523	129	1
26	*Mycobacterium diernhoferi* DSM 43524^T	734	4,275	297	1
27	*Mycobacterium duvalii* DSM 44244^T	734	3,967	238	0
28	*Mycobacterium elephantis* DSM 44368^T	734	4,002	148	2
29	*Mycobacterium fallax* DSM 44179^T	734	2,628	460	8
30	*Mycobacterium flavescens* DSM 43991^T	734	4,370	261	0
31	*Mycobacterium fluoranthenivorans* JCM 14741^T	734	4,452	422	25
32	*Mycobacterium fortuitum* JCM 6387^T	734	4,686	245	1
33	*Mycobacterium frederiksbergense* DSM 44346^T	734	4,688	213	3
34	*Mycobacterium gadium* DSM 44077^T	734	4,820	220	2
35	*Mycobacterium gilvum* DSM 45363^T	734	4,478	175	1
36	*Mycobacterium goodii* ATCC 700504^T	734	5,039	250	0
37	*Mycobacterium hassiacum* DSM 44199^T	734	3,307	392	15
38	*Mycobacterium helvum* JCM 30396^T	734	4,486	353	1

(Continued)

TABLE 2 (Continued)

GenomeID	Organism name	No. of core genes	No. of accessory genes	No. of unique genes	No. of exclusively absent genes
39	*Mycobacterium hodleri* DSM 44183^T	734	4,628	543	1
40	*Mycobacterium holsaticum* DSM 44478^T	734	3,917	278	0
41	*Mycobacterium insubricum* DSM 45132^T	734	2,195	703	250
42	*Mycobacterium iranicum* DSM 45541^T	734	4,706	229	0
43	*Mycobacterium komossense* DSM 44078^T	734	4,482	887	2
44	*Mycobacterium litorale* DSM 45785^T	734	4,159	176	0
45	*Mycobacterium llatzerense* DSM 45343^T	734	4,445	626	1
46	*Mycobacterium lutetiense* DSM 46713^T	734	4,280	379	14
47	*Mycobacterium madagascariense* DSM 45167^T	734	3,818	506	0
48	*Mycobacterium mageritense* JCM 12375^T	734	5,798	640	1
49	*Mycobacterium malmesburyense* CIP 110822^T	734	4,038	145	3
50	*Mycobacterium monacense* JCM 15658^T	734	4,462	186	1
51	*Mycobacterium moriokaense* JCM 6375^T	734	4,520	352	2
52	*Mycobacterium mucogenicum* DSM 44124^T	734	4,528	371	0
53	*Mycobacterium murale* DSM 44340^T	734	4,523	810	1
54	*Mycobacterium neoaurum* DSM 44074^T	734	4,022	197	1
55	*Mycobacterium novocastrense* DSM 44203^T	734	4,560	330	0
56	*Mycobacterium obuense* DSM 44075^T	734	4,213	215	4
57	*Mycobacterium pallens* JCM 16370^T	734	4,558	157	1
58	*Mycobacterium parafortuitum* ATCC 19686^T	734	4,539	165	0
59	*Mycobacterium porcinum* ATCC 33776^T	734	5,320	165	3
60	*Mycobacterium psychrotolerans* DSM 44697^T	734	4,170	226	3
61	*Mycobacterium pulveris* DSM 44222^T	734	3,992	281	0
62	*Mycobacterium pyrenivorans* DSM 44605^T	734	4,520	364	2
63	*Mycobacterium rhodesiae* DSM 44223^T	734	4,566	138	0
64	*Mycobacterium sarraceniae* JCM 30395^T	734	3,054	359	3
65	*Mycobacterium sediminis* DSM 45643^T	734	4,418	448	0
66	*Mycobacterium septicum* DSM 44393^T	734	4,930	235	11
67	*Mycobacterium setense* DSM 45070^T	734	4,702	166	0
68	*Mycobacterium smegmatis* NCTC 8159^T	734	5,069	417	0
69	*Mycobacterium sphagni* DSM 44076^T	734	4,269	526	0
70	*Mycobacterium thermoresistibile* DSM 44167^T	734	3,092	467	12
71	*Mycobacterium tusciae* DSM 44338^T	734	4,639	182	0
72	*Mycobacterium vaccae* NBRC 14118^T	734	4,564	233	3
73	*Mycobacterium wolinskyi* JCM 13393^T	734	5,598	562	0

of *Mycobacterium* and are responsible producing cell wall-associated lipids, siderophores, and other biologically active molecules (Stinear et al., 2008). AntiSMASH analysis revealed the presence of 14–21 biosynthetic gene clusters (BGCs) in the genomes of strain YC-RL4^T, MB418^T, and HX176^T that were especially enriched in genes encoding Type I polyketide synthases (PKSs) and non-ribosomal peptide synthases (NRPSs) (Supplementary Table S6). A BGC that was most similar to that encoding mycobactin was identified in all 73 genomes,

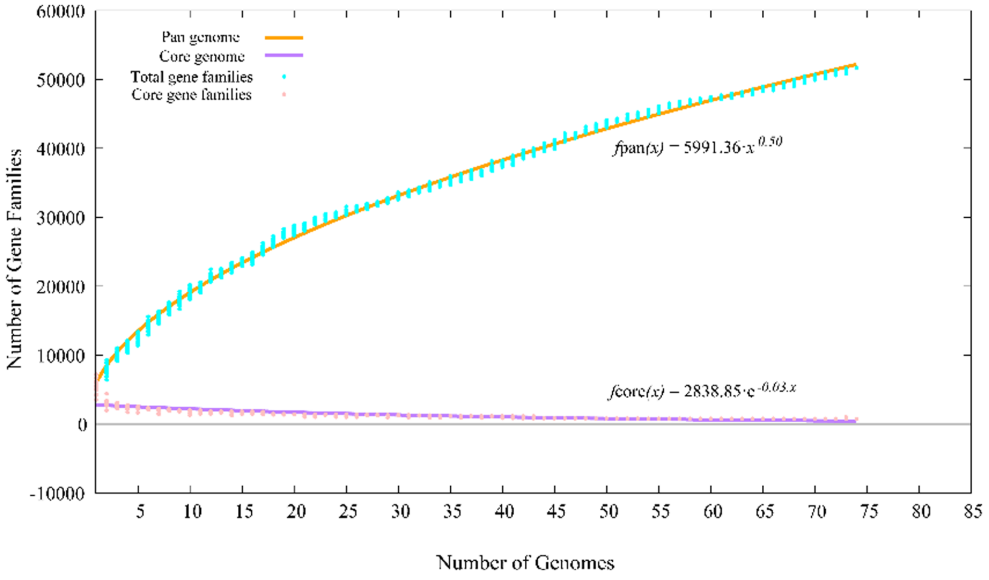

FIGURE 2
Pan-genome profiles of strains YC-RL4^T, MB418^T, HX176^T and 70 related *Mycobacterium* strains based on protein clustering.

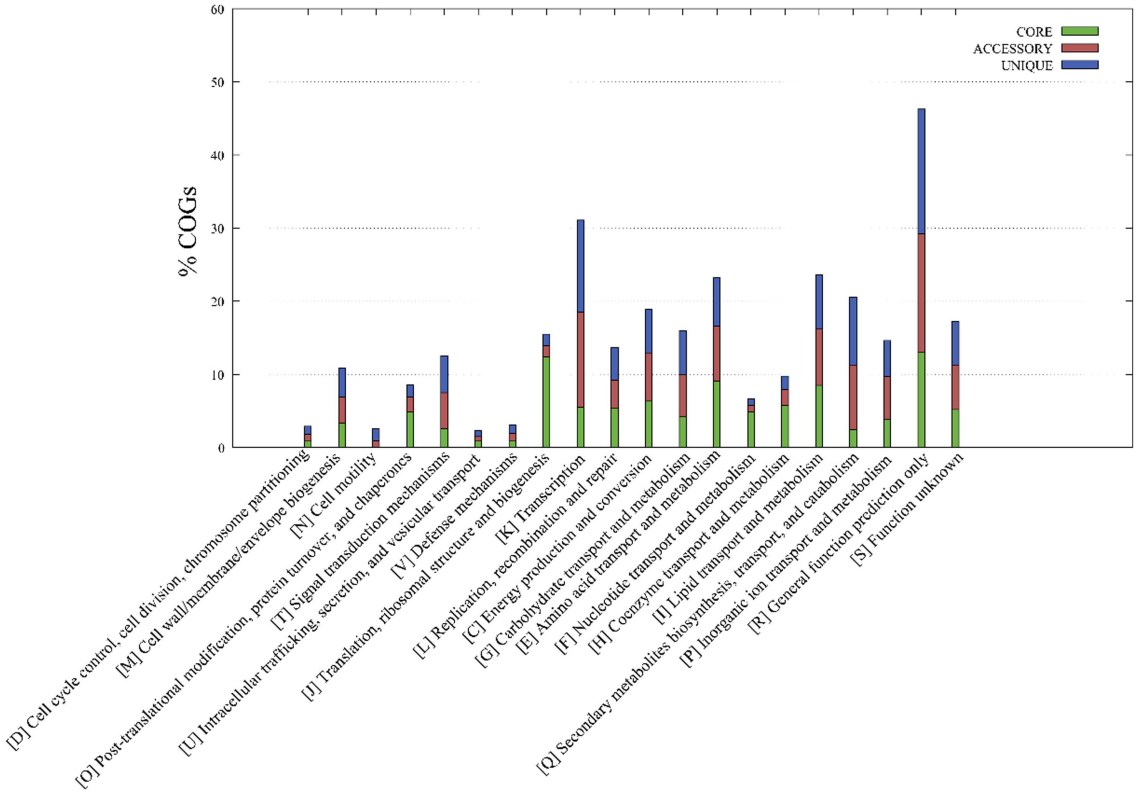

FIGURE 3
Metabolic pathways associated with the core, accessory, and unique genes of strains YC-RL4^T, MB418^T, HX176^T, and 70 other related *Mycobacterium* strains. The metabolic annotations are based on clusters of orthologous genes (COG) database annotations.

consistent with the production of mycobactin being essential for *Mycobacterium* strains to access iron (McMahon et al., 2012). In addition, several putative BGCs exhibited low similarities to known clusters, indicating their potential for synthesizing putatively novel secondary metabolites.

Conclusion

In this study, three strains of the genus *Mycobacterium* (YC-RL4^T, MB418^T, and HX176^T) were isolated from several petroleum-contaminated soil samples of China. The three strains exhibited highest

similarity to *Mycobacterium* species of the family *Mycobacteriaceae*. The 16S rRNA gene sequence of strain YC-RL4^T in comparison to other characterized *Mycobacterium* strains exhibited levels below the threshold for differentiating species (98.65%), while the 16S rRNA gene sequences of strains MB418^{T}and HX176^T compared to other characterized *Mycobacterium* strains were above 98.65%. However, the dDDH values among the three strains and the other characterized *Mycobacterium* species were very below the threshold value (70%) used to delineate bacterial strains of the same species (46). Moreover, the ANI values among all three strains and other type species of *Mycobacterium* were much lower than the threshold for bacterial species delineation (95–96%) (Kim et al., 2014). Thus, strains YC-RL4^T, MB418^T, and HX176^T likely represent three novel species of *Mycobacterium*. Chemotaxonomic, genomic, and phenotypic analyses of strains YC-RL4^T, MB418^T, and HX176^T confirmed their identification as novel species. Lastly, the genomes of strains YC-RL4^T, MB418^T, and HX176^T encoded proteins associated with PAH degradation and metal resistance, consistent with strain YC-RL4^T previously being shown to degrade phthalates (Ren et al., 2016). Consequently, these three species may hold considerable application potential in the bioremediation of PAH and metal-contaminated soils.

Description of *Mycobacterium adipatum* sp. nov.

(a.di.pa'tum. L. neut. adj. *adipatum*, fat, greasy)

Cells are Gram-positive, non-motile, and rod-shaped, producing opaque, ivory, and convex colonies on GYM and MB7H10 agar after cultivation at 48 h and 28°C. Cells are catalase-negative and oxidase-positive. Optimum growth was observed at 10–37°C, pH 6–7, and with NaCl concentrations ranging between 0 and 5%. Cells were negative for Voges–Proskauer, H_2S production, and starch hydrolysis tests. Acetic acid, D-gluconic acid, D-mannose, glucuronamide, glycerol, L-glutamic acid, L-malic acid, propionic acid, tween 40, α-D-glucose, β-hydroxy-D, and L-butyric acid can be utilized as carbon sources. 3-methyl glucose, acetoacetic acid, bromo-succinic acid, citric acid, D-arabitol, D-aspartic acid, D-cellobiose, dextrin, D-fructose, D-fucose, D-galactose, D-galacturonic acid, D-glucose-6-PO_4, D-glucuronic acid, D-lactic acid methyl ester, D-maltose, D-mannitol, D-melibiose, D-raffinose, D-saccharic acid, D-salicin, D-serine, D-sorbitol, D-trehalose, D-turanose, gelatin, gentiobiose, glycyl-L-proline, inosine, L-aspartic acid, L-fucose, L-galactonic acid lactone, L-histidine, L-pyroglutamic acid, L-rhamnose, L-serine, mucic acid, myo-inositol, N-acetyl neuraminic acid, N-acetyl-D-galactosamine, N-acetyl-D-glucosamine, N-acetyl-β-D-mannosamine, pectin, p-hydroxy-phenylacetic acid, quinic acid, stachyose, sucrose, α-D-lactose, α-keto-butyric acid, α-keto-glutaric acid, β-methyl-D-glucoside, and γ-amino-butyric acid are not used as carbon sources. D-fructose, D-glucose, D-xylose, esculin ferric citrate, glycerol, inositol, potassium 2-ketogluconate, and potassium gluconate can be assimilated and fermented to produce acid. Cells exhibit positive acid phosphatase, alkaline phosphatase, cystine arylamidase, esterase (C4), esterase lipase (C8), leucine arylamidase, lipase (C14), naphthol-AS-BI-phosphohydrolase, trypsin, valine arylamidase, and α-glucosidase activities *via* API ZYM strip assays. Whole-cell hydrolysates contain *meso*-diaminopimelic acid (*meso*-A_2pm), arabinose, galactose, glucose, mannose, and ribose. Cellular polar lipid profiles comprise diposphatidylglycerol (DPG), phosphatidylethanolamine (PE) and phosphatidylinositol (PI). The primary menaquinone is MK-9 (H_2). The major fatty acids were $C_{16:0}$ (15.3%) and $C_{17:1}\omega7c$ (15.3%). The mycolic acids primarily contain 60–70 carbon atoms. The type strain YC-RL4^T (= CPCC 205684^T = CGMCC 1.62027^T) was isolated from a petroleum-contaminated soil sample from Shandong, China. The draft genome of the type strain is 6.1 Mbp in size and exhibits a genomic G + C content of 67.4%.

Description of *Mycobacterium deserti* sp. nov.

(de.ser'ti. L. gen. n. *deserti*, from a desert)

Cells are Gram-positive, non-motile, and non-spore forming. Ivory colonies develop on GYM and MB7H10 agar after incubation for 48 h at 28°C. Optimal growth was observed at 15–45°C, pH 6–7, and NaCl concentrations ranging from 0 to 5%. Cells were oxidase-positive and catalase-negative, but exhibited negative results for Voges–Proskauer, H_2S production, and starch hydrolysis tests. Cells can utilize acetic acid, D-arabitol, D-fructose, D-galactose, D-gluconic Acid, D-mannitol, D-mannose, D-saccharic acid, D-sorbitol, myo-inositol, propionic acid, quinic acid, and α-D-glucose as sole carbon sources. API 50CH tests indicated that arbutin, D-lyxose, D-saccharose, D-tagatose, esculin ferric citrate, potassium 2-ketogluconate, and potassium gluconate are used as carbon sources. In contrast, amidon, amygdalin, D-arabinose, D-arabitol, D-ardonitol, D-cellobiose, D-fructose, D-fucose, D-galactose, D-glucose, D-lactose, D-maltose, D-mannitol, D-mannose, D-melezitose, D-melibiose, D-raffinose, D-ribose, D-sorbitol, D-trehalose, D-turanose, dulcitol, D-xylose, erythritol, gentiobiose, glycerol, glycogen, inositol, inulin, L-arabinose, L-arabitol, L-fucose, L-rhamnose, L-sorbose, L-xylose, mehyl-α-D-glucopyranoside, mehyl-α-D-mannopyranoside, Mehyl-β-D-xylopyranoside, N-acetylglucosamine, potassium 5-ketogluconate, salicin, and xylitol are not used as carbon sources. API ZYM analysis revealed the presence of positive acid phosphatase, alkaline phosphatase, cystine arylamidase, esterase (C4), leucine arylamidase, lipase (C14), naphthol-AS-BI-phosphohydrolase, trypsin, valine arylamidase, α-chymotrypsin, α-glucosidase, and β-glucosidase activities. Whole-cell hydrolysates contained *meso*-diaminopimelic acid (*meso*-A_2pm), arabinose, galactose, glucose, mannose, and ribose. Cellular polar lipid profiles comprised diposphatidylglycerol (DPG), phosphatidylethanolamine (PE), phosphatidylinositol (PI), and glycolipids (GL). The primary menaquinone was MK-9 (H_2). The major fatty acids were $C_{17:1}\omega7c$ (47.7%) and summed feature 9 (iso-$C_{17:1}\omega9c$/$C_{16:0}$ 10-methyl) (43.3%). The mycolic acids mainly contain 78–86 carbon atoms, with moderate amount of 76–84 carbon atoms, and minor of 62–70 carbon atoms. The type strain MB418^T (= CPCC 205710^T = KCTC 49782^T) was isolated from a gravel soil sample from the Gurbantunggut desert, China. The draft genome of the type strain is 5.6 Mbp in length and exhibits a genomic G + C content of 66.5%.

Description of *Mycobacterium hippophais* sp. nov.

(hip.po.pha'is. L. gen. n. *hippophais*, from *Hippophae*, a plant genus whose rhizosphere the type strain was isolated from)

Cells are Gram-positive, non-motile, and rod-shaped, producing yellow colonies. Cells were positive for oxidase activity, but negative

for catalase, Voges–Proskauer, H_2S production, and starch hydrolysis tests. Optimum growth was observed at 15–28°C, pH 6–7, and with NaCl concentrations ranging between 0 and 4%. Acetic acid, D-gluconic acid, D-saccharic Acid, propionic acid, and β-hydroxy-D,L-butyric acid can be used as substrates. API 50CH analysis revealed that D-fructose, D-glucose, D-ribose, esculin ferric citrate, potassium 2-ketogluconate, and potassium gluconate can be used as carbon substrates. Enzymatic activity analysis revealed the presence of alkaline phosphatase, esterase (C4), esterase lipase (C8), leucine arylamidase, lipase (C14), naphthol-AS-BI-phosphohydrolase, and valine arylamidase activities, but the lack of activity for acid phosphatase, cystine arylamidase, N-acetyl-β-glucosamimidase, trypsin, *α*-chymotrypsin, *α*-fucosidase, *α*-galactosidase, *α*-glucosidase, *α*-mannosidase, *β*-galactosidase, *β*-glucosidase, and *β*-glucuronidase. Whole-cell hydrolysates contained *meso*-diaminopimelic acid (*meso*-A_2pm), arabinose, galactose, glucose, mannose, and ribose. Cellular polar lipid profiles comprised diposphatidylglycerol (DPG), phosphatidylethanolamine (PE), phosphatidylinositol (PI), and glycolipids (GL). The primary menaquinone was MK-9 (H_2). The major fatty acids were $C_{17:1}\omega7c$ (43.2%), $C_{19:1}$ trans 7 (30.9%), and $C_{16:0}$ (8.8%). The mycolic acids primarily contain 68–78 carbon atoms. The type strain HX176^T (= CPCC 205372^T = KCTC 49413^T) was isolated from a rhizosphere soil sample of a medicinal plant in Xinjiang, China. The draft genome of the type strain is 5.9 Mbp in length and exhibits a genomic G + C content of 69.3%.

The 16S rRNA gene sequences of strains YC-RL4^T, MB418^T, and HX176^T were deposited in GenBank under the accession numbers OQ096616, OP522341 and OQ096617, respectively. The whole genome shotgun data for the genomes of strains YC-RL4^T, MB418^T, and HX176^T were deposited in the DDBJ, ENA, and GenBank databases under the accession numbers CP015596, JAODWD000000000, and JAPZPY000000000, respectively.

Data availability statement

The datasets presented in this study can be found in online repositories. The names of the repository/repositories and accession number(s) can be found in the article/Supplementary material.

Author contributions

YD, TM, JW, and JS carried out the experiments. YD, YY, and Y-QZ conceived the research, analyzed the data, and prepared the manuscript. All authors contributed to the article and approved the submitted version.

Funding

This research was supported by CAMS Innovation Fund for Medical Sciences (CIFMS, 2021-I2M-1-055), National Natural Science Foundation of China (32170021 and 81960712), Beijing Natural Science Foundation (5212018), Key project at central government level-the ability establishment of sustainable use for valuable Chinese medicine resources (2060302), and the National Infrastructure of Microbial Resources (NIMR-2021-3).

Acknowledgments

The authors sincerely thank Aharon Oren (The Institute of Life Sciences, The Hebrew University of Jerusalem, Jerusalem, Israel) and Bernhard Schink (Department of Biology, University of Konstanz, Konstanz, Germany) for their guidance in nomenclature.

Conflict of interest

The authors declare that the research was conducted in the absence of any commercial or financial relationships that could be construed as a potential conflict of interest.

Publisher's note

All claims expressed in this article are solely those of the authors and do not necessarily represent those of their affiliated organizations, or those of the publisher, the editors and the reviewers. Any product that may be evaluated in this article, or claim that may be made by its manufacturer, is not guaranteed or endorsed by the publisher.

Supplementary material

The Supplementary material for this article can be found online at: https://www.frontiersin.org/articles/10.3389/fmicb.2023.1225746/full#supplementary-material

References

Abbasnezhad, H., Gray, M., and Foght, J. M. (2011). Influence of adhesion on aerobic biodegradation and bioremediation of liquid hydrocarbons. *Appl. Microbiol. Biotechnol.* 92, 653–675. doi: 10.1007/s00253-011-3589-4

Arnesano, F., Banci, L., Bertini, I., Mangani, S., and Thompsett, A. R. (2003). A redox switch in CopC: an intriguing copper trafficking protein that binds copper(I) and copper(II) at different sites. *Proc. Natl. Acad. Sci. U. S. A.* 100, 3814–3819. doi: 10.1073/pnas.0636904100

Auch, A. F., Von Jan, M., Klenk, H. P., and Göker, M. (2010). Digital DNA-DNA hybridization for microbial species delineation by means of genome-to-genome sequence comparison. *Stand. Genomic Sci.* 2, 117–134. doi: 10.4056/sigs.531120

Augelletti, F., Tremblay, J., Agathos, S. N., Jousset, A., and Stenuit, B. (2020). Draft whole-genome sequence of the anthracene-degrading strain *Mycolicibacterium frederiksbergense* LB501T, isolated from a polycyclic aromatic hydrocarbon-contaminated soil. *Microbiol. Resour. Announc.* 9:e00671-20. doi: 10.1128/mra.00671-20

Bhattacharyya, M., Dhar, R., Basu, S., Das, A., Reynolds, D. M., and Dutta, T. K. (2023). Molecular evaluation of the metabolism of estrogenic di(2-ethylhexyl) phthalate in *Mycolicibacterium* sp. *Microb. Cell Factories* 22:82. doi: 10.1186/s12934-023-02096-0

Blin, K., Shaw, S., Steinke, K., Villebro, R., Ziemert, N., Lee, S. Y., et al. (2019). antiSMASH 5.0: updates to the secondary metabolite genome mining pipeline. *Nucleic Acids Res.* 47, W81–W87. doi: 10.1093/nar/gkz310

Butler, W. R., and Guthertz, L. S. (2001). Mycolic acid analysis by high-performance liquid chromatography for identification of Mycobacterium species. *Clin. Microbiol. Rev.* 14, 704–726. doi: 10.1128/cmr.14.4.704-726.2001

Chan, P. P., Lin, B. Y., Mak, A. J., and Lowe, T. M. (2021). tRNAscan-SE 2.0: improved detection and functional classification of transfer RNA genes. *Nucleic Acids Res.* 49, 9077–9096. doi: 10.1093/nar/gkab688

Chaudhari, N. M., Gupta, V. K., and Dutta, C. (2016). BPGA- an ultra-fast pan-genome analysis pipeline. *Sci. Rep.* 6:24373. doi: 10.1038/srep24373

Chemerys, A., Pelletier, E., Cruaud, C., Martin, F., Violet, F., and Jouanneau, Y. (2014). Characterization of novel polycyclic aromatic hydrocarbon dioxygenases from the bacterial metagenomic DNA of a contaminated soil. *Appl. Environ. Microbiol.* 80, 6591–6600. doi: 10.1128/aem.01883-14

Coyte, K. Z., Stevenson, C., Knight, C. G., Harrison, E., Hall, J. P. J., and Brockhurst, M. A. (2022). Horizontal gene transfer and ecological interactions jointly control microbiome stability. *PLoS Biol.* 20:e3001847. doi: 10.1371/journal.pbio.3001847

Dai, Y., Liu, R., Zhou, Y., Li, N., Hou, L., Ma, Q., et al. (2020). Fire Phoenix facilitates phytoremediation of PAH-cd co-contaminated soil through promotion of beneficial rhizosphere bacterial communities. *Environ. Int.* 136:105421. doi: 10.1016/j.envint.2019.105421

Deng, Y., Han, X. F., Jiang, Z. M., Yu, L. Y., Li, Y., and Zhang, Y. Q. (2022). Characterization of three Stenotrophomonas strains isolated from different ecosystems and proposal of *Stenotrophomonas mori* spnov. and *Stenotrophomonas lacuserhaii* sp. nov. *Front. Microbiol.* 13:1056762. doi: 10.3389/fmicb.2022.1056762

Deng, Y., Jiang, Z. M., Han, X. F., Su, J., Yu, L. Y., Liu, W. H., et al. (2023). Pangenome analysis of the genus Herbiconiux and proposal of four new species associated with Chinese medicinal plants. *Front. Microbiol.* 14:1119226. doi: 10.3389/fmicb.2023.1119226

di Lello, P., Benison, G. C., Valafar, H., Pitts, K. E., Summers, A. O., Legault, P., et al. (2004). NMR structural studies reveal a novel protein fold for MerB, the organomercurial lyase involved in the bacterial mercury resistance system. *Biochemistry* 43, 8322–8332. doi: 10.1021/bi049669z

Falkinham, J. O. 3rd. (2009). Surrounded by mycobacteria: nontuberculous mycobacteria in the human environment. *J. Appl. Microbiol.* 107, 356–367. doi: 10.1111/j.1365-2672.2009.04161.x

Gardner, P. P., Daub, J., Tate, J. G., Nawrocki, E. P., Kolbe, D. L., Lindgreen, S., et al. (2009). Rfam: updates to the RNA families database. *Nucleic Acids Res.* 37, D136–D140. doi: 10.1093/nar/gkn766

Guillemin, I., Cambau, E., and Jarlier, V. (1995). Sequences of conserved region in the a subunit of DNA gyrase from nine species of the genus Mycobacterium: phylogenetic analysis and implication for intrinsic susceptibility to quinolones. *Antimicrob. Agents Chemother.* 39, 2145–2149. doi: 10.1128/aac.39.9.2145

Gupta, R. S., Lo, B., and Son, J. (2018). Phylogenomics and comparative genomic studies robustly support division of the genus Mycobacterium into an emended genus Mycobacterium and four novel genera. *Front. Microbiol.* 9:67. doi: 10.3389/fmicb.2018.00067

Habe, H., Chung, J. S., Ishida, A., Kasuga, K., Ide, K., Takemura, T., et al. (2005). The fluorene catabolic linear plasmid in *Terrabacter* sp. strain DBF63 carries the beta-ketoadipate pathway genes, pcaRHGBDCFIJ, also found in proteobacteria. *Microbiology* 151, 3713–3722. doi: 10.1099/mic.0.28215-0

Hartmans, S., De Bont, J. A., and Stackebrandt, E. J. T. P. (2006). "The genus Mycobacterium--nonmedical" in *The prokaryotes*. eds. M. Dworkin, S. Falkow, E. Rosenberg, K. H. Schleifer and E. Stackebrandt (New York, NY: Springer)

Hormisch, D., Hormisch, D., Brost, I., Kohring, G. W., Giffhorn, F., Kroppenstedt, R. M., et al. (2004). *Mycobacterium fluoranthenivorans* sp. nov., a fluoranthene and aflatoxin B1 degrading bacterium from contaminated soil of a former coal gas plant. *Syst. Appl. Microbiol.* 27, 653–660. doi: 10.1078/0723202042369866

Kahl, S., and Hofer, B. (2003). A genetic system for the rapid isolation of aromatic-ring-hydroxylating dioxygenase activities. *Microbiology* 149, 1475–1481. doi: 10.1099/mic.0.25976-0

Kasai, H., Ezaki, T., and Harayama, S. (2000). Differentiation of phylogenetically related slowly growing mycobacteria by their gyrB sequences. *J. Clin. Microbiol.* 38, 301–308. doi: 10.1128/jcm.38.1.301-308.2000

Khan, A. A., Wang, R. F., Cao, W. W., Doerge, D. R., Wennerstrom, D., and Cerniglia, C. E. (2001). Molecular cloning, nucleotide sequence, and expression of genes encoding a polycyclic aromatic ring dioxygenase from Mycobacterium sp. strain PYR-1. *Appl. Environ. Microbiol.* 67, 3577–3585. doi: 10.1128/aem.67.8.3577-3585.2001

Kim, H., Kim, S. H., Shim, T. S., Kim, M. N., Bai, G. H., Park, Y. G., et al. (2005). Differentiation of Mycobacterium species by analysis of the heat-shock protein 65 gene (hsp65). *Int. J. Syst. Evol. Microbiol.* 55, 1649–1656. doi: 10.1099/ijs.0.63553-0

Kim, S. J., Kweon, O., Jones, R. C., Freeman, J. P., Edmondson, R. D., and Cerniglia, C. E. (2007). Complete and integrated pyrene degradation pathway in *Mycobacterium vanbaalenii* PYR-1 based on systems biology. *J. Bacteriol.* 189, 464–472. doi: 10.1128/jb.01310-06

Kim, M., Oh, H. S., Park, S. C., and Chun, J. (2014). Towards a taxonomic coherence between average nucleotide identity and 16S rRNA gene sequence similarity for species demarcation of prokaryotes. *Int. J. Syst. Evol. Microbiol.* 64, 346–351. doi: 10.1099/ijs.0.059774-0

Kweon, O., Kim, S. J., Holland, R. D., Chen, H., Kim, D. W., Gao, Y., et al. (2011). Polycyclic aromatic hydrocarbon metabolic network in *Mycobacterium vanbaalenii* PYR-1. *J. Bacteriol.* 193, 4326–4337. doi: 10.1128/jb.00215-11

Lagesen, K., Hallin, P., Rødland, E. A., Staerfeldt, H. H., Rognes, T., and Ussery, D. W. (2007). RNAmmer: consistent and rapid annotation of ribosomal RNA genes. *Nucleic Acids Res.* 35, 3100–3108. doi: 10.1093/nar/gkm160

Lévy-Frébault, V. V., and Portaels, F. (1992). Proposed minimal standards for the genus Mycobacterium and for description of new slowly growing Mycobacterium species. *Int. J. Syst. Bacteriol.* 42, 315–323. doi: 10.1099/00207713-42-2-315

Li, R., Zhu, H., Ruan, J., Qian, W., Fang, X., Shi, Z., et al. (2010). De novo assembly of human genomes with massively parallel short read sequencing. *Genome Res.* 20, 265–272. doi: 10.1101/gr.097261.109

Masindi, V., and Muedi, K. L. J. H. M. (2018). "Environmental contamination by heavy metals" in *Heavy metals*. eds. H. E. D. M. Saleh and R. F. Aglan (Chichester: IntechOpen)

Mcmahon, M. D., Rush, J. S., and Thomas, M. G. (2012). Analyses of MbtB, MbtE, and MbtF suggest revisions to the mycobactin biosynthesis pathway in *Mycobacterium tuberculosis*. *J. Bacteriol.* 194, 2809–2818. doi: 10.1128/jb.00088-12

Minnikin, D., O'donnell, A., Goodfellow, M., Alderson, G., Athalye, M., Schaal, A., et al. (1984). An integrated procedure for the extraction of bacterial isoprenoid quinones and polar lipids. *J. Microbiol. Methods* 2, 233–241. doi: 10.1016/0167-7012(84)90018-6

Møller, A. K., Barkay, T., Hansen, M. A., Norman, A., Hansen, L. H., Sørensen, S. J., et al. (2014). Mercuric reductase genes (merA) and mercury resistance plasmids in high Arctic snow, freshwater and sea-ice brine. *FEMS Microbiol. Ecol.* 87, 52–63. doi: 10.1111/1574-6941.12189

Nakamiya, K., Hashimoto, S., Ito, H., Edmonds, J. S., Yasuhara, A., and Morita, M. (2005). Microbial treatment of bis (2-ethylhexyl) phthalate in polyvinyl chloride with isolated bacteria. *J. Biosci. Bioeng.* 99, 115–119. doi: 10.1263/jbb.99.115

Nguyen, L. T., Schmidt, H. A., Von Haeseler, A., and Minh, B. Q. (2015). IQ-TREE: a fast and effective stochastic algorithm for estimating maximum-likelihood phylogenies. *Mol. Biol. Evol.* 32, 268–274. doi: 10.1093/molbev/msu300

Parks, D. H., Imelfort, M., Skennerton, C. T., Hugenholtz, P., and Tyson, G. W. (2015). CheckM: assessing the quality of microbial genomes recovered from isolates, single cells, and metagenomes. *Genome Res.* 25, 1043–1055. doi: 10.1101/gr.186072.114

Pereira, A. C., Ramos, B., Reis, A. C., and Cunha, M. V. (2020). Non-tuberculous mycobacteria: molecular and physiological bases of virulence and adaptation to ecological niches. *Microorganisms* 8:1380. doi: 10.3390/microorganisms8091380

Reis, A. C., and Cunha, M. V. (2021). The open pan-genome architecture and virulence landscape of *Mycobacterium bovis*. *Microb Genom* 7:000664. doi: 10.1099/mgen.0.000664

Ren, L., Jia, Y., Ruth, N., Qiao, C., Wang, J., Zhao, B., et al. (2016). Biodegradation of phthalic acid esters by a newly isolated *Mycobacterium* sp. YC-RL4 and the bioprocess with environmental samples. *Environ. Sci. Pollut. Res. Int.* 23, 16609–16619. doi: 10.1007/s11356-016-6829-4

Ren, L., Wang, G., Huang, Y., Guo, J., Li, C., Jia, Y., et al. (2021). Phthalic acid esters degradation by a novel marine bacterial strain *Mycolicibacterium phocaicum* RL-HY01: characterization, metabolic pathway and bioaugmentation. *Sci. Total Environ.* 791:148303. doi: 10.1016/j.scitotenv.2021.148303

Runyon, E. H. (1959). Anonymous mycobacteria in pulmonary disease. *Med. Clin. North Am.* 43, 273–290. doi: 10.1016/s0025-7125(16)34193-1

Sasser, M (2006). *Bacterial identification by gas chromatographic analysis of fatty acids methyl esters (GC-FAME)*. Newark, NY: Microbial ID Inc.

Schleifer, K. H., and Kandler, O. J. B. R. (1972). Peptidoglycan types of bacterial cell walls and their taxonomic implications. *Bacteriol. Rev.* 36, 407–477. doi: 10.1128/br.36.4.407-477.1972

Shamsuzzaman, M., Dahal, R. H., Kim, S., and Kim, J. (2023). Genome insight and probiotic potential of three novel species of the genus Corynebacterium. *Front. Microbiol.* 14:1225282. doi: 10.3389/fmicb.2023.1225282

Sherpa, M. T., Najar, I. N., Das, S., and Thakur, N. (2020). Distribution of antibiotic and metal resistance genes in two glaciers of North Sikkim, India. *Ecotoxicol. Environ. Saf.* 203:111037. doi: 10.1016/j.ecoenv.2020.111037

Skerman, V. B. D., Mcgowan, V., and Sneath, P. H. A. (1980). Approved lists of bacterial names. *Med. J. Aust* 30, 225–230. doi: 10.5694/j.1326-5377.1980.tb131800.x

Stahl, D. A., and Urbance, J. W. (1990). The division between fast- and slow-growing species corresponds to natural relationships among the mycobacteria. *J. Bacteriol.* 172, 116–124. doi: 10.1128/jb.172.1.116-124.1990

Stinear, T. P., Seemann, T., Harrison, P. F., Jenkin, G. A., Davies, J. K., Johnson, P. D., et al. (2008). Insights from the complete genome sequence of *Mycobacterium marinum* on the evolution of *Mycobacterium tuberculosis*. *Genome Res.* 18, 729–741. doi: 10.1101/gr.075069.107

Stone, B. B., Nietupski, R. M., Breton, G. L., and Weisburg, W. G. (1995). Comparison of Mycobacterium 23S rRNA sequences by high-temperature reverse transcription and PCR. *Int. J. Syst. Bacteriol.* 45, 811–819. doi: 10.1099/00207713-45-4-811

Takewaki, S. I., Okuzumi, K., Manabe, I., Tanimura, M., Miyamura, K., Nakahara, K. I., et al. (1994). Nucleotide sequence comparison of the mycobacterial dnaJ gene and PCR-restriction fragment length polymorphism analysis for identification of mycobacterial species. *Int. J. Syst. Bacteriol.* 44, 159–166. doi: 10.1099/00207713-44-1-159

Tamura, K., Stecher, G., and Kumar, S. (2021). MEGA11: molecular evolutionary genetics analysis version 11. *Mol. Biol. Evol.* 38, 3022–3027. doi: 10.1093/molbev/msab120

Tortoli, E. (2012). Phylogeny of the genus Mycobacterium: many doubts, few certainties. *Infect. Genet. Evol.* 12, 827–831. doi: 10.1016/j.meegid.2011.05.025

Tortoli, E., Brown-Elliott, B. A., Chalmers, J. D., Cirillo, D. M., Daley, C. L., Emler, S., et al. (2019). Same meat, different gravy: ignore the new names of mycobacteria. *Eur. Respir. J.* 54:1900795. doi: 10.1183/13993003.00795-2019

Vernikos, G., Medini, D., Riley, D. R., and Tettelin, H. (2015). Ten years of pan-genome analyses. *Curr. Opin. Microbiol.* 23, 148–154. doi: 10.1016/j.mib.2014.11.016

Willumsen, P., Karlson, U., Stackebrandt, E., and Kroppenstedt, R. M. (2001). *Mycobacterium frederiksbergense* sp. nov., a novel polycyclic aromatic hydrocarbon-degrading Mycobacterium species. *Int. J. Syst. Evol. Microbiol.* 51, 1715–1722. doi: 10.1099/00207713-51-5-1715

Wright, R. J., Bosch, R., Gibson, M. I., and Christie-Oleza, J. A. (2020). Plasticizer degradation by marine bacterial isolates: a Proteogenomic and Metabolomic characterization. *Environ. Sci. Technol.* 54, 2244–2256. doi: 10.1021/acs.est.9b05228

Yang, J., Gu, Y., Chen, Z., Song, Y., Sun, F., Liu, J., et al. (2021). Colonization and performance of a pyrene-degrading bacterium *Mycolicibacterium* sp. Pyr9 on root surfaces of white clover. *Chemosphere* 263:127918. doi: 10.1016/j.chemosphere.2020.127918

Yoon, S. H., Ha, S. M., Kwon, S., Lim, J., Kim, Y., Seo, H., et al. (2017a). Introducing EzBioCloud: a taxonomically united database of 16S rRNA gene sequences and whole-genome assemblies. *Int. J. Syst. Evol. Microbiol.* 67, 1613–1617. doi: 10.1099/ijsem.0.001755

Yoon, S. H., Ha, S. M., Lim, J., Kwon, S., and Chun, J. (2017b). A large-scale evaluation of algorithms to calculate average nucleotide identity. *Antonie Van Leeuwenhoek* 110, 1281–1286. doi: 10.1007/s10482-017-0844-4

Zeng, K., Hwang, H. M., Dong, S., Shi, X., Wilson, K., Green, J., et al. (2004). Photochemical transformation and phototoxicity of 1-aminopyrene. *Environ. Toxicol. Chem.* 23, 1400–1407. doi: 10.1897/03-415

Zeng, J., Zhu, Q., Wu, Y., Chen, H., and Lin, X. (2017). Characterization of a polycyclic aromatic ring-hydroxylation dioxygenase from *Mycobacterium* sp. NJS-P. *Chemosphere* 185, 67–74. doi: 10.1016/j.chemosphere.2017.07.001

Zhang, D. F., Cui, X. W., Zhao, Z., Zhang, A. H., Huang, J. K., and Li, W. J. (2020). *Sphingomonas hominis* sp. nov., isolated from hair of a 21-year-old girl. *Antonie Van Leeuwenhoek* 113, 1523–1530. doi: 10.1007/s10482-020-01460-z

Zhang, Y., Zhang, J., Fang, C., Pang, H., and Fan, J. (2012). *Mycobacterium litorale* sp. nov., a rapidly growing mycobacterium from soil. *Int. J. Syst. Evol. Microbiol.* 62, 1204–1207. doi: 10.1099/ijs.0.033449-0

Zimenkov, D. V., Kulagina, E. V., Antonova, O. V., Krasnova, M. A., Chernyaeva, E. N., Zhuravlev, V. Y., et al. (2015). Evaluation of a low-density hydrogel microarray technique for mycobacterial species identification. *J. Clin. Microbiol.* 53, 1103–1114. doi: 10.1128/JCM.02579-14

frontiers | Frontiers in Environmental Science

TYPE Original Research
PUBLISHED 13 October 2023
DOI 10.3389/fenvs.2023.1252926

OPEN ACCESS

EDITED BY
Vishal Tripathi,
Graphic Era University, India

REVIEWED BY
Titus Egbosiuba,
Chukwuemeka Odumegwu Ojukwu University, Nigeria
Naveen Bunekar,
Chung Yuan Christian University, Taiwan

*CORRESPONDENCE
Mariem Zouari,
mariem.zouari@innorenew.eu

RECEIVED 04 July 2023
ACCEPTED 02 October 2023
PUBLISHED 13 October 2023

CITATION
Zouari M, Marrot L and DeVallance DB (2023), Evaluation of properties and formaldehyde removal efficiency of biocarbon prepared at variable pyrolytic temperatures.
Front. Environ. Sci. 11:1252926.
doi: 10.3389/fenvs.2023.1252926

Evaluation of properties and formaldehyde removal efficiency of biocarbon prepared at variable pyrolytic temperatures

Mariem Zouari[1,2]*, Laetitia Marrot[3] and David Brian DeVallance[4]

[1]InnoRenew CoE, Izola, Slovenia, [2]Faculty of Mathematics, Natural Sciences, and Information Technologies, University of Primorska, Koper, Slovenia, [3]Fire Safe Sustainable Built Environment (FRISSBE), Slovenian National Building and Civil Engineering Institute (ZAG), Ljubljana, Slovenia, [4]College of Science and Technology, Commonwealth University, Lock Haven, PA, United States

Biocarbon (BC) represents a potential material for application in air remediation. This study investigated the efficiency of BC particles in the removal of formaldehyde. BC samples were prepared from *Arundo donax* (AD) and olive stone (OS) feedstocks at variable pyrolysis temperatures (from 300°C to 800°C). The BC particles were characterized using proximate, Fourier transform infrared, water contact angle, particle size, and physisorption analyses. The formaldehyde removal capacity was tested using an electrochemical formaldehyde sensor in a batch experiment. The physicochemical and structural properties depended on the pyrolysis temperature at which the BC was produced. The increase in pyrolysis temperature increased the BC's pH, hydrophobicity, and porosity. All the samples achieved a formaldehyde removal capacity ranging between 26% and 64% for BC pyrolyzed at 300°C and 800°C, respectively. In BC pyrolyzed at temperatures under 500°C, the formaldehyde capture was governed by a partitioning mechanism through diffusion in the noncarbonized organic fraction. In comparison, formaldehyde capture was controlled by a physical adsorption mechanism through pore filling for BC pyrolyzed at 500°C or above. BC pyrolyzed at 800°C was more efficient for formaldehyde adsorption due to the well-developed microporous structure for both AD and OS. AD-derived BC prepared at 800 °C (AD-BC800) was selected for the re-usability test, using thermal regeneration to remove the adsorbed components. The regenerated sample maintained a comparable formaldehyde removal capacity up to four re-use cycles. Moreover, the comparison between non-activated and activated AD-BC800 revealed that physical activation significantly enhanced BC's adsorptive ability.

KEYWORDS

biocarbon, pyrolysis temperature, partitioning, adsorption, volatile organic compounds, air purification

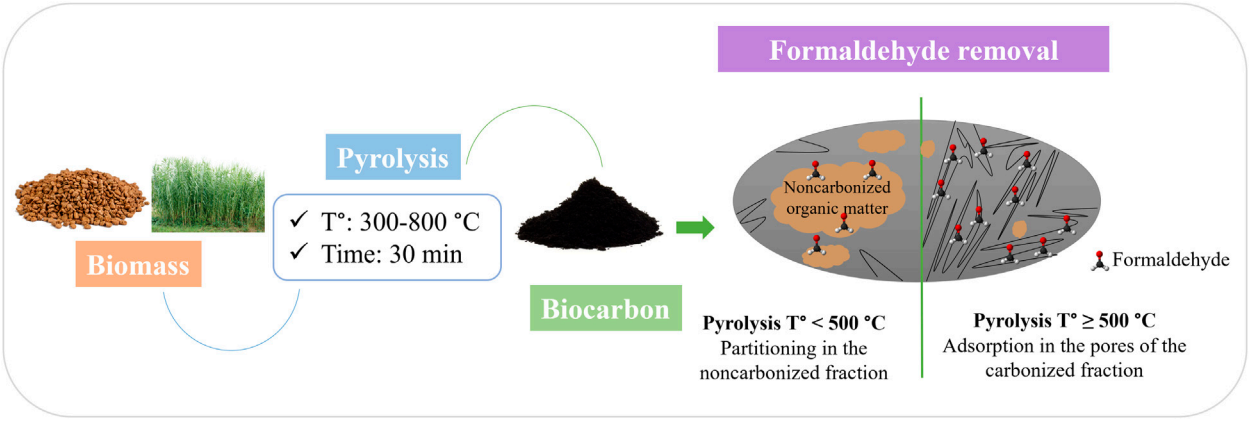

GRAPHICAL ABSTRACT

1 Introduction

Poor air quality is a severe problem linked to public health and environmental concerns. The World Health Organization reported in 2022 that air pollution is associated with 6.7 million premature deaths annually worldwide, from which 3.2 million deaths are caused by indoor air pollution (WHO, 2022). Among the wide range of airborne pollutants, volatile organic compounds (VOCs) have attracted more attention, given their high toxicity and negative environmental impact. VOCs are organic chemicals with high vapor pressure under ambient conditions, allowing them to evaporate and occur in the atmosphere. Depending on the boiling point range, VOCs can be categorized as very VOCs (from <0°C to 50°C–100°C), VOCs (from 50°C–100°C to 240°C–260°C), and semi-VOCs (from 240°C–260°C to 380°C–400°C) (WHO, 1989). VOCs represent a real threat to human health, given their high hazard and potential to provoke chronic severe diseases. Besides directly harming human health, VOCs damage the environment through photochemical smog formation and depletion of the ozone layer (Ling et al., 2019). Formaldehyde is an example of a common indoor VOC with a low evaporation point of about −19°C (IARC, 2006). In indoor conditions, formaldehyde is a colorless gas with an irritating odor and high reactivity. A large spectrum of indoor sources, such as flooring materials, carpets, cooking stoves, paints, and wall coverings, can emit formaldehyde. However, wood-based materials, such as furniture, are recognized as the primary emission source of formaldehyde in the indoor environment (Salthammer et al., 2010). Formaldehyde is a natural chemical in wood (Meyer and Boehme, 1997) primarily released during wood drying. Indoor emissions associated with wood product use are caused mainly by synthetic formaldehyde resin used as an adhesive component for commercial particle boards and furniture. Exposure to formaldehyde occurs by inhalation, and its consequences are various with several degrees of severity depending on concentration and exposure period: eye irritation, headache, dizziness, or acute symptoms such as respiratory tract damage, abortion, pneumonia, and hemorrhagic nephritis (US National Research Council, 1980). More serious concerns were raised after the classification of formaldehyde as a group 1 human carcinogen by the International Agency for Research on Cancer in 2006 (IARC, 2006).

Among the air remediation techniques, adsorption on porous support media has been recognized as a financially and technologically efficient method for trapping gaseous pollutants under ambient conditions. Carbonaceous materials such as carbon nanotubes (CNTs) (Liu et al., 2021), graphene (Guo et al., 2016), and activated carbon (Ryu et al., 2002) have been widely applied for the adsorption of a wide range of airborne pollutants. Biocarbon (BC), a member of the carbonaceous materials group, is a carbon-rich residue that can be prepared from the pyrolysis of almost any organic biomass, including underutilized feedstocks and by-products (Basu, 2013). BC, with and without activation, has been studied extensively as an adsorbent in soil or aqueous media for the removal of dye chemicals (Yu et al., 2021), heavy metals (Sachdeva et al., 2023), and antibiotics (Stylianou et al., 2021). BC has been shown to provide good adsorption performances in these applications due to its large porosity and surface functional groups. For instance, prior research (Egbosiuba et al., 2020) reported that activated BC from empty fruit bunch was successfully used for the removal of methylene blue from water. Results stated that the ultrasonic-assisted activation process enhanced the adsorption efficiency by increasing the porosity and surface chemistry of the adsorbent material. However, using BC for airborne contaminants removal has been less explored. BC's potential as an adsorbent is highly dependent on properties like porosity and carbon content (Angın, 2013). Pyrolysis temperature is the main factor determining the BC product's final properties and molecular structure (Leng and Huang, 2018). A prior study on the dynamic molecular structure of plant-derived BC (Keiluweit et al., 2010) revealed that depending on the pyrolysis temperature, BC could be categorized into four groups with differences in the chemical phases and physical states: 1) transition BC (from 200 °C to 300 °C with the release of light volatiles and evaporation of water, the crystalline structure of biomass is preserved), 2) amorphous BC (from 300°C to 600°C with depolymerization of the biomass and occurrence of random aromatic structures), 3) composite BC (from 600°C to 700°C with the generation of slightly ordered graphene-like arrangements merged into amorphous phases, and 4) turbostratic BC (above

700°C with the dominance of disordered graphitic crystallites). All these molecular and structural variations can influence the functionality of BC when used as an adsorbent (Keiluweit et al., 2010).

The efficiency of adsorbate-adsorbent interaction and the adsorption capacity can vary depending on the carbon material's properties. Thus, understanding the adsorption mechanism is crucial for preparing adequate material and achieving optimal pollutant removal. Yang et al. (2018) studied the kinetics of airborne pollutants adsorption on activated carbon with variable pores structures, and they concluded that the adsorption process occurs in three different phases. The first phase is external surface adsorption, when the adsorbate is transferred by convection and diffusion from the air to the adsorbent's surface. The rate of mass transfer depends on the specific surface area. The second phase is internal diffusion when the adsorbate molecules access the internal surface of the pores. The dominant factors in this phase are the pore size and volume. The final phase is the equilibrium stage, when the pores are filled with the adsorbate molecules. This stage depends on the ratio of different pore types (i.e., micro, meso, and macropores). Based on the above description of the adsorption mechanism, the adsorption capacity of porous materials, such as carbonaceous materials, was often associated with their physical structure. Notably, the specific surface area (SSA), pores size, and pores volume were believed to be key parameters controlling adsorption efficiency (Yang et al., 2018). For instance, Abdul Manap et al. (2018) studied formaldehyde adsorption on palm mesocarp-BC in a batch experiment. They reported that the formaldehyde adsorption increased with the increase of SSA and pores volume. However, their study did not investigate the microporous surface area, which could give complementary information to evaluate the relationship between adsorption capacity and the type of porosity.

Although the SSA and pores volume play an important role in the adsorption process, their effect in formaldehyde removal was not always dominant. Indeed, other factors could also contribute to formaldehyde adsorption on carbon-based materials, such as the basicity and the presence of surface functional groups. For instance, Lee et al. (2011) utilized sludge-derived activated carbon to remove formaldehyde. They reported that the sample activated with both KOH and ammonia performed better than the commercial activated carbon in removing formaldehyde despite the larger SSA of the commercial sample. They attributed the results to their prepared sample's higher surface basicity and content of oxygen and nitrogen functional groups. Based on their results, the surface basicity was favored by the occurrence of high amounts of metal components in the sewage sludge BC. However, this feature might not be representative of BC derived from other types of biomasses, such as AD and OS. Carter et al. (2011) also stated that the adsorption of low formaldehyde concentrations (3 and 7 ppm) was favored mainly by the presence of basic functional groups at the surface of activated carbon fibers (ACFs). Likewise, Yang et al. (2017) reported that CNTs-ACFs material exhibited three folds higher formaldehyde removal capacities than pure ACFs despite the significant difference in SSA (203.47 m^2/g and 1583.68 m^2/g for CNTs-ACFs and pure ACFs, respectively). They concluded that SSA could not accurately represent formaldehyde adsorption capacity. They also explained that the removal of formaldehyde, as a polar molecule, was likely enabled by chemisorption reactions that involve interaction and formation of strong covalent bonds between formaldehyde and the CNTs-ACFs material. The microporous surface area, pores distribution (i.e., micro, meso, and macropores), and composition of functional surface groups were not provided in their study which could further explain why CNTs-ACFs material performed better. The surface hydrophobicity of carbonaceous materials can also influence their adsorption capacity. In this regard, Boonamnuayvitaya et al. (2005) reported that the hydrophobic character of activated carbon samples lowered their ability to adsorb formaldehyde. They explained that formaldehyde, as a polar molecule, could better be adsorbed on hydrophilic surfaces. Based on their study, the formaldehyde adsorption capacity of activated carbon was more dependent on the surface chemical properties rather than the structural properties (i.e., surface area and pores volume).

During the present study, an in-depth investigation was performed to establish a better understanding of using BC as an efficient material for improving indoor air quality. The main objectives are: i) to investigate the effect of the pyrolysis temperature and physical activation on the properties of *Arundo donax* (AD) and olive stone (OS)-derived BC; ii) to investigate the influence of BC's properties on its formaldehyde removal capacity; and iii) to assess the re-usability of spent BC after thermal regeneration.

2 Materials and methods

2.1 Materials and reagents

Arundo donax (AD), an invasive species, and olive stone (OS), a by-product of the olive oil extraction industry, were selected as feedstocks. AD canes were harvested locally in Kampel, Slovenia. Crushed OS was provided by the Oljarna Krozera Franka Marzi sp olive oil extraction company (Srgaši, Slovenia) as by-products in 5 mm-sized dry particles.

The chemical composition of AD, is 21.1%, 37.9%, 34.0% for lignin, cellulose, and hemicellulose, respectively (Suárez et al., 2021).

The chemical composition of OS is 32.10%, 26.9%, and 34.8% for lignin, cellulose, and hemicellulose, respectively (Ferreiro-Cabello et al., 2022).

Technical N_2 with a purity of 99.998% (Grade 4.8) was used for the biomass pyrolysis and proximate analysis. N_2 and CO_2 gases with a purity of 99.999% (Grade 5.0) were used for physisorption analysis. Aqueous formaldehyde solution (37% w/v) was purchased from Carlo Erba reagents (Dasti group, Val de Reuil, France).

2.2 Preparation of the biomass

AD and OS were manually cleaned, ground with a cutting mill grinder (Pulverisette 25/19, Fritsch, Idar-Oberstein, Germany) using a 1 mm mesh, and dried in an oven for 24 h at 105°C to remove excessive moisture. The AD was then subjected to a demineralization

treatment by water washing under stirring at 60°C for 1 h to reduce the ash content. The OS, however, was not treated as our previous research indicated that the demineralization effect was negligible for this type of biomass (Zouari et al., 2023). Details about the characterization of the two biomasses can be found in (Zouari et al., 2023).

2.3 Preparation of the biocarbon particles

BC was prepared by pyrolysis of the two biomasses in a tube furnace (Nabertherm RSRC 120-1000/13, Nabertherm, Lilienthal, Germany). Each biomass, AD and OS, was pyrolyzed separately for 30 min at variable temperatures (300, 400, 500, 600, 700, and 800°C) under N_2 gas flow of 300 L/h and a heating rate of 1500°C/h, which is automatically controlled by the tube furnace and optimized to fit in the configuration of slow pyrolysis and to be able to control the thermal inertia of the furnace.

The pyrolysis process generated 12 specimens which were labelled based on the type of original biomass (AD or OS) and the pyrolysis temperature: AD-BC300, AD-BC400, AD-BC500, AD-BC600, AD-BC700, AD-BC800, OS-BC300, OS-BC400, OS-BC500, OS-BC600, OS-BC700, OS-BC800.

After cooling to room temperature, the BC samples were weighed to determine the pyrolysis yield using Eq. 1.

$$\text{Pyrolysis yield} = \frac{W_f}{W_i} \times 100 \quad (1)$$

Where W_i is the weight of the raw biomass (g), and W_f is to the weight of the derived BC (g).

The collected BC powders were then ball milled in distilled water media using a planetary ball miller (Pulverisette 5, Fritsch, Idar-Oberstein, Germany) for 30 min at 400 rpm. For milling, stainless-steel jars and 20 mm in diameter balls were utilized, and the ball: BC ratio was equal to 100. The ball-milled specimens were then dried at 105°C for 24 h to allow water evaporation, and the obtained powders were stored in glass containers until further characterization. The AD-BC800 sample was also processed through an activation phase to compare formaldehyde removal between non-activated and activated BC. AD-BC800 was selected for activation based on the formaldehyde removal results and a specific interest in valorizing AD as an invasive species. The BC activation was performed via physical activation under a CO_2 gas flow of 300 L/h at 800°C for 1 h. The obtained sample was identified as: Activated AD-BC800.

2.4 Characterization of the biocarbon particles

Proximate analysis was performed using a thermogravimetric analyzer (LECO TGA801, LECO corporation, Saint-Joseph, MI, United States). The volatiles, ash, and fixed carbon contents were determined according to the ASTM D7582 standard. Values for moisture, volatiles, ash, and fixed carbon were calculated using Eqs 2–5 detailed as specified in Section 14 of ASTM D7582 (ASTM, 2015).

$$\text{Moisture} = \frac{W_{initial} - W_{107°C}}{W_{initial}} \times 100 \quad (2)$$

$$\text{Volatiles} = \frac{W_{107°C} - W_{950°C}}{W_{initial}} \times 100 \quad (3)$$

$$\text{Ash} = \frac{W_{750°C}}{W_{initial}} \times 100 \quad (4)$$

$$\text{Fixed carbon} = 100 - (Moisture + Volatiles + Ash) \quad (5)$$

Where $W_{initial}$ is the initial weight of the BC sample (g), and $W_{*°C}$ refers to the weight of the BC sample (g) at the designated * temperature.

All tests were repeated three times, and the average values were reported.

The pH was measured in the leachate of the BC specimen by first mixing 0.5 g of BC with 10 mL of deionized water and agitating the mixture in an incubation shaker (IS-OS 20, Phoenix Instruments, Naperville, Illinois, United States) at 23 °C for 1 h. The solutions were then left to settle for 30 min, and the pH was determined using a pH meter equipped with an IS-68 × 591206-B-VSTAR pH/LogR Module (Orion Versa-Star Pro Meter, Thermo Fischer Scientific, Waltham, Massachusetts, United States).

Functional groups on the BC surface were analyzed using a Fourier transform infrared (FTIR) spectrometer (Alpha FT-IR Spectrometer Bruker, Billerica, MA, United States) connected to an ATR (attenuated total reflection) module. Wavelength ranges from 400 to 4,000 cm^{-1}, and a resolution of 4 cm^{-1} was set to record the FTIR spectra. For each sample, 64 scans were performed, and ten repetitions were done to obtain accurate results and minimize the effect of the atmospheric noise. Opus software was used to collect average spectra, which were further treated by eliminating CO_2 and atmospheric water vapor effects.

Hydrophobicity was assessed by an optical tensiometer (Attension Theta Flex Auto 4 system, Biolin Scientific, Gothenburg, Sweden) that measured the dynamic water contact angle (WCA). Following the method reported by Bachmann et al. (2000), the BC powders were evenly spread and pressed as a thin layer on a flat glass surface covered with adhesive tape (with the adhesive side exposed to the BC particles for proper fixation). The sessile drop method was used to determine the WCA. Five droplets, 4 µL each, were placed on the BC powders, and the WCA value was taken at 30 s. Averages with standard deviations were reported.

The particle size distribution was determined by laser diffraction technique using a Horiba Scientific LA-960A2 analyzer (HORIBA, Kyoto, Japan). The refractive index was set to 1.92. Before each measurement, 1 min of ultrasonication was done to facilitate homogeneous dispersion of the particles. Three repetitions were performed for each sample, and the average values were reported.

The internal porosity of the BC particles was investigated using a physisorption analyzer (Anton Paar Quantachrome Instruments, Boynton Beach, Florida, United States). N_2 and CO_2 gases were used to evaluate the surface area and pores distribution according to Brunauer-Emmett-Teller (BET) and Barrett, Joyner, and Halenda (BJH), and density functional theory (DFT) models, respectively. Before analysis, samples were degassed under vacuum for 12 h at 250°C to remove impurities trapped in the BC's cavities. Then, for the BET model, the N_2 adsorption-desorption isotherms were determined over a relative pressure range from 0.005 bar to 1 bar

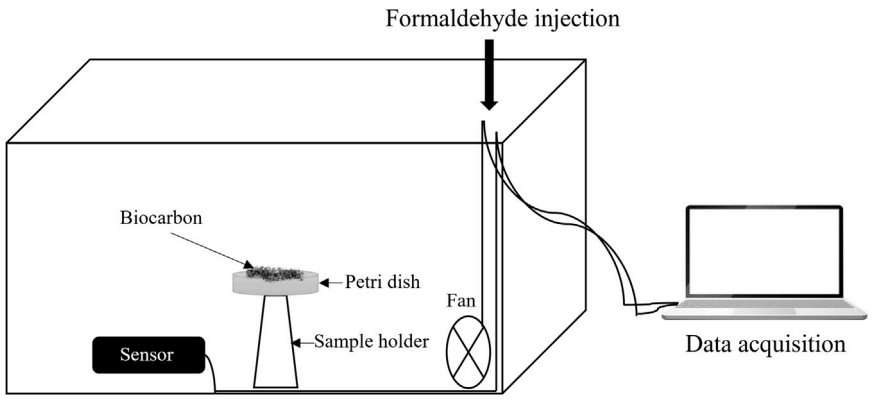

FIGURE 1
Schematic illustration of the formaldehyde removal capacity testing setup.

TABLE 1 Composition and pH of the biocarbon particles.

Sample ID	Proximate composition, % (mass-based)			pH	Pyrolysis yield, %
	Volatiles	Ash	Fixed carbon		
AD-BC300	58.21 ± 1.03	6.88 ± 0.14	31.81 ± 1.23	4.27 ± 0.05	53
AD-BC400	30.09 ± 0.60	6.29 ± 0.30	59.78 ± 0.79	4.28 ± 0.01	30
AD-BC500	20.96 ± 0.47	8.89 ± 0.28	65.43 ± 0.71	6.47 ± 0.05	27
AD-BC600	13.87 ± 0.30	7.24 ± 0.16	74.83 ± 0.46	8.43 ± 0.02	24
AD-BC700	12.65 ± 0.55	8.93 ± 0.10	76.02 ± 0.32	8.50 ± 0.06	23
AD-BC800	10.80 ± 0.52	10.75 ± 0.11	76.21 ± 0.59	8.63 ± 0.05	23
Activated AD-BC800	12.22 ± 0.39	13.11 ± 0.19	71.92 ± 0.66	8.92 ± 0.02	23
OS-BC300	49.36 ± 1.01	2.03 ± 0.04	46.87 ± 0.96	5.23 ± 0.01	53
OS-BC400	31.60 ± 0.70	2.47 ± 0.16	62.05 ± 0.94	5.69 ± 0.03	35
OS-BC500	22.21 ± 0.35	3.01 ± 0.03	73.24 ± 0.72	7.18 ± 0.04	33
OS-BC600	14.4 ± 0.41	2.29 ± 0.02	81.04 ± 0.73	8.33 ± 0.08	27
OS-BC700	11.45 ± 0.83	1.93 ± 0.58	83.78 ± 0.40	8.01 ± 0.07	27
OS-BC800	9.92 ± 0.60	4.29 ± 0.27	83.89 ± 0.87	8.71 ± 0.07	25

at 77 K to determine SSA and total pores volume, represented by mesopores (2 nm–50 nm in width) and macropores (>50 nm in width). In addition, the BJH method was used to determine the meso and macropores size distribution. For the DFT model, CO_2 adsorption-desorption isotherms were collected at a pressure range from 0.001 bar to 0.03 bar at 273 K to determine microporous surface area and micropores (<2 nm in width) volume.

2.5 Formaldehyde removal efficiency tests

The formaldehyde removal performance of the different BC samples was evaluated using a batch experiment setup, as shown in Figure 1. Before the tests, the samples were oven-dried overnight at 105 °C to remove any residual moisture. Tests were carried out in a closed glass chamber with a volume of 54 L equipped with an electrical fan. A Petri dish containing 1 g of BC powder sample was placed inside the testing chamber on a glass support, and 35 µL of formaldehyde solution was injected into the chamber through the inlet using a 50 µL micropipette. The chamber was hermetically sealed, and the fan was turned on to ensure a homogeneous distribution of the formaldehyde molecules. The initial formaldehyde concentration stabilized at 4 ppm. The experiment was conducted in standard ambient conditions: 23°C temperature, 50% relative humidity, and atmospheric pressure. The changes in formaldehyde concentration inside the chamber were continuously recorded using a formaldehyde electrochemical detection sensor (Stox-HCHO, EC Sense, Schäftlarn, Germany) with 0.1 ppm resolution and 1 s response time. The sensor was connected to the computer,

which enabled direct data acquisition using a TVOC-HCHO logger software (ADDproS, Celje, Slovenia).

The formaldehyde removal percentages were calculated according to Eq. 6 (Do et al., 2022), using the residual pollutant concentration measured in the chamber after 1 h.

$$\text{Formaldehyde removal} = \frac{C_0 - C_{1h}}{C_0} \times 100 \quad (6)$$

Where C_0 is the initial formaldehyde concentration (ppm) and C_{1h} is the measured formaldehyde concentration after 1 h of the experiment (ppm).

A blank test was carried out by repeating the same experiment without BC particles. The reduction in pollutant concentration calculated for the blank was subtracted from the values obtained for each sample for results correction. Three repetitions were conducted per BC substrate, and the average values were reported.

The re-usability of the spent adsorbent, AD-BC800, was assessed by determining the formaldehyde removal capacity after five cycles of thermal regeneration. The BC specimen was placed in the oven at 100 °C for 1 h to desorb the formaldehyde molecules captured in the BC pores during the previous cycle.

2.6 Statistical analysis

The Pearson correlation test was used to evaluate the relationship between BC's properties and the formaldehyde removal capacity. Furthermore, the effect of BC's properties on the formaldehyde removal capacity was evaluated by performing a multiple regression analysis. For both analyses, variables from all samples (AD-BC and OS-BC) were evaluated to remove the biomass type effect. NCSS software (NCSS, LLC, Version 07.1.21) was used for the statistical analysis. The effect of the independent variable was considered to be significant when the *p*-value was below 0.05.

The formaldehyde removal capacity of AD-BC and OS-BC was compared by unpaired *t*-test in Excel. A paired *t*-test was performed to compare the formaldehyde removal performance of non-activated and activated BC.

3 Results and discussion

3.1 Characteristics of biocarbon particles

3.1.1 Composition and pH

Results from proximate analysis, pH measurements, and pyrolysis yield of the BC samples derived from AD and OS at different pyrolytic temperatures are shown in Table 1.

The yield in BC decreased with the increase of the pyrolysis temperature from 300°C to 800°C. As the temperature increased from 300 °C to 500 °C, a decrease in the yield was observed from 53% to 27% for AD and from 53% to 33% for OS. However, when the temperature went from 600°C to 800°C, the yield slowly decreased from 24% to 23% for AD and 27%–25% for OS. The main lignocellulosic mass degradation occurred from 300°C to 500°C, resulting in a high amount of volatiles being released. Indeed, prior research (Marrot et al., 2021) on hemp stem pyrolysis reported that the maximum biomass degradation associated with maximum mass loss occurred at temperatures between 335 °C and 406 °C (for thermograms obtained with a heating rate of 2000 °C/h). Regardless of the pyrolysis temperature, OS yielded more BC compared to AD (Table 1), which can be assigned to the higher lignin content in OS of 26.50% (Rodríguez et al., 2008) *versus* 21.11% in AD (Suárez et al., 2021). Lignin-rich biomasses tend to generate more BC given the high thermal resistance and slow degradation of lignin polymers, starting at ambient temperature and continuing up to 900°C (Yang et al., 2007). This explanation aligns with the proximate analysis results (Table 1), revealing OS-derived BC samples' higher fixed carbon content.

When the pyrolysis temperature increased from 300°C to 800°C, the volatiles content decreased from 58.21% ± 1.03% to 10.80% ± 0.52% for AD-BC and from 49.36% ± 1.01% to 9.92% ± 0.60% for OS-BC samples. An opposite trend was obtained for ash and fixed carbon contents, which increased proportionally. As pyrolysis temperature increased, more volatile matter generated by the decomposition of biomass components was released in the form of condensable and non-condensable gases, promoting carbon-rich residue and concentration of ash minerals. Similar findings were reported by Marrot et al. (2021), who reported a decrease in volatiles and an increase in ash and fixed carbon percentages when the temperature increased from 400 °C to 1000 °C when preparing hemp stem-based BC. Egbosiuba (2022) also reported that the fixed carbon content of cassava peel-derived BC increased gradually with the increase in pyrolysis temperature from 300 °C to 600 °C regardless of the applied heating rate (10, 20, or 30 °C/min).

Regarding BC pH, the pH measurements increased progressively. They changed from an acidic character for samples prepared at 300 °C (4.27 ± 0.05 and 5.23 ± 0.01 for AD and OS, respectively) to an alkaline character for samples prepared at 800 °C (8.63 ± 0.05 and 8.71 ± 0.07 for AD and OS, respectively). Above 500°C, pH values fluctuated slightly for both biomasses, while it fluctuated clearly between samples prepared under 500°C. The lower pH observed for BC pyrolyzed at temperatures under 500 °C is likely related to higher amounts of acidic carboxyl groups in hemicellulose and celluloses, which were not degraded at these lower temperatures. Another reason for the increase in pH values could be the accumulation of ash components that have an alkaline nature. A prior study (Van Krevelen, 1993) assigned the decrease in BC's acidity at high temperatures to convert acidic aliphatic groups in the organic material into alkaline aromatic groups.

3.1.2 Surface functional groups of raw biomasses and their derived biocarbon particles

Figure 2 represents the FTIR spectra for raw biomasses, and the resultant BC produced at different pyrolysis temperatures. The detected peaks corresponding to surface functional groups were highlighted, and it can be observed that spectra from both biomasses revealed the presence of peaks in similar positions. Moreover, functional groups were more diverse in BC samples prepared at lower temperatures (<500 °C) regardless of the biomass type.

With the increase of pyrolysis temperature, a decrease in the polar O-H stretching (3,200–3,500 cm^{-1}) correspondent to hydroxyl groups was observed, which was attributed to the dehydration reactions due to water evaporation besides the degradation of alcohols and carboxylic groups (Keiluweit et al., 2010). The

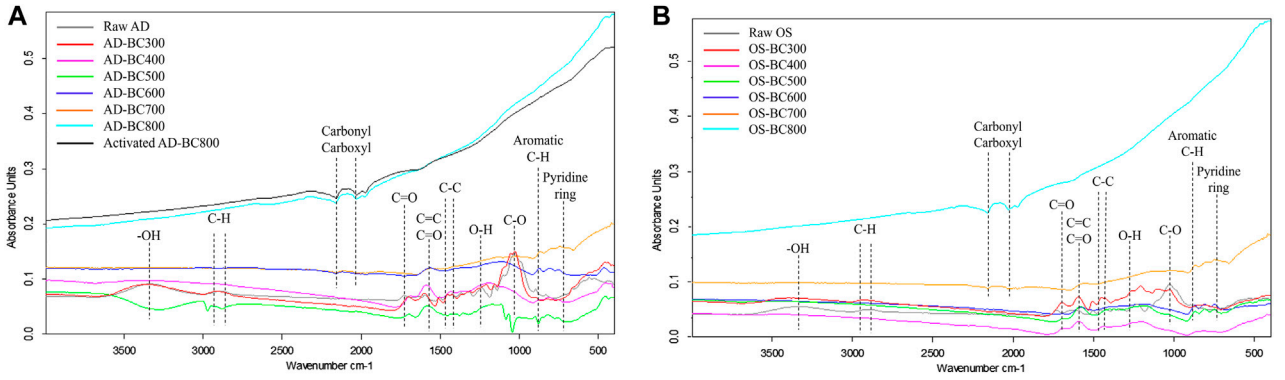

FIGURE 2
FTIR spectra of the raw biomasses and their derived biocarbon particles: **(A)** *Arundo donax* and **(B)** olive stone.

degradation of carboxylic groups correlated well with the reduction in BC's acidity (increase in pH) at higher temperatures (Table 1).

The peak at 2,925 cm^{-1} assigned to asymmetrical and symmetric-CH vibrations was detected in raw biomasses, and BC prepared at 300 °C. Then this peak faded to vanish in the rest of the BC samples. The -CH vibrations disappeared with the increase in pyrolysis temperature due to the decomposition of cellulose and hemicellulose, usually occurring at a temperature range of 220°C–400°C (Yang et al., 2007).

The band at 1750 cm^{-1} assigned to C=O functional groups from esters and anhydrides was present in the raw and carbonized biomasses at 300°C. The same band was also observed with lower intensity in BC samples prepared at 400°C. Then, this band disappeared as the pyrolysis temperature further increased.

The band at 1600 cm^{-1} associated with aromatic C=C and C=O stretching of alkenes and aldehydes, respectively (Uchimiya et al., 2011), was slightly present in the raw biomass spectra. This band then increased gradually with the increase in pyrolysis temperature up to 600°C, which positively correlates with the results from proximate analysis (Table 1) that revealed an increase in the fixed carbon content. However, the same band was not present in spectra corresponding to samples prepared at 700 °C and 800°C, likely because of high enough energy (high temperature), which enabled the breakage of these groups. Stretching around 890 cm^{-1} correspondent to C-H aromatic rings (Sahoo et al., 2020) was detected in all BC samples except for those prepared at 700°C and 800°C. During pyrolysis from 300°C to 600°C, the aromaticity of BC increased as the thermolabile aliphatic groups in raw biomass transformed into more stable aromatic structures. However, a further increase in the temperature (i.e., above 600°C) likely destroyed these structures. Similarly, Sahoo et al. (2020) observed an increase in C-H aromatic rings in BC from 350°C to 550°C, which was attributed to the simultaneous decrease in OH and CH alkyl groups. At 650 °C, they recorded a decrease in the peak of C-H aromatic rings, which was explained by the breakage of aromatics to generate more volatile compounds.

The wide band between 2050 cm^{-1} and 2,200 cm^{-1} was ascribed to carboxyl and carbonyl groups (Angin, 2013). This band was absent in BC prepared at 300°C–600°C, appeared slightly at 700°C and was visible at 800°C. The occurrence of this band is associated with the formation of different carbon structures (aromatic, carboxylic, and carbonyl carbon) at high pyrolytic temperatures. A prior study (Marrot et al., 2023) reported a similar trend in hemp BC samples pyrolyzed at 400°C–1000°C.

TABLE 2 Hydrophobicity test results.

Pyrolysis temperature, °C	Water contact angle, °	
	AD- BC	OS-BC
300	105 ± 13	97 ± 7
400	107 ± 5	125 ± 1
500	116 ± 4	126 ± 2
600	122 ± 1	130 ± 2
700	127 ± 1	131 ± 2
800	128 ± 1	141 ± 6
800 and CO_2 activation	128 ± 2	—

The stretching observed at 1400 cm^{-1} correspondent to C-C rings in lignin (Nandiyanto et al., 2016) was detected in raw biomasses, and BC prepared at 300°C and 400°C. As the pyrolysis temperature increased above 400°C, lignin polymers gradually degraded, leading to less pronounced peaks of C-C rings.

The FTIR spectra also revealed that the band at 1050 cm^{-1}, associated with C-O symmetric stretching for aliphatic functional groups, was soundly prominent in raw AD and OS. However, this band was detected with lower intensity in the BC sample prepared at 300°C and disappeared in BC prepared at temperatures above 300°C. This result was attributed to the depolymerization and degradation of celluloses and hemicelluloses during pyrolysis at high temperatures.

The activated AD-BC800 sample had an FTIR spectrum similar to the non-activated sample. Thus, the physical activation treatment did not influence the functional group composition at the surface of the BC sample in this case.

FTIR analysis results suggested that the pyrolytic temperature influenced the functional group composition of BC samples regardless of the raw biomass type. The change in functional

TABLE 3 Particle size representative diameters of the biocarbon samples.

Sample ID	Cumulative particle size distribution			
	D_{10}, μm	D_{50}, μm	D_{90}, μm	Mean, μm
AD-BC400	9 ± 4	20 ± 3	358 ± 11	88 ± 5
AD-BC500	5 ± 2	17 ± 2	270 ± 9	62 ± 4
AD-BC600	6 ± 1	15 ± 1	67 ± 5	31 ± 2
AD-BC700	5 ± 1	12 ± 2	37 ± 2	20 ± 2
AD-BC800	4 ± 2	11 ± 1	20 ± 3	16 ± 2
Activated AD-BC800	3 ± 1	11 ± 2	25 ± 1	13 ± 1
OS-BC300	6 ± 3	21 ± 3	101 ± 6	31 ± 3
OS-BC400	3 ± 1	12 ± 3	87 ± 4	31 ± 2
OS-BC500	2 ± 2	10 ± 2	64 ± 5	28 ± 3
OS-BC600	2 ± 1	7 ± 1	16 ± 3	9 ± 2
OS-BC700	2 ± 2	8 ± 2	17 ± 1	9 ± 2
OS-BC800	1 ± 1	6 ± 1	15 ± 2	7 ± 2

groups resulted from the biomass degradation reactions during the pyrolysis process.

3.1.3 Hydrophobicity of the biocarbon particles

The mean values of the water contact angle (WCA) of the BC powders are listed in Table 2.

Regardless of the original biomass type and pyrolysis temperature, all BC specimens exhibited a hydrophobic character (i.e., WCA higher than 90° (Law, 2014), and the higher the WCA, the stronger the water repellency). The WCA constantly increased with an increase in the pyrolysis temperature from 300 °C to 800 °C for both BC derived from AD and OS. Results were attributed to the changes in the chemical composition of the material prepared at different temperatures. With the increase in pyrolysis temperature, the extent of thermal degradation increased, and less hydrophilic natural polymers, namely cellulose and hemicellulose, were present in the final BC materials. Therefore, the BC prepared at higher temperatures exhibited higher hydrophobicity.

For BC prepared at 300°C, the WCA was higher (105° ± 13°) in the case of the AD-derived sample as compared to the OS-derived sample (97 ± 7). However, for BC prepared at temperatures from 400 °C to 800°C, the AD-derived samples had a lower WCA than the OS-derived samples (Table 2). These findings are likely related to the original chemical composition (i.e., the ratio of hemicellulose, cellulose, and lignin) of the two different feedstocks, which could affect the nature and intensity of the functional groups in the derived BC samples. The lower hydrophobicity of AD-derived BC was likely attributed to AD having a higher hemicellulose and cellulose content than OS. Suárez et al. (2021) reported a hemicellulose and cellulose content in AD of 34.02% and 37.95%, respectively, while Ferreiro-Cabello et al. (2022) reported a hemicellulose and cellulose content in OS of 34.8% and 26.9%, respectively.

The WCA of AD-BC800 remained steady after physical activation. Thus, the activation treatment did not affect the hydrophobicity of the material. The BC's hydrophobicity depended on the pyrolytic temperature and the original feedstock type. These results indicate that BC's hydrophobic properties can be tailored by selecting specific initial feedstock and processing temperatures.

3.1.4 Particles size of the biocarbon particles

Size distributions of the BC samples derived from AD and OS are represented in Table 3. Percentile values D_{10}, D_{50}, and D_{90} are statistical representatives for the cumulative particle size distribution where they indicate the size below which 10%, 50%, and 90% of all particles are obtained, respectively.

The ball-milling treatment of BC effectively reduced the particles' size as the particle size distributions of all samples fit into the micro-size range (Table 3). The AD-derived BC samples had a slightly higher particle size distribution than OS-derived BC. The mean size ranged between 13 μm and 88 μm and between 7 μm and 31 μm for BC derived from AD and OS, respectively. The difference in particle size between BC and different biomasses might be related to the shape of the raw biomass particles, round for OS and fibrous for AD (sheet-like particles). Indeed, the particle's shape can influence the particle size results when using laser diffraction, given that rod-shaped particles tend to appear larger (Naito et al., 1998).

Interestingly, the particle size decreased with the increase in pyrolysis temperature regardless of the biomass type. Exposure to higher temperatures provoked further degradation of the biomass components (i.e., hemicellulose, cellulose, and lignin), which likely decreased the resistance of the generated BC particles against the mechanical force during the ball-milling process. Thus, higher pyrolysis temperatures favored the grindability of BC.

3.1.5 Porosity of the biocarbon particles

The adsorption-desorption isotherms of N_2 and CO_2 in AD and OS-derived BC are represented in Figures 3, 4, respectively. Detailed results from the physisorption analysis are summarised in Table 4. The isotherms showed that BC samples prepared at variable temperatures possessed different N_2 and CO_2 uptake at a given relative pressure.

For N_2 adsorption-desorption isotherms, an open structure (i.e., separated adsorption-desorption branches) was observed, which is usually characteristic of carbon-based materials with narrow pores. For both biomasses, the N_2 isotherm of BC samples prepared at a temperature above 500 °C and the activated AD sample conformed with the type I isotherm characterized by strong N_2 uptake at low pressure according to the classification made by the International Union of Pure and Applied Chemistry (IUPAC) (Thommes et al., 2015). The sharp increase in the N_2 uptake close to the saturation vapor pressure (i.e., 1) is attributed to large meso- and macro-pores filling. The Activation of AD-BC800 further enhanced the N_2 uptake (Figure 3A), suggesting that physical activation further expanded the porosity of the BC sample.

The CO_2 adsorption-desorption isotherms had closed adsorption-desorption branches, and no hysteresis was observed, indicating that CO_2 molecules could be completely and easily desorbed. The capacity of CO_2 uptake increased gradually with

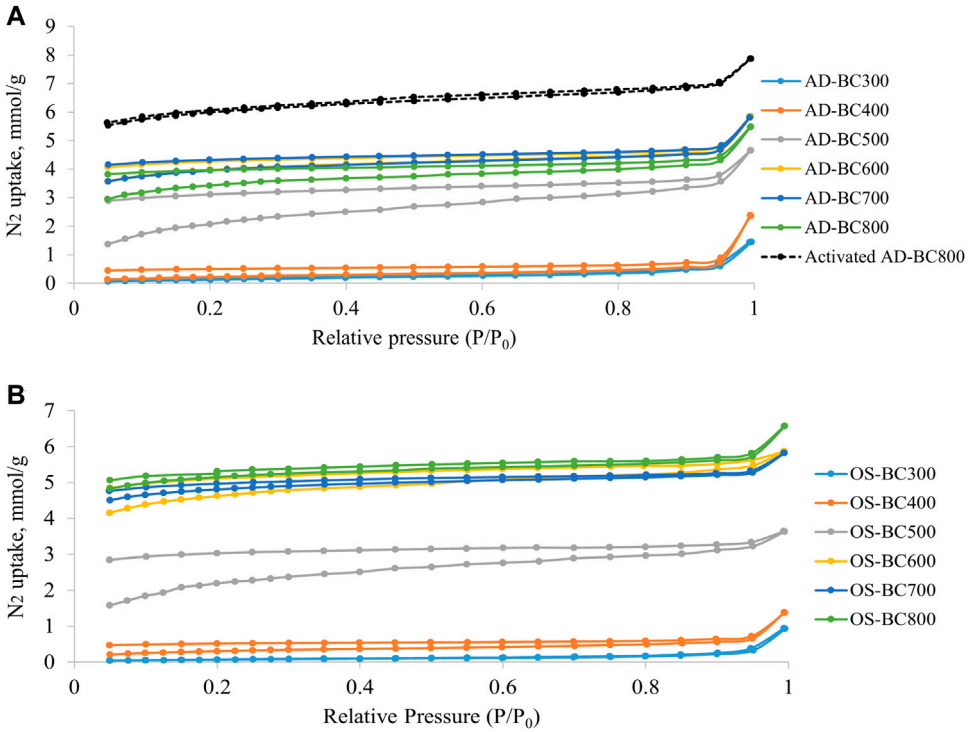

FIGURE 3
N_2 adsorption–desorption isotherms obtained at 77 K for **(A)** *Arundo donax* and **(B)** olive stone-derived biocarbon prepared at different pyrolysis temperatures.

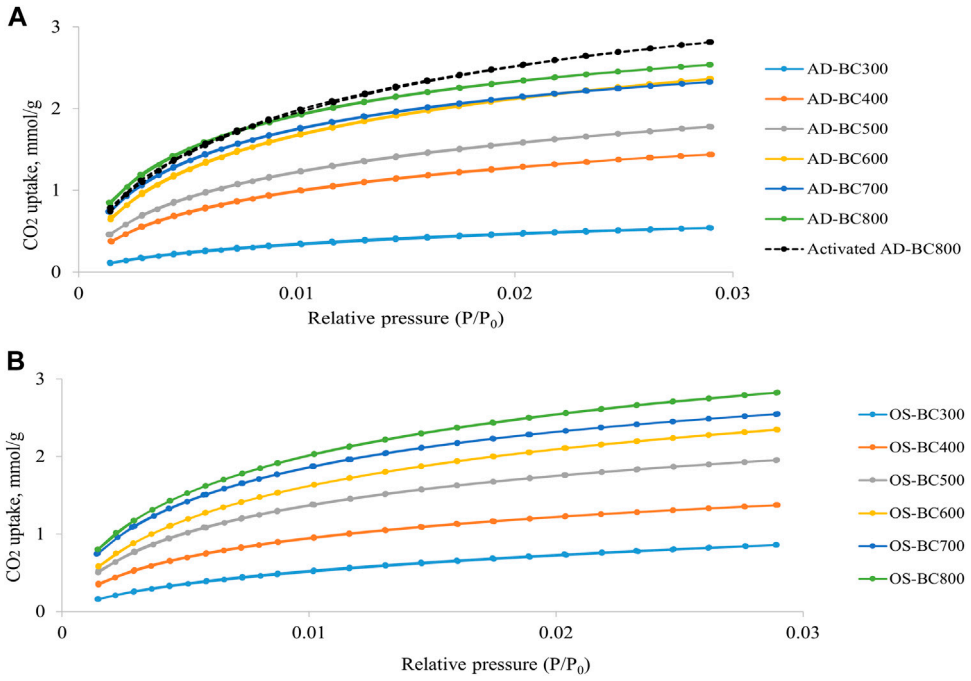

FIGURE 4
CO_2 adsorption–desorption isotherms obtained at 273 K for **(A)** *Arundo donax* and **(B)** olive stone-derived biocarbon prepared at different pyrolysis temperatures.

TABLE 4 Summary of physisorption analysis results.

Sample ID	Nitrogen		CO_2	
	Specific surface area, m^2/g	Total pore volume, cm^3/g	Microporous surface area, m^2/g	Micropores volume, cm^3/g
AD-BC300	13.82	0.050	125.27	0.038
AD-BC400	19.72	0.082	320.51	0.085
AD-BC500	177.15	0.162	414.50	0.116
AD-BC600	334.87	0.202	544.00	0.147
AD-BC700	332.80	0.203	540.20	0.140
AD-BC800	291.40	0.190	587.18	0.151
Activated AD-BC800	415.61	0.273	664.16	0.187
OS-BC300	6.01	0.032	208.96	0.067
OS-BC400	24.28	0.048	320.68	0.090
OS-BC500	167.44	0.126	450.57	0.123
OS-BC600	325.35	0.263	543.15	0.151
OS-BC700	330.94	0.202	589.38	0.156
OS-BC800	354.54	0.228	647.89	0.172

the increase of the relative pressure. The highest CO_2 uptakes were achieved by AD and OS BC prepared at 800°C, indicating that higher pyrolytic temperature favored the development of microporous structure in the BC samples. The Activated AD-BC800 exhibited higher CO_2 uptake as compared to the non-activated sample. Thus, physical activation treatment boosted the formation of micropores in the BC.

The specific and microporous surface areas and pore volumes of BC samples increased with the increase of pyrolysis temperature from 300°C to 800°C regardless of the original biomass type (Table 4). As pyrolysis temperature increased, the released volatiles generated cavities and pores in the BC structure. At higher pyrolysis temperatures, the extent of thermal degradation increased, and more volatiles were released, which was reflected by larger values of surface area and pores volume. A similar trend was observed by Mao et al. (2019), who found that the specific and micro porosities of the BC prepared from several types of feedstocks (pine wood, rice straw, rice bran, wood sawdust, and orange peels) were enhanced by increasing the pyrolysis temperature (250, 500, and 700 °C).

Except for the pyrolytic temperature of 300°C, AD-derived BC's SSA and microporous surface area were lower than those of OS-derived BC samples (Table 4). These results are likely related to the raw biomasses' original chemical composition, which might have influenced the thermal decomposition pathways during pyrolysis. Similarly, Lu and Zong. (2018) reported that the SSA of BC prepared from coniferous forest wastes was higher than that of BC prepared from herbaceous plant and broad-leaf forest wastes. They justified that the differences in porosity characteristics of BC from different feedstocks were related to the differences in cell morphology and structure in the raw materials. They also concluded that the precursor biomass types influenced BC's internal structure.

The increment in SSA was continuous in the function of the pyrolysis temperature for OS-derived BC samples. However, in the case of AD-derived BC, the SSA increased gradually up to 600 °C, then decreased slightly at 700°C and 800°C. These results can be seen in the N_2 adsorption-desorption isotherms (Figure 3A), where AD-BC600 had the highest N_2 uptake amongst other AD-BC. However, the microporous surface area of AD-BC800 was higher than AD-BC600, which was reflected in the CO_2 adsorption-desorption isotherms (Figure 4A). These findings suggest the effect of pyrolysis temperature on the BC's porosity could vary with the type of original biomass. Interestingly, regardless of the biomass type, BC's SSA increased sharply when the pyrolysis temperature went from 400°C to 500°C. This increase was attributed to the condensation of aromatics in lignin (happening around 500 C), which led to the generation and quick release of high amounts of gases and forced the opening of smaller pores). The total pore size distribution plots (Supplementary Figure S1) showed the dominance of mesopores with sizes ranging from 3 to 5 nm in all samples. However, these narrow mesopores occurred less in samples prepared under 500 C (Supplementary Figures S1A, B) than in samples pyrolyzed at 500 °C or above (Supplementary Figures S1C–F). Likewise, the micropore distribution (obtained from CO2 physisorption analysis) showed micropore sizes between 0.35 and 0.60 nm (Supplementary Figure S2). The structures of BC prepared at 500°C or above contained a larger volume of ultra-micropores. Therefore, the high pyrolytic temperatures favored biomass devolatilization and led to the resulting microporous structures in BC.

The activated AD-BC800 sample had larger surface areas and pore volume than the non-activated sample (Table 4). The SSA and

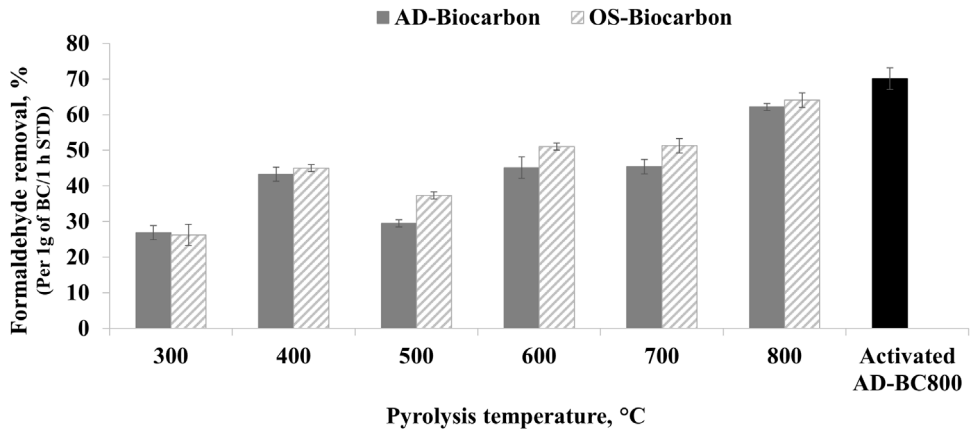

FIGURE 5
Formaldehyde removal capacities as a function of pyrolytic temperature.

TABLE 5 Correlation and multiple regression test results.

Independent variables	Correlation		Multiple regression
	Correlation coefficients	*p* Values	*p* Values
Fixed carbon, %	0.777	0.002*	0.421
Volatiles, %	−0.759	0.004*	0.250
Specific surface area, m^2/g	0.682	0.014*	0.054
Microporous surface area, m^2/g	0.815	0.001*	0.022*

* Statistically significant.

microporous surface area increased by 43% and 14% after activation. Therefore, the physical activation treatment further developed the BC's porosity.

3.2 Formaldehyde removal capacity

The formaldehyde removal percentages calculated after 1 h of experimental time in the presence of 1 g of BC are presented in Figure 5. The BC samples prepared at different temperatures exhibited different formaldehyde removal potentials. Indeed, the variation of pyrolytic temperature influenced the physicochemical and structural properties of the resulting BC samples and consequently changed the sorptive capacities. All BC samples achieved a certain formaldehyde removal activity. The percentage of formaldehyde removal ranged between 27% ± 2% and 62% ± 1% and between 26 ± 3%and 64% ± 2% for AD and OS-derived BC, respectively. Moreover, the amount of captured formaldehyde increased by 131% and 144% when the pyrolysis temperature increased from 300°C to 800 C for AD and OS-derived BC, respectively.

The correlation and multiple regression analysis results are represented in Table 5. The variables' effect was considered statistically significant when the corresponding *p*-value was below 0.05.

The correlation coefficients showed a positive correlation between formaldehyde removal capacity and fixed carbon, SSA, and microporous surface area. At the same time, a negative correlation was found between the formaldehyde removal capacity and the volatile content (Table 5). The *p* values from the correlation test showed a statistically significant relation between formaldehyde removal capacity and the four tested variables ($p < 0.05$). Results from the multiple regression analysis indicated that only microporous surface area was statistically significant when developing an equation to predict formaldehyde absorption based on BC properties. This result suggested that the occurrence of micropores in the BC's structure was the key parameter for efficient formaldehyde removal.

The unpaired *t*-test showed no statistically significant difference between the formaldehyde removal ability of BC prepared from AD and OS ($p = 0.311$). Therefore, the original feedstock did not influence the removal capacity. The slightly higher formaldehyde removal potential of OS-derived BC samples (Figure 5) was likely related to their larger microporous surface areas (Table 4) as compared to the AD-derived BC samples. Despite its lower SSA, AD-BC800 showed higher adsorption compared to AD-BC600. This result was attributed to the higher microporous surface area of AD-BC800 as compared to AD-BC600 (Table 4).

The presence of ultra-micropores concentrated in size range from 0.35 to 0.60 nm (Supplementary Figure S2) further confirms

the beneficial effect of smaller micropores occurrence on the BC's potential in removing formaldehyde. One possible explanation is the small size of the formaldehyde molecule, which has a diameter of 0.25 nm. The small size of the adsorbate was likely favorable for filling narrow micropores. Indeed, prior research reported that the adsorbate and pore size directly influence the adsorption capacity (Yang et al., 2018). Prior research (Yang et al., 2018) reported that the adsorption was not favored i) if the pore size of the porous material (i.e., adsorbent) is smaller than the target molecule's (i.e., adsorbate) size and ii) if the pore size is much larger than the molecule's size. Additionally, Liu et al. (2019) used molecular simulation models to investigate the kinetics of formaldehyde adsorption on carbonaceous materials and reported that ultra-micropores with 0.7 nm in width enabled optimal formaldehyde capture.

The increase in formaldehyde removal capacity by the different BC was not constant (Figure 5). Indeed, the formaldehyde removal increased when the temperature increased from 300°C to 400°C, then dropped at 500°C and increased again gradually from 600°C to 800°C. These results were attributed to two formaldehyde removal mechanisms and the predominance of one or the other. Indeed, Chen et al. (2008) highlighted that the pollutant removal by BC is ensured by either the partitioning effect and/or the adsorption effect. They also stated that the noncarbonized and carbonized fractions and surface and bulk properties of the BC material determine the contribution of either mechanism. In our study, the BC samples prepared at mild pyrolytic temperatures (under 500°C) had a higher noncarbonized organic matter content, reflected by the high volatiles and low fixed carbon content (Table 1). Noncarbonized organic matter likely favored the interaction with formaldehyde molecules and enabled the capture through a partitioning mechanism. During partitioning, the formaldehyde molecules diffused into the noncarbonized organic matter characterized by its amorphous aliphatic feature. This mechanism usually involves polar and non-polar interactions. Therefore, the presence of surface functional groups in BC samples prepared at 300°C and 400°C, observed in the FTIR spectra (Figure 2), likely helped to enable further the interaction forces between the formaldehyde molecules and the BC particles. Prior research by Meng et al. (2019) reported that functional groups on the surface of carbonaceous materials favored the interaction with gaseous VOCs.

For BC prepared at higher pyrolytic temperatures (500°C and above), the formaldehyde capture was assisted by the developed porous structure and large surface area. In this case, pores served as adsorption sites for the formaldehyde molecules and enabled the capture through a physical adsorption mechanism. Indeed, the adsorption phenomenon is mainly governed by Van der Waals forces, pores filling, and electrostatic adsorbent-adsorbate interaction (Vikrant et al., 2020). Therefore, the well-developed porosity, specifically microporosity, of the BC prepared at 500 °C and above (Table 4) was a key parameter in formaldehyde removal by BC, as verified by the multiple regression analysis (Table 5). Zhang et al. (2017) studied the performance of BC prepared from different biomasses at variable carbonization temperatures for air purification. They reported that the VOCs removal was governed by a partitioning mechanism in the case of BC prepared at 450°C or below and by a physical adsorption mechanism in the case of BC prepared at 600°C.

AD-BC800s formaldehyde removal capacity increased by 13% after physical activation (Figure 5). This increase was attributed to the improved microporous surface area and micropore volume (Table 4). The activation treatment enabled further development of the porous structure of BC by creating new internal pores and channels. The paired *t*-test results indicated that the effect of physical activation on the formaldehyde removal capacity was statistically significant (p = 0.001). A deeper study on the air purification performance of BC with and without activation is required to assess the environmental benefits of choosing non-activated or activated BC because of their pollutant removal capacity.

3.3 Formaldehyde removal in function of time and re-usability of the biocarbon

Figure 6 represents the evolution of formaldehyde concentrations inside the test chamber during 1 h of experimental time.

The decrease in formaldehyde concentrations was fast during the first 20 min of the experiment for AD and OS-derived BC. After approximately 20 min, the adsorption slowed, and the formaldehyde concentrations stabilized (Figure 5). Indeed, at the experiment's beginning, the BC structure pores were free and served as sites for the formaldehyde molecules. When most pores were occupied and the equilibrium time was reached, the adsorption process gradually decreased and stabilized, suggesting that the BC samples became saturated. The equilibrium time was slightly more delayed for samples prepared at temperatures above 500°C given that the formaldehyde capture mainly depended on pores filling. Similarly, Aziz et al. (2017) found that the adsorption capacity of zeolite-based adsorbents towards aromatic VOCs gradually decreased after reaching the respective equilibrium time (approximately 25 min).

Figure 7 represents the formaldehyde removal percentages of AD-BC800 after five cycles of thermal regeneration, which consists of using heat transfer forces to release the adsorbed formaldehyde molecules from the BC pores.

It was observed that the AD-BC800 sample maintained a comparable formaldehyde removal capacity up to the fourth cycle, indicating that it was possible to desorb formaldehyde molecules. After heating, BC's pores were freed and available for a new adsorption cycle. However, the removal capacity decreased by 13% after the fifth cycle, indicating that the re-usability of BC adsorbent tended to decline after several regeneration cycles. This result was attributed to the changes in structure and surface properties of the BC that likely occurred after repeated heating cycles. Prior research (Ahn et al., 2021) found that the formaldehyde adsorption capacity onto metal-BC decreased by about 50% and 65% after the first and second cycles of thermal regeneration at 80°C for 1 day, respectively. They explained that changes might have occurred in the pores structure and surface chemistry of the metal-BC, contributing to a partial loss in the adsorption performances. Moreover, Yang et al. (2018) investigated the adsorption-desorption cycles of toluene onto activated carbon samples with variable pore sizes. They reported that the pollutants' molecules accumulated in the activated carbon's narrow micropores, making it challenging to desorb at low regeneration temperatures. Hence, other methods should be pursued to free the BC pores and allow a long-lasting

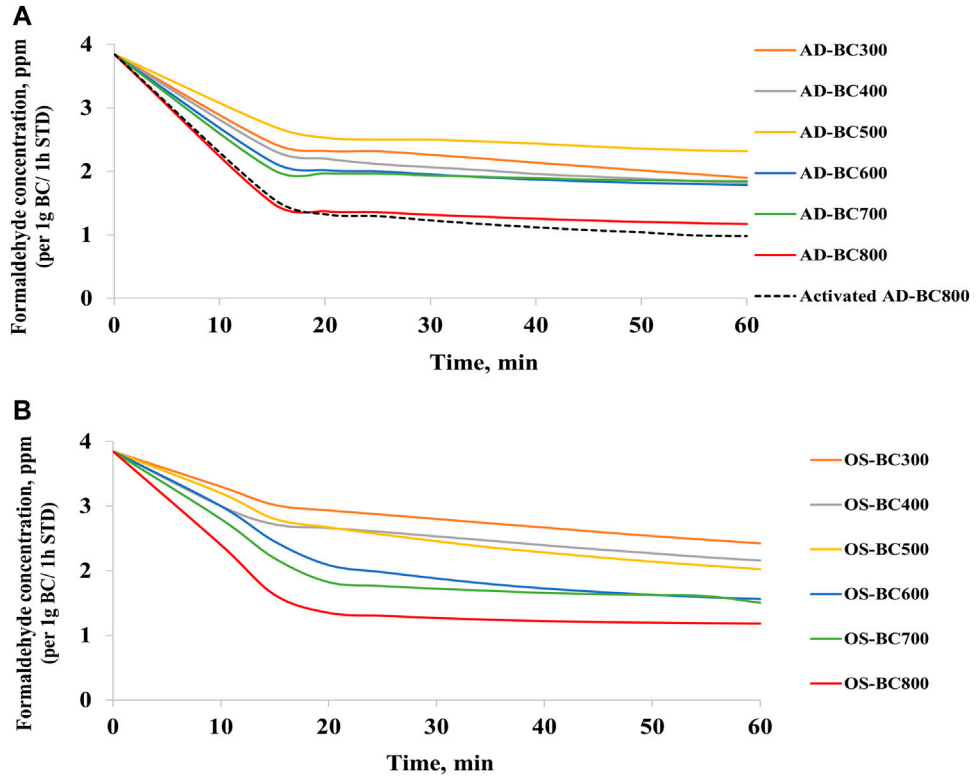

FIGURE 6
Variation of formaldehyde concentrations in the test chamber in the presence of **(A)** *Arundo donax* and **(B)** olive stone biocarbon.

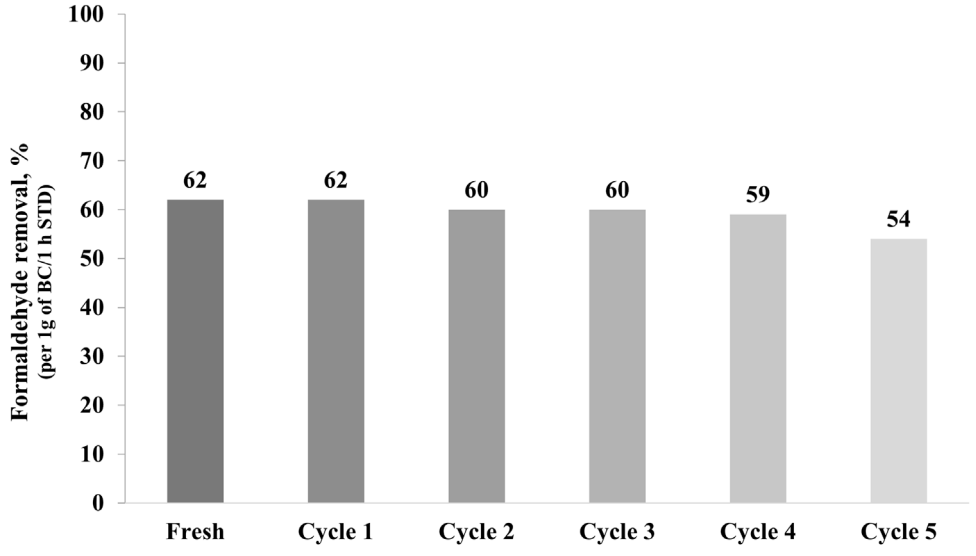

FIGURE 7
Formaldehyde removal capacity of AD-BC800 after five thermal regeneration cycles.

removal capacity. In this goal, follow-up research is conducted to dope BC particles with active photocatalysts and investigate the integrated adsorption-photocatalytic degradation potential.

The AD-BC800 sample was further tested using FTIR spectroscopy after the fifth adsorption and regeneration cycle to investigate eventual changes in the functional groups' composition. The spectra collected for

the fresh and re-used samples (Supplementary Figure S3) were similar. Hence, the second derivatives were also collected to enhance peak separation and reveal differences between the spectra. No obvious changes in the functional groups' composition were observed after the re-use and regeneration cycles except that the same peaks were slightly intensified. This result suggests that thermal regeneration effectively desorbs the formaldehyde from the spent material, especially since formaldehyde is characterized by high volatility. Prior research (Ahn et al., 2021) compared FTIR spectra of metallic biochar before and after interaction with formaldehyde. They observed new peaks at 2,900, 2,520, and 2,220 cm^{-1}, attributed to intermolecular hydrogen bonds of formate, carboxylic acid OH stretch, and alkyne stretching, respectively. However, they utilized metallic biochar, which facilitated the conversion of formaldehyde after adsorption and led to the appearance of intermediate molecules. Moreover, they collected the FTIR spectra directly after adsorption without performing a thermal regeneration step, which was not the case in the present study. Similarly (Chen et al., 2013), utilized Ag-containing catalysts for formaldehyde conversion, and they could identify several functional groups related to the occurrence of formaldehyde intermediates, such as formate species (HCOO) after interaction of the catalytic material with the formaldehyde gas. The investigation of variation in the adsorbent properties after several re-use cycles could be interesting to identify the cause of the decrease in formaldehyde removal efficiency after re-using, which will be considered in further research.

4 Conclusion

Biocarbon (BC) samples were prepared from *A. donax* (AD) and Olive stone (OS) at variable pyrolytic temperatures and used for capturing formaldehyde in batch experiments. The increase in pyrolysis temperature from 300°C to 800 °C increased the fixed carbon content of AD and OS-derived BC by 137% and 79%, respectively. The hydrophobicity and porosity of the BC increased with temperature. The FTIR showed that the surface functional groups occurred more in BC prepared at mild temperatures under 500 °C. The formaldehyde removal efficiencies ranged between 26% and 64%. The formaldehyde removal by BC prepared at temperatures under 500 °C was governed by a partitioning mechanism, favored by the presence of noncarbonized fraction that enabled the diffusion of formaldehyde molecules. Whereas for BC prepared at 500 °C or above, the formaldehyde removal was controlled by a physical adsorption mechanism assisted by pores filling. The occurrence of micropores in BC was a key parameter for optimal formaldehyde removal. The physical activation of AD-BC800 significantly increased the formaldehyde adsorption, which was attributed to the activated sample's enhanced microporosity. Thermally regenerated AD-BC800 exhibited comparable potential in removing formaldehyde for up to four re-use cycles. However, the formaldehyde removal percentage decreased by 13% in the fifth cycle, indicating that BC could partially lose its adsorptive function over long-term use. The saturation can limit BC's adsorptive potential after pores are filled with the adsorbate molecules. Therefore, for efficient use of BC in air remediation, it is necessary to find solutions to regenerate BC while preserving its performance effectively. Future research is warranted to develop BC particles that can degrade captured formaldehyde and investigate the adsorption degradation potential.

Data availability statement

The original contributions presented in the study are included in the article/Supplementary Material, further inquiries can be directed to the corresponding author.

Author contributions

MZ: Conceptualization, Investigation, Experimental, Formal analysis, Writing Original Draft. LM: Supervision, Review, Validation. DD: Supervision, Review, Editing. All authors contributed to the article and approved the submitted version.

Funding

This work was supported by the European Union's Horizon 2020 research and innovation program under H2020-WIDESPREAD-2018-2020-6 (grant agreement No 952395), the ForestValue Research Program and the Republic of Slovenia's Ministry of Education, Science and Sport (BarkBuild: grant agreement No C3330-21-252003), project BarkBuild is supported under the umbrella of ERA-NET cofund ForestValue 773324, and H2020 WIDESPREAD-2-Teaming (grant number 739574) and investment from the Republic of Slovenia and the European Regional Development Fund.

Conflict of interest

The authors declare that the research was conducted in the absence of any commercial or financial relationships that could be construed as a potential conflict of interest.

Publisher's note

Supplementary material

The Supplementary Material for this article can be found online at: https://www.frontiersin.org/articles/10.3389/fenvs.2023.1252926/full#supplementary-material

References

Abdul Manap, N. R., Shamsudin, R., Maghpor, M. N., Abdul Hamid, M. A., and Jalar, A. (2018). Adsorption isotherm and kinetic study of gas-solid system of formaldehyde on oil palm mesocarp bio-char: pyrolysis effect. *J. Environ. Chem. Eng.* 6, 970–983. doi:10.1016/j.jece.2017.12.067

Ahn, Y., Cho, D. W., Ahmad, W., Jo, J., Jurng, J., Kurade, M. B., et al. (2021). Efficient removal of formaldehyde using metal-biochar derived from acid mine drainage sludge and spent coffee waste. *J. Environ. Manage.* 298, 113468. doi:10.1016/j.jenvman.2021.113468

Angın, D. (2013). Effect of pyrolysis temperature and heating rate on biochar obtained from pyrolysis of safflower seed press cake. *Bioresour. Technol.* 128, 593–597. doi:10.1016/j.biortech.2012.10.150

ASTM (2015). *Standard Test Methods for Proximate Analysis of Coal and Coke by Macro Thermogravimetric Analysis*. West Conshohocken, PA: ASTM International.

Aziz, A., Kim, M., Kim, S., and Kim, K. S. (2017). Adsorption and kinetic studies of volatile organic compounds (VOCs) on seed assisted template free ZSM-5 zeolite in air. *J. Nanotechnol. Adv. Mater.* 9, 1–9. doi:10.18576/jnam/050101

Bachmann, J., Horton, R., van der Ploeg, R. R., and Woche, S. (2000). Modified sessile drop method for assessing initial soil–water contact angle of sandy soil. *Soil Sci. Soc. Am. J.* 64, 564–567. doi:10.2136/sssaj2000.642564x

Basu, P. (2013). "Chapter 5 - pyrolysis," in *Biomass gasification, pyrolysis and torrefaction*. Editor P. Basu (Boston: Academic Press), 147–176. doi:10.1016/B978-0-12-396488-5.00005-8

Boonamnuayvitaya, V., Sae-ung, S., and Tanthapanichakoon, W. (2005). Preparation of activated carbons from coffee residue for the adsorption of formaldehyde. *Sep. Purif. Technol.* 42, 159–168. doi:10.1016/j.seppur.2004.07.007

Carter, E. M., Katz, L. E., Speitel, G. E., and Ramirez, D. (2011). Gas-phase formaldehyde adsorption isotherm studies on activated carbon: correlations of adsorption capacity to surface functional group density. *Environ. Sci. Technol.* 45, 6498–6503. doi:10.1021/es104286d

Chen, B., Zhou, D., and Zhu, L. (2008). Transitional adsorption and partition of nonpolar and polar aromatic contaminants by biochars of pine needles with different pyrolytic temperatures. *Environ. Sci. Technol.* 42, 5137–5143. doi:10.1021/es8002684

Chen, D., Qu, Z., Sun, Y., Gao, K., and Wang, Y. (2013). Identification of reaction intermediates and mechanism responsible for highly active HCHO oxidation on Ag/MCM-41 catalysts. *Appl. Catal. B Environ.* 142–143, 838–848. doi:10.1016/j.apcatb.2013.06.025

Do, S. B., Lee, S. E., and Kim, T. O. (2022). Oxidative decomposition with PEG-MnO2 catalyst for removal of formaldehyde: chemical aspects on HCHO oxidation mechanism. *Appl. Surf. Sci.* 598, 153773. doi:10.1016/j.apsusc.2022.153773

Egbosiuba, T. C., Abdulkareem, A. S., Kovo, A. S., Afolabi, E. A., Tijani, J. O., Auta, M., et al. (2020). Ultrasonic enhanced adsorption of methylene blue onto the optimized surface area of activated carbon: adsorption isotherm, kinetics and thermodynamics. *Chem. Eng. Res. Des.* 153, 315–336. doi:10.1016/j.cherd.2019.10.016

Egbosiuba, T. C. (2022). Biochar and bio-oil fuel properties from nickel nanoparticles assisted pyrolysis of cassava peel. *Heliyon* 8, e10114. doi:10.1016/j.heliyon.2022.e10114

Ferreiro-Cabello, J., Fraile-Garcia, E., Pernia-Espinoza, A., and Martinez-de-Pison, F. J. (2022). Strength performance of different mortars doped using olive stones as lightweight aggregate. *Buildings* 12, 1668. doi:10.3390/buildings12101668

Guo, Z., Huang, J., Xue, Z., and Wang, X. (2016). Electrospun graphene oxide/carbon composite nanofibers with well-developed mesoporous structure and their adsorption performance for benzene and butanone. *Chem. Eng. J.* 306, 99–106. doi:10.1016/j.cej.2016.07.048

IARC (2006). *IARC monographs on the evaluation of carcinogenic risks to humans*. 1st ed. Lyon, France: IARC. Available at: https://publications.iarc.fr/Book-And-Report-Series/Iarc-Monographs-On-The-Identification-Of-Carcinogenic-Hazards-To-Humans/Formaldehyde-2-Butoxyethanol-And-1–Em-Tert-Em–Butoxypropan-2-ol-2006 (Accessed December 17, 2022).

Keiluweit, M., Nico, P. S., Johnson, M. G., and Kleber, M. (2010). Dynamic molecular structure of plant biomass-derived black carbon (biochar). *Environ. Sci. Technol.* 44, 1247–1253. doi:10.1021/es9031419

Law, K. Y. (2014). Definitions for hydrophilicity, hydrophobicity, and superhydrophobicity: getting the basics right. *J. Phys. Chem. Lett.* 5, 686–688. doi:10.1021/jz402762h

Lee, J. Y., Park, S. H., Jeon, J. K., Yoo, K. S., Kim, S. S., and Park, Y. K. (2011). The removal of low concentration formaldehyde over sewage sludge char treated using various methods. *Korean J. Chem. Eng.* 28, 1556–1560. doi:10.1007/s11814-011-0007-7

Leng, L., and Huang, H. (2018). An overview of the effect of pyrolysis process parameters on biochar stability. *Bioresour. Technol.* 270, 627–642. doi:10.1016/j.biortech.2018.09.030

Ling, Y., Wang, Y., Duan, J., Xie, X., Liu, Y., Peng, Y., et al. (2019). Long-term aerosol size distributions and the potential role of volatile organic compounds (VOCs) in new particle formation events in Shanghai. *Atmos. Environ.* 202, 345–356. doi:10.1016/j.atmosenv.2019.01.018

Liu, L., Liu, J., Zeng, Y., Tan, S. J., Do, D. D., and Nicholson, D. (2019). Formaldehyde adsorption in carbon nanopores – new insights from molecular simulation. *Chem. Eng. J.* 370, 866–874. doi:10.1016/j.cej.2019.03.262

Liu, W., Li, Z., Zhang, S., Jian, W., and Ma, D. (2021). Adsorption performance of multi-walled carbon nanotube-SiO2 adsorbent for toluene. *J. Fuel Chem. Technol.* 49, 861–872. doi:10.1016/S1872-5813(21)60090-7

Lu, S., and Zong, Y. (2018). Pore structure and environmental serves of biochars derived from different feedstocks and pyrolysis conditions. *Environ. Sci. Pollut. Res.* 25, 30401–30409. doi:10.1007/s11356-018-3018-7

Mao, J., Zhang, K., and Chen, B. (2019). Linking hydrophobicity of biochar to the water repellency and water holding capacity of biochar-amended soil. *Environ. Pollut.* 253, 779–789. doi:10.1016/j.envpol.2019.07.051

Marrot, L., Candelier, K., Valette, J., Lanvin, C., Horvat, B., Legan, L., et al. (2021). Valorization of hemp stalk waste through thermochemical conversion for energy and electrical applications. *Waste Biomass Valorization* 13, 2267–2285. doi:10.1007/s12649-021-01640-6

Marrot, L., Zouari, M., Schwarzkopf, M., and DeVallance, D. B. (2023). Sustainable biocarbon/tung oil coatings with hydrophobic and UV-shielding properties for outdoor wood substrates. *Prog. Org. Coat.* 177, 107428. doi:10.1016/j.porgcoat.2023.107428

Meng, F., Song, M., Wei, Y., and Wang, Y. (2019). The contribution of oxygen-containing functional groups to the gas-phase adsorption of volatile organic compounds with different polarities onto lignin-derived activated carbon fibers. *Environ. Sci. Pollut. Res.* 26, 7195–7204. doi:10.1007/s11356-019-04190-6

Meyer, B., and Boehme, C. (1997). Formaldehyde emission from solid wood. *For. Prod. J.* 47, 45–48.

Naito, M., Hayakawa, O., Nakahira, K., Mori, H., and Tsubaki, J. (1998). Effect of particle shape on the particle size distribution measured with commercial equipment. *Powder Technol.* 100, 52–60. doi:10.1016/S0032-5910(98)00052-7

Nandiyanto, A., Fadhlulloh, M., Rahman, T., and Mudzakir, A. (2016). Synthesis of carbon nanoparticles from commercially available liquified petroleum gas. *IOP Conf. Ser. Mater. Sci. Eng.* 128, 012042. doi:10.1088/1757-899X/128/1/012042

Rodríguez, G., Lama, A., Rodríguez, R., Jiménez, A., Guillén, R., and Fernández-Bolaños, J. (2008). Olive stone an attractive source of bioactive and valuable compounds. *Bioresour. Technol.* 99, 5261–5269. doi:10.1016/j.biortech.2007.11.027

Ryu, Y. K., Lee, H. J., Yoo, H. K., and Lee, C. H. (2002). Adsorption equilibria of toluene and gasoline vapors on activated carbon. *J. Chem. Eng. Data* 47, 1222–1225. doi:10.1021/je020044i

Sachdeva, S., Kumar, R., Sahoo, P. K., and Nadda, A. K. (2023). Recent advances in biochar amendments for immobilization of heavy metals in an agricultural ecosystem: a systematic review. *Environ. Pollut.* 319, 120937. doi:10.1016/j.envpol.2022.120937

Sahoo, K., Kumar, A., and Chakraborty, J. (2020). A comparative study on valuable products: bio-oil, biochar, non-condensable gases from pyrolysis of agricultural residues. *J. Mater. Cycles Waste Manag.* 39, 186–204. doi:10.1007/s10163-020-01114-2

Salthammer, T., Mentese, S., and Marutzky, R. (2010). Formaldehyde in the indoor environment. *Chem. Rev.* 110, 2536–2572. doi:10.1021/cr800399g

Stylianou, M., Christou, A., Michael, C., Agapiou, A., Papanastasiou, P., and Fatta-Kassinos, D. (2021). Adsorption and removal of seven antibiotic compounds present in water with the use of biochar derived from the pyrolysis of organic waste feedstocks. *J. Environ. Chem. Eng.* 9, 105868. doi:10.1016/j.jece.2021.105868

Suárez, L., Castellano, J., Romero, F., Marrero, M. D., Benítez, A. N., and Ortega, Z. (2021). Environmental hazards of giant reed (Arundo donax L.) in the macaronesia region and its characterisation as a potential source for the production of natural fibre composites. *Polymers* 13, 2101. doi:10.3390/polym13132101

Thommes, M., Kaneko, K., Neimark, A. V., Olivier, J. P., Rodriguez-Reinoso, F., Rouquerol, J., et al. (2015). Physisorption of gases, with special reference to the evaluation of surface area and pore size distribution (IUPAC Technical Report). *Pure Appl. Chem.* 87, 1051–1069. doi:10.1515/pac-2014-1117

Uchimiya, M., Wartelle, L. H., Klasson, K. T., Fortier, C. A., and Lima, I. M. (2011). Influence of pyrolysis temperature on biochar property and function as a heavy metal sorbent in soil. *J. Agric. Food Chem.* 59, 2501–2510. doi:10.1021/jf104206c

US National Research Council (1980). *Formaldehyde - an assessment of its health effects*. 1st ed. Washington DC: National Academies Press US. Available at: https://www.ncbi.nlm.nih.gov/books/NBK217652/(Accessed December 17, 2022).

Van Krevelen, W. D. (1993). *Coal: typology - physics - chemistry - constitution*. 1st ed. Amsterdam, Netherlands: Elsevier Science Publishers. Available at: https://www.osti.gov/etdeweb/biblio/5331158 (Accessed December 18, 2022).

Vikrant, K., Kim, K. H., Peng, W., Ge, S., and Sik Ok, Y. (2020). Adsorption performance of standard biochar materials against volatile organic compounds in air: a case study using benzene and methyl ethyl ketone. *Chem. Eng. J.* 387, 123943. doi:10.1016/j.cej.2019.123943

WHO (2022). Household air pollution. Available at: https://www.who.int/news-room/fact-sheets/detail/household-air-pollution-and-health (Accessed December 16, 2022).

WHO (1989). Indoor air quality: organic pollutants. *Environ. Technol. Lett.* 10, 855–858. doi:10.1080/09593338909384805

Yang, H., Yan, R., Chen, H., Lee, D. H., and Zheng, C. (2007). Characteristics of hemicellulose, cellulose and lignin pyrolysis. *Fuel* 86, 1781–1788. doi:10.1016/j.fuel.2006.12.013

Yang, S., Zhu, Z., Wei, F., and Yang, X. (2017). Enhancement of formaldehyde removal by activated carbon fiber via *in situ* growth of carbon nanotubes. *Build. Environ.* 126, 27–33. doi:10.1016/j.buildenv.2017.09.025

Yang, X., Yi, H., Tang, X., Zhao, S., Yang, Z., Ma, Y., et al. (2018). Behaviors and kinetics of toluene adsorption-desorption on activated carbons with varying pore structure. *J. Environ. Sci.* 67, 104–114. doi:10.1016/j.jes.2017.06.032

Yu, K. L., Lee, X. J., Ong, H. C., Chen, W. H., Chang, J. S., Lin, C. S., et al. (2021). Adsorptive removal of cationic methylene blue and anionic Congo red dyes using wet-torrefied microalgal biochar: equilibrium, kinetic and mechanism modeling. *Environ. Pollut.* 272, 115986. doi:10.1016/j.envpol.2020.115986

Zhang, X., Gao, B., Zheng, Y., Hu, X., Creamer, A. E., Annable, M. D., et al. (2017). Biochar for volatile organic compound (VOC) removal: sorption performance and governing mechanisms. *Bioresour. Technol.* 245, 606–614. doi:10.1016/j.biortech.2017.09.025

Zouari, M., Marrot, L., and DeVallance, D. B. (2023). Effect of demineralization and ball milling treatments on the properties of Arundo donax and olive stone-derived biochar. *Int. J. Environ. Sci. Technol.* doi:10.1007/s13762-023-04968-9

frontiers | Frontiers in Microbiology

TYPE Review
PUBLISHED 30 October 2023
DOI 10.3389/fmicb.2023.1207664

OPEN ACCESS

EDITED BY
Vaibhav Srivastava,
University of Allahabad, India

REVIEWED BY
Wang Feng,
Jiangsu University, China
Saibal Das,
ICMR-Center for Ageing and Mental Health, India

*CORRESPONDENCE
Irlon M. Ferreira
✉ irlon.ferreira@gmail.com

RECEIVED 17 April 2023
ACCEPTED 02 October 2023
PUBLISHED 30 October 2023

CITATION
Ferreira BL, Ferreira DP, Borges SF, Ferreira AM, Holanda FH, Ucella-Filho JGM, Cruz RAS, Birolli WG, Luque R and Ferreira IM (2023) Diclofenac, ibuprofen, and paracetamol biodegradation: overconsumed non-steroidal anti-inflammatories drugs at COVID-19 pandemic.
Front. Microbiol. 14:1207664.
doi: 10.3389/fmicb.2023.1207664

Diclofenac, ibuprofen, and paracetamol biodegradation: overconsumed non-steroidal anti-inflammatories drugs at COVID-19 pandemic

Beatriz L. Ferreira[1], Dionisia P. Ferreira[1], Swanny F. Borges[1], Adriana M. Ferreira[1], Fabricio H. Holanda[1], João G. M. Ucella-Filho[2], Rodrigo Alves S. Cruz[1], Willian G. Birolli[3], Rafael Luque[4] and Irlon M. Ferreira[1]*

[1]Biocatalysis and Applied Organic Synthesis Laboratory, Federal University of Amapá, Macapá, AP, Brazil, [2]Department of Forestry and Wood Sciences, Federal University of Espírito Santo, Jerônimo Monteiro, Espirito Santo, Brazil, [3]Molecular Oncology Research Center, Institute of Learning and Research, Barretos Cancer Hospital, Barretos, SP, Brazil, [4]Universidad ECOTEC, Via Principal Campus Ecotec, Samborondón, Ecuador

The consumption of non-steroidal anti-inflammatory drugs (NSAIDs) have increased significantly in the last years (2020–2022), especially for patients in COVID-19 treatment. NSAIDs such as diclofenac, ibuprofen, and paracetamol are often available without restrictions, being employed without medical supervision for basic symptoms of inflammatory processes. Furthermore, these compounds are increasingly present in nature constituting complex mixtures discarded at domestic and hospital sewage/wastewater. Therefore, this review emphasizes the biodegradation of diclofenac, ibuprofen, and paracetamol by pure cultures or consortia of fungi and bacteria at *in vitro*, *in situ*, and *ex situ* processes. Considering the influence of different factors (inoculum dose, pH, temperature, co-factors, reaction time, and microbial isolation medium) relevant for the identification of highly efficient alternatives for pharmaceuticals decontamination, since biologically active micropollutants became a worldwide issue that should be carefully addressed. In addition, we present a quantitative bibliometric survey, which reinforces that the consumption of these drugs and consequently their impact on the environment goes beyond the epidemiological control of COVID-19.

KEYWORDS

COVID-19, mycodegradation, contaminants, SARS-CoV-2, NSAIDs

1. Introduction

In a turnaround moment for humanity, 27 cases of pneumonia of unknown etiology were reported on 31 December 2019 in the city of Wuhan, Hubei Province, China. Later, the fast-spreading agent was identified and named as Severe Acute Respiratory Syndrome Coronavirus 2 (SARS-CoV-2) by the International Committee on Taxonomy of Viruses (ICTV), and the new disease was known as Coronavirus Disease 2019 (COVID-19) by the World Health Organization (WHO) (Oscanoa et al., 2020; Hu et al., 2021).

In March 2020, WHO warned governments to constitute a response and a containment initiative to an epidemic, later classified as a pandemic scenario. A series of measures were proposed and used in an attempt to contain the virus spreading, including home quarantine of infected people and those who entered in contact with them (Zhang et al., 2021). However, the available tools and resources were not enough to prevent this threat to mankind.

Mild symptoms of SARS-CoV-2, as fever, shortness of breath, and diarrhea, can be misunderstood with different viruses. Whereas severe cases can lead to pneumonia, severe acute respiratory syndrome, renal failure, multiple organ failure, and death (Singhal, 2020). Although the pathogenesis of this disease is still not completely understood, growing evidence indicate that a dysregulated inflammatory syndrome is narrowly associated with COVID-19 severity and poor prognosis (Zoulikha et al., 2022), which results from the high levels of inflammatory cytokines like IL2, IL7, IL10, GCSF, IP10, MCP1, MIP1A, and TNFα (Chen et al., 2020).

During the initial pandemic period, different known anti-viral, anti-malarial, and anti-inflammatory drugs were explored and introduced into the treatment. In this context, non-steroidal anti-inflammatory drugs (NSAIDs) were widely employed for COVID-19, especially for patients in home care. With over-the-counter availability, they have often been used without medical supervision to treat the basic symptoms of COVID-19, promoting excessive NSAIDs detection in wastewater treatment plants at both domestic and hospital sewage (Barcelo, 2020). Also, it is important to note that the consumption of these drugs increased significantly during the COVID-19 pandemic, even in comparison to other types of medication (Luis López-Miranda et al., 2022).

Before this period, these compounds were already among the most consumed drugs considering both with and without a prescription (Osafo et al., 2017). Therefore, it is important to note that the continuous use, even at sub-therapeutic concentrations, represents a potential risk to public health, although it is not possible to evaluate the effects of exposure at present (Stackelberg et al., 2004; Santos et al., 2010).

It is known that many non-target organisms (which possess human-and animal-alike metabolic pathways, similar receptors, or biomolecules) are inadvertently exposed to these active pharmaceuticals released into the environment (Fent et al., 2006; Santos et al., 2010). A problem that can be aggravated by the constitution of complex mixtures of biological products that, in some cases, can originate unknown super contaminants (Fent et al., 2006). Recently, the metabolic excretion of NSAIDs had received attention and became a relevant issue due to the impacts in aquatic species, more specifically in terms of chronic effects since low and constant contamination by these products were described (Banerjee and Maric, 2023). However, there is a large group of organisms whose exposure to these compounds and its effects have not yet been evaluated (Świacka et al., 2020).

Moreover, the removal of different NSAIDs through treatment stations has been reported as inefficient (Tiwari et al., 2017; Khasawneh and Palaniandy, 2021). Thus several strategies, including mycoremediation (Aracagök et al., 2018), bacterial remediation (Wojcieszyńska et al., 2022), membranes, and hybrid materials have been investigated for these purposes (Gu et al., 2018).

Based in the increased consumption of NSAIDs, especially by patients in COVID-19 treatment, these compounds were extensively detected in nature, as well as in domestic and hospital sewage/wastewater. Therefore, this review emphasizes the biodegradation of diclofenac, ibuprofen, and paracetamol, which are NSAIDs, by pure cultures and consortia of fungi or bacteria at *in vitro*, *in situ,* and *ex situ* processes over the past 10 years, as an efficient alternative for decontamination of these pharmaceuticals.

2. Pharmacology of the inflammatory process and possible COVID-19 impacts

The inflammatory process is considered a natural reaction of the organism in a protective response against harmful endogenous (immunological, neurological, and damaged cells) and exogenous effects (physical, chemical, and infectious), which involves different types of immune cells, blood vessels, chemical and molecular mediators. This process aims to block, inactivate, or eliminate harmful agents (Borges et al., 2018; Feehan and Gilroy, 2019). In most cases, the inflammation resolution occurs and the body returns to homeostasis after elimination. However, persistence of inflammatory cause and inefficient resolution can culminate in an exacerbated and prolonged inflammatory response that plays a key role in the development of multiple diseases (Badri et al., 2016; Feehan and Gilroy, 2019; Holanda et al., 2023).

The conventional pharmacologic intervention for the resolution of these inflammatory processes contemplate the use of anti-inflammatory drugs, which include the NSAIDs approached in this discussion, steroidal anti-inflammatory drugs (AIES) and/or glycocorticoids (Peesa et al., 2016).

Non-steroidal anti-inflammatory drugs present different chemical structures with similarities in the action mechanism, resulting in anti-inflammatory, antipyretic, and analgesic properties. These compounds are mainly indicated to treat symptoms of acute disorders (fever, edema, and pain), as well as in the treatment of chronic diseases. The main representatives of these drugs are diclofenac (DCF), ibuprofen (IBU), paracetamol (PAR), nimesulide, salicylic acid, piroxicam, meloxicam, naproxen, ketoprofen, mefenamic acid, and celecoxib (Chen et al., 2013; Wojcieszyńska et al., 2022).

Another active ingredient with increased consumption due to COVID-19 pandemic was paracetamol (PAR), also known as acetaminophen, which does not belong to the NSAIDs group because this compound does not present anti-inflammatory activity, but promotes analgesic and antipyretic properties similar to NSAIDs. Regardless of this, some studies have reported that PAR activity is also related to the inhibition of the cyclooxygenase (COX) enzymes, demonstrating a preferential inhibition of COX-2 (Ward and Alexander-Williams, 1999; Huntjens et al., 2005; Wojcieszyńska et al., 2022; Figures 1A,B).

The inflammatory process is considered an important part of the pathogenesis of various diseases (e.g., rheumatoid arthritis, diabetes, and cancer), and most of the time, it is a determinant factor regarding severity and complexity (Feehan and Gilroy, 2019). In this sense, several studies have already shown that, in the severe cases of COVID-19, the SARS-COV-2 virus infection promotes multisystem inflammation, generating intense tissue and cellular damage with respiratory, cardiovascular, liver, and renal complications concomitant with coagulation. Thus, demonstrating a strong relationship between

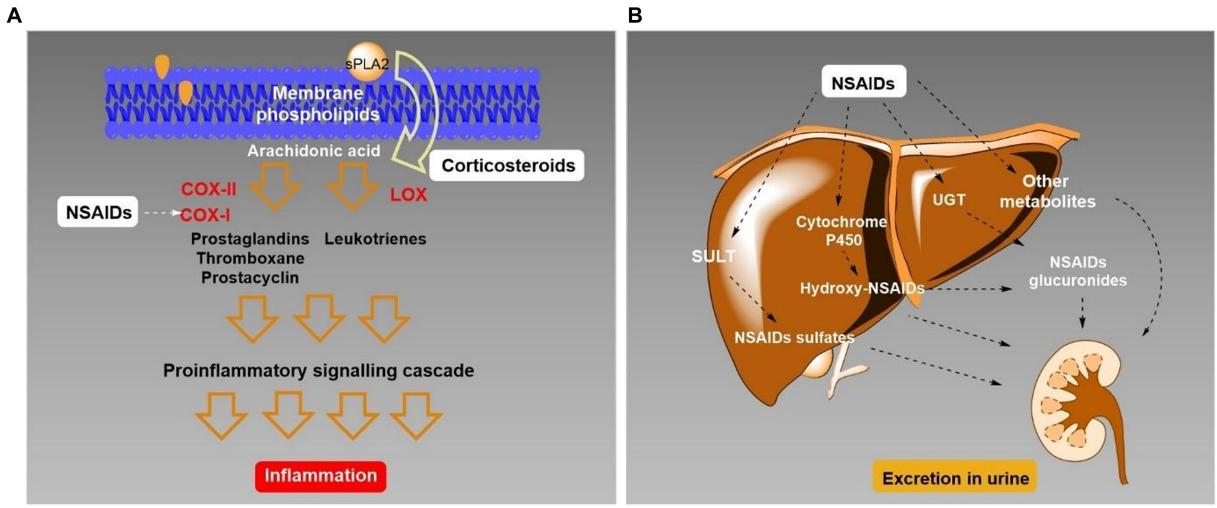

FIGURE 1
(A) Illustration of the simplified mechanism of action of nonsteroidal anti-inflammatory drugs (NSAIDs) in the inhibition of cyclooxygenase II.
(B) Biotransformation route of NSAIDs in the liver.

disease aggravation and hyperinflammatory response (de Almeida et al., 2020; Micallef et al., 2020; Perico et al., 2023). Therefore, the clinical manifestations of COVID-19 can be a result from exacerbated inflammatory conditions for a considerable number of cases, leading to the use of anti-inflammatory drugs as therapeutic strategy.

3. Ecotoxicity of non-steroidal anti-inflammatory drugs

Pharmaceutical products can be released into the environment in different manners during their life cycle, including steps of production, distribution, acquisition, and home use. The three main routes to transform drugs into micropollutants are excretion after ingestion, medicine or chemical removal during bathing, and direct disposal of unwanted products due to leftovers or expired validity (Ruhoy and Daughton, 2007). In addition, topical medications can contribute significantly with the environmental contamination by IBU and DCF in relation to the amount released by patients employing orally taken products (Austin et al., 2021). For instance, DCF and IBU were determined in wastewater from treatment plants (WWTPs) and effluent receiving waters in Nigeria. Maximum concentrations in wastewater were 166.1 $\mu g\,L^{-1}$ DCF and 62.0 $\mu g.L^{-1}$ IBU (Ajibola et al., 2021). In addition, these authors also demonstrated a high environmental risk of IBU to fish and DCF to bacteria.

In another study, DCF and PAR were also determined in rivers in South Africa in the range of 40 $ng\,L^{-1}$ to 51.94 $\mu g\,L^{-1}$ for DCF and from 96.70 to almost 152 $\mu g\,L^{-1}$ for PAR (Omotola and Olatunji, 2020). Furthermore, ketoprofen (42–133 $ng\,L^{-1}$), IBU (73–126 $ng\,L^{-1}$), DCF (199–469 $ng\,L^{-1}$), mefenamic acid (8–13 $ng\,L^{-1}$), and salicylic acid (54–109 $ng\,L^{-1}$) were detected in the Besós river at urbanized areas of Barcelona (Spain). In addition, the approached drugs were also observed in the aquifer (Jurado et al., 2021).

Besides the individual risk of pharmaceuticals, the mixture of contaminants might also pose an unacceptable risk to aquatic habitats (Kumari and Kumar, 2022). But unfortunately, few studies approached the effects of NSAIDs toxicity in the aqueous environment (Scheurell et al., 2009; Maculewicz et al., 2022). In this sense, the toxicity of IBU after photodegradation was investigated using the algae *Chlorella* sp. with the determination of the toxicity of the obtained byproducts mixture, as well as the toxicity of the main photodegradation product 4-acetylbenzoic acid alone. No effect of the mixture on algae viability was observed in comparison to IBU, whereas 4-acetylbenzoic acid significantly affected *Chlorella* sp. viability, starting from 0.25 mM to concentrations above 0.5 mM that caused the death of all cells (Gong et al., 2021).

Moreover, chronic toxicity trials performed on *Oncorhynchus mykiss* evidenced cytological changes in the liver, kidney, and gills after 28 days of exposure to just 1 $\mu g\,L^{-1}$ of DCF. When exposure reached concentration of 5 $\mu g\,L^{-1}$, renal lesions were evident as well as drug accumulation in liver, kidneys, gills, and muscle. DCF also inhibited the growth of marine phytoplankton *Dunaliella tertiolecta* at 25 $mg\,L^{-1}$ and above (DeLorenzo and Fleming, 2008). Approaching IBU ecotoxicity, it was reported generating growth stimulation of the cyanobacterium *Synechocystis* sp. for 5-day exposure to concentrations in the range of 1–1,000 $\mu g\,L^{-1}$, but inhibition of the duckweed plant *Lemna minor* after 7 days (Pomati et al., 2004).

Even though NSAIDs are characterized by relatively low environmental stability, especially through biotransformation in aerobic conditions and photolysis occurring in surface waters, these compounds and metabolic residues are frequently detected in surface water, marine water, freshwater reservoirs, rivers and lakes, from concentration of ng L^{-1} up to $\mu g\ L^{-1}$ (Świacka et al., 2020). Although physicochemical processes are commonly used in the remediation of NSAIDs, these processes need specific conditions for reaction, expensive operational costs, and may cause the formation of more toxic intermediate compounds (Sharma et al., 2020). Therefore, methods of green bioremediation processes are an attractive alternative for transformation of NSAIDs into low toxicity product and further mineralization.

4. Scope of research and bibliometric analysis

Search engines including Google Scholar, Web of Science, and Dimension were used to retrieve literature. Almost 32 research articles published between 2012 and 2023 (February) were employed for gathering relevant information. The primary search terms were "biodegradation and (diclofenac, ibuprofen, or paracetamol)," "bacteria removal and (diclofenac, ibuprofen, or paracetamol)," and "fungi removal and (diclofenac, ibuprofen or paracetamol)." In addition, a comprehensive bibliometric analysis was carried out using the international scientific database Scopus, aiming at mapping and understanding the interest and evolution of studies related to NSAIDs during the COVID-19 pandemic. To carry out this study, the methodology proposed by different authors was employed and adapted (Ucella-Filho et al., 2022; Lucas et al., 2023). In order to collect data relevant to the approached study topic, a search command was drawn up which included keywords pertinent to the focus of this review, and that were present in the titles or abstracts of articles. The following search formula was therefore used:: "TITLE (COVID-19 OR SARS-CoV-2 OR coronavirus OR COVID19) AND ABS (diclofenac OR 'diclofenac potassium' OR 'paracetamol' OR 'acetaminophen' OR 'n-acetyl-p-aminophenol' OR 'ibuprofen' OR '2-[4-(2-methylpropil) phenyl]propanoic acid)]') OR TITLE (diclofenac OR 'diclofenac potassium' OR 'paracetamol' OR 'acetaminophen' OR '*n*-acetyl-p-aminophenol' OR 'ibuprofen' OR '2-[4-(2-methylpropil)phenyl] propanoic acid)]')) AND PUBYEAR >2012 AND PUBYEAR <2024." The data collected was processed using the "biblioshiny" function in the "bibliometrix" package (Aria and Cuccurullo, 2017) of the R software (R Core Team, 2021), allowing us to obtain a structured and quantitative analysis of emerging trends in the field of NSAIDs research over the last 10 years (2013–2023).

Beyond the biodegradation process, several studies relating COVID-19 to drugs categorized as NSAIDs have received significant attention in the scientific community, increasing the number of articles aiming at a better understand of these drugs effects on the development of COVID-19. Therefore, justifying the environmental contamination by NSAIDs that might be present too in hospital, pre-clinical and clinical testing laboratories, as well as in universities and research institutes. In this context, it was carried out a comprehensive bibliometric analysis of articles mentioning relationships between NSAIDs and COVID-19, validating this information.

A total of 344 articles addressing this current topic under analysis were identified, of which 76 were classified as review articles, book chapters, letters, and communications, whereas 268 were categorized as research articles, which served as the basis for the data presented in this discussion. As expected, there were no studies relating COVID-19 to NSAIDs in the period from 2013 to 2018. However, in 2019, with the clinical urgency for information and treatments of this new disease, the first studies were already described (Cheng et al., 2020). However, the highest number of publications was observed in the year of 2022 with 89 documents addressing this connection. Although there was a sharp decline (>50 articles) in the number of publications from 2023 onwards (Figure 2A). The continuous increase in publications over these years focusing on the use of NSAIDs in relation to the treatment of COVID-19 symptoms has become important, given the mutations and adaptations of this virus and their variants (Markov et al., 2023), as well the need for effective strategies for symptoms relieve and complications prevention.

This research also plays a key role in adapting clinical protocols, discovering innovative therapies, and advancing scientific knowledge to understand future pandemics. Among the highlighted words recorded in these papers and processed by the bibliometric method, IBU and PAR appear among the five most cited words, indicating their relevance in the context of COVID-19 (Figure 2B). Therefore, without going into the merits of whether concomitant treatment with NSAIDs can be harmful or safe in COVID-19 patients, the production and consumption of NSAIDs, such as IBU, PAR, and DCF, as well as the involvement in clinical and pre-clinical trials, are still considered high and necessary, especially in developed countries such as the United States, Spain, the United Kingdom, Italy, and other European countries (Austin et al., 2022). Thus, contributing to the detection of these substances (IBU, PAR, and DIC), in some cases, at concentrations above the legislative limit. Furthermore, it is also necessary to reflect on the biodegradation methods, which are intrinsically related to the extensive use of NSAIDs and studies of the pharmacological and epidemiological profile of COVID-19.

Therefore, means of removal and methods of (bio)remediation such as those presented here by fungi or bacteria must be continued for the development of applied bioremediation alternatives, in synergy with the production and evaluation studies (*in vitro* or *in vivo*) of these drugs. Aiming at limiting the impacts possibly generated by the release of the drugs into the environment.

As showed in Figures 2A,B, COVID-19 has dominated the global scientific focus since the beginning of 2020, and as such, researchers were dedicated to add their contributions to what is known and what can be done to combat COVID-19, in addition, studies involving NSAIDs are accelerated to support some approaches. Furthermore, the exhibited ability of the virus to mutate rapidly and access to public or private funding for COVID-19 research is still attractive (Brandt et al., 2022), consequently, the use of related substances, such as NSAIDs, added to the usual worldwide consumption of these substance will keep the consumption high for several years. Therefore, efficient methods for bioremediation process for DCF, IBU, and PAR will be important for understanding the impact of these drugs on the environment and environmentally exposed population.

5. Biodegradation of diclofenac

Diclofenac, [2-(2-(2,6-dichlorophenylamino)phenyl] acetic acid, is a common non-steroidal anti-inflammatory drug (NSAID) used as oral tablets or topical gel with an estimated global consumption of up to 940 t per year (Zhang et al., 2008), its physicochemical properties are presented in Table 1. After oral administration, 65 and 70% of DCF is excreted in urine and 20–30% in feces as parent drug or metabolites, thus this pharmaceutical undergoes almost complete biotransformation in the human body (Vieno and Sillanpää, 2014; Davis et al., 2020).

Approaching the biodegradation by bacteria, strains isolated from a municipal wastewater treatment plant (WWTP) located in Northern Portugal (Ponte de Moreira, Portugal) were used for DCF biodegradation. *Brevibacterium* sp. D4 biodegraded 35% of 10 mg L^{-1} DCF as the sole carbon source, however the yield raised to 90% when periodic acetate addition as supplementary carbon source was employed (Table 2, entry 1; Bessa et al., 2017).

10.3389/fmicb.2023.1207664

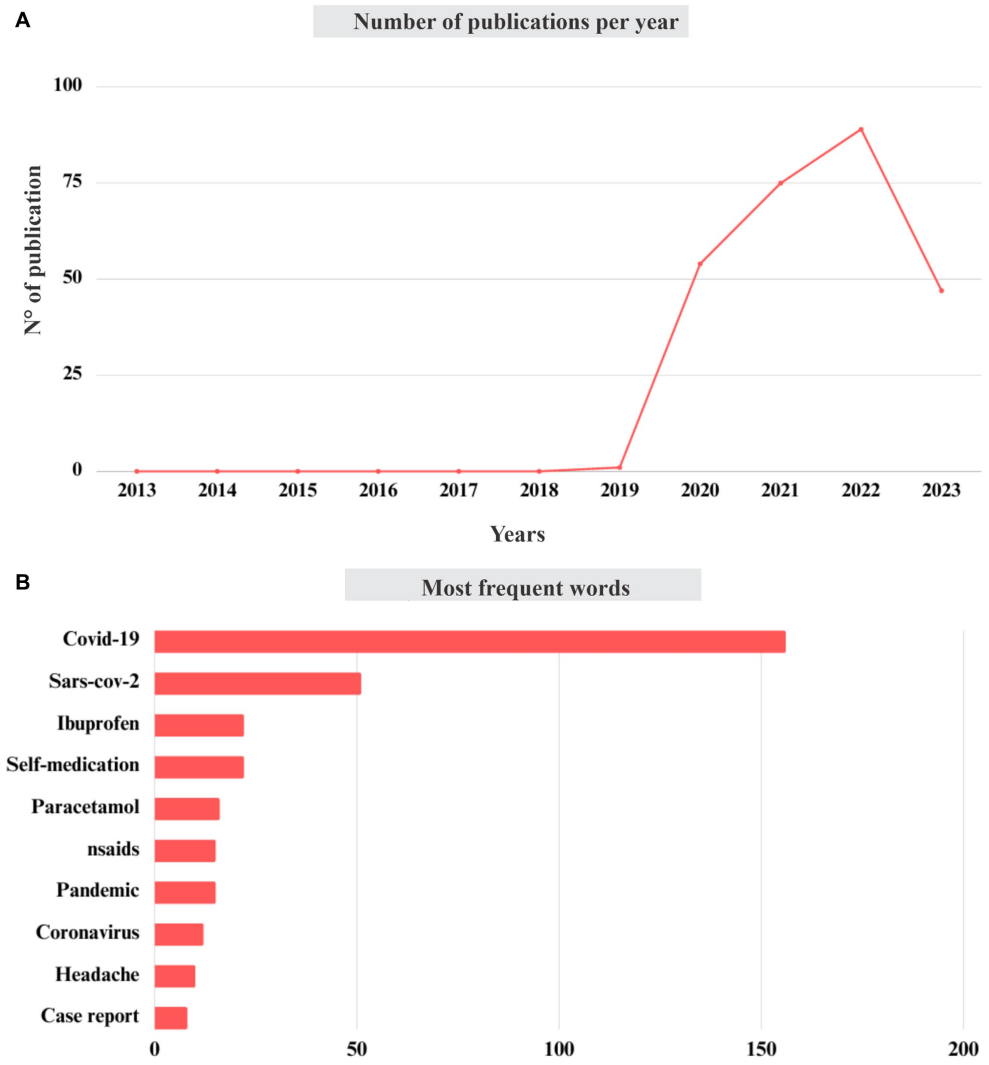

FIGURE 2
(A) Number of publications by year (2013–2023), and most frequent words **(B)** related to COVID-19 with NSAIDs.

TABLE 1 **Physicochemical properties of DCF, IBU, and PAR.**

Parameter	DCF	IBU	PAR
Chemical structure	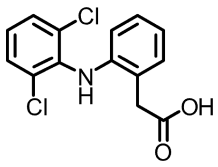	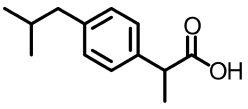	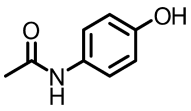
Chemical formula	$C_{14}H_{10}C_{l2}NO_2$	$C_{13}H_{18}0_2$	$C_8H_9NO_2$
CAS no	15307-86-5	15687-27-1	103-90-2
Water solubility	2.37 mg L^{-1}	21 mg L^{-1}	14 g L^{-1}
pKa	4.15[a]	4.5[b]	9.38[c]
logKow	4.51[a]	2.48[b]	0.46[c]

[a]Zhang et al. (2008); [b]Scheytt and Mersmann (2005); [c]Ward and Alexander-Williams (1999).

In another study, biodegradation of >99% DCF was reported by the bacterial strain *Labrys portucalensis* F11 (Table 2, entry 2) isolated from sediment of a polluted site in Portugal. Complete degradation was reached by co-metabolism with acetate after 6 days for 1.7 μM DCF, and after 25 days for 34 μM DCF both at 25°C and 130 rpm (Moreira et al., 2018). Furthermore, 12 metabolites were identified

TABLE 2 Summary of DCF, IBU, and PAR biodegradation.

Ent.	Microorganism	Isolation place	Drug	Biodegradation rate (conditions)	Ref
1.	*Brevibacterium* sp. *D4*	From wastwater treatment plant (Ponte de Moreira, Maia—Portugal)	DCF	90% (10 mg L^{-1}, at 25°C, 150 rpm by 30 days)	Bessa et al. (2017)
2.	*Labrys portucalensis* F11	From sediment of a polluted site in the northern Portugal	DCF	>99% (7.01 mg L^{-1} at 25°C, 130 rpm by 25 days)	Moreira et al. (2018)
3.	*Bacillus subtilis*	Provided by the Prodibio Company—Marseille, France	DCF	>99% (1,000 mg L^{-1}, at 20°C, 100 rpm by 17 h)	Grandclément et al. (2020)
4.	*Rhodococcus ruber* IEGM 346	From Regional Specialized Collection of Alkanotrophic Microorganisms	DCF	>99% (1,000 mg L^{-1}, at 28°C, 100 rpm by 6 days and 0.5% glucose).	Ivshina et al. (2019)
5.	*Klebsiella* sp. KSC	From livestock soil	DCF	90% (70,000 mg L^{-1}, at 30°C, pH 7, 100 rpm by 72 h)	Stylianou et al. (2018)
6.	*Microbial consortia*	Native microbial soil	DCF	90% (1,000 mg L^{-1}, at 25°C, 120 rpm by 10 days)	Facey et al. (2018)
7.	*Ganoderma applanatum*	Collection in the Department of Pure and Applied Botany—Nigeria	DCF	61% (15 mg L^{-1}, at 30°C, pH 4, 5 and 150 rpm by 72 h)	Bankole et al. (2020)
8.	*Laetiporus sulphureus*	Collection in the Department of Pure and Applied Botany, Federal University of Agriculture Abeokuta—Nigeria	DCF	73% (15 mg L^{-1}, at 30°C, pH 4.5 and 150 rpm by 72 h)	Bankole et al. (2020)
9.	*Talaromyces gossypii*	Sewage sludge composite samples were collected from the WWTPs—Granada—Spain	DCF	84.6% (20.62 mg L^{-1} at 28°C by 72 h)	Conejo-Saucedo et al. (2021)
10.	*Syncephalastrum monosporum*	Sewage sludge composite samples were collected from the WWTPs—Granada—Spain	DCF	82% (20.62 mg L^{-1} at 28°C by 72 h)	Conejo-Saucedo et al. (2021)
11.	*Aspergillus tabacinus*	Sewage sludge composite samples were collected from the WWTPs—Granada—Spain	DCF	76% (20.62 mg L^{-1} at 28°C by 72 h)	Conejo-Saucedo et al. (2021)
12.	*Talaromyces verruculosus*	Sewage sludge composite samples were collected from the WWTPs—Granada—Spain	DCF	37% (20.62 mg L^{-1} at 28°C by 72 h)	Conejo-Saucedo et al. (2021)
13.	*Aspergillus terreus*	Sewage sludge composite samples were collected from the WWTPs—Granada—Spain	DCF	49,7% (20.62 mg L^{-1} at 28°C by 72 h)	Conejo-Saucedo et al. (2021)
14.	*Aspergillus cejpii*	Sewage sludge composite samples were collected from the WWTPs—Granada—Spain	DCF	14.6% (20.62 mg L^{-1} at 28°C by 72 h)	Conejo-Saucedo et al. (2021)
15.	Microbial consortium (*Alcaligenes faecalis, Staphylococcus aureus, Staphylococcus, haemolyticus, Proteus mirabilis*)	Isolated from the vicinity of a pharmaceutical manufacturing unit—India	DCF	45% (150 mg.L^{-1}, at 25–30°C, pH 7 by 120 h)	Murshid and Dhakshinamoorthy (2019)
16.	*Penicillium oxalicum*	Isolated from a hydrocarbonpolluted pond in Motril—Granada	DCF sodium	99% (20.62 mg L^{-1}, 24 h, 28°C)	Murshid and Dhakshinamoorthy (2019)
17.	*Rhizophagus irregularis*	Institute of Botany, Czech Academy of Science—Czechia	IBU	80% (0.5 mg L^{-1}, 5–30°C, by 150 days,)	Hu et al. (2021)
18.	*Sphingopyxis granuli* RW412	River Elbe taken downstream of the Hamburg harbor-Germany	IBU	80% (800 mg L^{-1}, 30°C, 200 rpm, 3 days)	Aguilar-Romero et al. (2021)
19.	*Bacillus thuringiensis*	Soil of the Chemical factory "Organika-Azot" in Jaworzno, Poland	IBU	46.56% (25 mg L^{-1}, at 30°C,130 rpm by 20 days)	Marchlewicz et al. (2016)

(Continued)

TABLE 2 (Continued)

Ent.	Microorganism	Isolation place	Drug	Biodegradation rate (conditions)	Ref
20.	*Patulibacter* sp. Strain L11	Activated sludge collected from Beirolas WWTP—(Lisbon, Portugal)	IBU	92% (0.05 mg L^{-1}, at 28°C, 110 rpm by 90 h)	Almeida et al. (2013a)
21.	*Gordonia amicalis* EU266486.1	Activated sludge Beirolas WWTP (Lisbon, Portugal)	IBU	26% (0.1 mg L^{-1}, at 27°C, 110 rpm by 100 h)	Almeida et al. (2013b)
22.	*Acinetobacter bouvetti* JF681285	Activated sludge Beirolas WWTP (Lisbon, Portugal)	IBU	12.8% (0.1 mg L^{-1}, at 27°C, 110 rpm by 100 h)	Almeida et al. (2013b)
23.	*Bacillus siamensis* DSI-1	Isolated from wastewater—GenBank MT 039503	IBU	50% (3.5 mg $L^{-1,}$ at 30°C, pH 7, 165 rpm, by 18 h)	Chopra and Kumar (2022)
24.	*Microbacterium paraoxydans*	Isolated from pharmaceutical wastewater of East India Pharmaceutical Private Limited, Durgapur, West Bengal, India	IBU	92,01% (15 mg L^{-1}, at 30°C, pH 7, 150 rpm, 0.3% yeast extract)	Show et al. (2023)
25.	*Patulibacter medicamentivorans*	Isolated from activated sludge collected from Beirolas WWTP (Lisbon, Portugal)	IBU	>99% (0.25 mg L^{-1}, at 28°C, pH 7, 110 rpm by 7 days)	Salgado et al. (2020)
26.	*Nocardioides carbamazepini* sp. nov. CBZ_1T	Biofilm sample collected from a Pump and Treat system treating BTEX (benzene, toluene, ethyl-benzene, and xylenes) contaminated groundwater	IBU	70% (1.5 mg.L^{-1}, at 27°C, 145 rpm by 7 days)	Benedek et al. (2022)
27.	*Sphingomonas wottichii* MPO218	Sewage sludge of Copero (EMASESA, dos Hermanas, Seville, Spain), Company Almirall (Barcelona Spain)	IBU	>75% (4.4 mM at 4.5 h, 30°C and pH 7)	Aulestia et al. (2021)
28.	*Sphingomonas* sp		IBU	>99% (500 mg L^{-1}, 80 h, 37 ± 2°C)	Murdoch and Hay, 2013
29.	*Pseudoalteromonas* sp	GenBank accession number: KY583737	IBU	80%, (1.0 mg L^{-1}, 20 ± 1°C, 150 rpm by 72 h)	Li et al. (2022)
30.	*Rhodococcus cerastii IEGM 1278*	Regional specialized Collection of Alkano-trophic Microorganisms (acronym IEGM, the wprdl Federation for Culture)	IBU	14.1% (100 mg L^{-1}, at 28°C, 160 rpm by 7 days)	Ivshina et al. (2021)
31.	*R. cercidiphylli* IEGM 1184	Regional specialized Collection of Alkano-trophic Microorganisms (acronym IEGM, the wprdl Federation for Culture)	IBU	21.6% (100 mg L^{-1}, at 28°C, 160 rpm by 7 days)	Ivshina et al. (2021)
32.	*R. erythropolis* IEGM 501	Regional specialized Collection of Alkano-trophic Microorganisms (acronym IEGM, the wprdl Federation for Culture)	IBU	18.6% (100 mg L^{-1}, at 28°C, 160 rpm by 7 days)	Ivshina et al. (2021)
33.	*Paracoccus aminophilus* NR_042715.1	Activated sludge Beirolas WWTP (Lisbon, Portugal)	IBU	16.2% (0.1 mg L^{-1}, at 27°C, 110 rpm by 100 h)	Almeida et al. (2013b)
34.	*Patulibacter americanus* NR_042369	Activated sludge Beirolas WWTP (Lisbon, Portugal)	IBU	35% (0.1 mg L^{-1}, at 27°C, 110 rpm by 100 h)	Almeida et al. (2013b)
35.	*Pseudomonas stutzeri* CSW02	Sewage sludge was obtained from a Wastewater Treatment Plant (WWTP) in the city of Seville	PAR	100% (500 mg L^{-1}, at 30 ± 1°C, 150 rpm by 4 h)	Vargas-Ordóñez et al. (2023)
36.	*Pseudomonas extremaustralis* CSW01	Sewage sludge was obtained from a Wastewater Treatment Plant (WWTP) in the city of Seville	PAR	100% (500 mg L^{-1}, at 30 ± 1°C, 150 rpm, by 6 h)	Vargas-Ordóñez et al. (2023)
37.	*Pseudomonas* sp. PrS10	Sample wastewater collected from Cadila Pharmaceutical Limited, Gujarat, India	PAR	96.37% (3,000 mg L^{-1}, at 30°C, 140 rpm by 7 days)	Poddar et al. (2022)

(Continued)

TABLE 2 (Continued)

Ent.	Microorganism	Isolation place	Drug	Biodegradation rate (conditions)	Ref
38	*Pseudomonas moorei* KB4	From the activated sludge from the wastewater treatment plant Klimzowiec (Chorzów, Poland)	PAR	99% (50 mg L^{-1}, at 30°C, pH 7 by 1.5 h)	Żur et al. (2018b)
39.	*Pseudomonas aeruginosa*	Sludges from two Portuguese WWTPs	PAR	90% (50 mg L^{-1}, at r.t, by 2 days)	Palma et al. (2018)
40.	*Pseudomonas* sp. f2	PAR-degrading aerobic aggregate	PAR	100% (2.000 mg L^{-1}, at 30°C, 200 rpm by 70 h)	Zhang et al. (2013)
41.	*Pseudomonas* sp. fg-2	PAR-degrading aerobic aggregate	PAR	100% (2,500 mg L^{-1}, 30°C, 200 rpm by 45 h)	Zhang et al. (2013)
42.	*Stenotrophomonas* sp. f1	PAR-degrading aerobic aggregate	PAR	100% (2,000 mg L^{-1}, at 30°C, 200 rpm, by 16 h)	Zhang et al. (2013)
43.	*Pseudomonas aeruginosa strain* HJ1012	Isolated from stable microbial aggregate in a sequencing batch reactor	PAR	71.4% (2,200 mg L^{-1}, at 30°C, pH 7 by 18 h)	Hu et al. (2013)
44.	*Aspergillus niger*	Wastewater samples were collected from the effluent generated by YEDCO factory situated in Sana'a City, Yemen	PAR	37% (2,000 mg L^{-1}, at 25°C, pH 6.0 by 60 days)	Sana (2018)
45.	*Fusarium oxysporium*	Wastewater samples were collected from the effluent generated by YEDCO factory situated in Sana'a City, Yemen	PAR	26.1% (1,000 mg L^{-1}, at 25°C, pH 6.0 by 60 days)	Sana (2018)
46.	Microbial consortium (*Bacillus cereus; Corynebacterium nuruki; Enterococcus faecium*)	A sample of aerobic activated sludge was collected from the oxidation ditch of Faro Northwest WWTP's, Portugal.	PAR	> 90% (200 mg L^{-1}, at 28°C, by 48 h)	Palma et al. (2021)
47.	*Bacillus drentensis estirpe* S1	The sewage samples used in this study were collected from waste water drain in Sonipat, Haryana, India	PAR	93% (300 mg L^{-1}, at 40°C, pH 7, 165 rpm by 48 h)	Chopra and Kumar (2020)
48.	*M. yunnanensis* KGP04	Pharmaceutical industry wastewater and sludge samples were collected from VKIA (Vishwakarma Industrial Area), Jaipur	PAR	80% (1% w/v, at 25°C, pH 8, 200 rpm, by 6 h)	Sharma et al. (2020)
49.	*M. yunnanensis* TJPT4	Bacteria recovered from marine organisms, which were collected from the Catedral and Queijo Suiço marine caves, located in Sagres, Algarve, Portugal	PAR	>60% (15 mg L^{-1}, at 28°C, 150 rpm, by 360 h)	Palma et al. (2022)
50.	*Pseudomonas* spp.	Sludge of a hospital WWTP (Pharmafilter, Delft, NL)	PAR	>99% [250 mgL^{-1} (reactor conditions 500 rpm, pH 7, airflow 30 mL/min, and 20 ± 1°C) at 10 days]	Rios-Miguel et al. (2022)

using UPLC-QTOF analyses. Including mono-and di-hydroxylated compounds resulted from hydroxylation at the chlorine-substituted site, decarboxylation, methylation of a hydroxyl group, and formation of benzoquinone imine species (Figure 3).

In addition, mono-hydroxylated DCF products were reported at biodegradation by *Bacillus subtilis* and *Brevibacillus laterosporus* strains provided by the Prodibio Company (Marseille, France). Complete removal was observed in biodegradation with 1 mg mL^{-1} DCF after 17 h of an experiment at 20°C, pH 7, and 100 rpm (Table 2, entry 3; Grandclément et al., 2020).

Recently, Ivshina et al. (2019) reported the ability of 104 *Rhodococcal* strains isolated from municipal wastewater and deposited at the Regional Specialized Collection of Alkanotrophic Microorganisms (IEGM, WDCM 768, http://www.iegmcol.ru) to biodegrade DCF. The selected strain *Rhodococcus ruber* IEGM 346 (Table 2, entry 4) completely biodegraded 50 mg mL DCF after 6 days at 28°C in pH 7 with glucose (0.5%). Analysis by gas chromatography–mass spectrometry (GC–MS) confirmed the C-N bond cleavage and aromatic ring opening of DCF structure, generating benzoquinone the imine, mono-and di-hydroxylated

derivatives, which were the main biodegradation metabolites (Ivshina et al., 2019).

Some of these metabolites were also identified in the DCF biodegradation by *Klebsiella* sp. KSC isolated from livestock soil (Gen Bank, accession number KX500307). The best biodegradation results, 90%, was obtained at 70 mg L^{-1} DCF after 72 h at 30°C, pH 7, and 100 rpm (Table 2, entry 5). Furthermore, acute ecotoxicity assays with *Vibrio fischeri* were performed for the obtained biotransformation products, which were less toxic than the parent compound (Stylianou et al., 2018). In another study, up to 1.0 g L^{-1} DCF was fully biodegraded by a native microbial soil consortium obtained from 11 forest soil samples after 10 days at 25°C and 120 rpm (Table 2, entry 6; Facey et al., 2018).

Different bacterial strains previously isolated from a pharmaceutical manufacturing unit were also employed for DCF biodegradation. The consortium of bacteria composed of *Alcaligenes faecalis* (MG995024), *Staphylococcus aureus* (MG576208), *Staphylococcus haemolyticus* (MG995021), and *Proteus mirabilis* (MH021605) at pH 7 and temperature range of 25–30°C removed 45% DCF (Table 2, entry 7). Subsequently, at pH between 6 and 8 and 25–35°C, the consortium showed an efficiency increase to 55%. These results showed that consortia can be an interesting approach for the biodegradation of these micropollutants (Murshid and Dhakshinamoorthy, 2019).

Fungi species were also employed in the biodegradation process of DCF. *Ganoderma applanatum* and *Laetiporus sulphureus* deposited in the Microbial Collection of the Department of Pure and Applied Botany located at the Federal University of Agriculture Abeokuta (Nigeria) were explored. The removal of DCF reached 96% of 15 mg L^{-1} by the co-culture of both strains after 72 h at pH 4.5, 30°, and 150 rpm. It is important to note that the same strains, *G. applanatum* and *Laetiporus sulphureus*, exhibited reduced efficiencies of 61% (Table 2, entry 8) and 73% (Table 1, entry 9), respectively, when employed individually. Showing that the co-culture of fungi for biodegradation promoted synergistic effects (Bankole et al., 2020).

Fungal species isolated from sewage treatment plants at Granada (Spain) were also tested for DCF biodegradation. The consumption after 72 h at 28°C was assessed for six isolated strains (Table 2, entry 10–15). *Talaromyces gossypii* showed the maximum DCF removal of 85% (Table 1, entry 10), whereas *Syncephalastrum monosporum* presented 82% (Table 2, entry 11), and 76% removal was observed for *A. tabacinus* (Table 2, entry 12). In addition, *Aspergillus terreus*, *Talaromyces verruculosus*, and *Aspergillus cejpii* promoted lower biodegradation percentages of 50, 37, and 15% of DCF (Table 2, entries 13, 14, 15), respectively (Conejo-Saucedo et al., 2021).

The fungus *Penicillium oxalicum* previously isolated from a lake polluted by hydrocarbons in Motril (Spain) was also used for DCF biodegradation. Removal of 99% was observed after 24 h at 28°C, showing the interesting efficiency of this strain (Table 2, entry 16; Olicón-Hernández et al., 2019).

So, the literature shows that several microorganisms (fungi and bacterium) have been reported to biodegrade diclofenac with high rates of biodegradation through different metabolic pathways, including hydroxylation, dihydroxylation, decarboxylation, deschlorination, C-N bond cleavage, and aromatic ring opening. However, advances in the ecotoxicological study of metabolites of DCF are necessary.

6. Biodegradation of ibuprofen

Ibuprofen, ((2rs)-2-[4-(2-methylpropil)phenyl]propanoic acid), is a NSAIDs used in the form of tablet, capsule, oral suspension, granule, suppository, cream, gel, drop, and injection. Its physicochemical properties are described in Table 1. Approximately 80% of the IBU dose is absorbed in the gastrointestinal tract when administered orally. Then, its biotransformation occurs in the liver generating glucuronide metabolites that are excreted in the urine, in which less than 1% of the dose is excreted in untransformed form (Davies, 1998).

Microbial degradation of IBU has received attention from the worldwide scientific community due to its extensive consumption (Rastogi et al., 2021). The development of IBU was a result from the search for safe drugs in the middle of the 21st century, entering the English market in 1967 and in America in 1974, thus this was the first propionic acid to be used in the United States with non-steroidal anti-inflammatory therapeutic properties. In a comparison with other treatment options, IBU has weak anti-inflammatory activity, but the adverse effects are low, resulting in frequent use for pain and fever relief (Kantor, 1984; Ren et al., 2021).

Although different biocatalysts have been presented for IBU biodegradation, the search for new strains with unique properties continues using different perspectives aims at new information and insights for applied bioremediation.

The use of fungal strains in the biodegradation process of IBU is understudied, but some studies were described. In this regard, IBU-mineralizing bacteria isolated from sediments of the Elbe River taken downstream of the Hamburg harbor (Germany) were explored. These strains were characterized and tested for IBU remediation in different media. *Sphingopyxis granuli* (RW412) biodegraded 80% of 0.08 mg g^{-1} IBU in 3 days at 30°C and 200 rpm (Table 2, entry 17). These results indicated that RW412 bioaugmentation in a biopurification system can improve the dissipation rates of this active ingredient (Aguilar-Romero et al., 2021).

Wastewater was explored for strains isolation by different authors. Such as in the biodegradation of IBU by *Patulibacter* sp. L11 isolated from activated sludge collected from Beirolas WWTPs (Lisbon, Portugal), which was performed at different concentrations (1,000, 250, and 50 µg L^{-1}). Experiments at 28°C and 110 rpm resulted in 62% biodegradation of 50 µg L^{-1} initial concentration using M9 medium with yeast extract and tryptone (Table 2, entry 18). Moreover, 92% biodegradation was observed using OD2-medium (Almeida et al., 2013c).

Other strains obtained from activated sludge of Beirolas WWTPs were also explored for IBU biodegradation. The biodegradation reactions were performed at 27°C and 110 rpm for 100 h with an initial IBU concentration of 100 µg L^{-1}. The species with the highest percentage of biodegradation was *Patulibacter americanus* NR_042369 with 35%, followed by *Gordonia amicalis* EU266486.1 with 26%, *Paracoccus aminophilus* NR_042715.1 with 16%, and *Acinetobacter bouvetti* (JF681285) with 13% biodegradation (Table 2, entry 19–20; Almeida et al., 2013b).

Also from the WWTP located in Beirola, *Patulibacter medicamentivorans* I11^T was explored at IBU biodegradation (7 days, 28°C, pH 7.0, 110 rpm) with focus on metabolite identification in mineral medium supplemented with tryptone and yeast extract (Table 2, entry 21; Almeida et al., 2013a). GC–MS and LC–MS/MS

10.3389/fmicb.2023.1207664

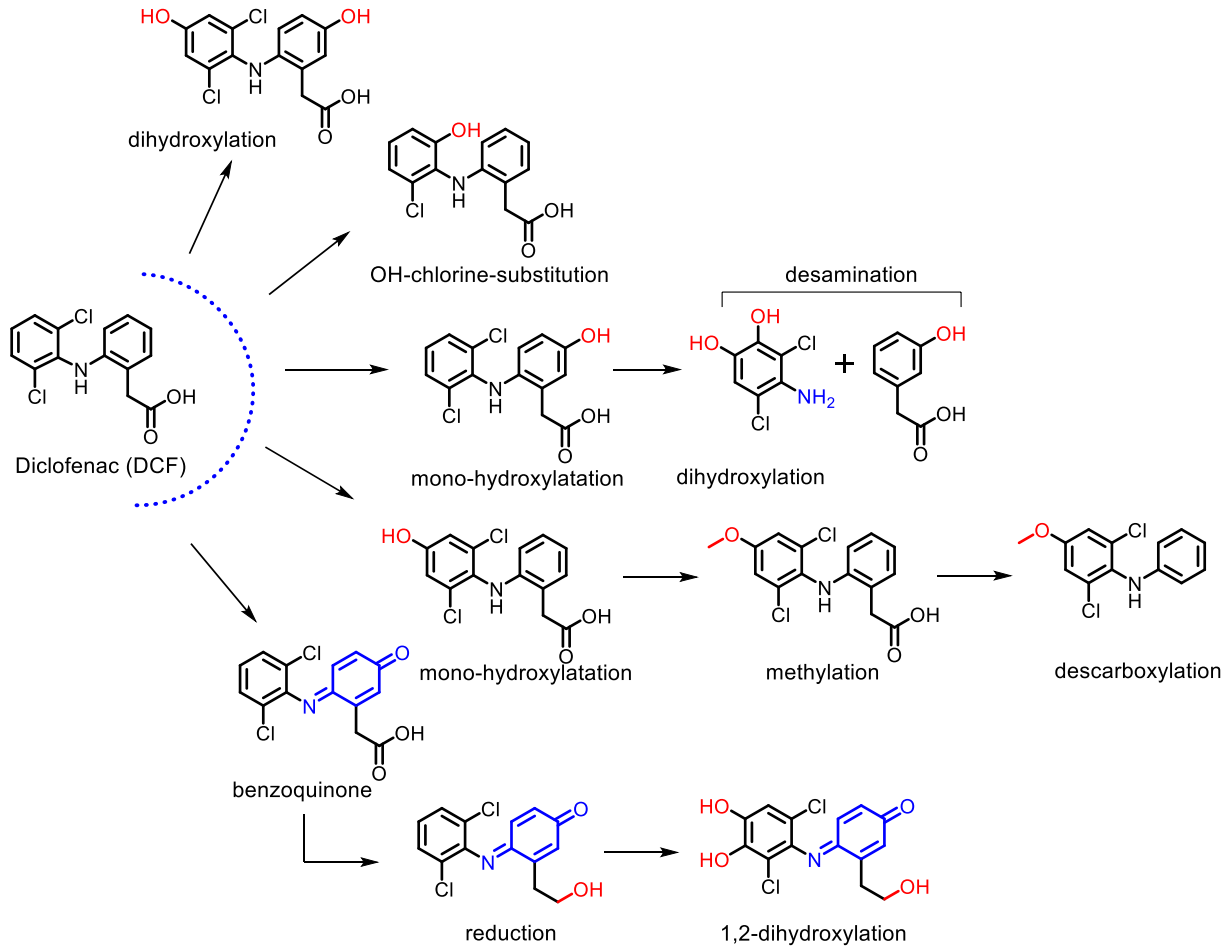

FIGURE 3
Schematic representation of DCF degradation by fungi or bacteria described in the literature (Bessa et al., 2017; Ivshina et al., 2019; Wojcieszyńska et al., 2023).

analyses revealed 22 byproducts and different biodegradation pathways were proposed based on hydroxylation reactions followed by the production of carboxylic acids and ring cleavage. Toxicity to different species and biodegradability prediction were performed using EPI Suite software, and it was concluded that compounds with increased hydrophilic character and reduced toxic effects were obtained (Almeida et al., 2013a; Salgado et al., 2020).

Active microbial cultures was also collected from treatment plants in India for isolation of bacterial IBU-degraders by enrichment culture technique. The identified strain *Bacillus siamensis* DSI-1 was assessed in an effluent sample supplemented with IBU. After 18 h, 50% biodegradation was determined and total removal was achieved in 15 days. The kinetic analysis was performed in batch experiments and optimum conditions were 30°C, pH 7, 165 rpm, and 3.5 mg L^{-1} of IBU initial concentration, reaching 86% of biodegradation and showing that optimization strategies should be employed for the obtention of higher process yields (Table 2, entry 22; Chopra and Kumar, 2022).

Microbacterium paraoxydans Genbank OL614700 and OL614701 (Table 2, entry 23) from an industrial wastewater facility at Durgapur, also at India, were screened in mineral salt medium and employed for IBU biodegradation. An interesting process optimization by central composite design was performed and a maximum biodegradation of 92% was obtained at pH 7, inoculum of 0.1 OD_{600}, 150 rpm, 30°C, and 0.3% yeast extract. It is important to note that the most significant factor for biodegradation were yeast extract content, showing the importance of co-metabolism for enhanced efficiency (Show et al., 2023).

In an omics approach, the use of metagenomic, metatranscriptomic, and metabolic analyses indicated that *Nocardioides carbamazepini* sp. nov. CBZ_1T was a new strain with an interesting ability to biodegrade pharmaceutics, emphasizing carbamazepine and IBU. This biocatalyst presented 70% biodegradation of 1.5 mg.L^{-1} IBU after 7 days in a medium supplemented with glucose (Table 2, entry 24). Therefore, a new strategy was employed with metagenome binning that resulted in a specific biocatalyst of interest, showing a new perspective for biodegradation studies (Benedek et al., 2022).

The enzymatic and genetic aspect of IBU biodegradation was also approached in the biodegradation of IBU by *Sphingomonas* sp. Ibu-2, which was isolated from a sewage treatment plant at Ithaca, United States (Table 2, entry 25). This strain received attention due to its ability to break IBU acid chain to the corresponding catechol. Seven genes (ipfABDEFHI) were identified in the fosmid pFOS3G7 obtained from the chromosomal library of *Sphingomonas* sp. Ibu-2, which

encoded the IBU and phenylacetate deacylation activity subsequently expressed in *E. coli*. These results expanded the knowledge about the genetic and enzymatic aspects of IBU biodegradation, enabling further process efficiency increase (Murdoch and Hay, 2013).

Recently, *Sphingomonas wittichii* MPO218 biodegraded IBU as the sole carbon source. Further exploration showed that this strain genome consisted of a circular chromosome and two circular plasmids. The plasmid pIBU218 presented a region with 100% identity with an IBU catabolic gene cluster previously described (Table 2, entry 26). Moreover, this plasmid was conjugative, enabling the horizontal transfer of the IBU consumption ability to *Sphingopyxis granuli* TFA, showing that gene transfer plays an important role in bacterial communities at biodegradation (Aulestia et al., 2021).

Industrial environments were also explored for the obtention of interesting biocatalysts. For instance, the Gram-positive *Bacillus thuringiensis* B1 was isolated from the soil of a chemical factory in Jaworzno (Poland). This strain biodegraded 20 mg L^{-1} of IBU in 6 days at 30°C using glucose as carbon source (Table 2, entry 27), showing its potential for biodegradation (Marchlewicz et al., 2016).

Marine aphotic environment was also explored for IBU biodegradation in the search for new biocatalysts, including *Pseudoalteromonas* sp. GCY isolated from sediment. Experiments with 1 mg.L^{-1} IBU at 20°C and 150 rpm for 72 h reached about 94% efficiency and five biodegradation products were suggested (Table 2, entry 28). Furthermore, an extensive approach showed that both abiotic and biotic degradation mechanisms occurred by the conversion of IBU by extracellular Reactive Oxygen Species to 4-ethylresorcinol, which was later converted by different intracellular enzymes. These results showed the importance of unifying different experimental data to reach an expanded overview of a biodegradation process (Li et al., 2022).

Extensive screenings of specific groups of strains were employed by some groups for xenobiotics biodegradation. In this regard, 100 actinobacteria strains were assessed, and *Rhodococcus cerastii* IEGM 1278 was selected by the total consumption of 100 mg.L^{-1} IBU after 144 h in the presence of n-hexadecane as alternative carbon source. IBU promoted the transition from the single to the multicellular form of *R. cerastii* IEGM 1278, which was accompanied by pronounced morphological changes in cell shape, size, and surface roughness. Moreover, the six obtained byproducts resulted from hydroxylation and decarboxylation reactions presented higher phytotoxicity than IBU. Thus, indicating a relevant environmental issue during this biodegradation process. In the case of medium supplemented with 100 mg L^{-1} IBU and 0.1% glycerol, *Rhodococcus cerastii* IEGM 1278, *R. cercidiphylli* IEGM 1184, and *R. erythropolis* IEGM 501 promoted 14, 22, and 19% biodegradation, respectively, after 7 days (Table 2, entry 29–31; Ivshina et al., 2021).

In an applied bioremediation approach, the effects of colonization of the arbuscular mycorrhizal fungus (AMF) *Rhizophagus irregularis* BEG140 on the growth and treatment of wetland plants (*Glyceria maxima*) under selective pressure by the presence of IBU were investigated in constructed wetlands. Two treatments were adopted in 52 days of reaction, sterilized inoculum and fungal inoculum, in which the removal efficiencies of 0.5 mg L^{-1} IBU were 74–87 and 88–93% (Table 2, entry 32), respectively. Therefore, bioaugmentation promoted a slight increase in IBU biodegradation rates (Hu et al., 2021).

Some studies reported the isolation and identification of IBU-biodegrading strains of bacteria, also approaching biodegradation pathways. However, few research groups have been performing integrative omics approaches, including genomic and metabolomics assessments aiming at deeper knowledge about the biodegradation of IBU, which is an extensively employed pharmaceutical and micropollutant. Furthermore, the potential of fungi for biodegradation of this compound is unknown, since an adequate number of studies are required for the obtention of wider conclusions.

Figure 4 shows IBU different biodegradation pathways, including the formation of isobutylbenzene, 2-(2-hydroxy-4-isobutylphenyl) propanoic acid, and 3-(4-(1-carboxyethyl)phenyl)-2-methylpropanoic acid, which were produced in the first step of degradation. Furthermore, the formation of 2-(4-formyl-2-hydroxyphenyl) propanoic acid can be observed, as well as other byproducts that results from decarboxylation and dehydrogenation reactions (Salgado et al., 2020; Li et al., 2022).

7. Biodegradation of paracetamol

Paracetamol or acetaminophen (*N*-acetyl-*para*-aminophenol, PAR) is an analgesic and antipyretic drug available in the form of tablet and oral suspension, its physicochemical properties are presented in Table 1. This pharmaceutical is administered orally and 90% of the dose is metabolized in the liver producing 5–15% of the hydroxylated product *N*-acetyl-*p*-benzoquinone imine by the enzyme cytochrome P-450, and the elimination of 5% through the kidneys in unchanged form (Wojcieszyńska et al., 2022).

Due to its large-scale use, this drug can be found in different environments, especially in water bodies. Regarding this, it is noteworthy that PAR is bioaccumulative in aquatic organisms and may induce reproductive and neurotoxic disorders (Vargas-Ordóñez et al., 2023). Therefore, this compound was considered an emerging pollutant that requires environmentally safe strategies for its removal.

Microorganisms, mainly bacteria, have been reported as efficient biocatalysts for PAR biodegradation in different environmental matrices, in which the most frequently detected products are 4-aminophenol, hydroquinone, 2-hexenoic acid, succinic acid, malonic acid, oxalic acid, formic acid, nitrate, and nitrite. However, the first step in PAR biodegradation is the cleavage of the amide bond by an amidase to produce 4-aminophenol and acetate (Figure 5; Hu et al., 2013).

The screening of bacterial strains has been an important tool for PAR biodegradation. For instance, 17 bacterial strains were isolated from the sewage of a Wastewater Treatment Plant (WWTP) in Seville (Spain), but only two of them (*Pseudomonas stutzeri* CSW02 and *Pseudomonas extremoustralis* CSW01) biodegraded high concentrations of PAR as sole carbon and energy source. The process reached 100% degradation at 500 mg L^{-1} PAR, 150 rpm, and 30°C for 6 h, showing the high efficiency of these strains (Table 2, entry 33 and 34, respectively; Vargas-Ordóñez et al., 2023).

In another study, several bacterial strains were isolated from wastewater at a pharmaceutical company in Gujarat (India). Recently, tests with *Pseudomonas* sp. PrS10 showed high biodegradation efficiency with removal of 96% of 3 g L^{-1} PAR at 30°C and 140 rpm for 7 days of reaction (Table 2, entry 35). Furthermore, experiments

indicated that both cell surface absorption and internalization of PAR were relevant processes (Poddar et al., 2022).

Wastewater treatment plants were the most explored source of biocatalysts for PAR biodegradation. Thus, six new bacterial strains isolated from activated sludge at the Klimzowiec wastewater treatment plant (Chorzów, Poland) removed PAR. *Pseudomonas moorei* KB4 was the most efficient strain in the initial concentration of 50 mg L^{-1} PAR at 30°C and pH 7.0 for 1.5 h (Table 2, entry 36). In addition, the biodegradation products *p*-aminophenol and hydroquinone were identified (Żur et al., 2018a), then, the hydroquinone aromatic ring might have been cleaved to 4-hydroxymuconic semialdehyde (Figure 5). Furthermore, this study showed that the concentrations of aromatic metabolites (phenol, 4-hydroxybenzoate, 4-chlorophenol, and 2-chlorophenol) were observed for a longer period than PAR, whereas aminophenol fast disappearing was determined. Indicating that these substrates may compete with the same enzymes, a phenomenon frequently observed during the degradation of aromatic compounds (Guzik et al., 2014).

Bacterial communities isolated from sludge of two Portuguese WWTPs were explored for PAR biodegradation under different media and oxygen conditions. Aerobic bacteria completely removed PAR in wastewater at a concentration of 50 mg L^{-1} after 2 days of incubation with aeration, and the metabolites 4-aminophenol and hydroquinone were identified as PAR degradation products. These results revealed that *Pseudomonas*, initially in 0.1%, reached the final relative abundance of 21.2% during the biodegradation process, confirming previous works reporting strains of this genus as paracetamol decomposers. Besides, the genera *Flavobacterium*, *Dokdonella,* and *Methylophilus* also deserve to be highlighted, since the initial relative abundances of 1.7%, 1.5 and 0.0% (not detected) in the inoculum reached 6.9, and 3.8 and 3.8% after incubation, respectively. Indicating the putative role of these genera in paracetamol biodegradation (Table 2, entry 37; Palma et al., 2018).

Still approaching the pseudomonas genus, three bacterial strains (*Pseudomonas* sp. f2, *Pseudomonas* sp. fg-2, and *Stenotrophomonas* sp. f1) were isolated from a PAR degrading aerobic aggregate using this drug as a unique source of energy. Complete biodegradation was observed for initial concentrations of 2.000 mg L^{-1} PAR after 70 h, 2.500 mg L^{-1} after 45 h, and 2.000 mg L^{-1} after 16 h at 30°C, showing the high efficiency and potential of these strains (Table 2, entry 38–40). Furthermore, the metabolites 4-aminophenol and hydroquinone were detected (Zhang et al., 2013).

The species *Pseudomonas aeruginosa* HJ1012 isolated from a stable microbial aggregate in a sequential batch reactor was also employed for PAR removal. Complete biodegradation of this active ingredient was obtained after 18 h at pH 7.0 and 30°C with an initial concentration of 2.200 mg L^{-1} (Table 2, entry 41). The consumption of PAR by *Pseudomonas aeruginosa* HJ1012 generated 71.4% of CO_2, showing that consumption occurred *via* mineralization (Hu et al., 2013).

Recently bacterial strains obtained from an oxidation ditch of a WWTP in Faro Norwest (Portugal) consumed PAR as carbon source. Strains were selected and *Bacillus cereus*, *Corynebacterium nuruki* and *Enterococcus faecium* removed 97 ± 4, 97 ± 6, and 87% PAR, respectively, at an initial concentration of 200 mg L^{-1} after 48 h at 28°C (Table 2, entry 42). Furthermore, the metabolites 4-aminophenol, hydroquinone, and 2-hexenoic acid were identified in this process, bringing new insights into the environmental fate of this drug (Palma et al., 2021).

In another study, *Bacillus drentensis* S1 obtained from sewage of a wastewater drainage in Sonipat (India) was employed in an experimental design in a 20 L batch reactor resulting in an increase from 28 to 93% of PAR removal in the optimized experimental

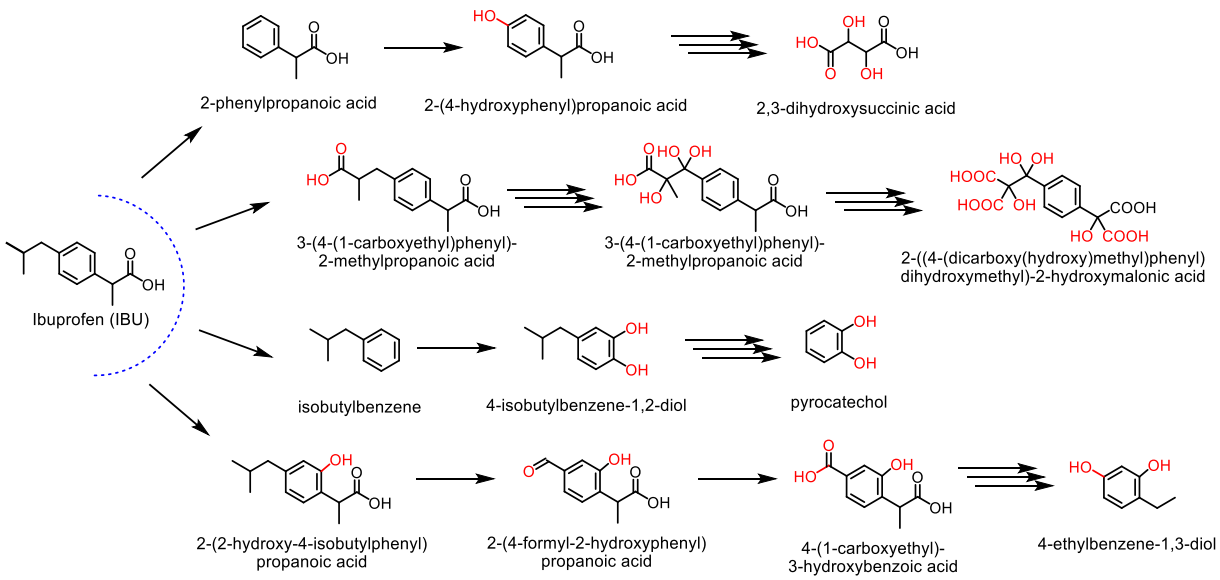

FIGURE 4
Some metabolites of IBU degradation from fungi or bacteria are described in the literature (Salgado et al., 2020; Li et al., 2022).

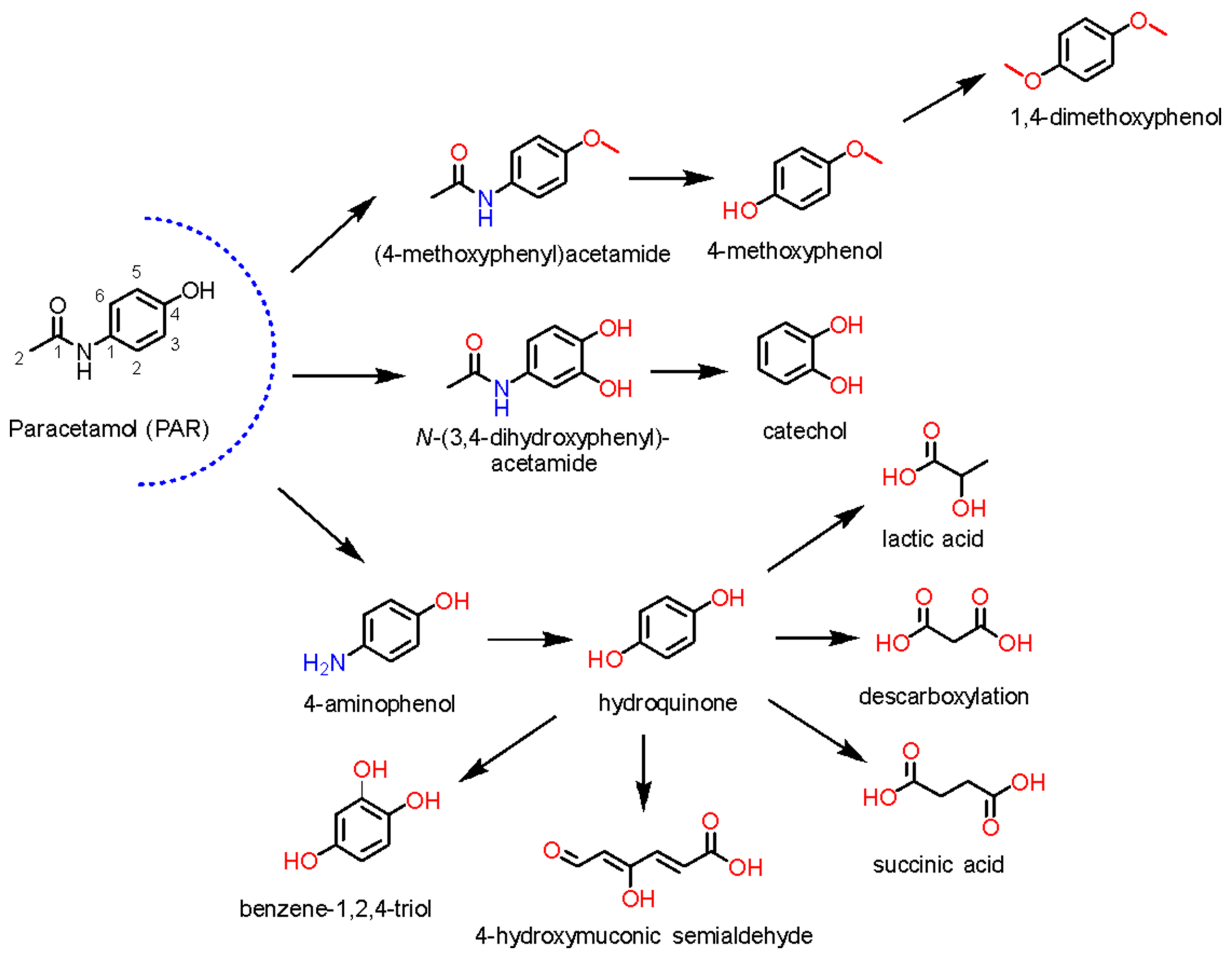

FIGURE 5
Some PAR metabolites from fungi or bacteria are described in the literature (Żur et al., 2018a; Rios-Miguel et al., 2022).

conditions of pH 7.0, 40°C, and 165 rpm and PAR initial concentration of 300 mg L^{-1}, showing that different factors can affect this biodegradation process (Table 2, entry 43; Chopra and Kumar, 2020).

Pharmaceutical industrial wastewater was also explored for PAR biodegradation. *Micrococcus yunnanensis* KGP04 was isolated for PAR biodegradation processes from sludge collected at the Vishwakarma industrial area (India). Removal of 43% was achieved in the initial screening and, after applying a Taguchi L8 experimental design for optimization, a biodegradation of 83% was obtained in optimized conditions [dextrose-0.15%, peptone 0.1%, inoculum size 4% (w v^{-1}), rpm 200, pH 8 at 25°C] after 6 h (Table 2, entry 44). Moreover, the biodegradation products were explored using nuclear magnetic resonance and Q-Tof spectrometry, aiming at expanding the knowledge about the fate of this drug in the environment (Sharma et al., 2020).

Another strain from the same species was employed in another PAR biodegradation study. *Micrococcus yunnanensis* strain TJPT4 was isolated from consortia of marine organisms collected at Catedral and Queijo Suijo marine caves (Sagres, Portugal). This strain showed high biodegradation capacity with 93% removal of 15 mg L^{-1} PAR after 360 h (Table 2, entry 45), also consuming the obtained metabolites. Therefore, promoting a cleaner residual medium (Palma et al., 2022).

A diverse microbial community obtained from a hospital WWTP enriched under low PAR concentrations in a membrane bioreactor was also approached, and two bacterial strains were isolated. A fast-growing *Pseudomonas* sp. that biodegraded 200 mg L^{-1} PAR in approximately 10 h producing 4-aminophenol, and a slow-growing *Pseudomonas* sp. that degraded PAR without obvious intermediates in more than 90 days were obtained. In addition, the metabolites 4-aminophenol, hydroquinone, hydroxyquinol, 4-hydroxymuconic semialdehyde, 2,5-dihydroxy-6-oxo-2,4-hexadienoic acid, and 3-hydroxy-2,4-hexadienedioic acid were identified as biodegradation products of PAR, expanding the available information about the biodegradation pathways of these compounds (Figure 5; Rios-Miguel et al., 2022).

Fungi strains were also employed for PAR biodegradation. *Aspergillus niger* and *Fusarium oxysporium* isolated from wastewater of a pharmaceutical industry located in Sana'a (Yemen) were assessed. The optimized conditions were 25°C and pH 6.0 for both species with 37% biodegradation for *A. niger* with an initial concentration of 2000 mg L^{-1} and 26% for *F. oxysporium* with an initial concentration

of 1,000 mg L^{-1} after 60 days of reaction, indicating that fungi strains can also be employed as biodegradation agents in PAR biodegradation processes (Table 2, entry 46 and 47; Sana, 2018).

Therefore, PAR can be degraded by different microorganisms, although bacteria were better explored than fungi for this purpose. Furthermore, the biodegradation of the obtained aromatic products includes hydroxylation reactions and cleavage of the aromatic ring, in general catalyzed by dioxygenases and monooxygenases. The main intermediates such as catechol, hydroquinone, 4-methoxyphenol, succinic, and lactic acid are formed as a result of these enzymatic hydroxylations (Rios-Miguel et al., 2022).

Many research groups focused their studies on optimizing the biodegradation process by different parameters, such as pH, temperature, oxygen availability, and nutrient supply, in interesting experiments that focused on the understanding how environmental factors influence efficiency. Regarding this, the obtained conditions were usually specific for each employed biocatalysts, but in general, extreme conditions jeopardized the process consumption rate. Furthermore, some results indicated that ideal conditions for strain growth and development can be an interesting starting point in terms of pH, temperature and oxygen supply, although the use of nutrient rich media or xenobiotics as sole carbon source can depend on the employed biocatalyst, since this ability to biodegrading these compounds as unique carbon source can be absent and other approaches should be employed for increased performance (Żur et al., 2018a).

In this context, tools from molecular biology should also be employed for obtaining increased efficiency, including characterization of microbial communities and identification of genus and species involved in high efficiency processes, as well as their relationships. Furthermore, omics approaches are necessary for a better comprehension of the genetic, enzymatic, and metabolic aspects involved in these reactions, since a comprehensive approach is necessary for the obtention of a process overview. Thus, these strategies could be employed in integration with previous studies in the development of applied technologies, especially for areas with increased NSAIDs at wastewater, as can occur at the surroundings of hospitals, clinics, and industrial plants.

8. Conclusion and future directions

Microbial degradation processes are a great alternative for the biodegradation of NSAIDs, especially using selected strains isolated from contaminated environments. Moreover, extensive studies about biodegradation pathways are required for the determination of the fate of these compounds, including the knowledge about enzymes and genes involved in these processes.

An increase in the amount of non-steroidal anti-inflammatory drugs, especially DCF, IBU, and PAR, present in domestic and hospital sewers was expected from the consumption of the population in the treatment of COVID-19-driven infections, resulting in aggravated environmental impact. Moreover, the consequences of NSAIDs should not be considered individually for each active ingredient, since complex mixtures and combinations with other xenobiotics can greatly enhance their impacts on nature and human health.

The growth of microbial degradation studies applied to NSAIDs mostly conducted with bacteria is remarkable, but the ecotoxicological consequences of biodegradation products are still unknown. Therefore, some topics require extensive advances, such as systematic monitoring of NSAIDs and its biodegradation products at *in vivo* models. Furthermore, studies addressing the effect of biodegradation products with mixtures of other active ingredients related to the treatment of different diseases, including COVID-19, are essential. Also, assessment on cost-performance and energetic efficiency of different degradation methods should be addressed.

It is important to emphasize the use of molecular biology for characterization of microbial communities integrated with omics tools for revealing the genetic, enzymatic and metabolic aspects behind these processes are desired, and should be in the mind of research groups. In addition to the selection and use of highly efficient strains for the development of applied technologies.

Therefore, the development of alternatives to minimize the increasing pollution promoted by the incorrect disposal, human excretion, or production activity of NSAIDs and related compounds will be essential for maintaining a healthy ecosystem and life.

Author contributions

BF, DF, SB, AF, FH, and JU-F: methodology, validation, investigation, data curation, and writing—original draft. WB, RL, and IF: conceptualization, supervision, writing—review and editing, and methodology.

Funding

The authors would like to acknowledge the *Fundação de Amparo à Pesquisa do Estado do Amapá* (FAPEAP); grant no. 88887.568501/2020-00 and the *Coordenação de Aperfeiçoamento de Pessoal de Nível Superior* (CAPES) grant no. 88881.716142/2022-01 for financial support. WB thanks the Brazilian Ministry of Health for his post-doctoral fellowship, grant no. 879335/2018. BF and IF thank for the scholarships financed *Coordenação de Aperfeiçoamento de Pessoal de Nível Superior* (CAPES) grant nos. 88887.637671/2021-00 (PDPG) and 88881.716142/2022-01 (PROCAD-AMAZONIA-DRI), respectively.

Conflict of interest

The authors declare that the research was conducted in the absence of any commercial or financial relationships that could be construed as a potential conflict of interest.

Publisher's note

References

Aguilar-Romero, I., De la Torre-Zúñiga, J., Quesada, J. M., Haïdour, A., O'Connell, G., McAmmond, B. M., et al. (2021). Effluent decontamination by the ibuprofen-mineralizing strain, *Sphingopyxis granuli* RW412: metabolic processes. *Environ. Pollut.* 274:116536. doi: 10.1016/J.ENVPOL.2021.116536

Ajibola, A. S., Adebiyi, A. O., Nwaeke, D. O., Ajibola, F. O., and Adewuyi, G. O. (2021). Analysis, occurrence and ecological risk assessment of diclofenac and ibuprofen residues in wastewater from three wastewater treatment plants in South-Western Nigeria. *J. Appl. Sci. Environ. Manag.* 25, 330–340. doi: 10.4314/jasem.v25i3.5

Almeida, B., Kjeldal, H., Lolas, I., Knudsen, A. D., Carvalho, G., Nielsen, K. L., et al. (2013a). Quantitative proteomic analysis of ibuprofen-degrading Patulibacter sp. strain I11. *Biodegradation* 24, 615–630. doi: 10.1007/s10532-012-9610-5

Almeida, B., Oehmen, A., Marques, R., Brito, D., Carvalho, G., and Barreto Crespo, M. T. (2013b). Modelling the biodegradation of non-steroidal anti-inflammatory drugs (497s) by activated sludge and a pure culture. *Bioresour. Technol.* 133, 31–37. doi: 10.1016/J.BIORTECH.2013.01.035

Almeida, B., Vaz-Moreira, I., Schumann, P., Nunes, O. C., Carvalho, G., and Crespo, M. T. B. (2013c). Patulibacter medicamentivorans sp. nov., isolated from activated sludge of a wastewater treatment plant. *Int. J. Syst. Evol. Microbiol.* 63, 2588–2593. doi: 10.1099/ijs.0.047522-0

Aracagök, Y. D., Göker, H., and Cihangir, N. (2018). Biodegradation of diclofenac with fungal strains. *Archiv. Environ. Protect.* 1, 55–62. doi: 10.24425/118181

Aria, M., and Cuccurullo, C. (2017). Bibliometrix: an R-tool for comprehensive science mapping analysis. *J. Inf. Secur.* 11, 959–975. doi: 10.1016/j.joi.2017.08.007

Aulestia, M., Flores, A., Mangas, E. L., Pérez-Pulido, A. J., Santero, E., and Camacho, E. M. (2021). Isolation and genomic characterization of the ibuprofen-degrading bacterium Sphingomonas strain MPO218. *Environ. Microbiol.* 23, 267–280. doi: 10.1111/1462-2920.15309

Austin, T., Bregoli, F., Höhne, D., Hendriks, A. J., and Ragas, A. M. J. (2022). Ibuprofen exposure in Europe; ePiE as an alternative to costly environmental monitoring. *Environ. Res.* 209:112777. doi: 10.1016/j.envres.2022.112777

Austin, T. J., Comber, S., Forrester, E., Gardner, M., Price, O. R., Oldenkamp, R., et al. (2021). The importance of over-the-counter-sales and product format in the environmental exposure assessment of active pharmaceutical ingredients. *Sci. Total Environ.* 752:141624. doi: 10.1016/j.scitotenv.2020.141624

Badri, W., Miladi, K., Nazari, Q. A., Greige-Gerges, H., Fessi, H., and Elaissari, A. (2016). Encapsulation of NSAIDs for inflammation management: overview, progress, challenges and prospects. *Int. J. Pharm.* 515, 757–773. doi: 10.1016/j.ijpharm.2016.11.002

Banerjee, S., and Maric, F. (2023). Mitigating the environmental impact of NSAIDs—physiotherapy as a contribution to one health and the SDGs. *Eur. J. Phys.* 25, 51–55. doi: 10.1080/21679169.2021.1976272

Bankole, P. O., Adekunle, A. A., Jeon, B.-H., and Govindwar, S. P. (2020). Novel cobiomass degradation of NSAIDs by two wood rot fungi, Ganoderma applanatum and Laetiporus sulphureus: ligninolytic enzymes induction, isotherm and kinetic studies. *Ecotoxicol. Environ. Saf.* 203:110997. doi: 10.1016/j.ecoenv.2020.110997

Barcelo, D. (2020). An environmental and health perspective for COVID-19 outbreak: meteorology and air quality influence, sewage epidemiology indicator, hospitals disinfection, drug therapies and recommendations. *J. Environ. Chem. Eng.* 8:104006. doi: 10.1016/j.jece.2020.104006

Benedek, T., Pápai, M., Gharieb, K., Bedics, A., Táncsics, A., Tóth, E., et al. (2022). Nocardioides carbamazepini sp. nov., an ibuprofen degrader isolated from a biofilm bacterial community enriched on carbamazepine. *Syst. Appl. Microbiol.* 45:126339. doi: 10.1016/J.SYAPM.2022.126339

Bessa, V. S., Moreira, I. S., Tiritan, M. E., and Castro, P. M. L. (2017). Enrichment of bacterial strains for the biodegradation of diclofenac and carbamazepine from activated sludge. *Int. Biodeterior. Biodegradation* 120, 135–142. doi: 10.1016/j.ibiod.2017.02.008

Borges, R. S., Lima, E. S., Keita, H., Ferreira, I. M., Fernandes, C. P., Cruz, R. A. S., et al. (2018). Anti-inflammatory and antialgic actions of a nanoemulsion of *Rosmarinus officinalis* L. essential oil and a molecular docking study of its major chemical constituents. *Inflammopharmacology* 26, 183–195. doi: 10.1007/s10787-017-0374-8

Brandt, M. D., Ghozy, S. A., Kallmes, D. F., McDonald, R. J., and Kadirvel, R. D. (2022). Comparison of citation rates between COVID-19 and non-COVID-19 articles across 24 major scientific journals. *PLoS One* 17, 1–8. doi: 10.1371/journal.pone.0271071

Chen, M., Yu, L., Gu, C., Zhong, D., Wu, S., and Liu, S. (2013). Celecoxib antagonizes the cytotoxic effect of cisplatin in human gastric cancer cells by decreasing intracellular cisplatin accumulation. *Cancer Lett.* 329, 189–196. doi: 10.1016/j.canlet.2012.10.030

Chen, N., Zhou, M., Dong, X., Qu, J., Gong, F., Han, Y., et al. (2020). Epidemiological and clinical characteristics of 99 cases of 2019 novel coronavirus pneumonia in Wuhan, China: a descriptive study. *Lancet* 395, 507–513. doi: 10.1016/S0140-6736(20)30211-7

Cheng, S.-C., Chang, Y.-C., Fan Chiang, Y.-L., Chien, Y.-C., Cheng, M., Yang, C.-H., et al. (2020). First case of coronavirus disease 2019 (COVID-19) pneumonia in Taiwan. *J. Formos. Med. Assoc.* 119, 747–751. doi: 10.1016/j.jfma.2020.02.007

Chopra, S., and Kumar, D. (2020). Characterization, optimization and kinetics study of acetaminophen degradation by *Bacillus drentensis* strain S1 and waste water degradation analysis. *Bioresour. Bioprocess* 7:9. doi: 10.1186/s40643-020-0297-x

Chopra, S., and Kumar, D. (2022). Characterization and biodegradation of ibuprofen by *Bacillus siamensis* strain DSI-1 isolated from wastewater. *Rendiconti Lincei* 33, 643–652. doi: 10.1007/s12210-022-01085-6

Conejo-Saucedo, U., Ledezma-Villanueva, A., Ángeles de Paz, G., Herrero-Cervera, M., Calvo, C., and Aranda, E. (2021). Evaluation of the potential of sewage sludge mycobiome to degrade high diclofenac and bisphenol-a concentrations. *Toxics* 9:115. doi: 10.3390/toxics9060115

Davies, N. M. (1998). Clinical pharmacokinetics of ibuprofen. *Clin. Pharmacokinet.* 34, 101–154. doi: 10.2165/00003088-199834020-00002

Davis, S. N., Wu, P., Camci, E. D., Simon, J. A., Rubel, E. W., and Raible, D. W. (2020). Chloroquine kills hair cells in zebrafish lateral line and murine cochlear cultures: implications for ototoxicity. *Hear. Res.* 395:108019. doi: 10.1016/j.heares.2020.108019

de Almeida, J. O., de Oliveira, V. R. T., dos Lucas, S. A. J., Simões Moita, B., Moreira Lima, L., Moita, B. S., et al. (2020). COVID-19: physiopathology and targets for therapeutic intervention. *Rev. Virtual Quim.* 12, 1464–1497. doi: 10.21577/1984-6835.20200115

DeLorenzo, M. E., and Fleming, J. (2008). Individual and mixture effects of selected pharmaceuticals and personal care products on the marine phytoplankton species *Dunaliella tertiolecta*. *Arch. Environ. Contam. Toxicol.* 54, 203–210. doi: 10.1007/s00244-007-9032-2

Facey, S. J., Nebel, B. A., Kontny, L., Allgaier, M., and Hauer, B. (2018). Rapid and complete degradation of diclofenac by native soil microorganisms. *Environ. Technol. Innov.* 10, 55–61. doi: 10.1016/J.ETI.2017.12.009

Feehan, K. T., and Gilroy, D. W. (2019). Is resolution the end of inflammation? *Trends Mol. Med.* 25, 198–214. doi: 10.1016/j.molmed.2019.01.006

Fent, K., Weston, A. A., and Caminada, D. (2006). Ecotoxicology of human pharmaceuticals. *Aquat. Toxicol.* 76, 122–159. doi: 10.1016/j.aquatox.2005.09.009

Gong, H., Chu, W., Huang, Y., Xu, L., Chen, M., and Yan, M. (2021). Solar photocatalytic degradation of ibuprofen with a magnetic catalyst: effects of parameters, efficiency in effluent, mechanism and toxicity evolution. *Environ. Pollut.* 276:16691. doi: 10.1016/j.envpol.2021.116691

Grandclément, C., Piram, A., Petit, M.-E., Seyssiecq, I., Laffont-Schwob, I., Vanot, G., et al. (2020). Biological removal and fate assessment of diclofenac using Bacillus subtilis and *Brevibacillus laterosporus* strains and ecotoxicological effects of diclofenac and 4′-hydroxy-diclofenac. *J. Chemother.* 2020, 1–12. doi: 10.1155/2020/9789420

Gu, Y., Huang, J., Zeng, G., Shi, L., Shi, Y., and Yi, K. (2018). Fate of pharmaceuticals during membrane bioreactor treatment: status and perspectives. *Bioresour. Technol.* 268, 733–748. doi: 10.1016/j.biortech.2018.08.029

Guzik, U., Hupert-Kocurek, K., Krysiak, M., and Wojcieszyńska, D. (2014). Degradation potential of protocatechuate 3,4-dioxygenase from crude extract of *Stenotrophomonas maltophilia* strain KB2 immobilized in calcium alginate hydrogels and on Glyoxyl agarose. *Biomed. Res. Int.* 2014:138768. doi: 10.1155/2014/138768

Holanda, F. H., Ribeiro, A. N., Sánchez-Ortiz, B. L., de Souza, G. C., Borges, S. F., Ferreira, A. M., et al. (2023). Anti-inflammatory potential of baicalein combined with silk fibroin protein in a zebrafish model (*Danio rerio*). *Biotechnol. Lett.* 45, 235–253. doi: 10.1007/s10529-022-03334-y

Hu, B., Hu, S., Chen, Z., and Vymazal, J. (2021). Employ of arbuscular mycorrhizal fungi for pharmaceuticals ibuprofen and diclofenac removal in mesocosm-scale constructed wetlands. *J. Hazard. Mater.* 409:124524. doi: 10.1016/J.JHAZMAT.2020.124524

Hu, J., Zhang, L. L., Chen, J. M., and Liu, Y. (2013). Degradation of paracetamol by *Pseudomonas aeruginosa* strain HJ1012. *J. Environ. Sci. Health A Tox. Hazard. Subst. Environ. Eng.* 48, 791–799. doi: 10.1080/10934529.2013.744650

Huntjens, D. R. H., Danhof, M., and Della Pasqua, O. E. (2005). Pharmacokinetic–pharmacodynamic correlations and biomarkers in the development of COX-2 inhibitors. *Rheumatology* 44, 846–859. doi: 10.1093/rheumatology/keh627

Ivshina, I. B., Tyumina, E. A., Bazhutin, G. A., and Vikhareva, E. V. (2021). Response of Rhodococcus cerastii IEGM 1278 to toxic effects of ibuprofen. *PLoS One* 16:e0260032. doi: 10.1371/journal.pone.0260032

Ivshina, I. B., Tyumina, E. A., Kuzmina, M. V., and Vikhareva, E. V. (2019). Features of diclofenac biodegradation by *Rhodococcus ruber* IEGM 346. *Sci. Rep.* 9:9159. doi: 10.1038/s41598-019-45732-9

Jurado, A., Vázquez-Suñé, E., and Pujades, E. (2021). Urban groundwater contamination by non-steroidal anti-inflammatory drugs. *Water* 13:720. doi: 10.3390/w13050720

Kantor, T. G. (1984). Summary: ibuprofen—past, present, and future. *Am. J. Med.* 77, 121–125. doi: 10.1016/S0002-9343(84)80030-3

Khasawneh, O. F. S., and Palaniandy, P. (2021). Occurrence and removal of pharmaceuticals in wastewater treatment plants. *Process. Saf. Environ. Prot.* 150, 532–556. doi: 10.1016/j.psep.2021.04.045

Kumari, M., and Kumar, A. (2022). Environmental and human health risk assessment of mixture of Covid-19 treating pharmaceutical drugs in environmental waters. *Sci. Total Environ.* 812, 1–10. doi: 10.1016/j.scitotenv.2021.152485

Li, Z., Wang, J., Gu, C., Guo, Y., and Wu, S. (2022). Marine bacteria-mediated abiotic-biotic coupling degradation mechanism of ibuprofen. *J. Hazard. Mater.* 435:128960. doi: 10.1016/J.JHAZMAT.2022.128960

Lucas, F. M. F., Araujo, E. C. G., Fiedler, N. C., da Silva Santana, J. A., and Tetto, A. F. (2023). Perspective: scientific gaps on forest fires in Brazilian protected areas. *For. Ecol. Manag.* 529:120739. doi: 10.1016/j.foreco.2022.120739

Luis López-Miranda, J., Molina, G. A., Esparza, R., Alexis González-Reyna, M., Silva, R., and Estévez, M. (2022). Ecofriendly and sustainable Sargassum spp.-based system for the removal of highly used drugs during the COVID-19 pandemic. *Arab. J. Chem.* 15, 1–15. doi: 10.1016/j.arabjc.2022.104169

Maculewicz, J., Kowalska, D., Świacka, K., Tański, M., Stepnowski, P., Białk-Bielińska, A., et al. (2022). Transformation products of pharmaceuticals in the environment: their fate, (eco)toxicity and bioaccumulation potential. *Sci. Total Environ.* 802, 1–31. doi: 10.1016/j.scitotenv.2021.149916

Marchlewicz, A., Domaradzka, D., Guzik, U., and Wojcieszyńska, D. (2016). *Bacillus thuringiensis* B1(2015) is a gram-positive Bacteria able to degrade naproxen and ibuprofen. *Water Air Soil Pollut.* 227:197. doi: 10.1007/s11270-016-2893-0

Markov, P. V., Ghafari, M., Beer, M., Lythgoe, K., Simmonds, P., Stilianakis, N. I., et al. (2023). The evolution of SARS-CoV-2. *Nat. Rev. Microbiol.* 21, 361–379. doi: 10.1038/s41579-023-00878-2

Micallef, J., Soeiro, T., and Jonville-Béra, A. P. (2020). Non-steroidal anti-inflammatory drugs, pharmacology, and COVID-19 infection. *Therapies* 75, 355–362. doi: 10.1016/j.therap.2020.05.003

Moreira, I. S., Bessa, V. S., Murgolo, S., Piccirillo, C., Mascolo, G., and Castro, P. M. L. (2018). Biodegradation of diclofenac by the bacterial strain *Labrys portucalensis* F11. *Ecotoxicol. Environ. Saf.* 152, 104–113. doi: 10.1016/j.ecoenv.2018.01.040

Murdoch, R. W., and Hay, A. G. (2013). Genetic and chemical characterization of ibuprofen degradation by Sphingomonas Ibu-2. *Microbiology* 159, 621–632. doi: 10.1099/mic.0.062273-0

Murshid, S., and Dhakshinamoorthy, G. P. (2019). Biodegradation of sodium diclofenac and mefenamic acid: kinetic studies, identification of metabolites and analysis of enzyme activity. *Int. Biodeterior. Biodegradation* 144:104756. doi: 10.1016/J.IBIOD.2019.104756

Olicón-Hernández, D. R., Camacho-Morales, R. L., Pozo, C., González-López, J., and Aranda, E. (2019). Evaluation of diclofenac biodegradation by the ascomycete fungus penicillium oxalicum at flask and bench bioreactor scales. *Sci. Total Environ.* 662, 607–614. doi: 10.1016/J.SCITOTENV.2019.01.248

Omotola, E. O., and Olatunji, O. S. (2020). Quantification of selected pharmaceutical compounds in water using liquid chromatography-electrospray ionisation mass spectrometry (LC-ESI-MS). *Heliyon* 6:e05787. doi: 10.1016/j.heliyon.2020.e05787

Osafo, N., Agyare, C., Obiri, D. D., and Antwi, A. O. (2017). "Mechanism of action of nonsteroidal anti-inflammatory drugs" in *Nonsteroidal Anti-Inflammatory Drugs*. ed. A. G. A. Al-kaf (Rijeka: Intech Open)

Oscanoa, T. J., Romero-Ortuno, R., Carvajal, A., and Savarino, A. (2020). A pharmacological perspective of chloroquine in SARS-CoV-2 infection: an old drug for the fight against a new coronavirus? *Int. J. Antimicrob. Agents* 56, 1–16. doi: 10.1016/j.ijantimicag.2020.106078

Palma, T. L., Donaldben, M. N., Costa, M. C., and Carlier, J. D. (2018). Putative role of Flavobacterium, Dokdonella and Methylophilus strains in paracetamol biodegradation. *Water Air Soil Pollut.* 229:200. doi: 10.1007/s11270-018-3858-2

Palma, T. L., Magno, G., and Costa, M. C. (2021). Biodegradation of paracetamol by some gram-positive bacterial isolates. *Curr. Microbiol.* 78, 2774–2786. doi: 10.1007/s00284-021-02543-4

Palma, T., Valentine, J., Gomes, V., Faleiro, M., and Costa, M. (2022). Batch studies on the biodegradation potential of paracetamol, fluoxetine and 17α-Ethinylestradiol by the *Micrococcus yunnanensis* strain TJPT4 recovered from marine organisms. *WaterSA* 14:3365. doi: 10.3390/w14213365

Peesa, J. P., Yalavarthi, P. R., Rasheed, A., and Mandava, V. B. R. (2016). A perspective review on role of novel NSAID prodrugs in the management of acute inflammation. *J. Acute Dis.* 5, 364–381. doi: 10.1016/j.joad.2016.08.002

Perico, N., Cortinovis, M., Suter, F., and Remuzzi, G. (2023). Home as the new frontier for the treatment of COVID-19: the case for anti-inflammatory agents. *Lancet Infect. Dis.* 23, 22–33. doi: 10.1016/S1473-3099(22)00433-9

Poddar, K., Sarkar, D., Chakraborty, D., Patil, P. B., Maity, S., and Sarkar, A. (2022). Paracetamol biodegradation by Pseudomonas strain PrS10 isolated from pharmaceutical effluents. *Int. Biodeterior. Biodegradation* 175:105490. doi: 10.1016/J.IBIOD.2022.105490

Pomati, F., Netting, A. G., Calamari, D., and Neilan, B. A. (2004). Effects of erythromycin, tetracycline and ibuprofen on the growth of Synechocystis sp. and Lemna minor. *Aquat. Toxicol.* 67, 387–396. doi: 10.1016/j.aquatox.2004.02.001

R Core Team (2021). R: A language and environment for statistical computing. Available at: https://www.r-project.org/

Rastogi, A., Tiwari, M. K., and Ghangrekar, M. M. (2021). A review on environmental occurrence, toxicity and microbial degradation of non-steroidal anti-inflammatory drugs (NSAIDs). *J. Environ. Manag.* 300:113694. doi: 10.1016/J.JENVMAN.2021.113694

Ren, Z., Romar, H., Varila, T., Xu, X., Wang, Z., Sillanpää, M., et al. (2021). Ibuprofen degradation using a co-doped carbon matrix derived from peat as a peroxymonosulphate activator. *Environ. Res.* 193:110564. doi: 10.1016/J.ENVRES.2020.110564

Rios-Miguel, A. B., Smith, G. J., Cremers, G., van Alen, T., Jetten, M. S. M., Op den Camp, H. J. M., et al. (2022). Microbial paracetamol degradation involves a high diversity of novel amidase enzyme candidates. *Water Res X* 16:100152. doi: 10.1016/J.WROA.2022.100152

Ruhoy, I. S., and Daughton, C. G. (2007). Types and quantities of leftover drugs entering the environment via disposal to sewage — revealed by coroner records. *Sci. Total Environ.* 388, 137–148. doi: 10.1016/j.scitotenv.2007.08.013

Salgado, R., Brito, D., Noronha, J. P., Almeida, B., Bronze, M. R., Oehmen, A., et al. (2020). Metabolite identification of ibuprofen biodegradation by Patulibacter medicamentivorans under aerobic conditions. *Environ. Technol.* 41, 450–465. doi: 10.1080/09593330.2018.1502362

Sana, A. (2018). Biodegradation of paracetamol by native fungal species inhabiting wastewater of a pharmaceutical factory in sana'a, Yemen. *Univ. J. Pharm. Res.* 2, 35–41. doi: 10.22270/ujpr.v2i6.r7

Santos, L. H. M. L. M., Araújo, A. N., Fachini, A., Pena, A., Delerue-Matos, C., and Montenegro, M. C. B. S. M. (2010). Ecotoxicological aspects related to the presence of pharmaceuticals in the aquatic environment. *J. Hazard. Mater.* 175, 45–95. doi: 10.1016/j.jhazmat.2009.10.100

Scheurell, M., Franke, S., Shah, R. M., and Hühnerfuss, H. (2009). Occurrence of diclofenac and its metabolites in surface water and effluent samples from Karachi, Pakistan. *Chemosphere* 77, 870–876. doi: 10.1016/j.chemosphere.2009.07.066

Scheytt, T., and Mersmann, P., Lindst¨adtlindst¨ Lindst¨adt, R., and Heberer, T. (2005). 1-octanol/water partition coefficients of 5 pharmaceuticals from human medical care: carbamazepine, clofibric acid, diclofenac, ibuprofen, and propyphenazone. *Water Air Soil Pollut.* 165, 3–11. doi: 10.1007/s11270-005-3539-9

Sharma, K., Kaushik, G., Thotakura, N., Raza, K., Sharma, N., and Nimesh, S. (2020). Enhancement effects of process optimization technique while elucidating the degradation pathways of drugs present in pharmaceutical industry wastewater using *Micrococcus yunnanensis*. *Chemosphere* 238:124689. doi: 10.1016/J.CHEMOSPHERE.2019.124689

Show, S., Sarkar, P., Barman, S., and Halder, G. (2023). Microbial remediation of ibuprofen contaminated water using novel isolate *Microbacterium paraoxydans*. *Chem. Pap.* 77, 517–531. doi: 10.1007/s11696-022-02499-0

Singhal, T. (2020). A review of coronavirus Disease-2019 (COVID-19). *Ind. J. Pediatr.* 87, 281–286. doi: 10.1007/s12098-020-03263-6

Stackelberg, P. E., Furlong, E. T., Meyer, M. T., Zaugg, S. D., Henderson, A. K., and Reissman, D. B. (2004). Persistence of pharmaceutical compounds and other organic wastewater contaminants in a conventional drinking-water-treatment plant. *Sci. Total Environ.* 329, 99–113. doi: 10.1016/j.scitotenv.2004.03.015

Stylianou, K., Hapeshi, E., Vasquez, M. I., Fatta-Kassinos, D., and Vyrides, I. (2018). Diclofenac biodegradation by newly isolated Klebsiella sp. KSC: microbial intermediates and ecotoxicological assessment. *J. Environ. Chem. Eng.* 6, 3242–3248. doi: 10.1016/j.jece.2018.04.052

Świacka, K., Michnowska, A., Maculewicz, J., Caban, M., and Smolarz, K. (2020). Toxic effects of NSAIDs in non-target species: a review from the perspective of the aquatic environment. *Environ. Pollut.* 273:115891. doi: 10.1016/j.envpol.2020.115891

Tiwari, B., Sellamuthu, B., Ouarda, Y., Drogui, P., Tyagi, R. D., and Buelna, G. (2017). Review on fate and mechanism of removal of pharmaceutical pollutants from wastewater using biological approach. *Bioresour. Technol.* 224, 1–12. doi: 10.1016/j.biortech.2016.11.042

Ucella-Filho, J. G. M., Freire, A. S. M., Carréra, J. C., Lucas, F. M. F., Zucolotto, S. M., Dias Júnior, A. F., et al. (2022). Tannin-rich bark extract of plants as a source of antimicrobial bioactive compounds: a bibliometric analysis. *S. Afr. J. Bot.* 150, 1038–1050. doi: 10.1016/j.sajb.2022.09.018

Vargas-Ordóñez, A., Aguilar-Romero, I., Villaverde, J., Madrid, F., and Morillo, E. (2023). Isolation of novel bacterial strains *Pseudomonas extremaustralis* CSW01 and Stutzerimonas stutzeri CSW02 from sewage sludge for paracetamol biodegradation. *Microorganisms* 11:196. doi: 10.3390/microorganisms11010196

Vieno, N., and Sillanpää, M. (2014). Fate of diclofenac in municipal wastewater treatment plant—a review. *Environ. Int.* 69, 28–39. doi: 10.1016/j.envint.2014.03.021

Ward, B., and Alexander-Williams, J. M. (1999). Paracetamol revisited: a review of the pharmacokinetics and pharmacodynamics. *Acute Pain* 2, 139–149. doi: 10.1016/S1366-0071(99)80006-0

Wojcieszyńska, D., Guzik, H., and Guzik, U. (2022). Non-steroidal anti-inflammatory drugs in the era of the COVID-19 pandemic in the context of the human and the environment. *Sci. Total Environ.* 834:155317. doi: 10.1016/J.SCITOTENV.2022.155317

Wojcieszyńska, D., Łagoda, K., and Guzik, U. (2023). Diclofenac biodegradation by microorganisms and with immobilised systems—a review. *Catalysts* 13, 1–18. doi: 10.3390/catal13020412

Zhang, Y., Geißen, S.-U., and Gal, C. (2008). Carbamazepine and diclofenac: removal in wastewater treatment plants and occurrence in water bodies. *Chemosphere* 73, 1151–1161. doi: 10.1016/j.chemosphere.2008.07.086

Zhang, L., Hu, J., Zhu, R., Zhou, Q., and Chen, J. (2013). Degradation of paracetamol by pure bacterial cultures and their microbial consortium. *Appl. Microbiol. Biotechnol.* 97, 3687–3698. doi: 10.1007/s00253-012-4170-5

Zhang, X., Wang, Y., Lyu, H., Zhang, Y., Liu, Y., and Luo, J. (2021). The influence of COVID-19 on the well-being of people: big data methods for capturing the well-being of working adults and protective factors nationwide. *Front. Psychol.* 12:681091. doi: 10.3389/fpsyg.2021.681091

Zoulikha, M., Huang, F., Wu, Z., and He, W. (2022). COVID-19 inflammation and implications in drug delivery. *J. Control. Release.* 346, 260–274. doi: 10.1016/j.jconrel.2022.04.027

Żur, J., Piński, A., Marchlewicz, A., Hupert-Kocurek, K., Wojcieszyńska, D., and Guzik, U. (2018b). Organic micropollutants paracetamol and ibuprofen—toxicity, biodegradation, and genetic background of their utilization by bacteria. *Environ. Sci. Pollut. Res.* 25, 21498–21524. doi: 10.1007/s11356-018-2517-x

Żur, J., Wojcieszyńska, D., Hupert-Kocurek, K., Marchlewicz, A., and Guzik, U. (2018a). Paracetamol—toxicity and microbial utilization. *Pseudomonas moorei* KB4 as a case study for exploring degradation pathway. *Chemosphere* 206, 192–202. doi: 10.1016/J.CHEMOSPHERE.2018.04.179

frontiers | Frontiers in Microbiology

TYPE Original Research
PUBLISHED 30 November 2023
DOI 10.3389/fmicb.2023.1298323

OPEN ACCESS

EDITED BY
Vaibhav Srivastava,
University of Allahabad, India

REVIEWED BY
Gaurav Saxena,
Shoolini University, India
Shangwei Zhang,
Beijing Normal University, China

*CORRESPONDENCE
Katsutoshi Hori
✉ khori@chembio.nagoya-u.ac.jp

RECEIVED 26 September 2023
ACCEPTED 08 November 2023
PUBLISHED 30 November 2023

CITATION
Takahashi S and Hori K (2023) Long-term continuous degradation of carbon nanotubes by a bacteria-driven Fenton reaction. *Front. Microbiol.* 14:1298323. doi: 10.3389/fmicb.2023.1298323

Long-term continuous degradation of carbon nanotubes by a bacteria-driven Fenton reaction

Seira Takahashi and Katsutoshi Hori*

Department of Biomolecular Engineering, Graduate School of Engineering, Nagoya University, Nagoya, Aichi, Japan

Very few bacteria are known that can degrade carbon nanotubes (CNTs), and the only known degradation mechanism is a Fenton reaction driven by *Labrys* sp. WJW with siderophores, which only occurs under iron-deficient conditions. No useful information is available on the degradation rates or long-term stability and continuity of the degradation reaction although several months or more are needed for CNT degradation. In this study, we investigated long-term continuous degradation of oxidized (carboxylated) single-walled CNTs (O-SWCNTs) using bacteria of the genus *Shewanella*. These bacteria are widely present in the environment and can drive the Fenton reaction by alternating anaerobic-aerobic growth conditions under more general environmental conditions. We first examined the effect of O-SWCNTs on the growth of *S. oneidensis* MR-1, and it was revealed that O-SWCNTs promote growth up to 30 μg/mL but inhibit growth at 40 μg/mL and above. Then, *S. oneidensis* MR-1 was subjected to incubation cycles consisting of 21-h anaerobic and 3-h aerobic periods in the presence of 30 μg/mL O-SWCNTs and 10 mM Fe(III) citrate. We determined key factors that help prolong the bacteria-driven Fenton reaction and finally achieved long-term continuous degradation of O-SWCNTs over 90 d. By maintaining a near neutral pH and replenishing Fe(III) citrate at 60 d, a degraded fraction of 56.3% was reached. *S. oneidensis* MR-1 produces Fe(II) from Fe(III) citrate, a final electron acceptor for anaerobic respiration during the anaerobic period. Then, ·OH is generated through the Fenton reaction by Fe(II) and H_2O_2 produced by MR-1 during the aerobic period. ·OH was responsible for O-SWCNT degradation, which was inhibited by scavengers of H_2O_2 and ·OH. Raman spectroscopy and X-ray photoelectron spectroscopy showed that the graphitic structure in O-SWCNTs was oxidized, and electron microscopy showed that long CNT fibers initially aggregated and became short and isolated during degradation. Since *Shewanella* spp. and iron are ubiquitous in the environment, this study suggests that a Fenton reaction driven by this genus is applicable to the degradation of CNTs under a wide range of conditions and will help researchers develop novel methods for waste treatment and environmental bioremediation against CNTs.

KEYWORDS

carbon nanotube, degradation, Fenton reaction, bacteria, *Shewanella*

1 Introduction

Carbon nanotubes (CNTs), especially single-walled CNTs (SWCNTs), have a wide range of applications due to their excellent properties, such as mechanical strength, optical properties, and electrical and thermal conductivity (Dresselhaus et al., 2004; Byrne et al., 2018; Hu et al., 2023). However, there are concerns about their impact on human health and ecosystems (Poland

et al., 2008). Some CNTs are needle-like, similar to asbestos, and can induce mesothelioma, pleural fibrosis, and lung cancer (Donaldson et al., 2013). Recent studies have reported that some CNTs are also toxic to plants, animals, and microorganisms, and may alter biodiversity (Chen et al., 2017; Mendonca et al., 2017; Chen et al., 2018; Kong et al., 2023); Such CNTs cause growth inhibition and reduced seed germination in plants (Begum and Fugetsu, 2012; Hatami, 2017), embryo growth inhibition and pneumonia in animals (Roman et al., 2013; Al Moustafa et al., 2016; Fujita et al., 2016), and cell membrane damage in microorganisms (Liu et al., 2009; Yadav et al., 2016). As the use of CNTs has become more widespread, the amount of CNTs released into the environment, either accidentally or as waste, may also increase, leading to additional concerns. Therefore, the safety against human health and biodegradability of CNTs have attracted great attention.

Allen et al. (2008, 2009) first reported the degradation of oxidized (carboxylated) SWCNTs (O-SWCNTs), which are functionalized SWCNTs, by horseradish peroxidase (HRP). Since then, the biodegradation of CNTs by incubation with heme enzymes, such as human myeloperoxidase (Kagan et al., 2010), human eosinophil peroxidase (Andon et al., 2013), bovine lactoperoxidase (Bhattacharya et al., 2015), fungal manganese peroxidase (Zhang et al., 2014) and lignin peroxidase (Chandrasekaran et al., 2014), in the presence of their substrate (H_2O_2) has been reported. However, Flores-Cervantes et al. (2014) were the first to quantitatively investigate the enzymatic degradation of CNTs and estimated a half-life of 80 years for SWCNT degradation by HRP. This result was largely different from the rapid degradation described in the paper by Allen et al. (2009), in which CNTs disappeared within 10 d. Quantitative studies and reproducibility have not yet been conducted for enzymes other than HRP. In addition, we recently demonstrated that the degradation of CNTs during incubation with heme enzymes and externally added H_2O_2 is not caused by enzymatic reaction but rather the Fenton reaction, which produces hydroxyl radicals (·OH) that are highly reactive and can oxidize most organic substances rapidly and nonselectively, via the decomposition of H_2O_2 catalyzed by Fe(II) (Qin et al., 2015; Takahashi et al., 2023). Peroxidases are easily inactivated by their substrate H_2O_2 via heme degradation, which is called suicide inactivation (Valderrama et al., 2002). In our previous study, the rapid suicide inactivation of peroxidases, including HRP, was observed; this process depended on the H_2O_2 concentration and was accompanied by the release of iron, which caused the Fenton reaction (Takahashi et al., 2023). Thus, enzymatic degradation of CNTs may not be as promising as previously expected.

Bacteria have an immense and diverse metabolic system and are utilized for environmental bioremediation and waste treatments. For CNTs, biotransformation or biodegradation by *Trabusiella guamensis* (Chouhan et al., 2016), *Mycobacterium vanbaalenii* PYR-1 (You et al., 2017), and a bacterial community consisting of *Burkholderia kururiensis*, *Delftia acidvorans* and *Stenotrophomonas maltophilia* (Zhang et al., 2013) has also been reported. However, the molecular mechanisms underlying these bacterial transformations of CNTs have never been elucidated. Wang et al. (2020) showed that *Labrys* sp. WJW secretes siderophores under iron-deficient conditions and degrades CNTs as the sole carbon source; this process occurs through an extracellular biogenic Fenton-like reaction induced by Fe(II) that is generated through the reduction of Fe(III) by siderophores and autocrine H_2O_2. This is the first and only report in which the mechanism underlying the degradation of carbon nanomaterials by bacteria was shown, suggesting that the Fenton reaction induced by microorganisms by different pathways may contribute to the degradation of CNTs.

Shewanella spp., environmentally ubiquitous facultative anaerobic bacteria, produce Fe(II) by reducing Fe(III) under anaerobic conditions and H_2O_2 by reducing O_2 under aerobic conditions, thus efficiently inducing the Fenton reaction by alternating anaerobic-aerobic cultures. The degradation of pentachlorophenol (McKinzi and Dichristina, 1999), 1,4-dioxane (Sekar and DiChristina, 2014), enrofloxacin (Yan et al., 2016), polybrominated diphenyl ethers (Peng et al., 2020; Shi et al., 2021), and polystyrene (Yang et al., 2022) by the Fenton reaction driven by *Shewanella* spp. has been reported. Therefore, the method should be effective in the degradation of CNTs, albeit much more recalcitrant than the other chemicals. The Fenton reaction driven by *Shewanella* spp., such as *S. oneidensis* and *S. putrefaciens*, could be applied to the degradation of CNTs under a wide range of environments, not limited to iron-deficient conditions. However, it is unclear whether *Shewanella* spp. is resistant to CNTs and whether the bacteria-driven Fenton reaction continues long enough to degrade CNTs. The purpose of this study is to determine the effectiveness of the Fenton reaction driven by *Shewanella* spp. for the continuous degradation of CNTs.

2 Materials and methods

2.1 Culture medium and chemical reagents

Dispersions of O-SWCNTs (Product No. ZEONANOR-SG101) were produced and provided by Zeon Nanotechnology Co., Ltd. (Japan). The dispersions of O-SWCNTs were stored in the dark, and it was confirmed that the properties of the pristine O-SWCNTs were unchanged from the beginning to the end of the experiment by Raman spectroscopy. Luria–Bertani (LB) broth and DL-sodium lactate were purchased from Nacalai Tesque Co., Ltd. (Japan). Mannitol and catalase were purchased from FUJIFILM Wako Pure Chemical Industries Co., Ltd. (Japan). Fe(III) citrate and horseradish peroxidase were purchased from Sigma–Aldrich, Ltd. (USA). 3′-(p-hydroxyphenyl) fluorescein (HPF) was purchased from Goryo Chemical, Inc. (Japan). N,N-diethyl-1.4-phenykenediamine sulfate (DPD) was purchased from Tokyo Chemical Industry Co., Ltd. (Japan). Ferrozine (3-(2-pyridyl)-5,6-bis (4-sulfophenyl)-1,2,4-triazine) was purchased from Dojindo Laboratories, Ltd. (Japan). N_2 gas (99.99% purity) was purchased from Alpha System Co. (Japan).

2.2 Evaluation of the effect of O-SWCNTs on *S. oneidensis* MR-1 growth

S. oneidensis MR-1 was precultured aerobically in LB medium until the optical density at 600 nm (OD_{600}) reached 1.0 and harvested by centrifugation. The cells were resuspended in M1 medium containing 20 mM sodium lactate (Peng et al., 2020; Supplementary Table S1) to an OD_{600} of 0.1 after they were washed three times with the medium and grown aerobically for 24 h at 30°C in 25 mL of M1 medium with different concentrations of O-SWCNTs in 100-mL flasks. The culture broth was periodically collected and

diluted stepwise in M1 medium, of which 100 µL was spread on LB agar plates. After 48 h of incubation at 30°C, the number of colonies was counted to determine the colony forming units (CFUs).

2.3 Degradation of O-SWCNTs by *S. oneidensis* MR-1

A suspension of *S. oneidensis* MR-1 cells in 25 mL of M1 medium containing 20 mM sodium lactate was prepared in a flask as described above. Fe(III) citrate and O-SWCNTs were added to the cell suspension at final concentrations of 10 mM and 30 µg/mL, respectively, and N_2 gas was bubbled from a gas exchange tube connected to a silicone plug capping the flask for 10 min. After the gas exchange tube was clamped, cells were incubated anaerobically in the flask at 30°C for 21 h. The culture was then continued aerobically and air was bubbled from the gas exchange tube for 3 h at 30°C. This 24 h cycle consisting of 21-h anaerobic and 3-h aerobic incubations was repeated 90 times (90 d) in the dark. Sodium lactate and/or lactic acid were supplied manually using a pipette daily as an electron donor at a final concentration of 10 mM at the end of the aerobic incubation. The approximate pH of the culture medium during incubation was checked using pH test strips at the end of the aerobic incubation. If intended, the pH was returned to approximately 7 daily using sodium lactate when the pH was below 8 and lactic acid and/or sodium lactate when the pH was above 8. For a control experiment, Fe(III) citrate was replaced by nitrate (10 mM). For other control experiments, 100 ng/mL catalase was supplied daily as an H_2O_2 scavenger, or 240 mM mannitol was initially added to M1 medium as a ·OH scavenger. The concentration of Fe(II) was measured at the end of each anaerobic and aerobic incubation with a ferrozine-based detection method (Dichristina, 1992; Yang et al., 2022). The concentration of H_2O_2 was measured at the end of each aerobic incubation using a method modified for iron-containing samples by Katsoyiannis et al. (2008) and Peng et al. (2020), based on peroxidase-catalyzed oxidation of DPD. The concentration of ·OH in the supernatant was measured 1.5 h after the start of each aerobic incubation using a fluorescent probe (HPF, 5 µmol/L) (Hessler et al., 2012; Wang et al., 2020).

2.4 Quantification and characterization of O-SWCNTs during and after incubation

To the whole culture broth sample (25 mL), 500 µL of 10 mg/mL lysozyme solution (in Tris–HCl buffer, pH 8) was added, and after the solution was stirred for 30 min, an equal volume of 5% SDS solution was added, and the broth was heated at 60°C for 2 h for cell lysis. The precipitate containing O-SWCNTs was collected by ultracentrifugation (35,000 rpm, 15 min, 20°C), rinsed with ultrapure water (resistivity at 25°C, >18 MΩ cm; TOC, <5 ppb), washed with 3 M HCl to remove iron oxides formed during incubation, rinsed with ethanol, and redispersed in ultrapure water. In every rinsing and washing process above, the pellet was redispersed and recovered by ultracentrifugation three times. The cellular components that could not be removed by rinsing and washing were sedimented by centrifugation (3,000 rpm, 2 min, 25°C). O-SWCNTs were recovered from the supernatant by subsequent ultracentrifugation (35,000 rpm, 15 min, 20°C) and redispersed in 25 mL of 5% SDS solution by sonication for 10 min. Our previous work confirmed that the properties of the O-SWCNTs used in this study are not affected by sonication (Takahashi et al., 2023). The absorbance of the resulting O-SWCNT dispersion at 750 nm (A_{750}) was measured to calculate the concentration of O-SWCNTs from a calibration curve prepared using stocks of O-SWCNT dispersion.

Prior to instrumental analysis, O-SWCNTs were collected again by ultracentrifugation under the same conditions above, washed with ultrapure water, and redispersed in methanol by sonication for 10 min. Specimens for Raman spectroscopy were prepared by drop-casting approximately 50 µL of the suspension on glass microscope slides and drying. All spectra were collected on a micro-Raman spectrometer (inVia Reflex, Renishaw, UK) using an excitation wavelength of 532 nm. The samples were scanned from 1,000–1,900 cm^{-1} to visualize the D and G bands of O-SWCNTs. Spectra were collected with a 10 s exposure time and averaged across 5 scans per sample. In each sample, at least 10 different spots were analyzed. For X-ray photoelectron spectroscopy (XPS) (ESCALAB250, VG Scientific, UK), specimens were prepared by drop-casting approximately 100 µL of the samples on carbon tape and drying. XPS was performed using monochromatized Al Kα radiation ($h\nu = 1486.6$ eV) as an X-ray source. For transmission electron microscopy (TEM), 10 µL of the appropriately diluted suspensions were dropped onto a carbon-coated copper grid (ELS-C10, Okenshoji Co., Ltd., Tokyo, Japan) and dried overnight under ambient conditions prior to TEM imaging. TEM images were acquired using a JEM-2100Plus (JEOL, Ltd., Tokyo, Japan) equipped with a CCD camera and operated at an acceleration voltage of 200 kV.

3 Results

3.1 Incubation conditions for the continuous Fenton reaction by *S. oneidensis* MR-1 in the presence of O-SWCNTs

Due to concerns that the cytotoxicity of O-SWCNTs would kill or inactivate bacterial cells and rapidly stop the bacteria-driven Fenton reaction, we first examined the effect of O-SWCNTs on the growth of *S. oneidensis* MR-1. For this purpose, cells were grown aerobically in the presence of different concentrations of O-SWCNTs at 30°C for 24 h, and the change in CFUs with incubation time was analyzed. Despite the reported toxicity of CNTs, the addition of 20 and 30 µg/mL O-SWCNTs unexpectedly promoted the growth of *S. oneidensis* MR-1, which was greater than that without O-SWCNTs (Figure 1 and Supplementary Figure S1). However, the growth was greatly inhibited at 40 µg/mL or greater. Accordingly, subsequent incubations of *S. oneidensis* MR-1 with O-SWCNTs in this study were conducted at an O-SWCNT concentration of 30 µg/mL.

Next, since the degradation of O-SWCNTs was expected to require a long period of time (several months or more), we investigated the conditions that would maintain the cell activity of *S. oneidensis* MR-1 and continue the Fenton reaction for a long period of time even in the presence of O-SWCNTs. Theoretically, under anaerobic conditions, this bacterium respirates using lactate as an electron donor and Fe(III) as a final electron acceptor and produces Fe(II). Then, the Fe(II) and H_2O_2 produced by the bacterium under aerobic conditions undergo the Fenton reaction, oxidizing Fe(II) to Fe(III) and generating

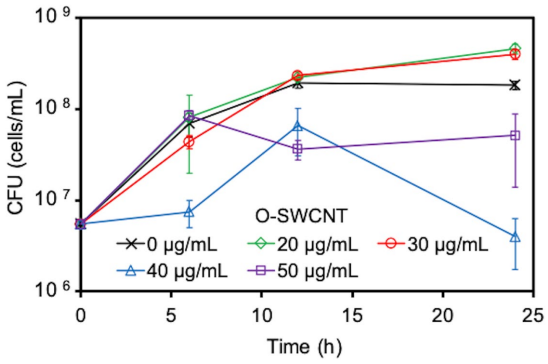

FIGURE 1
Effect caused by the concentration of O-SWCNTs on *S. oneidensis* MR-1 growth. Error bars indicate standard error from three independent cultures.

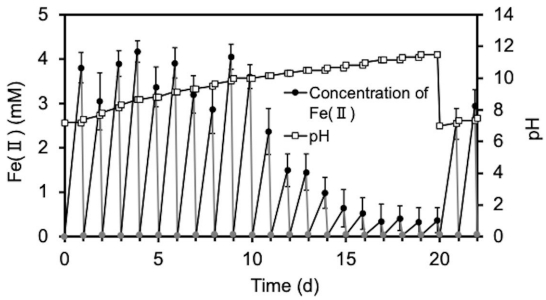

FIGURE 2
Time courses of pH and the Fe(II) concentration during the cultivation of *S. oneidensis* MR-1 with 24-h incubation cycles consisting of 21-h anaerobic and 3-h aerobic periods in the presence of O-SWCNTs and without controlling pH. The pH was adjusted to 7 at the end of the 20-d incubation. The square symbols indicate the pH values. Circular symbols indicate Fe(II) concentrations during the anaerobic (black) and aerobic (gray) periods. Error bars indicate standard error from three independent incubations.

·OH. Therefore, *S. oneidensis* MR-1 cells were subjected to alternating anaerobic-aerobic incubation in the presence of O-SWCNTs and 10 mM Fe(III) citrate, and the production of Fe(II), H_2O_2, and ·OH during the incubation was examined. Up to the first 10 d of the 24-h cycle consisting of 21-h anaerobic and 3-h aerobic incubations, the concentration of Fe(II) increased during the anaerobic period and reached 2.6 ~ 3.9 mM at the end of the 21-h anaerobic period (Figure 2). This result was almost consistent with the results obtained by previous studies in which 4 ~ 6.3 mM Fe(II) was produced after 24 h of anaerobic incubation of *Shewanella* spp. at the same concentration of Fe(III) citrate (Sekar and DiChristina, 2014; Peng et al., 2020). In contrast, Fe(II) became undetectable after each aerobic incubation. After 10 d of the incubation cycle, the amount of Fe(II) produced during the anaerobic period rapidly decreased, and its concentration became lower than 1 mM at 14 d, accompanied by an increase in the pH value of the culture medium. Then, the supplied electron donor was changed from sodium lactate to lactic acid after 20 d of the incubation cycle to return the pH to approximately 7, which restored Fe(II) production after the anaerobic period. Therefore, we performed a long-term incubation of *S. oneidensis* MR-1 for 90 d in the presence of O-SWCNTs and Fe(III) citrate. The pH of the culture medium was maintained at approximately 7 by using sodium lactate when the pH was less than 8 and lactic acid when the pH was above 8 as an electron donor. As a result, Fe(II) production was maintained at approximately 2 mM during the anaerobic period until approximately 60 d, despite an initial decrease from approximately 4 mM and daily fluctuations (Figure 3A). However, after 60 d, the amount of Fe(II) produced gradually decreased, and visible precipitation occurred, even though the pH was controlled near neutral. Then, Fe(III) citrate was added to the culture at 60 d at the same concentration as the initial concentration. This restored Fe(II) production after the anaerobic period to that at the beginning of the incubation cycle, and thereafter, the production of Fe(II) was maintained at a similar level until 90 d (Figure 3B). In the absence of *S. oneidensis* MR-1, no Fe(II) production was consistently observed during the incubation cycle, confirming that Fe(II) is produced by the anaerobic respiration of *S. oneidensis* MR-1. The H_2O_2 produced after the aerobic period was approximately 20 μM, a level similar to that reported in previous studies (Peng et al., 2020; Yang et al., 2022), and was maintained over 90 d (Figure 3C). It was also confirmed that H_2O_2 was produced by MR-1 cells because it was not detected in the absence of the cells. After each anaerobic-aerobic cycle, the production of ·OH was confirmed, and its concentration tended to change with the concentration of Fe(II) produced after the anaerobic period; ·OH production gradually decreased up to 60 d and was restored completely by the addition of Fe(III) citrate at 60 d (Figure 3D). No ·OH was consistently observed during the incubation cycle in the absence of *S. oneidensis* MR-1, confirming that it is produced through the Fenton reaction by H_2O_2 and Fe(II) produced by the bacterium. Thus, important factors were determined, including the nontoxic concentration of O-SWCNTs, pH level, and replenishment of Fe(III) citrate during the incubation cycle, that prolonged the bacterial Fenton reaction in the presence of O-SWCNTs using *S. oneidensis* MR-1 for a long time over 90 d.

3.2 Degradation of O-SWCNTs by anaerobic-aerobic incubation with *S. oneidensis* MR-1

We investigated whether long-term continuous degradation of O-SWCNTs is possible by the bacteria-driven Fenton reaction using *S. oneidensis* MR-1 under the conditions described in the previous section. After the bacterial cells and iron precipitate were removed, the concentration of O-SWCNTs during anaerobic-aerobic incubation with *S. oneidensis* MR-1 was quantified by measuring the A_{750} of the O-SWCNT redispersion solution (Yang et al., 2019; Takahashi et al., 2023). When O-SWCNTs were subjected to alternating anaerobic-aerobic incubation with *S. oneidensis* MR-1, at a pH of approximately 7, O-SWCNT degradation progressed continuously with incubation time; however, when Fe(III) citrate was not replenished, the degradation hardly progressed after 60 d, and the degraded fraction remained at 48.7% at 90 d (Figure 4). However, when Fe(III) citrate was replenished at 60 d, O-SWCNT degradation continued thereafter, eventually reaching the degraded fraction of 56.3% at 90 d. No degradation of O-SWCNTs was observed in the control sample without *S. oneidensis* MR-1. To confirm that O-SWCNT degradation was caused by a bacteria-driven Fenton reaction, we prevented the

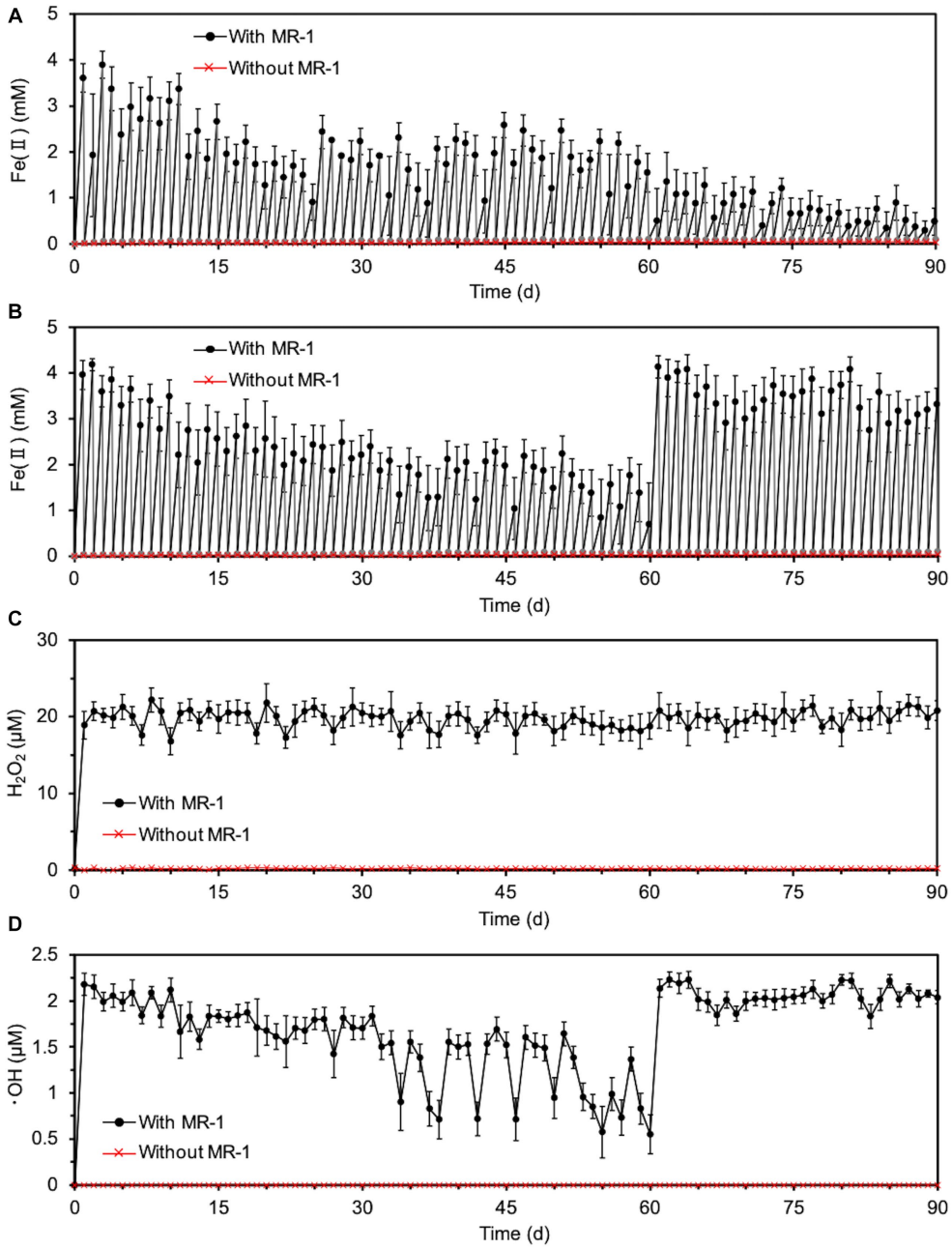

FIGURE 3
Long-term Fenton reaction driven by *S. oneidensis* MR-1 in 24-h incubation cycles consisting of 21-h anaerobic and 3-h aerobic periods under daily controlled pH near neutral in the presence of O-SWCNTs. Error bars indicate standard error from three independent incubations. **(A)** The time course of Fe(II) concentrations during the anaerobic (black) and aerobic (gray) periods without the replenishment of Fe(III) citrate. In the data without MR-1 (red), only the concentration of Fe(II) at the end of each anaerobic period was shown to simplify the figure. The concentration of Fe(II) was also almost zero at the end of each aerobic period, although the data were not shown. **(B)** The time course of Fe(II) concentrations during the anaerobic (black) and aerobic (gray) periods with the replenishment of Fe(III) citrate at 60 d. In the data without MR-1 (red), only the concentration of Fe(II) at the end of each anaerobic period was shown to simplify the figure. The concentration of Fe(II) was also almost zero at the end of each aerobic period, although the data were not shown. **(C)** The time course of H_2O_2 concentrations during alternating anaerobic-aerobic incubations of *S. oneidensis* MR-1 with the replenishment of Fe(III) citrate at 60 d. **(D)** The time course of ·OH concentrations during alternating anaerobic-aerobic incubations of *S. oneidensis* MR-1 with the replenishment of Fe(III) citrate at 60 d.

reaction from occurring in the absence of the reactants Fe(II) or H_2O_2. Fe(II) was not produced unless Fe(III) citrate was not added to the culture (Figure 5A), but H_2O_2 was produced with or without Fe(III) citrate (Figure 5B); the addition of catalase, an enzyme that consumes H_2O_2, eliminated H_2O_2 (Figure 5B) but did not inhibit Fe(II) production (Figure 5A). The product of the Fenton reaction ·OH did not form in the absence of Fe(III) citrate or in the presence of catalase (Figure 5C). Thus, under these incubation conditions, little degradation of O-SWCNTs occurred (5.0% without Fe(III) citrate and 8.9% with catalase). Furthermore, we investigated the addition of

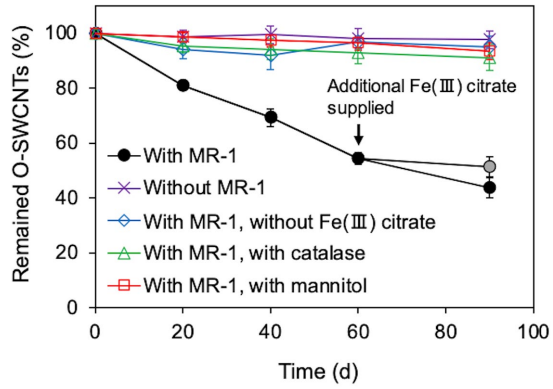

FIGURE 4
Long-term O-SWCNT degradation via the Fenton reaction driven by *S. oneidensis* MR-1 in 24-h incubation cycles consisting of 21-h anaerobic and 3-h aerobic periods under daily controlled pH near neutral. A gray circular symbol indicates that Fe(III) citrate was not replenished at 60 d. Error bars indicate standard error from three independent incubations.

mannitol to the culture, a scavenger of ·OH produced by the Fenton reaction. Mannitol was confirmed to eliminate ·OH (Figure 5C) without any effect on the production of Fe(II) or H_2O_2 (Figures 5A,B). In the presence of mannitol, O-SWCNTs were hardly degraded (the degraded fraction was 6.6%). These results suggest that O-SWCNTs were degraded by ·OH generated by the Fenton reaction caused by Fe(II) and H_2O_2 produced by the alternating anaerobic-aerobic incubation of *S. oneidensis* MR-1.

3.3 Transformation of O-SWCNTs during degradation by *S. oneidensis* MR-1

The transformation of O-SWCNTs during degradation by the bacteria-driven Fenton reaction using *S. oneidensis* MR-1 was also examined by spectroscopic analyses. The G-band (graphite) peak at 1,591 cm^{-1} and the D-band (disordered) peak at ~1,350 cm^{-1} are characteristic Raman bands of graphitic carbon materials, and the intensity ratio of the G-band to the D-band (G/D) is an index of structural disorder (Figure 6A; Miyata et al., 2011; Flores-Cervantes et al., 2014; Zhang M. F. et al., 2019; Wang et al., 2020). Raman spectra of O-SWCNTs after 90 d of incubation with *S. oneidensis* MR-1 showed a decrease in G/D from the initial value, suggesting an increase in the number of holes and defects on the surfaces of the O-SWCNTs. The trend of Raman spectral change was consistent with previous reports on bacterial biotransformation of CNTs (Chouhan et al., 2016; You et al., 2017; Wang et al., 2020). XPS analysis was performed to further investigate the changes in the chemical composition of O-SWCNTs. The acquired C1s spectrum of the samples resolved into different characteristic peaks (Figure 6B). The peak attributed to sp2 C-C decreased from 57.4 to 44.5% during 90 d of the incubation cycle with *S. oneidensis* MR-1, while the peak attributed to sp3 C-C increased from 6.8 to 16.7%. In addition, the oxygen functional groups (C-O and O-C=O) increased from 35.8 to 38.7%. These results imply that the graphitic structure in O-SWCNTs was oxidized, supporting the above interpretation obtained from the Raman spectral change.

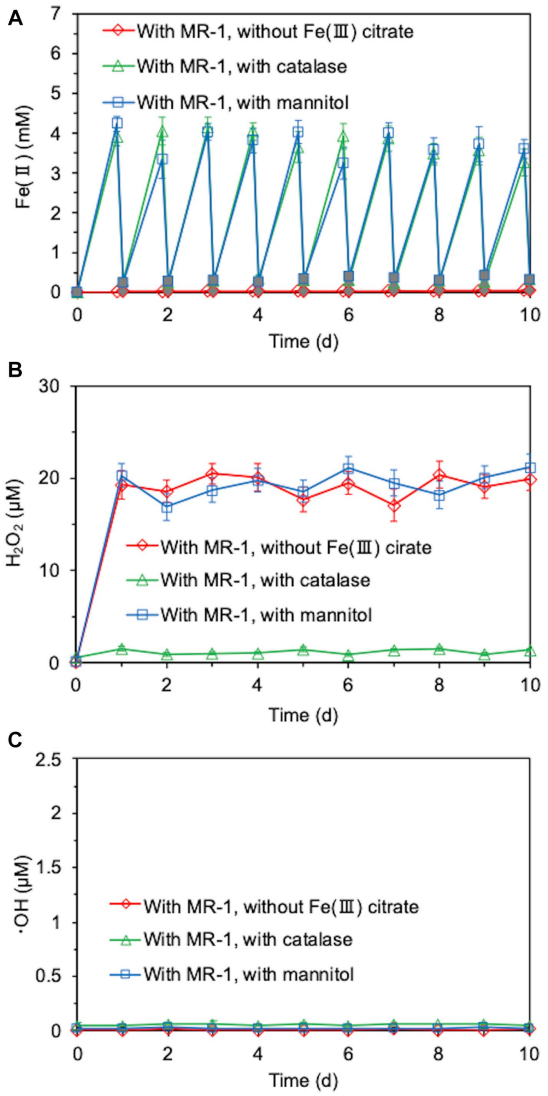

FIGURE 5
Time courses of Fe(II) **(A)**, H_2O_2 **(B)**, and ·OH **(C)** concentrations during the cultivation of *S. oneidensis* MR-1 with 24-h incubation cycles consisting of 21-h anaerobic and 3-h aerobic periods in the presence of O-SWCNTs. Fe(III) citrate was absent from the incubation solution or catalase or mannitol was added to the incubation solution. White and gray symbols in **(A)** indicate Fe(II) concentrations during the anaerobic period and aerobic period, respectively. Error bars indicate standard error from three independent incubations.

Morphological changes in O-SWCNTs were also confirmed by TEM observation. Before incubation (0 d), O-SWCNTs aggregated with entangled long fibers, and single O-SWCNT fibers were barely visible in any of the fields of view (Figure 6C). In contrast, after 90 d of the incubation cycle with *S. oneidensis* MR-1, most of the O-SWCNT fibers were observed to be short and isolated, along with fiber debris that appeared shredded (Figure 6D). The isolation of O-SWCNTs was presumably due to the progress of oxidation, which reduced van der Waals interactions between the nanotubes (Kim et al., 2012), which is consistent with the results obtained by Raman spectroscopy and XPS analysis.

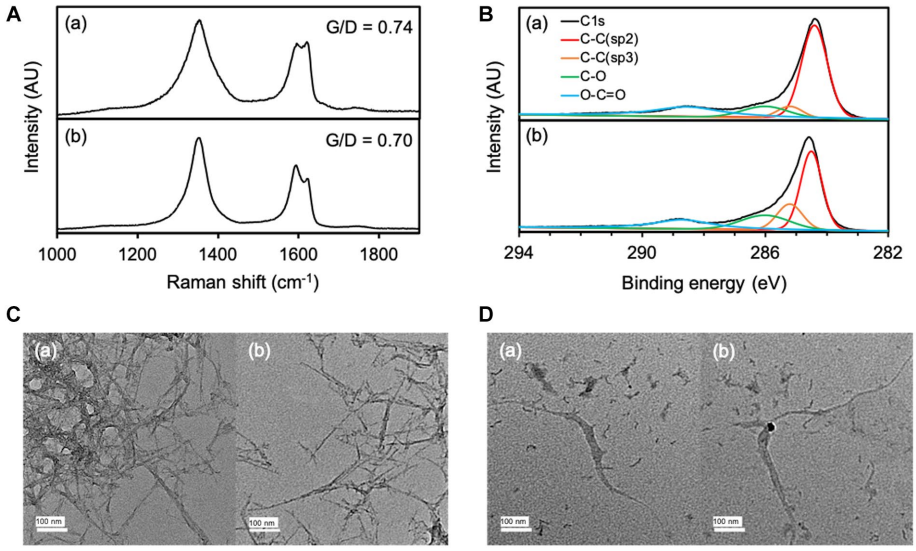

FIGURE 6
Raman spectra **(A)** and XPS spectra **(B)** of O-SWCNTs at 0 d **(a)** and 90 d **(b)** of incubation with *S. oneidensis* MR-1 in 24-h incubation cycles consisting of 21-h anaerobic and 3-h aerobic periods. TEM images of O-SWCNTs at 0 d **(C)** and 90 d **(D)** of incubation with *S. oneidensis* MR-1 in 24-h incubation cycles consisting of 21-h anaerobic and 3-h aerobic periods. Different views are shown in **(a)** and **(b)**.

4 Discussion

This is the first report that quantitatively demonstrates continuous bacterial degradation of CNTs for a long period of time over 90 d. We succeeded in O-SWCNT degradation utilizing the Fenton reaction driven by an alternating anaerobic-aerobic incubation cycle of *S. oneidensis* MR-1. Table 1 summarizes methods and results in previous papers about bacterial degradation of CNTs in comparison with those in this study. In all of the previous studies (Zhang et al., 2013; Chouhan et al., 2016; You et al., 2017; Wang et al., 2020, 2021), the degradation of CNTs was evaluated at only one time point; thus, the degradation rates or long-term stability and continuity of the degradation reaction could not be discussed. In addition, in most of the previous studies, the molecular mechanism underlying bacterial degradation of CNTs was unclear. In the studies by Wang et al. (2020, 2021) using *Labry* sp. WJW, CNT degradation was due to a bacteria-driven Fenton reaction, as in our present study. However, in their studies, unlike our present study, the Fenton reaction was induced by Fe(II) produced by the siderophore-mediated reduction of Fe(III). They observed the degraded fraction only after 20-d incubation of CNTs with the bacterium. Therefore, we do not know whether CNT degradation by the siderophore-mediated Fenton reaction can be maintained for a long period of time. The present study showed that the bacteria-driven Fenton reaction can stop in the middle of the process. Degradation of organic pollutants other than CNTs using the Fenton reaction driven by *Shewanella* spp. has also been reported, but the continuation of the Fenton reaction was only monitored for up to 7 d (McKinzi and Dichristina, 1999; Sekar and DiChristina, 2014; Yan et al., 2016; Peng et al., 2020; Yang et al., 2022). We found that to achieve long-term continuous Fenton reaction driven by *S. oneidensis* MR-1, the pH value of the culture medium must remain near neutral and Fe(III) citrate must be replenished during long-term incubation. We need to be careful not to raise the pH during incubation, which could result from the metabolism of the electron donor lactate (Tang et al., 2006). In addition, OH^- produced by the oxidation of Fe(II) and Fe(III) in the Fenton reaction may contribute to the pH increase (Brillas et al., 2009). It has been reported that alkaline conditions are unfavorable for microbial reduction of Fe(III) in the anaerobic respiration of *S. oneidensis* MR-1 (Wang et al., 2018; Zhu et al., 2022). Nevertheless, microbially driven Fenton reactions have been carried out without pH control in previous studies on the degradation of contaminants, with the exception of one study (Yang et al., 2022). Even when the pH was maintained near neutral, the Fe(II) production gradually decreased with the generation of visible precipitation after 60 d of the incubation cycle but recovered by the addition of Fe(III) citrate. This decrease in Fe(II) production could be due to the gradual oxidation and precipitation of iron into a form that was less available to *S. oneidensis* MR-1 for anaerobic respiration. It is well known that bare Fe(III) begins to precipitate above pH 3 in the form of oxyhydroxide, which is called iron sludge (Zhang M. H. et al., 2019). Although chelation of iron with citrate avoids iron sludge formation, its stability in bacterial culture for as long as 60 d in the presence of ·OH has never been reported. Therefore, some of the iron may be released from the decomposed citrate during long-term incubation. It was also important to determine the effect of O-SWCNTs on the growth of *S. oneidensis* MR-1 because, unlike many other contaminants, CNTs are known to possess antimicrobial activity (Kang et al., 2008; Liu et al., 2009; Mocan et al., 2017). At concentrations below 30 μg/mL, O-SWCNTs enhanced the growth of *S. oneidensis* MR-1, whereas at concentrations above 40 μg/mL, they inhibited growth. The reason why low concentrations of O-SWCNTs enhance growth is unknown. However, it has been reported that CNTs can enhance or inhibit bacterial growth depending on their concentration and bacterial species (Rodrigues and Elimelech, 2010; Zhang et al., 2015). By determining the conditions to maintain the bacteria-driven Fenton reaction for a long period of time, we succeeded in degrading O-SWCNTs continuously for 90 d and a final degraded fraction of 56.3%, which is the highest value obtained for bacterial degradation of CNTs (Table 1). Based on these results, the time necessary for the complete degradation of O-SWCNTs is approximately 150 d if their degradation by the Fenton reaction driven by *S. oneidensis* MR-1 linearly continues (Supplementary Figure S2). However, as the

TABLE 1 Reports on CNT degradation by bacteria.

Bacterial strain	Type of CNTs	Maximum degradation ratio (%)	Time period (d)	Continuity evaluation	Concentration of CNTs (μg/mL)	Quantitative evaluation methods	Mechanisms of degradation	Reference
Shewanella oneidensis MR-1	O-SWCNT	56.3	90	○	30	Measurement of absorbance of CNTs dispersion at 750 nm	Fenton reaction driven by alternating anaerobic-aerobic incubation	This study
Labrys sp. WJW	SWCNTs	33	20	×	100	Weighting of residual CNTs	Fenton reaction caused by Fe^{2+} produced by siderophores secreted under iron-deficient condition (Fe^{3+}: 1.2 μM) and H_2O_2	Wang et al. (2020)
	O-SWCNTs	10						
	MWCNTs	21.3						Wang et al. (2021)
Mycobacterium vanbaalenii PYR-1	MWCNTs	0.07	3	×	90	Measurement of headspace CO_2 level during incubation with CNTs	Bacterial co-metabolism (No molecuar mechanism)	You et al. (2017)
	O-MWCNTs	0.55						
Trabusiella guamensis	MWCNTs	–	30	×	15	–	–	Chouhan et al. (2016)
Burholderia kururiensis, *Delftia acidovorans*, *Stenotrophomonas maltophilia*	O-MWCNTs (^{14}C-labeled)	6.8	7	×	1	Mesurement of ^{14}C radioactivity in CO_2 released during incubation CNTs	–	Zhang et al. (2013)

degradation of O-SWCNTs progresses and their concentration becomes much lower, the degradation might gradually slow down and take longer to complete, as seen in our previous study (Takahashi et al., 2023).

The Fenton reaction should be among the most effective and suitable methods for removing organic pollutants. Even recalcitrant chemicals, including CNTs, can be degraded by the Fenton reaction (Li et al., 2017; Brillas, 2022; Takahashi et al., 2023). However, the classical Fenton reaction exhibits several drawbacks, such as continuity, operability, safety, and risk of secondary pollution. Although the Fenton reaction basically involves the oxidation of Fe(II) to Fe(III) by H_2O_2 along with ·OH generation and the reduction of Fe(III) to Fe(II) by H_2O_2, the rate of the latter reaction is 1/6000 of that of the former reaction (Zhang M. H. et al., 2019). Therefore, Fe(III) accumulates without effective cycling between Fe(II) and Fe(III) and begins to precipitate above pH 3, causing secondary pollution by iron sludge. To avoid this, acidic conditions of pH ≤3 must be used for the classical Fenton reaction. In addition, a continuous supply of H_2O_2, which is hazardous to handle, is necessary (Zhang M. H. et al., 2019; Brillas, 2022). In the Fenton reaction driven by *S. oneidensis* MR-1, anaerobic respiration promotes the reduction of Fe(III) to Fe(II), and H_2O_2 is self-supplied by this bacterium. Although Fe(III) accumulation causing iron sludge may be completely inevitable during a long-term reaction, shot replenishment of Fe(III) citrate can prolong the Fenton reaction and thereby O-SWCNT degradation. Therefore, this would lead to the establishment of safe, low-cost, and effective treatment technology for CNT waste and pollution in the future. The Fenton reaction driven by *Labrys* sp. WJW reported by Wang should also contribute to the development of another effective CNT treatment, but it requires iron-deficient conditions under which siderophores function (Wang et al., 2020). Furthermore, *Shewanella* spp. can produce Fe(II) from ferrihydrite and goethite, iron minerals that are widely present on the earth's surface (Peng et al., 2020). Given the ubiquity of *Shewanella* spp. and iron in the environment, it is expected that the Fenton reaction can be driven in a wide range of environments by *Shewanella* spp. and has potential applications for continuous *in situ* bioremediation of CNTs.

5 Conclusion

We first successfully demonstrated long-term continuous degradation of O-SWCNTs by a bacteria-driven Fenton reaction over 90 d using *S. oneidensis* MR-1 in alternating anaerobic-aerobic incubation cycles. This long-term Fenton reaction was achieved by maintaining a near neutral pH in the presence of O-SWCNTs at a concentration that did not inhibit bacterial growth and by replenishing Fe(III) citrate during the process (at 60 d). The final O-SWCNT degraded fraction after 90 d of incubation was 56.3%, which is the highest bacterial degradation of CNTs ever reported. *S. oneidensis* MR-1 produces Fe(II) from Fe(III) citrate, a final electron acceptor for anaerobic respiration during the anaerobic period, and ·OH is generated through the Fenton reaction by Fe(II) and H_2O_2 produced by MR-1 during the aerobic period. ·OH is responsible for O-SWCNT degradation, which is inhibited by scavengers of H_2O_2 and ·OH. Since *Shewanella* spp. and iron are ubiquitous in the environment, a bacteria-driven Fenton reaction can be used to degrade CNTs under a wider range of conditions. In addition, the study contributes to developing novel methods for waste treatment and environmental bioremediation against CNTs.

Data availability statement

The original contributions presented in the study are included in the article/Supplementary material, further inquiries can be directed to the corresponding author.

Author contributions

ST: Formal analysis, Investigation, Methodology, Writing – original draft. KH: Conceptualization, Writing – review & editing.

Funding

The author(s) declare financial support was received for the research, authorship, and/or publication of this article. Financial support was received from Zeon Nanotechnology Co. Ltd. for this research. The funder was not involved in the study design, collection, analysis, interpretation of data, the writing of this article or the decision to submit it for publication.

Acknowledgments

We thank Zeon Nanotechnology Co. Ltd. for providing the O-SWCNT sample. We also thank Kanie of Friend Microbe Inc. (Japan) for the helpful discussion about this study. The preprint of the paper has been submitted to ChemRxiv (https://doi.org/10.26434/chemrxiv-2023-rcjv5-v2).

Conflict of interest

The authors declare that this study was carried out in the absence of any commercial or financial relationships that could be construed as a potential conflict of interest.

Publisher's note

Supplementary material

The Supplementary material for this article can be found online at: https://www.frontiersin.org/articles/10.3389/fmicb.2023.1298323/full#supplementary-material

References

Allen, B. L., Kichambare, P. D., Gou, P., Vlasova, I. I., Kapralov, A. A., Konduru, N., et al. (2008). Biodegradation of single-walled carbon nanotubes through enzymatic catalysis. *Nano Lett.* 8, 3899–3903. doi: 10.1021/nl802315h

Allen, B. L., Kotchey, G. P., Chen, Y. N., Yanamala, N. V. K., Klein-Seetharaman, J., Kagan, V. E., et al. (2009). Mechanistic investigations of horseradish peroxidase-catalyzed degradation of single-walled carbon nanotubes. *J. Am. Chem. Soc.* 131, 17194–17205. doi: 10.1021/ja9083623

Al Moustafa, A. E., Mfoumou, E., Roman, D. E., Nerguizian, V., Alazzam, A., Stiharu, I., et al. (2016). Impact of single-walled carbon nanotubes on the embryo: a brief review. *Int. J. Nanomedicine* 11, 349–355. doi: 10.2147/Ijn.S96361

Andon, F. T., Kapralov, A. A., Yanamala, N., Feng, W. H., Baygan, A., Chambers, B. J., et al. (2013). Biodegradation of single-walled carbon nanotubes by eosinophil peroxidase. *Small* 9, 2721–2729. doi: 10.1002/smll.201202508

Begum, P., and Fugetsu, B. (2012). Phytotoxicity of multi-walled carbon nanotubes on red spinach (*Amaranthus tricolor* L) and the role of ascorbic acid as an antioxidant. *J. Hazard. Mater.* 243, 212–222. doi: 10.1016/j.jhazmat.2012.10.025

Bhattacharya, K., El-Sayed, R., Andon, F. T., Mukherjee, S. P., Gregory, J., Li, H., et al. (2015). Lactoperoxidase-mediated degradation of single-walled carbon nanotubes in the presence of pulmonary surfactant. *Carbon* 91, 506–517. doi: 10.1016/j.carbon.2015.05.022

Brillas, E. (2022). Fenton, photo-Fenton, electro-Fenton, and their combined treatments for the removal of insecticides from waters and soils. A review. *Sep. Purif. Technol.* 284:120290. doi: 10.1016/j.seppur.2021.120290

Brillas, E., Sires, I., and Oturan, M. A. (2009). Electro-Fenton process and related electrochemical technologies based on Fenton's reaction chemistry. *Chem. Rev.* 109, 6570–6631. doi: 10.1021/cr900136g

Byrne, C., Subramanian, G., and Pillai, S. C. (2018). Recent advances in photocatalysis for environmental applications. *J. Environ. Chem. Eng.* 6, 3531–3555. doi: 10.1016/j.jece.2017.07.080

Chandrasekaran, G., Choi, S. K., Lee, Y. C., Kim, G. J., and Shin, H. J. (2014). Oxidative biodegradation of single-walled carbon nanotubes by partially purified lignin peroxidase from *Sparassis latifolia* mushroom. *J. Ind. Eng. Chem.* 20, 3367–3374. doi: 10.1016/j.jiec.2013.12.022

Chen, M., Qin, X. S., and Zeng, G. M. (2017). Biodiversity change behind wide applications of nanomaterials? *Nano Today* 17, 11–13. doi: 10.1016/j.nantod.2017.09.001

Chen, M., Zhou, S., Zhu, Y., Sun, Y. Z., Zeng, G. M., Yang, C. P., et al. (2018). Toxicity of carbon nanomaterials to plants, animals and microbes: recent progress from 2015-present. *Chemosphere* 206, 255–264. doi: 10.1016/j.chemosphere.2018.05.020

Chouhan, R. S., Qureshi, A., Yagci, B., Gulgun, M. A., Ozguz, V., and Niazi, J. H. (2016). Biotransformation of multi-walled carbon nanotubes mediated by nanomaterial resistant soil bacteria. *Chem. Eng. J.* 298, 1–9. doi: 10.1016/j.cej.2016.04.019

Dichristina, T. J. (1992). Effects of nitrate and nitrite on dissimilatory iron reduction by *Shewanella putrefaciens* 200. *Abstr. Pap. Am. Chem. Soc.* 174:1891. doi: 10.1128/jb.174.6.1891-1896.1992

Donaldson, K., Poland, C. A., Murphy, F. A., MacFarlane, M., Chernova, T., and Schinwald, A. (2013). Pulmonary toxicity of carbon nanotubes and asbestos - similarities and differences. *Adv. Drug Deliv. Rev.* 65, 2078–2086. doi: 10.1016/j.addr.2013.07.014

Dresselhaus, M. S., Dresselhaus, G., Charlier, J. C., and Hernandez, E. (2004). Electronic, thermal and mechanical properties of carbon nanotubes. Philosophical Trans. *R. Soc. a-Mathematical Phys. Eng. Sci.* 362, 2065–2098. doi: 10.1098/rsta.2004.1430

Flores-Cervantes, D. X., Maes, H. M., Schaffer, A., Hollender, J., and Kohler, H. P. E. (2014). Slow biotransformation of carbon nanotubes by horseradish peroxidase. *Environ. Sci. Technol.* 48, 4826–4834. doi: 10.1021/es4053279

Fujita, K., Fukuda, M., Endoh, S., Maru, J., Kato, H., Nakamura, A., et al. (2016). Pulmonary and pleural inflammation after intratracheal instillation of short single-walled and multi-walled carbon nanotubes. *Toxicol. Lett.* 257, 23–37. doi: 10.1016/j.toxlet.2016.05.025

Hatami, M. (2017). Toxicity assessment of multi-walled carbon nanotubes on *Cucurbita pepo* L. under well-watered and water-stressed conditions. *Ecotoxicol. Environ. Saf.* 142, 274–283. doi: 10.1016/j.ecoenv.2017.04.018

Hessler, C. M., Wu, M. Y., Xue, Z., Choi, H., and Seo, Y. (2012). The influence of capsular extracellular polymeric substances on the interaction between TiO_2 nanoparticles and planktonic bacteria. *Water Res.* 46, 4687–4696. doi: 10.1016/j.watres.2012.06.009

Hu, X., Bao, X., Zhang, M., Fang, S., Liu, K., Wang, J., et al. (2023). Recent advances in carbon nanotube-based energy harvesting technologies. *Adv. Mater.* 2023:e2303035. doi: 10.1002/adma.202303035

Kagan, V. E., Konduru, N. V., Feng, W. H., Allen, B. L., Conroy, J., Volkov, Y., et al. (2010). Carbon nanotubes degraded by neutrophil myeloperoxidase induce less pulmonary inflammation. *Nat. Nanotechnol.* 5, 354–359. doi: 10.1038/Nnano.2010.44

Kang, S., Herzberg, M., Rodrigues, D. F., and Elimelech, M. (2008). Antibacterial effects of carbon nanotubes: size does matter! *Langmuir* 24, 6409–6413. doi: 10.1021/la800951v

Katsoyiannis, I. A., Ruettimann, T., and Hug, S. J. (2008). pH dependence of Fenton reagent generation and as(III) oxidation and removal by corrosion of zero valent iron in aerated water. *Environ. Sci. Technol.* 42, 7424–7430. doi: 10.1021/es800649p

Kim, S. W., Kim, T., Kim, Y. S., Choi, H. S., Lim, H. J., Yang, S. J., et al. (2012). Surface modifications for the effective dispersion of carbon nanotubes in solvents and polymers. *Carbon* 50, 3–33. doi: 10.1016/j.carbon.2011.08.011

Kong, L., Yan, G., Huang, X., Wu, Y., Che, X., Liu, J., et al. (2023). Sequential exposures of single walled carbon nanotubes and heavy metal ions to macrophages induce different cytotoxicity. *Sci. Total Environ.* 864:161059. doi: 10.1016/j.scitotenv.2022.161059

Li, T., Zhang, C. Z., Fan, X. X., Li, Y., and Song, M. X. (2017). Degradation of oxidized multi-walled carbon nanotubes in water via photo-Fenton method and its degradation mechanism. *Chem. Eng. J.* 323, 37–46. doi: 10.1016/j.cej.2017.04.081

Liu, S. B., Wei, L., Hao, L., Fang, N., Chang, M. W., Xu, R., et al. (2009). Sharper and faster "nano darts" kill more bacteria: a study of antibacterial activity of individually dispersed pristine single-walled carbon nanotube. *ACS Nano* 3, 3891–3902. doi: 10.1021/nn901252r

McKinzi, A. M., and Dichristina, T. J. (1999). Microbially driven Fenton reaction for transformation of pentachlorophenol. *Environ. Sci. Technol.* 33, 1886–1891. doi: 10.1021/es980810z

Mendonca, M. C. P., Rizoli, C., Avila, D. S., Amorim, M. J. B., and de Jesus, M. B. (2017). Nanomaterials in the environment: perspectives on *in vivo* terrestrial toxicity testing. *Front. Environ. Sci.* 5:71. doi: 10.3389/fenvs.2017.00071

Miyata, Y., Mizuno, K., and Kataura, H. (2011). Purity and defect characterization of single-wall carbon nanotubes using Raman spectroscopy. *J. Nanomater.* 2011, 1–7. doi: 10.1155/2011/786763

Mocan, T., Matea, C. T., Pop, T., Mosteanu, O., Buzoianu, A. D., Suciu, S., et al. (2017). Carbon nanotubes as anti-bacterial agents. *Cell. Mol. Life Sci.* 74, 3467–3479. doi: 10.1007/s00018-017-2532-y

Peng, Z. F., Shi, M. M., Xia, K. M., Dong, Y. R., and Shi, L. (2020). Degradation of 2, 2 ', 4, 4 '-Tetrabrominated diphenyl ether (BDE-47) via the Fenton reaction driven by the dissimilatory metal-reducing bacterium *Shewanella oneidensis* MR-1. *Environ. Pollut.* 266:115413. doi: 10.1016/j.envpol.2020.115413

Poland, C. A., Duffin, R., Kinloch, I., Maynard, A., Wallace, W. A. H., Seaton, A., et al. (2008). Carbon nanotubes introduced into the abdominal cavity of mice show asbestos-like pathogenicity in a pilot study. *Nat. Nanotechnol.* 3, 423–428. doi: 10.1038/nnano.2008.111

Qin, Y. X., Song, F. H., Ai, Z. H., Zhang, P. P., and Zhang, L. Z. (2015). Protocatechuic acid promoted alachlor degradation in Fe(III)/H_2O_2 Fenton system. *Environ. Sci. Technol.* 49, 7948–7956. doi: 10.1021/es506110w

Rodrigues, D. F., and Elimelech, M. (2010). Toxic effects of single-walled carbon nanotubes in the development of *E. coli* biofilm. *Environ. Sci. Technol.* 44, 4583–4589. doi: 10.1021/es1005785

Roman, D., Yasmeen, A., Mireuta, M., Stiharu, I., and Al Moustafa, A. E. (2013). Significant toxic role for single-walled carbon nanotubes during normal embryogenesis. *Nanomedicine* 9, 945–950. doi: 10.1016/j.nano.2013.03.010

Sekar, R., and DiChristina, T. J. (2014). Microbially driven Fenton reaction for degradation of the widespread environmental contaminant 1,4-dioxane. *Environ. Sci. Technol.* 48, 12858–12867. doi: 10.1021/es503454a

Shi, M. M., Xia, K. M., Peng, Z. F., Jiang, Y. G., Dong, Y. R., and Shi, L. (2021). Differential degradation of BDE-3 and BDE-209 by the *Shewanella oneidensis* MR-1-mediated Fenton reaction. *Int. Biodeterior. Biodegrad.* 158:105165. doi: 10.1016/j.ibiod.2020.105165

Takahashi, S., Taguchi, F., and Hori, K. (2023). Contribution of the Fenton reaction to the degradation of carbon nanotubes by enzymes. *Front. Environ. Sci.* 11:1184257. doi: 10.3389/fenvs.2023.1184257

Tang, Y. J. J., Laidlaw, D., Gani, K., and Keasling, J. D. (2006). Evaluation of the effects of various culture conditions on Cr(VI) reduction by *Shewanella oneidensis* MR-1 in a novel high-throughput mini-bioreactor. *Biotechnol. Bioeng.* 95, 176–184. doi: 10.1002/bit.21002

Valderrama, B., Ayala, M., and Vazquez-Duhalt, R. (2002). Suicide inactivation of peroxidases and the challenge of engineering more robust enzymes. *Chem. Biol.* 9, 555–565. doi: 10.1016/S1074-5521(02)00149-7

Wang, J. W., Ma, Q., Zhang, Z. J., Li, S. Z., Diko, C. S., Dai, C. X., et al. (2020). Bacteria mediated Fenton-like reaction drives the biotransformation of carbon nanomaterials. *Sci. Total Environ.* 746:141020. doi: 10.1016/j.scitotenv.2020.141020

Wang, J. W., Shan, S., Ma, Q., Zhang, Z. J., Dong, H. S., Li, S. Z., et al. (2021). Fenton-like reaction driving the degradation and uptake of multi-walled carbon nanotubes mediated by bacterium. *Chemosphere* 275:129888. doi: 10.1016/.chemosphere.2021.129888

Wang, X. N., Sun, G. X., Li, X. M., Clarke, T. A., and Zhu, Y. G. (2018). Electron shuttle-mediated microbial Fe(III) reduction under alkaline conditions. *J. Soils Sediments* 18, 159–168. doi: 10.1007/s11368-017-1736-y

Yadav, T., Mungray, A. A., and Mungray, A. K. (2016). Effect of multiwalled carbon nanotubes on UASB microbial consortium. *Environ. Sci. Pollut. Res.* 23, 4063–4072. doi: 10.1007/s11356-015-4385-y

Yang, M., Zhang, M. F., Nakajima, H., Yudasaka, M., Iijima, S., and Okazaki, T. (2019). Time-dependent degradation of carbon nanotubes correlates with decreased reactive oxygen species generation in macrophages. *Int. J. Nanomedicine* 14, 2797–2807. doi: 10.2147/Ijn.S199187

Yang, Y. T., Chen, J., Chen, Z., Yu, Z., Xue, J. C., Luan, T. G., et al. (2022). Mechanisms of polystyrene microplastic degradation by the microbially driven Fenton reaction. *Water Res.* 223:118979. doi: 10.1016/j.watres.2022.118979

Yan, W., Zhang, J. F., and Jing, C. Y. (2016). Enrofloxacin transformation on *Shewanella oneidensis* MR-1 reduced goethite during anaerobic-aerobic transition. *Environ. Sci. Technol.* 50, 11034–11040. doi: 10.1021/acs.est.6b03054

You, Y., Das, K. K., Guo, H., Chang, C. W., Navas-Moreno, M., Chan, J. W., et al. (2017). Microbial transformation of multiwalled carbon nanotubes by *Mycobacterium vanbaalenii* PYR-1. *Environ. Sci. Technol.* 51, 2068–2076. doi: 10.1021/acs.est.6b04523

Zhang, C., Chen, W., and Alvarez, P. J. J. (2014). Manganese peroxidase degrades pristine but not surface-oxidized (carboxylated) single-walled carbon nanotubes. *Environ. Sci. Technol.* 48, 7918–7923. doi: 10.1021/es5011175

Zhang, C. D., Li, M. Z., Xu, X., and Liu, N. (2015). Effects of carbon nanotubes on atrazine biodegradation by *Arthrobacter* sp. *J. Hazard. Mater.* 287, 1–6. doi: 10.1016/j.jhazmat.2015.01.039

Zhang, L. W., Petersen, E. J., Habteselassie, M. Y., Mao, L., and Huang, Q. G. (2013). Degradation of multiwall carbon nanotubes by bacteria. *Environ. Pollut.* 181, 335–339. doi: 10.1016/j.envpol.2013.05.058

Zhang, M. F., Deng, Y. M., Yang, M., Nakajima, H., Yudasaka, M., Iijima, S., et al. (2019). A simple method for removal of carbon nanotubes from wastewater using hypochlorite. *Sci. Rep.* 9:1284. doi: 10.1038/s41598-018-38307-7

Zhang, M. H., Dong, H., Zhao, L., Wang, D. X., and Meng, D. (2019). A review on Fenton process for organic wastewater treatment based on optimization perspective. *Sci. Total Environ.* 670, 110–121. doi: 10.1016/j.scitotenv.2019.03.180

Zhu, F., Huang, Y. H., Ni, H. Y., Tang, J., Zhu, Q., Long, Z. E., et al. (2022). Biogenic iron sulfide functioning as electron-mediating interface to accelerate dissimilatory ferrihydrite reduction by *Shewanella oneidensis* MR-1. *Chemosphere* 288:132661. doi: 10.1016/j.chemosphere.2021.132661

frontiers | Frontiers in Microbiology

TYPE Original Research
PUBLISHED 13 March 2024
DOI 10.3389/fmicb.2024.1297721

OPEN ACCESS

EDITED BY
Vaibhav Srivastava,
University of Allahabad, India

REVIEWED BY
Ahmed K. Badawi,
El-Madina Higher Institute for Engineering and Technology, Egypt
Bhuvan Vemuri,
Ardurra, United States

*CORRESPONDENCE
Tabarak Malik
✉ tabarak.malik@ju.edu.et
Aruliah Rajasekar
✉ rajasekargood@gmail.com;
✉ rajasekargood@tvu.edu.in
Rajaram Rajamohan
✉ rajmohanau@yu.ac.kr

RECEIVED 20 September 2023
ACCEPTED 20 February 2024
PUBLISHED 13 March 2024

CITATION
Kokilaramani S, Satheeshkumar A, Nandini MS, Narenkumar J, AlSalhi MS, Devanesan S, Natarajan PM, Rajamohan R, Rajasekar A and Malik T (2024) Application of photoelectrochemical oxidation of wastewater used in the cooling tower water and its influence on microbial corrosion. *Front. Microbiol.* 15:1297721. doi: 10.3389/fmicb.2024.1297721

Application of photoelectrochemical oxidation of wastewater used in the cooling tower water and its influence on microbial corrosion

Seenivasan Kokilaramani[1], Alagersamy Satheeshkumar[1], M. S. Nandini[2,3], Jayaraman Narenkumar[4], Mohamad S. AlSalhi[5], Sandhanasamy Devanesan[5], Prabhu Manickam Natarajan[6], Rajaram Rajamohan[7]*, Aruliah Rajasekar[8,1]* and Tabarak Malik[9]*

[1]Environmental Molecular Microbiology Research Laboratory, Department of Biotechnology, Thiruvalluvar University, Vellore, Tamilnadu, India, [2]Department of Microbiology, Sree Balaji Medical College and Hospital, Chennai, Tamil Nadu, India, [3]Sree Balaji Dental College and Hospital, BIHER University, Chennai, Tamil Nadu, India, [4]Department of Environmental and Water Resources Engineering, School of Civil Engineering, Vellore Institute of Technology, Vellore, Tamil Nadu, India, [5]Department of Physics and Astronomy, College of Science, King Saud University, Riyadh, Saudi Arabia, [6]Department of Clinical Sciences, Center of Medical and Bio-Allied Health Sciences and Research, College of Dentistry, Ajman University, Ajman, United Arab Emirates, [7]Organic Materials Synthesis Lab, School of Chemical Engineering, Yeungnam University, Gyeongsan-si, Republic of Korea, [8]Adjunct Faculty, Department of Prothodontics, Saveetha Dental College and Hospital, Chennai, Tamil Nadu, India, [9]Department of Biomedical Sciences, Institute of Health, Jimma University, Jimma, Ethiopia

Background: Cooling towers are specialized heat exchanger devices in which air and water interact closely to cool the water's temperature. However, the cooling water contains organic nutrients that can cause microbial corrosion (MC) on the metal surfaces of the tower. This research explores the combined wastewater treatment approach using electrochemical-oxidation (EO), photo-oxidation (PO), and photoelectrochemical oxidation (PEO) to contain pollutants and prevent MC.

Methods: The study employed electro-oxidation, a process involving direct current (DC) power supply, to degrade wastewater. MC studies were conducted using weight loss assessments, scanning electron microscopy (SEM), and x-ray diffraction (XRD).

Results: After wastewater is subjected to electro-oxidation for 4 h, a notable decrease in pollutants was observed, with degradation efficiencies of 71, 75, and 96%, respectively. In the wastewater treated by PEO, microbial growth is restricted as the chemical oxygen demand decreases.

Discussion: A metagenomics study revealed that bacteria present in the cooling tower water consists of 12% of *Nitrospira* genus and 22% of *Fusobacterium* genus. Conclusively, PEO serves as an effective method for treating wastewater, inhibiting microbial growth, degrading pollutants, and protecting metal from biocorrosion.

KEYWORDS

electro oxidation, photo-oxidation, photoelectrochemical oxidation, microbial corrosion, biofilm, cooling tower wastewater

Introduction

Cooling towers serve as specialized heat exchangers in which air and water interact closely to reduce the water temperature (Manh et al., 2019). The operational principle involves the passage of water through a heat exchanger, which absorbs heat and spreads it over the tower's top. The interaction with airflow causes the hot water to evaporate, increasing the air's temperature and relative humidity through heat transfer from the water stream to the air stream (Ortíz-Sánchez et al., 2023). This process results in a stream of cold water when the warmed air is released into the environment. The cycle is then repeated by pumping the cooled water from the basin through another heat transfer process (Abdulla et al., 2023). Cooling towers, often referred to as recirculating water systems, play a crucial role in removing excess heat and maintaining temperatures for industrial equipment, including heating, ventilation, and air conditioning (HVAC) systems. The key components of a cooling system include a recirculating pump, a heat exchanger, and a cooling tower (Fitch et al., 2022). Maintenance is a critical aspect of cooling towers. Poor maintenance leads to the accumulation of dust particles, microbes, debris, and other particles on cooling tower components. The accumulation of these particles can block airflow, constraining the operation of fans and pumps. As a consequence, cooling towers have a decreased lifespan and suffer from inefficiencies and loss of cooling efficacy, leading to economic losses and unreliable operations (Martínez-Huitle and Panizza, 2018). The uncontrolled growth of microbes that alter the chemical parameters of the cooling tower systems pose a significant challenge to the industry. Biofilms dominate cooling water systems, promoting micro-biofouling, which can obstruct the operations of these systems (Bhandari and Ranade, 2014; Reddy and Osborne, 2020).

Microbial corrosion occurs between metal surfaces and microbes present in wastewater (aqueous solution), with microbial growth, which depends on the volume of nutrients derived from organic matter, serving as a carbon source (Abdulla et al., 2023; Parthipan et al., 2023). Microbes adhere to exposed surfaces, leading to the production of biopolymers, primarily extracellular polymeric substances (EPS), forming biofilm layers. The subsequent oxidation and reduction processes occurring on metals result in the formation of pitting corrosion (Elumalai et al., 2021). Additionally, salts and organic compounds in the cooling tower water contribute to high salt concentrations and deposition, affecting its overall functioning (Saha et al., 2020). The parameters of cooling tower water, including calcium ions, total hardness, alkalinity, iron, phosphorus, orthophosphate, chloride, sulfur dioxide, conductance, turbidity, and chemical oxygen demand (COD), are analyzed and maintained to proper concentrations (Bustos-Terrones et al., 2021). Wastewater, characterized by a high concentration of inorganic compounds, induces heavy corrosion due to ion exchanges between compounds and metals (Guiamet and Gómez De Saravia, 2005). Industrial sectors frequently use ozonation and chlorination, among other disinfection processes, to treat and recycle wastewater; nevertheless, these systems have downsides, including high maintenance costs and operational concerns (Lazarova et al., 1999). Adsorption and electrochemistry are two removal methods that have been developed recently to clean wastewater (Fomina and Gadd, 2014; Reddy and Osborne, 2022). Wastewater is often subjected to mechanical biotreatment to remove hazardous substances and germs. Microbiological pollutants are assessed and tracked in relation to quality criteria (Musa et al., 2010). Photo-oxidation (PO), electrochemical oxidation (EO), and photoelectrochemical oxidation (PEO) are employed in industrial wastewater treatment due to their strong oxidation capacities to reduce contaminants (Zheng et al., 2022). There are primarily two approaches to electro-oxidation (EO). One is direct oxidation, which occurs on the electrode surface, and it can be stopped by the electric field effect, hydroxyl radicals (OH), hydrogen peroxide, ozone, or hydrogen radicals (Anadebe et al., 2020). The formation of various aqueous solution oxidants, such as sulfate or chlorine species, is the foundation of the second strategy, known as indirect oxidation (Sierra-Sánchez et al., 2022). When applied correctly, the efficient processes of anodic oxidation (EO) and ultraviolet radiation (PO) can both reduce and eliminate pollutants found in wastewater (Ungureanu et al., 2020). The EO process relies on the production of potent oxidants, such as hydroxyl radicals and oxide radicals (O_2^-), which react with contaminants to accelerate the degradation mechanisms (Cotillas et al., 2016). The straightforward method of PO relies on irradiating semiconductors with light to excite higher electron states (e^-), which move from the valence band to the conduction band and leave holes ("h^+") on the valence band. For the treatment of organic compounds involving oxidation, both e– and h+ can react with water molecules to form oxidative reactive species (for example, OH^-, O_2^-, and H_2O_2) (Fomina and Gadd, 2014). Although various publications discuss PEO, the chemicals that cause degradation in wastewater are classified as inorganic and organic pollutants. A recent study suggests that combining electrochemical oxidation and ultraradiation enhances the disinfection process by increasing the number of oxidizing products formed and activating them more effectively (de Vidales et al., 2015; Zapatero et al., 2015).

Therefore, the implementation of the photoelectrochemical oxidation (PEO) approach was effective in the treatment of cooling tower wastewater, leading to a reduction in contaminant levels. The study assessed the current density employed to reduce the chemical oxygen demand (COD) levels and investigated the activities of microbial populations that contribute to the formation of biofilms, a key factor in corrosion within cooling tower water (CTW). As a result of these findings, the oxidation process emerges as a markedly more favorable, efficient, cost-effective, environmentally friendly, and promising treatment option for the reduction or elimination of pollutants from wastewater.

Materials and methods

Sample collection

The cooling tower wastewater (CTW) was collected from the tannery industry (Ranipet Tannery Effluent Treatment Limited) (latitude 12.9149857° and longitude 79.3459513°) located in Ranipet, Tamil Nadu, India. The samples from the outlet of the cooling tower system were collected into a sterile container and stored at 4°C for future use.

Physicochemical parameters analysis

The collected samples were analyzed for specific parameters, such as temperature, pH, turbidity, total suspended solids (TSS), total dissolved solids (TDS), chloride (Cl^-), hardness, conductivity, and chemical oxygen demand (COD) using the dichromate method in the Merck Spectroquant TR 320 (Swaroop et al., 2016). The assessment followed the standard protocol outlined in the American Public Health Association (APHA) 200511, using which the physicochemical parameters of the cooling tower wastewater were evaluated both before and after treatment.

Metagenomic sequencing analysis

Genomic DNA extraction

GenomicDNA extraction was carried out from the collected CTW using commercially available kits such as the Xploregen kit. Before PCR amplification, the extracted DNA from the samples was subjected to NanoDrop and GEL Check. The NanoDrop readings of 260/280 at an approximate value of 1.8–2 are used to evaluate the quality of the DNA (Prakash et al., 2021).

Amplicon generation

The PCR amplification of the V3–V4 Region of 16s Gene: TAQ Master MIX contains High-Fidelity DNA Polymerase, 0.5 mM dNTPs, 3.2 mM MgCl2, PCR Enzyme Buffer. Primer information: 16s F:-5′ AGAGTTTGATGMTGGCTCAG3′ 16s R:-5′ TTACCGCGGCMGCSGGCAC3′. The following conditions were used: For amplification, 40 ng of the extracted DNA is utilized, along with 10 pM of each primer, with initial denaturation at 95°C, followed by 25 cycles of the following conditions: denaturation at 95°C for 15 s, annealing at 60°C for 15 s, elongation at 72°C for 2 min, and final extension at 72°C for 10 min, followed by a hold at 4°C. GEL Check and Nanodrop QC are performed on the amplified 16s PCR Product. The NanoDrop readings of 260/280 at an approximate value of 1.8–2 are used to evaluate the quality of the DNA (Shukla et al., 2021).

Library clean-up and sequencing

The amplicons from each sample were purified with Ampure beads to eliminate unneeded primers, and an additional eight cycles of PCR were performed using Illumina barcoded adapters to produce the sequencing libraries. Ampure beads were used to purify the libraries, and the Qubit dsDNA High Sensitivity assay kit was used to quantify them. Illumina Miseq with a 2x300PE v3–v4 sequencing kit was used for sequencing (Parthipan et al., 2023).

Bioinformatics analysis

NCBI is the database utilized for the 16s V3–V4 region. The sequencer's bcl data is de-multiplexed and converted into fastq raw data. The quality of the de-multiplexed data will be evaluated using the Fastqc (Version 0.11.9) and Multiqc (Version 1.10.1) tools. The QC-passed samples are qualified for further analysis, and for 16s metagenomics, we employed our own pipeline (Biokart Pipeline). The pipeline procedure is as follows: quality control, chimaera identification, OIU clustering, choosing representative sequence, assigning taxonomy, and creating a taxonomy table. When the run is finished, we have the final raw OTU table from which we can begin visualizing the results. Microsoft Excel is used to create the abundance feature tables and the top 10 organisms in each sample (2010). A microbiome analyst was used for additional studies such as a heat map, a core microbiome, a dendrogram, an alpha diversity index, a beta diversity index, a PCOA plot, a rarefaction curve, and so on (Chong et al., 2020; Mater et al., 2023). The metagenomic report is submitted to NCBI under the accession number PRJNA836405 (https://www.ncbi.nlm.nih.gov/bioproject/PRJNA836405).

Electrolytic system

The experimental setup involved bulk electrolysis utilizing a small, open, cylindrical, and hollow-shaped electrochemical tubular flow cell coated with a titanium tube. This tube had a diameter of 21 cm, a length of 3.9 cm, and a volume of 370 mL. The anode and cathode were positioned with a distance of 1.5 cm between them, and the cathode chamber was equipped with outlets and inlets for electrolyte flow. The inner side of the titanium tube housed the titanium-coated (Ti/TiO2-RuO2) expanded anode mesh, while the spacing between the cathode and anode was ~3.2 cm in length, with a diameter of 1 cm. The electrodes were arranged in parallel and vertically, maintaining an inter-electrode gap of 4 cm. The electrolyte sample, comprising 2,500 mL of CTW, was circulated through a peristaltic pump at a flow rate of 440 mL/min, and a DC supply was applied at a current density of about 12.21 mA/cm^2. This setup was employed for various electrochemical studies, following the methodologies outlined in previous studies (Su et al., 2019; Baaloudj et al., 2023). In the following studies, the three CTW systems were subjected to three treatments to test the comparative efficiency of the treatment process: (i) electro-oxidation (EO), (ii) photo-oxidation (PO), and (iii) photoelectro oxidation (PEO).

In the EO treatment (S2), current was applied to the electrolyte solution to treat the CTW (Martínez-Huitle and Panizza, 2018). In the PO (S3) setup, the UV lamp was only used to treat the CTW (Marszałek and Puszczało, 2020; Yi et al., 2022). In the PEO (S4) process, the rod-shaped UV lamp (6W) (Heber) was inserted in the middle of the anode mesh (Sierra-Sánchez et al., 2022) as the control system without treatment (S1). The total working volume flowed through the peristaltic pump to prevent temperature rise (Elawwad et al., 2017). The experiments were conducted under applied current conditions, by providing a direct DC supply (Aplab LD 6402). The entire experiment extended over 6 h, and samples were collected at 2-h intervals. The treated CTW underwent analysis post-treatment to examine COD levels and microbial growth to ensure adequate COD removal (Sundaravadivel and Vigneswaran, 2001). The processed water was further exposed

to sunlight to eliminate any residual contaminants present in the CTW.

Electro-oxidation

In this setup process, a circulating chamber is filled with the cooling tower water to a capacity of 2,500 mL. The electrolytic solution received an applied current of 1 A. On the anodic side, oxidation reaction takes place by breaking down the internal chemicals with the required current (Martínez-Huitle and Panizza, 2018).

Photo-oxidation

In this process, the sample is recirculated throughout the circulating chamber without using any applied current. The UV lamp is used in this setup to remove the organic contaminants and microbes present in the cooling tower system. The total viable bacterial counts and COD were estimated at the end of the experiment (Marszałek and Puszczało, 2020; Yi et al., 2022).

Photoelectro-oxidation

In this system, the electro-oxidation process and UV lamps were used in parallel. The UV and external current are applied in a sample time to achieve the removal of disinfectant in the cooling tower water (Sierra-Sánchez et al., 2022).

Ultraviolet–visible spectroscopy

The UV–visible spectrophotometer (UV-1800 SHIMADZU, Japan) was used to determine contaminants in the water sample both before and after treatment. APHA color measurements were quantified using the Hazen color index, and COD analysis was done at time intervals of 0, 2, 4, 6, and 8 h (Prakash et al., 2021).

Biocorrosion study

Weight loss measurement

Following the methodology outlined by Kokilaramani et al. (2021), the weighted samples in the form of coupons (2.5 × 2.5 cm^2) of the MS 1010 were introduced into the electro-oxidation (EO), photo-oxidation (PO), and photoelectro-oxidation (PEO) systems. The total number of corrosion formation systems was 4 ($n = 4$). Preweighted metal coupons, with each system having three coupons, were positioned in 500 mL conical flasks containing 400 mL of either pretreated or treated CTWs. These systems included S1—control (cooling tower water), S2—electro-oxidation-treated cooling tower water, S3—photo-oxidation-treated cooling tower water, and S4—photoelectro-oxidation treated cooling tower water, each in triplicate with an immobile condition. After 14 days of exposure, the coupons were retrieved from the flask, and non-metallic scrapers were employed to remove the corrosion products.

Following the completion of incubation, samples were taken from system and washed with pickling solutions. They were then dried at 40°C until they reached the desired weight consistency and then weighed again; the weight disparities were observed. The corrosion rate of MS was then analyzed and reported in mils per year (mpy), adhering to ASTM G1 standards. The weight loss calculation was performed to determine the corrosion rate (CR) using standard formulas and statistical significance.

Fourier-transformed infrared spectroscopy analysis

After the weight loss experiment, FT-IR was used to analyze the metal-scrap powdered samples. The FT-IR spectra with a wave number range of 400–4,000 cm^{-1}, a resolution of 8 cm^{-1}, and a scan rate of 64 scans/spectrum (PerkinElmer Spectrum IR Version 10.6.0, USA) were employed. Potassium bromide (KBr) was used to make pellets by applying hydrolytic pressure on metal samples (Gebreslassie et al., 2019). FT-IR was used to analyze the compounds present in the sample.

Scanning electron microscopy analysis

The surface morphologies and elemental compositions of mild steel samples exposed to pretreated and treated CTW for 21 days were examined by SEM/EDX by a Tescan VEGA 3SBH with an EDX detector on high magnification and resolution environmental scanning electron microscope (Morsi et al., 2016). After 21 days of exposure, the specimen surfaces S1, S2, S3, S5, S7, S9, and S11 were examined in order to assess the surface microstructure and composition of biofilm formation (Gebreslassie et al., 2019). To remove loosely adsorbed ions, the mild steel samples were finally washed thoroughly and then subjected to 15 min of ultrasonic cleaning.

X-ray diffraction studies

The XRD on metal powder, which had been previously prepared in a mortar, was analyzed by Bruker D8 Advance Equipment (Germany) with a LynxEye& Scintillation Counter detector with a 5°-140° angular range and at a rating between 40 and 30 kV. XRD analysis was applied directly to the mild steel samples in order to determine the types of oxide layers and corrosion products present on their surfaces (Narenkumar et al., 2019).

Electrochemical studies

The electrochemical analysis, including impedance spectroscopy and polarization, was conducted using the Metrohm Autolab instrument, USA, accompanied by Nova 2.1.5 software. This conventional three-electrode system has a capacity of ~50 mL of electrolyte, with MS specimens serving as the working electrode, platinum (Pt) as the counter electrode, and a saturated calomel electrode (SCE) as the reference electrode (Yue et al., 2014). After a 30-min immersion in the test fluid with a signal amplitude perturbation of 5 mV, the working electrode achieved a steady-state open circuit potential, E_{corr}. Impedance and potentiodynamic studies were performed on MS 1010 coupons (4 nos.) acting as the working electrode, with the reference electrode being a saturated calomel electrode (SCE) and a platinum electrode as the counter electrode (Mayrhofer et al., 2009). Impedance measurements were

conducted through an AC signal output with an amplitude of 10 mV at an open circuit potential (OCP) within the frequency range of 0.1–100 kHz. The impedance data were fitted to the most appropriate equivalent circuit, and the impedance parameters were obtained from Nyquist plots. The double-layer capacitance (Cdl) values were calculated from the frequency at the imaginary component of impedance (Grassini et al., 2018). The results were obtained 10 min after the startup process to reach a constant potential and were connected with multiple electrodes at a scan rate of 1,800 mV/h from an open circuit potential of +200 mV SCE to −200 mV SCE. The cooling tower water sample was analyzed after 21 days of immersion.

Results and discussion

Physicochemical characterization of cooling tower wastewater due to electrochemical oxidation

The physicochemical parameters of pretreated and treated CTW in EO, PO, and PEO are presented in Table 1. The pH of the CTW ranges from 5.71 to 4.28, having an average value of 5.70, which is permissible. The wastewater's turbidity exhibits a pale or dark yellow color, with a color unit of 0.48 Hazen. As the permissible limit of color according to the Central Pollution Control Board (CPCB) is 10 Hazen, the wastewater is treated to reduce the color before discharge (Srivastava et al., 2016). The average values of total suspended solids (TSS) and total dissolved solids (TDS) are found to be 133 ± 4 and 225 ± 0.5 mg/L, respectively. The chloride content in wastewater is determined to be 367.20 ± 3 mg/L, which is below the acceptable threshold of 1,000 mg/L. Additionally, the average value of conductivity is 1,348 ± 0.2 μS/cm, and the wastewater has chemical oxygen demand (COD) values (average) of 185 ± 6 mg/L. These results indicate that PEO treatment (2,512 ± 3 to 185 ± 6 mg/L) effectively reduced the COD values (Martínez-Huitle and Panizza, 2018). This result is in agreement with the data previously reported by Jallouli et al. (2020) for COD reduction in wastewater electrocoagulation (EC) or UV photolysis, which achieved 85.7 and 55.9% of COD reduction, respectively. Our results also broadly agree with these values. The average values of sulfide and sulfate are 112 ± 3.9 and 123 ± 2.1 mg/L, respectively, while the values of hardness and alkalinity are 170 ± 1 and 212 ± 1.5 mg/L, respectively. The COD test is crucial for detecting hazardous circumstances, biologically resistant organic substances, and the performance of treatment facilities due to the rapid results it provides. PEO emerges as the most efficient approach, as evidenced by the results of the electrochemical treatments. Thus, the efficiency of the methods is of the order PEO > EO > PO.

Metagenomic analysis

Isolation, characterization, and next-generation (metagenomic) sequencing of microbes

The taxonomic annotation of the predicted operational taxonomic units (OTUs) showed that CTW metagenomics was dominated by the domain bacteria (77.50%), followed by unknown (12.50%), and <10% OTUs were observed for archaea, viruses, and eukaryotes (Petrosino et al., 2009). Microbial diversity was accomplished in detail through taxonomic classification, which was performed using a ribosomal database project (RDP) classifier against the SILVA operational taxonomic units (OTUs) database. The detailed information of the CTW sample including total consensus reads chimeric sequences, pre-processed reads, OTUs, phylum (Supplementary Figure S1), class (Supplementary Figure S2), order (Supplementary Figure S3), family (Supplementary Figure S4), genus (Figure 1), and distribution for each sample based on OTUs and reads (Supplementary Figure S5) The findings of the metagenomic study were included in a submission to NCBI, with BioProject Accession number PRJNA836405 (https://www.ncbi.nlm.nih.

TABLE 1 Estimation of chemical parameters of cooling tower water.

Test parameter	Unit	Control	EO	PO	PEO
Temperature	°C	28 ± 0.1	35 ± 0.3	35 ± 0.5	35 ± 0.1
pH	1–14	5.71 ± 0.1	4.28 ± 0.3	4.93 ± 0.2	5.70 ± 0.6
Turbidity	NTU	5.09 ± 0.6	1.97 ± 0.1	2.13 ± 0.5	0.48 ± 0.2
TSS	mg/L	1,000 ± 5	202 ± 6	245 ± 2	133 ± 4
TDS	mg/L	700 ± 0.8	626 ± 0.6	689 ± 1.2	225 ± 0.5
Cl^-	mg/L	634.55 ± 6	570.74 ± 4	616.83 ± 7	367.20 ± 3
Conductivity	μS/cm	2,515 ± 0.4	2,076 ± 0.2	2,394 ± 0.3	1,348 ± 0.2
COD	mg/L	2,512 ± 3	1,380 ± 3	1,428 ± 5	185 ± 6
Sulfide	mg/L	888 ± 2.0	412 ± 3.3	682 ± 3.5	112 ± 3.9
Sulfate	mg/L	1,957 ± 1.0	582 ± 1.1	1,724 ± 3.3	123 ± 2.1
Hardness as CaCO3	mg/L	1,250 ± 2	1,120 ± 2	1,175 ± 3	170 ± 1
Alkalinity	mg/L	1,746 ± 1.3	741 ± 1.4	1,000 ± 2.2	212 ± 1.5

EO, electro-oxidation; PO, photo-oxidation; PEO, photoelectrochemical oxidation.

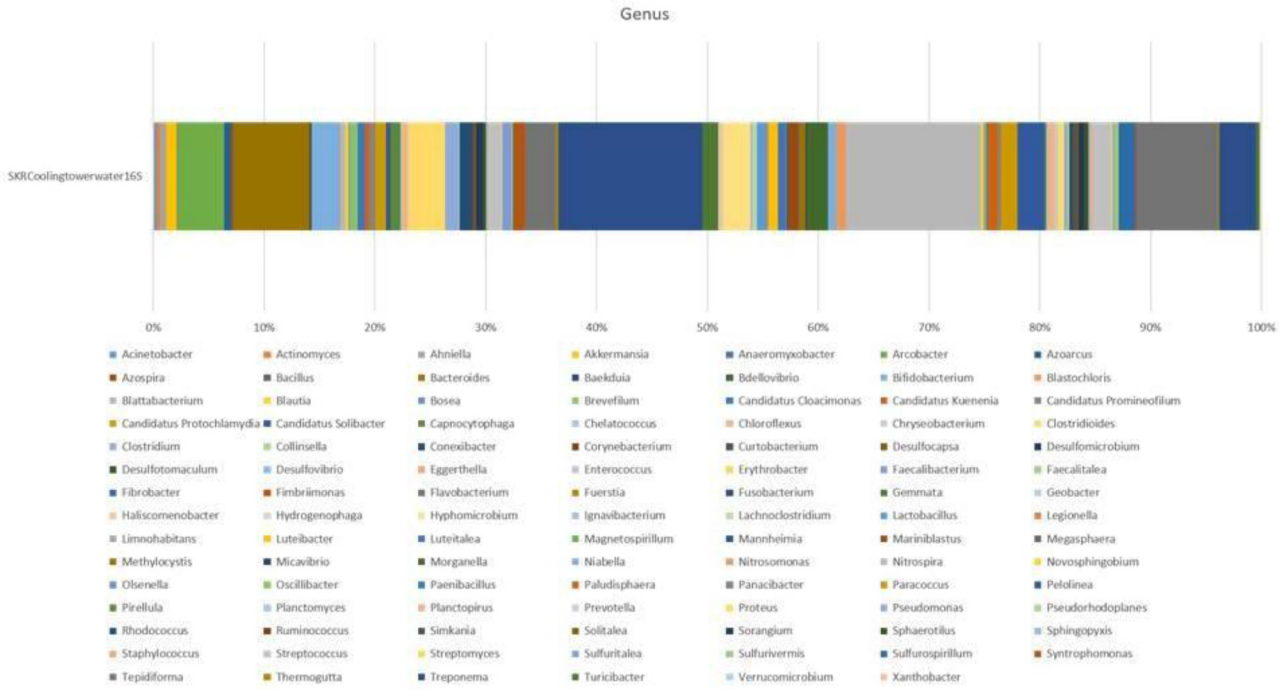

FIGURE 1
Genus revealed by metagenomics studies in the collective sample of cooling tower wastewater.

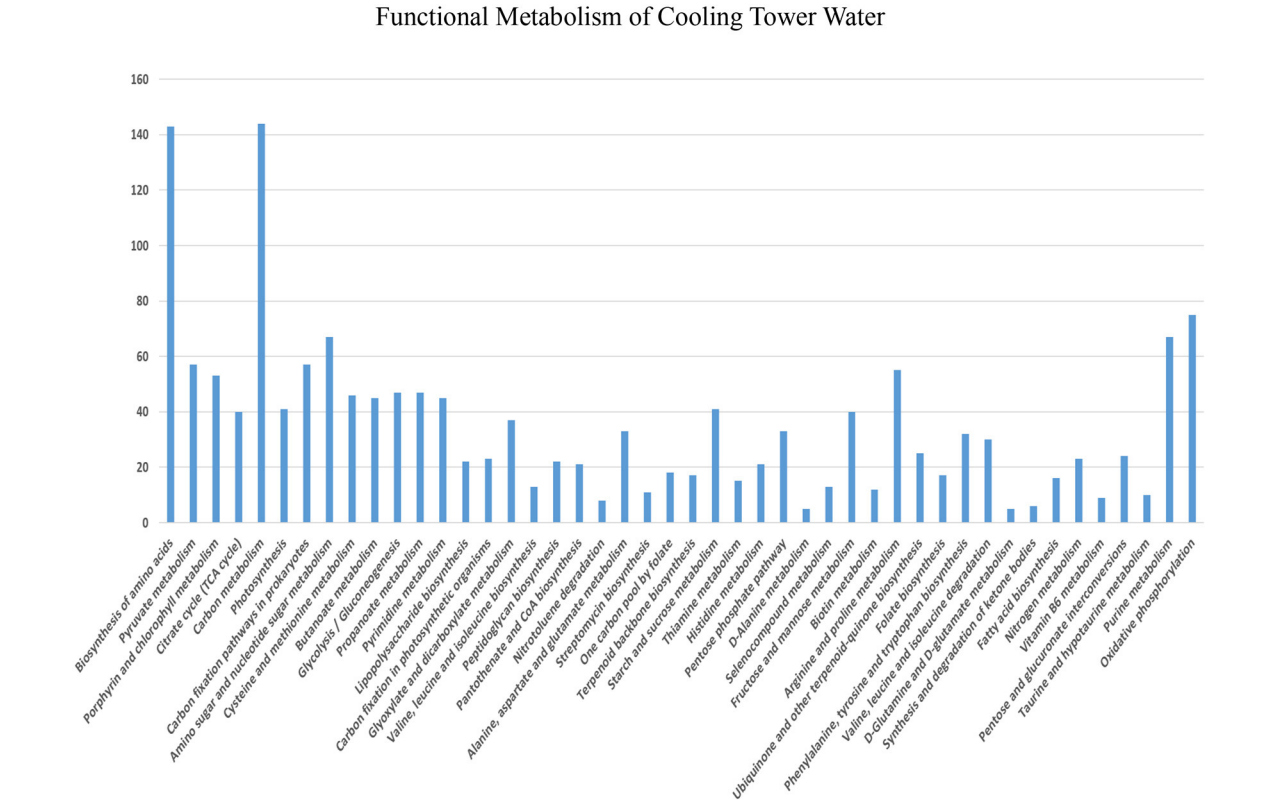

FIGURE 2
Metabolic activities in the collective sample of cooling tower wastewater.

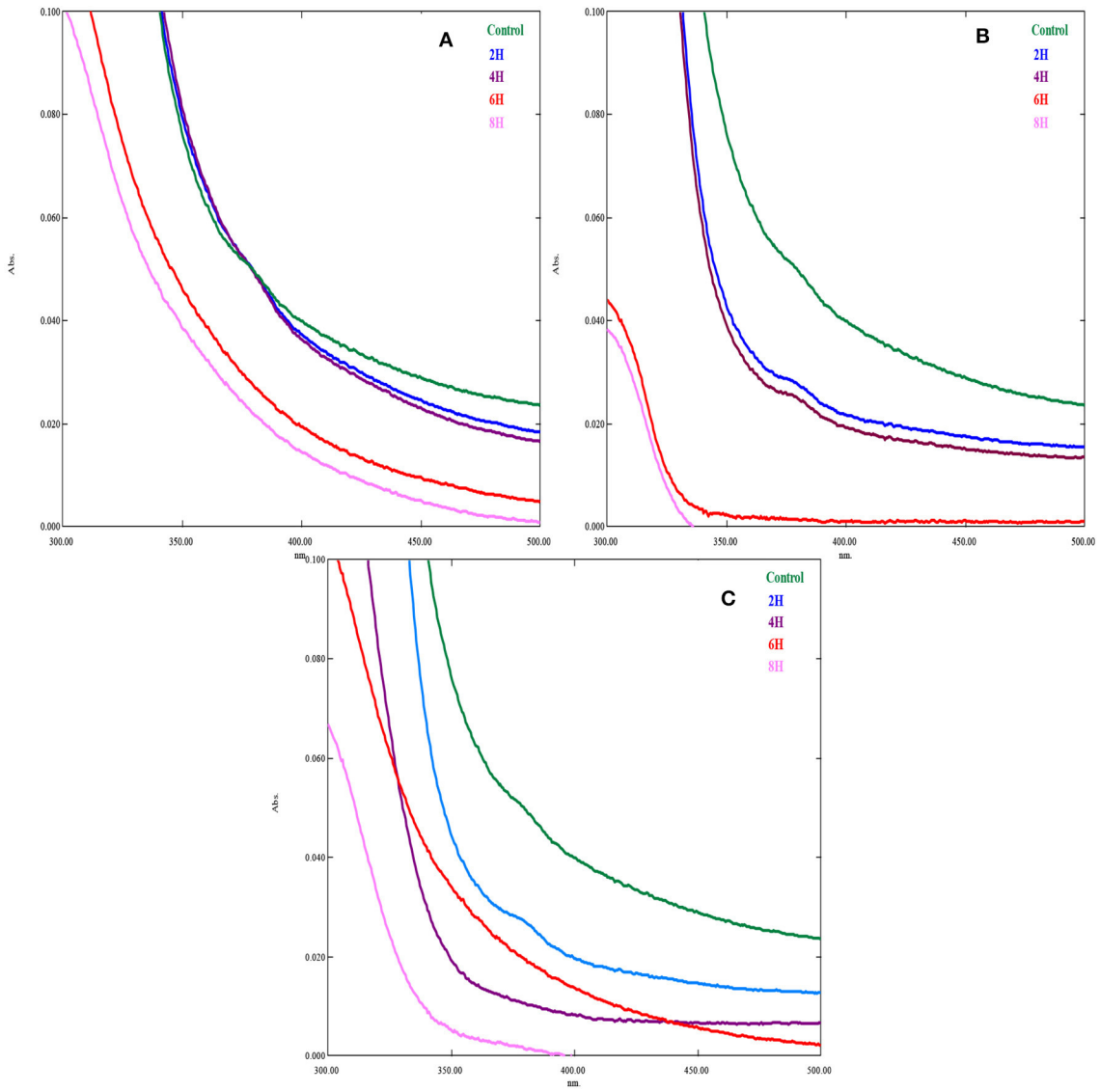

FIGURE 3
UV spectrum of treated and untreated cooling tower wastewater in different hours. **(A)** EO; **(B)** PO; **(C)** PEO.

gov/bioproject/PRJNA836405). It was noted that the taxa outside of top most 10 taxas are classified. At the genus level of taxonomic profiling, a total of 105 bacterial genera were detected in the CTW (Raji, 2017). Particularly when contrasted with variances within the individual treatments, the differences between the communities in the cooling tower systems, both in the planktonic cells and in the biofilm developed over the coupons, were significant. When the OTU numbers was investigated, *Fusobacteriia* class members predominated in planktonic communities (Gambino et al., 2022). The water sample consists of the most abundant bacterial OTU class (%) as follows (Figure 1): *Fusobacterium* (22), *Nitrospria* (21), *Tepidiforma* (13), *Bacteroides* (12), *Arcobacter* (7), *Clostridioides* (6), *Treponema* (6), *Flavobacterium* (5), *Bifidobacterium* (4), and *Hyphomicrobium* (4). The water sample contains diverse microbial genera (Figure 1) such as *Corynebacterium*, *Actinomyces*, *Streptomyces*, *Collinsella*, *Olsenella*, *Eggerthella*, *Baekduia*, *Clostridioides*, *Streptococcus*, *Lactobacillus*, *Bacillus*, *Xanthobacter*, *Erythrobacter*, *Sulfuritalea*, *Acinetobacter*, *Sulfurivermis*, *Desulfovibrio*, *Desulfomicrobium*, *Desulfotomaculum*, *Geobacter*, *Bacteroides*, *Fibrobacter*, *Pseudorhodoplanes*, *Nitrospira*, *Fimbriimonas*, *Flavobacterium*, *Pseudomonas*, *Clostridium*, and *Staphylococcus* (Figure 1) (Prakash et al., 2021). The metabolic activates of cooling tower water in the bar graphs representing microbial community composition revealed metagenomes at taxonomic levels in the cooling tower wastewater: (a) phylum, (b) class, (c) order, (d) family, and (e) genus. Microbial taxa showing <1% relative abundance are shown as "others" in the phylum level gto family level bar graphs, whereas those <1.5% are presented in the genus level bar graph (Pinel et al., 2020).

The functional metabolism of cooling tower water is shown in Figure 2. According to the results of the CTW metabolic

analysis (Supplementary Table S1), nearly 46 metabolic pathways were identified, and of these, carbon metabolism was ~308 (97.2%), biosynthesis of amino acids was 225 (71%), oxidative phosphorylation was 202 (63.8%), purine metabolism was 178 (56.2%), and arginine and proline metabolism stands at 129 (40.7%). Metabolism is a process involving the utilization of organic material for energy or the creation of cellular activities, occurring in all organic molecules to produce the acetate discharged as acetyl-CoA employed for biosynthetic reactions, which is oxidized to CO_2 accompanied by an equivalence reduction in tricarboxylic acid (TCA) cycle (Parthipan et al., 2023). The reduction equivalency was measured in the respiration chain with oxygen molecules. In this reaction, 2 M of acetate is oxidized to yield 34 M of ATP when the electron transport chain is phosphorylated, with oxygen acting as the terminal electron acceptor. This process preserves ATP. The ATP anhydridic phosphate bond energy has values up to 2 M upon 1 M glucose glycolysis. During metabolism, reducing equivalents participate in a controlled combustion process with molecular oxygen. Methane, CO_2, NH_3, and H_2S are produced by fermentative and acetogenic bacteria in conjunction with methanogens or sulfate reducers. It takes a low hydrogen partial pressure, mostly from interspecies hydrogen transfer, for biopolymers or monomers to completely degrade methanogenesis (Holtzapple et al., 2021). By arranging acetogens and hydrogenolytic methanogenic bacteria within short diffusion distances in flows or biofilms, interspecies hydrogen transfer

TABLE 2 Weight loss of biocorrosion system in cooling tower water.

Systems	Weight loss (mg)	Corrosion rate (mm/year)
S1—control (cooling tower water)	0.109 ± 0.04	1.970
S2—electro-oxidation treated cooling tower water	0.98 ± 0.06	0.859
S3—photo-oxidation treated cooling tower water	0.64 ± 0.03	0.566
S4—photo-electro-oxidation treated cooling tower water	0.33 ± 0.05	0.249

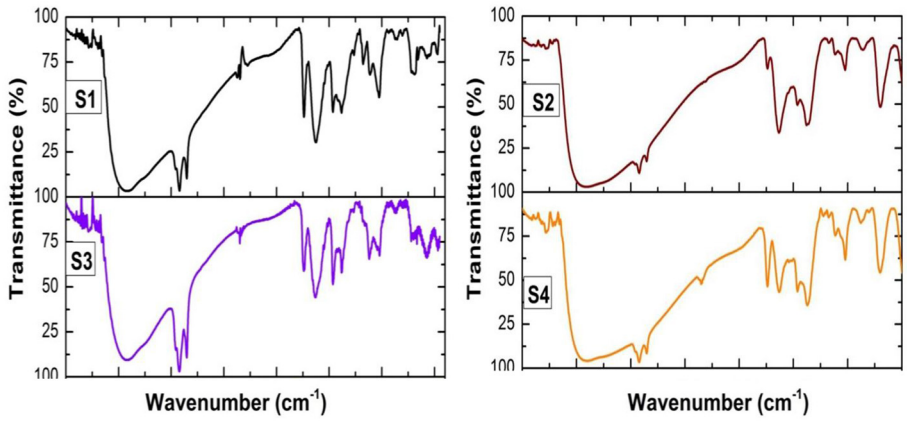

FIGURE 4
FTIR analysis of treated and untreated cooling tower wastewater. S1, Control; S2, EO; S3, PO; S4, PEO.

TABLE 3 FTIR analysis of biocorrosion system in cooling tower water.

Peak values (cm^{-1})	Bond	Intensity	Functional groups
3,423	N-H stretch	weak-medium	Amides R-C(O)-NH-R
2,924	C—H Strech	Strong	alkanes
2,347	R-C=N	Medium strong	Nitriles
1,727	R-C-H =O	Strong	Aldehydes
1,636	R-C(O)-NR′R"	Medium strong	Amides
1,363	–CH(CH3)2 or –(CH3)3	Medium	Alkanes and alkyls
1,109	RR′C-OH (2°) or C=C-CRR′-OH	Medium strong	Alcohol
1,010	=C-O-C	Medium strong	Ethers
864	=C-H	Strong	Alkenes
692	C-H	Strong	Aromatic compounds

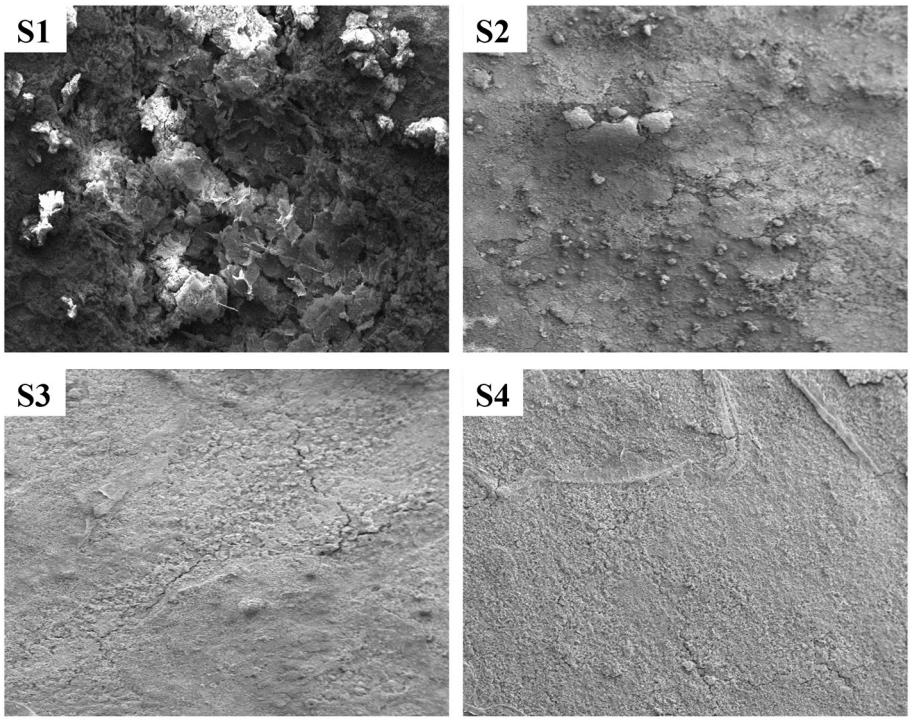

FIGURE 5
SEM analysis of treated and untreated cooling tower wastewater. S1, Control; S2, EO; S3, PO; S4, PEO.

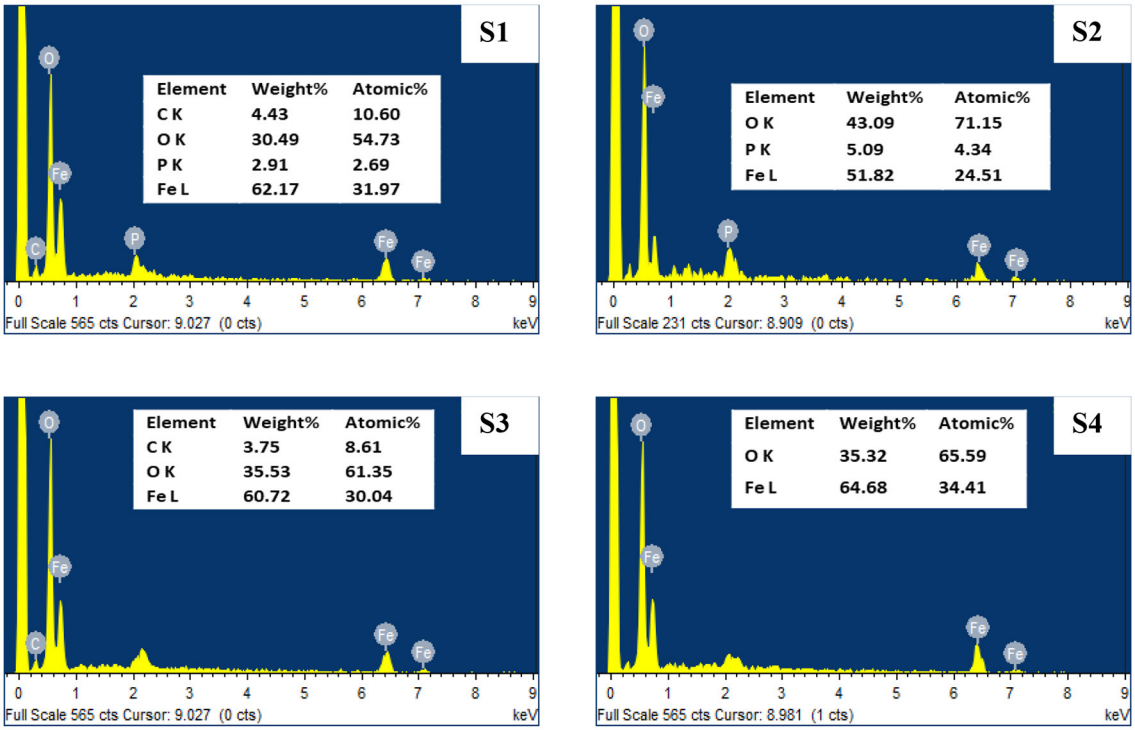

FIGURE 6
SEM analysis of treated and untreated cooling tower wastewater. S1, Control; S2, EO; S3, PO; S4, PEO.

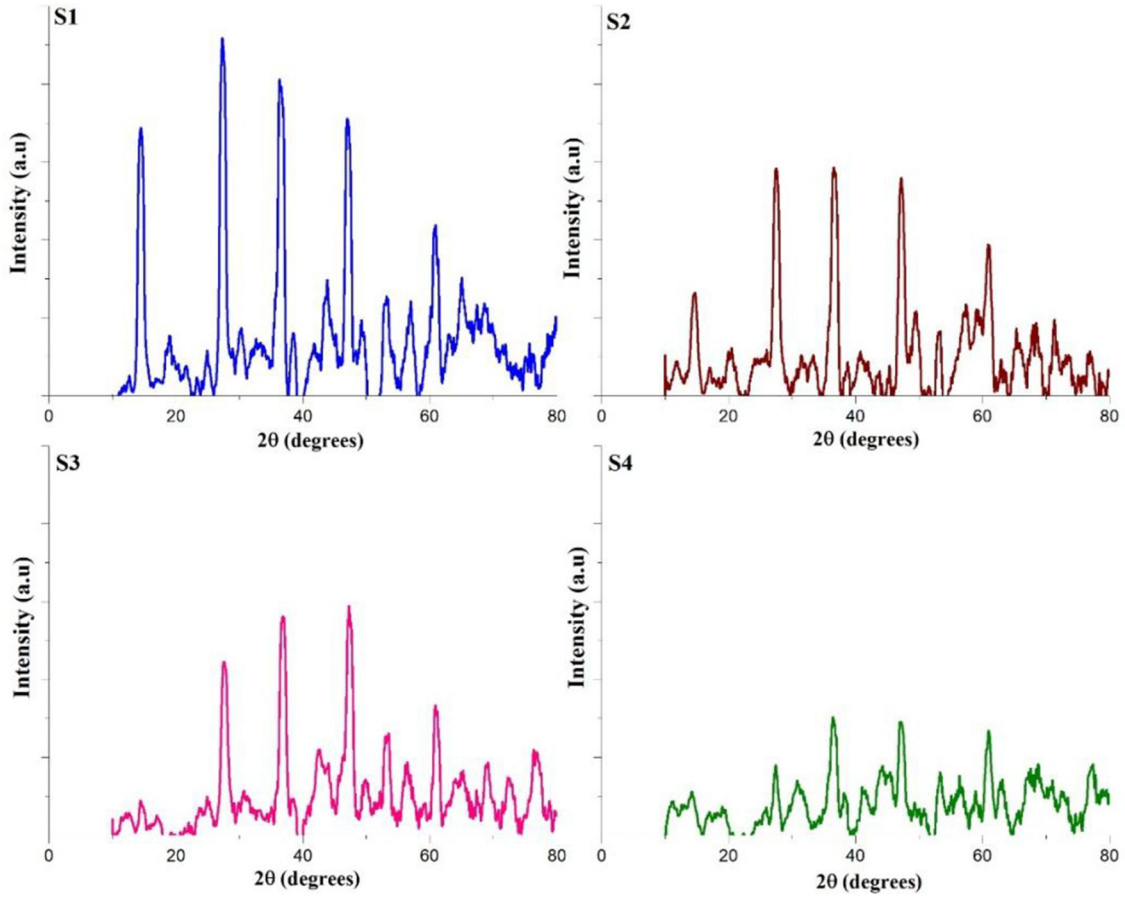

FIGURE 7
XRD analysis of treated and untreated cooling tower wastewater. S1, Control; S2, EO; S3, PO; S4, PEO.

is facilitated, and the fermentation process produces reducing equivalents for the reduction of carbon dioxide to methane and sulfate to sulfur dioxide (Gallert and Winter, 2005). The metabolism enzymes in the form of most toxic microorganisms catalyze the formation of analog chemicals, which are characterized as extracellular substances. These enzymes contribute to the mineralization of organic materials in water (Ahmad et al., 2022).

UV light spectrophotometric analysis

Figures 3A–C show the UV spectrum of cooling tower wastewater at different hours following EO, PO, and PEO. The adsorption UV spectrum indicates that the oxidation of CTW varies widely between the different hours (Ahmed et al., 2022). These entire spectrums are transformed in order for it to have an identical area between 300 and 500 nm, the range of the multicomponent method. The absorption spectra of the sample were identified in the visible range. The band at nearly 350 nm is distinctive of the unique aromatic rings and shows a considerable range of aromatic ring oxidation in the molecules of the wastewater. When the wastewater was exposed to UV light, a quick oxidation reaction takes place; this reaction time was virtually consistent for the photo-oxidation of the organic components in an aqueous solution (Zheng et al., 2022). The acquisition of a UV spectrum of a sample without treatment is carried out with a UV light (Advanced UV Examination of Wastewater). The existence of organic compound(s) present in the formulation that may absorb in the UV region is the primary explanation for the differences between the UV spectra of CTW (Yi et al., 2022). The whole spectrum range is between 200 and 800 nm, and for their dissolution in complex biological and environmental matrices, the working wavelengths are 325 and 395 nm. The slope break of the UV spectrum of fraction 4, at ~240 nm, is softened, confirming the presence of large particles (Physical and Aggregate Properties Marie-Florence Thomas) (Kinetics of decolourization of the azo structure in wastewater by UV/H2O2 process).

Weight loss measurement

The results of weight loss of biocorrosion system in cooling tower water are presented in Table 2. Initially, the MS coupon 1010 was weighed for the biocorrosion studies. In the control system, S1—pretreated CTW weight loss was recorded as 0.109 ± 0.04 mg, S2—EO-treated CTW weight loss was 0.98 ± 0.06 mg, S3—PO-treated CTW weight loss was 0.64 ± 0.03 mg, and S4—PEO-treated CTW weight loss was 0.33 ± 0.05. The corrosion rate

on exposure in S1, S2, S3, and S4 was 1.970, 0.859, 0.566, and 0.249, respectively (AlSalhi et al., 2023). After analyzing the statistical variance, it was found that the corrosion rate result, $p < 0.05$, is statistically significant.

The weight of the treated sample as a result of exposure period before the test is expressed as a ratio to its total mass. On a comparison of the pretreated and treated (EO, PO, and PEO) systems, the samples exhibiting the most severe metal loss behaviors offered superior conditions for the physical, chemical, and microbiological activities over a period of time. By using a mix of electric and UV light exposure to oxidize the microbial community and chemical substances, the PEO system exhibits negligible metal loss. The same set-equivalent corrosive conditions increased trust, and the parallel setup's identical corrosion conditions provided much more comfort (Rafieenia et al., 2022). The weight loss in the control system was also caused by the presence of inorganic chemicals and other metabolic processes.

FTIR analysis

The IR spectra reveal potential structural changes that may have occurred during the corrosion process. Figure 4 and Table 3 present the FT-IR spectra of CTW examined before and after oxidation. The FT-IR analysis of the biocorrosion system in CTW indicates several unique bands. A qualitative and quantitative comparison of the generated peaks for both pre-treatment and treated samples demonstrates the efficacy of the contaminant removal process. The FT-IR peaks show that compounds bind with samples S1, S2, S3, and S4. The value indicates the presence of 3,423 N–H stretches, denoting wide broad, amide R-C(O)-NH-R compounds. The peak at 2,924 cm^{-1} shows the presence of strong alkenes and narrow C—H stretch peaks. The peak at 727 cm^{-1} represents aldehydes R-C-H =O, a strong COH stretch compound. The peak at 1,636 cm^{-1}shows amides R-C(O)-NR′R" medium-strong C=O stretch. The peak at 1,363 cm^{-1} denotes the presence of alkenes and alkyls, medium –CH $(CH3)^2$ or – $(CH3)^3$ bend compound. The peak at 2,347 cm^{-1} indicates the presence of nitriles R-C = N medium strong C = N Stretch. The peak at 692 cm^{-1} shows aromatic compounds, mono-substituted strong C–H bend. The peak at 864 cm^{-1} represents alkenes RR′C=CH2 strong =C-H bend. The peak at 1,010 cm^{-1} demonstrates ethers Ar-O-R medium strong=C-O-C symmetric and asymmetric stretch. The peak at 1,109 cm^{-1} shows alcohols RR′C-OH (2°) or C=C-CRR′-OH medium strong C-O strong (Kamali et al., 2023).

SEM analysis

The SEM images of the pretreated and treated CTW specimens incubated for 21 days are depicted in Figure 5. Basically, a thick layer filled the entire specimen's surface. However, as can be observed, the arrangement of deposition on the metal surface and these oxide layers do not resemble each other. The deposition covering the pretreated corroded areas exhibits a layered structure, with dense aggregate in the top layer (Figure 5; S1). Deposits that create a thick, fragile oxide layer on top of the specimens exposed to EO are also heterogeneous, plain, and heterogeneous form (Figure 5; S3). On their oxide layer, the cell bodies were not easily discernible. In Figure 5 (S4), the mild steel was coated with a thick, homogeneous, and plain layer deposit in the treating conditions (Parthipan et al., 2023).

TABLE 4 Electrochemical impendence parameters of biocorrosion system in coolingtowerwater.

Sample name	CEP.Y0 (F)	R_s (Ωcm^2)	R_{ct} (Ωcm^2)	CEP.N
S1	1.2189E-8	−1.5714	102.43	1.0254
S2	1.1962E-8	−1.6794	121.32	0.9746
S3	1.2121E-8	−2.1749	112.83	0.95084
S4	1.4534E-8	−3.3364	102.66	0.88889

The energy-dispersive x-ray spectroscopy (EDX) examination for mild steel surface before and after treatment with CTW (Figure 6) revealed the reduction in ions to element in the reaction mixture, which may be used to determine the existence of the elements. Strong metallic ion signals were visible in the EDX spectrum, coupled with faint oxygen and carbon peaks, which could have come from surface-bound pretreatment water sample (Rocha et al., 2014). The EDX spectra of pretreatment water samples (Figure 6; S1) indicated the typical peaks (i.e., C, O, Fe, and P signals) of the formation of biofilm on the surface. The C, P, and some Fe singles are absent from the treated water (Figure 6; S2–S4), and the strength of the O peak is reduced. It is possible that these elements were completely oxidized during the treatment process (Sierra-Sánchez et al., 2022) (inhibition activity of Seaweed extract for mild carbon steel corrosion in saline formation water).

XRD analysis

The x-ray diffraction (XRD) pattern of corrosion products from mild steel in both pretreatment and treated CTW samples provides qualitative insights into the potential phases present (Linares-Hernández et al., 2010). The XRD data, showcasing the identified phases in the corrosion product samples, is illustrated in Figure 7. By cross-referencing and correlating the XRD data with patterns in the ICDD library, the main phase was determined to be FeOOH in all the samples. However, notable differences in peak intensity and breadth range were observed between pretreated CTW samples and treated CTW samples, indicating variations in the crystal structure (Peralta-Hernández et al., 2021). These findings suggest that the metal surfaces in the pretreatment samples had developed various types of FeOOH complexes, and the treatment process influenced the characteristics of the corrosion product phases.

Electrochemical studies

The I_{corr} value of system is 8.3514E-5 for S1, 0.00018628 for S2, 7.7287E-5 for S3, and 2.8717E-5 for S4. The R_p value system is 582.9 for S1, 408.61 for S2, 653.81 for S3, and 557.44 for S4, as shown in Table 4 and Figure 8. Electrochemical impendence parameters of CTW were also supported the the weight loss result. The S1 control cooling tower water results exhibit black color indicating a higher impedance rate, brown color indicating greater impedance for S2, violet color compared to control for S3, and

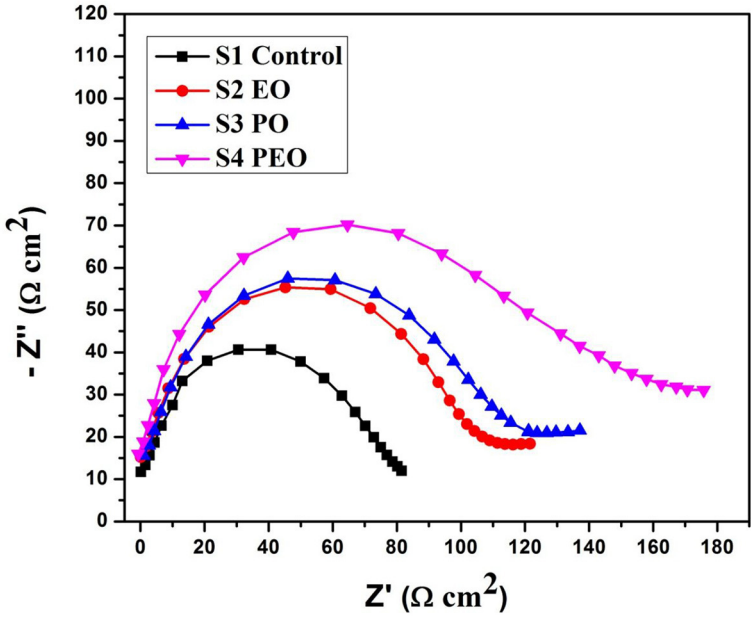

FIGURE 8
Electrochemical impendence parameters of treated and untreated cooling tower wastewater.

TABLE 5 Equivalent circuits for biocorrosion system in cooling tower water.

Element	Parameter	Value
S1		
R_s	R	−1.5714
R_p	R	104.45
CPE	Y0	1.2189E-08
		1.0254
S2		
R_s	R	−1.6794
CPE	Y0	1.1962E-08
	N	0.9746
R_p	R	122.88
S3		
R_s	R	−2.1749
R_p	R	114.94
CPE	Y0	1.2121E-08
	N	0.95084
S4		
R_s	R	−3.3364
R_p	R	106.35
CPE	Y0	1.4534E-08
	N	0.88889

red color indicating good result for S4 (Ungureanu et al., 2020). The Nyquist plots in the presence of control were depressed semicircles at a high frequency region when compared to EO, PO, and PEO, which might be due to inhomogeneity and roughness of the metal surface (Narenkumar et al., 2021). The superior semicircles were observed in inorganic chemicals, which indicates that the treated water inhibits the formation of the barrier layer on the surface and thereby inhibits electron transfer from the metal surface. The linear polarization S1 results show black color for control, brown color indicating the higher polarization rate for S2, blue color for S3 shows the effective rate, and red color for S4 shows a good result. The EIS and potentiodynamic graphs and tables show the corrosion rate and inhibition efficiency (Table 5; Figure 9). Haaken et al., also reported that PEO gives the best results and that the latter is unfavorable because the current density constitutes a limiting electrode parameter, on the one hand, and the enhancement of the current causes an increase in the resulting voltage and thus higher energy consumption, on the other hand (Butler et al., 2011). Potentiodynamic polarization parameters of cooling tower wastewater (Table 6) represent the consistency, stability, and intensity of the passive Fe oxide film generation, and this process was carried out according the study of Rocha et al. (2014). Using both the cathodic and anodic branches of the polarization curves, Tafel plots were used to derive the current densities *I* from the polarization curves. These findings support the metal alloy sample's inclination toward corrosion resistance that was inferred from the analysis of both equivalent circuit data and EIS diagrams (Yue et al., 2014). As a result, the increase of the electric charge input should be realized by the reduction of the flow rate.

10.3389/fmicb.2024.1297721

TABLE 6 Potentiodynamic polarization parameters of biocorrosion system in cooling tower water.

Sample name	E_{corr} (V)	i_{corr} (A)	R_p (Ω)	βa (V/dec)	βc (V/dec)
S1	−0.58692	8.3514E-5	582.9	0.21065	0.23957
S2	−0.58805	0.00018628	408.61	0.44053	0.29105
S3	−0.58371	7.7287E-5	653.81	0.22714	0.23855
S4	−0.57508	2.8717E-5	557.44	0.070169	0.077651

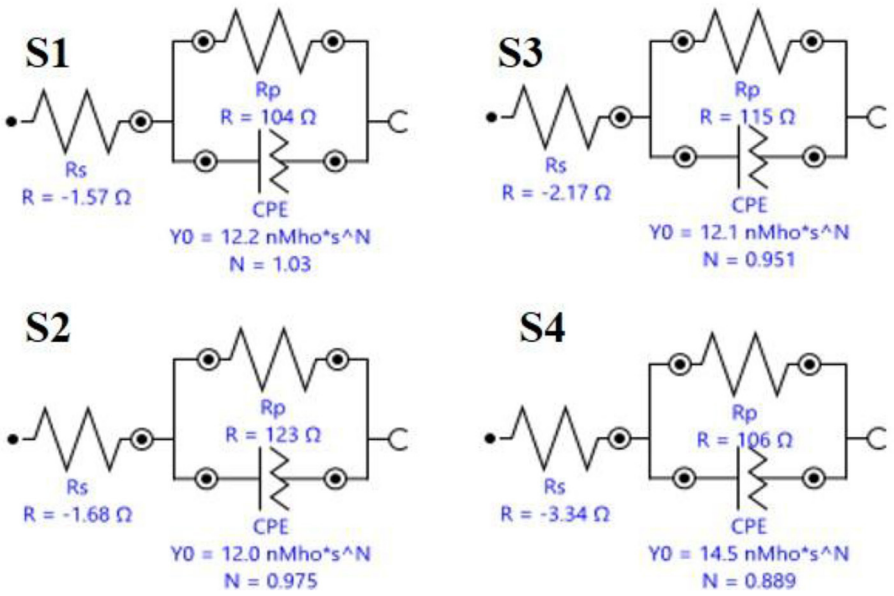

FIGURE 9
Equivalent circuits of cooling tower wastewater. S1, Control; S2, EO; S3, PO; S4, PEO.

Conclusion

The present study highlights the significant impact of photoelectro-oxidation (PEO) in controlling microbial corrosion on mild steel in cooling tower water. The impact of bacterial culture on the corrosion of mild steel has been studied by weight loss and electrochemical parameters. This bacterium effect was suppressed by PEO-treated cooling water compared to control, EO, and PO systems. FT-IR and COD tests confirmed that PEO is an efficient method to control corrosion. Ultraviolet (UV) light, a disinfection method employed in wastewater effluent treatment, was highlighted for its ability to destroy disease-causing organisms by disrupting their genetic material, preventing reproduction. The measurement of total suspended solids (TSS), including coarse fractions such as supracolloids and settleable matter, is crucial for the characterization of water and wastewater quality. The polarization study supported the observation that the corrosion current was lower in the PEO-treated system compared to control, EO, and PO systems. The electrochemical generation of sodium hypochlorite played a vital role in destroying microbial communities, subsequently reducing the corrosion rate of mild steel in the cooling tower water system.

Data availability statement

The datasets presented in this study can be found in online repositories. The names of the repository/repositories and accession number(s) can be found in the article/Supplementary material.

Author contributions

SK: Writing—original draft. AS: Methodology, Formal analysis, Writing—original draft. MN: Formal analysis, Methodology, Writing—review & editing. JN: Validation, Writing—original draft. MA: Software, Validation, Writing—review & editing. SD: Investigation, Validation, Writing—review & editing. PN: Validation, Writing—review & editing. RR: Validation, Visualization, Writing—review & editing. AR: Project administration, Supervision, Validation, Writing—review & editing. TM: Validation, Writing—review & editing.

Funding

The author(s) declare that no financial support was received for the research, authorship, and/or publication of this article.

Acknowledgments

The authors express their sincere appreciation to the RSP (RSP2024R398) King Saud University, Riyadh, Saudi Arabia.

Conflict of interest

The authors declare that the research was conducted in the absence of any commercial or financial relationships that could be construed as a potential conflict of interest.

Publisher's note

All claims expressed in this article are solely those of the authors and do not necessarily represent those of their affiliated organizations, or those of the publisher, the editors and the reviewers. Any product that may be evaluated in this article, or claim that may be made by its manufacturer, is not guaranteed or endorsed by the publisher.

Supplementary material

The Supplementary Material for this article can be found online at: https://www.frontiersin.org/articles/10.3389/fmicb.2024.1297721/full#supplementary-material

References

Abdulla, H., Zamorano, M., Rodríguez, M. L., El Shahawy, A., Hosny, S., Martín-Pascual, J., et al. (2023). An overview of agro-food industry wastewater treatment: a bibliometric analysis and literature review. *Appl. Water Sci.* 13:47. doi: 10.1007/s13201-022-01857-3

Ahmad, A., Ahmad, I., Kamal, T., Asiri, A. M., and Tabassum, S. (Eds.). (2022). *Sodium Alginate-Based Nanomaterials for Wastewater Treatment*. Elsevier.

Ahmed, M., Mavukkandy, M. O., Giwa, A., Elektorowicz, M., Katsou, E., Khelifi, O., et al. (2022). Recent developments in hazardous pollutants removal from wastewater and water reuse within a circular economy. *NPJ Clean Water* 5:12. doi: 10.1038/s41545-022-00154-5

AlSalhi, M. S., Devanesan, S., Rajasekar, A., and Kokilaramani, S. (2023). Characterization of plants and seaweeds based corrosion inhibitors against microbially influenced corrosion in a cooling tower water environment. *Arab. J. Chem.* 16:104513. doi: 10.1016/j.arabjc.2022.104513

Anadebe, V. C., Onukwuli, O. D., Abeng, F. E., Okafor, N. A., Ezeugo, J. O., and Okoye, C. C. (2020). Electrochemical-kinetics, MD-simulation and multi-input single-output (MISO) modeling using adaptive neuro-fuzzy inference system (ANFIS) prediction for dexamethasone drug as eco-friendly corrosion inhibitor for mild steel in 2 M HCl electrolyte. *J. Taiwan Inst. Chem. Eng.* 115, 251–265. doi: 10.1016/j.jtice.2020.10.004

Baaloudj, O., Nasrallah, N., Kenfoud, H., Bourkeb, K. W., and Badawi, A. K. (2023). Polyaniline/Bi12TiO20 hybrid system for cefixime removal by combining adsorption and photocatalytic degradation. *ChemEngineering* 7:4. doi: 10.3390/chemengineering7010004

Bhandari, V. M., and Ranade, V. V. (2014). *Advanced Physico-chemical Methods of Treatment for Industrial Wastewaters*.

Bustos-Terrones, Y. A., Hermosillo-Nevárez, J. J., Ramírez-Pereda, B., Vaca, M., Rangel-Peraza, J. G., Bustos-Terrones, V., et al. (2021). Removal of BB9 textile dye by biological, physical, chemical, and electrochemical treatments. *J. Taiwan Inst. Chem. Eng.* 121, 29–37. doi: 10.1016/j.jtice.2021.03.041

Butler, E., Hung, Y. T., Yeh, R. Y. L., and Al Ahmad, M. S. (2011). Electrocoagulation in wastewater treatment. *Water* 3, 495–525. doi: 10.3390/w3020495

Chong, J., Liu, P., Zhou, G., and Xia, J. (2020). Using MicrobiomeAnalyst for comprehensive statistical, functional, and meta-analysis of microbiome data. *Nat. Protoc.* 15, 799–821. doi: 10.1038/s41596-019-0264-1

Cotillas, S., de Vidales, M. J. M., Llanos, J., Sáez, C., Cañizares, P., and Rodrigo, M. A. (2016). Electrolytic and electro-irradiated processes with diamond anodes for the oxidation of persistent pollutants and disinfection of urban treated wastewater. *J. Hazard. Mater.* 319, 93–101. doi: 10.1016/j.jhazmat.2016.01.050

de Vidales, M. J. M., Sáez, C., Pérez, J. F., Cotillas, S., Llanos, J., Cañizares, P., et al. (2015). Irradiation-assisted electrochemical processes for the removal of persistent organic pollutants from wastewater. *J. Appl. Electrochem.* 45, 799–808. doi: 10.1007/s10800-015-0825-0

Elawwad, A., Zaghloul, M., and Abdel-Halim, H. (2017). Simulation of municipal-industrial full scale WWTP in an arid climate by application of ASM3. *J. Water Reuse Desalinat.* 7, 37–44. doi: 10.2166/wrd.2016.154

Elumalai, P., Parthipan, P., AlSalhi, M. S., Huang, M., Devanesan, S., Karthikeyan, O. P., et al. (2021). Characterization of crude oil degrading bacterial communities and their impact on biofilm formation. *Environ. Pollut.* 286:117556. doi: 10.1016/j.envpol.2021.117556

Fitch, A., Balderas-Hernandez, P., and Ibanez, J. G. (2022). Electrochemical technologies combined with physical, biological, and chemical processes for the treatment of pollutants and wastes: a review. *J. Environ. Chem. Eng.* 10:107810. doi: 10.1016/j.jece.2022.107810

Fomina, M., and Gadd, G. M. (2014). Biosorption: current perspectives on concept, definition and application. *Bioresour. Technol.*160, 3–14. doi: 10.1016/j.biortech.2013.12.102

Gallert, C., and Winter, J. (2005). *Bacterial Metabolism in Wastewater Treatment Systems. Environmental Biotechnology: Concepts and Applications*. Wiley-VCH Verlag GmbH & Co. KGaA, 1–48.

Gambino, E., Maione, A., Guida, M., Albarano, L., Carraturo, F., Galdiero, E., et al. (2022). Evaluation of the pathogenic-mixed biofilm formation of *Pseudomonas aeruginosa*/*Staphylococcus aureus* and treatment with limonene on three different materials by a dynamic model. *Int. J. Environ. Res. Public Health* 19, 3741. doi: 10.3390/ijerph19063741

Gebreslassie, G., Bharali, P., Chandra, U., Sergawie, A., Boruah, P. K., Das, M. R., et al. (2019). Novel g-C3N4/graphene/NiFe2O4 nanocomposites as magnetically separable visible light driven photocatalysts. *J. Photo Chem. Photobiola. Chem.* 382:111960. doi: 10.1016/j.jphotochem.2019.111960

Grassini, S., Corbellini, S., Parvis, M., Angelini, E., and Zucchi, F. (2018). A simple Arduino-based EIS system for in situ corrosion monitoring of metallic works of art. *Measurement* 114, 508–514. doi: 10.1016/j.measurement.2016.07.014

Guiamet, P. S., and Gómez de Saravia, S. G. (2005). Laboratory studies of biocorrosion control using traditional and environmentally friendly biocides: an overview. *Latin Am. Appl. Res.* 35, 295–300.

Holtzapple, M. T., Wu, H., Weimer, P. J., Dalke, R., Granda, C. B., Mai, J., et al. (2021). Microbial communities for valorizing biomass using the carboxylate platform to 1 produce volatile fatty acids: a review. *Bioresour. Technol.* 2:126253. doi: 10.1016/j.biortech.2021.126253

Jallouli, S., Wali, A., Buonerba, A., Zarra, T., Belgiorno, V., Naddeo, V., et al. (2020). Efficient and sustainable treatment of tannery wastewater by a sequential electrocoagulation-UV photolytic process. *J. Water Process Eng.* 38:101642. doi: 10.1016/j.jwpe.2020.101642

Kamali, M., Guo, Y., Aminabhavi, T. M., Abbassi, R., Dewil, R., and Appels, L. (2023). Pathway towards the commercialization of sustainable microbial fuel cell-based wastewater treatment technologies. *Renew. Sustain. Energy Rev.* 173:113095. doi: 10.1016/j.rser.2022.113095

Kokilaramani, S., Rajasekar, A., AlSalhi, M. S., and Devanesan, S. (2021). Characterization of methanolic extract of seaweeds as environmentally benign corrosion inhibitors for mild steel corrosion in sodium chloride environment. *J. Mol. Liq.* 340:117011. doi: 10.1016/j.molliq.2021.117011

Lazarova, V., Savoye, P., Janex, M. L., Blatchley Iii, E. R., and Pommepuy, M. (1999). Advanced wastewater disinfection technologies: state of the art and perspectives. *Water Sci. Technol.* 40, 203–213. doi: 10.2166/wst.1999.0593

Linares-Hernández, I., Barrera-Díaz, C., Bilyeu, B., Juárez-GarcíaRojas, P., and Campos-Medina, E. (2010). A combined electrocoagulation-electrooxidation treatment for industrial wastewater. *J. Hazard Mater*175, 688–694. doi: 10.1016/j.jhazmat.2009.10.064

Manh, T. D., Hien, P. V., Nguyen, Q. B., Quyen, T. N., Hinton, B. R. W., and Nam, N. D. (2019). Corrosion inhibition of steel in naturally-aerated chloride solution by rare-earth 4-hydroxycinnamate compound. *J. Taiwan Inst. Chem. Eng.* 103, 177–189. doi: 10.1016/j.jtice.2019.07.012

Marszałek, A., and Puszczało, E. (2020). Effect of photooxidation on nanofiltration membrane fouling duringwastewater treatment from the confectionery industry. *Water* 12, 1–13. doi: 10.3390/w12030793

Martínez-Huitle, C. A., and Panizza, M. (2018). Electrochemical oxidation of organic pollutants for wastewater treatment. *Curr. Opin. Electrochem.* 11, 62–71. doi: 10.1016/j.coelec.2018.07.010

Mater, Y., Kamel, M., Karam, A., and Bakhoum, E. (2023). ANN-Python prediction model for the compressive strength of green concrete. *Construct. Innovat.* 23, 340–359. doi: 10.1108/CI-08-2021-0145

Mayrhofer, K. J. J., Ashton, S. J., Kreuzer, J., and Arenz, M. (2009). An electrochemical cell configuration incorporating an ion conducting membrane separator between reference and working electrode. *Int. J. Electrochem. Sci*. 4, 1–8.

Morsi, R. E., Labena, A., and Khamis, E. A. (2016). Core/shell (ZnO/polyacrylamide) nanocomposite: *in-situ* emulsion polymerization, corrosion inhibition, anti-microbial and anti-biofilm characteristics. *J. Taiwan Inst. Chem. Eng.* 63, 512–522. doi: 10.1016/j.jtice.2016.03.037

Musa, A. Y., Khadom, A. A., Kadhum, A. A. H., Mohamad, A. B., and Takriff, M. S. (2010). Kinetic behavior of mild steel corrosion inhibition by 4-amino-5-phenyl-4H-1,2,4-trizole-3-thiol. *J. Taiwan Inst. Chem. Eng.* 41, 126–128. doi: 10.1016/j.jtice.2009.08.002

Narenkumar, J., AlSalhi, M. S., Arul Prakash, A., Abilaji, S., Devanesan, S., Rajasekar, A., et al. (2019). Impact and role of bacterial communities on biocorrosion of metals used in the processing industry. *Acs Omega* 4, 21353–21360. doi: 10.1021/acsomega.9b02954

Narenkumar, J., Devanesan, S., AlSalhi, M. S., Kokilaramani, S., Ting, Y. P., Rahman, P. K., et al. (2021). Biofilm formation on copper and its control by inhibitor/biocide in cooling water environment. *Saudi J. Biol. Sci.* 28, 7588–7594. doi: 10.1016/j.sjbs.2021.10.012

Ortíz-Sánchez, E., Guillén-Garcés, R. A., Morales-Arrieta, S., Ugochukwu Okoye, P., Olvera-Vargas, H., Sebastian, P. J., et al. (2023). Cultivation of carbohydrate-rich microalgae with great settling properties using cooling tower wastewater. *Environ. Sci. Pollut. Res.* 1–16. doi: 10.1007/s11356-023-28432-w

Parthipan, P., Cheng, L., Dhandapani, P., and Rajasekar, A. (2023). Metagenomics diversity analysis of sulfate-reducing bacteria and their impact on biocorrosion and mitigation approach using an organometallic inhibitor. *Sci. Total Environ.* 856:159203. doi: 10.1016/j.scitotenv.2022.159203

Peralta-Hernández, J. M., Coso, E. B., and González, R. S. (2021). Recent advances in the treatment of organic pollutants in synthetic and real wastewaters using photo-assisted electrochemical processes. *Chemosphere* 279:130581. doi: 10.1016/j.chemosphere.2021.130581

Petrosino, J. F., Highlander, S., Luna, R. A., Gibbs, R. A., and Versalovic, J. (2009). Metagenomic pyrosequencing and microbial identification. *Clin. Chem.* 55, 856–866. doi: 10.1373/clinchem.2008.107565

Pinel, I. S. M., Moed, D. H., Vrouwenvelder, J. S., and van Loosdrecht, M. C. M. (2020). Bacterial community dynamics and disinfection impact in cooling water systems. *Water Res.* 172:115505. doi: 10.1016/j.watres.2020.115505

Prakash, A. A., Rajasekar, A., Sarankumar, R. K., AlSalhi, M. S., Devanesan, S., Aljaafreh, M. J., et al. (2021). Metagenomic analysis of microbial community and its role in bioelectrokinetic remediation of tannery contaminated soil. *J. Hazard. Mater.* 412:125133. doi: 10.1016/j.jhazmat.2021.125133

Rafieenia, R., Sulonen, M., Mahmoud, M., El-Gohary, F., and Rossa, C. A. (2022). Integration of microbial electrochemical systems and photocatalyzis for sustainable treatment of organic recalcitrant wastewaters: main mechanisms, recent advances, and present prospects. *Sci. Total Environ.* 824:153923. doi: 10.1016/j.scitotenv.2022.153923

Raji, O. A. (2017). *Effect of Chitosan on Subterranean Termites (Reticulitermes Spp.) Mortality and Gut Bacterial Community*. Mississippi State University.

Reddy, S., and Osborne, J. (2022). An insight on the advancements of biological technologies in the bioremediation of textile effluents. *Urban Water J.* 19, 468–480. doi: 10.1080/1573062X.2022.2030369

Reddy, S., and Osborne, J. W. (2020). Biodegradation and biosorption of Reactive Red 120 dye by immobilized *Pseudomonas guariconensis*: kinetic and toxicity study. *Water Environ. Res.* 92, 1230–1241. doi: 10.1002/wer.1319

Rocha, J. H. B., Gomes, M. M. S., Dos Santos, E. V., De Moura, E. C. M., Da Silva, D. R., Quiroz, M. A., et al. (2014). Electrochemical degradation of Novacron Yellow C-RG using boron-doped diamond and platinum anodes: direct and Indirect oxidation. *Electrochim. Acta* 140, 419–426. doi: 10.1016/j.electacta.2014.06.030

Saha, P., Bruning, H., Wagner, T. V., and Rijnaarts, H. H. M. (2020). Removal of organic compounds from cooling tower blowdown by electrochemical oxidation: Role of electrodes and operational parameters. *Chemosphere* 259:127491. doi: 10.1016/j.chemosphere.2020.127491

Shukla, S. K., Khan, A., and Rao, T. S. (2021). "Microbial fouling in water treatment plants," in *Microbial and Natural Macromolecules* (Academic Press), 589–622.

Sierra-Sánchez, A. G., Linares-Hernández, I., Martínez-Miranda, V., Almazán-Sánchez, P. T., Teutli-Sequeira, E. A., Castañeda-Juárez, M., et al. (2022). Photo-electrooxidation treatment of Acetaminophen in aqueous solution using BDD-Fe and BDD-Cu systems. *Environ. Technol.* 43, 1189–1199. doi: 10.1080/09593330.2020.1822921

Srivastava, A. K., Gupta, A. K., Mehrotra, T., Choudhury, R., and Singh, R. (2016). Physicochemical, biochemical and statistical analysis of beverages industry effluent. *Res. J. Pharm Technol.* 9, 887–892. doi: 10.5958/0974-360X.2016.00169.4

Su, Y., Hu, H., Dong, M., and Azzam, R. (2019). *The Utilization of Electrokinetics for the Treatment of Industrial Wastewater-Industrial Size Experimental Study*.

Sundaravadivel, M., and Vigneswaran, S. (2001). Constructed wetlands for wastewater treatment. *Crit. Rev. Environ. Sci. Technol.* 31, 351–409. doi: 10.1080/20016491089253

Swaroop, B. S., Victoria, S. N., and Manivannan, R. (2016). Azadirachta indica leaves extract as inhibitor for microbial corrosion of copper by Arthrobacter sulfureus in neutral pH conditions-A remedy to blue green water problem. *J. Taiwan Inst. Chem. Eng.* 64, 269–278. doi: 10.1016/j.jtice.2016.04.007

Ungureanu, N., Vladut, V., Cristea, M., and Cujbescu, D. (2020). Wastewater electrooxidation using stainless steel electrodes. In: *E3S Web of Conferences, Vol. 180, EDP Sciences*.

Yi, G., Wang, B., Feng, Y., Fang, D., Yang, L., Liu, W., et al. (2022). The ins and outs of photo-assisted microbial electrochemical systems for synchronous wastewater treatment and bioenergy recovery. *Resour. Conserv. Recycl.* 181:106230. doi: 10.1016/j.resconrec.2022.106230

Yue, L., Wang, K., Guo, J., Yang, J., Luo, X., Lian, J., et al. (2014). Enhanced electrochemical oxidation of dye wastewater with Fe2O3 supported catalyst. *J. Ind. Eng. Chem.* 20, 725–731. doi: 10.1016/j.jiec.2013.06.001

Zapatero, A., Guerrero, A., Maldonado, X., Alvarez, A., San Segundo, C. G., Rodríguez, M. A., et al. (2015). High-dose radiotherapy with short-term or long-term androgen deprivation in localized prostate cancer (DART01/05 GICOR): a randomized, controlled, phase 3 trial. *Lancet Oncol.* 16, 320–327. doi: 10.1016/S1470-2045(15)70045-8

Zheng, Z., Deletic, A., Toe, C. Y., Amal, R., Zhang, X., Pickford, R., et al. (2022). Photo-electrochemical oxidation herbicides removal in stormwater: degradation mechanism and pathway investigation. *J. Hazard. Mater.* 436:129239. doi: 10.1016/j.jhazmat.2022.129239

frontiers | Frontiers in Environmental Chemistry

TYPE Original Research
PUBLISHED 04 June 2024
DOI 10.3389/fenvc.2024.1376079

OPEN ACCESS

EDITED BY
Gaurav Pant,
Graphic Era University, India

REVIEWED BY
Krishna Kumar Pandey,
Banaras Hindu University, India
Ajay Harit,
Mahatma Gandhi University, India

*CORRESPONDENCE
Sébastien Sauvé,
sebastien.sauve@umontreal.ca

RECEIVED 24 January 2024
ACCEPTED 22 April 2024
PUBLISHED 04 June 2024

CITATION
Teymoorian T, Dinh QT, Barbeau B and Sauvé S (2024), Performance of pitcher-type POU filters for the removal of 75 PFAS from drinking water: comparing different water sources.
Front. Environ. Chem. 5:1376079.
doi: 10.3389/fenvc.2024.1376079

Performance of pitcher-type POU filters for the removal of 75 PFAS from drinking water: comparing different water sources

Termeh Teymoorian[1], Quoc Tuc Dinh[1], Benoit Barbeau[2] and Sébastien Sauvé[1]*

[1]Department of Chemistry, Université de Montréal, Montreal, QC, Canada, [2]Department of Civil, Geological and Mining Engineering, Montreal, QC, Canada

This study presents a comprehensive assessment of the performance of popular pitcher-type point-of-use (POU) water filters to remove PFAS contaminants from tap waters. The evaluated filters, Brita (Elite and Standard), ZeroWater, Aquagear, and ClearlyFiltered, were tested for their efficacy in removing 75 targeted PFAS, total organic carbon (TOC), total dissolved solids (TDS), chloride, and sulfate from two Canadian tap waters with background Σ_{75} PFAS concentrations of 13 and 56 ng/L. Overall, the performances of the filters varied depending on the structure of the filter media, the water source, and the specific contaminants present. ZeroWater was the top performer in the case of total PFAS removal. The volume-weighted average removal of total PFAS after 160 L of filtration using Saint-Donat tap water was 99% for ZeroWater, 99% for ClearlyFiltered, 77% for Aquagear, and 20% for Brita (Elite). In the case of Montreal tap water, which had different water characteristics and lower total PFAS levels, the volume-weighted average removal for PFAS was ≈100% for ZeroWater, 96% for ClearlyFiltered, 60% for Aquagear, 48% for Brita (Elite), and 38% for Brita (Standard). Both laboratory and home tests involving ZeroWater filters yielded similar high-performance results using Montreal tap water. Although ZeroWater exhibited high PFAS removal (99%) in Saint-Donat water, TDS and TOC desorption and a significant drop in pH were observed after 80 L, a phenomenon which was explained by the higher total concentration of anions in this water. In contrast, no desorption was observed in Montreal tap water for TDS and TOC due to the lower concentrations of anions. The Aquagear filter demonstrated an unusual increase in concentrations of sulfate after the initial 20 L, which needs further evaluation. This study discusses individual filter performance, the influence of tap water characteristics, and the potential to meet the new NSF guidelines, which provides valuable insights for consumers seeking to choose an appropriate easy-to-use water filtration system to ensure safe and clean drinking water in different regions.

KEYWORDS

PFAS removal, point-of-use filters, drinking water, water quality, water treatment, environmental pollution, LC-HRMS

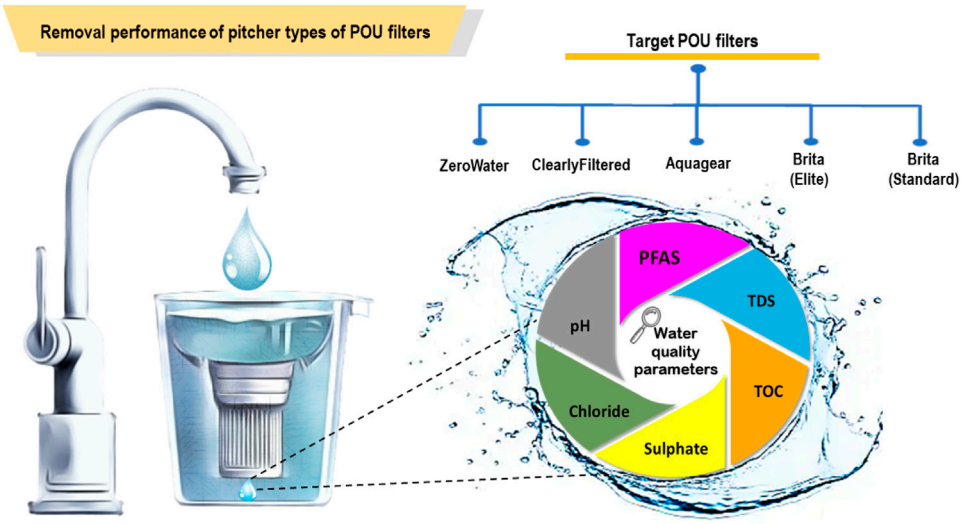

GRAPHICAL ABSTRACT

1 Introduction

Contamination of water with emerging contaminants, especially per- and polyfluoroalkyl substances (PFAS), is a growing concern worldwide. These chemicals are used in a wide range of industrial applications, and their persistence in the environment, as well as potential health impacts, have led to increased efforts to eliminate them from water bodies (Teymourian et al., 2021). However, PFAS are not effectively removed by conventional drinking water treatment processes, which means that even if drinking water meets other regulatory standards, it may still contain PFAS at levels of concern (Teymoorian et al., 2023). As a result, when contamination of tap water is discovered, further residential treatment may be required to remove PFAS from tap water before the community system upgrade is put in place.

Point-of-use (POU) drinking water filters are popular due to their ease of use and capacity to reduce exposure to various impurities and contaminants in drinking water. A POU filter is any device designed to provide treatment for an individual tap rather than the entire home. POU filters can be designed to remove chemical or microbial pollutants or improve water aesthetics. POU devices may consist of activated carbon (AC) with or without surface modifications, varied combinations of string-wound sediment filters, ultraviolet lamps, reverse osmosis membranes, redox media, and ion exchange filters, depending on the types of pollutants targeted (Wu et al., 2021).

For PFAS removal applications, using sorbent filters is a common treatment option. However, the adsorbent features (porosity, functional group, particle size), the chemistry of the water (pH, inorganic ions, organic matter) and PFAS characteristics (length of the C-F chain, functional group) all have impacts on adsorption efficiency (He et al., 2022). Consequently, it is important to assess the performance of POU filters under a range of operating conditions.

Herkert et al. (2020) investigated the effectiveness of point-of-entry (POE) and POU residential filters for drinking water for the elimination of seven perfluoroalkyl carboxylic acids (PFCAs), three perfluoroalkyl sulfonic acids (PFSAs), and six per- and polyfluoroalkyl ether acids (PFEAs) in 12 homes in southeastern and central (n = 61) North Carolina (NC, USA) (Herkert et al., 2020). All under-sink two-stage systems tested (>74% - >99% for Southeastern NC, >92% - >99% for Central NC) and reverse osmosis filters tested (>75% - >99% for Southeastern NC, >88%–100% for Central NC) demonstrated great removal for monitored perfluoroalkyl acids (PFAAs) and PFEAs. However, all other activated carbon-containing filters showed variable PFAS removal. PFAS removal efficiency of these filters was dependent on the length of the PFAS chain. Generally, PFAS with long-chains were more easily removed than short-chain PFAS. They also evaluated pitcher filters (n = 13), but only in Central NC, and the removal percentage varied between 36% and 71% for the PFAS they investigated. However, Herkert et al.'s study primarily focused on a limited range of PFAS, and the study was observational.

Another research by Anumol et al. (2015) evaluated the removal efficiency for different organic contaminants (including PFOS and PFOA) of three commercial pitcher-type POU devices (Brita® Riviera eight-cup filter, ZeroWater® eight-cup filter, and PUR™ CR-6000 seven-cup filter) and two refrigerator POU filters (Whirlpool®W10295370 filter and GE® MSWF) (Anumol et al., 2015). Each filter device had an exhaustion time determined by the manufacturer and defined as the time of service or maximum volume of water passed through the filter, which is called the manufacturer's expected lifetime (MEL). All filters had higher average removal for hydrophobic, nonionic compounds in comparison to hydrophilic compounds. Ionic compound removal (such as PFOS and PFOA) was improved by ion exchange resins in pitcher-type POU filters. The lifetime individual removal efficiencies of PFOS and PFOA were higher when using ZeroWater filter (96.7% and 97.5%, respectively) in comparison to other filters, such as PUR filter (~85% and 79%, respectively) and Brita filter (57% and 52%, respectively). However, this research evaluated the performance of POU filters only for two targeted anionic PFOS and PFOA, not for

the other types of PFAS with different lengths, charges, and functional groups, which can also affect the adsorption efficiency.

In another research in North Carolina (USA), 18 private well consumers were enlisted to evaluate the PFAS removal efficiency of under-sink, activated carbon block water filters. Sample collection was performed monthly for 8 months. Filters under investigation were certified for removing PFOS and PFOA under National Sanitation Foundation (NSF) certification P473, but they were not certified for short-chain PFAAs or PFEAs. A total of 17 PFAS were found in filter influent samples out of 47 targeted analytes (∑PFAS 4.7–131 ng/L). Overall, results showed that the filters effectively removed PFAS (97%–99%) in all influents, including short-chain PFEAs, for the total producer-recommended lifetime of the filters (Mulhern et al., 2021).

It has been reported that well water resources in the municipalities of Fountain, Security, and Widefield, (CO, USA) had PFOS and PFOA levels that exceeded the former U.S. Environmental Protection Agency (USEPA) health advisory level of 70 ng/L. Therefore, commercial POE/POU devices using granular activated carbon (GAC) adsorbents and reverse osmosis treatment were deployed to decrease PFAS exposure from household drinking water systems. All tested reverse osmosis systems were effective in removing PFAS from the influent water, lowering concentrations mostly under analytical detection levels (quantification level = 10 ng/L). The iSpring RCS5T and Flexeon LP-700 reverse osmosis filters did not exhibit any PFAS in the purified water; however, the HydroLogic Evolution™ RO1000 reverse osmosis filter exhibited low PFAS levels in the purified water after shutdown and startup (Patterson et al., 2019). No definite reason could be found to explain this observation.

He et al. (2022) collected 12 household water samples from Beijing (China), before and after POU filters. POU filters made with coconut shell activated carbon had removal percentages from 21% to 99% for 14 PFAS in tap water. Density functional theory (DFT) results demonstrated that the topological structures of PFAS and their hydrophobicity and electrostatic interactions between the adsorbent surface and the powerful electronegative F atoms are the most important factors that affect the adsorption of PFAS on the activated carbon (He et al., 2022). Competitive adsorption tests revealed that coconut shell AC had a higher affinity for PFSAs compared to PFCAs, and amongst the novel PFAS, 6:2 FTS and F-53B could be effectively eliminated from the water, but short-chain PFAAs and Gen-X were more challenging to remove. The FOSA energy of adsorption was higher than the same C_8 compound, which can be explained by the molecular structure, including polarizable amide groups that increase the affinity with coconut shell AC.

In this study, we evaluated the effectiveness of different brands of pitcher-type POU filters with or without NSF/ANSI Standard certifications to remove a wider range of targeted PFAS (n = 75) with different functional groups and chain lengths (although not all were detected in the unfiltered tap waters). Additionally, the impact of filtration on other water quality parameters, such as total organic carbon (TOC), total dissolved solids (TDS), chloride, and sulfate were evaluated to provide a comprehensive assessment of the filters' capabilities as well as gain insight into how the general quality of the tap water might influence PFAS removal. Each POU technology was tested using two different tap water sources from cities in Quebec province, Canada (Saint-Donat and Montreal) with distinct characteristics and PFAS levels. A recent study by Munoz et al. (2023) highlighted the presence of a high level of total PFAS in Saint-Donat's tap water, ranging from 68 to 82 ng/L (Munoz et al., 2023). This concentration exceeds Health Canada's newly proposed PFAS threshold of 30 ng/L (Health Canada, 2023). Hence, the results of this research can help the population of areas affected by PFAS contamination in their drinking water to make informed decisions when selecting the more suitable device to protect themselves against these harmful chemicals. The results also include a wide range of PFAS, including some PFAS that are not well studied and more difficult to remove using such filtration systems.

The selected pitcher filters are Brita® Elite™, Brita® Standard filter (model # OB03), ZeroWater (5-Stage), Aquagear, and ClearlyFiltered (Affinity® Filtration Technology). In this list, only ZeroWater and ClearlyFiltered currently hold NSF53 and Water Quality Association (WQA) certifications against PFOA/PFOS, respectively. To date, around 93 different sorbent filter products made by 15 manufacturers have been certified by NSF or the WQA to decrease PFOS and PFOA. However, PFAS are not limited to just these two compounds. There are around between 5,000 and more than 12,000 reported PFAS chemicals with various structures and chain lengths in the environment (Karamat et al., 2023; Sosnowska et al., 2023), which can remain in the water after filtration or may affect the adsorption of other PFAS due to competition effects. Given that previous studies evaluated POU filters with a limited number of targeted PFAS compounds, studies using the natural mixture of PFAS are of interest. Hence, we explored the effectiveness of these filters in removing up to 75 different targeted PFAS compounds using the un-spiked water matrices. It is important to mention that NSF certifications (previously as P473 and now categorized as 53 or 58) were originally based on a threshold of 70 ppt for PFOS and PFOA, the previous advisory limit set by the EPA. However, the NSF 53/58 is currently under review to include more stringent certification criteria for PFAS removal as the EPA has recently updated much lower enforceable levels, called Maximum Contaminant Levels (MCLs). These MCLs now stand at 4 ppt for PFOS and PFOA, alongside thresholds for PFHxS, PFNA, and Gen-X at 10 ppt (EPA, 2024).

The evaluation of pitcher-type POU filters for the removal of different contaminants is more important compared to other types of POU filters. Pitcher-type filters can be deployed more rapidly than plumbed-in systems following contamination and they offer an interesting interim option prior to the implementation of community treatment. These filters are also widely used due to their low initial purchase cost, high availability, and convenience in residential homes. Evaluating the performance of different types of pitcher filters can provide valuable information to consumers and policymakers to ensure that people have access to safe and clean drinking water, especially in areas with high detected and quantified PFAS in tap water. Dissolved ions such as natural organic matter (NOM), chloride, and sulfate can also impact the performance of POU filters, given that several treatment pitcher-filter technologies rely on ion exchange. NOM also competes with PFAS for adsorption onto activated carbon media. This can lead to decreased PFAS removal efficiency and a shorter filter lifetime by clogging the filter. Therefore, considering the impact of dissolved ions is also important when selecting and using POU filters.

TABLE 1 Name of selected POU filters, removal elements, lifetime, and NSF/ANSI certificates.

Brand	Name of filter	Removal processes[&]	Lifetime[&]	WQA -NSF/ANSI standards certificates	PFOA/PFOS reduction claim
ClearlyFiltered	Affinity® Filtration Technology	Woven mesh screen + Granulated activated carbon + Composite shell	100 gallons (378 L) or 4 months	Equivalent to 42, 53, 401 and P473	✓ (Certified by WQA)
Aquagear		Activated carbon and ion exchange media	120 gallons (454 L) or 6 months	N/A	✓ (From a 3rd party accredited laboratory)
Brita	Standard	Coconut-based activated carbon with ion exchange resin	40 gallons (151 L) or 2 months	42 and 53	–
	Elite	Adsorbents + pleated filters + Activated carbon + Fibrous matrix	120 gallons (454 L) or 6 months	42 and 53	–
ZeroWater		Coarse Basic + Foam divider + Activated Carbon & Oxidation Reduction Alloy + Negative and positive ion exchanger + Ultra-fine sieve and non-woven membrane layers	20 or 40 gallons (76 L or 151 L)	42 and 53	✓ (Certified by NSF)

Note: NSF P473: Specific certification for PFAS, among mentioned NSF/ANSI, standards. NSF P473 certificate came into effect in 2016 as a provisional standard, which was incorporated into NSF/ANSI, 53 or 58 standards in June 2021; NSF, 53: Health effects (for PFAS, if the certification included PFAS); NSF, 42: Aesthetic effects (not for PFAS); NSF, 401: Emerging Contaminants (Excludes PFAS), and: Manufacturer information.

2 Materials and methods

2.1 Chemicals and standards

Certified and surrogate PFAS standards were provided by different sources, including Wellington Laboratories (Guelph, ON, Canada), DuPont (Wilmington, DE, USA), Fluobon (Beijing, China), Apollo Scientific, and Synquest Laboratories. Details are provided in Supplementary Tables S1-S2. Methanol, HPLC grade water, HPLC grade water with 0.1% formic acid, and acetonitrile were provided by Fisher Scientific (ON, Canada). NH_4OH was purchased from Sigma-Aldrich (MO, USA).

2.2 Sample collection

The tap waters of Saint-Donat, originating from a municipal system fed by untreated groundwater, and Montreal in Quebec, Canada (whose water is produced from the St-Lawrence River) were chosen to evaluate the performance of POU filters. Each device was evaluated with these two tap water sources in order to determine how well the filters perform under different water characteristics. Unfiltered tap waters were collected in multiple pre-cleaned high-density polyethylene (HDPE, 19 L) buckets, stored at 4°C, and analyzed within a week. The tap waters were used without spiking any PFAS. Therefore, the PFAS mixture was different for each tap water.

Before starting the analysis, each POU filter was preconditioned based on the manufacturer's recommendations. The POU filters were kept at ambient temperature during the experiment (~20 C°). Pre-cleaned HDPE bottles (500 mL) were used for the collection of filtered and unfiltered tap water at each level of sample collection. The bottles had been rinsed with deionized water, followed by 50: 50 methanol/HPLC grade water and HPLC water prior to PFAS sampling. Filtered water samples in the lab batch experiment were collected directly under each POU filter after passing 20 L, 40 L, 80 L, and 160 L of tap water, ensuring no contact with the pitcher materials. The filter was then returned to the pitcher to proceed to the next sampling point. Controls (unfiltered samples) were collected at the same time as collecting the filtered samples to have an accurate removal percentage. In order to describe the average exposure of consumers using the filtration devices, the volume-weighted average removals were calculated for each POU device using the following equation:

$$\text{Removal (\%)} = \frac{R_1.V_1 + \left[\sum_{i=2}^{n} \frac{(R_i+R_{i-1})}{2}.\ (V_i - V_{i-1})\right]}{V_n} \times 100\% \quad (1)$$

n is the number of volumes tested (4), R_i is the removal measured after V_i, V_i is the volume of water filtered at step i (each i corresponds to a specific interval between two consecutive data points), and V_n is the total volume filtered = 160 L.

Each POU filter was operated for 8 h per day with a rest period of 16 h. Pitcher filters were gravity-fed using sequential batches of water (2 L) pumped in the top receptacle of the pitcher. All samples were kept at 4°C immediately after collection and tested within a month for PFAS analysis.

2.3 POU devices

This research evaluated the performance of five commercially available pitcher-type POU filters, including Brita® Elite™, Brita® Standard filter (model # OB03), ZeroWater (5-Stage), Aquagear, and ClearlyFiltered (Affinity® Filtration Technology) (Table 1). The choice of these pitcher filter devices is due to their small size, ease of use, cartridge replacement, and ease of transport in each area, and the choice of these brands is due to their availability in the North American area, which also has NSF/ANSI or similar certificates. NSF, as a non-profit organization, certifies a broad range of industrial and domestic products, such as home water purification systems. Each filter was tested in duplicate (except Brita

TABLE 2 General chemistry of tap water sources in this research.

	Saint-Donat, QC (n = 15)	Montreal, QC (n = 24)	NSF/ANSI 53–2021 conditions for chemical reduction claims
pH	6.00–7.14 (Mean = 6.61; *n* = 10)	7.28–7.97 (Mean = 7.73; *n* = 10)	7.5 ± 0.5
TOC (mg/L)	0.80–0.86 (Mean = 0.82)	2.08–2.46 (Mean = 2.24)	>1
TDS (mg/L)	155–208 (Mean = 179)	92–103 (Mean = 99)	200–500
Turbidity (NTU)	0.085	0.143	≤1
Fluoride (mg/L)	< MDL[a]	< MDL[a]	
Chloride (mg/L)	104–133 (Mean = 122)	22–26 (Mean = 24)	
Nitrite (mg/L)	< MDL[b]	<MDL[b]	
Sulphate (mg/L)	9.2–11 (Mean = 10.2)	18–21 (Mean = 19.7)	
Phosphate (mg/L)	< MDL[c]	< MDL[c]	
Alkalinity (mg $CaCO_3$/L)	≈30–40	≈80	
Anions (mEq/L)[d]	~4.9	~2.7	
Total 75 PFAS (ng/L)	38.7–63.3 (Mean = 56.4; n = 16)	8.4–16.1 (Mean = 12.7; n = 24)	

[a]Fluoride method detection level (MDL), 0.05 mg/L.
[b]Nitrite MDL, 0.03 mg/L.
[c]Phosphate MDL, 0.05 mg/L.
[d]Sum of bicarbonate, chloride and sulfate.

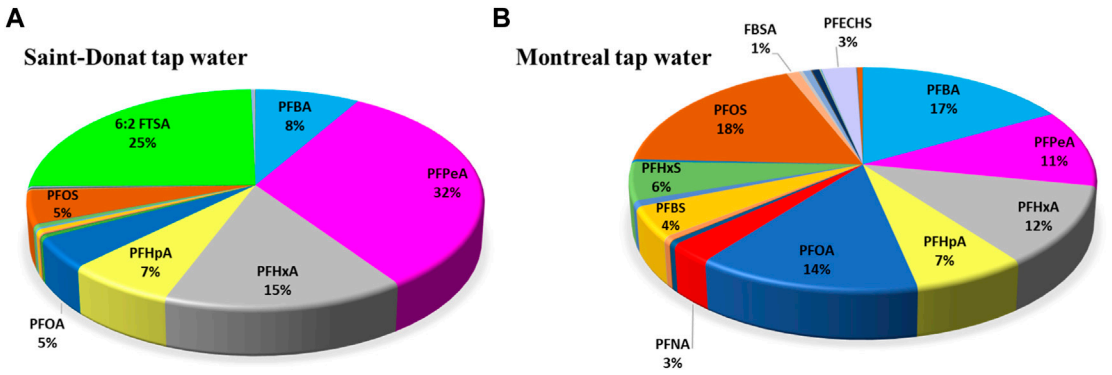

FIGURE 1
The average contribution percentages of each detected PFAS in the tap water of **(A)** Saint-Donat (Σ_{75} PFAS = 56 ng/L), **(A)** and Montreal (Σ_{75} PFAS = 13 ng/L).

Standard) but with different tap water sources. The selected POU filters all contain activated carbon and/or ion exchange resin media. The inside structure of each device can be seen in Supplementary Figures S1-S5.

2.4 Analysis methods

Off-line automated solid phase extraction (SPE) (Thermo/Dionex Autotrace 280 system) was used for the extraction of PFAS from water using Strata X-AW, 200 mg/6 mL from Phenomenex as SPE cartridge. A 100 µL surrogate internal standards (IS) mixture (10 µg/L in MeOH) was spiked to each of the tap water samples before doing SPE, and the pH of the samples was adjusted to 6.5 with acetic acid to improve retention of short-chain PFAS. The cartridges were first conditioned with 0.2% (v/v) NH_4OH (from 28% to 30% solution) in MeOH (2 × 4 mL) followed by 2 × 4 mL of HPLC-grade water. After loading the samples (flow rate of 10 mL/min), cartridges were dried using nitrogen flow for about 30 min. Finally, PFAS analytes were eluted with 2 × 4 mL of 0.2% (v/v) ammonium hydroxide in methanol. Further evaporation was done for all samples under mild nitrogen gas and temperature (40°C) to reach 250 µL. Extracted samples were injected into an ultra-high-performance liquid chromatograph coupled with a high-resolution Q Exactive Orbitrap mass spectrometry (UHPLC-HRMS) with negative and positive ionization modes (150–1,000 m/z, full scan mode) (Munoz et al., 2023). More information about the UHPLC-HRMS acquisition method is provided in (Supplementary Table S3).

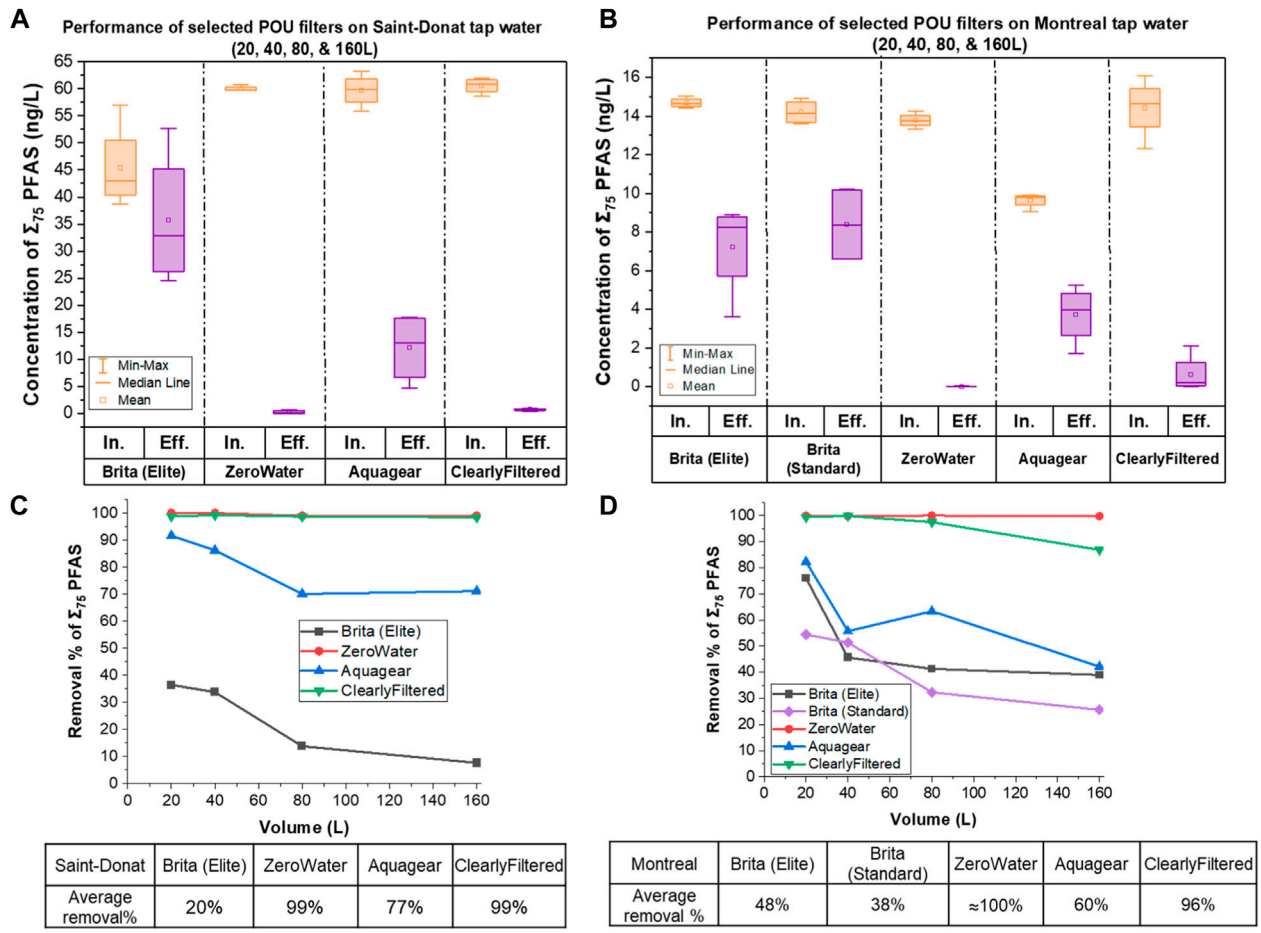

Saint-Donat	Brita (Elite)	ZeroWater	Aquagear	ClearlyFiltered
Average removal%	20%	99%	77%	99%

Montreal	Brita (Elite)	Brita (Standard)	ZeroWater	Aquagear	ClearlyFiltered
Average removal %	48%	38%	≈100%	60%	96%

FIGURE 2
The removal performance of a Σ_{75} PFAS for selected POU filters with increasing filtered volumes (20, 40, 80, and 160 L). **(A)** and **(B)** show the changes in concentrations of the Σ_{75} PFAS in influents and effluents in Saint-Donat and Montreal tap water, respectively. Removal (in %) of Σ_{75} PFAS for each POU filter as well as volume-weighted average removal % for **(C)** Saint-Donat and **(D)** Montreal tap waters.

The TOC of the influents and effluents was determined using a TOC analyzer (Sievers M5310 C, USA). Anions were measured with an ion chromatograph (ICS 5000 AS-DP DIONEX, USA) equipped with an AS18 column. The TDS of influent and effluent samples were also measured.

2.5 Quality assurance and quality control

Method blanks were used during each batch of SPE to check for any contamination that may have arisen during the analysis. After the initial calibration verification, continuing calibration verification was performed after every 10th water sample in LC-HRMS. Limits of detection (LODs) are presented in Supplementary Table S4. As HRMS yielded PFAS signals with low or unmeasurable background noise within the set mass tolerance threshold, the traditional signal-to-noise method used to derive LODs of LC-MS/MS methods could not be reproduced here. Instead, the LODs were calculated by multiplying the standard deviation of the blanks by the (n-1, 95) student coefficient (n is the number of replicate blanks), when applicable (Muir and Sverko, 2006). LODs were also calculated based on the peak intensity of low-end calibration curve levels or field samples with low concentrations (the LOD was derived using an absolute height of 1E4) (Kaboré et al., 2018). The reporting method LODs were then set at either the blank-derived or height-derived value, whichever was greater. We note that an alternative method described in EPA LC-MS/MS methods for PFAS in drinking water derives detection limits (DL) from the standard deviation of spike replicates (e.g., EPA method 537.1), which likely would be valid for LC-HRMS. Accuracy (Supplementary Table S5) was also assessed by ensuring that the mean accuracy values were within 70%–130% (for n = 3), with relative standard deviations mostly lower than 20% according to the US EPA method (Shoemaker and Tettenhorst, 2018; EPA, 2019; Goeury et al., 2022).

3 Results and discussion

Table 2 provides the water quality parameters for the two tap water sources. The turbidity of unfiltered tap water of Montreal and Saint-Donat was less than 1 NTU (0.143 and 0.085 NTU, respectively). Saint-Donat tap water generally exhibited higher levels of TDS and chloride compared to Montreal tap water. On the other hand, Montreal tap water showed higher levels of TOC and sulfate in contrast to Saint-Donat tap water.

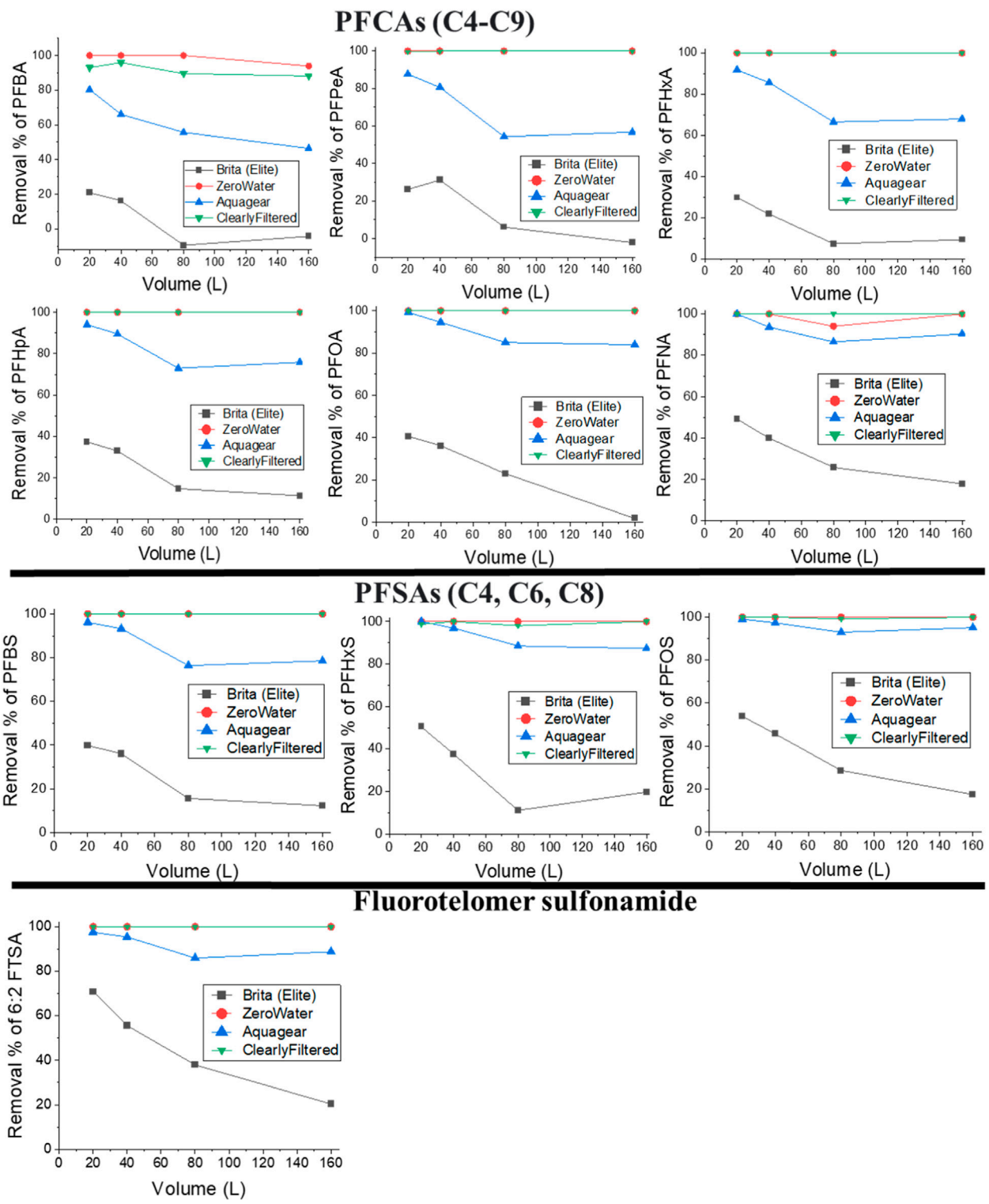

FIGURE 3
Removals (in %) of the highest quantified PFAS, categorized into three groups: PFCAs, PFSAs, and fluorotelomer sulfonamide in Saint-Donat tap water after filtration of 20–160 L.

The observed flow rate of each POU device was different for Saint-Donat and Montreal tap waters as the physicochemical characteristics of the water can affect the flow rate. The average flow rate of ZeroWater was 99 mL/min for Saint-Donat tap water; however, it was 127 mL/min for Montreal (+28%), even though Montreal tap water had slightly higher turbidity (0.143 vs.

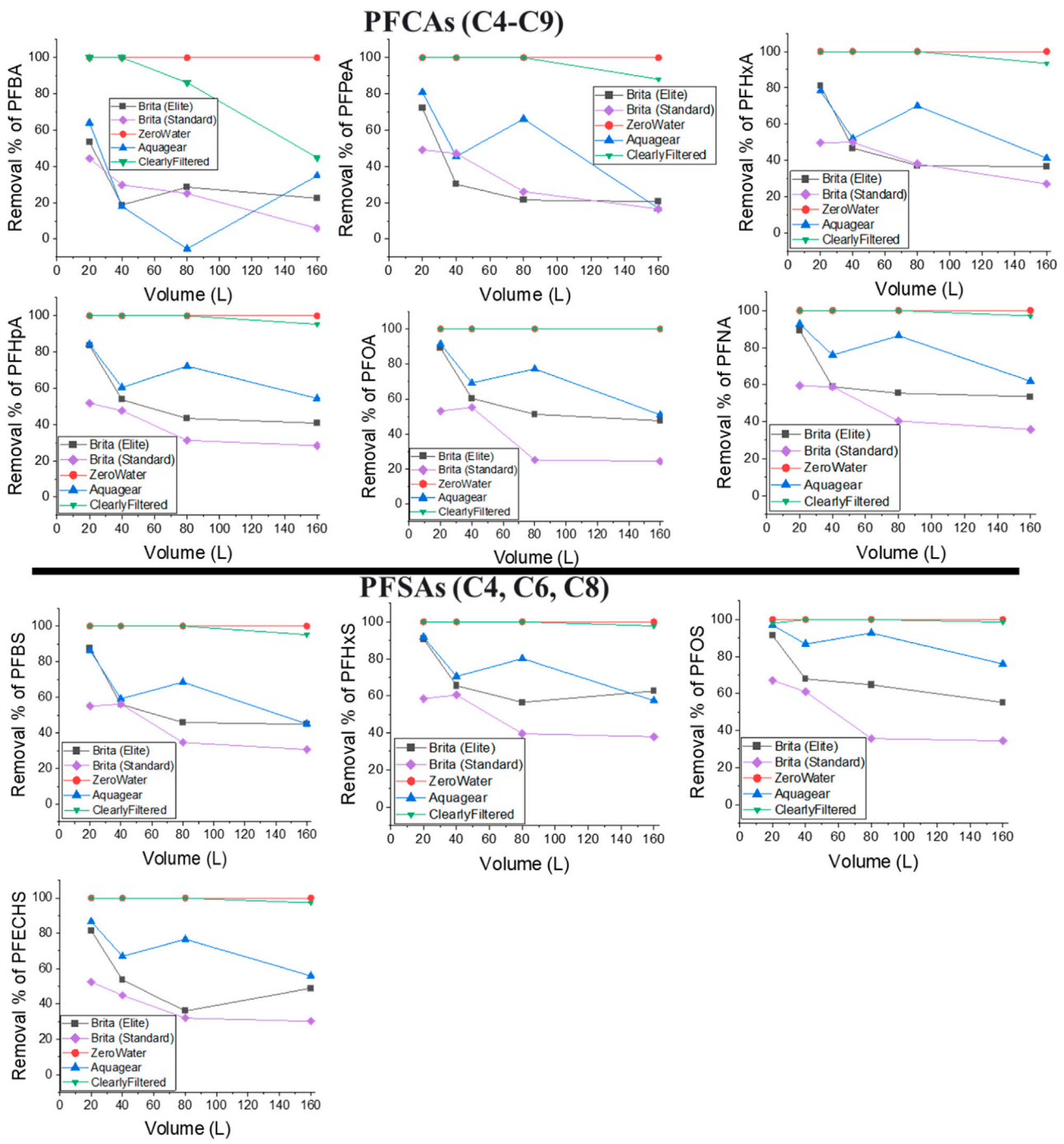

FIGURE 4
Removals (in %) of the highest quantified PFAS, categorized into two groups: PFCAs and PFSAs (linear and cyclic) in Montreal tap water after filtration of 20–160 L.

0.085 NTU). Aquagear filter had a 70 mL/min average flow rate for Saint-Donat tap water, and for Montreal tap water, it was 89 mL/min (+27%). The average flow rate for the Brita (Elite) filter was 115 mL/min for Montreal but was not recorded for Saint-Donat tap water. ClearlyFiltered also had a +29% higher average flow rate (53 mL/min) for Montreal tap water compared to Saint-Donat (41 mL/min), and it was the product with the lowest flow rate among all investigated POU devices. As the flow rate is correlated with the contact time of water inside the filter, such variation in flow could also contribute to variability in sorption performance (Belkouteb et al., 2020).

The average total concentration of PFAS in the source water of Saint-Donat was also higher than in Montreal, with different contribution percentages of each PFAS (Figure 1). During the analysis of influent water samples from Saint-Donat, 27 out of the 75 targeted PFAS compounds were not detected. Similarly,

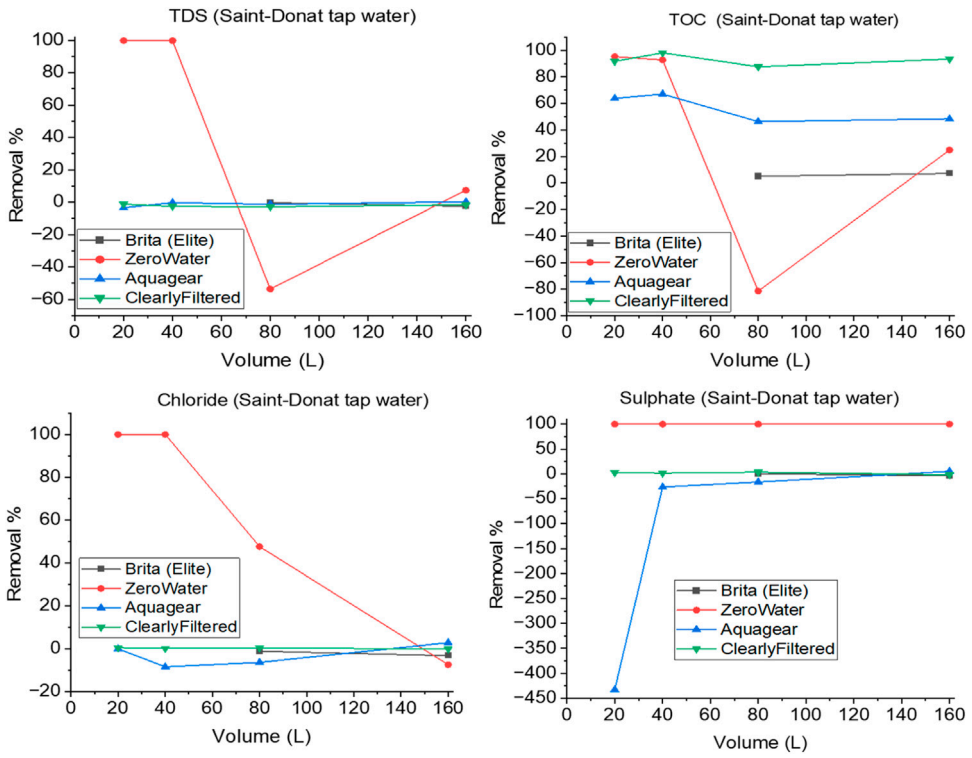

FIGURE 5
TDS, TOC, chloride, and sulfate removal % for selected POU filters using Saint-Donat tap water. Note: The data for the collected samples at 20 L and 40 L for Brita (Elite) is not available.

29 out of the 75 targeted PFAS compounds were also not detected in the Montreal influents. Generally, higher initial contaminants concentrations can result in a faster breakthrough, as the filter may become saturated sooner.

ZeroWater performance: Following the implementation of the ZeroWater filter, a majority of the detected PFAS compounds in both sources of effluents were successfully reduced below the detection limit throughout the entire test period (160 L). This filter demonstrated superior PFAS reduction in the effluents with volume-weighted average removal after 160 L above 99% for Σ_{75} PFAS (as well as for PFOS + PFOA) for both sources of water (Figure 2) during water sampling volumes (20–160 L) compared to all other POU filters tested likely due to its five-stage filtration system, in which activated carbon and anionic and cationic ion exchangers (AIX and CIX) play a prominent role (Supplementary Figure S1). While this explanation offers insights, it is crucial to acknowledge that definitive conclusions would require further investigations, considering factors such as contact time and carbon selection, as well as other key design criteria that could influence the adsorption performance.

Figures 3, 4 also present the removal percentages of the most quantified PFAS compounds found in the tap water of Saint-Donat and Montreal, respectively (compounds that were not detected were considered as 0). ZeroWater consistently maintained high removal percentages, reaching mainly ~100% for all chain lengths and different functional groups using Montreal tap water. However, in the case of PFBA in Saint-Donat waters, removal was slightly reduced at 94%, after 160 L, probably due to higher levels of total PFAS, chloride and TDS (Table 2) and the challenges in sorbing short-chain PFAS on activated carbon and AIX due to the more hydrophilic nature of shorter chain PFAS. Earlier studies have indicated that the primary mechanism responsible for removing short-chain PFAS is the electrostatic interaction with the adsorbent (Li et al., 2023). However, in the case of Saint-Donat water, this mechanism in ZeroWater may have been exhausted sooner compared to Montreal tap water. Although the PFAS removal was quite stable over 160 L of operation, large fluctuations in other monitored water quality parameters were observed, especially in Saint Donat waters.

Supplementary Tables S6, S7 present pH variations of the Saint-Donat and Montreal influents and effluents, focusing on the performance of evaluated POU filters. ZeroWater exhibited a remarkable pH drop for Saint-Donat tap water after processing 80 L, decreasing from 6.03 to an acidic pH of 2.67, indicating highly acidic conditions in the filtered water. The ZeroWater instructions indicate that when the filtered water becomes acidic, the filter is exhausted and must be replaced. Finally, after filtering 160 L, the effluent pH slightly improved to 5.63, probably due to the exhaustion of the CIX resin. Such a sharp decrease in pH after 80 L suggests that the filter includes an AIX resin loaded with OH^- which was exhausted before the H^+ loaded CIX resin and, therefore, no longer able to neutralize the H^+ released by the CIX. The results suggest that there may be more CIX than AIX resin in the filer (in terms of capacity, not necessarily volume), causing the AIX to

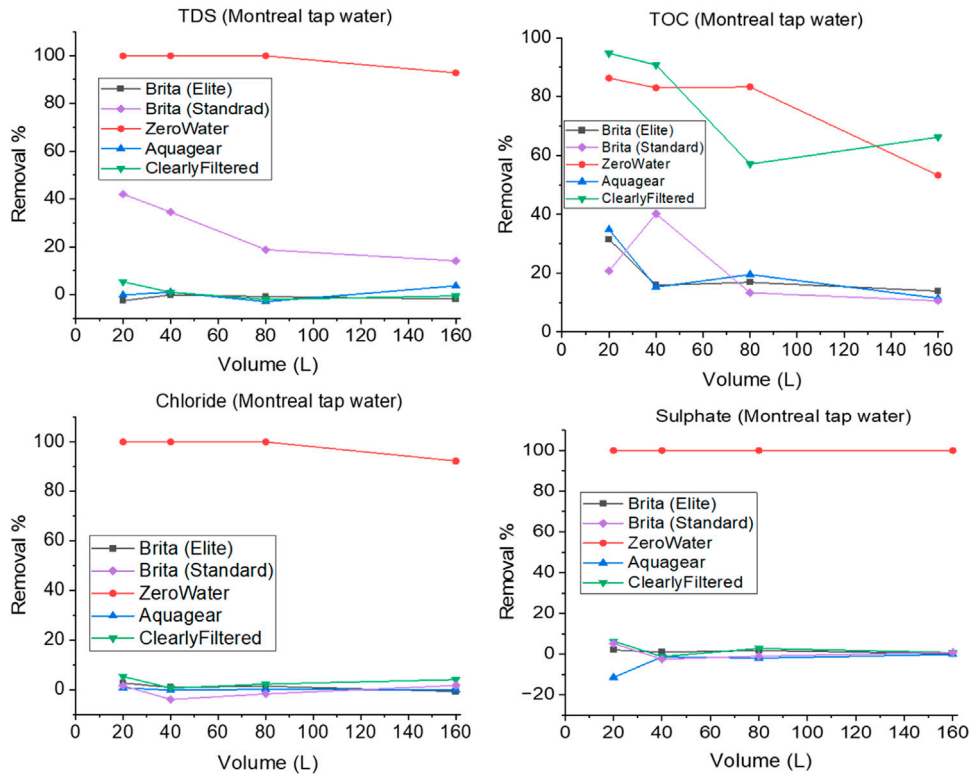

FIGURE 6
TDS, TOC, chloride, and sulfate removal % for selected POU filters using Montreal tap water.

become exhausted before the CIX. This imbalance leads to a rapid drop in pH, resulting in a lemon-like taste in the filtered water, which is unpalatable for drinking. This observation raises an intriguing possibility for future research on optimizing the resin composition in ZeroWater filters by introducing more AIX resin to balance it with CIX in the system to potentially enhance their lifespan.

Similar fluctuations were also observed for TOC and TDS after 80 L. TOC removal in the case of Saint-Donat tap water (initial concentration (n = 4) of 0.83 mg C/L) showed an efficiency of about 93% after 40 L, but after reaching 80 L, the removal decreased to −81%, i.e., organic matter actually desorbed from the filter media during the low pH event. Fortunately, PFAS removal was not impacted during this event. The filter freed up adsorption sites during the desorption event, resulting in approximately 25% TOC removal after 160 L of water sampling (Figure 5). A similar trend was also observed for TDS using Saint-Donat tap water (average in influents (n = 4): 191 mg/L), where ZeroWater achieved about 100% removal after 40 L, but the removal dropped to −54% after 80 L, indicating desorption of some TDS. Subsequently, with additional filtration (160 L), the removal efficiency increased to only 7%, presumably because of the same reason for TOC. IX is notorious for producing elution peaks in relation to the affinity of the contaminants (Liu et al., 2021).

In contrast to Saint-Donat, ZeroWater exhibited better and more stable performance in Montreal tap water, likely due to lower levels of anions (2.7 vs. 4.9 mEq/L in Saint-Donat tap water Table 2), which may have resulted in less competition for adsorption on the filter structure. As a result, in Montreal tap water, ZeroWater achieved around 83% TOC removal after 80 L with an initial average concentration of 2.3 mg C/L (n = 4), which reached 53% at the end of water sampling (160 L). The high removal of TDS was also stable after 80 L, with a reduction to 93% after 160 L (Figure 6).

Notably, chloride removal by ZeroWater showed differences between the two water sources (Figures 5, 6). For Montreal, ZeroWater, with an initial average concentration of 23 mg/L (n = 4), achieved a consistently high removal of about 100% up to 80 L (Figure 6), and this figure decreased slightly to approximately 92% after 160 L. However, in Saint-Donat tap water, which had a higher initial average chloride concentration (122 mg/L), the performance decreased to 48% after 80L, and after 160 L, the recorded removal was −7%, indicating that the filter had reached its saturation point for chloride and started to release previously exchanged chloride. On the other hand, sulfate removal percentages for ZeroWater were consistently high in both water sources, demonstrating almost 100% removal. Sulfate is known to exhibit a higher affinity than chloride for AIX resin, and the concentrations were less than chloride, especially at Saint Donat (Table 2). Therefore, monitoring chloride removal was a better predictor of PFAS removal.

ClearlyFiltered performance: ClearlyFiltered, as a PFAS reduction-certified product, had the second-best performance with ~96% and ~99% removal of total PFAS in Montreal and Saint-Donat tap water, respectively. This filter also had nearly 100% removal for PFOS + PFOA during the experiment for both tap waters. Specific details about the filter's structure are not provided to explain the exact removal mechanisms. This filter is

considered an advanced water filter with a higher price point and a significantly longer manufacturer-expected lifetime (approximately 2.5–5 times longer than ZeroWater). The filtration method employs a distinctive dual-technology approach to achieve this performance (carbon layers and proprietary composite layer).

As contaminants like PFAS pass through this filter constructed with *Affinity® Filtration Technology*, they undergo a complex pathway with multiple twists and turns, different from a direct trajectory, resulting in higher removal rates than simple filters, according to the manufacturer. This structure might also be the reason for its lower average flow rate compared to other evaluated POU filters (Supplementary Figure S2). ClearlyFiltered consistently maintained high removal percentages (near 100%) for most quantified PFAS in Saint-Donat water throughout the experiment for all chain lengths and functional groups (Figure 3). However, for PFBA, the volume-weighted average removal percentage over 160 L was 91%, while the specific removal after 160 L was 88%, attributed to the challenge in sorbing more hydrophilic short-chain PFAS in this adsorption-based filter. This filter also demonstrated high removal of PFAS in Montreal tap water but less than in Saint-Donat tap water when the filtration volume reached 160 L for PFCAs (C4-C7 &C9) and PFSAs (C4, C6, C8). The removal of PFBA changed from 100% to 45% after 160 L, probably due to the impacts of higher levels of TOC in Montreal tap water, which caused more competition from hydrophobic organic matter on adsorption sites, which also means ClearlyFiltered probably relies more on the hydrophobic effect of activated carbon for adsorption.

Other removal performances were also different using ClearlyFiltered in comparison with ZeroWater. The TOC volume-weighted average removal rate was 92%, with an average initial concentration of 0.8 mg/L in Saint-Donat influent water. However, in the case of Montreal tap water, which had a notably higher initial average TOC concentration of 2.2 mg/L, the removal dropped to 73%. This again suggests that the filter's efficiency is influenced by the level of TOC in the water. In contrast with ZeroWater, ClearlyFiltered did not remove TDS, chloride, and sulfate, as shown in Figures 5, 6, which suggests that the filter does not rely on ion exchange as the primary removal mechanism.

Brita (Elite) performance: Brita filters are not NSF-53 certified for PFAS removal and lower performances were therefore expected. The Brita (Elite) filter showed a 36% removal for Σ_{75} PFAS after filtering 20 L of Saint-Donat tap water, which decreased to a mere 8% after filtering 160 L, with a volume-weighted average removal rate of 20%. Even though the TOC was higher in Montreal tap water, this filter exhibited better performance, achieving a 76% Σ_{75} PFAS removal after 20 L, which decreased to 39% after filtering 160 L, with a volume-weighted average removal rate of 48% after 160 L (vs. 20% in Saint-Donat). Volume-weighted average removal of the sum of PFOS and PFOA for this filter for Montreal tap water was relatively better (64%) than Saint-Donat tap water (29%). The type of PFAS present (Saint-Donat tap water includes higher levels of shorter chain PFAS with low AC affinity) is a potential explanation for this difference in performance.

These overall lower performances of the Brita (Elite) filter might be linked to its simpler filtration system (Supplementary Figure S3), which is not as effective in targeting PFAS contaminants. The main part of the structure of Brita that can help to reduce the PFAS is AC adsorption and hydrophobic interactions between the hydrophobic parts of the PFAS and the hydrophobic nature of the AC (Hakimabadi et al., 2023).

As can be seen in Figures 3, 4, the Brita (Elite) filter offered lower removal efficiencies of the shorter perfluorocarbon chains. As expected, the removal increased with the length of the PFAS chains. This filter also showed greater removal efficiencies for PFAS with sulfonate functional groups compared to carboxylate functional groups for both water sources, a common observation for AC sorption of PFAS. This difference can be attributed to the stronger negative inductive effect of the sulfonate functional group compared to carboxylate, primarily due to the presence of an additional oxygen atom in the sulfonate's resonance structure (Park et al., 2020).

The 6:2 FTSA was also quantified (6.6–17.1 ng/L, mean = 14.0 ng/L) in all unfiltered Saint-Donat tap water samples (n = 16), which Brita (Elite) removed better than the total PFAS concentration, starting from 71% removal at 20 L to 20% after 160 L (with a volume-weighted average removal rate of 43%).

It must be mentioned that for Brita (Elite), the Saint-Donat raw waters were sampled over a period of about 2 weeks, which explains the higher influent variability (Figure 2A). This filter demonstrated low removal performance for TOC with a volume-weighted average removal rate of 19% and was ineffective in removing TDS, chloride, and sulfate. For this filter, the initial pH remained relatively stable throughout the filtration process for both water sources.

Brita (Standard) performance: The performance of the Brita (Standard) filter in Montreal tap water was also low, with a low volume-weighted average removal rate of 38% for Σ_{75} PFAS with about 42% for PFOS + PFOA. Therefore, it was not evaluated for Saint-Donat tap water. Similar to Brita (Elite), this filter also had better removal performance with increasing chain length. For instance, PFBA (C4) had a volume-weighted average removal rate of 25%, and this rate increased for PFNA (C9) to 46% during the experiment. Additionally, the removal efficiencies of PFSAs were greater than PFCAs but with less magnitude compared to the Brita (Elite) (Figure 4). The structure of this filter is presented in Supplementary Figure S4.

Aquagear performance: Aquagear is not NSF-certified for PFAS removal, but the manufacturer provides third-party performance data on its website. Aquagear's performance also varied depending on the water source. It showed better removal efficiency for PFAS in Saint-Donat, with a volume-weighted average removal rate of 77% in comparison to Montreal tap water, with a volume-weighted average removal rate of 60%. The same removal trends were also observed for PFOS + PFOA, with volume-weighted average removals of 93% and 79% for Saint-Donat and Montreal tap waters, respectively. It means that despite Montreal tap water having lower PFAS levels, higher levels of other parameters in the water seemed to affect the PFAS adsorption on this filter, which is made from activated carbon and ion exchange media (Supplementary Figure S5). Aquagear also offered improved PFAS removals for longer chain lengths and sulfonated functional groups, as can be seen in Figures 3, 4. This removal trend suggests that activated carbon likely has a more important role in this filter, which is more effective in capturing longer-chain PFAS compounds.

The pH was not significantly impacted after the filtration of both tap waters. TOC removal by Aquagear was higher in Saint-Donat tap water, starting from 64% after 20 L and declining to 48% after 160 L with a volume-weighted average removal rate of 54% and in the case of Montreal tap water, ranging from 35% after 20 L to 11% after 160 L with a volume-weighted average of 20%.

This filter was also ineffective in removing TDS, chloride, and sulfate, suggesting that adsorption relies mostly on hydrophobicity.

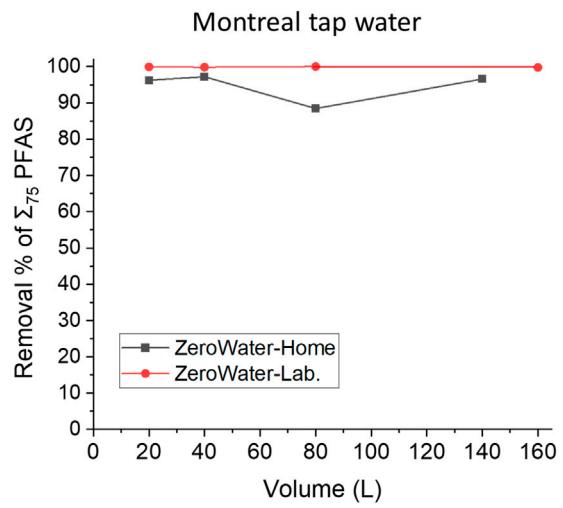

FIGURE 7
Comparison of Σ_{75}PFAS removal in the home versus laboratory experiment using Montreal tap water.

Notably, for sulfate, there was a significant release from 10 to 55 mg/L (removal rate −438%) after 20 L in Saint-Donat tap water. The negative removal rate continued although in smaller rates, until volume of 80 L (−16 removal % was recorded after reaching 80 L). A similar trend was also seen for Montreal tap water but with a smaller magnitude. After 20 L, the removal rate of sulfate was −11% but was insignificant after 160L. Further investigations would be needed to understand the exact source of this release as IX can be operated in sulfate mode. It is crucial to note that these sulfate leachings, though observed, remained below the EPA's secondary maximum contaminant level (SMCL) of 250 mg/L (EPA, 2022).

Testing ZeroWater in domestic settings: As ZeroWater demonstrated the best performance in removing PFAS compared to other filters, further evaluation was done in a home setting using Montreal tap water to assess its PFAS removal performance under normal use. Since the house residents prefer to drink cold water, the filter was kept in the refrigerator (4°C) between use. The results are illustrated in Figure 7, where the volume-weighted average removal percentage for Σ_{75} PFAS reached 94%, while it was up to 100% for the laboratory test. Due to the low flow rate resulting from filter clogging, the residents faced challenges in reaching the 160-L volume needed to compare with lab tests. Consequently, data points for 160 L are missing in the home batch results, and the last volume recorded was 140 L. Globally, the home test provided performance data coherent with the laboratory test, given the numerous factors that differed in both tests.

4 Conclusion

The study compared the performance of various POU water filters, including Brita (Elite and Standard), ZeroWater, Aquagear, and ClearlyFiltered, in removing ambient PFAS concentrations from two different tap waters from Saint-Donat and Montreal, Canada. The findings revealed that the efficiency of the filters varied depending on their structure, water source, and the specific PFAS present.

The two NSF or WQA certified filters with advanced and multi-stage filtration systems, named ZeroWater and ClearlyFiltered filters, demonstrated the highest PFAS removal performances. Initial water quality, such as TOC, TDS, and anions levels can significantly influence PFAS filtration outcomes. Volume-weighted average removal of total PFAS over 160 L were 99%, 99%, 77%, and 20% for ZeroWater, ClearlyFiltered, Aquagear, and Brita (Elite), respectively, using Saint-Donat tap water. In the case of Montreal tap water with different water characteristics and lower total PFAS level, the volume-weighted average removal of PFAS were ~100%, 96%, 60%, 48%, and 38% for ZeroWater, ClearlyFiltered, Aquagear, Brita (Elite) and Brita (Standard) respectively. Laboratory and home tests performed using ZeroWater filters provided similar performances.

ZeroWater demonstrated a noticeable pH drop after filtering 80 L in Saint-Donat tap water. Although desorption of organic matter and anions was noted during this event, PFAS removal was not impacted. Nevertheless, ZeroWater indicates that the acidic filtered water means the filter is exhausted and must be replaced. Aquagear also demonstrated an unusual sulfate release during the early sampling taken after 20 L, which needs further evaluation.

The findings of this study can provide guidance, especially for communities, particularly those residing in regions with notably elevated PFAS levels in tap water, as well as those relying on private wells as their source of drinking water facing PFAS contamination issues. This information aids them in selecting the most effective POU filter to protect them against PFAS that meets their specific water quality needs.

While this study aimed to assess the competitive PFAS removal efficiency of selected filters by considering some important water parameters, future investigations are required to evaluate their PFAS removal performance alongside a broader range of emerging contaminants such as pesticides, pharmaceuticals, or microplastics, especially for well-sourced tap water.

Furthermore, investigations on the environmental implications of POU filters are also important, including their material composition, disposal processes for used cartridges, and recyclability assessments to better clarify the overall sustainability of these filtration systems.

Data availability statement

The original contributions presented in the study are included in the article/Supplementary Material, further inquiries can be directed to the corresponding author.

Author contributions

TT: Conceptualization, Formal Analysis, Investigation, Methodology, Writing–original draft. QD: Investigation, Validation, Writing–review and editing, Methodology. BB: Conceptualization, Supervision, Writing–review and editing, Formal Analysis, Investigation, Validation. SS: Conceptualization, Funding acquisition, Methodology, Project administration, Supervision, Writing–review and editing.

Funding

The author(s) declare financial support was received for the research, authorship, and/or publication of this article. We want to thank the Natural Sciences and Engineering Research Council, the Canada Foundation for Innovation and PURE CREATE for funding this research.

Conflict of interest

The authors declare that the research was conducted in the absence of any commercial or financial relationships that could be construed as a potential conflict of interest.

Publisher's note

All claims expressed in this article are solely those of the authors and do not necessarily represent those of their affiliated organizations, or those of the publisher, the editors and the reviewers. Any product that may be evaluated in this article, or claim that may be made by its manufacturer, is not guaranteed or endorsed by the publisher.

Supplementary material

The Supplementary Material for this article can be found online at: https://www.frontiersin.org/articles/10.3389/fenvc.2024.1376079/full#supplementary-material

References

Anumol, T., Clarke, B. O., Merel, S., and Snyder, S. A. (2015). Point-of-Use devices for attenuation of trace organic compounds in water. *Journal-American Water Works Assoc.* 107, E474–E485. doi:10.5942/jawwa.2015.107.0129

Belkouteb, N., Franke, V., Mccleaf, P., Köhler, S., and Ahrens, L. (2020). Removal of per-and polyfluoroalkyl substances (PFASs) in a full-scale drinking water treatment plant: long-term performance of granular activated carbon (GAC) and influence of flow-rate. *Water Res.* 182, 115913. doi:10.1016/j.watres.2020.115913

EPA (2019). Method 533: determination of per- and polyfluoroalkyl substances in drinking water by isotope dilution anion exchange solid phase extraction and liquid chromatography/tandem mass spectrometry. Available at: https://www.epa.gov/dwanalyticalmethods/method-533-determination-and-polyfluoroalkyl-substances-drinking-water-isotope (Accessed November 07, 2023).

EPA (2022). Sulfate in drinking water. Available at: https://archive.epa.gov/water/archive/web/html/sulfate.html#:~:text=Sulfate%20in%20drinking%20water%20currently,i.e.%2C%20taste%20and%20odor (Accessed December 12, 2023).

EPA (2024). Per- and polyfluoroalkyl substances (PFAS)-Final PFAS national primary drinking water regulation. Available at: https://www.epa.gov/sdwa/and-polyfluoroalkyl-substances-pfas (Accessed May 6, 2024)

Goeury, K., Duy, S. V., Munoz, G., Prévost, M., and Sauvé, S. (2022). Assessment of automated off-line solid-phase extraction LC-MS/MS to monitor EPA priority endocrine disruptors in tap water, surface water, and wastewater. *Talanta* 241, 123216. doi:10.1016/j.talanta.2022.123216

Hakimabadi, S. G., Taylor, A., and Pham, A. L.-T. (2023). Factors affecting the adsorption of per-and polyfluoroalkyl substances (PFAS) by colloidal activated carbon. *Water Res.* 242, 120212. doi:10.1016/j.watres.2023.120212

He, A., Lu, Y., Chen, F., Li, F., Lv, K., Cao, H., et al. (2022). Exploring the origin of efficient adsorption of poly-and perfluoroalkyl substances in household point-of-use water purifiers: deep insights from a joint experimental and computational study. *Sci. Total Environ.* 831, 154988. doi:10.1016/j.scitotenv.2022.154988

HEALTH-CANADA (2023) *Draft objective for per- and polyfluoroalkyl substances in Canadian drinking water: overview*.

Herkert, N. J., Merrill, J., Peters, C., Bollinger, D., Zhang, S., Hoffman, K., et al. (2020). Assessing the effectiveness of point-of-use residential drinking water filters for perfluoroalkyl substances (PFASs). *Environ. Sci. Technol. Lett.* 7, 178–184. doi:10.1021/acs.estlett.0c00004

Kaboré, H. A., Duy, S. V., Munoz, G., Méité, L., Desrosiers, M., Liu, J., et al. (2018). Worldwide drinking water occurrence and levels of newly-identified perfluoroalkyl and polyfluoroalkyl substances. *Sci. total Environ.* 616, 1089–1100. doi:10.1016/j.scitotenv.2017.10.210

Karamat, A., Tehrani, R., Foster, G. D., and VAN Aken, B. (2023). Plant responses to per-and polyfluoroalkyl substances (PFAS): a molecular perspective. *Int. J. Phytoremediation* 26, 219–227. doi:10.1080/15226514.2023.2232874

Li, D., Lee, C.-S., Zhang, Y., Das, R., Akter, F., Venkatesan, A. K., et al. (2023). Efficient removal of short-chain and long-chain PFAS by cationic nanocellulose. *J. Mater. Chem. A* 11, 9868–9883. doi:10.1039/d3ta01851b

Liu, Z., Papineau, I., Mohseni, M., Peldszus, S., Bérubé, P. R., Sauvé, S., et al. (2021). Operating bicarbonate-form versus chloride-form ion exchange resins without regeneration for natural organic matter removal. *ACS ES&T Water* 1, 1456–1463. doi:10.1021/acsestwater.1c00040

Muir, D., and Sverko, E. (2006). Analytical methods for PCBs and organochlorine pesticides in environmental monitoring and surveillance: a critical appraisal. *Anal. Bioanal. Chem.* 386, 769–789. doi:10.1007/s00216-006-0765-y

Mulhern, R., Bynum, N., Liyanapatirana, C., Destefano, N. J., Knappe, D. R., and Macdonald Gibson, J. (2021). Longitudinal assessment of point-of-use carbon filters for removal of per-and polyfluoroalkyl substances from private well water. *AWWA Water Sci.* 3, e1262. doi:10.1002/aws2.1262

Munoz, G., Liu, M., Duy, S. V., Liu, J., and Sauvé, S. (2023). Target and nontarget screening of PFAS in drinking water for a large-scale survey of urban and rural communities in Québec, Canada. *Water Res.* 233, 119750. doi:10.1016/j.watres.2023.119750

Park, M., Daniels, K. D., Wu, S., Ziska, A. D., and Snyder, S. A. (2020). Magnetic ion-exchange (MIEX) resin for perfluorinated alkylsubstance (PFAS) removal in groundwater: roles of atomic charges for adsorption. *Water Res.* 181, 115897. doi:10.1016/j.watres.2020.115897

Patterson, C., Burkhardt, J., Schupp, D., Krishnan, E. R., Dyment, S., Merritt, S., et al. (2019). Effectiveness of point-of-use/point-of-entry systems to remove per-and polyfluoroalkyl substances from drinking water. *AWWA water Sci.* 1, 11311–e1212. doi:10.1002/aws2.1131

Shoemaker, J., and Tettenhorst, D. (2018) *EPA Method 537.1: determination of selected per-and polyfluorinated alkyl substances in drinking water by solid phase extraction and liquid chromatography/tandem mass spectrometry (LC/MS/MS)*. Washington, DC: National Center for Environmental Assessment.

Sosnowska, A., Bulawska, N., Kowalska, D., and Puzyn, T. (2023). Towards higher scientific validity and regulatory acceptance of predictive models for PFAS. *Green Chem.* 25, 1261–1275. doi:10.1039/d2gc04341f

Teymoorian, T., Munoz, G., Vo Duy, S., Liu, J., and Sauvé, S. (2023). Tracking PFAS in drinking water: a review of analytical methods and worldwide occurrence trends in tap water and bottled water. *ACS ES&T Water* 3, 246–261. doi:10.1021/acsestwater.2c00387

Teymourian, T., Teymoorian, T., Kowsari, E., and Ramakrishna, S. (2021). A review of emerging PFAS contaminants: sources, fate, health risks, and a comprehensive assortment of recent sorbents for PFAS treatment by evaluating their mechanism. *Res. Chem. Intermed.* 47, 4879–4914. doi:10.1007/s11164-021-04603-7

Wu, J., Cao, M., Tong, D., Finkelstein, Z., and Hoek, E. (2021). A critical review of point-of-use drinking water treatment in the United States. *Npj Clean. Water* 4, 40–25. doi:10.1038/s41545-021-00128-z

frontiers | Frontiers in Microbiology

TYPE Original Research
PUBLISHED 07 June 2024
DOI 10.3389/fmicb.2024.1403279

OPEN ACCESS

EDITED BY
Gaurav Pant,
Graphic Era University, India

REVIEWED BY
Cheng Zhang,
Jiangnan University, China
Dirk Tischler,
Ruhr University Bochum, Germany

*CORRESPONDENCE
Desong Yang
✉ yds_agr@shzu.edu.cn

RECEIVED 19 March 2024
ACCEPTED 21 May 2024
PUBLISHED 07 June 2024

CITATION
Hu Z, Qian C, Wang H, Sun L, Wu C, Zhang G, Han X, Wang C, Ma T and Yang D (2024) Comprehensive toxicological, metabolomic, and transcriptomic analysis of the biodegradation and adaptation mechanism by *Achromobacter xylosoxidans* SL-6 to diuron. *Front. Microbiol.* 15:1403279. doi: 10.3389/fmicb.2024.1403279

Comprehensive toxicological, metabolomic, and transcriptomic analysis of the biodegradation and adaptation mechanism by *Achromobacter xylosoxidans* SL-6 to diuron

Zhixu Hu, Cancan Qian, Haodong Wang, Lanlan Sun, Cailan Wu, Guoqiang Zhang, Xiaoqiang Han, Chunjuan Wang, Ting Ma and Desong Yang*

College of Agriculture/Key Laboratory of Oasis Agricultural Pest Management and Plant Protection Resources Utilization, Shihezi University, Shihezi, China

Biodegradation was considered a promising and environmentally friendly method for treating environmental pollution caused by diuron. However, the mechanisms of biodegradation of diuron required further research. In this study, the degradation process of diuron by *Achromobacter xylosoxidans* SL-6 was systematically investigated. The results suggested that the antioxidant system of strain SL-6 was activated by adding diuron, thereby alleviating their oxidative stress response. In addition, degradation product analysis showed that diuron in strain SL-6 was mainly degraded by urea bridge cleavage, dehalogenation, deamination, and ring opening, and finally *cis, cis*-muconic acid was generated. The combined analysis of metabolomics and transcriptomics revealed the biodegradation and adaptation mechanism of strain SL-6 to diuron. Metabolomics analysis showed that after the strain SL-6 was exposed to diuron, metabolic pathways such as tricarboxylic acid cycle (*cis, cis*-muconic acid), glutathione metabolism (oxidized glutathione), and urea cycle (arginine) were reprogrammed in the cells. Furthermore, diuron could induce the production of membrane transport proteins in strain SL-6 cells and overexpress antioxidant enzyme genes, finally ultimately promoting the up-regulation of genes encoding amide hydrolases and dioxygenases, which was revealed by transcriptomics studies. This work enriched the biodegradation mechanism of phenylurea herbicides and provided guidance for the removal of diuron residues in the environment and promoting agriculture sustainable development.

KEYWORDS

***Achromobacter xylosoxidans*, degradation, bioremediation, diuron, multiomics**

1 Introduction

Diuron (3-(3,4 dichlorophenyl)-1,1 dimethylurea) was a phenylurea herbicide that was extensively acted to Broadleaf weeds and grassy weeds in diverse crops fields such as cotton, fruit, and cereals (Li et al., 2021; Wang et al., 2022). Its function was to block the binding sites of plastid quinones in photosynthetic system II, and then destroy electron transport, thereby

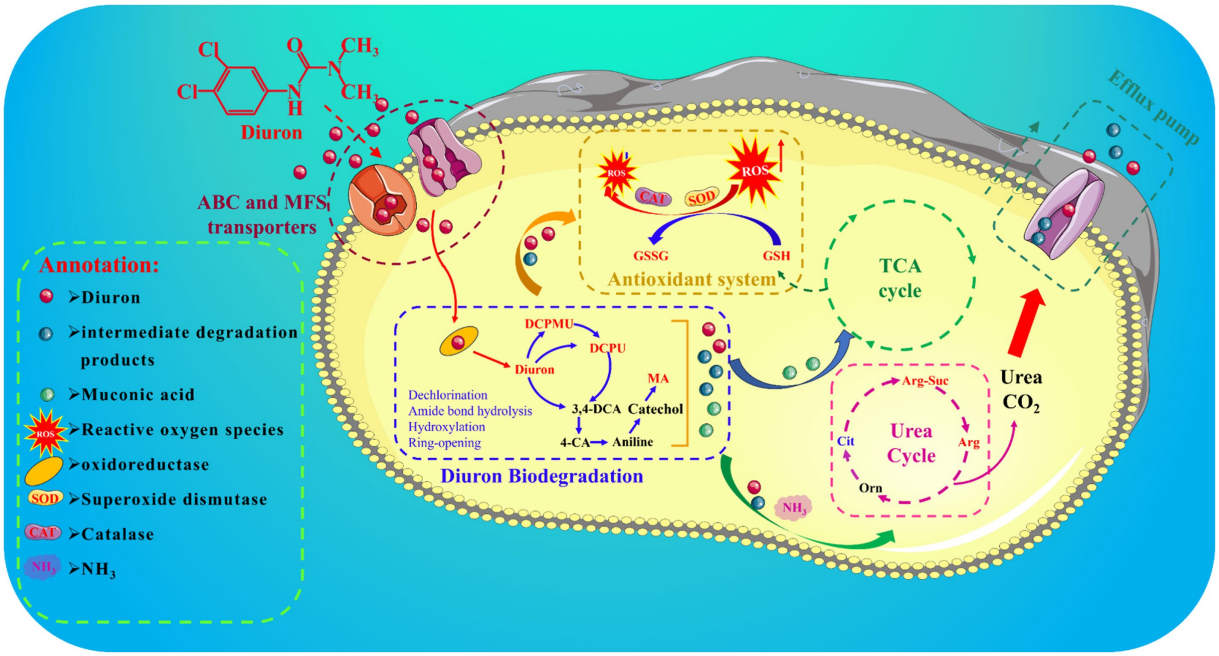

GRAPHICAL ABSTRACT

leading to weed death. However, most studies indicated that diuron was not easily volatile and photolytic in the soil, which could cause phytotoxicity and damage to subsequent sensitive crops, and induce environmental contamination of groundwater (Tandon and Pant, 2019). In addition, the ecological toxicity of diuron on non-target organisms was also reported, thereby raising community worry about its adverse impact on human health (Kao et al., 2019). Previous studies indicated that the diuron could cause endocrine and respiratory system disorders through its carcinogenic, mutagenic, and neurotoxic properties (Rocha et al., 2013; Huovinen et al., 2015; Behrens et al., 2016). Therefore, it is an urgent development for researchers to find a safe and effective method to manage the environmental pollution problem of diuron.

Currently, diuron could be degraded by means of physical adsorption, photocatalysis, chemistry, and microorganisms in the environment (Park and Jhung, 2020). Among them, microbial degradation was a safe and effective method to control organic contaminants from the natural environment (Bhatt et al., 2021). At present, only a few bacterial strains have been reported to degrade diuron, such as *Neurospora intermedia* (Wang et al., 2017), and *Bacillus licheniformis* (Singh and Singla, 2019). However, most of these bacterial isolates were unable to achieve complete mineralization of diuron and ended up producing only 1-(3,4-dichlorophenyl)-3-methyl urea (DCPMU), 1-(3,4-dichlorophenyl) urea (DCPU), or 3,4-dichloroaniline (3,4-DCA). In addition, previous research mainly focused on improving biodegradation efficiency, biodegradation characteristics, and identification of biodegradation products. There were relatively few reports on the resistance and transformation mechanism of microorganisms to diuron (Bhatt et al., 2021). Importantly, multi-omics technology provides new research ideas for elucidating the degradation mechanism of organic contaminants (Manzoni et al., 2018; Chunyan et al., 2023). Transcriptomics was used to explore key genes and degradation principles of microorganisms degrading pollutants (Filiatrault, 2011). Furthermore, metabolomics provided key information for us to further understand related metabolic pathways and their changes in the biodegradation process of aromatic compounds (Gao et al., 2021). Therefore, analyzing transcriptome and metabolome data could help us systematically understand the adaptation and biodegradation mechanisms of bacteria to diuron.

In this study, *Achromobacter xylosoxidans* SL-6 obtained in the early stage was used as the experimental object to investigate the biodegradation mechanism of diuron. Therefore, we combined toxicological evaluation, biodegradation product identification, metabolome analysis, and transcriptome analysis to reveal: (1) the adaptation mechanism of strain SL-6 to the oxidative stress caused by diuron; (2) the transport mechanism of strain SL-6 to diuron in cells; (3) the degradation mechanism of strain SL-6 to diuron in cells.

2 Materials and methods

2.1 Chemicals and medium

Diuron (analytically pure ≥97.0%) was provided by Shanghai McLean Biochemical Technology Co., Ltd. HPLC grade *n*-hexane and methanol were obtained from Thermo Fisher Scientific, United States. Mineral salt medium (0.2 g $MgSO_4{\cdot}7H_2O$, 1 g $(NH4)_2$ SO_4, 1.5 g K_2HPO_4, 0.5 g NaCl, and 0.5 g KH_2PO_4 per litre of water; Sigma-Aldrich; purity ≥99%). Luria-Bertani (LB) medium (10.0 g tryptone, 5.0 g yeast extract, and 10.0 g NaCl per litre of water; Sigma-Aldrich; purity ≥99%). All chemicals were analytical reagent grade.

2.2 Biodegradation characteristics of strain SL-6 to diuron

Previously, our research team has successfully discovered a strain that efficiently degrades diuron. The strain was isolated from the agricultural test site of Shihezi University, Shihezi City, Xinjiang Uygur Autonomous Region, China. The strain was identified and named *Achromobacter xylosoxidans* SL-6. Supplementary Figure S1 displays the colony morphology and evolutionary tree of the SL-6 strain. The results of the biological characteristics study of strain SL-6 are shown in Supplementary Figure S2. It was found that when the diuron dose reached 200 mg/L, the biodegradation efficiency of strain SL-6 was 93.1% within 5 days.

2.3 Determination of the cytotoxicity of diuron to the strain SL-6

Strain SL-6 was inoculated into MSM medium containing several doses of diuron (0, 50, 100, 200, 400, 600 mg/L) and cultured for 24 h and 48 h, respectively. After washing three times with PBS, the cells were performed at 4°C and 8,000 rpm to obtain bacterial cells. The reactive oxygen species (ROS) level, malondialdehyde (MDA) content, and lactate dehydrogenase (LDH) activity in strain SL-6 were measured, which was described in Supplementary Section SI-1.

2.4 Strain SL-6 antioxidant enzyme activity assay

Superoxide dismutase (SOD), catalase (CAT), and glutathione (GSH) were essential antioxidants for maintaining redox homeostasis in organisms (Staerck et al., 2017). The strain SL-6 was inoculated in several doses of diuron (0, 50, 100, 200, 400, 600 mg/L) and cultured for 24 h and 48 h, respectively. The cells were ultrasonically fragmented at 0°C for 15 min and centrifuged at 8,000 rpm to collect the supernatant. The activity of SOD, CAT, and the content of GSH in strain SL-6 cells was detected by the reagent kit (Jiancheng Bioengineering Institute, Nanjing, China).

2.5 Degradation of diuron and identification of metabolites

The sample was extracted twice with *n*-hexane and the organic phase was combined. The organic solution was removed by the rotary evaporator and then redissolved with methanol. The degradation products of diuron were detected by GC-MS (Agilent 8,890-5977B, Agilent Technologies, CA, United States). The column temperature program, scan range, and the parameters of the mobile phase are shown in Supplementary Section SI-2.

2.6 Metabolomic analysis

To detect alterations in intracellular metabolites, we performed a nontargeted metabolomic analysis (Gika et al., 2019). Strain SL-6 cells grown in LB medium supplemented with 200 mg/L diuron were harvested. The appropriate amount of sample was added to 1,000 μL pre-cooled methanol/acetonitrile/water solution (2:2:1, v/v/v) and treated with a vortex oscillator for 30 s. After ultrasonication at 4°C for 25 min, it was placed at −20°C for 15 min. The samples were placed in a centrifuge at 4°C, 14,000 rpm for 15 min. The supernatant was dried in a vacuum concentrator. Then it was redissolved with 100 μL acetonitrile/water (1:1, v/v) solvent and vortexed for 30 s, and then placed in a 4°C, 14000 rpm centrifuge for 15 min. The extracted samples were detected by UPLC-Q-TOF/MS. The specific parameters of LC-MS/MS analysis were described in Supplementary Section SI-3.

2.7 Transcriptome analysis

The strain SL-6 was inoculated into MSM liquid medium containing diuron (200 mg/L) and without diuron by 10% inoculation volume, and three replicates were set up, respectively, (An et al., 2020). The cells were cultured in a shaker at 30°C and 180 rpm for 72 h. Centrifugation was performed at 4°C and 10,000 rpm for 10 min to collect bacterial sediment. Washed twice with PBS, frozen in liquid nitrogen for 5 min, and stored at −80°C. The transcriptome sequencing service of the test samples was carried out by Wuhan Kangce Technology Co., Ltd. (Wuhan, China). The specific process of transcriptome sequencing was described in Supplementary Section SI-4.

2.8 Statistical analysis

Statistical analysis was performed using IBM SPSS statistics software (version 26.0, IBM Corporation, New York, United States). The significance of the difference between the treatment group and the control group was compared by single factor analysis of variance and Duncan test. All data were expressed as the means ± standard deviation (SD) at the $p < 0.05$ level. Data visualization was performed using Origin 2023 software (OriginLab, Massachussets, United States).

3 Results

3.1 Effect of diuron on the antioxidant system of strain SL-6

It was reported diuron could induce lipid peroxidation of the cell membrane by generating ROS, thereby leading to oxidative stress injury (Wang et al., 2022). ROS, MDA, and LDH were common indicators of cellular oxidative damage (Wakeel et al., 2020). Therefore, the intracellular ROS, MDA content, and LDH activity of strain SL-6 during treatment with diuron at different initial concentrations were determined. The results indicated that the ROS level, MDA content, and LDH activity of strain SL-6 cells treated with diuron was enhanced in a concentration-dependent manner (Figure 1). In addition, after 600 mg/L diuron treatment for 48 h, the ROS level, MDA content, and LDH activity of cells were increased by 4.29, 3.89, and 1.80 times than that of the control group, respectively. This indicated that diuron could induce the production of ROS in strain SL-6 cells, leading to enhanced lipid peroxidation and ultimately causing cell damage of strain SL-6. Previous studies indicated that SOD, CAT, and GSH were the primary

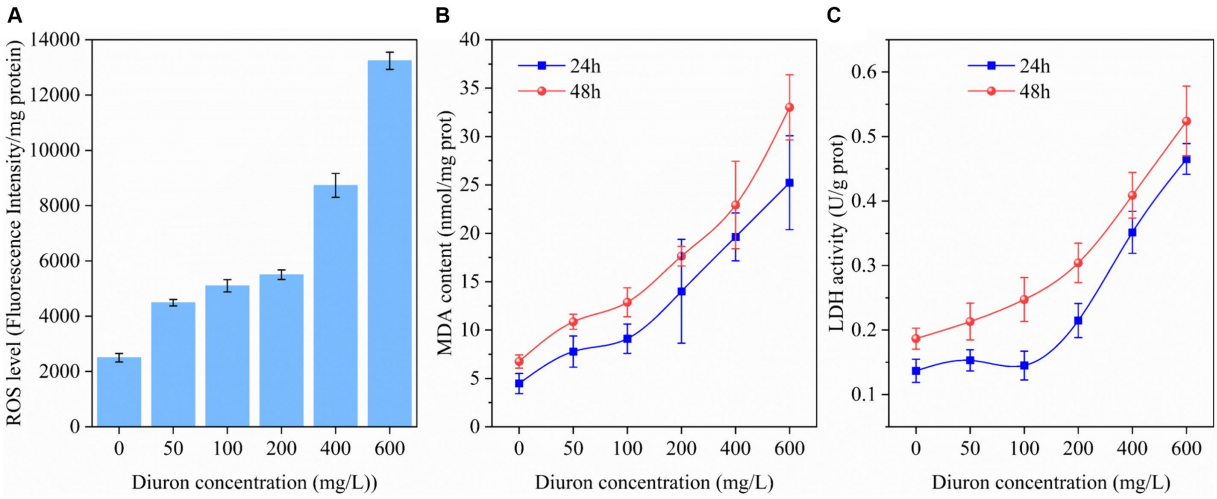

FIGURE 1
Effects of different concentrations of diuron on **(A)** ROS level (48 h), **(B)** MDA content, and **(C)** LDH activity of *Achromobacter xylosoxidans* SL-6 after treatment for 24 h and 48 h, respectively. Error bars represent standard deviation ($p < 0.05$).

antioxidant active substances in cells and played an important role in scavenging excessive ROS to maintain cellular redox balance (Hernández et al., 2015). Therefore, the SOD, CAT activity, and GSH content in the cells exposed to diuron were measured (Supplementary Figure S3). The results showed that after treatment with 200 mg/L diuron, the SOD, CAT activity and GSH content of strain SL-6 cells increased by 80, 159, and 81%, respectively, compared with the control group. This indicated that the addition of low concentration of diuron (≤200 mg/L) could stimulate the increase of SOD, POD activity, and GSH content in strain SL-6 cells, and reduce the oxidative damage of cells by removing excessive ROS in strain SL-6 cells.

3.2 Identification of intermediate degradation products of diuron

Combined with previous research results, we found that strain SL-6 had the highest biodegradation efficiency to 200 mg/L diuron (Supplementary Figure S2D), and the addition of 200 mg/L diuron had a relatively small effect on the oxidative damage of strain SL-6 cells. Therefore, 200 mg/L was selected as the optimal application dose of diuron in subsequent experiments. At present, the study found that the use of reference mass spectral database is still one of the best approaches to annotate the structure of known metabolites (Vinaixa et al., 2016). A total of seven metabolites were identified according to the mass spectra information by GC/MS detection (Supplementary Figure S4), including demethylation products: DCPMU and DCPU ($C_8H_8Cl_2N_2O$ and $C_7H_5Cl_2NO$), amide bond hydrolysis product: 3,4-DCA ($C_6H_5Cl_2N$), dechlorination products: 4-CA and aniline (C_6H_6ClN and C_6H_7N), and hydroxylation products: catechol and *cis, cis*-muconic acid ($C_6H_6O_2$ and $C_6H_6O_4$). The results confirmed that a series of continuous transformations of diuron occurred in the cells of strain SL-6, including demethylation, urea bridge cleavage, dehalogenation, deamination, hydroxylation, and ring-opening (Figure 2).

3.3 Metabolomic analysis of intracellular metabolites of strain SL-6

Metabolomics method was used to analyze the changes of intracellular metabolites of the strain SL-6 after diuron treatment. The results showed that 1,338 metabolites were detected and analyzed. Principal component analysis (PCA) revealed a clear distinction between the diuron treatment group and the control group on PC1, which represented 79.3% of the total variance (Supplementary Figure S5A). This indicated that the changes in endogenous metabolites of the degrading bacteria SL-6 cells were caused by diuron. Further analysis of metabolites was performed to clarify the differences in metabolites among the two groups. Among them, 388 were significantly up-regulated and 172 were significantly down-regulated (Supplementary Figure S5B). In addition, VIP score plots of relevant metabolites were obtained by PLS-DA (Supplementary Figure S5C). It is worth noting that the addition of 200 mg/L diuron had effects on a variety of metabolites related to diuron degradation or antioxidants by strain SL-6, such as DCPMU, DCPU, malic acid, arginine, eta-carotene, phosphatidylethanolamine, citric acid, and glutathione. Furthermore, KEGG pathways indicated that the metabolic pathways mainly affected by diuron treatment were the biosynthesis of amino acids, 2-oxocarboxylic acid metabolism, alanine, aspartate and glutamate metabolism, and arginine biosynthesis (Supplementary Figure S5D). The above results showed that strain SL-6 could efficiently degrade diuron by the diuron biodegradation pathway, the TCA cycle, glutathione metabolism, and the urea cycle (Figure 3).

There were three degradation products involved in the biodegradation pathway of diuron, namely DCPMU, DCPU, and *cis, cis*-muconic acid (MA) (Figure 3A). The metabolites involved in the TCA cycle were divided into two categories: organic acids and amino acids (Figure 3B). Among them, the contents of succinyl coenzyme A, malic acid, and citric acid increased significantly, and their relative abundance increased by 32.15, 3.60, and 17.78%, respectively, compared with the control group (Supplementary Figure S6). The

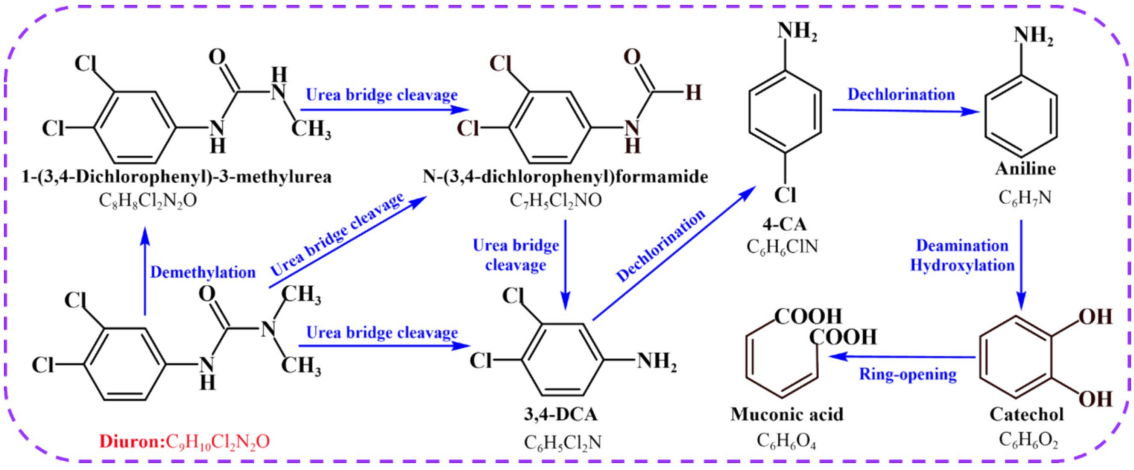

FIGURE 2
Proposed transformation pathway of diuron by *Achromobacter xylosoxidans* SL-6.

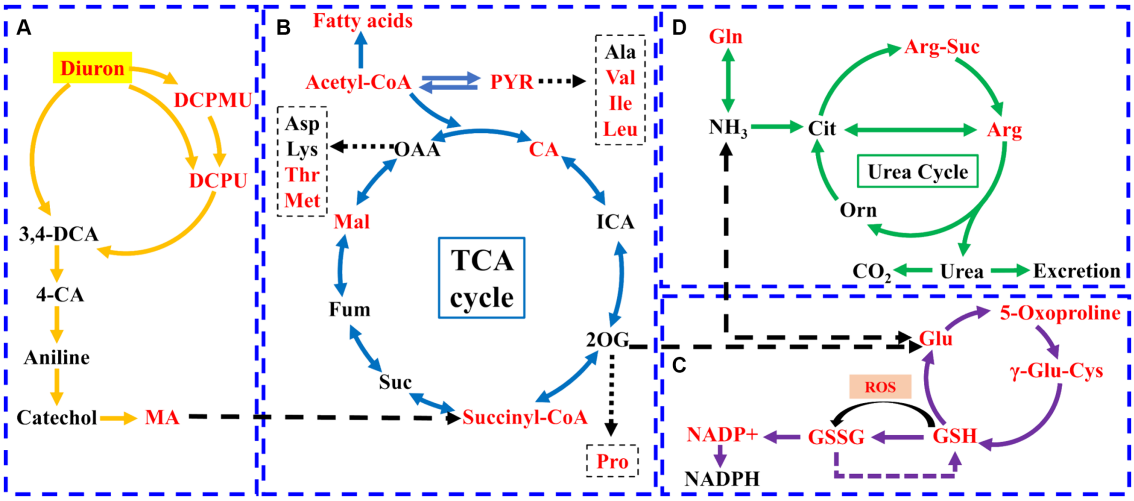

FIGURE 3
Schematic diagram of the metabolic pathways of strain SL-6 cells exposed to 200 mg/L diuron. **(A)** Diuron degradation pathway. **(B)** TCA cycle. **(C)** Glutathione metabolism. **(D)** Urea cycle. Red represents upregulation. Gln, glutamine; Glu, glutamic acid; Orn, ornithine; Cit, citrulline; Arg-Suc, L-argininosuccinic acid; γ-Glu-Cys, γ-L-glutamyl-L-cysteine; DCPMU, 1-(3,4-dichlorophenyl)-3-methyl urea; DCPU, 1-(3,4-dichlorophenyl) urea; MA, cis, cis-muconic acid; CA, citric acid; ICA, isocitrate; PYR, pyruvate; 2-OG, 2-Oxopentanoic acid; Suc, succinic acid; Fum, fumarate; Mal, malic acid.

contents of arginine, glutamic acid, methionine, isoleucine, valine, proline, and threonine were up-regulated (Supplementary Figure S6). This suggested that the TCA cycle could provide energy and various nutrients required for the strain SL-6 to adapt and degrade diuron, and was the center of the degradation metabolic reaction. In addition, the levels of glutamic acid, oxoproline, glutathione, and oxidized glutathione (GSSH) involved in glutathione metabolism were increased, and their relative abundances increased by 12.45, 13.39, 20.43, and 29.72%, respectively, compared with the control group (Figure 3C; Supplementary Figure S6). At the same time, the content of arginine and arginine succinic acid involved in the urea cycle were significantly up-regulated, and their relative abundances increased by 24.59 and 36.53%, respectively, compared with the control group (Figure 3D; Supplementary Figure S6). This indicated that strain SL-6 could reduce the oxidative stress induced by diuron through glutathione metabolism and urea cycle pathway, enhance the detoxification ability of diuron cytotoxicity, and better serve the degradation of diuron.

3.4 Transcriptome enrichment analysis of DEGs

Illumina MiSeq sequencing technology was used to research the differentially expressed genes during the degradation of diuron by strain SL-6, and the biodegradation mechanism of diuron was discussed. The PCA analysis showed that the diuron treatment group (200 mg/L) was significantly separated from the control group along PC1, which explained 42.84% of the total variance (Figure 4A). The results of the volcano plot showed that compared with the control group, the total number of differentially expressed genes (DEGs) after diuron induction was 1,057, of which 445 were up-regulated and 612

were down-regulated (Figure 4B). The 1,057 DEGs were annotated by the GO database and divided into three categories: molecular function, cellular component, and biological process (Figure 4C). In the molecular function classification, some up-regulated genes were annotated as oxidoreductase, dehydrogenase, cytochrome P450 and hydrolase activities (Ma et al., 2023). These DEGs involving the above GO entries might participate in the degradation of diuron by strain SL-6. The most important GO term in the classification of cellular components was ATPase-dependent transmembrane transport complex, followed by transmembrane transport protein complex, plasma membrane protein complex, and transport complex. These DEGs involved in the transmembrane transport of substances might help strain SL-6 transport diuron into cells. In the classification of biological processes, the up-regulated genes were mainly concentrated in carbon metabolism, nitrogen metabolism, fatty acid metabolism, and TCA cycle, while the down-regulated genes focused on cellular carbohydrate metabolism, glucan metabolism, polysaccharide metabolism, and glycogen metabolism (Qi et al., 2023). The above genes might participate in the energy metabolism process in strain SL-6 cells, providing energy to degrade and adapt to diuron. Similar results were observed for KEGG annotated pathway distribution. In KEGG pathway analysis, DEGs were mainly concentrated in multiple metabolic items, such as oxidative phosphorylation, glyoxylic acid and dicarboxylic acid metabolism, nitrogen metabolism, transmembrane transport, the TCA cycle, and glycolysis (Figure 5A).

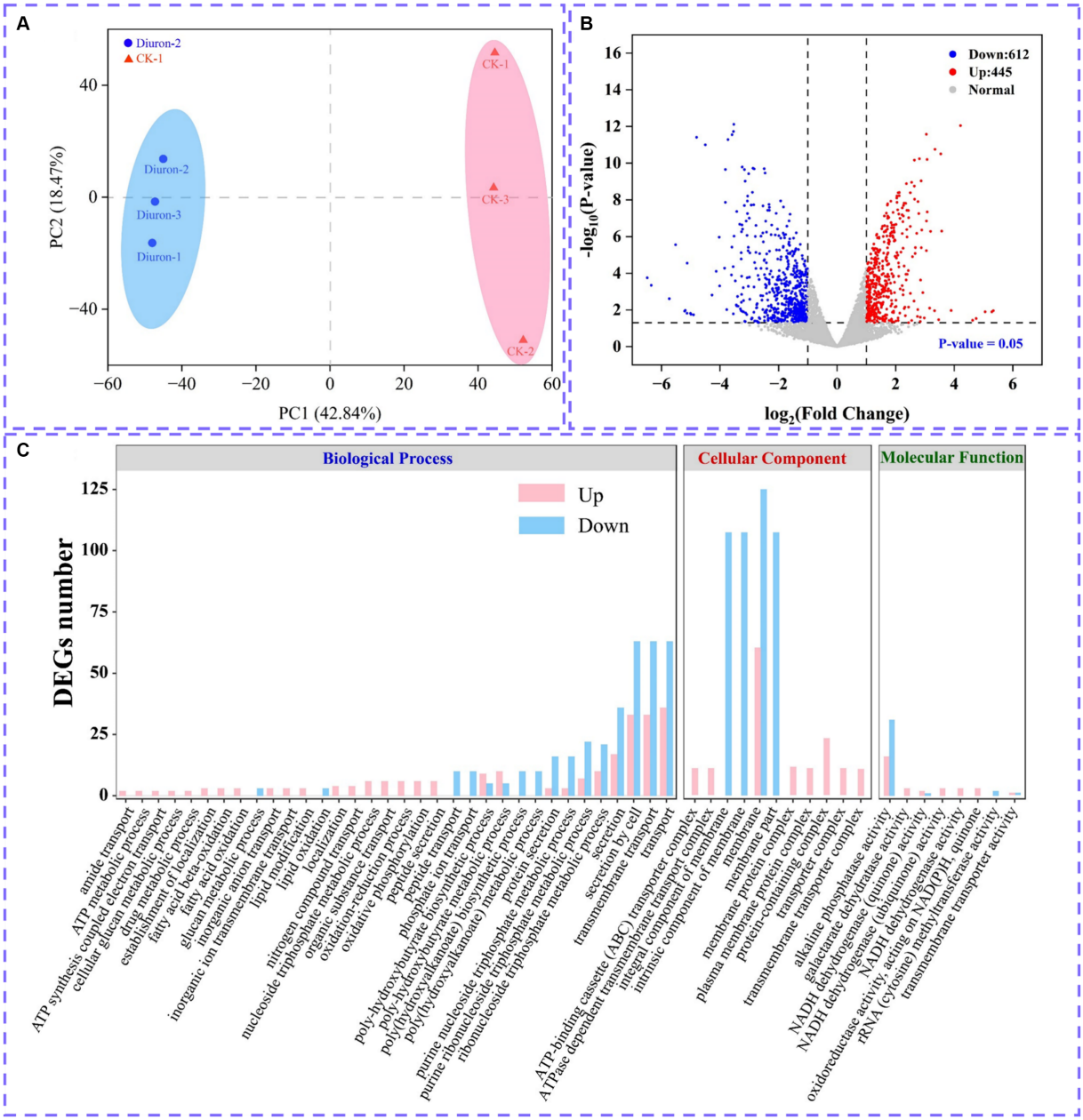

FIGURE 4
(A) PCA analysis plot. **(B)** Volcano plot of all differentially expressed genes. **(C)** Significantly enriched GO terms in differentially expressed genes.

10.3389/fmicb.2024.1403279

3.5 DEGs related to strain SL-6 adaptation and degradation of diuron

The degradation of diuron in strain SL-6 cells involved a variety of biological processes, including material transmembrane transport, antioxidant response, and the role of diuron degradation enzymes. Hierarchical clustering analysis was performed on DEGs related to the above biological processes (Figure 5B).

Cell transmembrane transport system: genes encoding transmembrane proteins, ATP-binding cassette (ABC), and major facilitator superfamily (MFS) transporters. According to the transcriptome results, we found that the expression of the genes (I6I48_RS07135 and *livG*) encoding Lipopolysaccharide export system ATP-binding protein LptB synthesis were significantly increased by 3.80-fold and 3.34-fold than that of the control group, respectively (Supplementary Table S1). The genes encoding outer membrane protein (I6I48_RS11310, *adeC*, and I6I48_RS00580) were up-regulated by 3.01-fold, 2.99-fold, and 3.19-fold than that of the control group, respectively (Supplementary Table S1). The expressions of nine ABC transporters (I6I48_RS03180, I6I48_RS10650, I6I48_RS28500, I6I48_RS29915, I6I48_RS19805, I6I48_RS18970, I6I48_RS23815 *dctP*, and *pstS*) and one MFS transporters (I6I48_RS22785) were significantly up-regulated (Supplementary Table S1). In summary, we speculate that the strain SL-6 cells had a transmembrane transport system capable of transporting exogenous organic substances, which could transport diuron into the cells to complete the next step of degradation.

Antioxidant system: genes encoding catalase, peroxidase, glutathione metabolism, and redox homeostasis. According to the transcriptome of diuron-treated cells, the genes encoding peroxidase (I6I48_RS30485, I6I48_RS29650, and I6I48_RS11345) and catalase (I6I48_RS02815) were significantly up-regulated (Supplementary Table S2). The genes encoding glutathione S-transferase (I6I48_RS26100) and glutaredoxin (I6I48_RS17070) were up-regulated by 2.34-fold and 2.47-fold than that of the control group, respectively (Supplementary Table S2). Three cellular redox homeostasis-related genes (I6I48_RS18035, I6I48_RS30485, and I6I48_RS05390) were up-regulated by 2.05-fold, 2.48-fold, and 2.57-fold than that of the control group, respectively (Supplementary Table S2). Taken together, we speculate that there was an antioxidant system in the cells of strain SL-6 that could resist exogenous toxic substances and help the strain cells maintain normal survival, so as to ensure the degradation of diuron.

Diuron degradation system: genes encoding demethylase, amidase, amidohydrolase, dehalogenase, monooxygenase and dioxygenase. The results of transcriptome showed that the expression level of the cytochrome P450 (*adhP*) gene encoding xenobiotic metabolism increased by 2.73-fold than that of the control group (Supplementary Table S3), which might be involved in the demethylation reaction of strain SL-6 to diuron. The gene expressions of N-formylglutamate amidohydrolase (I6I48_RS16595), amidohydrolase family (I6I48_RS20465), amidohydrolase family protein (I6I48_RS04995), and N-acetylmuramyl-L-alanine amidase (I6I48_RS09150) were significantly up-regulated

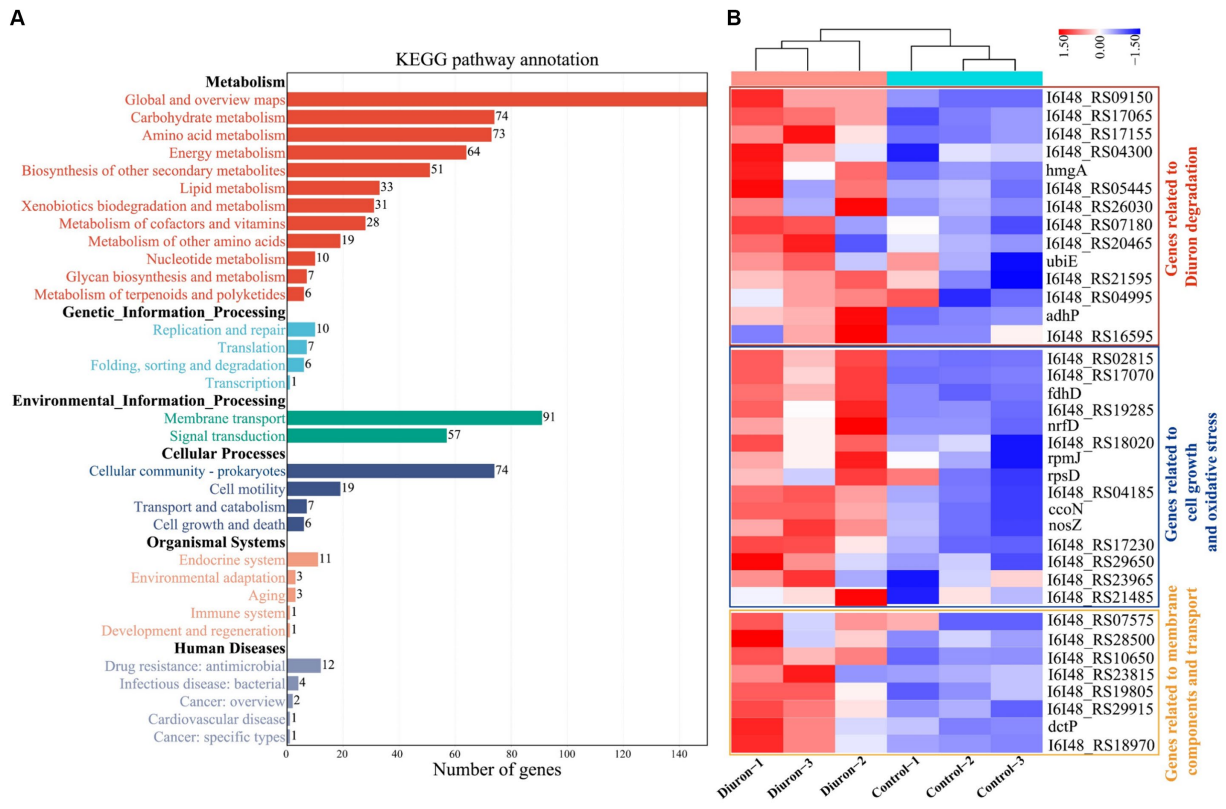

FIGURE 5
(A) KEGG secondary classification of differentially expressed genes. **(B)** Cluster heat map of differentially expressed genes related to transmembrane transport of substances, antioxidant reactions, and the action of diuron-degrading enzymes.

(Supplementary Table S3), indicating that they could be involved in the hydrolysis of amide bonds and act as hydrolases to catalyze the cleavage of urea bridges in this process. The gene expression of 4-chlorobenzoyl-CoA dehalogenase (I6I48_RS07180) was up-regulated by 2.20-fold than that of the control group (Supplementary Table S3), which might be related to the reductive dechlorination reaction during the biodegradation of diuron. The gene expression of nitrate monooxygenase (I6I48_RS21595) was up-regulated by 2.35-fold than that of the control group (Supplementary Table S3), which could be relevant to the deamination oxidation reaction of aniline during the biodegradation of diuron. The expression of genes encoding multiple dioxygenases was significantly up-regulated, including quercetin 2,3-dioxygenase (I6I48_RS17155), aromatic ring hydroxylating dioxygenase (I6I48_RS26030), homogentisate 1,2-dioxygenase (*hmgA*) and phytanoyl-CoA dioxygenase family protein (I6I48_RS04300) (Supplementary Table S3), indicating that they might be responsible for ring-opening cleavage. Therefore, we speculate that there was a diuron degradation system composed of genes encoding multiple degradation enzymes in the strain SL-6 cells, which helped the strain SL-6 cells degrade and utilize diuron.

4 Discussion

The analysis of diuron degradation products provided information on the degradation pathway for the biodegradation mechanism of diuron by bacterial SL-6 cells. Previous studies indicated that microorganisms first generate DCPMU and DCPU by removing one or two methyl groups on diuron (Ellegaard-Jensen et al., 2013). This was followed by the hydrolysis of the amide bond, generating the metabolite 3,4-DCA, which was the common microbial diuron degradation product (Egea et al., 2017). According to previous reports, the biodegradation of 3,4-DCA mainly included two diverse reactions (dehalogenation and hydroxylation), followed by the formation of 4-chloroaniline (4-CA) and 1,2-dichlorobenzene (1,2-DCB) (Silambarasan et al., 2020). 4-CA was dechlorinated and hydroxylated to generate aniline and 4-chlorocatechol respectively, and then, aniline was deaminated to generate catechol (Mohlam et al., 2018; Li et al., 2022). Ultimately, ring-opening cleavage of catechol produced *cis, cis*-muconic acid (Shahryari et al., 2018; Yu et al., 2020). According to the seven degradation products identified by GC-MS, the degradation pathway of diuron in the cells of strain SL-6 was clarified. Mainly demethylation, urea bridge cleavage, dehalogenation, deamination and ring opening, which provided a basis for subsequent research on the biodegradation mechanism of diuron by strain SL-6.

Metabolomics was a science that reflects the physiological state of organisms by detecting changes in endogenous metabolites (Liang et al., 2021). Through metabolomic research, it was found that strain SL-6 requires the joint participation of the TCA cycle, glutathione metabolism, and urea cycle to adapt to and degrade diuron. As the center of metabolic pathways, the TCA cycle provided energy for other metabolic pathways in organisms (Liu et al., 2017; Ke et al., 2018). The degradation products of diuron could be utilized by SL-6 cells through the TCA cycle. Importantly, the TCA cycle could also produce organic acids to biosynthesize other amino acids (Arnold and Finley, 2023). These newly generated amino acids could participate in the regulation of energy metabolism, signaling pathways, and antioxidant defense responses in cells (Nesterov et al., 2020). The up-regulated arginine, glutamic acid, methionine, isoleucine, valine, proline, and threonine could directly or indirectly be involved in glycolysis, fat metabolism, pyruvate metabolism, and the TCA cycle, providing various nutrients for strain SL-6. Furthermore, Previous studies reported that glutathione was a common antioxidant in organisms and played an important role in maintaining cellular redox homeostasis, regulating cellular signals, and improving protein activity (Hasanuzzaman et al., 2017). Therefore, we speculated that the glutathione metabolic pathway could continuously provide antioxidants for SL-6 strain cells. The purpose was to remove the excessive ROS induced by diuron and maintain the redox homeostasis of SL-6 cells. Previous studies reported that arginine serves as an intermediate in the urea cycle, which could relieve ammonia poisoning and involved in the energy metabolism and antioxidant stress response of various microorganisms (Charlier and Bervoets, 2019; Hirose et al., 2021). Therefore, we speculate that the ammonia (NH_3) removed during the degradation of diuron might eventually be excreted by the strain SL-6 cells via the urea cycle to achieve detoxification. Metabolomic analysis helped us to further expand our understanding of the mechanisms of degradation and adaptation of strain SL-6 to diuron.

Transcriptomics studies had shown that in order to fully degrade diuron, strain SL-6 cells might have cell transmembrane transport system, antioxidant system, and degradation system composed of a variety of different coding genes. Previous research had confirmed that most of the transmembrane transport of exogenous substances was mediated by the membrane transport system (Wu et al., 2023). Lipopolysaccharide, outer membrane protein, ABC, and MFS transporters were components of the cell transmembrane transport system. Studies had shown that lipopolysaccharide could adjust the hydrophobicity of bacterial cell surfaces and play an important role in the adsorption of organic contaminants (Okuda et al., 2016). Outer membrane proteins (OMPs) were structural proteins on the outer membrane of bacterial cells, which could participate in the passive and active transport of substances (Sun et al., 2022). It has been reported that ABC transporters and MFS transporters play important roles in cell transmembrane nutrient absorption (Mutanda et al., 2022). In addition, ABC and MFS transporters participated in the excretion of various toxic compounds within microbial cells and provided microorganisms with resistance to various compounds (Wilkens, 2015; Pasqua et al., 2021). We considered that diuron could enter the strain SL-6 cells through the cell transmembrane transport system to achieve multi-step degradation of diuron.

At present, research has shown that there was an endogenous antioxidant system in organisms, which could counteract free radicals and neutralize oxidants to maintain cellular redox homeostasis (He et al., 2017). The common antioxidants include catalase, peroxidase, glutathione metabolism, and redox homeostasis genes. It was reported that catalase and peroxidase in cells participate in the scavenging of ROS and reduce cytotoxicity (Hasanuzzaman et al., 2017). Glutathione S-transferase and glutaredoxin mediate the reduction of glutathione and were involved in the detoxification of xenobiotics and oxidative stress response (Dasari et al., 2018; Chai and Mieyal, 2023). Furthermore, genes related to cellular redox homeostasis play an important role in maintaining the normal physiological activities of cells and responding to oxidative stress (He et al., 2017). We considered that the genes encoding catalase, peroxidase, glutathione metabolism, and redox homeostasis together constitute the antioxidant system, which could help the strain SL-6 better adapt to the toxicity of diuron

and provide a healthy and stable cell environment for the degradation of diuron in the cell.

In addition, the biodegradation of diuron mainly involved demethylase, amidase, amidohydrolase, dehalogenase, monooxygenase, and dioxygenase, which played different roles in the biodegradation of diuron. Demethylation reaction: the DCPMU and DCPU generated by diuron degradation indicate that the enzyme catalyzes the sequential demethylation of diuron (Silva Moretto et al., 2019). Cytochrome P450 was proved to participate in the demethylation of diuron by *Arthrobacter* N2 (Giacomazzi and Cochet, 2004). It was also involved in the demethylation reaction of diuron in humans and other mammals (Abass et al., 2007; Uno et al., 2011). Amide bond hydrolysis reaction: the most important enzymatic reaction of diuron biodegradation was the hydrolysis and cleavage of the amide bond to produce the metabolite 3,4-DCA (Hussain et al., 2015; Silambarasan et al., 2020). It was found that amidohydrolases and amidases played a role in the hydrolysis of amide bonds during the biodegradation of phenylurea herbicides. Seven species were reported, including PuhA, PuhB, LibA, HylA, Phh, Mhh, and LahB (Dejonghe et al., 2003; Khurana et al., 2009; Bers et al., 2012; Zhang et al., 2018, 2020).

Dechlorination reaction: the literature states that the next step after the biodegradation of 3,4-DCA was the sequential dechlorination reaction, which resulted in the production of aniline (Hongsawat and Vangnai, 2011). Dehalogenases could catalyze the removal of halogen groups and then were used by many bacteria to degrade halogenated aromatic hydrocarbons (Ang et al., 2018; Pimviriyakul et al., 2020). Therefore, the gene encoding dehalogenase might be involved in the reductive dechlorination reaction during the biodegradation of diuron. Oxidative deamination reaction: it has been reported that aniline was converted into catechol by deamination and hydroxylation (Arora, 2015). Monooxygenases could catalyze the deamination and oxidation of aromatic nitrogen oxides to generate hydroxylated products (Paul et al., 2021). The gene encoding monooxygenase might be involved in the biodegradation of diuron by strain SL-6 and play a role in the deamination of aniline to catechol. Ring-opening reaction: catechol could be further degraded into *cis, cis*-muconic acid (MA) through the ortho-cleavage pathway (Liu et al., 2023). According to various studies, dioxygenase had the ability to catalyze the ring-opening cleavage reaction of catechol (Zhang et al., 2021). The generated *cis, cis*-muconic acid was ultimately metabolized through the TCA cycle (He et al., 2023). We considered that there was a diuron degradation system composed of genes encoding demethylase, amidase, amidohydrolase, dehalogenase, monooxygenase, and dioxygenase in strain SL-6 cells, which helped the strain SL-6 cells to degrade and utilize diuron step by step, and finally realize the complete mineralization of diuron.

In summary, the biodegradation and adaption mechanisms of *Achromobacter xylosoxidans* SL-6 to diuron were further revealed through toxicological assessment, identification of intermediate metabolites, metabolome, and transcriptome analysis. Toxicological evaluation results showed that diuron could activate the antioxidant system (superoxide dismutase, catalase, and glutathione) in the cells of strain SL-6, and relieve the oxidative damage induced by a large number of reactive oxygen species. The analysis of degradation metabolites indicated that the diuron underwent a sequence of reactions in strain SL-6 cells, urea bridge cleavage, dehalogenation, deamination oxidation, and ring-opening. Metabolomic analysis revealed that the degradation of diuron by strain SL-6 mainly involved four metabolic pathways: diuron biodegradation, tricarboxylic acid cycle, glutathione metabolism, and the urea cycle. Furthermore, transcriptome data analysis identified differentially expressed genes that participated in substance transmembrane transport, antioxidant response, and diuron degradation in strain SL-6 cells. Overall, our research results offered a new perspective on the biodegradation and adaptation mechanism of strain SL-6 to diuron and promoted the environmental remediation strategy to a deeper level.

Data availability statement

The original contributions presented in the study are publicly available. This data can be found here: NCBI Sequence Read Archive (SRA) database, accession number: PRJNA1118467.

Author contributions

ZH: Data curation, Investigation, Software, Writing – original draft. CQ: Conceptualization, Writing – review & editing. HW: Conceptualization, Writing – review & editing. LS: Investigation, Writing – review & editing. CaW: Conceptualization, Funding acquisition, Methodology, Writing – review & editing. GZ: Resources, Supervision, Writing – review & editing. XH: Resources, Supervision, Writing – review & editing. ChW: Resources, Supervision, Writing – review & editing. TM: Resources, Supervision, Writing – review & editing. DY: Data curation, Project administration, Supervision, Writing – review & editing.

Funding

The author(s) declare that financial support was received for the research, authorship, and/or publication of this article. This work was financially supported by the National Natural Science Foundation of China (No. 3230688).

Conflict of interest

The authors declare that the research was conducted in the absence of any commercial or financial relationships that could be construed as a potential conflict of interest.

Publisher's note

Supplementary material

The Supplementary material for this article can be found online at: https://www.frontiersin.org/articles/10.3389/fmicb.2024.1403279/full#supplementary-material

References

Abass, K., Reponen, P., Turpeinen, M., Jalonen, J., and Pelkonen, O. (2007). Characterization of diuron N-demethylation by mammalian hepatic microsomes and cDNA-expressed human cytochrome P450 enzymes. *Drug Metab. Dispos.* 35, 1634–1641. doi: 10.1124/dmd.107.016295

An, X., Tian, C., Xu, J., Dong, F., Liu, X., Wu, X., et al. (2020). Characterization of hexaconazole-degrading strain *Sphingobacterium multivorum* and analysis of transcriptome for biodegradation mechanism. *Sci. Total Environ.* 722:137171. doi: 10.1016/j.scitotenv.2020.137171

Ang, T.-F., Maiangwa, J., Salleh, A. B., Normi, Y. M., and Leow, T. C. (2018). Dehalogenases: from improved performance to potential microbial dehalogenation applications. *Molecules* 23:1100. doi: 10.3390/molecules23051100

Arnold, P. K., and Finley, L. W. S. (2023). Regulation and function of the mammalian tricarboxylic acid cycle. *J. Biol. Chem.* 299:102838. doi: 10.1016/j.jbc.2022.102838

Arora, P. K. (2015). Bacterial degradation of monocyclic aromatic amines. *Front. Microbiol.* 6:820. doi: 10.3389/fmicb.2015.00820

Behrens, D., Rouxel, J., Burgeot, T., and Akcha, F. (2016). Comparative embryotoxicity and genotoxicity of the herbicide diuron and its metabolites in early life stages of *Crassostrea gigas*: implication of reactive oxygen species production. *Aquat. Toxicol.* 175, 249–259. doi: 10.1016/j.aquatox.2016.04.003

Bers, K., Sniegowski, K., De Mot, R., and Springael, D. (2012). Dynamics of the linuron hydrolase *libA* gene pool size in response to linuron application and environmental perturbations in agricultural soil and on-farm biopurification systems. *Appl. Environ. Microbiol.* 78, 2783–2789. doi: 10.1128/AEM.06991-11

Bhatt, P., Gangola, S., Bhandari, G., Zhang, W., Maithani, D., Mishra, S., et al. (2021). New insights into the degradation of synthetic pollutants in contaminated environments. *Chemosphere* 268:128827. doi: 10.1016/j.chemosphere.2020.128827

Chai, Y.-C., and Mieyal, J. J. (2023). Glutathione and glutaredoxin—key players in cellular redox homeostasis and signaling. *Antioxidants* 12:1553. doi: 10.3390/antiox12081553

Charlier, D., and Bervoets, I. (2019). Regulation of arginine biosynthesis, catabolism and transport in *Escherichia coli*. *Amino Acids* 51, 1103–1127. doi: 10.1007/s00726-019-02757-8

Chunyan, X., Qaria, M. A., Qi, X., and Daochen, Z. (2023). The role of microorganisms in petroleum degradation: current development and prospects. *Sci. Total Environ.* 865:161112. doi: 10.1016/j.scitotenv.2022.161112

Dasari, S., Ganjayi, M. S., Yellanurkonda, P., Basha, S., and Meriga, B. (2018). Role of glutathione S-transferases in detoxification of a polycyclic aromatic hydrocarbon, methylcholanthrene. *Chem. Biol. Interact.* 294, 81–90. doi: 10.1016/j.cbi.2018.08.023

Dejonghe, W., Berteloot, E., Goris, J., Boon, N., Crul, K., Maertens, S., et al. (2003). Synergistic degradation of linuron by a bacterial consortium and isolation of a single linuron-degrading *Variovorax* strain. *Appl. Environ. Microbiol.* 69, 1532–1541. doi: 10.1128/AEM.69.3.1532-1541.2003

Egea, T. C., da Silva, R., Boscolo, M., Rigonato, J., Monteiro, D. A., Grünig, D., et al. (2017). Diuron degradation by bacteria from soil of sugarcane crops. *Heliyon* 3:e00471. doi: 10.1016/j.heliyon.2017.e00471

Ellegaard-Jensen, L., Aamand, J., Kragelund, B. B., Johnsen, A. H., and Rosendahl, S. (2013). Strains of the soil fungus *Mortierella* show different degradation potentials for the phenylurea herbicide diuron. *Biodegradation* 24, 765–774. doi: 10.1007/s10532-013-9624-7

Filiatrault, M. J. (2011). Progress in prokaryotic transcriptomics. *Curr. Opin. Microbiol.* 14, 579–586. doi: 10.1016/j.mib.2011.07.023

Gao, J., Song, J., Ye, J., Duan, X., Dionysiou, D. D., Yadav, J. S., et al. (2021). Comparative toxicity reduction potential of UV/sodium percarbonate and UV/hydrogen peroxide treatments for bisphenol a in water: an integrated analysis using chemical, computational, biological, and metabolomic approaches. *Water Res.* 190:116755. doi: 10.1016/j.watres.2020.116755

Giacomazzi, S., and Cochet, N. (2004). Environmental impact of diuron transformation: a review. *Chemosphere* 56, 1021–1032. doi: 10.1016/j.chemosphere.2004.04.061

Gika, H., Virgiliou, C., Theodoridis, G., Plumb, R. S., and Wilson, I. D. (2019). Untargeted LC/MS-based metabolic phenotyping (metabonomics/metabolomics): the state of the art. *J. Chromatogr. B* 1117, 136–147. doi: 10.1016/j.jchromb.2019.04.009

Hasanuzzaman, M., Nahar, K., Anee, T. I., and Fujita, M. (2017). Glutathione in plants: biosynthesis and physiological role in environmental stress tolerance. *Physiol. Mol. Biol. Plants* 23, 249–268. doi: 10.1007/s12298-017-0422-2

He, L., He, T., Farrar, S., Ji, L., Liu, T., and Ma, X. (2017). Antioxidants maintain cellular redox homeostasis by elimination of reactive oxygen species. *Cell. Physiol. Biochem.* 44, 532–553. doi: 10.1159/000485089

He, S., Wang, W., Wang, W., Hu, H., Xu, P., and Tang, H. (2023). Microbial production of *cis,cis*-muconic acid from aromatic compounds in engineered *Pseudomonas*. *Synth. Syst. Biotechnol.* 8, 536–545. doi: 10.1016/j.synbio.2023.08.001

Hernández, L. E., Sobrino-Plata, J., Montero-Palmero, M. B., Carrasco-Gil, S., Flores-Cáceres, M. L., Ortega-Villasante, C., et al. (2015). Contribution of glutathione to the control of cellular redox homeostasis under toxic metal and metalloid stress. *J. Exp. Bot.* 66, 2901–2911. doi: 10.1093/jxb/erv063

Hirose, Y., Yamaguchi, M., Sumitomo, T., Nakata, M., Hanada, T., Okuzaki, D., et al. (2021). *Streptococcus pyogenes* upregulates arginine catabolism to exert its pathogenesis on the skin surface. *Cell Rep.* 34:108924. doi: 10.1016/j.celrep.2021.108924

Hongsawat, P., and Vangnai, A. S. (2011). Biodegradation pathways of chloroanilines by *Acinetobacter baylyi* strain GFJ2. *J. Hazard. Mater.* 186, 1300–1307. doi: 10.1016/j.jhazmat.2010.12.002

Huovinen, M., Loikkanen, J., Naarala, J., and Vähäkangas, K. (2015). Toxicity of diuron in human cancer cells. *Toxicol. In Vitro* 29, 1577–1586. doi: 10.1016/j.tiv.2015.06.013

Hussain, S., Arshad, M., Springael, D., SøRensen, S. R., Bending, G. D., Devers-Lamrani, M., et al. (2015). Abiotic and biotic processes governing the fate of phenylurea herbicides in soils: a review. *Crit. Rev. Environ. Sci. Technol.* 45, 1947–1998. doi: 10.1080/10643389.2014.1001141

Kao, C. M., Ou, W.-J., Lin, H.-D., Eva, A. W., Wang, T.-L., and Chen, S. C. (2019). Toxicity of diuron in HepG2 cells and zebrafish embryos. *Ecotoxicol. Environ. Saf.* 172, 432–438. doi: 10.1016/j.ecoenv.2019.01.036

Ke, M., Qu, Q., Peijnenburg, W. J. G. M., Li, X., Zhang, M., Zhang, Z., et al. (2018). Phytotoxic effects of silver nanoparticles and silver ions to *Arabidopsis thaliana* as revealed by analysis of molecular responses and of metabolic pathways. *Sci. Total Environ.* 644, 1070–1079. doi: 10.1016/j.scitotenv.2018.07.061

Khurana, J. L., Jackson, C. J., Scott, C., Pandey, G., Horne, I., Russell, R. J., et al. (2009). Characterization of the phenylurea hydrolases a and B: founding members of a novel amidohydrolase subgroup. *Biochem. J.* 418, 431–441. doi: 10.1042/bj20081488

Li, C., Sun, Y., Sun, G., Zang, H., Sun, S., Zhao, X., et al. (2022). An amidase and a novel phenol hydroxylase catalyze the degradation of the antibacterial agent triclocarban by *Rhodococcus rhodochrous*. *J. Hazard. Mater.* 430:128444. doi: 10.1016/j.jhazmat.2022.128444

Li, J., Zhang, W., Lin, Z., Huang, Y., Bhatt, P., and Chen, S. (2021). Emerging strategies for the bioremediation of the phenylurea herbicide diuron. *Front. Microbiol.* 12:686509. doi: 10.3389/fmicb.2021.686509

Liang, Y., Zhang, H., and Cai, Z. (2021). New insights into the cellular mechanism of triclosan-induced dermal toxicity from a combined metabolomic and lipidomic approach. *Sci. Total Environ.* 757:143976. doi: 10.1016/j.scitotenv.2020.143976

Liu, S., Guo, C., Dang, Z., and Liang, X. (2017). Comparative proteomics reveal the mechanism of Tween80 enhanced phenanthrene biodegradation by *Sphingomonas* sp. GY2B. *Ecotoxicol. Environ. Saf.* 137, 256–264. doi: 10.1016/j.ecoenv.2016.12.015

Liu, Y., Wei, F., Xu, R., Cheng, T., and Ma, Y. (2023). Insights into the binding interaction of catechol 1,2-dioxygenase with catechol in *Achromobacter xylosoxidans* DN002. *Appl. Biochem. Biotechnol.* 195, 298–313. doi: 10.1007/s12010-022-04129-7

Ma, Q., Han, X., Song, J., Wang, J., Li, Q., Parales, R. E., et al. (2023). Characterization of a new chlorimuron-ethyl-degrading strain *Cedecea* sp. LAM2020 and biodegradation pathway revealed by multiomics analysis. *J. Hazard. Mater.* 443:130197. doi: 10.1016/j.jhazmat.2022.130197

Manzoni, C., Kia, D. A., Vandrovcova, J., Hardy, J., Wood, N. W., Lewis, P. A., et al. (2018). Genome, transcriptome and proteome: the rise of omics data and their integration in biomedical sciences. *Brief. Bioinform.* 19, 286–302. doi: 10.1093/bib/bbw114

Mohlam, F., Bakeer, W., El-Gebaly, E., and Amin, M. (2018). Molecular characterization of aniline biodegradation by some bacterial isolates having unexpressed catechol 2,3-dioxygenase gene. *J. Pure Appl. Microbiol.* 12, 2027–2039. doi: 10.22207/JPAM.12.4.39

Mutanda, I., Sun, J., Jiang, J., and Zhu, D. (2022). Bacterial membrane transporter systems for aromatic compounds: regulation, engineering, and biotechnological applications. *Biotechnol. Adv.* 59:107952. doi: 10.1016/j.biotechadv.2022.107952

Nesterov, S. V., Yaguzhinsky, L. S., Podoprigora, G. I., and Nartsissov, Y. R. (2020). Amino acids as regulators of cell metabolism. *Biochemistry* 85, 393–408. doi: 10.1134/S000629792004001X

Okuda, S., Sherman, D. J., Silhavy, T. J., Ruiz, N., and Kahne, D. (2016). Lipopolysaccharide transport and assembly at the outer membrane: the PEZ model. *Nat. Rev. Microbiol.* 14, 337–345. doi: 10.1038/nrmicro.2016.25

Park, J. M., and Jhung, S. H. (2020). Polyaniline-derived carbons: remarkable adsorbents to remove atrazine and diuron herbicides from water. *J. Hazard. Mater.* 396:122624. doi: 10.1016/j.jhazmat.2020.122624

Pasqua, M., Bonaccorsi di Patti, M. C., Fanelli, G., Utsumi, R., Eguchi, Y., Trirocco, R., et al. (2021). Host-bacterial pathogen communication: the wily role of the multidrug efflux pumps of the MFS family. *Front. Mol. Biosci.* 8:723274. doi: 10.3389/fmolb.2021.723274

Paul, C. E., Eggerichs, D., Westphal, A. H., Tischler, D., and van Berkel, W. J. H. (2021). Flavoprotein monooxygenases: versatile biocatalysts. *Biotechnol. Adv.* 51:107712. doi: 10.1016/j.biotechadv.2021.107712

Pimviriyakul, P., Wongnate, T., Tinikul, R., and Chaiyen, P. (2020). Microbial degradation of halogenated aromatics: molecular mechanisms and enzymatic reactions. *Microb. Biotechnol.* 13, 67–86. doi: 10.1111/1751-7915.13488

Qi, X., Zhu, M., Yuan, Y., Rong, X., Dang, Z., and Yin, H. (2023). Integrated toxicology, metabolomics, and transcriptomics analyses reveal the biodegradation and adaptation mechanisms to BDE-47 in *Pseudomonas plecoglossicida*. *Chem. Eng. J.* 454:140412. doi: 10.1016/j.cej.2022.140412

Rocha, M. S. D., Arnold, L. L., Dodmane, P. R., Pennington, K. L., Qiu, F., Camargo, J. L. V. D., et al. (2013). Diuron metabolites and urothelial cytotoxicity: in vivo, in vitro and molecular approaches. *Toxicology* 314, 238–246. doi: 10.1016/j.tox.2013.10.005

Shahryari, S., Zahiri, H. S., Haghbeen, K., Adrian, L., and Noghabi, K. A. (2018). High phenol degradation capacity of a newly characterized *Acinetobacter* sp. SA01: bacterial cell viability and membrane impairment in respect to the phenol toxicity. *Ecotoxicol. Environ. Saf.* 164, 455–466. doi: 10.1016/j.ecoenv.2018.08.051

Silambarasan, S., Logeswari, P., Ruiz, A., Cornejo, P., and Kannan, V. R. (2020). Influence of plant beneficial *Stenotrophomonas rhizophila* strain CASB3 on the degradation of diuron-contaminated saline soil and improvement of *Lactuca sativa* growth. *Environ. Sci. Pollut. Res.* 27, 35195–35207. doi: 10.1007/s11356-020-09722-z

Silva Moretto, J. A., Rueda Furlan, J. P., Tonelli Fernandes, A. F., Bauermeister, A., Lopes, N. P., and Stehling, E. G. (2019). Alternative biodegradation pathway of the herbicide diuron. *Int. Biodeterior. Biodegradation* 143:104716. doi: 10.1016/j.ibiod.2019.06.004

Singh, A. K., and Singla, P. (2019). Biodegradation of diuron by endophytic *Bacillus licheniformis* strain SDS12 and its application in reducing diuron toxicity for green algae. *Environ. Sci. Pollut. Res.* 26, 26972–26981. doi: 10.1007/s11356-019-05922-4

Staerck, C., Gastebois, A., Vandeputte, P., Calenda, A., Larcher, G., Gillmann, L., et al. (2017). Microbial antioxidant defense enzymes. *Microb. Pathog.* 110, 56–65. doi: 10.1016/j.micpath.2017.06.015

Sun, J., Rutherford, S. T., Silhavy, T. J., and Huang, K. C. (2022). Physical properties of the bacterial outer membrane. *Nat. Rev. Microbiol.* 20, 236–248. doi: 10.1038/s41579-021-00638-0

Tandon, S., and Pant, R. (2019). Kinetics of diuron under aerobic condition and residue analysis in sugarcane under subtropical field conditions. *Environ. Technol.* 40, 86–93. doi: 10.1080/09593330.2017.1380709

Uno, T., Kaji, S., Goto, T., Imaishi, H., Nakamura, M., Kanamaru, K., et al. (2011). Metabolism of the herbicides chlorotoluron, diuron, linuron, simazine, and atrazine by CYP1A9 and CYP1C1 from Japanese eel (*Anguilla japonica*). *Pestic. Biochem. Physiol.* 101, 93–102. doi: 10.1016/j.pestbp.2011.08.005

Vinaixa, M., Schymanski, E. L., Neumann, S., Navarro, M., Salek, R. M., and Yanes, O. (2016). Mass spectral databases for LC/MS- and GC/MS-based metabolomics: state of the field and future prospects. *Trends Analyt Chem* 78, 23–35. doi: 10.1016/j.trac.2015.09.005

Wakeel, A., Xu, M., and Gan, Y. (2020). Chromium-induced reactive oxygen species accumulation by altering the enzymatic antioxidant system and associated cytotoxic, genotoxic, ultrastructural, and photosynthetic changes in plants. *Int. J. Mol. Sci.* 21:728. doi: 10.3390/ijms21030728

Wang, Y., Li, H., Feng, G., Du, L., and Zeng, D. (2017). Biodegradation of diuron by an endophytic fungus *Neurospora intermedia* DP8-1 isolated from sugarcane and its potential for remediating diuron-contaminated soils. *PLoS One* 12:e0182556. doi: 10.1371/journal.pone.0182556

Wang, X. D., Zhang, C. Y., Yuan, Y., Hua, Y. F., Asami, T., Qin, Y., et al. (2022). Molecular responses and degradation mechanisms of the herbicide diuron in rice crops. *J. Agric. Food Chem.* 70, 14352–14366. doi: 10.1021/acs.jafc.2c05142

Wilkens, S. (2015). Structure and mechanism of ABC transporters. *F1000Prime Rep.* 7:14. doi: 10.12703/P7-14

Wu, J., Zhao, R., Zhao, L., Xu, Q., Lv, J., and Ma, F. (2023). Sorption of petroleum hydrocarbons before transmembrane transport and the structure, mechanisms and functional regulation of microbial membrane transport systems. *J. Hazard. Mater.* 441:129963. doi: 10.1016/j.jhazmat.2022.129963

Yu, H., Wang, L., Lin, Y., Liu, W., Tuyiringire, D., Jiao, Y., et al. (2020). Complete metabolic study by dibutyl phthalate degrading *Pseudomonas* sp. DNB-S1. *Ecotoxicol. Environ. Saf.* 194:110378. doi: 10.1016/j.ecoenv.2020.110378

Zhang, C., Chen, H., Xue, G., Liu, Y., Chen, S., and Jia, C. (2021). A critical review of the aniline transformation fate in azo dye wastewater treatment. *J. Clean. Prod.* 321:128971. doi: 10.1016/j.jclepro.2021.128971

Zhang, L., Hang, P., Hu, Q., Chen, X.-L., Zhou, X.-Y., Chen, K., et al. (2018). Degradation of phenylurea herbicides by a novel bacterial consortium containing synergistically catabolic species and functionally complementary hydrolases. *J. Agric. Food Chem.* 66, 12479–12489. doi: 10.1021/acs.jafc.8b03703

Zhang, L., Hu, Q., Liu, B., Li, F., and Jiang, J.-D. (2020). Characterization of a linuron-specific amidohydrolase from the newly isolated bacterium *Sphingobium* sp. strain SMB. *J. Agric. Food Chem.* 68, 4335–4345. doi: 10.1021/acs.jafc.0c00597

frontiers | Frontiers in Microbiology

TYPE Review
PUBLISHED 14 August 2024
DOI 10.3389/fmicb.2024.1424825

OPEN ACCESS

EDITED BY
Vishal Tripathi,
Graphic Era University, India

REVIEWED BY
Arun Karnwal,
Lovely Professional University, India
Amit Srivastava,
University of Jyväskylä, Finland

*CORRESPONDENCE
Wenping Zhang
✉ wpzhang@kust.edu.cn
Ye Yang
✉ yangyekm@163.com

†These authors have contributed equally to this work

RECEIVED 28 April 2024
ACCEPTED 02 August 2024
PUBLISHED 14 August 2024

CITATION
Zhou Y, Wang T, Wang L, Wang P, Chen F, Bhatt P, Chen S, Cui X, Yang Y and Zhang W (2024) Microbes as carbendazim degraders: opportunity and challenge. *Front. Microbiol.* 15:1424825. doi: 10.3389/fmicb.2024.1424825

Microbes as carbendazim degraders: opportunity and challenge

Yi Zhou[1†], Tianyue Wang[1†], Liping Wang[1], Pengfei Wang[1], Feiyu Chen[1], Pankaj Bhatt[2], Shaohua Chen[2], Xiuming Cui[1], Ye Yang[1*] and Wenping Zhang[1*]

[1]Key Laboratory of Sustainable Utilization of Panax Notoginseng Resources of Yunnan Province, Faculty of Life Science and Technology, Kunming University of Science and Technology, Kunming, Yunnan, China, [2]State Key Laboratory for Conservation and Utilization of Subtropical Agro-bioresources, Guangdong Province Key Laboratory of Microbial Signals and Disease Control, Integrative Microbiology Research Centre, South China Agricultural University, Guangzhou, China

Carbendazim (methyl benzimidazol-2-ylcarbamate, CBZ) is a systemic benzimidazole carbamate fungicide and can be used to control a wide range of fungal diseases caused by *Ascomycetes*, *Basidiomycetes* and *Deuteromycetes*. It is widely used in horticulture, forestry, agriculture, preservation and gardening due to its broad spectrum and leads to its accumulation in soil and water environmental systems, which may eventually pose a potential threat to non-target organisms through the ecological chain. Therefore, the removal of carbendazim residues from the environment is an urgent problem. Currently, a number of physical and chemical treatments are effective in degrading carbendazim. As a green and efficient strategy, microbial technology has the potential to degrade carbendazim into non-toxic and environmentally acceptable metabolites, which in turn can dissipate carbendazim from the contaminated environment. To date, a number of carbendazim-degrading microbes have been isolated and reported, including, but not limited to, *Bacillus*, *Pseudomonas*, *Rhodococcus*, *Sphingomonas*, and *Aeromonas*. Notably, the common degradation property shared by all strains was their ability to hydrolyze carbendazim to 2-aminobenzimidazole (2-AB). The complete mineralization of the degradation products is mainly dependent on the cleavage of the imidazole and benzene rings. Additionally, the currently reported genes for carbendazim degradation are MheI and CbmA, which are responsible for breaking the ester and amide bonds, respectively. This paper reviews the toxicity, microbial degradation of carbendazim, and bioremediation techniques for carbendazim-contaminated environments. This not only summarizes and enriches the theoretical basis of microbial degradation of carbendazim, but also provides practical guidance for bioremediation of carbendazim-contaminated residues in the environment.

KEYWORDS

carbendazim, toxicity, microbial degradation, biodegradation pathway, bioremediation

1 Introduction

Fungal pathogens cause significant damage to crops every year during crop production, which results in reduced crop yields, reduced nutritional value and significant economic losses. Thus, the usage of fungicides is growing in popularity as a way to prevent these losses (Singh et al., 2016). However, while fungicides are widely used, their residues also seriously jeopardize human health and ecological safety (Huang et al., 2018). Carbendazim (CBZ), also known as Methyl 1H-benzimidazol-2-ylcarbamate, is a benzimidazole, specifically 2-aminobenzimidazole with a methoxycarbonyl group substituting the primary amino group. It has the chemical formula $C_9H_9N_3O_2$, a structural formula shown in Figure 1, and a molecular weight of 191.19 (Bai et al., 2017). CBZ is a broad-spectrum systemic fungicide that is used to control various fungal diseases in agriculture, horticulture, and forestry. The antifungal mechanism of CBZ is by interfering with the synthesis and function of the fungal cell wall, thus leading to fungal cell death. Specifically, polymyxin binds to fungal cell wall synthase, blocking the enzyme activity and inhibiting the synthesis of fungal cell wall polysaccharides, which leads to the termination of fungal cell wall synthesis. This results in severe disruption of fungal cell wall synthesis and thinning of the cell wall. In addition to interfering with the synthesis of the fungal cell wall, CBZ can also interfere with the activity of enzymes related to the fungal cell wall, affecting the function of the fungal cell wall, so that the fungal cell cannot normally absorb nutrients and excrete metabolites, resulting in the inability of the fungal cell to grow and reproduce normally. CBZ can also inhibit the metabolic process of fungal cells by interfering with the enzyme activity inside the fungal cells, leading to the death of fungal cells. In addition, CBZ controls fungal diseases of *Ascomycetes* and Anamorphic fungi by preventing the growth of fungal bud tubes, attachment formation, and mycelial growth, as well as interfering with the formation of spindle bodies during mitosis of pathogenic fungi (Salunkhe et al., 2014; Zhang T. et al., 2022). It is extensively utilized globally to control a wide range of diseases in crops, fruits, and vegetables (Wang et al., 2010), including but not limited to bananas, mangoes, strawberries, oranges, pineapples, pears, cereals, sugar beets, fodder beets, rapeseed, and ornamental plants against rice blight, wheat blast, cucumber anthracnose, and canola botrytis (Liu et al., 2022). In addition, CBZ is also used in the paint, textile, and paper industries (Ebedy et al., 2022). Recently, it has also been approved for use in the leather and paint industries to improve the quality and longevity of materials (Singh et al., 2019).

Potential residue buildup in the finished product is the main issue farmers face. According to studies, CBZ has a half-life of 2 to 25 months in water under aerobic and anaerobic conditions, 3 months on turf, and 6 to 12 months in bare soil (Alvarado-Gutiérrez et al., 2017). People are growing more aware of the need of eating healthily and are also increasingly sensitive to pesticide residues in food. The discovery that CBZ is one of the main pollutants found in food has drawn a lot of attention (Shi et al., 2022). Food, contaminated water, and air are known to be the ways that CBZ enters the human body and the food chain. Nearly all of the CBZ in the dried tea leached into the brewed tea, according to Zhou et al. (2018) evaluation of the residue transfer and risk assessment of CBZ in green tea. According to Li et al. (2017), who evaluated the transfer of CBZ residues from rapeseed flowers to beekeeping products, the CBZ residues in pollen on day eighteen were 1.10 ± 0.03 mg/kg, in honey on day twenty-four were 0.032 ± 0.001 mg/kg, and in royal jelly on day twenty-two were 0.077 ± 0.002 mg/kg. A concentration of 0.01 μg/L of CBZ is detected in the surface water at the Kibuye sampling point of Lake Kivu (Houbraken et al., 2017). CBZ leftovers were detected in over 80% of African palm crop samples, samples taken close to cities, and samples taken in locations where maize crops predominated. The concentration of CBZ residues in urban areas was found to be the highest at 31 ng/L (Cabrera et al., 2023). According to Rico et al. (2022), CBZ was found in 80% of water samples taken from urban streams in the Brazilian Amazon, with concentrations as high as 214 ng/L. Because of the buildup of residues from the continuous use of CBZ, human health is today seriously threatened (Salunkhe et al., 2014). Numerous studies have shown that CBZ not only affects development, but also damages the kidneys, interferes with the body's endocrine system, causes hematologic toxicity, forms aberrations, is toxic to reproductive tissues, leads to abnormalities in liver function, causes changes in the kinetics of microtubule assembly and disassembly, alters the stability of the meiotic spindle microtubules and the integrity of the spindle poles, and causes neuroinflammation (Prashantkumar et al., 2012; Rama et al., 2014; Alvarado-Gutiérrez et al., 2017; Long et al., 2021; Shi et al., 2022).

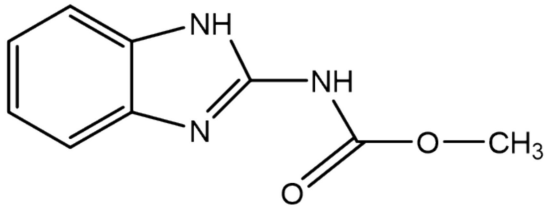

FIGURE 1
Structural formula of carbendazim.

The following two factors can be our starting points for resolving the conflict between environmental pollution and high and consistent agricultural product yields. Pesticides with low toxicity, high efficiency, and low residue should be searched out and produced; on the other hand, essential emphasis should be paid to techniques of degradation pesticide residues (Huang et al., 2018). While CBZ can naturally deteriorate, the degrading effects of sunlight are not readily apparent (Bai et al., 2017). Hence, there is a pressing need to develop more efficient degrading techniques. Several techniques, including abiotic degradation and biodegradation, have been developed to efficiently degradation CBZ. It has been demonstrated that a few abiotic degradation processes, including photodegradation (Yogesh Kumar et al., 2022), molecular hydrogen degradation (Zhang T. et al., 2022), acoustic ozone (O_3/US) degradation (Siddique et al., 2021), and gamma radiation (Ciarrocchi et al., 2021), are efficient in degrading CBZ. However, in addition to being harmful to the environment, the degradation of CBZ through gamma radiation, burning, electro-oxidation, microwave induction, or chemical oxidation also necessitates a large and costly infrastructure (Zhang et al., 2020). Therefore, microbial degradation—a technology that is low-cost and environmentally friendly compared to abiotic degradation methods—is attracting increasing attention.

Since it started in the 1940s, microbial degradation of bactericides has proven an efficient way to degrading complex organic pollutants into smaller, simpler molecules. For example, the majority of the

pollutants are either entirely broken down into CO_2 and H_2O or degrading into less hazardous forms (Mishra et al., 2021b). Furthermore, microbial decomposition can withstand harsh environmental conditions and is inexpensive, making it a very viable and efficient remediation method (Mishra et al., 2021a). Numerous microbes have been shown to be efficient in degrading CBZ to date, including: *Bacillus subtilis* (Salunkhe et al., 2014), *Pseudomonas* (Alvarado-Gutiérrez et al., 2017), *Stenotrophomonas* sp. (Alvarado-Gutiérrez et al., 2017), *Rhodococcus* (Long et al., 2021), *Ralstonia* (Zhang et al., 2005), *Sphingomonas paucimobilis*, *Aeromonas hydrophila*, *Burkholderia cepacian* (Pandey et al., 2010), *Microbacterium* sp. (Zhang Y. et al., 2017), *Brevibacillus* sp. (Kanjilal et al., 2018), *Streptomyces* sp., *Rhizobium leguminosarum* (Kanjilal et al., 2018), *Klebsiella*, *Flavobacterium*, *Stenotrophomonas* (Alvarado-Gutiérrez et al., 2020), *Ralstonia* sp. (Silambarasan and Abraham, 2020), *Chryseobacterium* sp., *Aeromonas caviae* (Silambarasan and Abraham, 2020), *Enterobacter* (Cycoń et al., 2011), *Alternaria alternata and Trichoderma* sp. (Chuang et al., 2021), *Nocardioides* (Pandey et al., 2010). It was discovered that *Rhodococcus* sp. had the highest number of bacterial strains capable of degrading CBZ, and that the number of bacterial strains degrading CBZ was significantly larger than that of fungal and actinomycete strains. Such as CBZ can be effectively degraded by *Rhodococcus jialingiae* djl-6-2, *Rhodococcus qingshengii* djl-6, *Rhodococcus erythropolis* djl-11, *Rhodococcus* sp. CX-1, *Rhodococcus erythropolis* JAS13, *Rhodococcus* sp. D-1, *Rhodococcus erythropolis* CB11.

As CBZ residues receive increased attention, there has been a deeper examination of CBZ's degradation process and mechanism (Huang et al., 2018). The primary degradation process involves the hydrolysis of CBZ to 2-aminobenzimidazole (2-AB), the predominant degradation product. It is subsequently changed into 2-hydroxybenzimidazole (2-HB), which undergoes ring cleavage to progressively degrade into CO_2 and H_2O (Bai et al., 2017; Long et al., 2021). According to the mechanisms of degradation that have been documented, CBZ is broken down by hydroxylation of C-N bonds in the parent molecule, which results in the formation of metabolites (Alvarado-Gutiérrez et al., 2017). Moreover, it was discovered that one of the major transformations in the degradation process of benzimidazole was aromatic hydroxylation (Shi et al., 2022). With the in-depth exploration of the degradation mechanism, there are more and more reports on CBZ degradation by functional enzymes encoded by genes (Zhang et al., 2020). including MheI (Alpha/beta fold hydrolase), CbmA (Amidase), and CYPs1A2 (Cytochrome P450 Enzyme 1A2) are the primary enzymes in charge of CBZ degradation (Shi et al., 2022; Zhang M. et al., 2022). Furthermore, degradation genes found in plasmids and chromosomes may control CBZ degradation. The hydroxylase and exo-diol dioxygenase-encoding *hdx* and *edoA* genes, as well as the aggregation of the *edoB3*, *edoB1, edoB2,* and *edoC* genes, and the aggregation of the *mno, benA,* and *catA* genes, are all implicated in the degradation of the CBZ, according to later investigations (Long et al., 2021). Much of the current discussion of carbendazim focuses on its toxicity, ecological risks, and potential risks to human health and physicochemical degradation pathways. Thus, the purpose of this review is to clarify the risks associated with CBZ residues. To describe the methods and metabolic pathways of CBZ degradation, in particular the microbial degradation pathway and to outline the metabolic pathways of the genes and enzymes that degrade CBZ and are essential to the biodegradation process. Furthermore, a number of bioremediation techniques for cleaning up soil polluted with CBZs were discussed. It is dedicated to removing CBZ residues even further and offering the theoretical foundation required for the advancement and use of the technique for utilizing microorganisms to remediate CBZ-contaminated soil.

2 Toxicity of carbendazim

As frequently as every 10 to 15 d, fungicides are used in agricultural production to control crop diseases. The majority of fungicides used find their way into the soil environment, where they leave behind residues that contaminate the environment (Liang et al., 2023). According to a growing body of research, fungicide residues influence soil microbial activity, microbial community structure, and function in addition to causing the emergence of microbial community resistance and the transmission of related resistance genes (Fang et al., 2016). Because of its strong toxic effects and high degree of non-degradability, CBZ has been categorized by the World Health Organization as dangerous (Ling et al., 2016). Australia, the European Union (except Portugal), and the United States have outlawed the use of CBZ; but, the United Kingdom, Portugal, and some developing countries (China, Brazil, and India) continue to permit the production and use of CBZ in various formulations (Chuang et al., 2021).

CBZ has a lengthy half-life of 6 to 12 months in bare soils because of its slow breakdown. In water, however, it dissipates rather rapidly as indicated by short half-life of about 2–25 days (Singh et al., 2016). In addition to the possible persistence of CBZ residues on leaves. Furthermore, plants have the ability to absorb CBZ through their roots, seeds, or leaves, and subsequently distribute it throughout their entire body (Silambarasan and Abraham, 2020). More dangerously, CBZ has the ability to transferred throughout the food chain, leading to bioaccumulation and biomagnification (Salunkhe et al., 2014) (Figure 2). Even CBZ has been discovered in house dust and drains (Shi et al., 2022). It has been documented that CBZ has harmful effects on amphibians, macroinvertebrates, zooplankton, and primary producers that live in freshwater, as well as people (Ling et al., 2016). Hepatocyte dysfunction, for instance, can result from CBZ-induced hepatic necrosis, hepatocyte edema, and hepatocyte degeneration (Shi et al., 2022). Significant histopathological alterations in the kidney may also result from it. These include elevated levels of blood urea nitrogen and plasma creatinine, which can cause renal dysfunction; a decrease in the kidney's ability to eliminate excess metabolic waste products like urea and creatinine, which can cause renal vascular congestion, peritubular and periglomerular inflammatory cell infiltration, renal necrosis, and vacuolization (Sharma et al., 2022). Research has also indicated that CBZ can lead to hematological toxicity, alter hemopoiesis, have endocrine-disrupting effects, lower total platelet counts, and diminish red blood cell counts by 3–19% and white blood cell counts by 18–35% (Singh et al., 2016). Additionally, when exposed to CBZ at levels greater than 0.79 mg/L, reproductive tissues may become toxic and developmental consequences may occur (Ebedy et al., 2022). Specifically, CBZ can lead to oxidative stress on the testes and inert cells, cause testicular damage and infertility through the shedding of the germinal epithelium, affect the levels of testosterone, luteinizing hormone, follicle-stimulating hormone, inhibit testicular steroidogenesis, increase estrogen, and increase levels of androgen receptor mRNA. CBZ has also been linked to the hypothalamus-pituitary-gonadal axis being affected, the hypothalamic–pituitary-gonadal axis is impacted by CBZ, which can lead to severe estrogen-mediated lesions, changes in testicular weight,

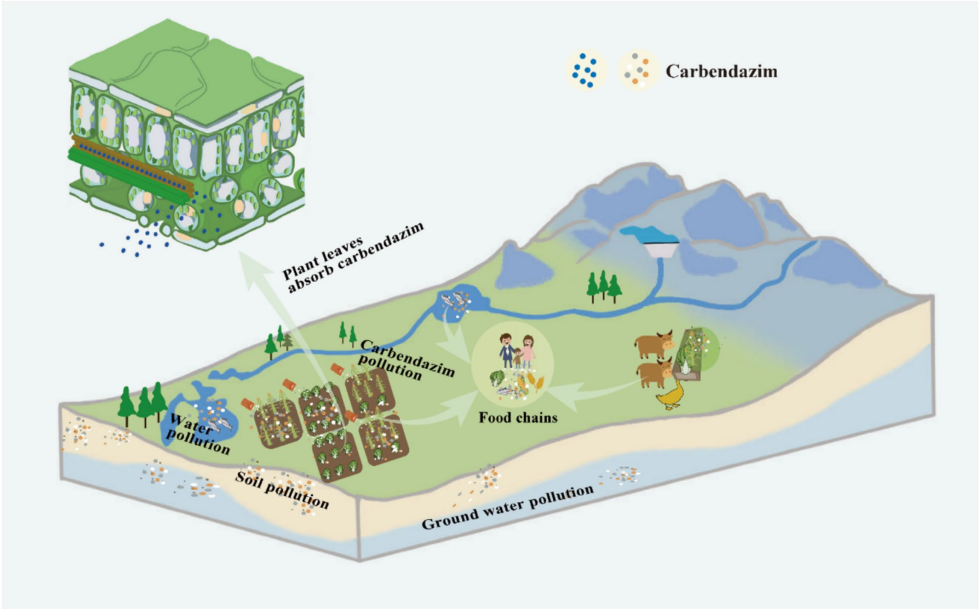

FIGURE 2
Mobility of carbendazim in the environment.

obstruction of the output ducts, shedding of germ cells, decreased spermatocyte counts and spermatozoa viability, morphologic abnormalities, failure of spermatogenesis by apoptosis of the germ cells, and infertility. Worrisomely, it has been shown that CBZ is hazardous to the fetus and can induce fetal malformation (Sharma et al., 2022).

Moreover, CBZ disrupts spindle protein meiosis, resulting in chromosomal abnormalities and aneuploidy, both of which increase the risk of cancer (Ling et al., 2016; Bai et al., 2017; Long et al., 2021). CBZ disrupts microtubule assembly and impairs chromosome segregation during cell division in fungal and mammalian cells by inhibiting both the binding of guanosine triphosphate (GTP) to microtubule proteins and microtubule polymerization through interaction with β-microtubule proteins (Rama et al., 2014), it also modifies the stability of meiotic spindle microtubules and the integrity of the spindle pole by interfering with the dynamics of microtubule construction and disassembly (Prashantkumar et al., 2012). Additionally, by activating the NF-kB signaling pathway linked to IL-1 and TNF-α cytokines, CBZ caused neuroinflammation. This resulted in time-and dose-dependent oxidative stress injury, neurobehavioral changes, and neuropathological changes, including neuronal death in various brain regions (Ebedy et al., 2022). Crucially, scientists tracked how phytotoxicity changed as CBZ biodegraded and discovered that toxicity progressively dropped as CBZ degradation (Bai et al., 2017). Thus, there has been a lot of focus in public health on the breakdown of CBZ into less dangerous molecules or its direct breakdown into CO_2 and H_2O.

3 Abiotic degradation of carbendazim

3.1 Overview of abiotic degradation strategies

As the general population's worry over CBZ residues grows, more scientists are looking into the best ways to degrade CBZ. Numerous abiotic techniques have been reported to degrade CBZ, according to the literature. One of the numerous methods that contributes to CBZ degradation, for instance, is photolytic degradation (Yogesh Kumar et al., 2022). Furthermore, the inclusion of catalysts in the presence of light can efficiently degrade CBZ; Photocatalysts are widely used for the photodegradation of a wide range of pollutants, and through their use many organic, inorganic and microbiological pollutants can be converted into less harmful metabolites. One of the most often used and effective photocatalysts for the photodegradation of CBZ is titanium dioxide. Additionally, was demonstrated that when exposed to sunshine, Fe doped with TiO_2 exhibits higher photoactivities than undoped TiO_2. The combination of Iron (Fe) and sunlight enhances the photocatalytic activity of TiO_2. Fe-doped TiO_2 broke down 98% of the CBZ in direct sunlight (Kaur et al., 2016). Mungsuk et al. (2023) used particulate and sol–gel coated filters to degrade CBZ using TiO_2 photocatalysis under sunlight, it achieved 89–91% degradation of CBZ with an optimum kinetic rate constant of 0.048 min^{-1}. The type II $Bi_2S_3/BiFeO_3$ heterojunction system is also a photocatalyst that can effectively degrade CBZ, $BiFeO_3$ nanoplates and Bi_2S_3 nanorods are in intimate microscopic contact within the $Bi_2S_3/BiFeO_3$ materials. The $Bi_2S_3/BiFeO_3$ materials demonstrated superior absorption of visible light, heightened separation of charge carriers, and effective photocatalytic activity, attaining 96% degradation in just 2 hours of reaction time (Bhoi et al., 2018). Another photocatalyst, Two-dimensional (2D) gadolinium tungstate nanosheets (GW Nfs) were synthesized by Periyasamy et al. (2019). using co-precipitation. These unique structures are particularly effective because they catalyze the degradation of CBZ, a post-harvest fungicide, and other reactions. GW Nfs effectively degrades 98% of CBZ when exposed to visible light. Moreover, using electroless template synthesis, Altynbaeva et al. (2022) created a new Cu_2O/ZnO@PET hybrid composite. The Cu_2O/ZnO@PET composite showed increased photocatalytic activity with 98% CBZ breakdown when exposed to UV–visible light. For the first time, Wang H. et al. (2023) used Bismuth Oxyhalide (BiOCl, BiOBr, and BiOI) photocatalysts for the

mineralization and degradation of CBZ. After 3 hours of exposure to a metal halide lamp at a pH of 7, the degradation efficiency reached 99%, and more than 90% of the CBZ molecules could be mineralized.

Based on physiological and genetic evidence, molecular hydrogen is thought to be a key player in controlling the degradation of CBZ in plant leaves by encouraging the synthesis of glutathione (GSH). The reasoning behind this is that two enzymes involved in the metabolism of reduced GSH are glutathione reductase (GR) and glutathione S-transferase (GST). The reduction of oxidized glutathione (GSSG) to GSH is carried out by GR, whereas the generation of GSH is stimulated by molecular hydrogen through the enhancement of γ-glutamylcysteine synthetase (γ-ECS) activity. CBZ residues have the potential to bind to GSH and create less reactive and toxic conjugates that can be transported and degraded later on, thanks to increased GST activity (Zhang T. et al., 2022). In addition, it was demonstrated that gamma radiation was useful in lowering CBZ residues in strawberries, the degradation rate according to the gamma radiation dose and the fungicide's chemical composition (Ciarrocchi et al., 2021). Dielectric barrier discharge (DBD) plasma can cause CBZ in sealed containers to degrade either directly or indirectly. It can do this by producing a range of physical (UV and shockwave) and chemical (-OH, -O, -H radicals, O_3, and H_2O_2). CBZ (0.5 ug/mL) was degraded by 89.54% under ideal circumstances (Wang J. et al., 2023). Also, by encapsulating CBZ in superabsorbent hydrogels (SHs), CBZ's dissipation rate increased dramatically by 34.2–54.1%, reducing its persistence in the soil matrix (Yang et al., 2018). And in order to treat various forms of CBZ-polluted wastewater, aluminum carbide nanosheets (AlC_3NS) were employed as an effective adsorbent. It was shown that the adsorption energy of CBZ through-C=O groups interacting with Al atoms of AlC_3NS was around 30.14 kcal/mol (Kadhim et al., 2022). Besides, the fungicide CBZ is degraded by the combined application of ozone and ultrasound (O3/US), which reduces the average CBZ residue in fruits and vegetables by 72% (Siddique et al., 2021). Yogesh Kumar et al. (2022) synthesized gadolinium sesquisulfide anchored with nitrogen-doped reduced graphene oxide (Gd_2S_3/NRGO) by a simple microwave-assisted method. It was found that Gd_2S_3/NRGO could effectively degrade CBZ, and 94% of CBZ was degraded within 90 min in the presence of Gd_2S_3/NRGO.

In summary, the degradation of CBZ by these abiotic degradation methods mainly focuses on the application of photocatalysts, and a few of them use some physical or chemical means to degrade CBZ. The non-biological degradation method is mainly characterised by high degradation efficiency, but there are some disadvantages of this method, such as the slow degradation rate and the long period required for natural photolytic degradation; and the degradation of CBZ by gamma radiation is not environmentally friendly; The study of CBZ degradation by particulate and sol–gel coated filters, Bi_2S_3/$BiFeO_3$ heterojunction materials and novel composite materials requires a large amount of costly infrastructure, which is expensive; Photocatalyst degradation of CBZ is inexpensive, green and environmentally friendly, but the production process of photocatalysts is cumbersome and takes a long time; therefore, the development of microbial degradation of CBZ, which is cheaper, greener and easier to implement, is gradually becoming a hot research topic.

3.2 Abiotic degradation pathways

The spontaneous degradation of CBZ in soil occurs via three different metabolic routes (Figure 3). The first route involves producing TP159 by methylating, deoxymethylation, and dehydroxylating CBZ. The second pathway of degradation involves the production of TP 149 through the demethylation, decarboxylation, and hydroxylation of CBZ. Alternatively, TP 159 can be formed through deoxymethylation and hydroxylation. Deoxymethylation and deamidation resulted in the production of TP 108 (1,2-diaminobenzene), and comparatively high quantities of TP 149 and TP 159 were found, indicating that these intermediates are the main metabolites. The third degradation process produces TP 213 by hydroxylating and demethylating CBZ. After the benzene ring is split, TP 165, TP 143, TP 133, and TP 129 are formed as

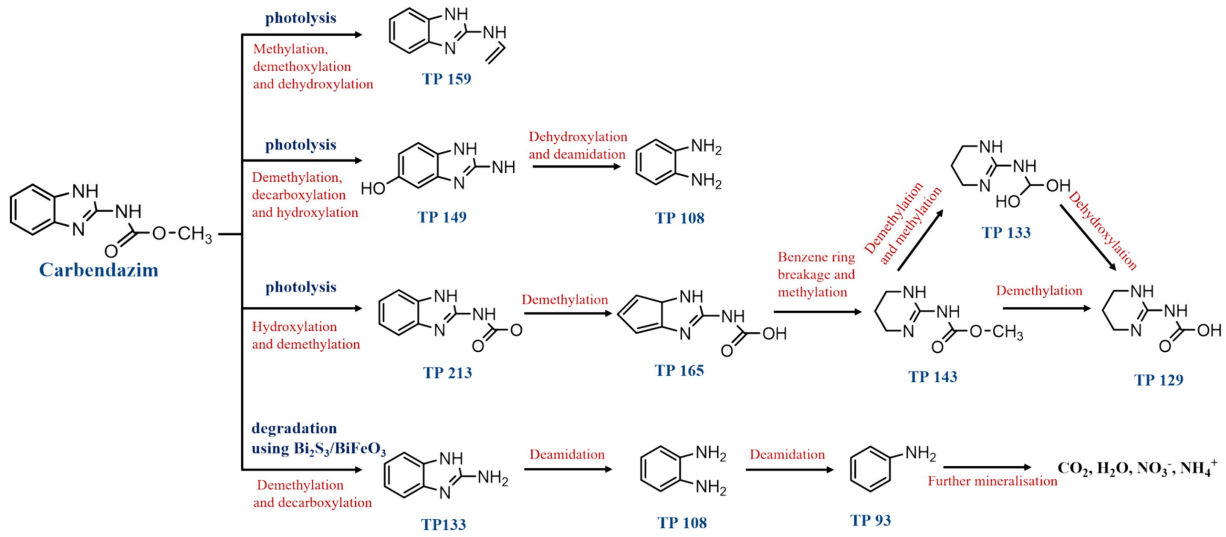

FIGURE 3
Degradation pathways of carbendazim by non-biodegradable.

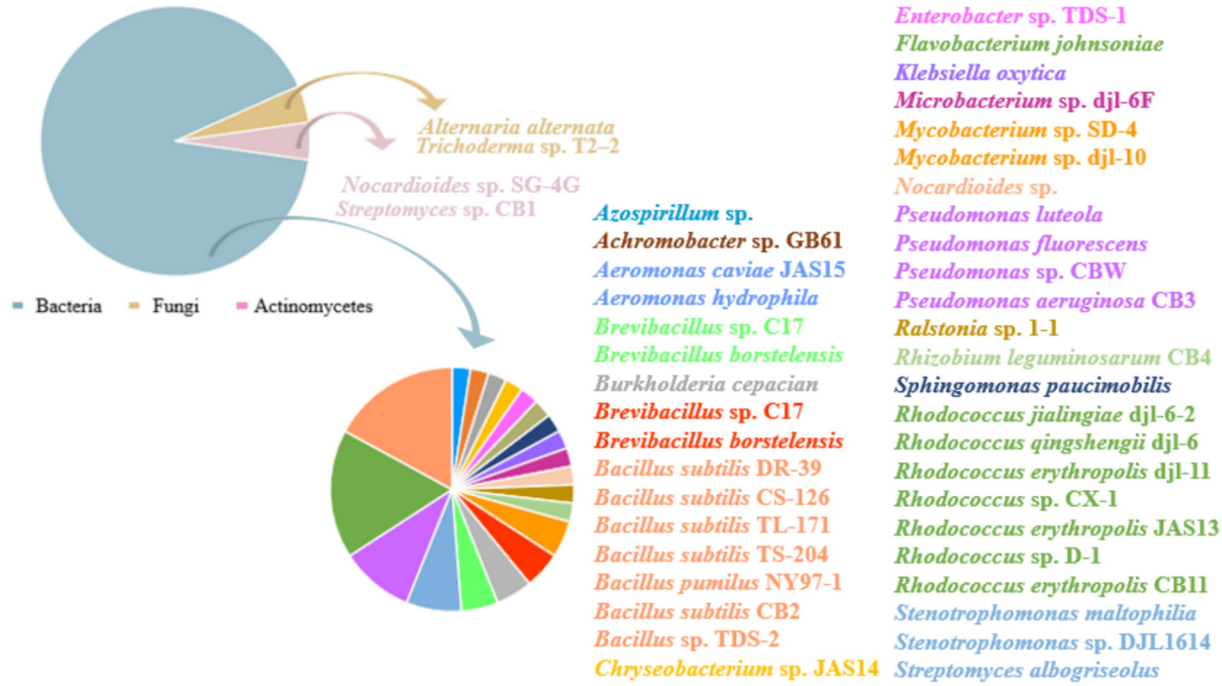

FIGURE 4
Carbendazim degrading strains. Different color block regions in the pie chart indicate the proportion of this species to found strains.

a consequence of a number of processes, including deoxymethylation, demethylation, and methylation (Huang et al., 2020). Moreover, employing $Bi_2S_3/BiFeO_3$ heterojunction materials as photocatalysts, a fourth degradation route has been discovered for the effective photocatalytic breakdown of CBZ fungicide under visible light irradiation. When CBZ broke down on the surface of the $Bi_2S_3/BiFeO_3$ catalysts, aliphatic organic intermediates were released and the intermediates TP = 133 and TP = 108 formed. Following the release of NH_3, the intermediate TP = 108 produces aniline (intermediate TP = 93). TP = 93 takes over as the primary intermediate in the photocatalytic mineralization of CBZ after 60 min. CO_2, H_2O, NH_4^+, and $NO_3^-$are produced when the generated intermediate is further mineralized on the catalyst surface (Bhoi et al., 2018). Numerous studies have been conducted on the abiotic degradation of CBZ, Nevertheless, the majority of them solely concentrate on creating novel degrading techniques and raising the effectiveness of degradation. Few comprehensive studies have been conducted on the mechanism and degradation pathway of CBZ; therefore, it is important to continue researching the degradation pathway in order to degrade the CBZ more quickly and effectively. The investigation of the CBZ degradation process needs more attention in the future.

4 Microbial degradation of carbendazim

4.1 Potential microorganisms for degradation of carbendazim

Multiple methods have been developed to degrade CBZ in response to growing environmental awareness. Nevertheless, it was discovered that photolysis was weak for CBZ degradation (Bai et al., 2017), and that certain abiotic degradation techniques typically call for the use of specific catalysts or high doses of radiation and ozone, which could present new hazards to food safety (Wang J. et al., 2023). Consequently, the development of an environmentally acceptable and efficient approach for CBZ degradation becomes very vital. More and more efforts are being made to use microbial degradation for the degradation of CBZ because, as scientific research technology advances, researchers have discovered that microbial degradation is crucial to the biodegradation of pesticides, which can transform pesticides into forms that are safe for the environment and non-toxic (Ling et al., 2016).

Numerous microbial strains have been discovered that degrade CBZ at this time. In general, bacteria are more important in CBZ biodegradation than fungi and actinomycetes are in the dissipation of CBZ in soil (Figure 4) (Yarden et al., 1990). A multitude of *Rhodococcus* sp. strains were discovered to be efficient in degrading CBZ, as indicated in Table 1. Among these strains were *Rhodococcus erythropolis* JAS13 (Silambarasan and Abraham, 2020), *Rhodococcus* CX-1 (Long et al., 2021), *Rhodococcus jialingensis* djl-6-2 (Wang et al., 2010), *Rhodococcus erythropolis* djl-11 (Zhang et al., 2013), *Rhodococcus* sp. D-1 (Bai et al., 2017), *Rhodococcus qingshengii* djl-6 (Jing-Liang et al., 2006; Chuang et al., 2021), The ability of these strains to degrade CBZ is demonstrated in Table 1. Additionally, it has been discovered that certain bacteria from different genera may effectively degrade CBZ. For example, *Achromobacter* sp. GB61 can degrade CBZ quite effectively. Following treatment with *Achromobacter* sp. GB61, the half-life of CBZ was 8.45 d, as opposed to 63 d in the absence of this strain. Furthermore, the breakdown intermediates' metabolites were found to be environmentally acceptable and non-toxic (Ling et al., 2016). The degradation of CBZ

TABLE 1 Carbendazim-degrading strains and degradation efficiency.

Strain	Environment	Time	Concentration	Degradation
Bacillus pumilus NY97-1	MSM	24 h	300 mg/L	Degradation rate of 90.07%
Brevibacillus panacihumi C17	MSM	36 h	100 mg/L	Degradation rate of 87.25%
Bacillus velezensis HY-3479	M9 minimal medium	48 h	250 mg/L	Degradation rate of 76.99%
Rhodococcus jialingensis djl-6-2	MSM	60 h	100 mg/L	Degradation rate of 94%
Rhodococcus sp. D-1	MSM	3 d	200 mg/L	Degradation rate of 98.2%
Streptomyces CB1	MSM	14 d	1,000 mg/L	Degradation rate of 91.65%
Pseudomonas aeruginosa CB3	MSM	14 d	1,000 mg/L	Degradation rate of 87.35%
Bacillus subtilis CB2	MSM	14 d	1,000 mg/L	Degradation rate of 81.85%
Rhodococcus erythropolis JAS13	MSM	-	150 mg/L	Degradation rate of 100%
Rhizobium leguminosum CB4	MSM	14 d	1,000 mg/L	Degradation rate of 76.54%
Brevibacillus borstelensis and *Streptomyces albogriseolus*	MSM	12 h	30 ug/mL	Degradation rate of 97%
Mycobacterium sp. SD-4	MSM	72 h	50 mg/L	Average degradation rate of 0.63 mg/L/h
Rhodococcus erythropolis djl-11	MSM	–	1,000 mg/L	Average degradation rate of 333.33 mg/L/d
Rhodococcus sp. CX-1	MSM	5 h	50 mg/L	Average degradation rate of 9.90 mg/L/h
Rhodococcus qingshengii djl-6	M9 minimal medium	36 h	100 mg/L	Average degradation rate of 55.56 mg/L/d
Pseudomonas sp. CBW	Mineral salts medium	3 d	10.0 mg/L	Degradation rate of 99.1%
Ralstonia sp. 1–1	Addition of yeast extract in liquid MSM medium	24 d	500 mg/L	Degradation rate of 95.96%
Bacillus subtilis DR-39, CS-126, TL-171, TS-204	Thompson Seedless	25 d	1.0 g/L	Degradation rate of 95.45%
Chryseobacterium sp. JAS14	Soil	9 d	200 mg/L	Degradation rate constant of 27.30 d^{-1}
Aeromonas caviae JAS15	Soil	9 d	200 mg/L	Degradation rate constant of 23.87 d^{-1}
Trichoderma sp. T2-2	Sterilized soil	6 d	50 mg/L	Degradation rate of 100%

by four strains of *Bacillus subtilis* (DR-39, CS-126, TL-171 and TS-204) was examined by Salunkhe et al. (2014). Thompson Seedless was sprayed with 1.0 g/L of CBZ, and after 25 d, the residual on control grapes was 0.44 mg/kg; however, the residue on grapes treated with the four *Bacillus subtilis* strains was just 0.02 mg/kg. In treated grapes, degradation kinetics revealed a reduced half-life, ranging from 3.1 to 5.2 d, as opposed to 8.8 d in the control group. Moreover, when concentrations increased (10 to 300 mg/L), *Bacillus pumilus* NY97-1's CBZ degradation ranged from 42.44 to 90.07% (Zhang et al., 2009). In M9 Minimal Medium supplemented with 250 mg/L CBZ, Song and Hwang (2023) demonstrated that the *Bacillus velezensis* HY-3479 strain could digest CBZ. Its optimal degradation efficiency was achieved 48 h after the addition of 12.5 mM NH_4NO_3.

Besides, CBZ was demonstrated that *Brevibacillus panacihumi* C17 also efficiently degraded CBZ by 87.25% at a concentration of 100 mg/L over an incubation period of 36 h, pH 7.0, and 180 rpm/min (Kanjilal et al., 2018). After 3 d of incubation at concentrations of 1.0 and 10.0 mg/L, respectively, *Pseudomonas* sp. CBW decomposed approximately 87.1 and 99.1% of CBZ in MSM (Fang et al., 2010). *Streptomyces* CB1, *Pseudomonas aeruginosa* CB3, *Bacillus subtilis* CB2, and *Rhizobium leguminosum* CB4 decompose 91.65, 87.35, 81.85, and 76.54% of CBZ, respectively, throughout the degradation process (Singh et al., 2019). And the degradation rate constants were 27.30 d^{-1} and 23.87 d^{-1}, respectively, after *Chryseobacterium* sp. JAS14 and *Aeromonas caviae* JAS1 were introduced into soil without additional nutrients (Silambarasan and Abraham, 2020). *Ralstonia* sp. 1-1's degradation rate constants in MSM supplemented with yeast extract (150 mg/L) and CBZ (500 mg/L) revealed a degradation rate of 19.16 and 95.96%, respectively, within 24 d (Zhang et al., 2005). Using CBZ as the only source of carbon and nitrogen for development, *Mycobacterium* sp. SD-4 was able to degrade 50 mg/L CBZ at an average degradation rate of 0.63 mg/L/h (Zhang Y. et al., 2017). In addition, *Stenotrophomonas* sp. DJL1614 also is a kind of bacteria that breaks down CBZ pesticide residues, according to a Chinese patent (Alvarado-Gutiérrez et al., 2017). And LC–MS analysis showed that the combined degradation of CBZ by *Streptomyces albogriseolus* and *Brevibacillus borstelensis* decreased the concentration of CBZ from 30 ug/mL to 0.86 ug/mL in 12 h with a degradation rate of 97%, and to 0.60 ug/mL in 20 h with a degradation rate of 98% (Arya and Sharma, 2015). CBZ is also broken down by *Klebsiella oxytica*, *Flavobacterium johnsoniae*, and *Stenotrophomonas maltophilia*. All three bacteria have been shown to carry genes encoding the mheI, which is implicated in CBZ degradation (Alvarado-Gutiérrez et al., 2020). With a high conversion rate and no need for cofactors, the MheI-6F protein purified from the CBZ-degrading strain *Microbacterium* sp. djl-6F catalyzed the direct hydrolysis of CBZ to 2-aminobenzimidazole (2-AB) (Lei et al., 2017). *Bacillus* sp. TDS-2 and *Enterobacter* sp. TDS-1 strains may also be able to convert CBZ to 2-AB, which could be used for bioremediation of CBZ-contaminated soil (Cycoń et al.,

10.3389/fmicb.2024.1424825

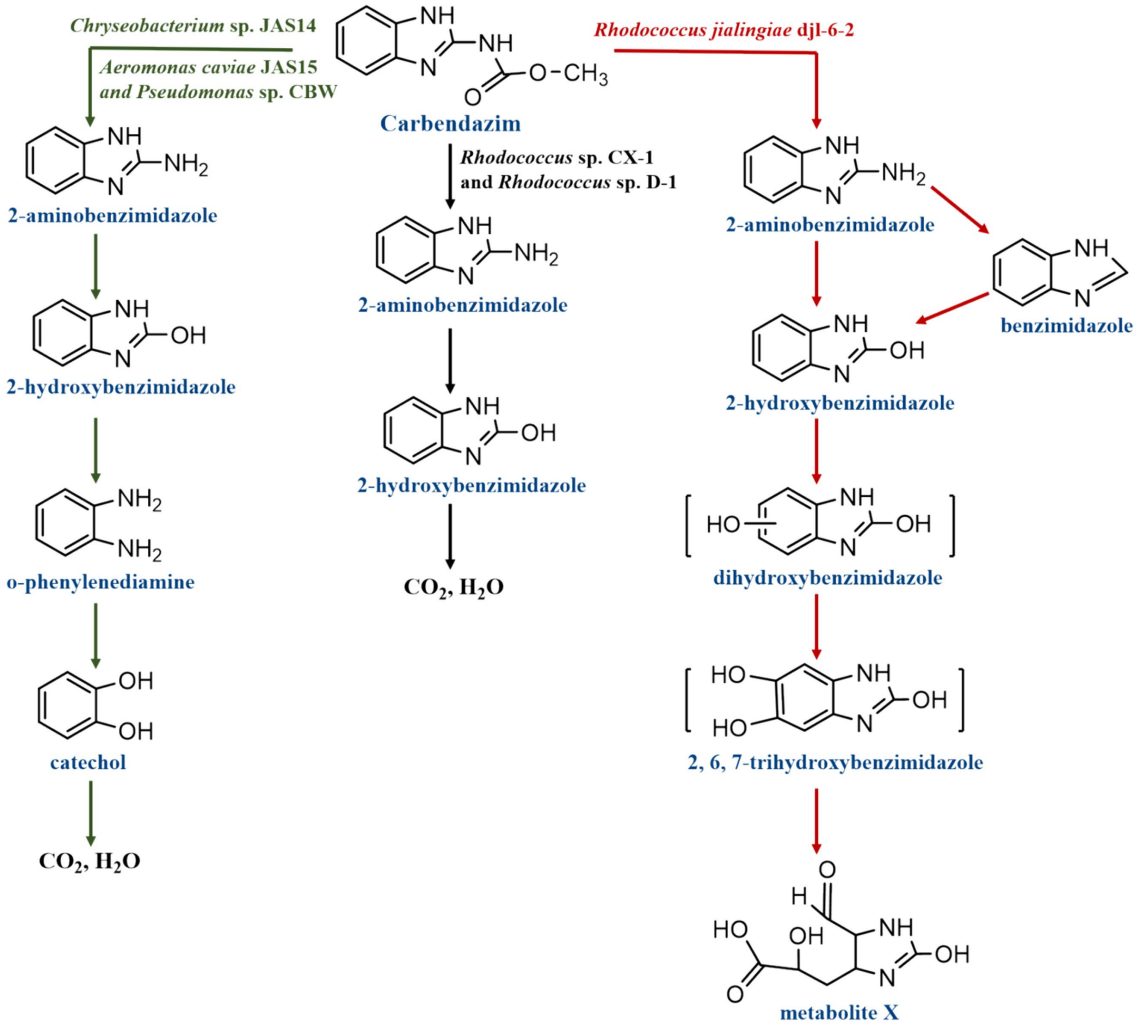

FIGURE 5
Degradation pathways of carbendazim by microbial strains.

2011). And six d after being inoculated with *Trichoderma* sp. T2-2, CBZ in sterile soil was fully destroyed (Liansheng and Fei, 2009).

To sum up, there are a lot of microbial species that can break down CBZ. However, different strains have varying capacities to break down CBZ. This is because different strains have different functional enzymes, which causes differences in the strains' ability to break down CBZ. On the other hand, different culture conditions can affect the growth of microorganisms, which can affect the efficiency of the strains' CBZ degradation. The ideal growth conditions for various microorganisms vary depending on factors like temperature, pH, concentration of CBZ, extra sources of carbon and nitrogen, duration of incubation, etc. The ideal growth temperature for some bacteria is 37°C, whereas for others it is 30°C. Elevations or decreases in temperature will impact the development of bacterial strains. In addition, some microorganisms can use the nutrients in the soil for their growth, but some microorganisms cannot grow well in the soil environment, so in the work of soil microbial remediation, it is not only necessary to screen strains with the ability of efficiently degrading CBZ, but also need this strain to have the ability to grow well in the soil environment. For example, it was found that strains *Achromobacter* sp. GB61, *Rhodococcus qingshengii* djl-6 and *Actinomucor elegans* LBM 239 had good bioremediation effects on CBZ-contaminated soils under different conditions, which can be used for bioremediation of CBZ-contaminated environment.

4.2 Pathways of microbial degradation of carbendazim

While numerous strains have been employed for CBZ degradation, only a small number of strains have been suggested for their particular degradation pathways. Only *Rhodococcus* sp. CX-1, *Rhodococcus* sp. D-1, *Chryseobacterium* sp. JAS14, *Aeromonas caviae* JAS15, *Pseudomonas* sp. CBW and *Rhodococcus jialingiae* djl-6-2 now describe their metabolic pathway for degrading CBZ, as illustrated in Figure 5. After analyzing the molecular weight and structural formula of CBZ intermediate metabolites using HPLC-MS/MS, the following was inferred about the biodegradation process of CBZ by the strains of *Rhodococcus* sp. D-1 and CX-1: First, 2-AB was produced by hydrolyzing CBZ. Next, 2-hydroxybenzimidazole (2-HB) was

produced, and finally, 2-HB was progressively broken down into CO_2 and H_2O (Bai et al., 2017; Long et al., 2021). In addition, *Pseudomonas* sp. CBW, *Chryseobacterium* sp. JAS14 and *Aeromonas caviae* JAS15 biodegraded CBZ by the following pathway: After converting CBZ to 2-AB, 2-HB was quickly converted. 2-HB was then further transformed by ring cleavage to o-phenylenediamine and catechol, and ultimately even to CO_2 and H_2O (Fang et al., 2010; Silambarasan and Abraham, 2020). The first step in *Rhodococcus jialingiae* djl-6-2's degradation of CBZ is the hydrolysis of methyl carbonate's side chain, which yields 2-AB or benzimidazole (BZ). It was discovered that NH_4NO_3 inhibits the conversion of 2-AB during this process. After then, both are transformed to 2-HB. Ring cleavage of 2-HB further opens the benzene ring to catechol (BZ) (Wang et al., 2010).

From the degradation pathway of CBZ by the six strains of bacteria, it was found that the mineralization of CBZ occurs through the hydroxylation of C-N bonds in the parent molecule to form metabolites. The CBZ degradation pathways of three strains, *Pseudomonas* sp. CBW, *Chryseobacterium* sp. JAS14 and *Aeromonas caviae* JAS15 were more clearly defined compared to the CBZ degradation pathways of *Rhodococcus* sp. D-1 and CX-1: CBZ undergoes demethylation and decarboxylation to form 2-AB, then hydroxylation to form 2-HB, after which it undergoes dehydroxylation to form o-phenylenediamine, which undergoes hydroxylation to form catechol, which is finally mineralized to CO_2 and H_2O. In contrast, *Rhodococcus* sp. D-1 and CX-1 were insufficient for the intermediate steps of the CBZ degradation pathway, and only CBZ was subjected to demethylation and decarboxylation to generate 2-AB, then hydroxylation to generate 2-HB, and finally 2-HB was mineralized to CO_2 and H_2O. In addition, a new degradation process was identified in the degradation pathway of CBZ by *Rhodococcus jialingiae* djl-6-2, whereby 2-AB can be degraded to benzimidazole and then hydroxylated to produce 2-HB. Overall, smaller molecule degradation products have yet to be discovered and further additions to the CBZ degradation pathway are still necessary.

4.3 Functional enzymes/genes involved in carbendazim degradation

Researchers have been studying the degradation process of CBZ more and more depth as a result of the low toxicity, efficiency, and direct degradation of pesticides by microbial enzymes that have attracted attention (Huang et al., 2018). Various enzymes have been shown to be able to achieve the degrading reaction of any organic contaminant. This is because, by catalyzing the creation of new proteins, microbial enzymes might decrease the toxicity and duration of these substances while hastening the degradation of organic contaminants (Zhang et al., 2020). Such as organic contaminants of all kinds are frequently degraded by enzymes such as ligninases, hydroxylases, cytochrome P450, hydrolases, and oxidases (Ciarrocchi et al., 2021).

According to Zhang M. et al. (2022), the primary cause of the breaking of the CBZ ester bond to provide methanol and 2-benzimidazole carbamic acid is the CBZ hydrolase. Such as, MheI and CbmA were individually classified as esterase and amidase according to different catalytic mechanisms. Based on the conserved signature GXSXXG motif and the shared catalytic site Ser-His, MheI was identified as a member of the Abhydrolase superfamily. MheI hydrolyzed methyl salicylate, α-naphthyl acetate, and p-nitrophenyl acetate. The esterase MheI was in charge of cleaving the CBZ ester bond to produce methanol and 2-benzimidazole carbamic acid. The latter was unstable since it included both an amino and a carboxyl group that may separate spontaneously to result in 2-AB (Figure 6). With only one amino acid change at position 150, the *mheI* gene is highly conserved (>99% identity) across several CBZ degradation strains (Zhang M. et al., 2022). *mheI* was discovered to be present in the following strains: *Rhodococcus* sp. CX-1 (Long et al., 2021), *Microbacterium* sp. djl-6F (Fang et al., 2010), *Mycobacterium* sp. SD-4 (Zhang Y. et al., 2017), *Mycobacterium* sp. djl-10 (Zhang J. et al., 2017), *Nocardioides* sp. SG-4G (Pandey et al., 2010), *Rhodococcus qingshengii* djl-6 (Zhang et al., 2005; Chuang et al., 2021), *Rhodococcus erythropolis* djl-11 (Zhang et al., 2013). Furthermore, CbmA is an amidase signature superfamily enzyme containing a highly conserved catalytic triad Ser-Ser-Lys. it might have catalytic activity for compounds with the secondary aromatic amine and the N atom attached to relatively simple structures, such as acetic acid, propionic acid, or formate. It was shown to be highly conserved in *Rhodococcus* sp., hydrolyzing p-nitroacetanilide, and it was classified as a member of the amidase superfamily with catalytic site residues Lys82, Ser187, and Ser181. The amide bond of CBZ was broken by CbmA, resulting in the formation of 2-AB and methyl formate (Zhang M. et al., 2022) (Figure 6). It has also been demonstrated that the primary enzyme in the metabolism of CBZ is CYP1A2, one of the Cytochrome P450 enzymes (CYP450). CYP450 participates in the metabolism of many substances, including endogenous substances, exogenous substances and drugs. CYP450 has been found to be effective in degrading a variety of fungicides and herbicides, among others. For example, CYP90D5 one of the CYP450, promotes the degradation of isoproturon (IPU) and acetochlor (ACT) in rice tissues and grains (Su et al., 2023). CYP1A2 was found to be effective in degrading CBZ. It is most likely hydroxylated by CYP1A2 to M1 (5-hydroxycarbendazim), which is then oxidized by CYP1A2 enzymes to a quinone-imine intermediate. The resulting electrophilic species then interacted with glutathione (GSH) and N-acetylcysteine (NAC). As the most important bio-thiol, GSH, an excellent soft nucleophile, can readily react with and degrade the contaminant, a soft electrophile, with or without the assistance of glutathione transferases. In other words, quinone-imine forms M2 (glutathione conjugate) by binding to GSH, and M2 forms M3 (N-acetyl cysteine conjugate) by binding to NAC (Shi et al., 2022) (Figure 6).

When it comes to the degradation of organic compounds of genes, bacterial plasmids are crucial. In microbial strains, fungicide degradation genes are found on chromosomes, transposons, or, most frequently, plasmids (Dionisio et al., 2019). The genome of strain *Rhodococcus* sp. CX-1 was found to have 7,651 predicted genes, of which the *amh* genes located on plasmids 2_orf0354, 2_orf0356, and chr_orf9440 were determined to be crucial in the conversion of CBZ to 2-AB. Plasmids chr_orf2214 and 2_orf0061, which carry *hdx* genes, are responsible for the degradation of 2-AB to 2-HB and then 2-HB to 2, 6, 7-trihydroxybenzimidazole (2,6,7-HBM). Extradiol dioxygenase in plasmid 2_orf0059 and plasmid chr_orf2213 is responsible for the degradation step of 2,6,7-HBM to X1(C7H8N2O5), which is essential for the cleavage of the benzene ring in CBZ. In addition, it was found that the *mno* gene in plasmid chr_orf8524 was involved in the imidazole ring cleavage reaction for the degradation of 2-benzimidazolone (2-BME) to o-phenylenediamine, which could be converted to catechol by the $FADH_2$-encoded $FADH_2$-dependent monooxygenase encoded by plasmid chr_orf85527. Catechol was

10.3389/fmicb.2024.1424825

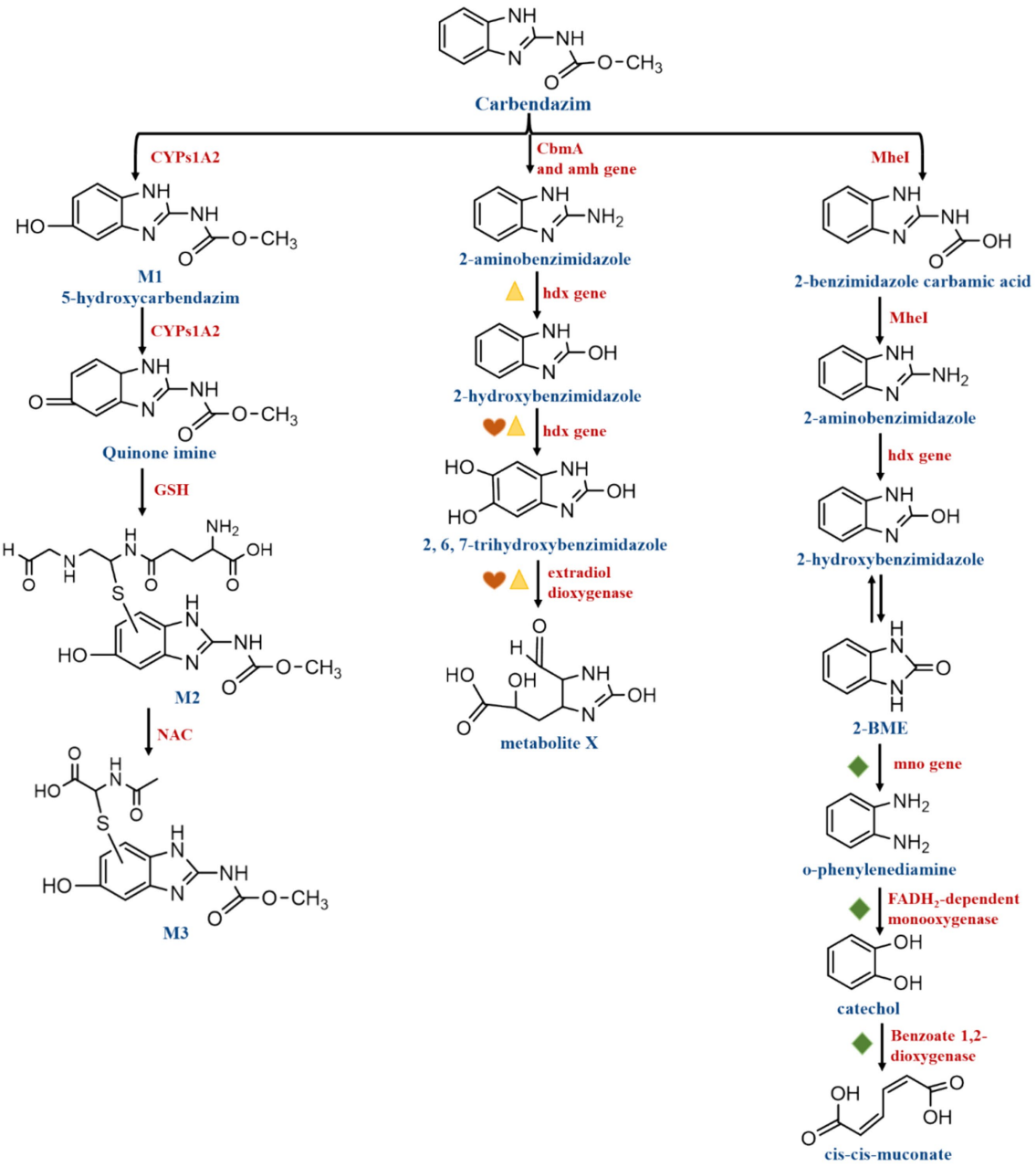

FIGURE 6
Carbendazim degradation pathways involving functional enzymes and genes. Indicate *hdx* and *edo*A genes were clustered, indicate *edo*B3, *edo*B1, *edo*B2, and *edo*C genes were clustered, indicate *mno*, *ben* A, and *cat* A genes were clustered.

considered to be cleaved by Benzoate 1,2-dioxygenase. Dependent monooxygenase encoded by plasmid chr_orf8527 to catechol. Catechol cleavage can be achieved by Benzoate 1,2-dioxygenase encoded by chr_orf8517, and catechol is considered to be a common intermediate in the degradation of aromatic compounds. The enzymes hydroxylase and estradiol dioxygenase, encoded by the genes *hdx* and *edoA*, were found to be clustered. These genes participate in the degradation processes of 2-AB to 2-HB, then 2-HB to 2,6,7-HBM and 2,6,7-HBM to X1 ($C_7H_8N_2O_5$). The *edoB3*, *edoB1*, *edoB2*, and *edoC* genes were also clustered and may be involved in the degradation of 2-HB to 2,6,7-HBM, and then 2,6,7-HBM to X1 ($C_7H_8N_2O_5$). In the degradation of 2-BME to o-phenylenediamine, o-phenylenediamine to catechol, and catechol to cis-cis-muconate, The genes *mno*, *ben A*, and *cat A* were clustered to participate in the degradation process described above (Long et al., 2021) (Figure 6).

5 Bioremediation of carbendazim-contaminated environments

In modern agriculture, CBZ is widely used to keep pests out of crops, but if sprayed improperly, it can have detrimental effects on the environment and living beings (Wei et al., 2023). Because it kills or

inhibits pathogenic fungi and sensitive bacteria in the soil, and because the remains of dead microorganisms can be used as a substrate to promote the growth of other resistant microorganisms, cause bacteria to become resistant to CBZ, and change the overall makeup of the bacterial community (Tarla et al., 2020). CBZ residues have the ability to alter the functional and structural diversity of soil microbial communities through both direct and indirect effects (Zhou et al., 2023). Additionally, they have the ability to significantly lower soil nitrification, ammonification, and dehydrogenase activities (Zhang M. et al., 2022).

Significantly, the stability and productivity of agroecosystems are primarily determined by soil microbial populations and related activities (Van Der Heijden et al., 2008). The removal of CBZ residues from agricultural soils has thus emerged as a pressing issue. Degradation of CBZ has been demonstrated to be an environmentally beneficial option through sustainable bioremediation of CBZ-contaminated soils. The term "bioremediation" refers to a biodegradation process that breaks down organic chemicals (such as pesticides, biocides, and other natural contaminants) contaminated by using microorganisms' metabolic capabilities. In addition, bioremediation has drawn a lot of interest as a widely used, affordable, effective, and ecologically friendly method of cleaning up contaminated areas (Kour et al., 2021). It is commonly known that a variety of microorganisms, including bacteria, fungi, and algae, may efficiently metabolize pesticides or alter their chemical structures, accelerating their breakdown and cleaning up contaminated environments. As a result, an increasing number of people are attempting to bioremediate CBZ-contaminated environments using microbial strains or consortia (Giri et al., 2021; Sarker et al., 2021). For instance, strain *Achromobacter* sp. GB61 played a significant role in the bioremediation of CBZ-contaminated habitats and was successful in bioremediating CBZ-contaminated soil under various conditions. It also contributed to the large-scale degradation of CBZ (Ling et al., 2016). The inoculation of strain *Rhodococcus qingshengii* djl-6 into the soil was found to be beneficial for the remediation of CBZ-contaminated soil, as more than 93% of the CBZ was eliminated from the soil after 14 d of incubation, according to the researchers. It was also discovered that members of the soil microbial community, particularly soil bacteria, may benefit from the intermediate metabolites of strain djl-6's CBZ breakdown. Thus, it also encourages the formation of additional potential CBZ-degrading microorganisms from the local microbial community in the soil (Chuang et al., 2021). Moreover, other *Rhodococcus* sp. strains that degrade CBZ also have good potential for bioremediation. One such strain is *Rhodococcus jialingiae* djl-6-2, which was inoculated into CBZ-contaminated soil. Regardless of whether the soil had been sterilized or not, the degradation rate of CBZ was higher than that of the uninoculated soil, indicating that strain djl-6-2 has a good bioremediation effect on the CBZ-contaminated soil. This suggests that on CBZ-contaminated soil, strain djl-6-2 has a good bioremediation impact. This is because *Rhodococcus* sp. exhibits a remarkable capacity to metabolize chemicals that are challenging to degrade, including pesticide derivatives that include amino and nitro, haloaromatics, aromatic compounds, and PAHs (Wang et al., 2010). Using *Actinomucor elegans* LBM 239 in combination with biostimulation proved to be a good treatment for CBZ elimination, detoxification, and soil fertility, according to Baumann et al. (2024).

Chen et al. (2021) evaluated the effectiveness of the CBZ-degrading bacterium *Streptococcus densiflorus* WJD-55 and its safety in shed tomato soils. It was found that dense *Streptomyces* sp. WJD-55 could effectively play the role of degrading CBZ and rapidly reducing the residual CBZ content in the soil. The initial soil CBZ mass concentration was about 42 mg/kg, and the use rate of the fungicide was 0.1%. On the 10th day after the treatment, the mass concentration of CBZ in the soil was 9.27 mg/kg, which decreased by 78%, while the mass concentration of CBZ in the control soil was 30.2 mg/kg, which declined by 29%. In addition, it was found that dense *Streptococcus* sp. WJD-55 could stably colonize the soil and could improve the fungal microbial diversity of contaminated soil, with no adverse effects on the soil's physicochemical properties and the growth of tomato crops. Tian and Chen (2009) used corn stover powder as raw material to produce *Xylomycetes* T2-2 bioremediation agent through solid fermentation. The soil was artificially inoculated with the T2-2 bioremediation agent at an inoculum level of 107 cfu/g of dry soil and a CBZ content of 0.1 mg/g of dry soil for the remediation of sterilized and natural soils. It was found that the inoculation of CBZ in sterilized soil was completely degraded in 6 d, whereas the complete degradation of CBZ in natural soil was shortened to 4 d. This suggests that straw meal acts as a co-metabolizing substrate and promotes co-metabolizing degradation of T2-2 and Indigenous microorganisms. In addition, strain T2-2 was found to degrade CBZ in the soil and control plant diseases. According to Xiao et al. (2013), native soil microbes, CBZ-degrading strains, and *Sedum alfredii* worked together to remove CBZ from polluted soil. Sedum alfredii changed the community structure of the soil, boosted microbial activity, and enhanced microbial diversity. Remarkably, rather than coming from direct plant absorption, CBZ dissipation is the outcome of encouraging biodegradation. Furthermore, *Sedum alfredii* were demonstrated superior efficacy in the biodegradation of CBZ in conjunction with *Flavobacterium* and *Pseudomonas* sp. These strains enhanced microbial activity, enriched microbial diversity, and modified the structure of microbial communities, all of which contributed to the biodegradation of CBZ in the soil. To sum up, the landscape and scope of environmental remediation are being dramatically altered by these bioremediation technologies in the direction of sustainable bioremediation.

6 Conclusion

Fungicides are indispensable for sustainable crop production. However, as a commonly used fungicide, carbendazim, while promoting production, also caused severe fungicide contamination. Carbendazim can enter the human body and food chain through food, contaminated air and water, posing a serious threat to biological health and ecological environment. Therefore, the degradation of carbendazim residues is urgent. Studies have shown that many microbial strains have excellent carbendazim degradation properties, especially *Rhodococcus* sp. Thus far, the enzyme and gene resources related to CBZ degradation are very limited. It is expected that more new genes and enzymes for carbendazim degradation will be explored further, which will facilitate further understanding of the mechanism of carbendazim microbial degradation. In addition, advanced molecular biological methods, enzyme engineering techniques and emerging materials will provide better tools for the remediation of

carbendazim contamination, which lays the foundation for low-cost, efficient and complete degradation of carbendazim in the future.

Author contributions

YZ: Data curation, Formal analysis, Investigation, Visualization, Writing – original draft. TW: Formal analysis, Investigation, Writing – review & editing. LW: Writing – review & editing. PW: Writing – review & editing. FC: Writing – review & editing. PB: Writing – review & editing. SC: Writing – review & editing. XC: Writing – review & editing. YY: Funding acquisition, Writing – review & editing. WZ: Funding acquisition, Project administration, Writing – review & editing.

Funding

The author(s) declare financial support was received for the research, authorship, and/or publication of this article. This work was support by the National Key Research and Development Program of China (No: 2023YFC3503802), Yunnan Fundamental Research Projects (Nos: 202301AT070797 and 202301BE070001-060), National Natural Science Foundation of China (No: 82360744), Yunnan Major Scientific and Technological Projects (No: 202202AG050021), and New think tank of Kunming University of Science and Technology (No: XXZK2023004).

Conflict of interest

The authors declare that the research was conducted in the absence of any commercial or financial relationships that could be construed as a potential conflict of interest.

The author(s) declared that they were an editorial board member of Frontiers, at the time of submission. This had no impact on the peer review process and the final decision.

Publisher's note

References

Altynbaeva, L. S., Barsbay, M., Aimanova, N. A., Jakupova, Z. Y., Nurpeisova, D. T., Zdorovets, M. V., et al. (2022). A novel Cu2O/ZnO@PET composite membrane for the photocatalytic degradation of Carbendazim. *Nano* 12:1724. doi: 10.3390/nano12101724

Alvarado-Gutiérrez, M. L., Ruiz-Ordaz, N., Galíndez-Mayer, J., Curiel-Quesada, E., and Santoyo-Tepole, F. (2020). Degradation kinetics of carbendazim by *Klebsiella oxytoca*, Flavobacterium johnsoniae, and *Stenotrophomonas maltophilia* strains. *Environ. Sci. Pollut. Res.* 27, 28518–28526. doi: 10.1007/s11356-019-07069-8

Alvarado-Gutiérrez, M. L., Ruiz-Ordaz, N., Galíndez-Mayer, J., Santoyo-Tepole, F., Curiel-Quesada, E., García-Mena, J., et al. (2017). Kinetics of carbendazim degradation in a horizontal tubular biofilm reactor. *Bioprocess Biosyst. Eng.* 40, 519–528. doi: 10.1007/s00449-016-1717-3

Arya, R., and Sharma, A. K. (2015). Bioremediation of Carbendazim, a Benzimidazole fungicide using Brevibacillus borstelensis and *Streptomyces albogriseolus* together. *Curr. Pharm. Biotechnol.* 17, 185–189. doi: 10.2174/1389201016666150930115737

Bai, N., Wang, S., Abuduaini, R., Zhang, M., Zhu, X., and Zhao, Y. (2017). Rhamnolipid-aided biodegradation of carbendazim by Rhodococcus sp. D-1: characteristics, products, and phytotoxicity. *Sci. Total Environ.* 590-591, 343–351. doi: 10.1016/j.scitotenv.2017.03.025

Baumann, A. J., Sadañoski, M. A., Marino, D. J. G., Alvarenga, A. E., Silva, C. G., Argüello, B., et al. (2024). Carbendazim mycoremediation: a combined approach to restoring soil. *Mycol. Prog.* 23:7. doi: 10.1007/s11557-023-01943-z

Bhoi, Y. P., Nayak, A. K., Gouda, S. K., and Mishra, B. G. (2018). Photocatalytic mineralization of carbendazim pesticide by a visible light active novel type-II Bi2S3/BiFeO3 heterojunction photocatalyst. *Catal. Commun.* 114, 114–119. doi: 10.1016/j.catcom.2018.06.018

Cabrera, M., Capparelli, M. V., Ñacato-Ch, C., Moulatlet, G. M., López-Heras, I., Díaz González, M., et al. (2023). Effects of intensive agriculture and urbanization on water quality and pesticide risks in freshwater ecosystems of the Ecuadorian Amazon. *Chemosphere* 337:139286. doi: 10.1016/j.chemosphere.2023.139286

Chen, R., Men, X., Qu, J., Sun, X. Y., and Zhao, L. X. (2021). Study on remediation of Carbendazim-contaminated soil by microbial agent W55. *Guangdong Agric. Sci.* 48, 92–102. doi: 10.16768/j.issn.1004-874X.2021.07.012

Chuang, S., Yang, H., Wang, X., Xue, C., Jiang, J., and Hong, Q. (2021). Potential effects of *Rhodococcus qingshengii* strain djl-6 on the bioremediation of carbendazim-contaminated soil and the assembly of its microbiome. *J. Hazard. Mater.* 414:125496. doi: 10.1016/j.jhazmat.2021.125496

Ciarrocchi, I. R., Mendes, K. F., Pimpinato, R. F., Spoto, M. H. F., and Tornisielo, V. L. (2021). The effect of radiation in the degradation of carbendazim and azoxystrobin in strawberry. *Radiat. Phys. Chem.* 179:109269. doi: 10.1016/j.radphyschem.2020.109269

Cycoń, M., Wójcik, M., and Piotrowska-Seget, Z. (2011). Biodegradation kinetics of the benzimidazole fungicide thiophanate-methyl by bacteria isolated from loamy sand soil. *Biodegradation* 22, 573–583. doi: 10.1007/s10532-010-9430-4

Dionisio, F., Zilhão, R., and Gama, J. A. (2019). Interactions between plasmids and other mobile genetic elements affect their transmission and persistence. *Plasmid* 102, 29–36. doi: 10.1016/j.plasmid.2019.01.003

Ebedy, Y. A., Hassanen, E. I., Hussien, A. M., Ibrahim, M. A., and Elshazly, M. O. (2022). Neurobehavioral toxicity induced by Carbendazim in rats and the role of iNOS, Cox-2, and NF-κB Signalling pathway. *Neurochem. Res.* 47, 1956–1971. doi: 10.1007/s11064-022-03581-5

Fang, H., Han, L., Cui, Y., Xue, Y., Cai, L., and Yu, Y. (2016). Changes in soil microbial community structure and function associated with degradation and resistance of carbendazim and chlortetracycline during repeated treatments. *Sci. Total Environ.* 572, 1203–1212. doi: 10.1016/j.scitotenv.2016.08.038

Fang, H., Wang, Y., Gao, C., Yan, H., Dong, B., and Yu, Y. (2010). Isolation and characterization of Pseudomonas sp. CBW capable of degrading carbendazim. *Biodegradation* 21, 939–946. doi: 10.1007/s10532-010-9353-0

Giri, B. S., Geed, S., Vikrant, K., Lee, S. S., Kim, K.-H., Kailasa, S. K., et al. (2021). Progress in bioremediation of pesticide residues in the environment. *Environ. Eng. Res.* 26, 200446–200440. doi: 10.4491/eer.2020.446

Houbraken, M., Habimana, V., Senaeve, D., López-Dávila, E., and Spanoghe, P. (2017). Multi-residue determination and ecological risk assessment of pesticides in the lakes of Rwanda. *Sci. Total Environ.* 576, 888–894. doi: 10.1016/j.scitotenv.2016.10.127

Huang, T., Ding, T., Liu, D., and Li, J. (2020). Degradation of Carbendazim in soil: effect of sewage sludge-derived biochars. *J. Agric. Food Chem.* 68, 3703–3710. doi: 10.1021/acs.jafc.9b07244

Huang, Y., Xiao, L., Li, F., Xiao, M., Lin, D., Long, X., et al. (2018). Microbial degradation of pesticide residues and an emphasis on the degradation of Cypermethrin and 3-phenoxy benzoic acid: a review. *Molecules* 23:2313. doi: 10.3390/molecules23092313

Jing-Liang, X., Xiang-Yang, G., Biao, S., Zhi-Chun, W., Kun, W., and Shun-Peng, L. (2006). Isolation and characterization of a Carbendazim-degrading Rhodococcus sp. djl-6. *Curr. Microbiol.* 53, 72–76. doi: 10.1007/s00284-005-0474-3

Kadhim, M. M., Alomar, S., Hachim, S. K., Abdullaha, S. A. H., Zedan Taban, T., and Alnasod, N. (2022). Aluminium carbide nano-sheet as a promising adsorbent for removal of carbendazim. *Inorg. Chem. Commun.* 144:109844. doi: 10.1016/j.inoche.2022.109844

Kanjilal, T., Panda, J., and Datta, S. (2018). Assessing Brevibacillus sp. C17: an indigenous isolated bacterium as bioremediator for agrochemical effluent containing toxic carbendazim. *J. Water Process Eng.* 23, 174–185. doi: 10.1016/j.jwpe.2018.03.016

Kaur, T., Sraw, A., Toor, A. P., and Wanchoo, R. K. (2016). Utilization of solar energy for the degradation of carbendazim and propiconazole by Fe doped TiO2. *Sol. Energy* 125, 65–76. doi: 10.1016/j.solener.2015.12.001

Kour, D., Kaur, T., Devi, R., Yadav, A., Singh, M., Joshi, D., et al. (2021). Beneficial microbiomes for bioremediation of diverse contaminated environments for environmental sustainability: present status and future challenges. *Environ. Sci. Pollut. Res.* 28, 24917–24939. doi: 10.1007/s11356-021-13252-7

Lei, J., Wei, S., Ren, L., Hu, S., and Chen, P. (2017). Hydrolysis mechanism of carbendazim hydrolase from the strain Microbacterium sp. djl-6F. *J. Environ. Sci.* 54, 171–177. doi: 10.1016/j.jes.2016.05.027

Li, Y.-H., Zhou, B.-L., Qian, M.-R., Wang, Q., and Zhang, H. (2017). Transfer assessment of Carbendazim residues from rape flowers to apicultural products. *J. Anal. Methods Chem.* 2017:e6075405, 1–7. doi: 10.1155/2017/6075405

Liang, X., Li, Y., Zheng, Z., Tian, F., Du, Y., Yang, Y., et al. (2023). Effects of mixed application of avermectin, imidacloprid and carbendazim on soil degradation and toxicity toward earthworms. *Sci. Rep.* 13:14115. doi: 10.1038/s41598-023-41206-1

Liansheng, T., and Fei, C. (2009). Characterization of a carbendazim-degrading Trichoderma sp. T2-2 and its application in bioremediation. *Wei Sheng Wu Xue Bao*. Available at: https://www.x-mol.com/paper/1212957631469920262?adv (accessed February 27, 2023).

Ling, L., Sun, J., Fang, J., and Shang, C. (2016). Kinetics and mechanisms of degradation of chloroacetonitriles by the UV/H2O2 process. *Water Res.* 99, 209–215. doi: 10.1016/j.watres.2016.04.056

Liu, W., Li, Y., Wang, Y., Zhao, Y., Xu, Y., and Liu, X. (2022). DFT insights into the degradation mechanism of carbendazim by hydroxyl radicals in aqueous solution. *J. Hazard. Mater.* 431:128577. doi: 10.1016/j.jhazmat.2022.128577

Long, Z., Wang, X., Wang, Y., Dai, H., Li, C., Xue, Y., et al. (2021). Characterization of a novel carbendazim-degrading strain Rhodococcus sp. CX-1 revealed by genome and transcriptome analyses. *Sci. Total Environ.* 754:142137. doi: 10.1016/j.scitotenv.2020.142137

Mishra, S., Lin, Z., Pang, S., Zhang, W., Bhatt, P., and Chen, S. (2021a). Recent advanced Technologies for the Characterization of xenobiotic-degrading microorganisms and microbial communities. *Front. Bioeng. Biotechnol.* 9:632059. doi: 10.3389/fbioe.2021.632059

Mishra, S., Pang, S., Zhang, W., Lin, Z., Bhatt, P., and Chen, S. (2021b). Insights into the microbial degradation and biochemical mechanisms of carbamates. *Chemosphere* 279:130500. doi: 10.1016/j.chemosphere.2021.130500

Mungsuk, C., Yommee, S., Supothina, S., and Chuaybamroong, P. (2023). Solar photocatalytic degradation of carbendazim in water using TiO2 particle-and sol-gel dip-coating filters. *Results Eng.* 19:101348. doi: 10.1016/j.rineng.2023.101348

Pandey, G., Dorrian, S. J., Russell, R. J., Brearley, C., Kotsonis, S., and Oakeshott, J. G. (2010). Cloning and biochemical characterization of a novel Carbendazim (Methyl-1 *H-Benzimidazol*-2-ylcarbamate)-hydrolyzing esterase from the newly isolated *Nocardioides* sp. strain SG-4G and its potential for use in enzymatic bioremediation. *Appl. Environ. Microbiol.* 76, 2940–2945. doi: 10.1128/AEM.02990-09

Periyasamy, S., Vinoth Kumar, J., Chen, S.-M., Annamalai, Y., Karthik, R., and Erumaipatty Rajagounder, N. (2019). Structural insights on 2D gadolinium tungstate Nanoflake: a promising Electrocatalyst for sensor and Photocatalyst for the degradation of postharvest fungicide (Carbendazim). *ACS Appl. Mater. Interfaces* 11, 37172–37183. doi: 10.1021/acsami.9b07336

Prashantkumar, W., Sethi, R. S., Pathak, D., Rampal, S., and Saini, S. P. S. (2012). Testicular damage after chronic exposure to carbendazim in male goats. *Toxicol. Environ. Chem.* 94, 1433–1442. doi: 10.1080/02772248.2012.693493

Rama, E. M., Bortolan, S., Vieira, M. L., Gerardin, D. C. C., and Moreira, E. G. (2014). Reproductive and possible hormonal effects of carbendazim. *Regul. Toxicol. Pharmacol.* 69, 476–486. doi: 10.1016/j.yrtph.2014.05.016

Rico, A., de Oliveira, R., de Souza, S., Nunes, G., Rizzi, C., Villa, S., et al. (2022). Ecological risk assessment of pesticides in urban streams of the Brazilian Amazon. *Chemosphere* 291:132821. doi: 10.1016/j.chemosphere.2021.132821

Salunkhe, V. P., Sawant, I. S., Banerjee, K., Wadkar, P. N., Sawant, S. D., and Hingmire, S. A. (2014). Kinetics of degradation of carbendazim by *B. subtilis* strains: possibility of in situ detoxification. *Environ. Monit. Assess.* 186, 8599–8610. doi: 10.1007/s10661-014-4027-8

Sarker, A., Nandi, R., Kim, J.-E., and Islam, T. (2021). Remediation of chemical pesticides from contaminated sites through potential microorganisms and their functional enzymes: prospects and challenges. *Environ. Technol. Innov.* 23:101777. doi: 10.1016/j.eti.2021.101777

Sharma, M., Maheshwari, N., Khan, F. H., and Mahmood, R. (2022). Carbendazim toxicity in different cell lines and mammalian tissues. *J. Biochem. Mol. Toxicol.* 36:e23194. doi: 10.1002/jbt.23194

Shi, J., Zhao, M., Li, K., Zhao, Y., Li, W., Peng, Y., et al. (2022). Metabolic activation and cytotoxicity of fungicide Carbendazim mediated by CYP1A2. *J. Agric. Food Chem.* 70, 4092–4101. doi: 10.1021/acs.jafc.1c08144

Siddique, Z., Malik, A. U., Asi, M. R., Inam-ur-Raheem, M., Iqbal, M., and Abdullah, M. (2021). Impact of sonolytic ozonation (O3/US) on degradation of pesticide residues in fresh vegetables and fruits: case study of Faisalabad, Pakistan. *Ultrason. Sonochem.* 79:105799. doi: 10.1016/j.ultsonch.2021.105799

Silambarasan, S., and Abraham, J. (2020). Biodegradation of carbendazim by a potent novel Chryseobacterium sp. JAS14 and plant growth promoting *Aeromonas caviae* JAS15 with subsequent toxicity analysis. *3 Biotech* 10:326. doi: 10.1007/s13205-020-02319-w

Singh, S., Kumar, V., Singh, S., and Singh, J. (2019). Influence of humic acid, iron and copper on microbial degradation of fungicide Carbendazim. *Biocatal. Agric. Biotechnol.* 20:101196. doi: 10.1016/j.bcab.2019.101196

Singh, S., Singh, N., Kumar, V., Datta, S., Wani, A. B., Singh, D., et al. (2016). Toxicity, monitoring and biodegradation of the fungicide carbendazim. *Environ. Chem. Lett.* 14, 317–329. doi: 10.1007/s10311-016-0566-2

Song, S., and Hwang, C.-W. (2023). Microbial degradation of the benzimidazole fungicide carbendazim by *Bacillus velezensis* HY-3479. *Int. Microbiol.* 27, 797–805. doi: 10.1007/s10123-023-00427-0

Su, X. N., Liu, X. S., Li, C. Y., and Zhang, Y. P. (2023). Cytochrome P450 CYP90D5 enhances degradation of the herbicides Isoproturon and Acetochlor in Rice plants and grains. *J. Agric. Food Chem.* 70, 17399–17409. doi: 10.1021/acs.jafc.3c05963

Tarla, D. N., Erickson, L. E., Hettiarachchi, G. M., Amadi, S. I., Galkaduwa, M., Davis, L. C., et al. (2020). Phytoremediation and bioremediation of pesticide-contaminated soil. *Appl. Sci.* 10:1217. doi: 10.3390/app10041217

Tian, L., and Chen, F. (2009). Characterization of a carbendazim-degrading Trichoderma sp. T2-2 and its application in bioremediation. *Wei Sheng Wu Xue Bao* 49, 925–930. doi: 10.13343/j.cnki.wsxb.2009.07.011

Van Der Heijden, M. G. A., Bardgett, R. D., and Van Straalen, N. M. (2008). The unseen majority: soil microbes as drivers of plant diversity and productivity in terrestrial ecosystems. *Ecol. Lett.* 11, 296–310. doi: 10.1111/j.1461-0248.2007.01139.x

Wang, H., Shi, G., Wang, G., Wang, R., Chen, W., Li, J., et al. (2023). Investigation on the photocatalytic degradation properties of BiOX on carbendazim and its mechanism. *ChemistrySelect* 8:e202204707. doi: 10.1002/slct.202204707

Wang, Z., Wang, Y., Gong, F., Zhang, J., Hong, Q., and Li, S. (2010). Biodegradation of carbendazim by a novel actinobacterium *Rhodococcus jialingiae* djl-6-2. *Chemosphere* 81, 639–644. doi: 10.1016/j.chemosphere.2010.08.040

Wang, J., Xing, C., Xia, J., Chen, H., Zhang, J., and Yan, W. (2023). Degradation of carbendazim in aqueous solution by dielectric barrier discharge cold plasma: identification and toxicity of degradation products. *Food Chem.* 403:134329. doi: 10.1016/j.foodchem.2022.134329

Wei, J., Wang, X., Tu, C., Long, T., Bu, Y., Wang, H., et al. (2023). Remediation technologies for neonicotinoids in contaminated environments: current state and future prospects. *Environ. Int.* 178:108044. doi: 10.1016/j.envint.2023.108044

Xiao, W., Wang, H., Li, T., Zhu, Z., Zhang, J., He, Z., et al. (2013). Bioremediation of cd and carbendazim co-contaminated soil by cd-hyperaccumulator Sedum alfredii associated with carbendazim-degrading bacterial strains. *Environ. Sci. Pollut. Res.* 20, 380–389. doi: 10.1007/s11356-012-0902-4

Yang, Y., Zhang, S., Yang, J., Bai, C., Tang, S., Ye, Q., et al. (2018). Superabsorbent hydrogels coating increased degradation and decreased bound residues formation of carbendazim in soil. *Sci. Total Environ.* 630, 1133–1142. doi: 10.1016/j.scitotenv.2018.02.178

Yarden, O., Salomon, R., Katan, J., and Aharonson, N. (1990). Involvement of fungi and bacteria in enhanced and nonenhanced biodegradation of carbendazim and other benzimidazole compounds in soil. *Can. J. Microbiol.* 36, 15–23. doi: 10.1139/m90-004

Yogesh Kumar, K., Prashanth, M. K., Parashuram, L., Palanivel, B., Alharti, F. A., Jeon, B.-H., et al. (2022). Gadolinium sesquisulfide anchored N-doped reduced graphene oxide for sensitive detection and degradation of carbendazim. *Chemosphere* 296:134030. doi: 10.1016/j.chemosphere.2022.134030

Zhang, M., Bai, X., Li, Q., Zhang, L., Zhu, Q., Gao, S., et al. (2022). Functional analysis, diversity, and distribution of carbendazim hydrolases MheI and CbmA, responsible for the initial step in carbendazim degradation. *Environ. Microbiol.* 24, 4803–4817. doi: 10.1111/1462-2920.16139

Zhang, X., Huang, Y., Harvey, P. R., Li, H., Ren, Y., Li, J., et al. (2013). Isolation and characterization of Carbendazim-degrading *Rhodococcus erythropolis* djl-11. *PLoS One* 8:e74810. doi: 10.1371/journal.pone.0074810

Zhang, G.-S., Jia, X.-M., Cheng, T.-F., Ma, X.-H., and Zhao, Y.-H. (2005). Isolation and characterization of a new carbendazim-degrading Ralstonia sp. strain. *World J. Microbiol. Biotechnol.* 21, 265–269. doi: 10.1007/s11274-004-3628-8

Zhang, W., Lin, Z., Pang, S., Bhatt, P., and Chen, S. (2020). Insights into the biodegradation of Lindane (γ-Hexachlorocyclohexane) using a microbial system. *Front. Microbiol.* 11:522. doi: 10.3389/fmicb.2020.00522

Zhang, L., Qiao, X., and Ma, L. (2009). Influence of environmental factors on degradation of carbendazim by *Bacillus pumilus* strain NY97-1. *Int. J. Environ. Pollut.* 38, 309–317. doi: 10.1504/IJEP.2009.027231

Zhang, Y., Wang, H., Wang, X., Hu, B., Zhang, C., Jin, W., et al. (2017). Identification of the key amino acid sites of the carbendazim hydrolase (MheI) from a novel carbendazim-degrading strain Mycobacterium sp. SD-4. *J. Hazard. Mater.* 331, 55–62. doi: 10.1016/j.jhazmat.2017.02.007

Zhang, T., Wang, Y., Zhao, Z., Xu, S., and Shen, W. (2022). Degradation of Carbendazim by molecular hydrogen on leaf models. *Plan. Theory* 11:621. doi: 10.3390/plants11050621

Zhang, J., Yuan, Q., Yang, W., and Wang, X. (2017). Complete genome sequence of Carbendazim-degrading *Mycobacterium* sp. strain djl-10. *Genome Announc.* 5, e01683–e01616. doi: 10.1128/genomeA.01683-16

Zhou, L., Jiang, Y., Lin, Q., Wang, X., Zhang, X., Xu, J., et al. (2018). Residue transfer and risk assessment of carbendazim in tea. *J. Sci. Food Agric.* 98, 5329–5334. doi: 10.1002/jsfa.9072

Zhou, T., Wang, F., Tahmasbian, I., Ma, B., Liu, M., and Zhang, M. (2023). Linking Carbendazim accumulation with soil and endophytic microbial community diversities, compositions, functions, and assemblies: effects of urea-hydrogen peroxide and nitrification inhibitors. *J. Agric. Food Chem.* 71, 17689–17699. doi: 10.1021/acs.jafc.3c04777

frontiers | Frontiers in Environmental Science

TYPE Original Research
PUBLISHED 24 September 2024
DOI 10.3389/fenvs.2024.1426203

OPEN ACCESS

EDITED BY
Leonardo Fernandes Fraceto,
São Paulo State University, Brazil

REVIEWED BY
Sikandar I. Mulla,
REVA University, India
Yanju Liu,
The University of Newcastle, Australia

*CORRESPONDENCE
John Yang,
yangj@lincolnu.edu

RECEIVED 30 April 2024
ACCEPTED 03 September 2024
PUBLISHED 24 September 2024

CITATION
Li N, Yang K, Lin C and Yang J (2024) Enhanced biodegradation of trinitrotoluene in rhizosphere soil by native grasses.
Front. Environ. Sci. 12:1426203.
doi: 10.3389/fenvs.2024.1426203

Enhanced biodegradation of trinitrotoluene in rhizosphere soil by native grasses

Na Li[1], Kenny Yang[2], Chungho Lin[3] and John Yang[2]*

[1]Tillage and Cultivation Research Institute, Liaoning Academy of Agricultural Sciences, Shenyang, China, [2]Department of Agriculture and Environmental Science & Cooperative Research, Lincoln University of Missouri, Jefferson City, MO, United States, [3]Center of Agroforestry, University of Missouri, Columbia, MO, United States

Soil contamination by the munition explosive residues of 2,4,6-trinitrotoluene (TNT) and its metabolites resulting primarily from military operations has been identified as a threat to human health and ecosystems. Biodegradation by native plants to remove this hazardous compound or reduce its toxicity is considered a cost-effective and environmentally sound approach for the cleanup or restoration of TNT-contaminated soils. This study aims to investigate the TNT biodegradation and kinetics by two selected native grasses in the species-specific rhizosphere soils through growth chamber experiments. Native eastern gamma grass (*Tripsacum dactyloides*) and switchgrass (*Panicum virgatum L.*) were grown in soil spiked with ^{14}C-TNT for 8 weeks. The ^{14}C-TNT degradation and degradative metabolite profile in the rhizosphere soils were determined by liquid scintillation counter and high-performance liquid chromatography, respectively. The results indicated that both native grass species significantly enhanced the TNT degradation in the rhizosphere soils as compared with the control rhizosphere soils. More than 95% of the applied ^{14}C-TNT was degraded in the first 7 days, and the rate then reached a steady state afterward, but less than 10% of the TNT applied was completely mineralized and transformed into CO_2. The degradative reaction was found to follow second-order kinetics. Six major TNT degradative metabolites have been detected and identified in the rhizosphere soils. Overall, switchgrass appeared more effective for biodegrading TNT than eastern gamma grass. This research demonstrated that the native grass species, especially switchgrass, has the potential to mitigate the adverse human health and ecological risks of TNT-contaminated sites and can be considered an environmentally friendly, sustainable approach to safeguarding human health from TNT contamination.

KEYWORDS

TNT, biodegradation, native grass, rhizosphere soil, remediation

Introduction

Soil contamination with munition explosives such as TNT (2,4,6-trinitrotoluene) resulting from military operations or wastewater discharge has been identified as a threat to human health and ecosystems. TNT is one of two explosive munitions most widely used in the world (USEPA, 2014). Massive TNT production started in 1902 and peaked during the two world wars (Nyanhongo et al., 2005). Since World War I, TNT has been used as a major explosive by the United States Army (Lewis et al., 2004). Annual TNT production was reported to be approximately one million kilograms (Harter and Ricket,

1985). The manufacture, use, and disposal of TNT explosives has resulted in environmental contamination, such as soil, water, or ecosystems, which is a public health and environmental concern (Pennington and Brannon, 2002). Wastewater generated during TNT production, also called "pink water," could result in land contamination adjacent to the manufacturing facilities (Gilbert et al., 1980; Lindner, 1980). It was reported that up to 2 million liters of pink water could be produced annually by a single factory (Jenkins et al., 1986). At the Louisiana Army Ammunition Plant in Louisiana and the Cornhusker Army Ammunition Plant in Nebraska, land contamination by TNT was reported at up to 87,000 mg/kg in soil, 711,000 mg/kg in sediment, and 3,375 mg/L in surface water (Steevens et al., 2002). In the United States, more than 12 million tons of soil have been contaminated by the explosives (Lewis et al., 2004), and at least 20 of 1,397 hazardous waste sites listed on the USEPA National Priorities List have been identified as being contaminated by TNT (Agency for Toxic Substances and Disease Registry, 1995).

TNT is a highly toxic, single-ring nitroaromatic compound that is relatively persistent in the environment. Environmental contamination by TNT is a severe human health and environmental concern. Human exposure to TNT or other nitroaromatic compounds such as DNT (dinitrotoluene) and nitrophenols can cause several health problems, such as anemia, abnormal liver function, cataract development, skin irritation, and even cancers (Yinon, 1990; Honeycutt et al., 1996; Mulla and Talwar, 2013; Mulla et al., 2019). The TNT-exposure-related death of 475 people has been reported in the United States (McConnell and Flinn, 1946).

Conventional remediation approaches for TNT-contaminated sites include incineration, compost, or bioslurry. However, those remediation technologies are often destructive, high-cost, or labor-intensive (Habineza et al., 2016). In contrast, biodegradation to detoxify the TNT explosives by *in situ* microorganisms, green plants, or natural processes is often non-destructive with low maintenance and costs (Glick, 2003) and could be considered as a cost-effective, environmental-sound sustainable strategy for cleanup of the soils contaminated by the explosives (Habineza et al., 2016; Mulla et al., 2019).

Biodegradation of TNT by microorganisms has been extensively studied for decades (Habineza et al., 2016). Kao et al. (2016) studied indigenous microorganisms for TNT biodegradation in soil and concluded that the effectiveness was less satisfactory. Most previous studies showed that TNT or other nitroaromatic compounds in the environments preferred to be transformed into other degradative compounds rather than completely mineralized into CO_2 (Habineza et al., 2016). Major TNT metabolites detected in the biodegradative pathway were 2-amino-4,6-dinitrotoluene (2-A-4,6-DNT), 4-amino-2,6- dinitrotoluene (4-A-2,6-DNT), 2,4-diamino-6-nitrotoluene (2,4-DA-6-NT), 2,6-diamino- 4-nitrotoluene (2,6-DA-4-NT) (Wang et al., 2010). Little TNT mineralization was reported (Hawari et al., 2000). This is probably due to the symmetric location of nitro groups on the toluene ring of TNT that limits enzymatic attack by classic dioxygenase during the microbial metabolism of aromatic compounds and the high electronegativity and partially positive charge of N atoms in the nitro group that make TNT easily reducible (Esteve-Nunez et al., 2001).

Biodegradation of TNT by native plants or grasses through a species-specific rhizosphere microbial community is little reported and remains largely unknown. The transgenic *Arabidopsis* plant study by Wang and Su (2024) indicated that TNT treatment would induce the overexpression of the *CYP81D11* gene in *Arabidopsis* and enhance plant resistance or tolerance to TNT stress through enhanced TNT uptake rather than induced biodegradation. It has been suggested that native plants have a promising ability to degrade organic pollutants such as chlorinated hydrocarbons, nitroaromatic compounds, pesticides, and petroleum by species-specific microbial communities in rhizosphere soil (Anderson et al., 1993; Haby and Crowley, 1996; Reilley et al., 1996; Siciliano and Greer, 2000; Chaudhry and Schroeder, 2001; Schwitzguebel and Auberrt, 2001; Via and Zinnert, 2016). The objectives of this study were to use growth chamber experiments to i) investigate *in situ* TNT degradation and mineralization in rhizosphere soils by two selected native grasses, ii) determine the kinetics or mechanisms of native grass-specific TNT degradative processes, and iii) identify the profile of TNT metabolites in the degradative pathways.

Materials and methods

Experimental procedures: Two native grass species grown in Missouri, United States, Eastern gamma grass (*Tripsacum dactyloides,* EG) and Switchgrass (*Panicum virgatum* L, SW), were selected for this experiment based on our previous screening results. The seeds of EG and SW were sterilized in 30% ethanol for 30 s, rinsed with deionized water for 1 min, and then seeded in plastic pots (15 cm diameter, 20 cm height) filled with soil containing a mixture of 50% sand and 50% silt at a rate of 10 seeds per pot. The EG and SW pots, three pots per grass plus control (total nine pots), were grown in a walk-in growth chamber under the conditions of light intensity at 1,400 E m^{-2}·sec^{-1}, light/dark period at 15/9 h, humidity at 50%, and temperature at 25°C (light)/20°C (dark) for 8 weeks to develop microbial communities in grass species-specific rhizosphere soil. Soil moisture was maintained by adding deionized water weekly to a plastic pan placed under each pot. At maturity, fresh rhizosphere soils (soil near roots) were collected at the end of 8-week growth period from each of the EG or SW pots. The rhizosphere soils were collected by gently pulling five plants from each pot and carefully separating the soil from the roots. The soil samples were placed in plastic bags and stored at −4°C until treatment.

Twenty (20) grams of each of the collected fresh rhizosphere soils were treated with 0.5 μCi C^{14}-TNT (PerkinElmer Life and Analytical Sciences) and 17.86 μg of 1,000 μg mL^{-1} TNT (Spex Certiprep, Inc.) to make total TNT concentration of 1.0 mg kg^{-1} soil. The C^{14} spiked soil was placed in 15-mL Erlenmeyer flasks, and a 20-mL scintillation vial containing 10 mL 1 M NaOH (Fisher Scientific) was also prepared as a $^{14}CO_2$ trap. Both spiked soil flask and scintillation vial were placed in a mason jar and sealed with parafilm and duct tape. The jars were incubated at room temperature in the dark for 8 weeks. Each treatment was triplicated, and blank soil was included as controls. During the incubation period, soil moisture was maintained at 15%. The NaOH trap was replaced every week and stored at room temperature in the dark until $^{14}CO_2$ analysis. Samples (1.0 g) of spiked soil were also

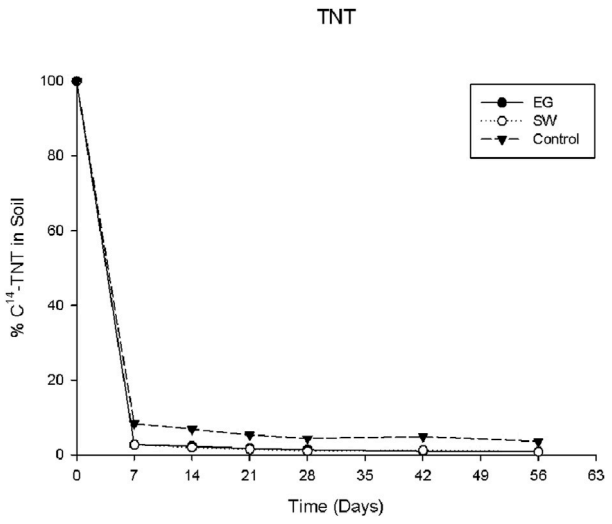

FIGURE 1
Percentage of applied C^{14}-TNT remaining in the rhizosphere soil of EG and SW grasses during the 8-week incubation period.

collected from the jars at 0 days, 7 days, 14 days, 21 days, 42 days, and 56 days, respectively, and then extracted using 10 mL 100% acetonitrile (Fisher Scientific). The soil extracts were passed through a 0.45 μm filter, concentrated to 200 μL by an N_2 evaporator, and stored at −20°C prior to TNT analysis. After the extraction, the soils were oven-dried at 65°C overnight, ground into a fine powder, and stored in 20-mL scintillation vials at room temperature in the dark.

Analytical procedures: A 1.0 mL aliquot of the 10-mL 1 M NaOH traps was transferred into a 7 mL scintillation vial, mixed with 4 mL cocktail (Ultima Gold™ AB, PerkinElmer), and measured for $^{14}CO_2$ radioactivity by a Beckman LS 6000SC liquid scintillation counter. The amount of C^{14}-TNT in the traps was determined, and the TNT mineralization rate was calculated. A 0.5 g sample of the spiked soil after acetonitrile extraction was weighed in a 7-mL scintillation vial and mixed with 4 mL of cocktail (Ultima Gold™ AB, PerkinElmer). The mixtures were vortexed, allowed to precipitate for 3 days, and measured for $^{14}CO_2$ radioactivity by a Beckman LS 6000SC liquid scintillation counter. The amount of non-extractable TNT fraction in soil was determined. Concentrations of acetonitrile-extractable C^{14}-TNT and its metabolites were analyzed by a Shimadzu High Performance Liquid Chromatogram equipped with a Phenomenex Columbus C8110A column and a radioactivity detector. The mobile phase consisted of 100% acetonitrile and 0.1% phosphoric acid (1:9, v:v) at a flow rate of 1 mL min^{-1}.

Statistical analysis: Data were analyzed using non-parametric two-way ANOVA for treatment using SAS software.

Results and discussion

TNT degradation

As the data in Figure 1 show, the disappearance of TNT in the rhizosphere soil appeared to be rapid during the first 7 days and gradually leveled off during the incubation period. It was estimated that more than 95% of the applied TNT degraded in the first 7 days. Two selected native grasses significantly enhanced the TNT degradation compared with the control, but the degradative capacity of the two grasses did not significantly differ. The grasses' ability to enhance the TNT degradation was less effective than expected under the experimental conditions. Enhanced degradation in the rhizosphere soil by the native grasses could be a result of the biodegradative or biochemical reactions mediated by enriched specific microbial communities due to the activity of the grass roots. It is well known that rhizosphere soil differs in chemical and biochemical properties such as pH, redox, and organic composition from bulk soil, as induced by plant root activities, including root exudation, respiration, and nutrient uptake. Plant species could create differential or species-specific biochemical and ecological conditions in the rhizosphere because of genetic differences. The unique rhizosphere environment may help develop or differentiate a species-specific microbial group or community enabled to attack nitroaromatic compounds and promote TNT degradation or detoxification (Su et al., 2024). The rapid degradation of TNT in the early incubation stage has been observed in the previous studies by Hawari et al. (2000). This suggested that the original TNT molecule may be transformed to other nitroaromatic forms without a complete cleavage of the aromatic ring rather than a complete mineralization to CO_2. As reported previously, the chemical structure of TNT could strongly limit the possibility of aromatic ring cleavage. In this case, the TNT that disappeared in the rhizosphere soil might be transformed into nitroso-, hydroxylamino-, or amino-TNT derivatives because of the easily reducible nitro groups (Wang et al., 2010).

Major mechanisms of TNT biodegradation have been proposed, including successive two-electron reduction and denitration (Nyanhongo et al., 2005; Smets et al., 2007), which involves a sequential reduction of TNT to nitroso-TNT, hydroxylamino-TNT, and amino-TNT derivatives. The degradative intermediates that were frequently detected included 2-hydroxylamino-4,6-dinitrotoluene (2HA46DNT), 4-hydroxylamino-2,6-dinitrotoluene (4HA26DNT), 2-amino-4,6-dinitrotoluene (2A46DNT), 4-amino-2,6-dinitrotoluene (4A26DNT) and 2,4-diamino-6-nitrotoluene. No nitroso derivative was detected (Koder and Miller, 1998; Esteve-Nunez et al., 2001; Yin et al., 2004; Nyanhongo et al., 2005; Yin et al., 2005). These partially reduced TNT intermediates have been reported to react with each other in the presence of oxygen to form azoxytetranitrotoluene, which is more recalcitrant and mutagenic than TNT (Haidour and Ramos, 1996; George et al., 2001). Although the oxygenolytic metabolism of TNT rarely occurred, a possible oxygenolytic attack of aminodinitrotoluene was observed. 2-amino-4,6-dinitrotoluene and 4-amino-2,6-dinitrotoluene has been reported to be oxidized to 3-amino-4-methyl-5-nitrocatechol and 3-amino-6methyl-5-nitrocatechol with the release of nitrite, respectively (Johnson et al., 2001). Hydroxylamino-TNT derivatives were observed to go through a Bamberger-like rearrangement to produce vicinal amino and hydroxyl substituents with the release of ammonium (Hughes et al., 1998; Caballero et al., 2005a; Caballero et al., 2005b; Caballero and Ramos, 2006).

Denitration refers to the direct hydride addition to the aromatic ring of TNT with the formation of a TNT hydride-Meisenheimer

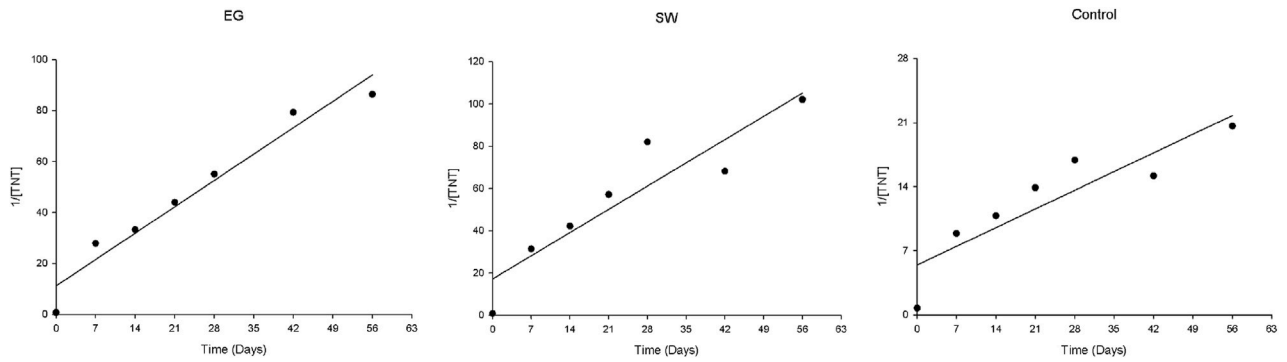

FIGURE 2
Kinetic order of TNT degradation in EG and SW rhizosphere soils.

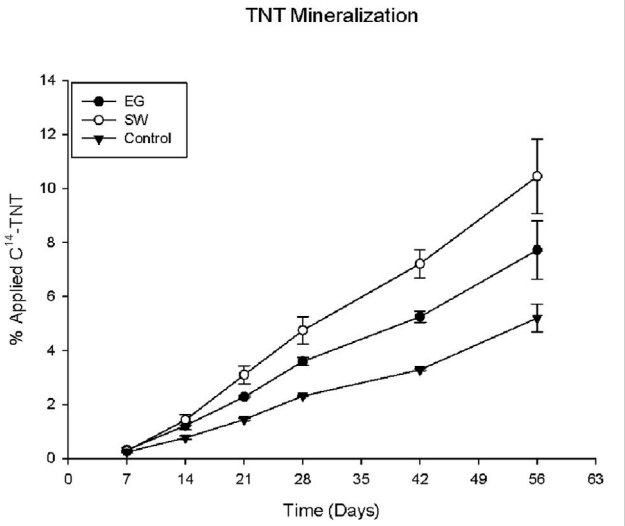

FIGURE 3
Percentage of C^{14}-TNT mineralization in EG and SW rhizosphere soils.

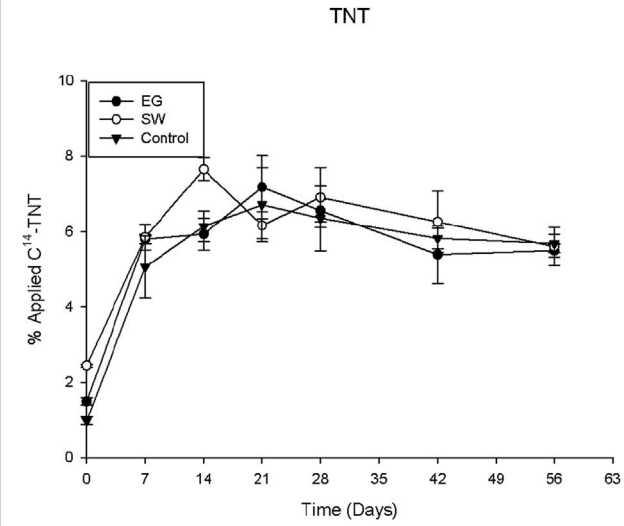

FIGURE 4
Percentage of non-extractable C^{14}-TNT in EG and SW rhizosphere soils.

complex (H^--TNT) (Esteve-Nunez et al., 2001; Nyanhongo et al., 2005; Smets et al., 2007). H^--TNT would be quickly converted to a TNT dihydride-Meisenheimer complex ($2H^-$-TNT). $2H^-$-TNT is an unstable orange product that could be further transformed with nitrite release. A one-electron reduction of TNT may also occur (Spain, 1995; Esteve-Nunez et al., 2001). One nitro group of TNT could be reduced to a nitroso group with the formation of a nitroanion radical. This nitroanion radical would react with oxygen to form a superoxide and original nitro aromatic compound through a futile cycle.

Degradation kinetics

TNT degradation in soil can be considered an irreversible reaction. The rate law of TNT degradation can be expressed as follows:

$$d[TNT]/dt = -k[TNT]^n,$$

where *[TNT]* is concentration, *t* is time, *k* is a constant, and *a* is kinetic order. If $n = 0$, the TNT degradation would be a zero-order reaction, and the equation can be rewritten as follows:

$$d[TNT]/dt = -k[TNT]^0 = -k.$$

Then, the equation can be integrated as follows:

$$[TNT] = [TNT]_0 - kt.$$

If $n = 1$ or 2, the TNT degradation would be a first- or second-order reaction, and the equation can be integrated as follows:

$$ln[TNT] = ln[TNT]_0 - kt$$

or

$$1/[TNT] = 1/[TNT]_0 + kt.$$

When *[TNT], ln[TNT], or 1/[TNT]* is plotted against the incubation time, a linear line would indicate the kinetic order for the TNT degradation. Based on data shown in Figure 1, in all

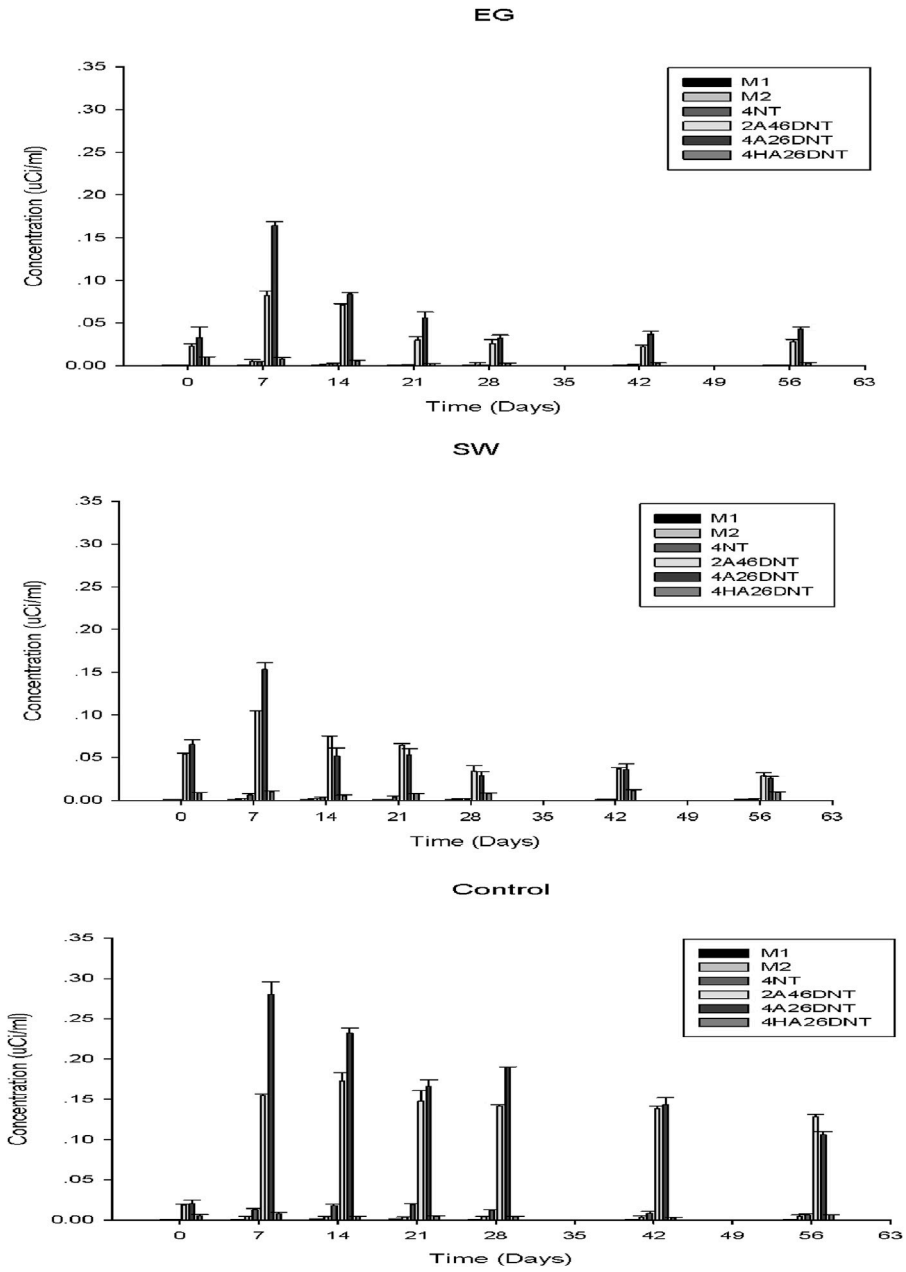

FIGURE 5
Concentrations of TNT degradative metabolites detected in EG and SW rhizosphere soils.

cases, the TNT biodegradation in rhizosphere soil by both grasses presented second-order reaction kinetics (Figure 2). The regression coefficients of the linearity were r^2 = 0.9525, r^2 = 0.8514, and r^2 = 0.8002 in EG and SW rhizosphere soils and control soil, respectively. This second-order kinetics indicated that, like most biodegradation processes of organic contaminants, the biodegradation of TNT was a microbial-driven transformation reaction. The degradation rate was initially fast and then gradually reached a steady state, as shown in Figure 1. This suggested that oxygen availability or TNT concentration may be a primary rate-limiting factor during the biodegradation process.

TNT mineralization

As indicated in Figure 1, the two selected native grasses significantly enhanced the TNT degradation or biotransformation in the rhizosphere soils. More than 95% of applied TNT was degraded in the first 7 days, and the rate remained in a steady state afterward during the incubation. Among the amount of the TNT degraded, only a fraction of the applied TNT was completely mineralized into harmless CO_2 by the native grasses, as indicated in Figure 3. It was estimated that approximately 10% and 8% of applied TNT was transformed into CO_2 by SW and EG, respectively, during the 8 weeks compared with 5% in the control. Both SW and EG

demonstrated a significantly higher capacity than the control to enhance or stimulate the complete TNT mineralization or CO_2 transformation, and SW was shown to be more effective than EG. This result was still less satisfactory and consistent with previous reports (Habineza et al., 2016), indicating that only a limited fraction of TNT applied had experienced complete cleavage of the aromatic ring and larger amounts of TNT were transformed to smaller molecules rather than CO_2. A relatively low TNT mineralization rate was also reported in many other studies (Hawari et al., 2000; Nyanhongo et al., 2005). Meanwhile, the chemical-stable ring structure or properties of TNT that make the aromatic ring intact could resist or limit TNT mineralization. In addition to the TNT applied, the mineralization may also result from the TNT metabolites or smaller degradative molecules in the rhizosphere that were attacked by the species-specific activity of the soil rhizosphere microbes enhanced by native EG and SW grasses, causing the aromatic ring cleavage and transformation of CO_2.

TNT residue

TNT residue was the fraction of non-extractable TNT remaining in the soil after acetonitrile extraction and presented the fraction of non-degradable TNT. TNT and its degradative metabolites may be able to interact with clays and humic substances in soil, which form relatively stable compounds resistant to acetonitrile extraction. Thus, those residual TNT compounds in soil could be considered less toxic or non-harmful fractions to the environment and human health because of their very limited bioavailability and leachability. The more non-extractable compounds are in soil, the less toxic they are to humans and ecosystems. Data presented in Figure 4 indicate that there was no significant difference among the treatments in the amounts of non-extractable TNT in the rhizosphere soils. In all cases, the non-extractable contents increased rapidly in the first 7 days of the incubation period and then remained relatively stable at around 6%–7% afterward, indicating that the rapid formation of relatively stable TNT complexes could prevent TNT from further degradation or mineralization by soil microorganisms. This was in agreement with the degradation data presented in Figure 1, which shows that approximately 95% TNT was degraded during the incubation.

TNT degradative metabolites

Six major degradative metabolites of TNT have been identified in the acetonitrile extracts of the rhizosphere soils collected (Figure 5), which included 4-nitrotoluene (4NT), 2-amino-4,6-dinitrotoluene (2A46DNT), 4-amino-2,6-dinitrotoluene (4A26DNT), 4-hydroxylamino-2,6-dinitrotoluene (4HA26DNT), and two unknowns, M1 and M2. Based on the metabolite profiles, the TNT degradative pathway in soil seemed to undergo the sequential two-electron reduction mechanism mentioned above. Hydroxylamino- and amino-TNT derivatives have been detected in this study, but no nitroso-TNT derivative was identified. This observation is in good agreement with other studies reported, in which hydroxylamino- and amino-TNT derivatives were frequently observed as TNT metabolites, and no nitroso-TNT derivatives were detected (Koder and Miller, 1998; Esteve-Nunez et al., 2001; Yin et al., 2004; Nyanhongo et al., 2005; Yin et al., 2004).

Relatively higher concentrations of the identified TNT metabolites were observed during the first 7 days of the incubation, which corresponded to the rapid dissipation of TNT in early incubation (Figure 1). Overall, 2A46DNT and 4A26DNT appeared to be the major metabolites of TNT degradation in the soils. 4HA26DNT concentrations were very low in both soils. Compared with the control, the concentrations of TNT metabolites were significantly lower in the grass rhizosphere soils during the incubation period. This indicated that both native grasses enhanced not only TNT degradation but also the degradation of TNT metabolites in soil. Nevertheless, some TNT metabolites may be more toxic than the parent molecule; for example, nitroso and hydroxylamino groups were reported to be responsible for the mutagenicity and carcinogenicity of nitroaromatic compounds. Hydroxylamino-dinitrotoluene was reported to cause hemotoxic symptoms in humans exposed to TNT (Esteve-Nunez et al., 2001). Further reduction of the nitro group to an amino group may decrease the toxicity or mutagenicity of the compounds.

Conclusion

This growth chamber experiment showed that two selected EG and SW native grasses significantly enhanced the degradation of TNT in species-specific rhizosphere soil. SW appeared to be more effective in degrading TNT than EG. More than 95% of the TNT applied was degraded or transformed to other metabolic derivatives in the soil during the incubation period. The degradation rate was initially fast at the first 7 days of incubation and then remained low and steady afterward. The biodegradation was identified as a second-order reaction. Approximately 10% of the TNT applied was completely mineralized or transformed into harmless CO_2. There was approximately 6%–7% non-acetonitrile-extractable TNT or TNT residue that may form relatively stable metabolic derivatives or complexes with soil constituents and limit further TNT degradation in soil. Six major TNT degradative metabolites were identified in the degradative pathway. This study demonstrated that the native grasses have the potential to mitigate the adverse human and environmental risks of TNT-contaminated sites through enhanced biodegradation and could be considered as a cost-effective, environmental-sound remediation approach for safeguarding human health and ecosystems from TNT contamination.

Data availability statement

The original contributions presented in the study are included in the article/supplementary material; further inquiries can be directed to the corresponding author.

Author contributions

NL: writing–original draft, writing–review and editing, formal analysis, software, and validation. KY: data curation,

writing–original draft, formal analysis, and methodology. CL: data curation, methodology, and writing–review and editing. JY: funding acquisition, project administration, supervision, writing–review and editing, methodology, and writing–original draft.

Funding

The author(s) declare that financial support was received for the research, authorship, and/or publication of this article. This research was funded by the USEPA-NCE-STAR and the USDA-NIFA through grants to Lincoln University of Missouri (EPA no. RD83107101; NIFA no. 0206403).

Conflict of interest

The authors declare that the research was conducted in the absence of any commercial or financial relationships that could be construed as a potential conflict of interest.

Publisher's note

References

Agency for Toxic Substances and Disease Registry, (1995). *Toxicological profile for TNT*. Atlanta, GA: Dpartment of Health and Human Services.

Anderson, T., Guthrie, E., and Walton, B. T. (1993). Bioremediation in the rhizosphere: plant roots and associated microbes clean contaminated soil. *Environ. Sci. Technol.* 27, 2630–2636. doi:10.1021/es00049a001

Caballero, A., Esteve-Nunez, A., Zylstra, G. J., and Ramos, J. L. (2005a). Assimilation of nitrogen from nitrite and trinitrotoluene in *Pseudomonas putida* JLR11. *Bacteriol* 187, 396–399. doi:10.1128/JB.187.1.396-399.2005

Caballero, A., Lazaro, J., Ramos, J. L., and Esteve-Núñez, A. (2005b). PnrA, a new nitroreductase-family enzyme in the TNT-degrading strain *Pseudomonas putida* JLR11. *Environ. Microbiol.* 7, 1211–1219. doi:10.1111/j.1462-2920.2005.00801.x

Caballero, A., and Ramos, J. (2006). A double mutant of *Pseudomonas putida* JLR11 deficient in the synthesis of the nitroreductas PnrA and assimilatory nitrite reductase NasB is impaired for growth on 2,4,6-trinitrotoluen (TNT). *Environ. Microbiol.* 8, 1306–1310. doi:10.1111/j.1462-2920.2006.01012.x

Chaudhry, Q., Schroeder, P., Werck-Reichhar, D., Grajek W Mulla, S., Talwar, M., Ninnekar, H., et al. (2001). Prospects and limitations of phytoremediation for the removal of persistent pesticides in the environment. *Environ. Sci. Pollut. Res.* 9, 4–17. doi:10.1065/espr2001.09.084.1

Esteve-Nunez, A., Caballero, A., and Ramos, J. L. (2001). Biological degradation of 2,4,6-Trinitrotoluene. *Microbiol. Mol. Biol. Rev.* 65, 335–352. doi:10.1128/mmbr.65.3.335-352.2001

George, S., Huggins-Clark, G., and Brooks, L. (2001). Use of a *Salmonella* microsuspension bioassay to detect the mutagenicity of munitions compounds at low concentrations. *Mutat. Res.* 490, 45–56. doi:10.1016/s1383-5718(00)00150-9

Gilbert, E., Kaye, S., and Herman, H. (1980) "TNT," in *Encyclopedia of explosives and related items*. Dover NJ, US Army armament research and development commmand, 235–287.

Glick, B. R. (2003). Phytoremediation: synergistic use of plants and bacteria to clean up the environment. *Biotechnol. Adv.* 21, 383–393. doi:10.1016/s0734-9750(03)00055-7

Habineza, A., Zhai, J., Mai, T., Mmereki, D., and Ntakirutimana, T. (2016). Biodegradation of 2, 4, 6-trinitrotoluene (TNT) in contaminated soil and microbial remediation options for treatment. *Period. Polytech. Chem. Eng.* 61 (3), 171–187. doi:10.3311/ppch.9251

Haby, P., and Crowley, D. (1996). Biodegradation of 3-chlorobenzoate as affected by rhizodeposition and selected carbon substrates. *Environ. Qual.* 25, 304–310. doi:10.2134/jeq1996.00472425002500020014x

Haidour, A., and Ramos, J. (1996). Identification of products resulting from biological reduction of 2,4,6-trinitrotoluene, 2,4-dinitrotoluene and 2,6-dinitrotoluene by *Psedudomonas* sp. *Environ. Sci. Technol.* 30, 2365–2370. doi:10.1021/es950824u

Harter, D., and Ricket, D. (1985) "The use and importance of nitroaromatic chemicals in the chemical industry," in *Toxicity of nitroaromatic chemical industry*. New York: Hemisphere Publishing, 1–14.

Hawari, J., Beaudet, S., Halasz, A., Thiboutot, S., and Ampleman, G. (2000). Microbial degradation of explosives: biotransformation versus mineralization. *Appl. Microbiol. Biotechnol.* 54, 605–618. doi:10.1007/s002530000445

Honeycutt, M. E., Jarvis, A. S., and McFarland, V. A. (1996). Cytotoxicity and mutagenicity of 2,4,6-trinitrotoluene and its metabolites. *Ecotoxicol. Environ. Saf.* 35, 282–287. doi:10.1006/eesa.1996.0112

Hughes, J., Wang, C., Yesland, K., Richardson, A., Bhadra, R., Bennett, G., et al. (1998). Bamberger rearrangement during TNT metabolisn by *Clostridium acetobutylicum*. *Environ. Sci. Technol.* 32, 494–500. doi:10.1021/es970612s

Jenkins, T., Leggett, D., Grant, C. L., and Bauer, C. F. (1986). Reversed-phase high-performance liquid chromatographic determination of nitroorganics in munitions wastewater. *Anal. Chem.* 58, 170–175. doi:10.1021/ac00292a042

Johnson, G., Smets, B., and Spain, J. C. (2001). Oxidative transformation of aminodinitrotoluene isomers by multicomponent dioxygenases. *Appl. Environ. Microbiol.* 67, 5460–5466. doi:10.1128/aem.67.12.5460-5466.2001

Kao, C., Lin, B., Chen, S. C., Wei, S. F., Chen, C. C., Yao, C. L., et al. (2016). Biodegradation of trinitrotoluene (TNT) by indigenous microorganisms from TNT-contaminated soil, and their application in TNT bioremediation. *Bioremediation* 20 (3), 165–173. doi:10.1080/10889868.2016.1148007

Koder, R., and Miller, A. (1998). Steady-state kinetic mechanism, stereospecificity, substrate and inhibitor specificity of *Enterobacter cloacae* nitroreductase. *Biochim. Biophys. Acta* 1387, 395–405. doi:10.1016/s0167-4838(98)00151-4

Lewis, T. A., Newcombe, D. A., and Crawford, R. L. (2004). Bioremediation of soils contaminated with explosives. *Environ. Manag.* 70, 291–307. doi:10.1016/j.jenvman.2003.12.005

Lindner, V. (1980) "Explosives and propellants," in *Kirk-Othmer encyclopedia of chemical technology*. NY: Wiley, 561–620.

McConnell, W., and Flinn, R. (1946). Summary of twenty-two trinitrotoluene fatalities in World War II. *Ind. Hyg. Tox* 28, 76–86.

Mulla, S., Bharagava, R., Belhaj, D., Saratale, G. D., Bagewadi, Z. K., Saxena, G., et al. (2019). "An overview of nitro group-containing compounds and herbicides degradation in microorganisms," in *Metabolism of xenobiotic compounds. Microorganisms for sustainability*. Editor P. Arora (Singapore: Springer), 10, 319–335. doi:10.1007/978-981-13-7462-3_16

Mulla, S., Talwar, M., et al. (2013). "Biodegradation of 2, 4, 6-trinitrotoluene explosive residues," in *Biological remediation of explosive residues. Environmental science and engineering*. Editor S. Singh (Cham: Springer), 201–233.

Nyanhongo, G. S., Schroeder, M., Steiner, W., and Gübitz, G. M. (2005). Biodegradation of 2,4,6-trinitrotoluene (TNT): an enzymatic perspective. *Biocatal. Biotransformation* 23 (2), 53–69. doi:10.1080/10242420500090169

Pennington, J. C., and Brannon, J. M. (2002). Environmental fate of explosives. *Thermochim. Acta* 384, 163–172. doi:10.1016/s0040-6031(01)00801-2

Reilley, K., Banks, M., and Schwab, A. P. (1996). Dissipation of polycyclic aromatic hydrocarbons in the rhizosphere. *Environ. Qual.* 25, 212–219. doi:10.2134/jeq1996.0047242500250002002x

Schwitzguebel, J., Auberrt, S., et al. (2001). Sulphonated aromatic pollutants: limits of microbial degradability and potential of phytoremediation. *Environ. Sci. Pollut. Res.* 9, 62–72. doi:10.1065/espr2001.09.084.4

Siciliano, S., and Greer, C. (2000). Plant-bacterial combinations to phytoremediate soil contaminated with high concentrations of 2,4,6-trinitrotoluene. *Environ. Qual.* 29, 311–316. doi:10.2134/jeq2000.00472425002900010039x

Smets, B. F., Yin, H., and Esteve-Nuñez, A. (2007). TNT biotransformation: when chemistry confronts mineralization. *Appl. Microbiol. Biotechnol.* 76, 267–277. doi:10.1007/s00253-007-1008-7

Spain, J. (1995). Biodegradation of nitroaromatic compounds. *Annu. Rev. Microbiol.* 49, 523–555. doi:10.1146/annurev.mi.49.100195.002515

Steevens, J. A., Duke, B. M., Lotufo, G. R., and Bridges, T. S. (2002). Toxicity of the explosives 2,4,6-trinitrotoluene, hexahydro-1,3,5-trinitro-1,3,5-triazine, and octahydro-1,3,5,7-tetranitro-1,3,5,7- tetrazocine in sediments to *Chironomus tentans* and *Hyalella azteca*: low-dose hormesis and high-dose mortality. *Environ. Toxicol. Chem.* 20 (7), 1475–1482. doi:10.1897/1551-5028(2002)021<1475:toteth>2.0.co;2

Su, K., Wu, Z., Liu, Y., Wang, Y., Wang, H., Liu, M., et al. (2024). UDP-glycosyltransferase UGT96C10 functions as a novel detoxification factor for conjugating the activated dinitrotoluene sulfonate in switchgrass. *Plant Biotechnol.* 22, 2530–2540. doi:10.1111/pbi.14366

United States Environmental Protection Agency (USEPA) (2014). Washington, DC: USEPA. Technical Fact Sheets. 2,4,6-Trinitrotoluene (TNT).

Via, S., and Zinnert, J. (2015). Impacts of explosive compounds on vegetation: a need for community scale investigations. *Environ. Pollut.* 208, 495–505. doi:10.1016/j.envpol.2015.10.020

Wang, H., Su, K., et al. (2024). Overexpressing *CYP81D11* enhances 2,4,6-trinitrotoluene tolerance and removal efficiency in *Arabidopsis*. *Physiol. Plantarium*. doi:10.1111/pbl.14364

Wang, Z., Ye, Z., Zhang, M., and Bai, X. (2010). Degradation of 2,4,6-trinitrotoluene (TNT) by immobilized microorganism-biological filter. *Process Biochem.* 45, 993–1001. doi:10.1016/j.procbio.2010.03.006

Yin, H., Wood, T., and Smets, B. F. (2004). Reductive transformation of TNT by *Escherichia coli*: pathway description. *Appl. Microbiol. Biotechnol.* 67, 397–404. doi:10.1007/s00253-004-1736-x

Yin, H., Wood, T., and Smets, B. F. (2005). Reductive transformation of TNT by *Escherichia coli* resting cells: kinetic analysis. *Appl. Microbiol. Biotechnol.* 69, 326–334. doi:10.1007/s00253-005-1988-0

Yinon, J. (1990). *Toxicity and metabolism of explosives*. Boca Raton, Florida: CRC Press.

Frontiers in Microbiology

Explores the habitable world and the potential of microbial life

The largest and most cited microbiology journal which advances our understanding of the role microbes play in addressing global challenges such as healthcare, food security, and climate change.

Discover the latest Research Topics

See more →

Frontiers

Avenue du Tribunal-Fédéral 34
1005 Lausanne, Switzerland
frontiersin.org

Contact us

+41 (0)21 510 17 00
frontiersin.org/about/contact